Biopolymeric coating of nanodiamonds to increase their stability for applications *in vitro* and *in vivo*

Dissertation zur Erlangung des Doktorgrades Dr. rer. nat. der Fakultät für Naturwissenschaften der Universität Ulm

vorgelegt von

M. Sc. Marco Raabe

geboren in Rheinfelden (Baden)

2020

Abstract

In the past decade, nanodiamonds emerged as promising candidates in the field of nanomedicine, bioimaging, and nanoscale sensing due to their outstanding magnetic and optical properties. Nanodiamonds containing negatively-charged nitrogen vacancy centers possess a stable fluorescence with a wavelength close to the near infrared and show no photobleaching or blinking. Furthermore, nanodiamonds are biocompatible which was demonstrated in various organisms. Taken together, these are the optimal prerequisites for long-term fluorescence imaging or super-resolution microscopy. In addition, polarization of spins of ^{13}C enriched nanodiamonds could pave the way for magnetic resonance imaging in future.

Next to imaging, the negatively-charged nitrogen vacancy centers located inside the nanodiamond lattice act as nanoscale sensors due to their magneto-optical properties. This enables to measure external single spins, electric and magnetic fields, temperature, pH-value, and electric charges.

However, nanodiamonds tend to aggregate very strongly in physiological environments and hence designing proper coating material is inevitable. Therefore, before nanodiamonds can be applied routinely in bioimaging or nanoscale sensing these limitations need to be overcome. Coating of nanodiamonds must not only improve their colloidal stability and retain their good biocompatibility but also should not interfere with their magneto-optical properties. In the past years, various coating materials have been invented but they were mostly designed for a specific application and not for broad usage.

In this thesis, we present two bio-inspired coating materials for nanodiamond stabilization and functionalization. The first coating has been inspired by protein corona formation around nanoparticles in Nature. Starting from the blood plasma protein human serum albumin, we designed a positively-charged copolymer by attaching polyethylene glycol chains. Negatively-charged nanodiamonds were coated by electrostatic, non-covalent adsorption of the polycationic protein. This protein coating could be easily functionalized and applied in different fields of bioimaging. In cells, we used correlative light–electron microscopy to visualize nanodiamond clusters in nanoscale resolution allowing to distinguish individual nanodiamonds. Furthermore, we applied energy filtered transmission electron microscopy to identify single nanodiamonds, which did not belong to a cluster, inside cells for the first time. Using this technique, we showed single nanodiamond uptake into cells as well as single nanodiamonds which were located in a mitochondrion. *In vivo*, we proved the integrity of the coating and the successful crossing of coated nanodiamonds of the blood–brain barrier. Furthermore, we designed a protein material which allowed us to perform magnetic resonance imaging with high contrast in chick embryos. This new material could pave the way to magnetic resonance imaging of coated nanodiamonds.

The second coating strategy has been inspired by mussel foot proteins. The small molecule L-3,4-dihydroxyphenylalanine (L-DOPA) self-polymerized starting from the surface of nanodiamonds and formed a three-dimensional polymer network. In contrast to the flexible protein coating, the poly(L-DOPA) allowed us to control the thickness of the shell very precisely. Due to its strong absorption, poly(L-DOPA) is known to possess a photothermal effect which was conferred to poly(L-DOPA) coated nanodiamonds. After absorbing indocyanine green and transferrin to improve the photothermal effect and induce cell targeting, a strong photothermal effect of the construct was observed in HeLa cells with spatial control by adjusting the diameter of the laser beam. Notably, the photothermal effect could be induced in HeLa cells even at a very low power of the laser beam.

In summary, we developed two bio-inspired coatings of nanodiamonds and applied these coated nanodiamonds in different fields, such as photothermal application and bioimaging, as well as in different living systems from 2D cell culture up to *in vivo* applications.

Table of Contents

1. Introduction

1.1 Carbon Nanomaterials

Over the past years, carbon nanomaterials gained increasing interest due to their low intrinsic toxicity, low cost for large-scale production, and versatile surface functionalization. Different allotropes of carbon at the nanoscale emerged such as fullerenes and carbon nanodots, carbon nanotubes/nanohorns and graphene nanoribbons, graphene and graphene oxides, and nanodiamonds (NDs, see Figure 1).[1] The whole family of carbon nanomaterial has been successfully applied in the fields of sensing[2], imaging[1], drug delivery[1], and theranostics[3]. In the following, the different allotropes of carbon nanomaterials are discussed briefly.
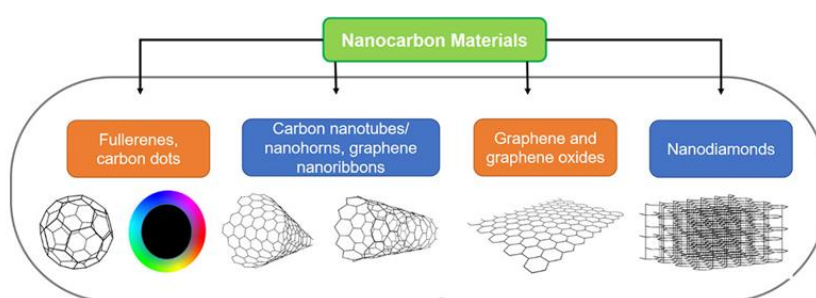
Figure 1 Overview of carbon nanomaterials. Over the past years, carbon materials developed into different directions including fullerenes and carbon nanodots, carbon nanotubes/nanohorns and graphene nanoribbons, graphene and graphene oxides, and nanodiamonds.[1] Adapted with permission from Panwar, N.; Soehartono, A. M.; Chan, K. K.; Zeng, S.; Xu, G.; Qu, J.; Coquet, P.; Yong, K.-T.; Chen, X. Nanocarbons for Biology and Medicine: Sensing, Imaging, and Drug Delivery. *Chem. Rev.* **2019**, *119* (16), 9559–9656. Copyright (2019) American Chemical Society.

Fullerenes are spherical all-carbon nanomaterials which were firstly predicted in 1970[3] and discovered in 1985[4]. Around ten years after their discovery, this achievement was awarded with the Nobel Prize in Chemistry. Fullerenes exist with different numbers of carbon atoms (C_{60}, C_{70}, C_{80}) and all of these carbon atoms are sp^2 hybridized.[3] The C_{60} fullerene, so called Buckminsterfullerene, is composed of 32 faces, 12 of these are pentagonal and 20 hexagonal.[4] A special feature of fullerenes is their potential to act as sensitizers for the photo-production of singlet oxygen ($^1O_2$) and thus are applied for photodynamic cancer therapy.[3]

Closely related to fullerenes are carbon nanotubes, which are buildup of only hexagons and forming a tube structure. Carbon nanotubes can contain single or multiple walls based on the number of layers.[3] For biomedical applications, carbon nanotubes need to be functionalized further, e.g. by oxidation, because they possess a poor dispersibility and a high toxicity.[3] Functionalized carbon nanotubes were utilized in biomedical imaging, drug delivery, and biosensing. Next to carbon tubes, also flat carbon sheets exist. Graphene is a single or few-layer 2D material composed of sp^2 hybridized carbon which was discovered in 2004.[3] Certainly, graphene became the most prominent carbon material and was decorated with the Nobel Prize in Physics in 2010. This is due

to its outstanding properties as high loading of aromatic drugs, thermal conductivity, and thermal stiffness.[3] However, pristine graphene possesses a poor aqueous solubility. Therefore, various derivatives have been developed as graphene oxide, reduced graphene oxide, few-layer graphene oxide, and chemically changed graphene.[3] Noteworthy, many layers of graphene can also stack on each other forming a 3D material, so called graphite. The isolation of graphene from bulk graphite has been achieved by simple exfoliation.[5]

While fullerenes, carbon nanotubes, and graphene are of uniform chemical structure, carbon dots can combine various carbon interactions. Carbon dots are mainly classified into three types: graphene quantum dots, carbon nanodots, and polymer dots.[6] Graphene quantum dots contain at least one layer of graphene as a carbon core. These carbon dots show a size-dependent fluorescence between 1 to 8 nm and the emission changes from blue to orange-red.[7] Carbon nanodots are composed of sp^2/sp^3 carbons or amorphous carbon together with embedded sp^2-hybridized nanocrystalline regions. Finally, polymer dots are composed of aggregated or cross-linked polymers.[6]

NDs differ from the mentioned carbon materials strongly because NDs are buildup of a crystalline carbon lattice in which carbon atoms are sp^3 hybridized. In contrast to graphene, diamond is only metastable at ambient temperatures and the production of diamond requires a much higher temperature and pressure.[8] While the fluorescence of NDs origins from defects in the lattice, the fluorescence of the other carbon materials mainly origins from conjugated π-electron systems. These defects in NDs enable imaging without bleaching and sophisticated sensing of magnetic and electric fields, temperature, and electron spins. Similar to the other carbon nanomaterials, the surface of NDs must be functionalized for biomedical applications because unmodified NDs tend to aggregate strongly in aqueous solutions. In the following introduction, all features of NDs will be discussed as physical properties, synthesis, post-modification, coating, and applications in biomedicine, imaging as well as sensing.

1.2 Physical Properties of Nanodiamonds

NDs possess outstanding magneto-optical properties, which enable a variety of applications in the fields of bioimaging and nanoscale sensing. In this chapter, these physical properties are discussed in detail.

Graphite vs. Diamond

While graphite is the most stable form of carbon material, diamond is only metastable at ambient temperatures. Although the energy difference between the phase of graphite and diamond is small (0.02 eV/atom), the two phases are separated by a high energy barrier (~0.4 eV/atom). Therefore, graphite can be only transferred into diamond at high temperatures and high pressures.[8] Interestingly, at nanoscale, the stabilities of the diamond and graphite phases are reversed because the surface energy becomes more dominant. Consequently, small NDs (3–6 nm) are more stable than nanographite.[9]

Chemical Structure of the ND Core

Regarding the chemical composition, NDs can be divided into a core and a surface unit. While the core of NDs is composed of sp^3 hybridized carbon atoms forming tetragonally coordinated carbon–carbon bonds, so-called diamond cubic, the surface is of complex chemical structure and can contain a various number of different chemical functionalities. These first subchapters will focus on the nature of the core.

Diamond is the strongest and most inert material known up to date due to the dense packing of the carbon atoms. Because of the sp^3 hybridization of the carbon atoms in the core, diamond possesses a large band gap of 5.49 eV (see Figure 2A), which is equivalent to the energy of light with a wavelength of 225 nm. This means that diamond is transparent for light with a higher wavelength than 225 nm, which is essential to understand the optical properties of NDs. The large bandgap of diamond materials allows optically active crystal defects to emit light with a fluorescence spectra in the visible and infrared regions. In addition, the diamond core possesses a high refractive index (~2.4) providing strong scattering of light, especially in the ultraviolet (UV) region.[10]
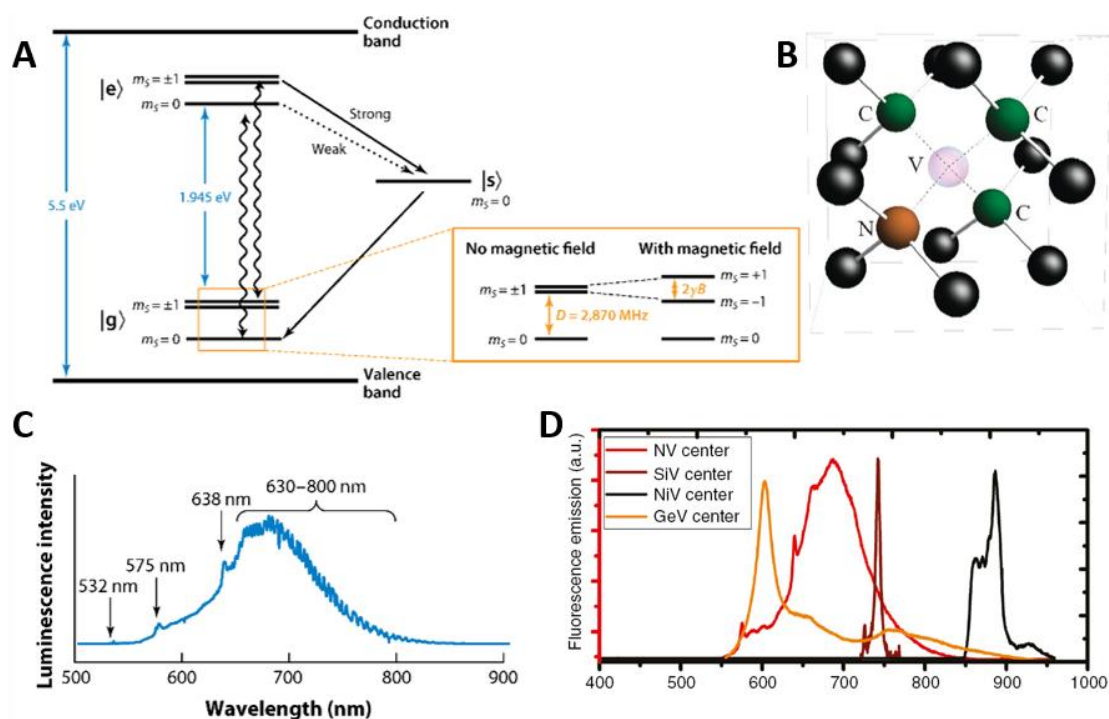
Figure 2 Characteristics of nitrogen-vacancy (NV) centers in fluorescent nanodiamonds (FNDs). (A) Energy diagram of a negatively-charged NV (NV⁻) center. NV⁻ centers possess a spin triplet in ground (|g›) and excited (|e›) state as well as a metastable singlet state (|s›). Wiggling arrows indicate radiative transition and black arrows either strong or weak non-radiative relaxation *via* the singlet state. In the ground state, the spin sublevels m_s=0 and m_s=±1 are separated by 2.87 MHz at zero magnetic field. At nonzero magnetic field, m_s=+1 and m_s=−1 are split according to the strength of the magnetic field. (B) Schematic representation of a NV center. (C) Typical photoluminescence spectrum of different NV centers in a FND with a zero phonon line of a neutral NV at 575 nm, of a NV⁻ at 638 nm, and vibrational side of NV⁻ at 630–800 nm. (D) Photoluminescence spectra of different color centers such as germanium-vacancy (GeV), NV, silicon-vacancy (SiV), and nickel-vacancy (NiV). (A)+(C) are adapted with permission from Schirhagl, R.; Chang, K.; Loretz, M.; Degen, C. L. Nitrogen-Vacancy Centers in Diamond: Nanoscale Sensors for Physics and Biology. *Annu. Rev. Phys. Chem.* **2014**, *65* (1), 83–105. Copyright (2013) Annual Reviews. (B) is adapted with permission from Wu, Y.; Jelezko, F.; Plenio, M. B.; Weil, T. Diamond Quantum Devices in Biology. *Angew. Chemie - Int. Ed.* **2016**, 6586–6598. Copyright (2016) John Wiley and Sons. (D) is adapted with permission from M. H. Alkahtani, F. Alghannam, L. Jiang, A. Almethen, A. A. Rampersaud, R. Brick, C. L. Gomes, M. O. Scully, P. R. Hemmer, *Nanophotonics* **2018**, *7*, 1423–1453. Published by De Gruyter.

Crystal Defects and Color Centers in NDs

Ironically, imperfections in the diamond carbon lattice are a main reason for the rapid success of NDs in the fields of bioimaging and sensing. As mentioned before, pure NDs are entirely transparent and possess no optical properties. However, impurities and vacancy defects in the ND lattice can absorb and emit light. There are hundreds of luminescent defects in diamonds known including boron, nickel, silicon, nitrogen, among many others.[11] The latter gained especially high interest in the research during the last decade due to its optical features and the possibility of sensing. The nitrogen-vacancy (NV) center is a point defect in the carbon lattice of the diamond and consists of a substitutional nitrogen atom, which is directly located next to a vacancy (see Figure 2B) and can occur in different charge states.[12] While the neutral (NV⁰) and positive (NV⁺)

charge states show no magneto-optical activity, the negatively charged NV center (NV⁻) does and therefore, is the most attractive one especially in sensing. In total, six electrons are involved in the formation of the NV⁻ center. Two electrons originate from the nitrogen atom, three electrons are dangling bonds from the three carbon atoms located around the vacancy, and the last electron is captured from the lattice.[13] The NV⁻ center has a sharp optical zero-phonon line at λ=638 nm (E=1.945 eV, see Figure 2A+C) and a phonon sideband at 600–800 nm (see Figure 2C). However, the zero phonon line contributes less than 5% to the total emission. The vibrational side band can be removed by cooling down the diamond to 10 K or lower. Interestingly, the fluorescence of the NV⁻ center does not bleach and is independent of the size of NDs in contrast to quantum dots (QDs), which show a size-dependent change in the color.[14] The NV⁻ center has an electron spin which equals to 1. Due to this, the ground and excited states of the NV⁻ center are triplets, for which m_s=0 and m_s=±1 states are split at zero-field by 2.88 GHz and 1.42 GHz, respectively. For both ground and excited states m_s=+1 and m_s=−1 are degenerate levels, this degeneracy can be removed by external magnetic field or lattice strain. The relaxation from excited to ground state is spin dependent. In case of m_s=0, the electron will relax by a radiative process. However, if the electron spin equals m_s=±1, the relaxation to the ground state can go directly with photon emission or with 30% probability through the intermediate state by a non-radiative path and with spin conversion from m_s=±1 to m_s=0 (see Figure 2A). Therefore, the number of emitted photons is spin-dependent and is lower for m_s=±1. Due to this, the electronic spin state can be detected by optically detected magnetic resonance (ODMR). The principle of ODMR is discussed in the next chapter »Sensing Properties of Color Centers« in detail. Furthermore, the spin states possess long relaxation times (T1, T2).[12] All these features enable sensing using NV⁻ centers which is discussed in the next chapter.

So far, the NV center is the best studied color center in NDs. However, there is extensive research to identify and characterize new color centers mainly because of three reasons: (1) the emission of the NV center is very broad and there is a need for color centers with sharp and narrow emissions; (2) a stronger fluorescence signal would be beneficial which is comparable to small molecular dyes allowing the use of commonly available imaging instruments; (3) color centers with an emission peak shifted more into the near-infrared (NIR) region would enable bioimaging *in vivo* because it overcomes the problem of the penetration depth of the light.[14]

Another interesting color-center is the silicon-vacancy (SiV) center. SiV centers possess a sharp and narrow zero-phonon line at around 738 nm (see Figure 2D). In addition, the excitation wavelength can be chosen in the NIR window. Therefore, the silicon vacancy center is of great interest for bioimaging and sensing. Nickel color centers in diamonds possess a photoluminescence doublet around 883/885 nm and are also promising candidates for bioimaging (see Figure 2D). Finally, tin-vacancy centers and germanium-vacancy centers are studied as well with zero-phonon lines at 619 nm and 602 nm, respectively (see Figure 2D).[14]

Sensing Properties of Color Centers

NDs with color centers are interesting optical markers. However, they can be used as nanoscale sensors too depending on the type of color center which is located inside the diamond lattice. NDs containing NV^- centers can be used as nanosensors not only with high sensitivity but also with nanoscale spatial resolution. For example, the NV^- center can detect magnetic or electrical fields as well as temperature changes due to its physical properties. The detection of magnetic fields is possible because of the spin properties of the NV^- center. As mentioned earlier, the NV^- center possesses a spin of 1 and a spin triplet at the ground and excited states. The ground states $m_s=0$ and $m_s=\pm1$ are separated by 2.88 GHz (see Figure 2A) and in a similar way the excitation states $m_s=0$ and $m_s=\pm1$ are separated by 1.42 GHz. Optical excitation (by laser excitation) allows transitions only with spin state conservation. In simpler terms, transitions from the ground state $m_s=0$ to the excited state $m_s=\pm1$ and from the ground state $m_s=\pm1$ to the excited state $m_s=0$ are forbidden. However, a microwave with a resonance frequency allows the spin conversion from $m_s=0$ to $m_s=\pm1$ of either ground states or excited states. This enables the manipulation of the spin states of the NV^- center. The relaxation from the excited state to the ground state is also spin dependent. As mentioned above, every electron relaxation at $m_s=0$ releases one photon. However, in case of $m_s=\pm1$ the relaxation can go through the intermediate state (30% chance) without photon emission and with spin conversion to $m_s=0$ (see Figure 2A). This phenomenon optically distinguishes the spin states of NV^- centers: $m_s=0$ emits more photons and is called bright state while $m_s=\pm1$ emits less photons and is called dark state. The technique which measures this is called ODMR. The highest contrast which can be achieved between bright and dark states is 30% (see Figure 3A). Furthermore, a long laser excitation (pulse longer than 500 ns) always transfers the electrons of NV^- centers into the spin state $m_s=0$ due to the relaxation and spin conversion over the intermediate state (see Figure 2A). In summary, the NV^- center is a spin system, which can be optically transferred to special spin states (laser light to $m_s=0$), which allows manipulation of spin states by microwaves (microwave to change $m_s=0$ to $m_s=\pm1$), and which allows optical readout (different number of photons for different spin states). An external magnetic field splits the spin states $m_s=+1$ and $m_s=-1$ and shifts them relatively to $m_s=0$ due to the Zeeman Effect (Figure 3C). Therefore, ODMR measurements with an external magnetic field give not one minimum as it is the case at zero-field conditions (Figure 3A), but two (Figure 3C). How strong the two minima are separated from each other depends on the strength of the magnetic field ($2\gamma B$). Therefore, any external permanent magnetic fields can be sensed by the splitting of $m_s=+1$ and $m_s=-1$ spin states and consequently, a change in the frequency which can be directly measured by ODMR.[13] The splitting between $m_s=+1$ and $m_s=-1$ can also appear due to lattice strain especially for NV^- centers located closely to the surface. However, this internal splitting does not affect external splitting and NDs can be used to sense magnetic field in the same manner. Oscillating magnetic field can be measured by their effect to the spin-lattice (T1, see Figure 3B) and spin-spin (T2)

relaxation times. In a perfect system, the present spin states should keep the state forever. However, in the real system, there are a lot of different fluctuating magnetic fields, which decrease the relaxation times of the spin. Measurements of T1 and T2 are most useful to detect different parts of external magnetic fields. In principle, the NV⁻ center is sensitive for all kind of spins which are located close enough (less than 30 nm). This enables a number of sensing possibilities such as nanoscale NMR, ion concentration, pH values, electric charges, and single molecular-spins.[13]

Other than magnetic fields, changes in temperature can also be measured. One way to detect the change in temperature is to observe the shift of the zero-phonon line due to the crystal expansion which occurs due to the temperature increase. This is applicable for all color centers in diamonds. However, for NV centers it is not very effective, since only less than 5% of the total emission goes through the zero-phonon line. Therefore, this method is more effective for silicon-vacancy centers. NV⁻ centers rely on another technique to measure changes in temperature. The crystal field which is responsible for splitting the $m_s=0$ and $m_s=\pm 1$ is temperature dependent. That is why, a shift of ODMR lines will be observed due to the change in temperature (Figure 3D).[14] This effect can be amplified by external magnetic fields. The accuracy of sensing the temperature is roughly 1 °C.[15]

These are the physical fundamentals of sensing using fluorescent nanodiamonds (FNDs). To illustrate the sensing potential better, examples from literature will be given in Chapter 1.8.
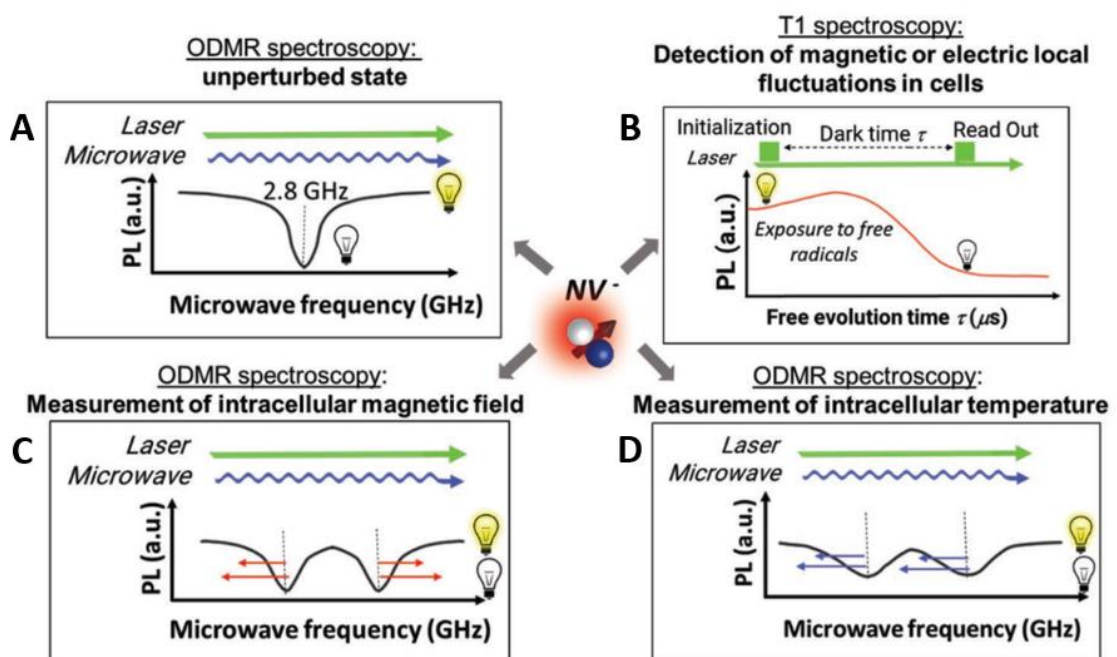
Figure 3 Schematic illustration of different spectroscopic methods for sensing. (A) In ODMR spectroscopy FNDs are illuminated by a laser constantly while a microwave with changing frequency is applied. At the frequency matching the zero-field splitting, the fluorescence intensity drops by about 30% because electrons in the excited state with a spin state of $m_s=\pm 1$ can relax over the single state by a non-radiative process. (B) In T1 spectroscopy, electron spins are first transferred into $m_s=0$ by optical pumping. After

switching off the laser, the electron spins return into the equilibrium. Because m_s=0 is brighter than the equilibrium spin states, the time until the equilibrium is reached can be measured by the photoluminescence intensity of the FNDs. (C) In presence of an external magnetic field, m_s=+1 and m_s= −1 split according to the strength by the magnetic field. This can be measured by ODMR spectroscopy. (D) Other than external magnetic fields, the spin states are also sensitive to temperature. If the temperature changes, the resonance frequencies will change as well. (A)–(D) are adapted with permission from Torelli, M. D.; Nunn, N. A.; Shenderova, O. A. A Perspective on Fluorescent Nanodiamond Bioimaging. *Small* **2019**, 1902151. Copyright (2019) John Wiley and Sons.

Surface Properties of NDs

While the composition of the core is simple from the chemical point of view, the surface of NDs is chemically highly complicated and can contain a various number of different chemical functionalities. The surface of NDs is important for further modification and for the dispersion of NDs in different solvents. A major limitation is the presence of mostly sp^2 carbon. These graphitic structures could form onion rings around the carbon materials and are strongly quenching the luminescence of the color centers in the ND core.[10] These diverse chemical functionalities on the ND surface are also causing the risk of strong batch-to-batch variations. Therefore, numerous techniques were invented to remove sp^2 carbon and to homogenize the surface of NDs.[16] These treatments are discussed in chapter 1.4.

Size and Shape of NDs

Sizes of NDs vary usually from a few to hundreds of nanometers depending on the synthesis method. NDs produced by detonation techniques are commonly small (4–5 nm) and of spherical shape.[10] Micron-sized NDs synthesized by high pressure–high temperature approaches require further crushing to reach nanoscale sizes. Therefore, these NDs possess usually sharp edges and form various non-regular shapes.[10]

It is well known that the size of nanoparticles (NPs) in general is important for biomedical applications. However, there are also investigations about the behavior of NDs with different shapes. For example, there are indications that NDs with sharp edges can penetrate into cells easier compared to spherical NDs.[17,18]

1.3 Synthesis of Nanodiamonds

NDs are produced by either top-down or bottom-up approaches. In the top-down process, micron-sized NDs are fragmented by milling or ultrasound.[19] However, these vigorous mechanical processes can easily damage the optical properties of NDs. In contrast, during the bottom-up process, the carbon lattice is formed from molecular precursors. Often, bottom-up and top-down processes are combined. Therefore, micron-sized NDs are fabricated by bottom-up approaches and are fragmented into nanometer sizes afterwards by top-down processes. Among these many methods[20], three approaches became more relevant and are discussed in the following.

Detonation, Chemical Vapor Deposition, and High Pressure–High Temperature Synthesis

Over the past decades, three prominent methods to produce NDs distinguished themselves. Firstly, the detonation technique which was already reported in the 1960s and produces nanometer sized NDs. Secondly, chemical vapor deposition (CVD) which is mostly applied to create coated surfaces and ND films. Thirdly, the production under high pressure and high temperature (HPHT) which is the mildest and most controllable technique and therefore is applicable to produce FNDs.

The production of diamonds by detonation was invented by Danilenko in 1963.[21] The detonation takes place in a closed chamber filled with molecules of explosives (Composition B) which provide both, the carbon source for diamond formation and the high energy which is needed for the conversion. Composition B is a mixture containing TNT (2,4,6-trinitrotoluene) and hexogen (1,3,5-trinitroperhydro-1,3,5-triazine) among others.[19,22] In addition, the reaction chamber is either filled with an inert gas or ice, so-called 'dry' or 'wet' synthesis. After the detonation, a soot is formed which contains diamonds, graphitic carbon materials, and other impurities. Therefore, intensive purification is necessary to remove sp^2 carbon and metal impurities. NDs produced by detonation techniques are polycrystalline and are only of a few nanometer in size.[22]

Another attractive method to produce NDs is CVD. Usually, a gas phase composed of hydrogen and methane is ionized into chemically active radicals using microwave, radiofrequency, laser induced, direct current, hot filament, or chemical activation. While methane acts only as carbon source, hydrogen is very important because it terminates the dangling carbon bonds, creates reactive carbon radicals, and prevents the growth of graphite. The growth process of the NDs in CVD takes place on a substrate surface. Commonly used substrates are molybdenum, silicon nitride, and tungsten carbide which require special pretreatments before the CVD process. The temperature of the substrates is set from 1000 to 1400 K during the CVD process. Due to the substrate surface and growth time, NDs can either form individual NDs or a thin film in CVD.[23]

The classical HPHT approach is considered milder and better controllable compared to the detonation method and single-crystalline NDs are formed. Therefore, this process

gained much attention to produce FNDs. Synthesis occurs often in a diamond anvil cell (see Figure 4B) but also other methods are reported, e.g. piston-cylinder or multi-anvil devices.[24] Using a diamond anvil cell, carbon materials are usually located in a chamber which can be heated up to high temperatures (~2000 K). Two diamond anvils, one from the top and one from the bottom, are exerting the high pressures to the chamber. Traditionally, graphite, carbon nanotubes or fullerenes are used as a carbon source.[19] Under high pressure and high temperature, a thermodynamic transition of the carbon phase from sp^2 to sp^3 hybridization takes place. Afterwards, bulk diamonds, which are formed during HPHT, are fragmented into nanometer-sized diamonds by bead-assisted sonic disintegration or mechanical ball milling (see Figure 4A).[8] Recently, the direct production of nanometer-sized NDs using HPHT was achieved whereby damage during milling processes was avoided. A more detailed description can be found in chapter »HPHT Synthesis using Adamantane Seeds«.
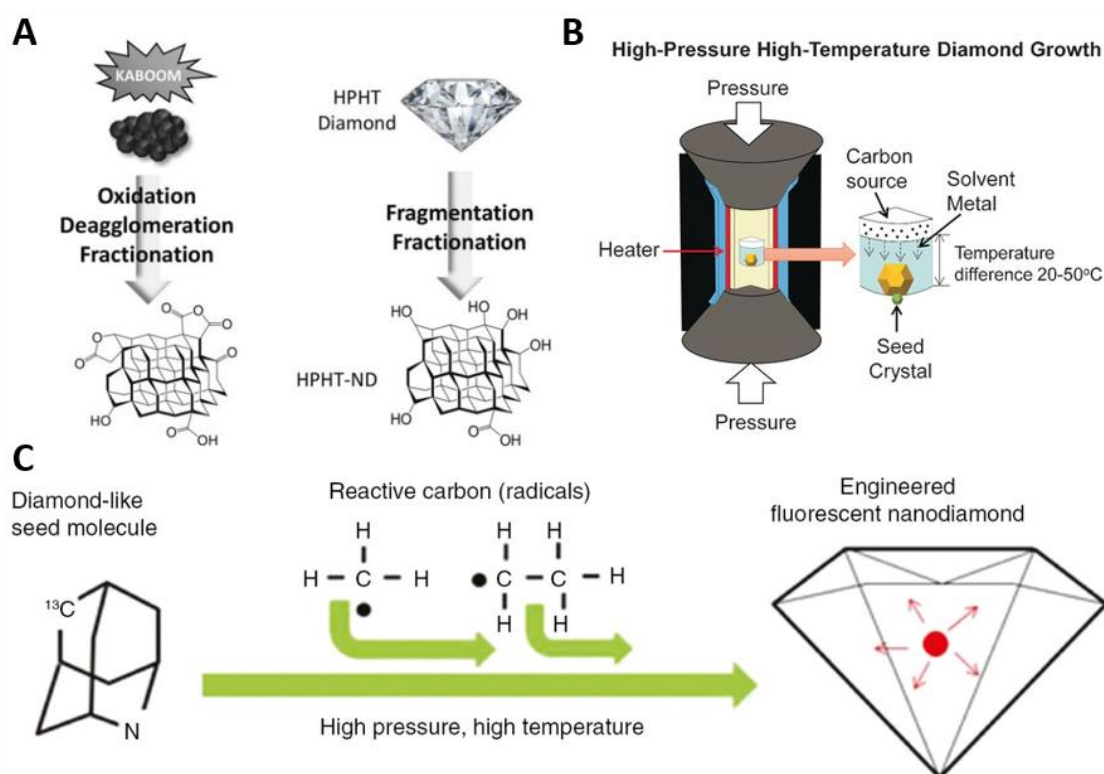
Figure 4 (A) The detonation and high pressure–high temperature (HPHT) synthesis routes are shown. (B) Scheme of a typical diamond anvil cell. (C) Scheme of a HPHT synthesis using adamantane derivates as seed. Adamantane containing a nitrogen atom allows to introduce nitrogen into NDs during the growth phase. (A) is adapted with permission from Reina, G.; Zhao, L.; Bianco, A.; Komatsu, N. Chemical Functionalization of Nanodiamonds: Opportunities and Challenges Ahead. Angew. Chemie Int. Ed. 2019. Copyright (2019) John Wiley and Sons. (B) is adapted with permission from Wu, Y.; Jelezko, F.; Plenio, M. B.; Weil, T. Diamond Quantum Devices in Biology. *Angew. Chemie - Int. Ed.* **2016**, 6586–6598. Copyright (2016) John Wiley and Sons. (C) is adapted with permission from M. H. Alkahtani, F. Alghannam, L. Jiang, A. Almethen, A. A. Rampersaud, R. Brick, C. L. Gomes, M. O. Scully, P. R. Hemmer, *Nanophotonics* **2018**, *7*, 1423–1453. Published by De Gruyter.

Implementation and Stabilization of Vacancy Centers

Most of the natural formed bulk diamonds possess nitrogen impurities in the carbon lattice. However, the number of active NV centers is typically too low for applications. There are several ways to improve the number of active NV centers. If bulk diamonds do not contain any or too less nitrogen atoms such as natural bulk diamonds, nitrogen atoms can be introduced into the diamond lattice subsequently using ion implantation.[25] For example, the group of Wrachtrup successfully introduced a single NV center into diamonds using a ^{14}N or ^{15}N ion beam.[26,27] In contrast to the detonation method, CVD and HPHT syntheses allow the introduction of nitrogen atoms during the growth process.[28–30] This is accomplished by introduction of N_2 gas during the CVD process[28] or using nitrogen containing carbon sources, such as adamantane carbonitrile, during the HPHT synthesis.[29,30] However, the introduced nitrogen atoms do not form active NV centers instantaneously. Vacancies in the diamond lattice can be created by high-energy electron or ion irradiation (10 MeV and 8 mA[31]). To form active NV centers, these vacancies need to move to a nitrogen atom in the lattice which is accomplished by high-temperature annealing (800 °C under vacuum, 2 h[31]).[13]

Next to nitrogen, also other atoms were explored. Recently, the group of Krivitsky[32] synthesized NDs containing silicon vacancy center by adding tetrakis(trimethylsilyl)-silane during the growth process. Furthermore, germanium vacancy centers were successfully introduced by ion-implantation.[33]

High Pressure–High Temperature Synthesis using Adamantane Seeds

Traditionally, diamonds produced by HPHT synthesis are of micrometer size and need to be fragmented to reach nanometer scale. These processes are costly and time-consuming because the milling is accompanied by metal impurities which need to be removed again. In addition, fragmentation by bead-assisted sonic disintegration or ball milling can create thin cracks in the NDs lattice or destroy vacancy centers. Therefore, it would be beneficial to synthesize directly nanometer-sized diamonds using the HPHT method. Usually, the carbon sources are completely decomposed under the high pressure and high temperature conditions. To gain more control over the formation of diamonds, a synthesis using carbon seeds was proposed. These seeds should help to initiate the formation of diamond and lead to a more controllable growth even at lower pressures and temperatures (see Figure 4C). The smallest unit in a diamond is of similar shape as adamantane. The carbon atoms of adamantane possess already a sp^3 hybridization. Although the idea to use adamantane as carbon source for diamond synthesis is not new, it was reported in 1965 firstly[34], there were strong disagreements about the behavior of adamantane during the diamond formation in the literature in the past decades.[30] Mostly, there was no difference between adamantane and other hydrocarbons because of the very high pressure (12.5 GPa) and high temperature (2000 K) which was applied. Under these conditions, adamantane is decomposed completely and cannot act as a seed. Onodera *et al.* reduced the pressure and

temperature (8 GPa, 1590 K) significantly but received only ND aggregates.[30] In the past two years, several articles dealing with HPHT synthesis using adamantane seeds were published which emphasizes the importance of this topic.[29,30,35,36] For the first time, the group of Vlasov[30] reported synthesis of nanodiamonds using a pressure (9 GPa) which is below the pressure limit required for the direct conversion of graphite (>11 GPa) and temperature values ranging from 1900 to 1270 K. The formed NDs had sized of 2–10 nm in diameter. Using a mixture of adamantane and adamantane carbonitrile (adamantane containing a nitrogen atom), the formed NDs possessed different types of NV centers (NVN, NV^0, NV^-).[30] Recently, the group of Hemmer[29] reported ND formation at a low temperature but still a high pressure (400 °C, 10 GPa). It was speculated that the low temperature slows down the reaction and gives higher quality NDs. In addition, the temperature is below the decomposition temperature of the seed (2-azaadamantane hydrochloride). NDs with sizes of 10 to 150 nm were formed which possessed NV^0 and NV^- centers upon irradiation and annealing.[29] Next to this, it was recently shown that using polymeric adamantane seeds (poly(1-vinyladamantane)), ND formation took place at very low temperatures (250 °C, 7 GPa).[36] However, the production of FNDs with intrinsic NV centers has not yet been achieved.

Post-Synthetic Purification

During the synthesis of NDs and also during the irradiation processes, samples are contaminated with non-diamond carbon and metal impurities. In general, diamonds synthesized by detonation techniques require a more intensive purification compared to NDs produced by HPHT.[19] A common protocol to remove sp^2 carbon (graphite) and metal impurities is oxidation of the ND surface using strong acids.[16,19] The reactivity of the sp^2 carbon is significantly higher than the reactivity of sp^3 carbon towards oxidation.[37] The most popular procedure which is used throughout the literature is a mixture of concentrated sulfuric, nitric, and per-chloric acid (HCl, HNO_3, and H_2SO_4).[16] Another popular way to purify the ND surface is air oxidation. By adjusting the temperature carefully, only sp^2 carbon can be removed selectively (425 °C). Using a temperature above 450 °C, sp^2 and sp^3 carbon will be oxidized. The latter method is more efficient in removing the sp^2 carbon completely but comes along with the loss of sp^3 carbon.[16] It is important to note that the purification of the ND surface is not only critical to prevent aggregation but it also strongly affects the NV centers within the NDs. Graphite on the ND surface quenches the NV luminescence and a highly oxidized ND surface can influence the charge state of the NV centers closely located to the surface.[38] Oxygen or fluorine terminated NDs showed a higher ratio of NV^-/NV^0 compared to hydrogen or nitrogen terminated NDs.[39,40] Especially for applications in the field of sensing a high number of NV^- centers is required because only NV^- possess magneto-optical properties. After the surface purification, the deagglomeration of the NDs is necessary because single NDs are forming aggregates. NDs produced by detonation require stronger deagglomeration methods compared to NDs from HPHT which tend to aggregate less. High-energy ball milling is the most promising method for detonation

20

NDs and the milder sonication is the method of choice for NDs produced by HPHT synthesis.[19] Depending on the size-distribution of the NDs, a size fractionation could be useful. Especially for NDs produced by fragmentation, fractionation is crucial because the size-distribution of the NDs is broad.[19] Fractionation can be performed by centrifugation, ultra-centrifugation or density-gradient centrifugation.[41]

1.4 Primary Surface Functionalization of Nanodiamonds

Primary Surface Functionalization by Oxidation, Reduction or Gas Phase

The application of NDs in drug delivery, bioimaging, and sensing comes along with special demands on the quality of the ND surface. While the ND core is inert, of simple molecular composition, and shielded from the external environment, the surface of NDs is highly complicated on the molecular level and is in direct contact with the surrounding environment. Therefore, the surface chemistry is crucial for the colloidal stability in solution of NDs and for further modification. As mentioned before, the ND surface also influences the NV centers in the diamond lattice. To reiterate, oxygen or fluorine terminated NDs (~30 nm) showed a higher ratio of NV^-/NV^0 compared to hydrogen or nitrogen terminated NDs.[39,40] In addition, surface functionalization is important to standardize the surface properties of NDs from different batches or even from different synthesis methods to prevent batch-to-batch variations. The surface of NDs can contain various functional groups such as COOH, C=O, different alcohol functions (tertiary, secondary, primary), and ether groups. Therefore, the surface charge can vary strongly, with zeta potentials ranging from -50 to 50 mV.[16] Other than standardizing the surface characteristics, surface functionalization is an important starting point for further chemical modification of NDs. In this chapter, there is a clear distinguishment between primary surface functionalization and coating of NDs. Primary functionalization refers to the conversion of functional groups such as a transformation of hydroxyl groups into carboxylic acid groups, whereas coating includes covalent and non-covalent interactions taking place at the ND surface such as polymerization from the ND surface or non-covalent attachment of proteins.
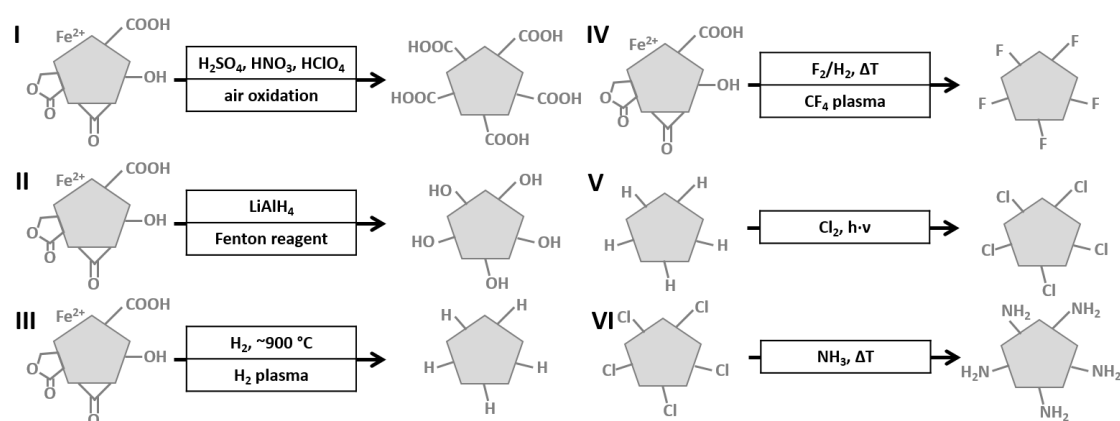
Figure 5 Schematic overview of different primary post-functionalization methods of nanodiamonds.

Carboxylated NDs. COOH-terminated NDs have already been discussed previously because oxidation is a standard procedure to purify the ND surface. To recap, the oxidation of the ND surface is mainly performed using a mixture of concentrated acids or by heating above 400 °C (see Figure 5I).[16] Oxidized NDs possess a hydrophilic character with a zeta potential between -30 to -50 mV.[16]

Hydroxylated NDs. OH-terminated NDs are of interest because they allow silylation or acylation reactions. A common way is to reduce C=O groups using borane or $LiAlH_4$. A harsher way is the use of the Fenton reagent, a mixture of hydrogen peroxide and $FeSO_4$ in a strongly acidic solution. First, this reagent removes non-diamond carbon followed by a reaction of generated OH radicals with the surface of the ND yielding a highly hydroxylated surface (see Figure 5II).[16]

Hydrogenated NDs. The reduction of functional groups to C–H groups is rather difficult because it typically results in just different types of hydroxyl functions. The introduction of C–H groups using elemental hydrogen at high temperatures (~900 °C) was reported.[16] However, the number of C–OH increases as well and the high temperature cannot be used for nanometer-sized diamonds because this would produce significant amounts of graphitic carbon.[16] Therefore, a more elegant method has been to perform hydrogenation in a plasma reactor. Loh *et al.*[42] created a hydrogenated surface of detonation NDs using a microwave plasma reactor at 800 °C twice for 60 min (see Figure 5III). Another method describes to use hydrogen gas in a microwave plasma generator at a pressure of 15 mbar.[43]

Fluorinated NDs. Fluorination of NDs was achieved by Khabashesku *et al.* using a gas phase reaction of F_2/H_2 mixture at high temperatures (see Figure 5IV). Another method is to apply atmospheric pressure plasma with CF_4 to graft fluorine atoms to the ND surface.[16]

Chlorinated NDs. The most efficient way to produce a chlorinated surface of NDs is the photochemical reaction of gaseous chlorine with hydrogenated NDs (see Figure 5V).[16]

Aminated NDs. Amine-terminated NDs were produced using chlorinated NDs in gaseous ammonia at elevated temperatures (see Figure 5VI). So far, amination by photochemistry or plasma treatment was only achieved for ND films but protocols could be transferrable to single ND particles.[16]

Primary Surface Functionalization using Small Molecules

Functionalization of the surface of nanodiamonds is also possible using small molecules especially when it comes to functional groups which are difficult to introduce in another way. Azide-terminated NDs were prepared using dopamine derivatives transforming the primary amine group of dopamine into the azide group. By mixing hydroxylated NDs with the dopamine derivatives, a monolayer shell of dopamine was formed where the azide groups were on the surface.[44] A dopamine derivative was also used to prepare perfluorophenyl azide-terminated NDs for further photochemical reactions.[45] Hydroxylated NDs were functionalized using the coupling agent, 3-aminopropyltriethoxysilane, yielding in amine-terminated NDs.[46,47] Furthermore, treatment of hydroxylated NDs with firstly 3-bromopropyltrichlorosilane and secondly sodium azide also enabled the formation of azide-terminated NDs.[48] Another way to

produce azide-terminated NDs is coupling of 4-azidobenzoic acid to hydroxylated NDs using *N*,*N'*-dicyclohexylcarbodiimide (DCC).[49] Alkynyl-terminated NDs were functionalized by coupling of 4-pentynoic acid in the presence of DCC.[50] Carboxylated NDs can be also transferred into hydroxylated NDs by reaction with ethanolamine in the presence of 1-ethyl-3-(3-dimethylaminopropyl)carbodiimide (EDC)/*N*-hydroxysuccin-imide (NHS).[51] Furthermore, these NDs can be functionalized with an azide group by esterification of the hydroxyl groups of the NDs with 2-(2-azidoethoxy)ethyl 4-chloro-4-oxobutanoate.[51]

As pointed out above, there are many different possibilities to functionalize the surface of NDs. How these functionalization strategies help to further coat the surface of NDs for various applications is explained in the next chapter in detail.

1.5 Surface Coating Strategies of Nanodiamonds

For most applications, simply relying on primary surface functionalization of NDs is not sufficient because the NDs often still aggregate strongly in aqueous buffer systems. Therefore, further coating of NDs is necessary. In this chapter, different strategies to coat NDs are discussed and classified by covalent or non-covalent interactions as well as the type of modification.

Covalent Surface Coatings

A good starting point for covalent modifications of NDs is a carboxylated surface. Carboxylic acid groups can be easily activated and react with amine groups subsequently. Mostly, carboxylic acid groups on the surface of NDs are activated by either thionyl chloride or simple EDC/NHS chemistry. Hydroxylated NDs are often used for esterification or reactions with siloxanes.[19] In contrast, amine-terminated NDs seldom find a use because the preparation is rather difficult. However, amine-terminated NDs allow the access to reactions with activated carboxylic acid groups. In the following, representative examples are given.

Linear Polymers. Introducing a polyethylene glycol (PEG) shell is a common strategy to modify NPs because PEG possesses a high biocompatibility, a low immunogenicity, and prevents protein adsorption. Most importantly, PEG chains improve the colloidal stability of NPs. Therefore, modifications with PEG chains are also of interest for NDs and several different methods for the attachment of PEG units are described in literature.[52–58] Carboxylated NDs were either activated using thionyl chloride (SOCl$_2$)[52,53] or EDC/Sulfo-NHS[54]. Afterwards, PEG chains were grafted onto the surface of the activated NDs by esterification of the hydroxyl or amine groups located at one end of the PEG chains. Furthermore, PEG units, end-functionalized with a thiol, were grafted onto NDs by thiol-ene click chemistry reacting with the sp^2 carbon on the surface of NDs.[55] Although, amine-terminated NDs are not often used in literature, due to the more challenging functionalization and the normally bad dispersity of amine-terminated NDs, Lu *et al.*[56] synthesized PEGylated amine-terminated NDs using the "grafting onto" approach. Firstly, two different polymers were synthesized by reversible addition-fragmentation chain transfer (RAFT) polymerization and end-functionalized with a carboxylic acid group to enable coupling to the amine-terminated NDs. Another approach[47] described amine-functionalized NDs which were coupled to *o*-methylbenzaldehydes to enable light-induced ligation of polymers (see Figure 6A). Using different maleimide end-functionalized polymers synthesized by RAFT polymerization, UV-light promoted Diels-Alder reactions with *o*-methylbenzaldehydes was demonstrated to be an efficient modification strategy.[47] Finally, azide-terminated NDs were modified with polymers by strain-promoted alkyne–azide cycloaddition click-chemistry. Two polymers were synthesized by RAFT copolymerization or block copolymerization and end-functionalized with dibenzocyclooctyne which allowed ligation to the azide-terminated NDs.[51]

To increase the density of the PEG units, grafting from approaches were exploited as well. Zhang *et al.*[57] compared "grafting to" and "grafting from" approaches of PEG units (see Figure 6C). "Grafting to" was achieved by activation of the carboxylic acid groups of NDs followed by esterification of hydroxyl groups of PEG chains (1900 Da). "Grafting from" was performed by atom transfer radical polymerization (ATRP). Hydroxylated NDs were modified using 2-bromoisobutyryl bromide as initiator. Afterwards, poly(poly(ethylene glycol) methacrylate) chains were polymerized on the ND surface through ATRP using Cu(Br)/N,N,N',N'',N''-pentmethyl diethylenetriamine as the catalyst/ligand. However, grafted polymer weight ratios of "grafted to" and "grafted from" approaches, in numbers 29.8% and 34.4%, respectively, differed only slightly.
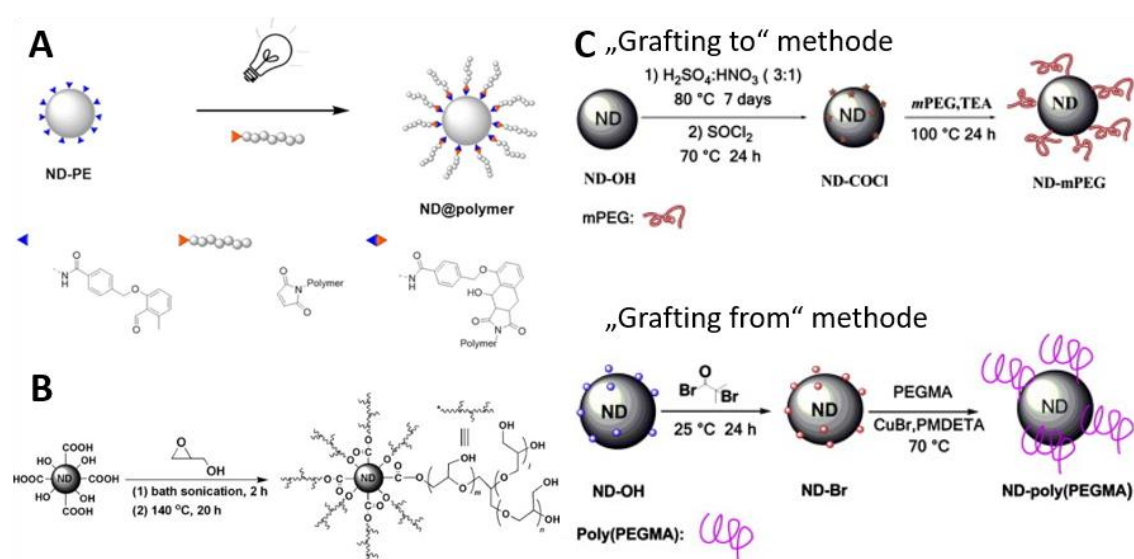

Figure 6 (A) Nanodiamonds (NDs) were modified with *o*-methylbenzaldehyde and maleimide end-functionalized polymers were synthesized. Upon UV irradiation, o-methylbenzaldehydes was transferred into quinodimethane which underwent Diels−Alder reactions with the maleimide of the polymers. (B) Synthesis of ND functionalized with hyperbranched polyglycerol through the ring-opening polymerization of glycidol. (C) "Grafting to": Carboxylated NDs were prepared by oxidation with H_2SO_4 and HNO_3 and afterwards, were activated with thionyl chloride followed by an esterification of hydroxyl groups of PEG chains (1900 Da). "Grafting from": Hydroxylated NDs were modified using 2-bromoisobutyryl bromide as initiator. Afterwards, poly(poly(ethylene glycol) methacrylate) chains were polymerized on the ND surface through atom transfer radical polymerization using Cu(Br)/N,N,N',N'',N''-pentmethyl diethylenetriamine as the catalyst/ligand. (A) is adapted with permission from Wuest, K. N. R.; Trouillet, V.; Goldmann, A. S.; Stenzel, M. H.; Barner-Kowollik, C. Polymer Functional Nanodiamonds by Light-Induced Ligation. *Macromolecules* **2016**, *49* (5), 1712–1721. Copyright (2016) American Chemical Society. (B) is adapted with permission from Zhao, L.; Takimoto, T.; Ito, M.; Kitagawa, N.; Kimura, T.; Komatsu, N. Chromatographic Separation of Highly Soluble Diamond Nanoparticles Prepared by Polyglycerol Grafting. *Angew. Chemie Int. Ed.* **2011**, *50* (6), 1388–1392. Copyright (2011) John Wiley and Sons. (C) is adapted with permission from Zhang, X.; Fu, C.; Feng, L.; Ji, Y.; Tao, L.; Huang, Q.; Li, S.; Wei, Y. PEGylation and PolyPEGylation of Nanodiamond. *Polymer*. **2012**, *53* (15), 3178–3184. Copyright (2012) Elsevier.

A common problem of modification is the low number of functional groups which is presented on the surface of NDs. Therefore, it is very difficult, even with "grafting from" approaches, to achieve high densities of linear polymers. In addition, a high density of

polymers is especially important for biomedical applications to prevent unspecific adsorption of proteins. To overcome this limitation, hyperbranched polymers were investigated. They seem to be more suitable because even with a small number of starting points a high density is formed due to the branching of the polymer chains.

Hyperbranched Polymers. Polyglycerol (PG) emerged as a promising candidate for the modification of NDs and has often been used in literature in the last years.[59–68] PG possesses a high biocompatibility and hydrophilicity which makes PG a potential replacement for PEG.[67] The group of Komatsu[67] reported the modification of carboxylated ND with hyperbranched PG by ring-opening polymerization of glycidol for the first time (see Figure 6B). For this purpose, NDs and glycidol were mixed, sonicated, and stirred at 140 °C under neutral conditions for 20 h. The carboxylic acid groups as well as hydroxyl groups served as initiation sites for the polymerization. Free PG which was formed by self-polymerization was removed by centrifugation. To completely remove free PG and to narrow down the size distribution of the PG coated NDs, size-exclusion chromatography was performed. In the following years, PG surfaces were further modified to enable the attachment of drugs or targeting groups. Carboxylic groups were introduced by reaction of PG with succinic anhydride.[60,63] After reaction of the PG with tosyl chloride, a substitution by azido groups was possible enabling easy click chemistry.[63] The azido groups can be reduced to amino groups as well allowing reaction with activated carboxylic acids such as dyes.[61] Furthermore, hydrazine moieties, allowing immobilization and pH-responsive cleavage of drugs, were introduced.[66] The group of Shirakawa[65] invented a one pot synthesis of PG coating to produce directly carboxylic acid terminated PG surfaces. Separately, Hsieh *et al.* produced alkyne-functionalized PG coated ND in a one pot synthesis.[64] As direct polymerization of glycidyl propargyl ether at the surface of NDs led to strong aggregation, a thin coating of PG using glycidol was first synthesized. After 2 h of reaction, glycidyl propargyl ether was added to the mixture forming an additional PG coating bearing alkyne groups (see Figure 7A). Next to PG, the dendrimer poly(amidoamine) (PAMAM, 3rd generation, ethylene diamine core) was attached covalently to NDs.[69] PAMAM was added under anhydrous conditions to couple the primary amines of PAMAM with the acyl chlorides on the surface of activated NDs.[69]

Although PG coatings seem to be a prominent coating there are still some limitations of this approach. So far the coating is very thick which makes application in sensing difficult. Furthermore, the yield of coated NDs is relatively low because of the purification steps and the uncontrolled polymerization mechanism.

Non-Classical Polymers. Next to linear and hyperbranched polymers, non-classical polymers such as polydopamine were also used to coat NDs. Especially in the last two years, several works reporting dopamine or analogues of dopamine were published emphasizing the potential of this class of material.[70–75] Under mild alkaline conditions dopamine self-polymerizes into polydopamine on many different surfaces. Zeng *et al.*[70]

reported a protocol to form polydopamine coated NDs by mixing and stirring a solution of dopamine and solution of NDs under mild alkaline conditions (0.01 M Tris buffer, pH=8.5) for 12 h. Free dopamine and small polydopamine particles, formed by self-polymerization, were removed by centrifugation. Noteworthy, the thickness of the polydopamine shell which was formed around the surface of NDs could be controlled by the concentration of dopamine during the self-polymerization. The dopamine surface contains many reactive groups including catechol and quinone groups enabling reactions with thiol or amine groups through Michael addition and/or Schiff base reactions.[70] This allowed further modification of the polydopamine coated NDs using thiol group end-functionalized single deoxyribonucleic acid (DNA) strands[70] or PEG chains[73] and non-covalent adsorption of dyes[72]. Furthermore, the catechol groups presented at the polydopamine surface are known to reduce metal ions into metal NPs such as silver ions.[70] However, polydopamine is extremely adhesive and often causes problems with aggregation. Therefore, dopamine analogues were explored too. We[75] showed successfully that L-3,4-dihydroxyphenylalanine (L-DOPA), a dopamine derivative containing an additional carboxylic acid group, could be used to coat FNDs. The polymerization of L-DOPA was performed using sodium periodate and Milli-Q water to avoid buffer salts which can cause problems with aggregation of NDs. The work is described in detail in chapter 3.4.

Silica. Silica coatings are used often to coat NDs because silica is highly stable over a range of pH values, chemically inert, optical transparent, and the coating process can be easily regulated with the possibility to produce porous silica coatings.[76] The group of Neuman[77] produced silica coated FNDs using a liposome-based encapsulation process (see Figure 7C). A mixture of FNDs and tetraethyl orthosilicate were trapped in multi-lamellar vesicles. Ultrasonication broke multilamellar vesicles into small unilamellar vesicles with sizes of around 100 nm in diameter while subsequent conversion of tetraethyl orthosilicate into silica was catalyzed by triethylamine. The liposome-based encapsulation process promotes the formation of monodisperse silica-encapsulated NDs. The group of Rosenholm[78] used cetyltrimethylammonium bromide and tetraethoxy orthosilicate to form a (meso)porous silica shell around FNDs to enable loading of active compounds. A cross-linked silica shell, using bis(triethoxysilyl)ethane, bearing a flexible PEG layer was presented by Rehor *et al.*[79]. Finally, an ultrathin silica shell (< 1 nm) which was further modified with polymethacrylate copolymers was synthesized by the same group.[80]
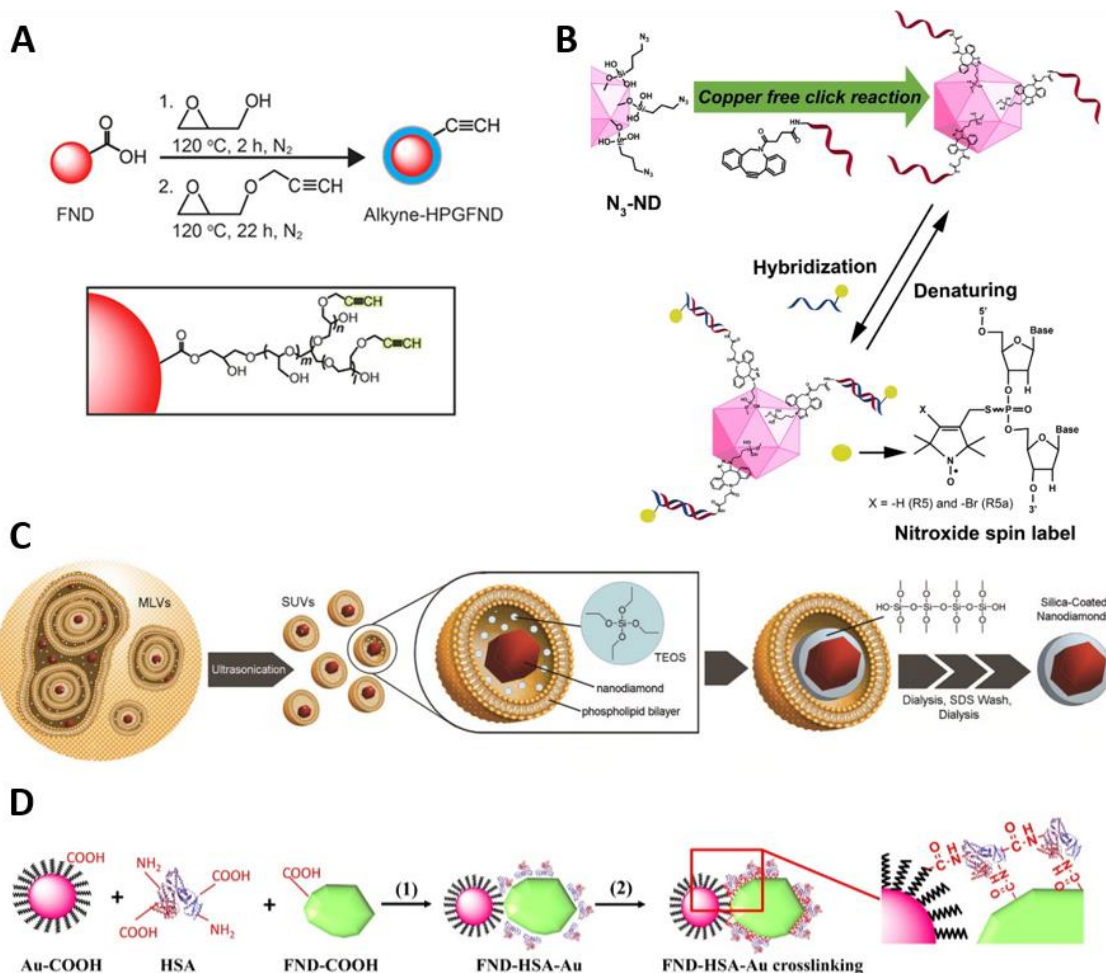
Figure 7 (A) Fluorescent nanodiamonds (FNDs) with a thin coating of golyglycerol (PG) using glycidol was formed. After 2 h of reaction, glycidyl propargyl ether was added to the mixture forming an additional PG coating bearing alkyne groups. (B) Azide-funcionalized nanodiamonds were prepared to enable copper free click chemistry with dibenzocyclooctyne (DBCO) modified single DNA strands. Complementary single DNA strands were hybridized afterwards. (C) FNDs and tetraethyl orthosilicate were trapped in multilamellar vesicles. Ultrasonication broke multilamellar vesicles into small unilamellar vesicles with sizes of around 100 nm in diameter. The conversion of tetraethyl orthosilicate into silica was catalyzed by triethylamine. (D) FNDs, gold nanoparticles, and human serum albumin were mixed, purified by centrifugation, and finally cross-linked by addition of NHS/EDC. (A) is adapted with permission from Hsieh, F.-J.; Sotoma, S.; Lin, H.-H.; Cheng, C.-Y.; Yu, T.-Y.; Hsieh, C.-L.; Lin, C.-H.; Chang, H.-C. Bioorthogonal Fluorescent Nanodiamonds for Continuous Long-Term Imaging and Tracking of Membrane Proteins. *ACS Appl. Mater. Interfaces* **2019**, *11* (22), 19774–19781. Copyright (2019) American Chemical Society. (B) is adapted with permission from Akiel, R. D.; Zhang, X.; Abeywardana, C.; Stepanov, V.; Qin, P. Z.; Takahashi, S. Investigating Functional DNA Grafted on Nanodiamond Surface Using Site-Directed Spin Labeling and Electron Paramagnetic Resonance Spectroscopy. *J. Phys. Chem. B* **2016**, *120* (17), 4003–4008. Copyright (2016) American Chemical Society. (C) is adapted with permission from Bumb, A.; Sarkar, S. K.; Billington, N.; Brechbiel, M. W.; Neuman, K. C. Silica Encapsulation of Fluorescent Nanodiamonds for Colloidal Stability and Facile Surface Functionalization. *J. Am. Chem. Soc.* **2013**, *135* (21), 7815–7818. Copyright (2013) American Chemical Society. (D) is adapted with permission from Liu, W.; Naydenov, B.; Chakrabortty, S.; Wuensch, B.; Hübner, K.; Ritz, S.; Cölfen, H.; Barth, H.; Koynov, K.; Qi, H.; et al. Fluorescent Nanodiamond–Gold Hybrid Particles for Multimodal Optical and Electron Microscopy Cellular Imaging. *Nano Lett.* **2016**, *16* (10), 6236–6244. Copyright (2016) American Chemical Society.

Proteins. Proteins are an interesting class of biopolymers because they are monodisperse and can possess various functions. The group of Weil[17] used human serum albumin (HSA) to coat NDs and to link them to gold NPs (see Figure 7D). COOH-terminated gold NPs, HSA, and carboxylated FNDs were mixed and stirred for 4 h. After adsorption of the gold particles and HSA onto the surface of FND, free HSA was removed by centrifugation. A solution of EDC and NHS was added to cross-link the amine groups of HSA with the –COOH groups of the gold NPs and the FNDs to form stable ND-gold hybrids. The constructs were purified by ultracentrifugation to ensure that only one ND is bound to several gold NP.[17] Transferrin, a protein binding membrane-anchored transferrin receptors, was connected covalently to carboxylated NDs after activation of the carboxylic acid groups.[81,82] Streptavidin is often used in nanoarchitecture because it has four binding pockets for the small molecule biotin with a high binding affinity. To preserve the quaternary structure of streptavidin, a linker was used to attach the protein to the surface of NDs. Cordina *et al.*[83] firstly, coupled a PEG linker onto carboxylated NDs. Afterwards, streptavidin was attached to the free end of the PEG linkers. Streptavidin coated NDs are highly beneficial because they easily allow to attach different biotinylated compounds such as polymers[83] or gold NPs[84]. One of the most interesting class of proteins in modern biomedical applications are antibodies due to their highly specific binding to antigens. There are not many publications showing direct modifications of NDs with antibodies probably because the quaternary structure of antibodies can be easily damaged. Li *et al.*[85] coupled the antibody cetuximab successfully to carboxylated NDs simply by mixing and stirring a solution of NDs, a solution of antibodies, and a mixture of EDC/NHS. Afterwards, unbound antibodies were removed by centrifugation. A similar strategy was also possible for enzymes. Papain or chymotrypsin were covalently coupled onto the surface of activated NDs.[86] Noteworthy, papain or chymotrypsin, which were attached to NDs, retained their enzymatic activity.

Peptides. Next to proteins, also peptides were connected to NDs.[87–93] Mostly carboxylated NDs were coupled to amine groups of peptides using different kinds of carbodiimide crosslinker chemistry. These peptides include a bone morphogenetic protein 2 derived peptide (sequence: KIPKASSVPTELSAISTLYLGGC)[90], an enzymatically cleavable peptide (sequence: LGRMGLPGK)[87], a mitochondrial targeting peptide[93], and a targeting peptide (sequence: DGEA) for $\alpha 2\beta 1$ integrins.[92] Furthermore, carboxylated NDs were modified with polypeptides such as poly-L-arginine.[88] The poly-L-arginine coating enabled to adsorb gold nanorods onto NDs. Finally, the group of Xiao[89] grafted a PEGylated polypeptide onto amine-terminated NDs.

Deoxyribonucleic acid/peptide nucleic acid. DNA became a highly interesting material in fabrication of nanoarchitecture because it allows highly precise constructions due to the hybridization of DNA single strands. However, there are very few examples of covalent modification of NDs with DNA. Dibenzocyclooctyne (DBCO) end-functionalized single DNA strands were connected to azide-terminated NDs by click chemistry (see Figure 7B). Afterwards, complementary strands could be hybridized which were

functionalized with a single electron radical.[48] Dopamine coated NDs enabled to attach single DNA strands which were end-functionalized with a thiol group. In this way, gold nanorods decorated with complementary DNA strands could be hybridized to the NDs.[70] Peptide nucleic acid (PNA) is closely related to DNA but the backbone is built up of peptide bonds. Carboxylated NDs were firstly activated using a solution of EDC and NHS and after removal of the coupling agents, PNA was added to enable the reaction of the primary amine groups of the N-terminus of PNAs with the activated carboxylic acids of the surface of NDs.[94]

Non-Covalent Surface Coatings

Non-covalent modifications of NDs can be divided into two classes of interactions: electrostatic interactions and hydrophobic interactions.[19] Because electrostatic interactions rely on the charge state of both the surface of NDs and the coating material, mostly carboxylated NDs and positively charged coating materials are used. Hydrophobic interactions describe an apolar interaction of the coating molecule and the surface of NDs. Here, often small molecules such as hydrophobic drugs are used.

Polymers. Because of the negative surface charge of carboxylated NDs, positively charged polymers can be used for non-covalent modification. Polyethylenimine (PEI) is a highly positive charged polymer which is capable of complexing DNA and therefore is often used to coat NDs.[95–99] A solution of NDs was mixed with a solution of PEI (800 Da) and the mixture was stirred before free PEI was removed by centrifugation to form PEI coated NDs.[96,98,99] Single chain NPs prepared by glycopoylmers can be used to coat NDs as well.[100] Glycopolymers were produced by RAFT polymerization and NPs were formed by light-induced single chain cross-linking. Afterwards, these NPs were adsorbed onto the surface of NDs by interaction of hydrogen bonds and carboxylic acid groups as proposed.[100] Lee *et al.*[101] synthesized a copolymer containing a hydrophilic PEG block and a mixed cationic–hydrophobic block (2-(dimethylamino)ethyl methacrylate-*co*-butyl methacrylate) to coat NDs by non-covalent adsorption.

Proteins. Next to synthetic polymers, biopolymers like proteins are ideal candidates because they tend to adsorb to surfaces easily. The adsorption of proteins to the surface of NDs includes many kinds of interactions: electrostatic, hydrophobic, hydrogen bonding, and van der Waals interactions.[102] Some of the proteins, among them bovine serum albumin (BSA) and myoglobin, are known to form a thin monolayer coating around the NDs due to the strong protein surface interaction.[103] The process of how NDs are coated with proteins by non-covalent adsorption is very simple and similar throughout the whole literature. Thus, it will not be discussed in detail for each publication but a general description will be given instead. Usually, a solution of NDs and a solution of proteins were mixed and stirred at 4 °C or room temperature for a few hours up to overnight depending on the literature. Afterwards, unbound proteins were removed by centrifugation to give protein-coated NDs. There are different strategies why proteins are a beneficial coating material for NDs. Firstly, proteins can function as

a structural material to prevent aggregation of NDs and increase their colloidal stability. Often members of the albumin family, a highly robust class of proteins, were used for these purposes such as HSA[101,104], BSA[102,103,105,106], and α-lactalbumin[106]. Secondly, proteins were also used because of their functional properties and many proteins were explored from families of signaling proteins (carbohydrate-modified BSA[105], horse heart myoglobin[103], bone morphogenetic proteins[107], basic fibroblast growth factor[107], recombinant viral envelope protein[108]), storage proteins (ferritin[109]), enzymes (lysozyme[102], luciferase[110]), and antibodies (cetuximab[111], transforming growth factor β antibody[112]).

The group of Weil[113–116] developed a protein-based copolymer to coat NDs which was successfully applied in various fields including drug delivery[115], correlative microscopy[114], DNA-origami[113], and crossing of the blood–brain barrier (BBB)[116]. In this system, based on BSA or HSA, proteins were first cationized by transferring all negatively charged amino acid side chain groups into positively charged groups to increase the electrostatic interaction with the negatively charged surface of NDs (see Figure 20, Figure 22). Afterwards, PEG chains were attached to proteins to improve the colloidal stability. Finally, protein–PEG conjugates were denatured to increase the flexibility and exposure of the protein backbone. For drug delivery applications, doxorubicin (DOX) was attached to the cysteines of the proteins *via* a pH-responsive hydrazone linker. Coated NDs were prepared by mixing diluted solutions of NDs and copolymers in either Milli-Q water or boric acid buffer (20 mM, pH 8.4) and stirring at room temperature overnight. Afterwards, free copolymers were removed by centrifugation from the coated NDs. This design is further discussed in the chapters 3.1 and 3.2.

Peptides. Although it seems to be much more common to attach peptides covalently to the surface of NDs, there are also a few examples of non-covalent adsorption of peptides. Similar to the adsorption of proteins, insulin was adsorbed to the surface of carboxylated NDs just by mixing and stirring a solution of NDs and a solution of insulin.[103,117] Afterwards, free insulin was removed by centrifugation. The same strategy was also used to coat carboxylated NDs with a peptide containing a trans-activator of transcription (TAT) and a nuclear localization signal (NLS) unit (see Figure 8B).[118] Morales-Zavala *et al.*[119] used a bi-functional peptide to coat NDs successfully. The peptide was composed of two segments: The first segment contains seven units of arginine and therefore possess a highly positive net charge which facilitates an interaction with the carboxylated surface of NDs (see Figure 8A). The second segment (sequence: CLPFFD) was able to recognize amyloid β aggregates. After coating NDs, the positive charged segment of the peptides was facing to and interacting with the surface of the NDs while the bioactive segment was facing to the surrounding.
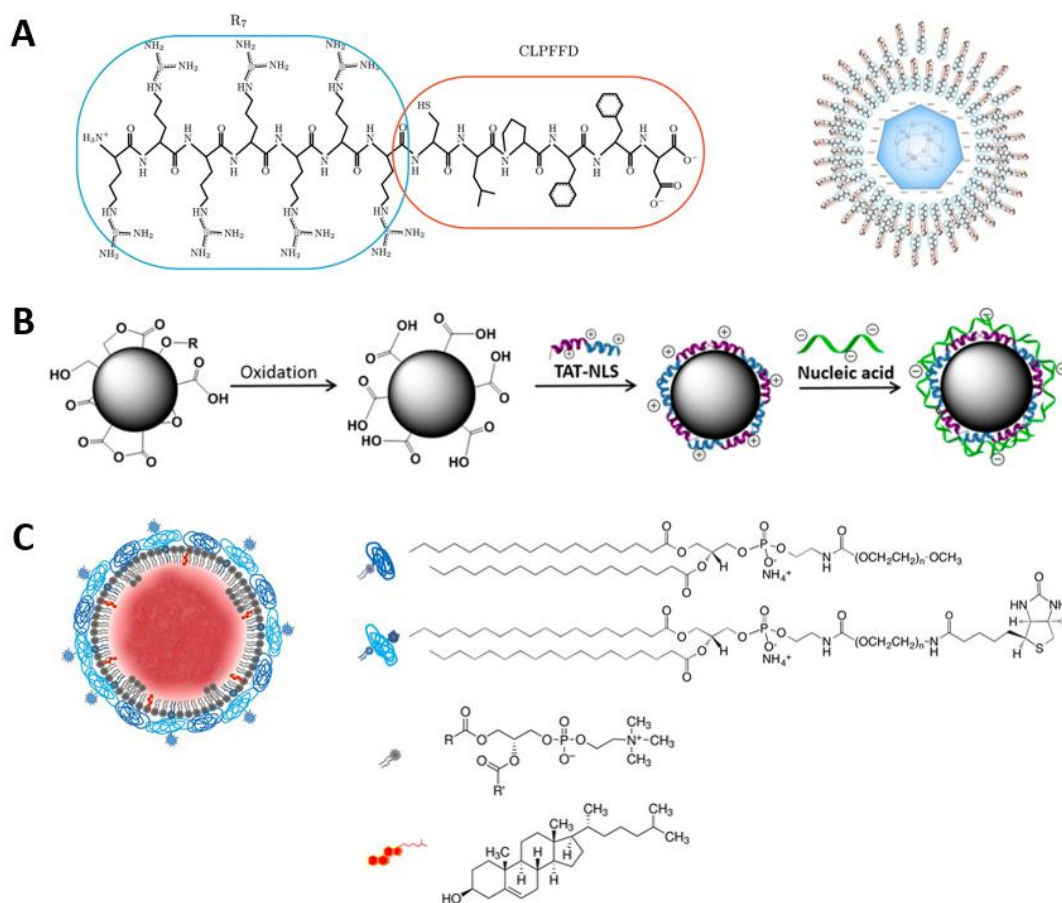
Figure 8 (A) Nanodiamonds (NDs) were coated by a peptide which was composed of two segments: The first segment contains seven units of arginine and therefore possess a highly positive net charge which facilitates an interaction with the carboxylated surface of NDs. The second segment (sequence: CLPFFD) was able to recognize amyloid β aggregates. (B) NDs were oxidized and coated with a peptide which was composed of a trans-activator of transcription and a nuclear localization signal sequence. Finally, nucleic acid chains were adsorbed onto the NDs. (C) Different phospholipids were used to coat NDs. The biotin end-group allowed further modification using streptavidin as a linker. (A) is adapted with permission from Morales-Zavala, F.; Casanova-Morales, N.; Gonzalez, R. B.; Chandía-Cristi, A.; Estrada, L. D.; Alvizú, I.; Waselowski, V.; Guzman, F.; Guerrero, S.; Oyarzún-Olave, M.; et al. Functionalization of Stable Fluorescent Nanodiamonds towards Reliable Detection of Biomarkers for Alzheimer's Disease. *J. Nanobiotechnology* **2018**, *16* (1), 1–14. Published by BioMed Central. (B) is adapted with permission from Leung, H. M.; Chan, M. S.; Liu, L. S.; Wong, S. W.; Lo, T. W.; Lau, C.-H.; Tin, C.; Lo, P. K. Dual-Function, Cationic, Peptide-Coated Nanodiamond Systems: Facilitating Nuclear-Targeting Delivery for Enhanced Gene Therapy Applications. *ACS Sustain. Chem. Eng.* **2018**, *6* (8), 9671–9681. Copyright (2018) American Chemical Society. (C) is adapted with permission from Hsieh, F.-J.; Chen, Y.-W.; Huang, Y.-K.; Lee, H.-M.; Lin, C.-H.; Chang, H.-C. Correlative Light-Electron Microscopy of Lipid-Encapsulated Fluorescent Nanodiamonds for Nanometric Localization of Cell Surface Antigens. *Anal. Chem.* **2018**, *90* (3), 1566–1571. Copyright (2018) American Chemical Society.

Deoxyribonucleic acid/ribonucleic acid. While covalent conjugation of DNA strands to the surface of NDs is mostly used to design specific nanoarchitectures, non-covalent adsorption of DNA/ribonucleic acid (RNA) single- or double-strands are mostly applied in the field of gene delivery. The group of Arnault[43] used hydrogenated NDs to adsorb small interfering RNA (siRNA) successfully. Hydrogenated NDs have the advantage that

their surface is positively charged and therefore able to interact with the negatively charged RNA. However, the usage of hydrogenated NDs is uncommon because the functionalization is challenging. Instead carboxylated NDs are used much more often. Because DNA/RNA is highly negatively charged, carboxlyated NDs were pre-coated with positively charged substances to enable adsorption of RNA/DNA strands. The procedure of coating NDs with DNA/RNA is very similar throughout the literature, hence in the following there is a general description given followed by examples of positive pre-coating materials as well as DNA/RNA from the literature. Carboxylated NDs were either covalently or non-covalently modified with a positively charged material. Positively charged materials include small molecules (lysine[120,121]), polymers (PEI800[96,98,99,122] and polyglycerol[123]), dendrimers (PAMAM[69]), proteins (BSA-PEG copolymer[113]), and peptides (TAT-NLS[118], see Figure 8B). A solution of pre-coated NDs and a solution of DNA/RNA were mixed and shaken or sonicated for 0.5 to 2 h. Different types of DNA/RNA which were adsorbed onto the pre-coated surface of NDs cover siRNA[43,69,120], antisense RNA[99,122], single-strand DNA[113,118], double-strand DNA[98], and plasmid DNA[96,120,123]. Furthermore, a layer-by-layer method to attach microRNA to NDs was introduced by the group of Sheng.[124]

Lipid Bilayer. Another less popular coating method of NDs are lipid bilayers.[125–127] Hsieh *et al.*[125,126] developed a lipid coating by adding a solution of lipids in an organic solvent miscible directly into an aqueous solution of carboxylated NDs (see Figure 8C). Afterwards, the organic solvent was removed by rotary evaporation. Using biotinylated phospholipids allowed further modification by streptavidin linkers. Vavra *et al.*[127] used another strategy to prepare a self-assembled phospholipid bilayer, the so-called supported lipid bilayer. This technique forms a uniform lipid shell in comparison to the method developed by Hsieh *et al.*[125]. Firstly, NDs were functionalized with a 4-5 nm thick silica shell. Afterwards, the phospholipid bilayer was formed using a microfluidic device.[127]

Hydrophobic Interaction. The last class of non-covalent interactions are hydrophobic interactions which were mainly used to adsorb hydrophobic drugs directly onto the lipophilic surface of NDs. There is an enormous number of publications reporting adsorption of small molecules including drugs such as DOX, epirubicin, daunorubicin, mitoxantrone, paclitaxel or cis-platin[85]. All these small molecular drugs cannot be discussed here in detail but are nicely summarized in a review by Lai *et al.*[76].

1.6 Biomedical Applications

NDs are interesting candidates for biomedical applications because their fluorescence, which shows no bleaching, is ideal for tracing the delivery of active compounds, such as drugs or genes. Furthermore, NDs have been successfully applied for photothermal and photodynamic therapy. After a detailed discussion about the biocompatibility of NDs, a major requisite for biomedical applications, delivery of drugs and genes as well as photothermal and photodynamic applications are described.

Biocompatibility

As many applications aim at *in vitro* or *in vivo* usage, the biocompatibility of NDs is an important parameter. The core of NDs is composed of almost only carbon and is chemically inert. Therefore, there is no risk of cytotoxicity caused by the core. However, in contrast to the core, the surface of NDs is chemically complicated and can contain various reactive groups as well as metal impurities which could cause toxicity. In general, it is very difficult to make a statement about the biocompatibility of NDs because the toxicity depends highly on the present surface of the NDs. For example, NDs which were bought and used as-received often showed a higher toxicity compared to NDs which were bought and further oxidized by the customers.[20] Mainly, this might be due to metal impurities or remaining sp^2 carbon which can increase the toxicity.[76] Therefore, proper purification of the surface of NDs is highly crucial. Furthermore, the synthesis rout of NDs also influences the cytotoxicity. For instance, the average NDs produced by HPHT possess a better biocompatibility compared to NDs synthesized by detonation.[128] Next to this, applying NDs at high concentrations showed toxicity as well. An increased level of apoptosis was observed at concentrations of 200–1000 µg/ml of NDs. In contrast, a concentration below 50 µg/ml of NDs showed no evident toxicity.[20] Immunotoxicity, indicated by an increased secretion of chemokines and cytokines, was studied using NDs in many different cell types. For instance, mesenchymal stem cells which were incubated with carboxylated NDs did not alter secretion of cytokines, chemokines, and growth factors.[20] Furthermore, the oxidative stress level of cells caused by NDs was investigated. For example, no signs of oxidative stress have been observed in neuroblastoma cells, macrophages, keratinocytes, and PC-12 cells.[20] The cell division and differentiation was not altered after applying NDs to 3T3-L1 embryonic fibroblasts, neuron cells derived from embryonal carcinoma stem cells, and *C. elegans*.[76] Nontoxicity of NDs was evaluated in zebra fish embryo.[129] Only higher concentrations of NDs (>1 mg/ml) effected the early developmental states of the embryo. Another risk for *in vivo* application is induced-toxicity by the accumulation of NDs in organs especially because NDs are not biodegradable. Biodistribution of NDs *in vivo* showed mostly accumulation of NDs in liver lung tissues after 2 h. Zhang *et al.*[130] reported an inflammatory response in the lung. Furthermore, Yuan *et al.*[131] showed accumulation of NDs in murine lung and liver for at least up to 28 days. These NDs mostly accumulated in macrophages in the liver, maybe captured by the reticuloendothelial system. There

are not much data on excretion of NDs. In rats, excretion of NDs took place over the urinary tract.[128]

In summary, it remains difficult to make a general statement about the biocompatibility of NDs because NDs occur in different shapes and sizes which complicates comparisons in the literature. Furthermore, batch-to-batch variations influence the toxicity as well. However, NDs seem to be more biocompatible compared to other carbon nanomaterials[132,133] or semiconductor QDs[134].

Drug Delivery

The therapeutic effect of hydrophobic drugs is often limited by their poor stability and solubility. To overcome the insolubility, hydrophobic drugs are attached or loaded onto NPs. In addition, due to the bigger size of NPs, these systems possess often a longer circulation time *in vivo* and benefit from the enhanced permeability and retention (EPR) effect. Non-fluorescent NDs were used in preliminary studies for drug delivery mainly by non-covalent adsorption of the drug molecule onto the surface of NDs.[135,136] For this purpose, negatively charged NDs were mixed with positively charged DOX and DOX-ND composites (NDX) were precipitated by addition of NaCl. The Cl⁻ ions were substantial for the drug loading. Without NaCl, a drug loading of only 0.5 wt% of DOX was observed whereas in presence of NaCl, over 10 wt% adsorption of DOX onto the NDs was achieved.[135] Release of the DOX from the NDs was achieved by desalination. NDXs were incorporated successfully into murine macrophages as well as human colorectal carcinoma cells and showed slow and sustained DOX release.[135] *In vivo*, the NDX complex showed increased apoptosis and tumor growth inhibition in murine liver tumor and mammary carcinoma models compared to conventional DOX.[136]

With improvement of the ND quality and especially the defect centers, FNDs became highly attractive for drug delivery applications because they also facilitate imaging in conjugation with therapy.[137] FNDs are especially interesting for tracing drug delivery because they possess a fluorescence without bleaching combined with tunable sizes in the "nano"-regime and a very high carrier stability. There are various publications about drug delivery and imaging using FNDs. Therefore, only a selection will be discussed in this chapter. The group of Weil[115] developed a protein-based copolymer coating for FNDs which allowed a pH-responsive cleavage of DOX (see Figure 9A). HSA was cationized by transferring all negative charges into positives by reacting with ethylene diamine and statistical PEGylation using NHS activated PEG (MW=2000 Da). Afterwards, the protein was denatured and the disulfide bridges were reduced to attach maleimide functionalized DOX *via* Michael addition reactions. DOX was linked to the maleimide through a hydrazone bond which allowed cleavage and drug release in an acidic environment. Carboxylated FNDs were simply coated by non-covalent adsorption of the protein due to its positive charges and by hydrophobic interactions of the lipophilic domains of the protein. Through this method, around 80 nm sized coated FNDs were received which were stable in various buffer systems. A lysosomal mimicking

36

environment revealed a drug release of 70% after 24 h following a two-step procedure. Firstly, the protein backbone was partly degraded by proteases and secondly, the drug was released by pH-induced cleavage of the hydrazone bond. Furthermore, the DOX release was studied by confocal laser scanning microscopy (CLSM) *in vitro* (see Figure 9B). Interestingly, DOX signals were found in endosomes, cytosol, and nuclear, while FND signals were only found in endosomes indicating the release and escape of DOX in the endosome (see Figure 9C–E). Confocal studies strongly benefited from the fact that the fluorescence of FNDs does not bleach in contrast to DOX. Therefore, it was possible to distinguish between the fluorescence of FNDs and DOX. Finally, the coated FNDs revealed antitumor efficacy in a human breast cancer xenograft model. The cancer xenograft viability as well as the tumor growth were significantly decreased compared to conventional DOX.
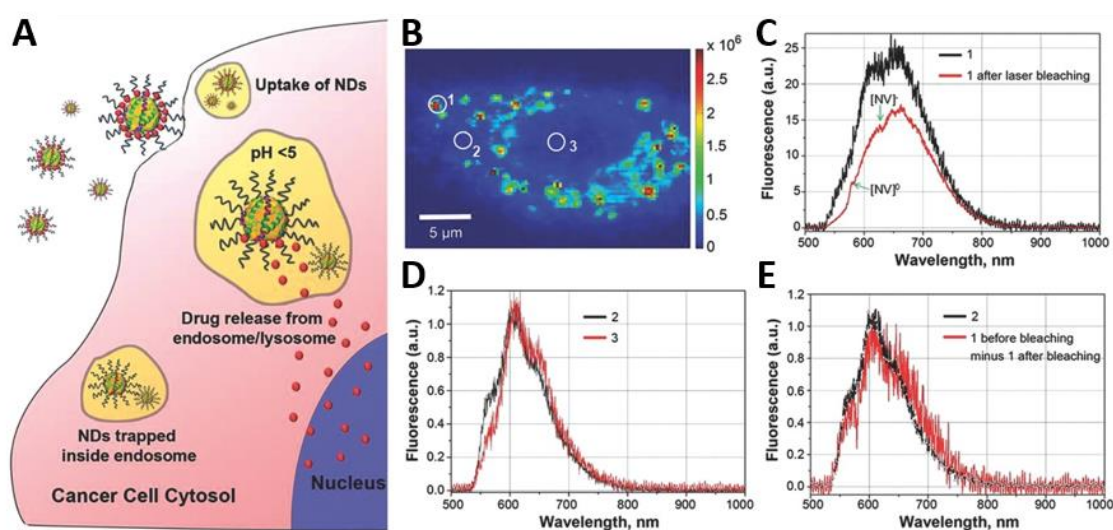

Figure 9 (A) Illustration of the drug release inside endosomes due to the acidic environment. (B) Confocal image of fluorescent nanodiamonds inside A549 cells. (C) Fluorescence intensity spectra of the area in circle 1 in (B) which captured an endosome. After laser bleaching of the fluorescence of doxorubicin, the characteristic fluorescence intensity spectrum of FNDs remained. This indicated the presence of FNDs in the endosome. (D) Fluorescence intensity spectra of circle 2 and 3 in (B) showing only a typical spectra of doxorubicin. This indicates that in the cytosol (circle 2) and nucleus (circle 3) only free doxorubicin is present. (E) Subtraction of the FND typical spectrum from the original spectrum of circle 1 showed a typical spectrum of doxorubicin which matches with the spectrum of circle 2. (A)–(E) are adapted with permission from Wu, Y.; Ermakova, A.; Liu, W.; Pramanik, G.; Vu, T. M.; Kurz, A.; McGuinness, L.; Naydenov, B.; Hafner, S.; Reuter, R.; et al. Programmable Biopolymers for Advancing Biomedical Applications of Fluorescent Nanodiamonds. *Adv. Funct. Mater.* **2015**, *25* (42), 6576–6585. Copyright (2015) John Wiley and Sons.

PG-coated FNDs too were used for various drug delivery applications. A particularly interesting system combined drugs and targeting groups was composed of RGD as a targeting unit and either DOX[62,66] or cisplatin[63] as drug (see Figure 10A+B). In the first step, PG coating was prepared by ring-opening polymerization of glycidol. To introduce RGD peptides, some hydroxyl groups of PG were transferred into azide groups using tosyl chloride followed by substitution of the tosylates with azido groups. RGD propiolic

amide was attached by Cu(II) catalyzed click chemistry. To introduce DOX, a pH cleavable hydrazine moiety was synthesized. Thereafter, bis(4-nitrophenyl) carbonate reacted with the hydroxyl groups of the PG and after the formation of p-nitrobenzoate, the p-nitrophenyl group was substituted by hydrazine. Finally, DOX was attached under formation of a hydrazone bond.[66] Under acidic conditions (pH 5.0), a drug release of 63% was shown. *In vitro*, the PG coating hindered unspecific uptake of NDs into A549 tumor cells and U937 macrophages which is an important prerequisite for targeted delivery. The RGD units target the integrin receptor $\alpha_v\beta_3$ which is overexpressed in many tumor cell types. RGD modified PG-coated NDs showed increased uptake into A549 (integrin receptor $\alpha_v\beta_3$ positive) and no difference in uptake into U937 macrophages (integrin receptor $\alpha_v\beta_3$ negative) compared to NDs without RGD. Consequently, after incubating cells with DOX attached to NDs, A549 showed almost no cytotoxic effect in the absence of RGD but a strong cytotoxicity in the presence of RGD while U937 macrophages showed no cytotoxicity with or without RGD (see Figure 10C+D). In another study, the same material was used to investigate a dendritic cell-mediated delivery system to stimulate glioblastoma cell immunogenicity.[62] Recently, in a deeper study was shown, that stimulation of glioblastoma cell immunogenicity was achieved by activation of autophagy induced by PG-coated FNDs connected to DOX.[59]
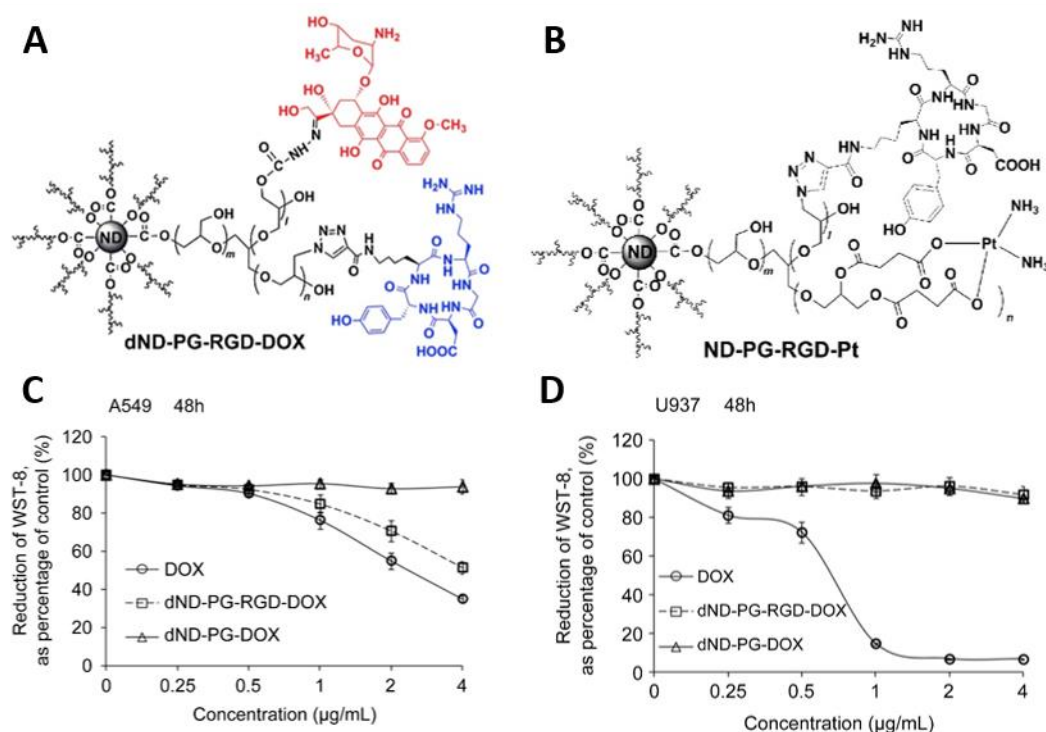

Figure 10 (A) Scheme of a polyglycerol coated nanodiamond (ND) which was functionalized with doxorubicin and cyclic RGD. (B) Scheme of a polyglycerol coated ND which was functionalized with cisplatin and cyclic RGD. (C) A549 (integrin receptor $\alpha_v\beta_3$ positive) showed an enhanced cytotoxic effect after applying NDs with cyclic RGD. (D) U937 macrophages (integrin receptor $\alpha_v\beta_3$ negative) showed no cytotoxic effect for NDs with or without cyclic RGD. (A)+(C)+(D) are adapted with permission from Zhao, L.; Xu, Y.-H.; Akasaka, T.; Abe, S.; Komatsu, N.; Watari, F.; Chen, X. Polyglycerol-Coated Nanodiamond as a Macrophage-Evading Platform for Selective Drug Delivery in Cancer Cells. *Biomaterials* **2014**, *35* (20), 5393–5406. Copyright (2014) Elsevier. (B) is adapted with permission from Zhao, L.; Xu, Y. H.; Qin, H.; Abe,

S.; Akasaka, T.; Chano, T.; Watari, F.; Kimura, T.; Komatsu, N.; Chen, X. Platinum on Nanodiamond: A Promising Prodrug Conjugated with Stealth Polyglycerol, Targeting Peptide and Acid-Responsive Antitumor Drug. *Adv. Funct. Mater.* **2014**, *24* (34), 5348–5357. Copyright (2014) John Wiley and Sons.

Based on the PG-coated NDs, a system for delivery of cisplatin, a chemotherapy medication, was invented.[63] To introduce cisplatin, carboxylic acid groups were created by nucleophilic ring-opening of succinic anhydride. Afterwards, cis-(NH$_3$)$_2$Pt(II) moiety was immobilized through ligand exchange to form coated FNDs with a size of 64 nm. Under acidic conditions, the platinum was released two times faster than at pH 7.4. Further addition of RGD allowed specific uptake into U87MG cells but not into HeLa cells. Finally, the cytotoxic effect was investigated in U87MG cells which was comparable to free cisplatin.[63]

FNDs connected to the drug paclitaxel and the antibody cetuximab were designed to target epidermal growth factor receptor (EGFR)-positive triple-negative breast cancer (TNBC) cells.[111] Paclitaxel-2'-succinate, a paclitaxel derivative containing a free carboxylic acid group, was covalently coupled to amine-terminated FNDs.[138] Paclitaxel-2'-succinate contains an ester which is pH-responsive and allows release of paclitaxel under acidic conditions.[138] Afterwards, cetuximab, an antibody binding EGFR, was attached to the surface of FNDs by non-covalent adsorption.[111] The complex was tested in various breast cancer tumor cell types and showed targeted delivery only in EGFR positive (MDA-MB-231) but not EGFR negative (MCF-7) tumor cell lines. *In vitro*, FNDs with cetuximab showed a significant induced apoptosis level of MDA-MB-231 cells compared to FNDs without cetuximab or the control. Finally, the MDA-MB-231 tumor inhibition *in vivo* was most enhanced after treatment using FNDs coated with cetuximab compared to FNDs without cetuximab or the control.[111]
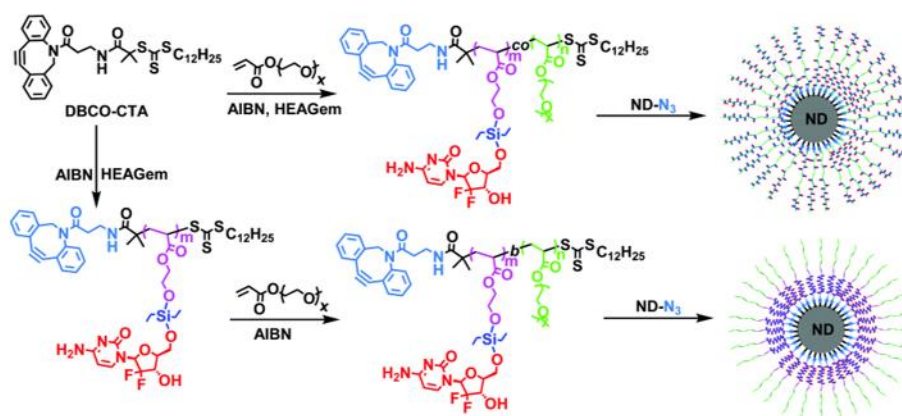

Figure 11 Reaction rout to form nanodiamonds (ND) coated with block copolymers or statistical copolymers containing the drug gemcitabine. Adapted with permission from Lai, H.; Lu, M.; Lu, H.; Stenzel, M. H.; Xiao, P. PH-Triggered Release of Gemcitabine from Polymer Coated Nanodiamonds Fabricated by RAFT Polymerization and Copper Free Click Chemistry. *Polym. Chem.* **2016**, *7* (40), 6220–6230. Copyright (2016) The Royal Society of Chemistry.

Carboxylated FNDs were successfully functionalized with a mitochondrial localizing sequence (MLS) peptide as well as folic acid for delivery of DOX.[93] To achieve this,

carboxylated FNDs were activated by EDC/Sulfo-NHS and coupled to the amine groups of MLS peptides and PEGylated folic acids. Afterwards, DOX was physically adsorbed to the surface of FNDs. These constructs showed strong uptake into HeLa and MCF-7 cells due to folic acid receptor-mediated endocytosis and were selectively localized in mitochondria. FNDs lacking the MLS peptide were only localized in lysosomes. After adsorption of DOX, a significantly improved cytotoxicity of MCF-7/ADR cells was revealed compared to free DOX. MCF-7/ADR cells possess a transporter protein which pumps free DOX, located intracellular, out of the cell and hinders DOX to reach the nucleus. MLS peptide-modified FNDs loaded with DOX were transported into mitochondria where DOX was released and caused cell death.[93]

Gemcitabine was attached to FNDs functionalized with polymers to improve the IC_{50} value in AsPC-1 cells, a human pancreas adenocarcinoma, as well as to trace the drug delivery.[51] The prodrug gemcitabine is intracellular converted by deoxycytidine kinase into its therapeutically active metabolites but applications are often hindered by the short half-life during blood circulation. The life-time can be improved by attaching gemcitabine to a polymer backbone. To allow RAFT polymerization, gemcitabine was connected to a polymerizable unit *via* an acid sensitive bifunctional silyl ether linker. The acid sensitive linker allowed drug release under acidic conditions. Next to the drug, oligo ethylene glycol methyl ether acrylate was used as a co-monomer and block copolymers as well as statistical copolymers were synthesized (see Figure 11). The polymers were end-functionalized with a DBCO group which allowed to graft the polymers onto the surface of azide-terminated FNDs by copper free click-chemistry. However, *in vitro* experiments revealed that block copolymer polymers do not behave noticeably different to the statistical polymers regarding cytotoxicity which was only in the same range as for free gemcitabine.[51]

FNDs functionalized with transferrin and DOX were synthesized to induce clathrin-dependent and transferrin receptor-mediate endocytosis.[82] Firstly, transferrin was mixed with DOX to form transferrin-DOX complexes. Afterwards, carboxlyated FNDs were activated using EDC/NHS chemistry and after purification, the transferrin-DOX complexes were covalently attached to the surface of FNDs. However, it is very likely that next to the covalently bound monolayer of transferrin-DOX further layers of transferrin-DOX were formed by non-covalent, physical adsorption. The final construct had an average size of 235 nm. The construct was strongly uptaken into cells expressing the transferrin receptor such as HeLa and HepG2. The uptake could be reduced by blocking the receptor with free transferrin or using cells (HEK293) which express a low level of receptors. Consequently, the complex showed a higher cytotoxicity in cells expressing more transferrin receptors. However, *in vivo*, no difference in the inhibition of the tumor growth was measured of mice treated with free DOX or the construct indicating the absence of the targeting effect. Most probably, a protein corona was formed *in vivo*, shielded the transferrin coating and hindered the interaction of transferrin with the transferrin receptor.[82]

40

In summary, in the beginning NDs were used as drug carriers by absorption of hydrophobic drugs onto the surface of NDs. However, simple absorption causes the risk of uncontrolled leaking of drugs during *in vivo* applications. Therefore, in the past years, drugs and targeting groups were mainly attached to the coating materials of FNDs, while FNDs functioned as imaging probes. On this basis, FNDs are not good drug carrier regarding loading of drugs but due to their fluorescence, which shows no bleaching, FNDs are perfect imaging probes for tracing drug delivery. Targeted delivery of coated FNDs was shown for several different cell lines as well as intracellular. Next to tracing of drug delivery, FNDs also offer the potential to function as sensors of drug release in future.

Gene Delivery

As it has been already discussed in chapter 1.5, most of the DNA/RNA delivery systems are composed of a FND core coated with a positive material which can further condensate DNA/RNA. The positively charged polymer PEI (800 Da) is used most often in literature.[96,98,99,122] Coating of carboxylated FNDs was achieved by mixing and stirring a solution of FNDs and a solution of PEI. After purification, DNA/RNA was added and physically adsorbed onto the PEI-coated NDs. Ho *et al.*[96] adsorbed luciferase plasmids or GFP plasmids onto PEI (800 Da)-coated NDs to transfect cells. These constructs revealed a high uptake and a good biocompatibility in HeLa cells. Furthermore, these constructs showed the highest transfection rate for luciferase and GFP in HeLa cells compared to systems where the plasmids were adsorbed to only PEI, amine-terminated NDs, or carboxylated NDs.[96] The group of Benson used PEI-coated FNDs to transport antisense RNA into cancer cells.[99,122] Inside the cells, the antisense RNA was released and inhibited oncogenic microRNA. Successful knockdown of microRNA-135b in mammary carcinoma was shown in 3D organoids as well as *in vivo*.[99]

A layer-by-layer hybrid system was invented by the group of Sheng[124] to deliver microRNA into TNBC cells. Carboxylated FNDs were non-covalently coated with one layer of positively charged protamine sulfate firstly. After purification, microRNA (miR-34a) was physically adsorbed to form a second layer. Protamine sulfate was added to form a third layer. Finally, folic acid was physically adsorbed. The different layers were characterized by zeta-potential measurements due to the opposite charges of the coating materials. The final construct had a size of around 200 nm in diameter. miR-34a has been identified as a tumor suppressor which is dramatically downregulated in TNBC cells. The construct showed a high uptake in MDA-MB-231 cells, a TNBC cell line. In contrast to untreated cells, the treated cells showed an increased level of miR-34a as well as a reduction of the expression of the target gene, *Fra-1*. These results were confirmed in a MDA-MB-231 xenograft mouse model which also revealed an inhibited tumor growth compared to control groups.[124]
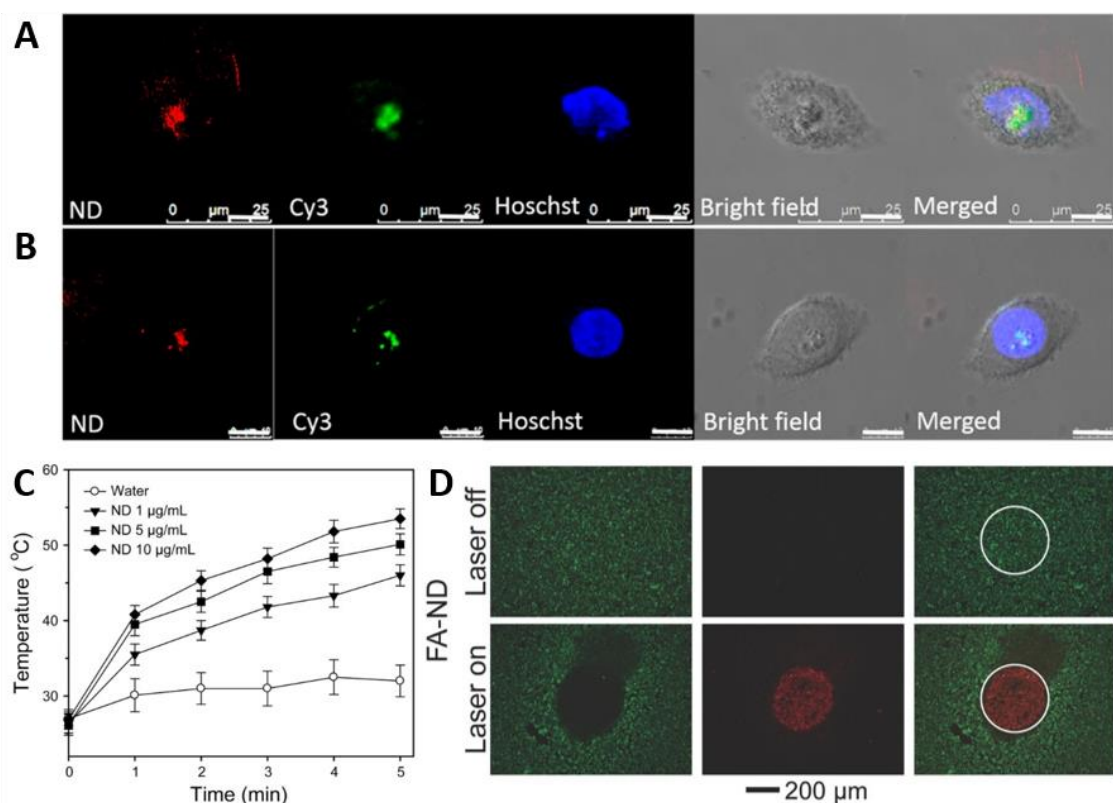
Figure 12 Fluorescence nanodiamonds (FNDs) coated with a peptide containing a TAT and a NLS sequence showed uptake into the nucleus of (A) MCF-7 and (B) HeLa cells. Scale bar = 10 µm. (C) FND clusters revealed a photothermal effect upon irradiation with a laser beam (808 nm, 2 W/cm^2). (D) FND clusters showed successful photothermal applications *in vitro* with spatial control by adjusting the laser beam diameter (circle). (A)+(B) are adapted with permission from Leung, H. M.; Chan, M. S.; Liu, L. S.; Wong, S. W.; Lo, T. W.; Lau, C.-H.; Tin, C.; Lo, P. K. Dual-Function, Cationic, Peptide-Coated Nanodiamond Systems: Facilitating Nuclear-Targeting Delivery for Enhanced Gene Therapy Applications. *ACS Sustain. Chem. Eng.* **2018**, *6* (8), 9671–9681. Copyright (2018) American Chemical Society. (C)+(D) are adapted with permission from Ryu, T.-K.; Baek, S. W.; Kang, R. H.; Choi, S.-W. Selective Photothermal Tumor Therapy Using Nanodiamond-Based Nanoclusters with Folic Acid. *Adv. Funct. Mater.* **2016**, *26* (35), 6428–6436. Copyright (2016) John Wiley and Sons.

Delivery of antisense oligonucleotides into the nucleus using a FND system was shown by the group of Lo[118]. Carboxylated FNDs were non-covalently coated with a peptide containing a TAT and a NLS segment. After purification, antisense oligonucleotide ANA4625 was loaded by physical adsorption to form the final construct with a size of around 280 nm. In cells, this antisense oligonucleotide causes suppression of target *bcl-2* and *bcl-xL* mRNA/protein expressions and induces cell apoptosis. Due to the TAT and NLS sequences, the constructs were located in the nucleus of MCF-7 and HeLa cells (see Figure 12A+B). However, the transport into nucleus was only successful for smaller FNDs. Compared to gene silencing in the cytoplasm, the antisense activity of ANA 4625 was much stronger in MCF-7 cells for the construct which was transported into the nucleus.[118]

Photothermal and Photodynamic Therapy

Photothermal therapy is based on the effect that the energy of absorbed photons by a material is not released by emission of light but by production of heat (by emission of phonons).[139] Due to their huge Stokes shift, FNDs might be assumed as good materials for photothermal therapies. However, so far only one publication reported a sufficient photothermal effect of bare FND nanoclusters.[140] These FND nanoclusters were prepared using a fluidic device and an acetone and a water phase.[141] After only 5 min of irradiation (808 nm, 2 W/cm^2), an increase in temperature of around 25 °C was discovered at a very low concentration of FND nanoclusters (10 µg/ml, see Figure 12C). Furthermore, these nanoclusters showed effective killing of cells *in vitro* (see Figure 12D) as well as a therapeutic effect *in vivo*.[140] For individual FNDs, only very weak photothermal effects are reported which are insufficient for biomedical applications.[72,75] Hence, these FNDs were further functionalized with dopamine/L-DOPA and indocyanine green (ICG)[72,75], chlorin e6[142], or polyaniline[143] to amplify the effect. The group of Mrówczyński[72] designed a system composed of FNDs coated by a polydopamine shell which allowed further loading of ICG by physical adsorption. After irradiation (808 nm laser, 2 W), FNDs coated with polydopamine revealed an increase in temperature of 25 °C (without ICG) or 50 °C (with ICG) compared to bare FNDs (5 °C). *In vitro*, the ICG loaded polydopamine-coated FNDs showed a moderate cytotoxicity and demonstrated spatial control due to the focus of the laser beam.[72] We contributed to the field of photothermal therapy by inventing a system based on FNDs which were coated by poly(L-DOPA), transferrin, and ICG.[75] This work will be elaborated in chapter 3.4.

In contrast to photothermal effects, photodynamic therapy requires a photo-sensitizer which generates cytotoxic reactive oxygen species (singlet oxygen, $^1O_2$) after irradiation. To achieve this, NDs were connected to chlorin e6[142], periodic mesoporous organosilica[144], or BODIPY-phthalocyanines[145]. For example, chlorin e6, from "chlorophyll *a*", is a typical photosensitizer but the use has been limited due to its intrinsic hydrophobicity.[142] Therefore, phase-change material NPs were synthesized containing chlorin e6 and NDs. These NPs show both, a photodynamic effect caused by the chlorin e6 and a photothermal effect due to the NDs. Furthermore, the photothermal effect induced a controlled release of chlorin e6 from the NPs.[142]

1.7 Imaging

Imaging methods have become powerful tools over the last decades allowing investigations of cellular processes up to diagnostics in a whole human body depending on the applied technique. These different imaging techniques require specific imaging probes. For example, while electron microscopy (EM) needs probes with a dense structure which can scatter electrons, fluorescence microscopy requires probes which can absorb and emit light. However, often imaging probes only fit for one technique. Due to its special optical features, FNDs are promising candidates for various imaging methods. The dense carbon lattice of NDs enables EM in cells and Raman imaging in cells and organisms. The NV centers of FNDs, which do not bleach, are ideal for tracking and super-resolution microscopy in cells and for ODMR imaging in organisms. Furthermore, the use of other defect centers enables photoacoustic imaging in organisms. The potential of hyperpolarization might allow magnetic resonance imaging (MRI) in future. In this chapter, different imaging techniques are discussed in detail.

Comparison to Other Optical Particles and Organic Dyes

Before the details of imaging using FNDs are discussed, it is of interest to compare FNDs to other existing optical particles or small organic dyes. One emerging class of optical particles are QDs. As mentioned in chapter 1.2, the fluorescence of FNDs originates from defect centers in the crystal lattice. Therefore, the emission wavelength is independent of the size of FNDs and the brightness depends on the number of color centers located inside the crystal lattice. Consequently, larger FNDs are usually brighter because they possess more defect centers. However, the emission wavelength can be tuned by using different color centers. In contrast, QDs show a size-dependent change in the emission wavelength. Furthermore, QDs are blinking which is not the case for FNDs. The brightness of QDs is usually much higher than the brightness of FNDs.[14]

The group of Gipson[146] studied the brightness and photostability of red or near-IR fluorescent nanomaterials in detail. For their comparison, FNDs of a size of 120 nm were used. Compared to small organic dye such as Alexa 647 or QDs, FNDs do not possess a high mass based brightness which is not surprisingly because FNDs consists of mainly carbon atoms which are not contributing to the fluorescence (see Figure 13A). However, comparing the molar brightness, FNDs and fluorescent beads, which are fluorescent dyes embedded in a polymer or silica matrix, are showing the highest values (see Figure 13B). That the fluorescence cannot be bleached is an outstanding property of FNDs, which is highly attractive for tracking. As depicted in Figure 13C, most of the other materials showed strong bleaching after only a few minutes under continuous laser illumination. QDs were bleached after 25 min but only FNDs and nanorubies showed no bleaching.[146]
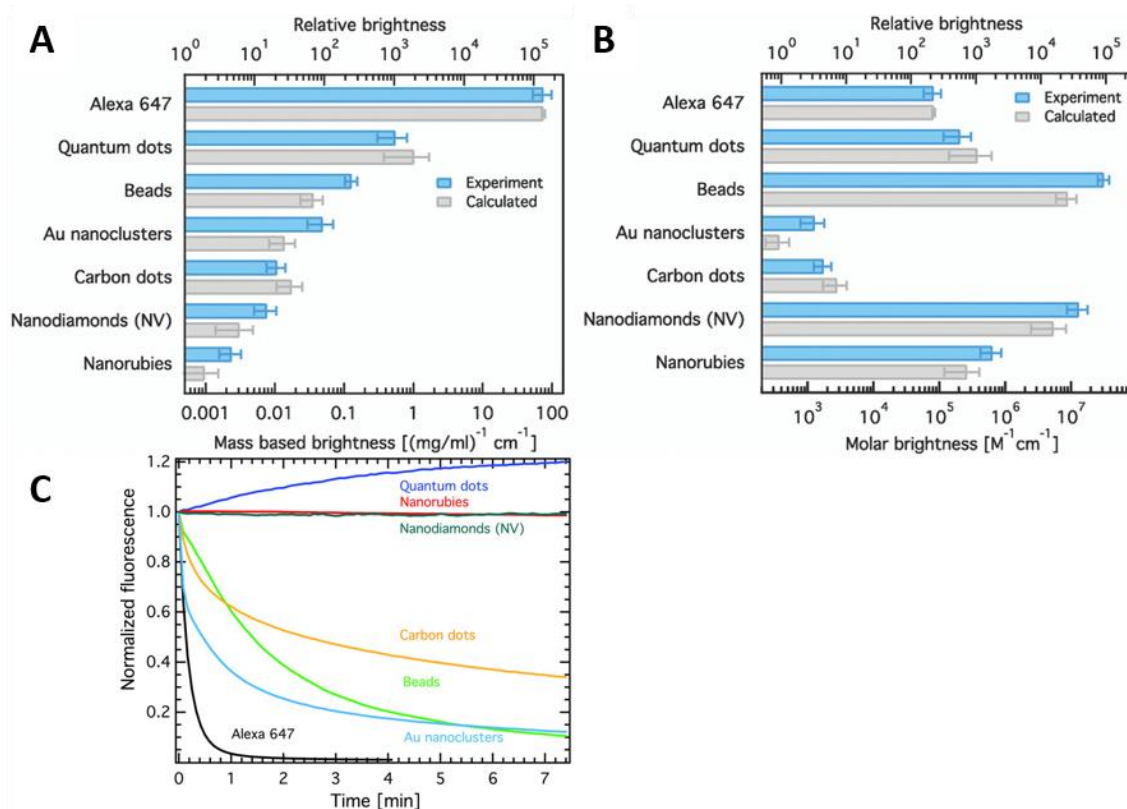
Figure 13 (A) Comparison of the relative brightness and the mass based brightness of different optical materials. (B) Comparison of the relative brightness and the molar brightness of different optical materials. (C) Comparison of the quenching behavior of different optical materials up to 7 min of irradiation. (A)–(C) are adapted with permission from Reineck, P.; Francis, A.; Orth, A.; Lau, D. W. M.; Nixon-Luke, R. D. V.; Rastogi, I. Das; Razali, W. A. W.; Cordina, N. M.; Parker, L. M.; Sreenivasan, V. K. A.; et al. Brightness and Photostability of Emerging Red and Near-IR Fluorescent Nanomaterials for *Bioimaging. Adv. Opt. Mater.* **2016**, *4* (10), 1549–1557. Copyright (2016) John Wiley and Sons.

Fluorescence Imaging in Cells

FNDs are highly attractive for tracking experiments *in vitro* due to their presumably high biocompatibility and because the NV centers cannot be bleached. Especially, the high photostability of FNDs allows tracking over a long time frame. 2D single particle tracking (SPT) in HeLa cells using FNDs was introduced in 2007 by the groups of Chang and Fann for the first time.[147] SPT of FNDs in 3D was achieved using a home-built servo control fluorescence microscopy system which was able to follow the fluorescence signal of a single FND in HeLa cells in real-time (see Figure 14A).[148] Furthermore, two-photon excitation enabled to suppress the autofluorescence of the HeLa cells strongly compared to single-photon excitation.[148] The SPT allowed to study biological processes such as receptor-mediated endocytosis using folic acid-modified FND.[149] Next to this, FNDs can be used as optical tags to follow the movements of proteins on the cell membrane or intracellular.[60,64,126,150]   For example, TGF-β signaling was investigated using SPT of TGF-conjugated FNDs.[150] SPT allowed to calculate the diffusion coefficient of TGF-modified FNDs after binding to the TGF-β receptor. This revealed new insights of the dynamics such as three different states of diffusion: immobile, intermediate, and

fast which are probably related to the different steps in the signaling. The group of Tochio was tracking an interleukin receptor by using FNDs.[60] Interleukin-18 receptor alpha chain was recombinant modified with a β-lactamase-tag. The β-lactamase-tag allowed to bind FND which were connected to an ampicillin structure specifically to the receptor *via* the tag. Using SPT, trajectories of the receptors could be imaged and diffusion coefficients could be calculated.[60] Recently, the group of Chang[64] presented a strategy to biorthogonal label membrane proteins with alkyne-functionalized FNDs (see Figure 7A). The first strategy was to introduce an azide group into sialoglycoproteins, located in the membrane, by adding azide-modified sugars into the culture of HeLa cells. Afterwards, alkyne-functionalized FNDs could bind to these sugar motives by Cu(I) catalyzed click chemistry. Another strategy was to use azide-modified anti-integrin α5 antibodies (see Figure 14C). Integrin α5 belongs to the group of sialoglycoproteins which is located in the membrane. After incubating human fibroblasts with the antibody, alkyne-functionalized FNDs were again conjugated to the antibodies by click chemistry to allow tracking. SPT allowed to image random and active movement of the labeled integrin α5 as well as calculation of the diffusion coefficient (see Figure 14B). Furthermore, FND allowed to track the movements of integrin α5 for long time (2 h) which is not possible with commercial dyes because of bleaching. Long-time tracking revealed movements of the integrin α5 to front side of the cell migration route which could not be visualized by short-term imaging.[64]

Next to tracking the movement of membrane protein, FNDs were also used to reveal dynamics inside of cells. Tunneling nanotubes are thin membranous bridges connecting cells and are important for exchange of proteins and cytoplasmic components. Tracking of FNDs was successfully used to study these transport dynamics in HEK293T[151], endothelia cells (bEnd.3)[116], and neuronal cells[116]. In HEK293T cells a random movement of FNDs in the cytoplasm was revealed followed by a direct movement once the FNDs entered the tunneling nanotube.[151] We confirmed these findings using bEnd.3 and neuronal cells.[116] Furthermore, transport of FNDs inside the branches of dissociated neurons were studied (see Figure 14D).[152] By tracking FNDs, many parameters of the transport could be assessed such as stop and go phases, velocity, run length, pausing time, and the diffusion coefficient among others.[152]

Tracking of FNDs was also used to visualize the movement of whole cells.[153–155] The group of Chao[155] prepared various FND-bearing cancer cells to track their movement. Furthermore, labeling of lung stem/progenitor cells using FNDs was achieved too which allowed tracking of the cells *in vivo*.[154]

The group of Hollenberg[156] performed quantum measurement and tracking of the orientation of FNDs inside living cells. Firstly, the group revealed that FNDs located inside HeLa cells can be distinguished from each other by ODMR spectroscopy. Because every FND is unique, the ODMR spectra of a FND is like a fingerprint which does not change even after long time periods and movements of FNDs. Furthermore, FNDs only

with a single NV⁻ center can be used to track the orientation of the NV center. By applying a magnetic field, the ODMR peaks split into m_s=+1 and m_s=−1. The magnitude of the splitting depends on the orientation of the NV⁻ center in regard to the magnetic field. The group of Hollenberg showed that tracking of the orientation is even possible in HeLa cells.[156]
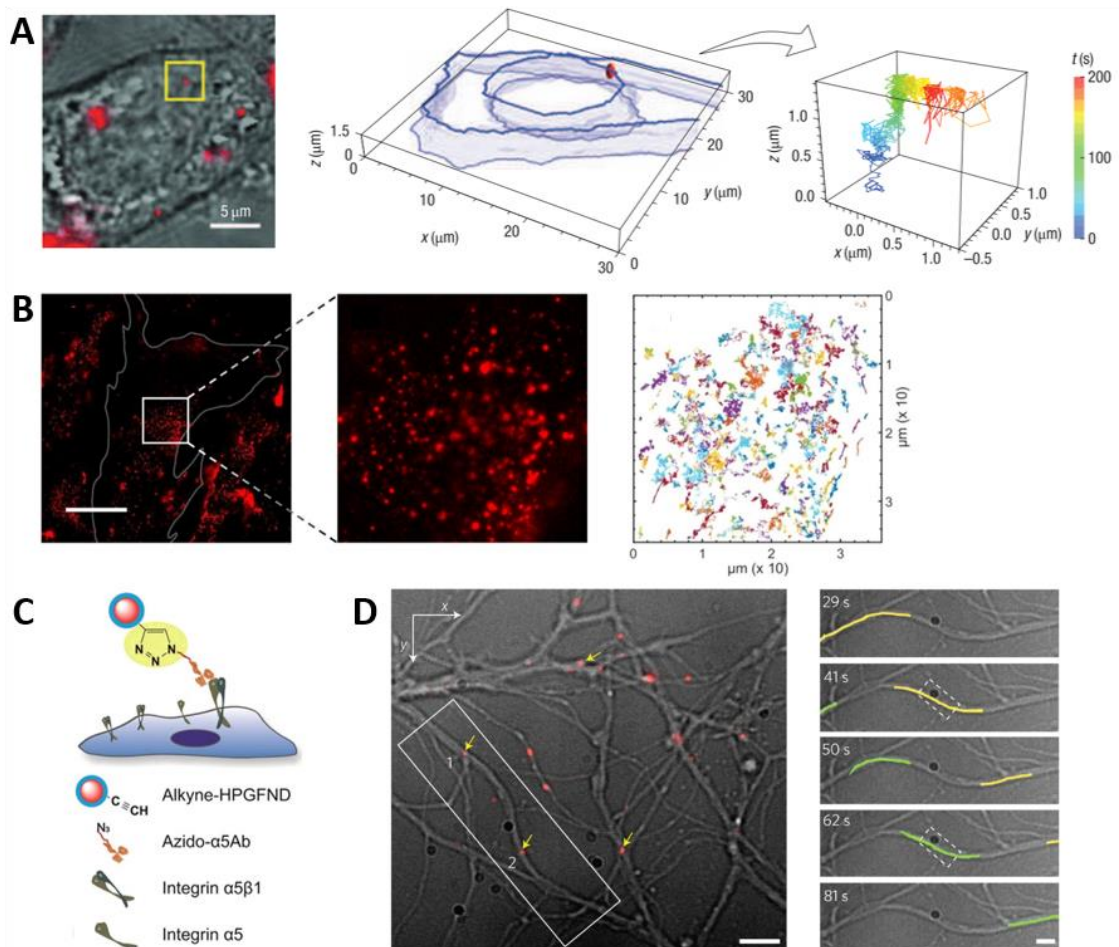

Figure 14 (A) Bight-field and epifluorescence images of a cell after uptake of fluorescent nanodiamonds (FNDs). A FND was tracked over time and the three-dimensional trajectory (shown in pseudo-color) and displacements are shown. Scale bar = 5 μm. (B) The movement of integrin α5 on the membrane was investigated after labelling them with FNDs. Scale bar = 50 μm. (C) Illustration of labelling of integrin α5 with FNDs. Firstly, azide modified antibodies against integrin α5 were bound. Secondly, alkyne-modified FNDs were able to bind to the antibodies. (D) Tracking of FNDs allowed investigation of transport mechanism in branches of dissociated neurons. Scale bar = 5 μm. (A) is adapted with permission from Chang, Y.-R.; Lee, H.-Y.; Chen, K.; Chang, C.-C.; Tsai, D.-S.; Fu, C.-C.; Lim, T.-S.; Tzeng, Y.-K.; Fang, C.-Y.; Han, C.-C.; et al. Mass Production and Dynamic Imaging of Fluorescent Nanodiamonds. *Nat. Nanotechnol.* **2008**, *3* (5), 284–288. Copyright (2008) Springer Nature. (B)+(C) are adapted with permission from Hsieh, F.-J.; Sotoma, S.; Lin, H.-H.; Cheng, C.-Y.; Yu, T.-Y.; Hsieh, C.-L.; Lin, C.-H.; Chang, H.-C. Bioorthogonal Fluorescent Nanodiamonds for Continuous Long-Term Imaging and Tracking of Membrane Proteins. *ACS Appl. Mater. Interfaces* **2019**, *11* (22), 19774–19781. Copyright (2019) American Chemical Society. (D) is adapted with permission from Haziza, S.; Mohan, N.; Loe-Mie, Y.; Lepagnol-Bestel, A.-M.; Massou, S.; Adam, M.-P.; Le, X. L.; Viard, J.; Plancon, C.; Daudin, R.; et al. Fluorescent Nanodiamond Tracking Reveals Intraneuronal Transport Abnormalities Induced by Brain-Disease-Related Genetic Risk Factors. *Nat. Nanotechnol.* **2017**, *12* (4), 322–328. Copyright (2016) Springer Nature.

Next to NV centers, also FNDs containing SiV were used for imaging.[157–159] Applying both kinds of FNDs, containing either SiV or NV centers, to cells at the same time allowed multi-color imaging.[158]

Fluorescence Imaging in Organisms

Using FNDs for imaging *in vivo* was already performed in various organisms including *Caenorhabditis elegans*[160–162], *drosophila melanogaster* embryos[163], mice[116,154,162,164], miniature pig[165], and zebrafish embryos[129,166]. The group of Chang[166] used BSA-coated FND to study their dynamics in zebrafish yolk cells by SPT. These FNDs showed unidirectional and stop-and-go traffic in the yolk cell with a velocity of 0.19–0.40 µm/s. Furthermore, these FNDs stayed in dividing cells even when the embryos developed into larvae and into adult fish.[166] FNDs were applied in a very similar way to study diffusion in both furrow periplasm and sub-nuclear periplasm of a *drosophila melanogaster* embryo.[163] SPT of single FNDs allowed to record and analyze the trajectory and calculate the diffusion coefficient and mean driven velocity. The diffusion rates of FNDs in the furrow periplasm and sub-nuclear periplasm differed by the factor of 10.
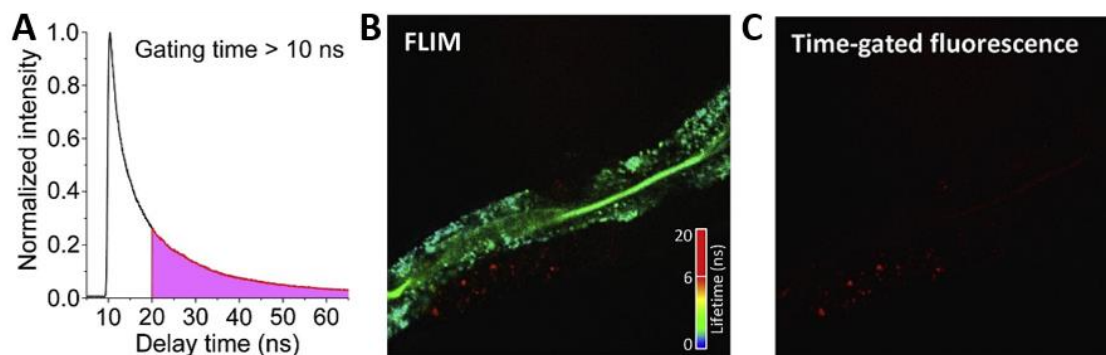

Figure 15 (A) The fluorescent decay time of FNDs. The shaded area represents the fluorescence signal collected during gating time. (B) Fluorescence lifetime imaging microscopy image of *C. elegans*. (C) Image showing only fluorescent decay time > 10 ns. (A)–(C) are adapted with permission from Kuo, Y.; Hsu, T.-Y.; Wu, Y.-C.; Chang, H.-C. Fluorescent Nanodiamond as a Probe for the Intercellular Transport of Proteins in Vivo. *Biomaterials* **2013**, *34* (33), 8352–8360. Copyright (2013) Elsevier.

Time gating was discovered to be an elegant method to remove the background signal *in vivo* because NV⁻ (11.6 ns) possess a substantial longer fluorescence life time compared to cell or tissue autofluorescence (1–4 ns).[160] The group of Chang[160] showed a much increased image contrast of FNDs in *C. elegans* using fluorescence lifetime imaging microscopy with a gating time longer than 10 ns (see Figure 15A–C). The same group translated this technique to enable wide-field time-gated fluorescence imaging in mice.[164] Using Raman shifting, a green laser (532 nm) was changed to an orange laser (599 nm) to prevent strong absorption and emission of hemoglobin, a main factor of autofluorescence. Furthermore, a nanosecond intensified charge-coupled device, a highly sensitive camera capable of high-speed gating operation, was used as the detector.[164] So far the most sophisticated *in vivo* experiments were performed by the group of Chang[165] using mini pigs. Albumin-coated FNDs were used for quantitative

tracking of mesenchymal stem cells in miniature pigs. However, experiments were performed after sacrificing the pigs but not in living animals, which would be most desirable.[165]

Optically Detected Magnetic Resonance Microscopy

Next to time gating, ODMR microscopy also enabled background free imaging.[68,162,167,168] ODMR microscopy benefits from the effect that the fluorescence of NV⁻ centers can be stimulated by microwaves. As discussed previously, using a microwave of 2.87 GHz results in a reduction of about 30% of the fluorescence intensity of the NV⁻ centers. However, the fluorescence of other optical objects is not effected in the presence of a microwave. During ODMR microscopy, images are acquired with and without 2.87 GHz microwave irradiation (see Figure 16A+B). Afterwards, pixel-by-pixel subtraction between these two images is performed to remove the background. This technique was successfully applied to image background free *in vivo*[162], e.g. *C. elegans* and mice, as well as fine nanostructures such as a single actin filament[68].
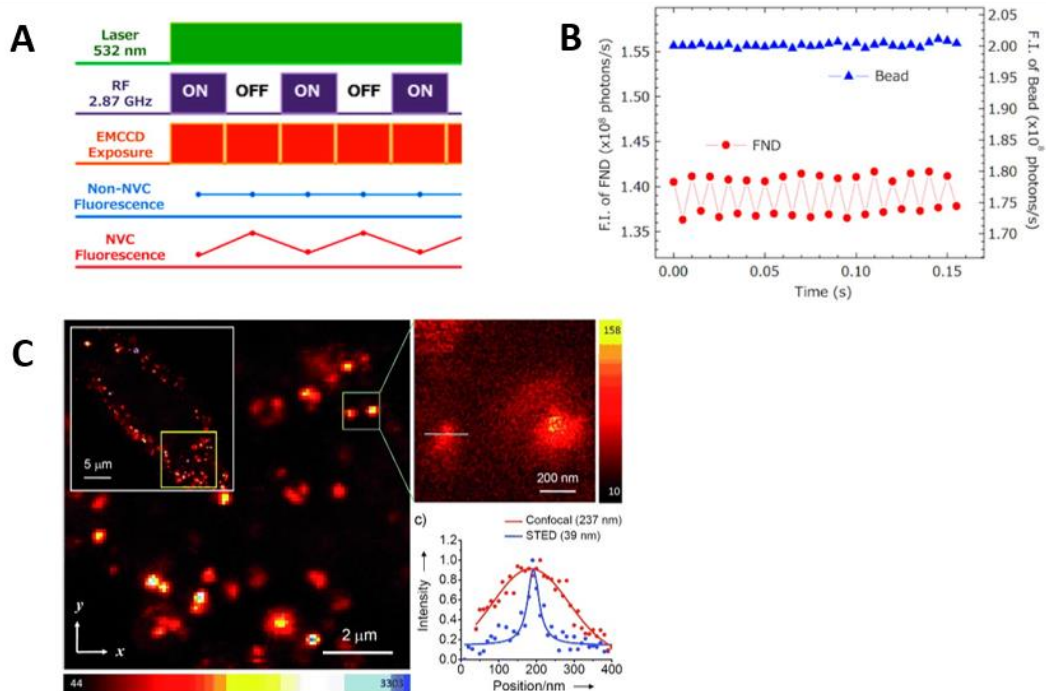

Figure 16 (A) Time chart of an ODMR measurement. The laser is continuously on and a microwave (radiofrequency) is alternatingly switched on and off. (B) Fluorescence spectra over time of an optical bead and a fluorescent nanodiamond (FND). The optical bead is not influenced by the microwave but the fluorescence intensity of the FNDs dropped whenever the microwave is witched on. (C) Left: Image of FNDs inside a cell recorded by confocal microscopy. Right top: Image of FNDs inside a cell recorded by stimulated emission depletion (STED) microscopy. Right bottom: Improvement of the resolution provided by STED microscopy. (A)+(B) are adapted with permission from Igarashi, R.; Yoshinari, Y.; Yokota, H.; Sugi, T.; Sugihara, F.; Ikeda, K.; Sumiya, H.; Tsuji, S.; Mori, I.; Tochio, H.; et al. Real-Time Background-Free Selective Imaging of Fluorescent Nanodiamonds in Vivo. *Nano Lett.* **2012**, *12* (11), 5726–5732. Copyright (2012) American Chemical Society. (C) is adapted with permission from Tzeng, Y.-K.; Faklaris, O.; Chang, B.-M.; Kuo, Y.; Hsu, J.-H.; Chang, H.-C. Superresolution Imaging of Albumin-Conjugated Fluorescent

A new imaging technique of FNDs was presented by the group of Yablonovitch[169]. The group designed a magnetic field free point which is surrounded by a magnetic field. By applying a microwave (2.87 GHz) and moving the magnetic field free point over a sample, only FNDs which are located in the magnetic field free point showed a decrease in fluorescence due to the microwave. FNDs which were exposed to a magnetic field showed no decrease in fluorescence because of the Zeeman splitting of the m_s=±1 and consequently, the microwave resonance change by a rate of 56 GHz T^{-1}. This technique allowed high sensitivity for detecting ~100 fg NDs and high spatial resolution (~100 µm).[169]

Correlative Microscopy

Correlative light–electron microscopy (CLEM) has emerged quickly in the field of bioimaging because it combines the individual strengths of both light microscopy (LM) and EM. LM allows fast screening as well as live and multi-color imaging. In contrast, EM can be only performed on fixed samples in grey scale but provides the highest resolution. Because FNDs can be visualized by EM, due to their dense carbon lattice, and LM, without bleaching, they became prominent candidates for CLEM.[114,170–173] The group of Schirhagl[173] used FNDs of 40 nm and 70 nm size and proofed that the fluorescence of the FNDs survived fixation and embedding which is necessary for the EM. Hsieh *et al.*[171] applied FNDs, which were encapsulated in a lipid layer, on HeLa cells to target CD44. CLEM was used, transmission electron microscopy (TEM) and scanning electron microscopy, to reveal the successful binding of the FNDs to the cellular membrane. However, in these two publications EM served mainly to reveal the cellular structure in nanoscale while the FNDs were only visualized by LM. The group of Hänninen[170] improved the contrast of FNDs in TEM, so that it was possible to visualize clusters of FNDs in intracellular vesicles. The positions of the clusters in TEM matched with the fluorescence signals recorded by stimulated emission depletion (STED) microscopy. We[114] contributed to this field significantly by improving the contrast of FNDs in TEM further and performing TEM tomography which allowed to visualize individual FNDs forming a cluster in 3D. Furthermore, using energy filtered transmission electron microscopy (EFTEM) enabled to visualize single FND which are not belonging to a cluster for the first time intracellular. This work is described in detail in chapter 3.1.

Super-Resolution Microscopy

In the past decades, super-resolution microscopy revolutionized the field of bioimaging indicated by the huge number of techniques which are available up to date.[174] Among these techniques, STED, stochastic optical reconstruction (STORM), and photoactivated localization microscopy are the most popular because they are commercialized and user-friendly. Because of their high photostability, FNDs gained great interest for STED microscopy instead of STORM microscopy which requires

stochastic blinking. The group of Hell[175] revealed an optical resolution of 7.6 nm in a bulk diamond containing NV centers using ground state depletion microscopy, a STED related method. Using a solid immersion lens, the resolution could be even improved down to 2.4 nm.[176] Furthermore, classical STED microscopy was enabled by implementing a depletion laser with a wavelength above 700 nm.[177,178] A resolution of around 10 nm was achieved resolving NV centers in 40–250 nm sized FNDs.[178] However, STED microscopy in combination with FNDs has not found many applications in bioimaging so far. The group of Chang[106] used albumin-coated FNDs and investigated their potential as biomarkers in cells by STED. Compared to classical CSLM, the resolution dropped from around 240 nm to 40 nm upon STED microscopy (see Figure 16C).

Photoacoustic Imaging

Photoacoustic (PA) imaging is based on the PA effect where light is converted into sound. Compared to classical fluorescence microscopy, PA imaging has the great advantage that light only needs to go one-way through the tissue and that the detection is based on ultrasound generation. This allows deeper tissue penetration.[179] Because of their strong optical absorbance, FNDs are promising candidates as contrast agents for PA imaging.[58,180–185] Due to better tissue penetration, usually NIR light is used for PA imaging. Because NDs have only limited absorbance in the NIR, the group of Forrest[185] prepared radiation-damaged NDs. Using a high-dose He$^+$ irradiation, they created a lot of vacancies in the diamond crystal lattice which are termed GR1 defects. These GR1 defects possess a zero-phonon line at 741 nm and showing absorption up to 800 nm. Most importantly, the fluorescence quantum yield of the GR1 defects is only around 1%. Therefore, 99% of the energy absorbed by these GR1 defects is released by nonradiative processes such as vibration heating, which may contribute to the PA signal intensity. Using NDs containing GR1 defects led to a 71-fold higher PA signal on a molar basis compared to gold nanorods. In rodents these ND could be clearly imaged 3 mm below the skin.[185] Based on this, the same group[58] functionalized radiation-damaged NDs with an anti-human epidermal growth factor receptor 2 (HER2) peptide and showed targeted delivery into HER2-positive tumors as visualized by PA imaging.

Raman Imaging

The group of Zhi[85,186–188] performed several studies regarding Raman imaging of NDs. Upon irradiation using a laser with a wavelength of 532 nm, NDs possess a sharp Raman peak at 1332 cm^{-1} which can be easily distinguished from the Raman bands, 2800–3200 cm^{-1}, caused by symmetric stretching vibration of CH_2 and CH_3 groups of the lipids in HeLa cells (see Figure 17A–C). Raman mapping allowed to image the interaction of EGF-modified NDs with the EGF receptor on the membrane of HeLa cells.[187] Furthermore, the group performed 3D confocal Raman imaging to get an better understanding of the location of EGF- or cetuximab-modified NDs in cells (see Figure 17D).[85,188]
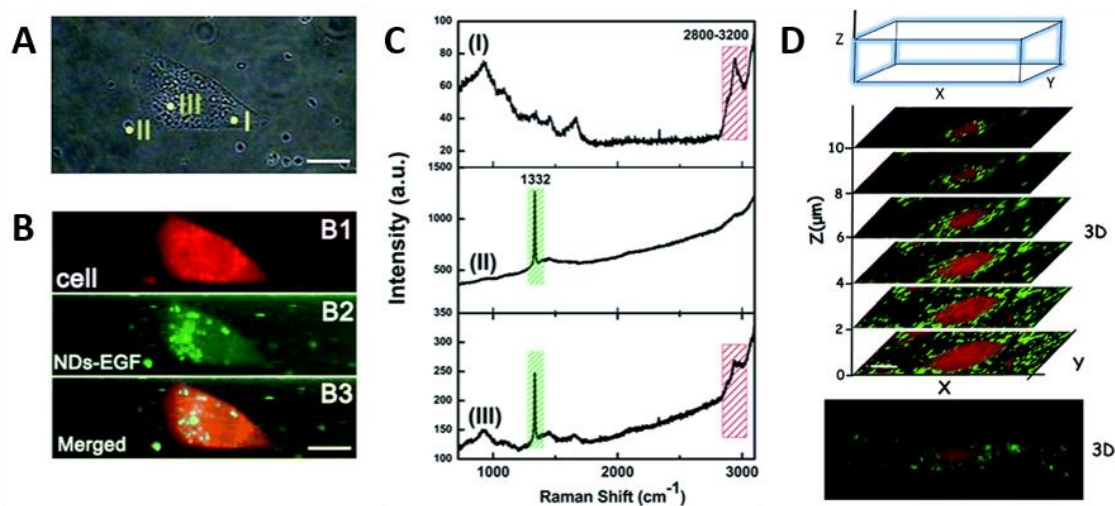
Figure 17 (A) Positions inside a cell which were investigated by Raman imaging. Scale bar = 10 μm. (B) Top: Raman signal of the cellular structures (2800–3200 cm^{-1}); Center: Raman signal of nanodiamonds (1332 cm^{-1}); Bottom: Merged Raman signals of the cellular structures (red) and nanodiamonds (green). Scale bar = 10 μm. (C) Corresponding Raman spectra of (I) cytoplasm, (II) extracellular nanodiamonds, and (III) nanodiamonds in a cell. The labeled regions are shown in (A). (D) 3D Raman imaging of nanodiamonds (green) uptaken into cells. (A)–(C) are adapted with permission from Li, D.; Chen, X.; Wang, H.; Yu, Y.; Liu, J.; Wang, Y.; Zhang, J.; Zheng, M.; Zhi, J. Nanodiamonds as Raman Probes for Specifically Targeted Bioimaging: Visualization and Mechanism Study of the Biorecognition between Nanodiamonds-EGF and EGFR. *RSC Adv.* **2017**, *7* (21), 12835–12841. Published by The Royal Society of Chemistry. (D) is adapted with permission from Chen, X.; Li, D.; Wang, H.; Jiao, Y.; Wang, H.; Yu, Y.; Zhi, J. Fabrication of an EGF Modified Nanodiamonds-Based Anti-Cancer Drug Targeted Delivery System and Drug Carrier Uptake Visualization by 3D Raman Microscopy. *RSC Adv.* **2016**, *6* (50), 44543–44551. Copyright (2016) The Royal Society of Chemistry.

Next to Raman imaging, coherent anti-Stokes Raman scattering (CARS) microscopy was used to image single non-fluorescent NDs as well.[189] In general, CARS microscopy is promising for bioimaging as it is faster than Raman imaging and possesses a high spatial resolution because CARS is a non-linear process in contrast to Raman scattering.[189] The group of Borri[189] has not only shown that non-fluorescent NDs exhibit strong CARS but also that CARS microscopy can be used to image NDs in HeLa cells.

Magnetic Resonance Imaging

At the moment there are three ways how NDs are used for MRI. Firstly, classical contrast agents such as gadolinium[190–194] or iron[195,196] are attached to NDs. Gadolinium has been introduced by functionalizing the ND surface with chelator molecules like DOTA derivates[190,191] or DTPA[193] which can bind Gd^{3+} ions or by grafting Gd^{3+} ions directly onto the surface of NDs[192]. Iron doped NDs were produced by ion implementation.[195,196] However, in these systems NDs just function as carrier and the improvement in the MRI contrast is only due to the decreased diffusion time. Secondly, paramagnetic impurities on the surface of NDs can be polarized and the spin polarization can be transferred to surrounding H^1 spins of the water molecules.[197] This can be achieved due to the Overhauser effect which describes the transfer of polarized electron

spins to nuclear spins. NDs provide partially polarized electron spins in form of paramagnetic impurities such as NV centers, substitutional nitrogen (P1) centers, and unpaired electrons at the surface. By using a radiofrequency, the transfer of spins can be induced creating MRI contrast on-demand. The group of Rosen[197] has shown this principle. Thirdly, hyperpolarization of ^{13}C spins in NDs with the option to polarize liquid solutions by spin diffusion in future is under study.[198,199] The electron spins of NV$^−$ centers can be hyperpolarized and a transfer of these spins to the nuclear spins of surrounding ^{13}C atoms in the ND lattice is possible. A major problem to transfer hyperpolarization protocols from bulk diamonds to NDs is the constantly changing orientation of the NV$^−$ centers in NDs due to their mobility in solution. To overcome this limitation, the group of Pines[198] described now an orientation-independent, optical ^{13}C hyperpolarization method at room temperature for diamond powder.

In summary, FNDs are outstanding imaging probes because they can be applied widely across different techniques. Due to its high photostability, the fluorescence of the NV centers is ideal for tracking of FNDs in cells and simple organisms. Furthermore, the long fluorescent lifetime enables time gating measurements to suppress the background. ODMR microscopy is another method which has been successfully applied to reduce the background. Next to background-free imaging, high resolution has been achieved using STED microscopy or EM. Even EM of FNDs in cells was possible because of the dense carbon lattice of NDs. The dense carbon core of NDs has also enabled Raman imaging due to its distinct scattering properties. Other than NV centers, defect centers, which showed a bad quantum yield, have been applied for photoacoustic imaging because they converted light into heat. Finally, MRI has been performed with NDs.

1.8 Nanoscale Sensing

Next to imaging, one important research field is nanoscale sensing. Nanoscale sensing would enable to reveal changes in temperature, pH value or ion flow during biological processes. Furthermore, often certain dysfunctions or disorders are associated with a change in temperature or pH value as cancer tissue.[200] NV$^-$ centers in diamond are promising candidates for various sensing application because due to their magneto-optical properties they possess a high spatial resolution and sensitivity.[201]

Electron Spins

As mentioned in chapter 1.2, external electron spins can be measured by magnetic relaxometry which is more sensitive than ODMR spectroscopy.[174] During a T1 measurement the spin equilibration is disturbed by applying laser light. Because many electrons in the excited state with a total spin of $m_s=\pm1$ relax over a singlet state into the ground state and changing the total spin to $m_s=0$, more NV$^-$ centers possess a spin of $m_s=0$ due to the laser irradiation (see Figure 2A). After switching off the laser, the equilibrium is restored after a certain time (T1 time) by spin-lattice relaxation (see Figure 3B). This T1 relaxation is effected by spin-lattice interaction and external spin bath in the surrounding. Because in the NV$^-$ center the magnetic and optic properties are coupled, $m_s=0$ is brighter than $m_s=\pm1$, the T1 time can be measured by the decrease of the photoluminescence intensity (see Figure 3B). Based on this method it was possible to sense the spin of Gd^{3+} ions[202–205] and Fe^{3+} ions[109] using FND containing NV$^-$ centers. The group of Jacques[202] was able to measure Gd^{3+} ions with a sensitivity of around 14 electron spins detected within 10 s using 10 nm FNDs containing a single NV$^-$ center. The group of Hollenberg[203] improved this system which allowed to measure Gd^{3+} concentration inside the bilayer of an artificial cell membrane represented by a lipid bilayer on a glass surface (see Figure 18A+B). The group of Jelezko[109] coated FNDs with Ferritin, a Fe^{3+} containing protein, and showed a shortening of the spin-spin relaxation time T2 and the spin-lattice relaxation time T1 compared to uncoated FNDs.
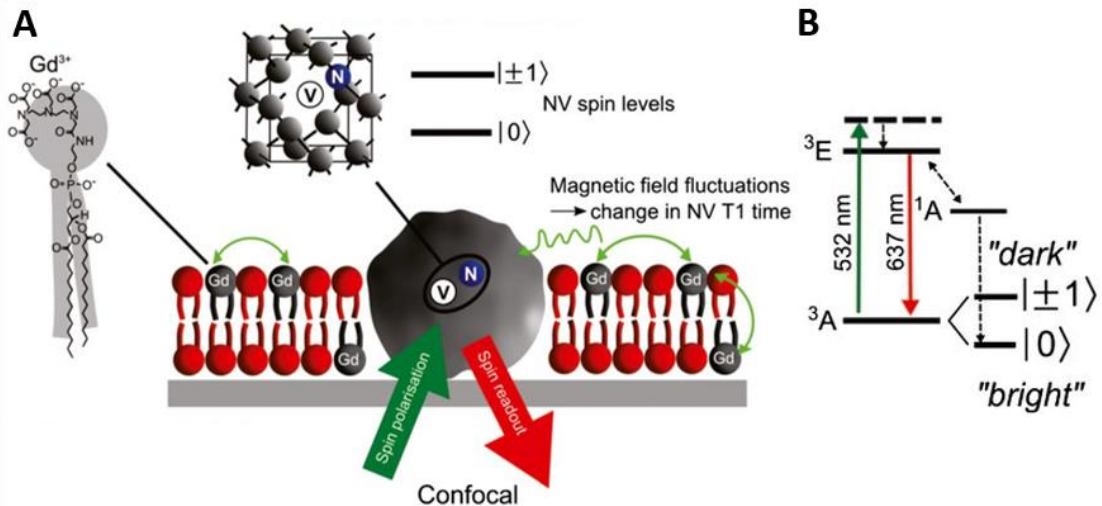
Figure 18 (A) Experimental setup to sense Gd^{3+} ions. A lipid bilayer was prepared on a glass surface and a nanodiamond was incorporated. Phospholipids were modified with a Gd^{3+} ion to enable a movement of Gd^{3+} along the membrane. The change in the spin concentration was measured by T1 time. (B) Energy diagram of negatively charged nitrogen vacancy containing nanodiamonds illustrating the "dark" and "bright" states. (A)+(B) are adapted with permission from Kaufmann, S.; Simpson, D. A.; Hall, L. T.; Perunicic, V.; Senn, P.; Steinert, S.; McGuinness, L. P.; Johnson, B. C.; Ohshima, T.; Caruso, F.; et al. Detection of Atomic Spin Labels in a Lipid Bilayer Using a Single-Spin Nanodiamond Probe. *Proc. Natl. Acad. Sci.* **2013**, *110* (27), 10894–10898.

Electric and Magnetic Fields

In the year 2008 three important publications, two by the group of Lukin[206,207] and one by the group of Wrachtrup[208], reported the principle of nanoscale magnetic sensing using NV⁻ centers in diamonds. The group of Lukin[207] proposed a method of high magnetic sensitivity either a single NV⁻ center containing ND connected to the tip of an atomic force microscopy (AFM) for high spatial resolution or a bulk diamond with a high density of NV⁻ centers for higher sensitivity. While the single ND improved the spatial resolution down to 10 nm, the bulk diamond served as an optical magnetic-field imager with a sensitivity approaching a few fT $Hz^{-1/2}$.[207] A slightly different approach was used by the group of Wrachtrup[208]. The group combined an AFM and confocal setup which was furthermore equipped with a microwave generator to enable electron spin resonance (ESR) measurements. A diamond nanocrystal containing a single NV⁻ center was placed onto the glass substrate and a magnetic tip was used in the AFM setup. As discussed in the introduction, an increasing external magnetic field resulted in separation of the m_s=±1 (see Figure 19A). Calculation of the external magnetic field strength was possible from the ESP resonance ω_1 and ω_2. Moving the cantilever in x and y position enabled to measure a line profile of the magnetic field strength and calculating the exact position of the NV⁻ center.[208]

Furthermore, the group of Wrachtrup[209] designed an experiment to sense an electric-field in 3D using a single nitrogen-vacancy defect center spin in a bulk diamond (see Figure 19B). Hereby, a sensitivity of an electric-field of 202±6 V cm^{-1} $Hz^{-1/2}$ was achieved.

The group of Hollenberg[210] were monitoring ion-channel function in a cell-membrane using a diamond nanocrystal. A single ND connected to an AFM tip was brought in close contact to an ion channel to measure the change in the quantum decoherence time.

Temperature

Sensing of temperature using FNDs was performed in living cells for the first time in 2013[211] and gained more interest in the following years.[15,88,212] As discussed in chapter 1.2, the zero-field splitting of $m_s=0$ and $m_s=\pm1$ is temperature depended. Therefore, a change in temperature can be measured by ODMR spectroscopy (to recap see Figure 3D). The group of Harada[15] showed that their method to sense the temperature is highly independent of pH value, ion concentration, viscosity, molecular interaction, and organic solvent. To perform temperature measurements in cells, the group used fixed cells to create a calibration curve with known temperatures against measured zero-field splitting values. This allowed to measure the temperature in cells more precisely (see Figure 19C). Building up on this principle, the group of Hollenberg[212] measured the change of the zero-field splitting values of many FND located in different parts of a cell to receive an intracellular temperature map of primary cortical neurons (see Figure 19D). The group of Chang[88] prepared ND-gold nanorods hybrids. Upon irradiation with a laser (808 nm), the gold nanorods converted photon energy into heat. It was possible, to calculate the increase in temperature by measuring the change of the zero-field splitting of the NV^- centers.
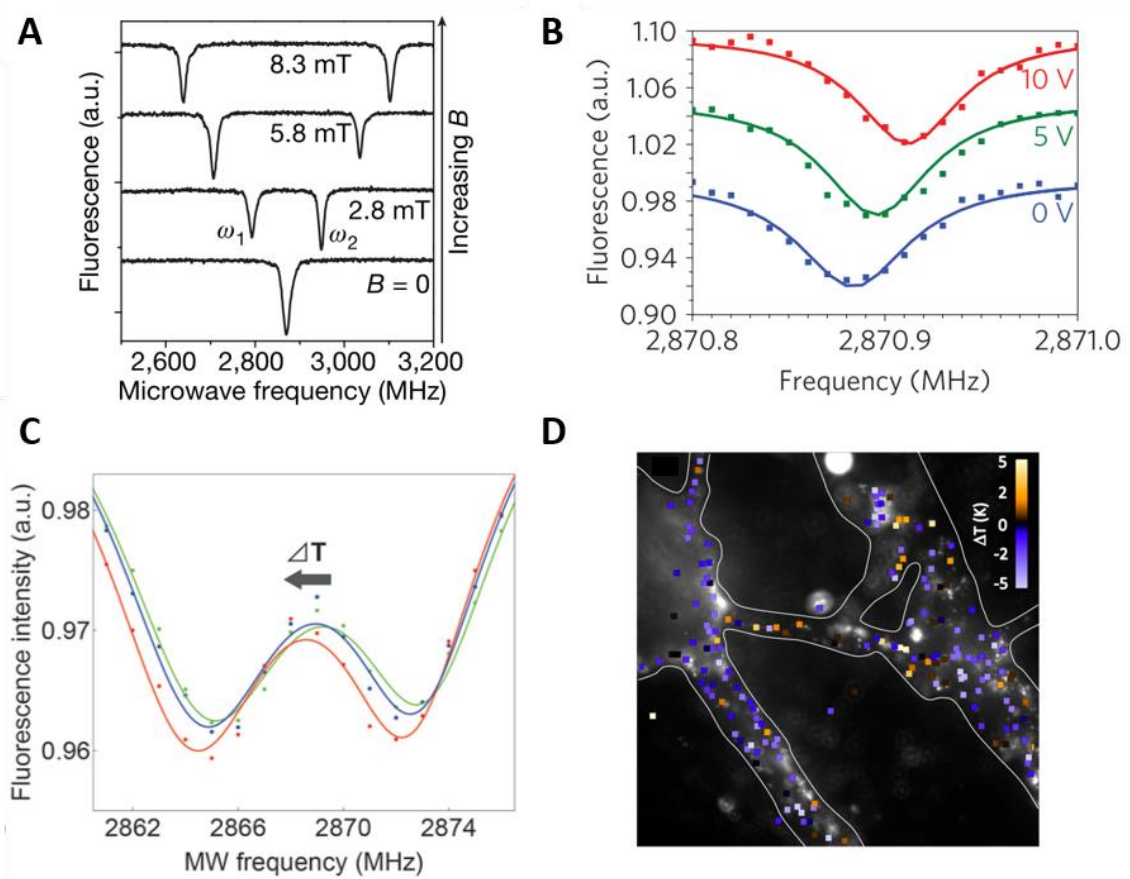
Figure 19 (A) Optically detected magnetic resonance (ODMR) spectra at different external magnetic fields illustrating the effect of the magnetic strength on the separation of $m_s=\pm1$. (B) ODMR spectra at different electric fields revealing the change in the frequency of the zero-field splitting. (C) ODMR spectra at different temperatures showing the change in the frequency of the zero-field splitting. (D) Temperature mapping in primary cortical neurons. (A) is adapted with permission from Balasubramanian, G.; Chan, I. Y.; Kolesov, R.; Al-Hmoud, M.; Tisler, J.; Shin, C.; Kim, C.; Wojcik, A.; Hemmer, P. R.; Krueger, A.; et al. Nanoscale Imaging Magnetometry with Diamond Spins under Ambient Conditions. *Nature* **2008**, *455* (7213), 648–651. Copyright (2008) Springer Nature. (B) is adapted with permission from Dolde, F.; Fedder, H.; Doherty, M. W.; Nöbauer, T.; Rempp, F.; Balasubramanian, G.; Wolf, T.; Reinhard, F.; Hollenberg, L. C. L.; Jelezko, F.; et al. Electric-Field Sensing Using Single Diamond Spins. *Nat. Phys.* **2011**, *7* (6), 459–463. Copyright (2011) Springer Nature. (C) is adapted with permission from Sekiguchi, T.; Sotoma, S.; Harada, Y. Fluorescent Nanodiamonds as a Robust Temperature Sensor inside a Single Cell. Biophys. *Physicobiology* **2018**, *15*, 229–234. Copyright: https://creativecommons.org/licenses/by-nc-sa/4.0/. (D) is adapted with permission from Simpson, D. A.; Morrisroe, E.; McCoey, J. M.; Lombard, A. H.; Mendis, D. C.; Treussart, F.; Hall, L. T.; Petrou, S.; Hollenberg, L. C. L. Non-Neurotoxic Nanodiamond Probes for Intraneuronal Temperature Mapping. *ACS Nano* **2017**, *11* (12), 12077–12086. Copyright (2017) American Chemical Society.

Because the sensitivity of NV⁻ centers is much better for magnetic fields than for changes in temperature, the group of Li[213] proposed to use magnetic NPs which are docked to a stimulus-responsive hydrogel. FNDs were coated with poly(N-isopropylacrylamide) and afterwards magnetic NPs were connected to the coating. Upon temperature changes, the hydrogel either expanded or shrunk which consequently changed the distance between the NV⁻ centers in the FNDs and the

magnetic NPs. According to the distance, the $m_s=+1$ and $m_s=-1$ spin states either strongly or weakly drifted apart due to the magnetic field in the ODMR spectra.

pH-Values

The group of Igarashi[214] revealed that uniformly carboxylated FNDs are sensitive to a pH ranging from pH 3 to pH 7. In a basic environment, the carboxylic acid groups located on the surface of the FNDs turn more and more negative. These negative charges are probably perturbing the electric field in the FNDs and shortening the T_1 time. Indeed, this shortening of the T_1 time was found between pH 3 and pH 7 but the T_1 time stayed constant for pH > 7. To cover also measurements of pH values > 7, FNDs were coated with poly-L-cysteine which contains thiol groups with a pK_a of 8–11. The coated FNDs showed a clear shortening of the T_1 time for an increasing pH from pH 7 to pH 11.

Electric Charges

Next to sensing electric charges by measuring of the T1 time as it has been done for pH-values, it is also possible to sense them by measuring the ratio of the charge states of the NV centers because the charge state of coating materials influences the charge state of the NV centers.[98] For instance, FNDs which were coated with positively charged PEI showed an enhanced NV^0 to NV^- center ratio due to manipulation of the Fermi level position by the surface band bending. In contrast, after adsorbing negatively charged DNA onto the FNDs-PEI the number of NV^- centers increased again. Because NV^0 and NV^- centers possess different zero-phonon lines, the charge ratio can be easily revealed by measuring the photoluminescence intensity fluorescence. This allowed to follow the release of DNA in cells.

Optical and Anti-Brownian Electrokinetic Trapping

Recently, FNDs were applied for different trapping approaches such as optical trapping[215,216], near-field optical trapping[217], and anti-Brownian electrokinetic (ABEL) trapping[218]. The group of Awschalom[216] used an infrared laser (1,064 nm) to trap an ensemble of FND particles. In parallel, a 532 nm laser was applied to enable optically detected ESR measurements with 3D control in solution. This precise trapping of FNDs also allows mapping of magnetic fields in 3D in solution. An estimated sensitivity of about 50 µT/$\sqrt{\text{Hz}}$ was achieved by this approach.[216] The group of Reece[215] improved the optical trapping system by eliminating the spin decoherence effect of the trapping laser which allowed measurements of the spin–lattice relaxation time (T1). Because optical trapping requires very high laser powers when the objects become small (< 100 nm), the group of Radenovic[218] performed ABEL trapping. ABEL trapping cancels the Brownian motion of objects by applying an electric field which induces an electrokinetic drift. This approach allowed optically detected ESR measurements of FND with a size of 30 nm.[218]

In summary, FNDs are promising candidates for biomedical applications, bioimaging, and nanoscale sensing due to their outstanding properties. In the field of biomedical applications, FNDs have mainly been used as imaging probes for tracing drug delivery. Coating materials have been designed which enabled to attach drugs *via* responsive linkers. These responsive linkers released the drug at the targeting site. In the field of bioimaging, FNDs are of interest due to their special optical properties such as a high photostability without bleaching, a long fluorescence lifetime, a dense carbon-based core structure, a high reflection index, a distinct Raman scattering, and a fluorescence which can be stimulated by a microwave. Taking all these features together, FNDs could be employed in various imaging techniques including long-time fluorescence tracking, time-gate imaging, ODMR and super-resolution microscopy, CLEM, and Raman imaging. Furthermore, hyperpolarization of paramagnetic impurities on the surface or of NV centers located inside the FNDs paved the way for MRI. Most prominently, FNDs containing NV^- centers allow sensing at nanoscale. For example, FNDs are capable of sensing electron spins, magnetic and electric fields, temperature, pH-values, and electric charges by magnetic relaxometry as well as ODMR and fluorescence spectroscopy. However, there are still obstacles which limit the applications of NDs. In the field of imaging, applications *in vitro* are demanding bright and small FNDs (few nm) which would enable to track proteins without influencing the behavior of these proteins significantly. Up to now, applied FNDs have a size of at least 30 nm in diameter. Applications *in vivo* are still limited due to the weak emission, especially of smaller FNDs (<40 nm). Therefore, smaller FNDs with a higher number of active NV centers would be beneficial to track these FNDs in living animals. Furthermore, other optical defect centers such as SiV centers need to be explored further because their emission, which is shifted to the infrared, would be more suitable for imaging *in vivo*. Sensing applications are often limited by the inhomogeneous properties of FNDs. FNDs usually contain a broadly distributed number of NV^- centers, a broad size distribution, and various shapes of FNDs is too big. Furthermore, coatings of FNDs are mostly very thick and therefore, the distance of the NV^- centers to the substance, which should be detected, is too long. Finally, measurements are very time consuming and do not allow to sense fast processes. All these drawbacks are hindering sensing applications up to now and need to be overcome in future.

2. Motivation

In the introduction current applications and future potentials of NDs were discussed. However, there is still a huge gap between on one hand synthesis and further functionalization of FNDs and on the other hand sophisticated applications such as bioimaging or nanoscale sensing. For bioimaging, stringent requirements are needed in biocompatibility, colloidal stability, size distribution of FNDs, and quantity of optical active centers, whereas sensing demands uniform surface modifications, thin coatings, and sufficient amount of NV⁻ centers or other defect centers. Up to now, there are many activities improving surface purification, functionalization, and post-modifications based on covalent and non-covalent interactions of NDs and coating materials. Especially, coating materials are important because they form the intersection between the hard and dense diamond material and the mostly soft materials present in biological environments. However, often coating materials which are designed are of complex structure, only applicable for a specific application, and cannot easily be applied across different fields.

Therefore, in this dissertation, bio-inspired coatings are proposed, which are easy to fabricate, translatable, and very variable in their applications. Inspired by Nature two coating materials were designed: firstly, a non-covalent coating strategy was developed which originates from protein adsorption and protein corona formation in Nature. Secondly, a covalent coating induced by self-polymerization of small molecules inspired by mussel foot proteins was developed.

Non-covalent coatings possess certain advantages over covalent modifications. For example, they are easier to functionalize and characterize because this can be done before the coating is adsorbed onto the NDs. Furthermore, preliminary studies can be performed only with the coating material. Our group gained a lot of experience with HSA-based carrier systems. As common for proteins, HSA possesses a specific amino acid sequence and therefore can be functionalized in a precise way. The conversion of negatively charged amino acid side chains into positively charged ones allowed a higher degree of functionalization as well as an increase in cellular uptake. The immune response was reduced and the colloidal stability improved by attaching PEG chains. The high number of functional groups on the HSA allowed to vary the modifications easily such as the attachment of small molecular dyes for multi-color imaging, chelator units to bind contrast agents for MRI, and drugs *via* a pH-responsive linker. Furthermore, the positive charge of the protein enables simple coating of the negatively-charged NDs by convenient electrostatic adsorption. To show the applicability of this coating material for different bioimaging applications, we performed various imaging methods in different scales. *In vitro*, we demonstrated the use of coated FNDs for CLEM in combination with EFTEM providing the highest and finest resolution. By moving to *in vivo* experiments, the transport of coated FNDs into the mouse brain through the BBB

was proven. Finally, we prepared a coating material for MRI by attachment of Gd^{3+} ions and evaluated the coating material *in ovo*.

In the second approach, we used the ability of L-DOPA to directly self-polymerize from the surface of FNDs. Because poly(L-DOPA) is a less soft and flexible material than the HSA-based coating, the poly(L-DOPA) coating gave us better control over the thickness of the shell which was formed around the FNDs. Next to the various present functional groups which allowed post-modification of the coated FNDs, poly(L-DOPA) is a functional coating material which shows a photothermal effect. In combination with the abilities of FNDs this allowed us to perform photothermal applications in parallel to bioimaging. After addition of the protein transferrin and the small molecular dye ICG, coated FNDs showed uptake into cancer cells and a photothermal effect at low laser powers. Furthermore, FNDs offer the possibility to confirm the photothermal effect on a nanoscale level intracellular by sensing of the temperature using ODMR spectroscopy. It was shown that the poly(L-DOPA) coating does not influence or weaken the ODMR signal.

3. Investigated Systems

3.1 An *In Vitro* Study of Coated Fluorescent Nanodiamonds With Nanoscale Resolution Using Correlative Microscopy Techniques

In the first publication, we investigated the behavior of coated FNDs in cells. To achieve this with a high resolution, we used a combination of different microcopy techniques including CLEM and EFTEM. Often, the spatial information is limited to a microscopic level, which is recorded by fluorescence microscopy techniques *in vitro* or tomography techniques, such as MRI, computed tomography (CT) or positron-emission tomography (PET), *in vivo* but there is not much known about the intracellular behavior of coated FNDs on a nanoscale level. This information would be crucial to further develop modern nanomedicine, high standard bioimaging or sensing probes by avoiding the risk of coated FND-induced toxicity and to get a better understanding of coated FND–cell interactions such as uptake mechanisms, intracellular release, and trafficking.

Classical LM is restricted to the wavelength of light and therefore does not provide resolution beyond the diffraction limit (~200 nm).[219] Super-resolution microscopy was invented to overcome these limitations. In the last decade, a huge step forward in nanoscale resolution was made which is also shown by the increasing number of different techniques such as STED, STORM, photoactivated localization microscopy, and super-resolution optical fluctuation imaging.[220] However, there are still special requirements which need to be fulfilled for the different techniques. Fluorophores should possess a high photostabiliy and/or special optical behaviors such as blinking. A resolution down to 40 nm could be achieved for NDs in HeLa cells using STED, which is still around 100 times lower than the resolution of TEM (below 1 nm).[106,221] In addition, super-resolution microscopy cannot visualize most of the cellular structures caused by the absence of fluorescent signals. EM is the method of choice when it comes to nanoscale resolution because it can reveal cellular structures at the highest resolution even without special marker molecules. However, reaching such high resolutions comes along with several drawbacks. EM works only under high vacuum preventing any kind of live cell imaging. Next to this, imaging works only in grayscale. CLEM was invented to combine the two powerful microscopy techniques and to overcome the hurdles of each individual technique. LM allows fast screening and live cell imaging using multi-color detection, whereas EM provides the best resolution even without marker molecules. This makes CLEM a powerful tool in modern nanomedicine. Several obstacles arise during CLEM studies of NPs. Firstly, NPs need a dense core structure, which must be detectable by EM. Secondly, the NP must not be destroyed by the sophisticated preparation procedure for EM. This can easily occur during cutting the specimen into a few hundred nanometer thin slices using a diamond knife. Thirdly, the fluorophore must survive the embedding method and the emission must be strong enough to be distinguishable from the background signal. QDs and gold NPs have been analyzed by

CLEM but they suffer from their weak fluorescence, blinking of QDs, and their cytotoxicity, which limits long-term studies *in vitro* and *in vivo*.[134,222–224]

Considering these prerequisites, FNDs appear as excellent candidates for CLEM studies. The diamond core is composed of mainly carbon atoms building up a dense structure which can be visualized by EM. More importantly, the fluorescence of FNDs arises from NV centers inside the carbon lattice which are not easily affected by the chemical surrounding and therefore are not quenched by embedding procedures. In addition, they show a high photostability and low cytotoxicity.[225] Previously, the application of FNDs in cells for CLEM was limited due to the weak contrast of FNDs in TEM.[170,171,173] Therefore, FNDs were attached to gold NPs which showed a much higher contrast in TEM.[17] Especially, single FNDs could not be visualized by CLEM in cells so far due to the too weak fluorescence signal in CLSM and too low signal-to-noise ratio in TEM.

In this work, we used CLEM to identify FND clusters in cells with a very high resolution in bright-field TEM. Furthermore, EFTEM enabled the visualization of single FNDs in cells for the first time.
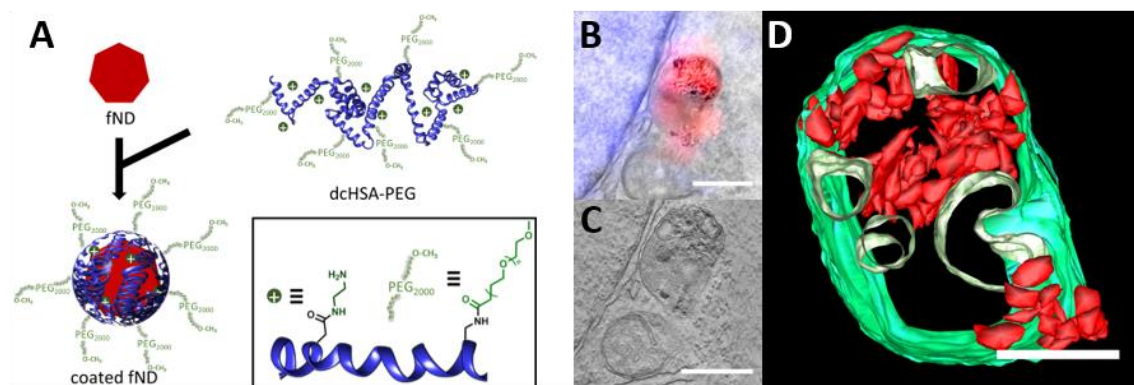
Figure 20 (A) Overview of the coating procedure of fluorescent nanodiamonds with cationized and PEGylated human serum albumin. (B) Correlative light–electron microscopy image of nanodiamonds (red) in an intracellular vesicle after merging light and electron microscopy images. (C) Transmission electron microscopy tomogram of the region in (B) allowing to identify individual nanodiamonds in a cluster. (D) 3D model of the intracellular vesicles with nanodiamonds (red) and membrane (green). Scale bar = (B+C) 500 nm, (D) 250 nm. (A–D) are adapted with permission from Han, S.; Raabe, M.; Hodgson, L.; Mantell, J.; Verkade, P.; Lasser, T.; Landfester, K.; Weil, T.; Lieberwirth, I. High-Contrast Imaging of Nanodiamonds in Cells by Energy Filtered and Correlative Light-Electron Microscopy: Toward a Quantitative Nanoparticle-Cell Analysis. *Nano Lett.* **2019**, *19* (3), 2178–2185.

FNDs with a diameter of around 35 nm in average (determined by TEM) were used in our study. The surface of the FNDs was oxidized by the manufacturer using strong acids (usually nitric acid, perchloric acid, and sulfuric acid) yielding a high number of carboxylic acid groups. The negative surface groups stabilize the NV⁻ centers and lead to a high colloidal stability in MilliQ water. However, FNDs tend to aggregate strongly in aqueous buffer systems even at low salt concentrations. Thus, coating the surface of FNDs is essential for studies in cellular environments. Previously, we established a protocol to

coat FNDs using a bioinspired copolymer.[115] The coating is derived from the human plasma protein HSA and the modification were done according to literature.[115] In summary, all negatively charged amino acids of the HSA backbone reacted with ethylendiamine resulting in a high positive surface charge. This allowed further modification and increased cellular uptake due to the interaction with the negative cell membrane. Next, the cationized HSA was PEGylated by addition of NHS activated poly(ethylene oxide). The PEG chains increased the colloidal stability and reduced the immunogenicity. In the final step, the PEGylated HSA was denatured using a phosphate buffer containing a high concentration of urea as well as tris(2-carboxyethyl)phosphine (TCEP) to reduce the disulfide bonds. To prevent refolding, the free thiols were capped by 1-(2-aminoethyl)-1H-pyrrole-2,5-dione.

FNDs were diluted (0.1 mg/ml) in MilliQ water and sonicated to prevent aggregates. Afterwards, the copolymer solution (low concentration of 0.1 mg/ml) and the FND solution were mixed and stirred overnight (see Figure 20A). Unbound copolymer was removed by centrifugation. After the coating, the negative surface charge of the FNDs changed to a positive value and the hydrodynamic radius (R_h) increased from 44.5 nm to 61.7 nm measured by dynamic light scattering (DLS). One reason for the relatively high increase in the R_h is the loss of smaller FNDs during the centrifugation steps. More importantly, the coated FNDs showed a monomodal distribution in the DLS indicating a single, narrowly distributed species. This was confirmed by DLS measurements over several angles. In addition, coated FNDs showed no aggregation in TEM imaging compared to uncoated FNDs. The NV⁻ centers provide an emission in the range of 660–700 nm after excitation with a 561 nm laser using a commercial available confocal microscope. The emission intensity depends very much on the number of NV⁻ centers. Therefore, bigger FNDs (~100–200 nm) emit much stronger than smaller FNDs. However, smaller FNDs are more attractive for biomedical applications. We have chosen FNDs with a size of 35 nm in diameter containing around 15 NV⁻ centers per FND. Noteworthy is that our coating does not affect the fluorescent properties of the FNDs.

For CLEM studies, we incubated HeLa cells with FNDs (75 μg/ml, 37 °C, 5% CO_2, 4 h). TEM requires sophisticated sample preparation including fixation and embedding of cells in polymeric resigns.

Two methods were used in the following:

(1) "in-resign CLEM"; The samples were vitrified and embedded before LM and TEM was performed. This allowed a high precision of the signals in LM and TEM.

(2) "in-dish CLEM"; First LM was performed allowing live cell imaging. Afterwards, the samples were prepared for TEM. Due to the time gap between performing LM and TEM, the signals were slightly shifted which is mainly caused by shrinking of the cells during preparation for TEM.

Both methods, in-resin and in-dish CLEM, showed spherical clusters of FNDs in CLSM and TEM. As expected, the signals in CLSM and TEM merged perfectly in the in-resin CLEM but there slightly offset in the in-dish CLEM. The in-dish CLEM showed more fluorescence signals in CLSM in exchange because the sample is not embedded into a polymeric resin. Furthermore, the in-dish CLEM allows 3D tomography because the CLSM is performed before embedding the cells for TEM. In this way, we obtained spatial information of the fluorescence signals by performing z-stacks in CLSM (see Figure 20B). Afterwards, the sample was prepared for TEM and a tomogram was taken (see Figure 20C). The tomography using TEM allowed us not only to distinguish single FNDs in a FND cluster but also gave us information about the cellular surroundings. We visualized a cellular vesicle which is filled with 101 FNDs forming three clusters (see Figure 20D). In the tomogram, it is clearly visible that one cluster of FNDs is breaking through the membrane of the vesicle, which was described in literature before.[17,226]

CLEM provided us detailed information about FND clusters but was not able to identify single FNDs beyond clusters. There were two reasons for this; Firstly, single FNDs showed a low fluorescence intensity which was not strong enough to be detectable by CLSM. Secondly, without the information of the CLSM it was not possible to identify single FNDs in cells using TEM because many cellular structures were of similar shape and contrast.

We used three different electron microscopy techniques to visualize and identify single FNDs in cells.

High-angle annular dark-field imaging scanning transmission electron microscope. It was possible to identify single FNDs using a high-angular annular dark-field detector in scanning TEM. However, the method relies strongly on the orientation of the FND crystals. Therefore, not all single FNDs could be visualized.

Transmission electron microscopy (overfocus). The discontinuous potential change at the FND edges leads to bright Fresnel fringes around single FNDs in overfocus bright-field TEM micrographs. However, other phase objects in the specimen could be misinterpreted as FNDs too.

Energy filtered transmission electron microscopy. EFTEM allows to differentiate between elastic and inelastic scattering of the electron beam. The inelastic scattering relies strongly on the material on which the electron beam is directed. EFTEM has been used to identify QDs and gold NPs before but has not yet been used for imaging of FNDs.[227] Using electron energy loss spectroscopy we could show that the inelastic scattering intensity increased for FNDs compared to the surrounding materials. Based on this, we used EFTEM imaging to identify single FNDs. Compared to classical bright-field TEM, the signal-to-noise ratio in EFTEM imaging improved by the factor two. In addition, we estimated the resolution using a line plot through two individual FNDs which were close by. After applying a Gaussian fit (R^2=0.974), we calculated the distance

between the two single FNDs which was around 30 nm. This allowed us to study the behavior of single FNDs in cells for the first time.

There is not much known about FND uptake into cells on a nanoscale level. Therefore, we applied EFTEM to imaged FNDs which were located close to the extracellular matrix of the cellular membrane. Several FNDs formed a cluster composed of about 4 FNDs. However, we also visualized a single FND which was already partly encapsulated by the cellular membrane. We performed tomography and created a model of the FND afterwards. The 3D tomography clearly visualized a single FND uptake for the first time. Hereby, the cellular membrane is not completely encapsulated but there is still a tunnel from the inside of the early endosome to the outside of the cell.

Next to cellular uptake, intracellular delivery is of high interest regarding sensing,[225] drug delivery,[228] and NP-related toxicity.[225] We were able to visualize two single FNDs which are located inside a mitochondrion using EFTEM, 3D tomography, and 3D modelling (see Figure 21A–D). Interestingly, next to the mitochondrion was a vesicle located containing a FND cluster with a size of about 200 nm in diameter. Probably, the FND cluster is too bulky to enter the mitochondrion. The two individual FNDs inside the mitochondrion were not encapsulated by a membrane. We could speculate that the single FNDs escaped from a vesicle and that the membrane of the FND merged with the mitochondrial membrane. However, deeper studies are necessary to reveal the detailed uptake process of FND into mitochondria.
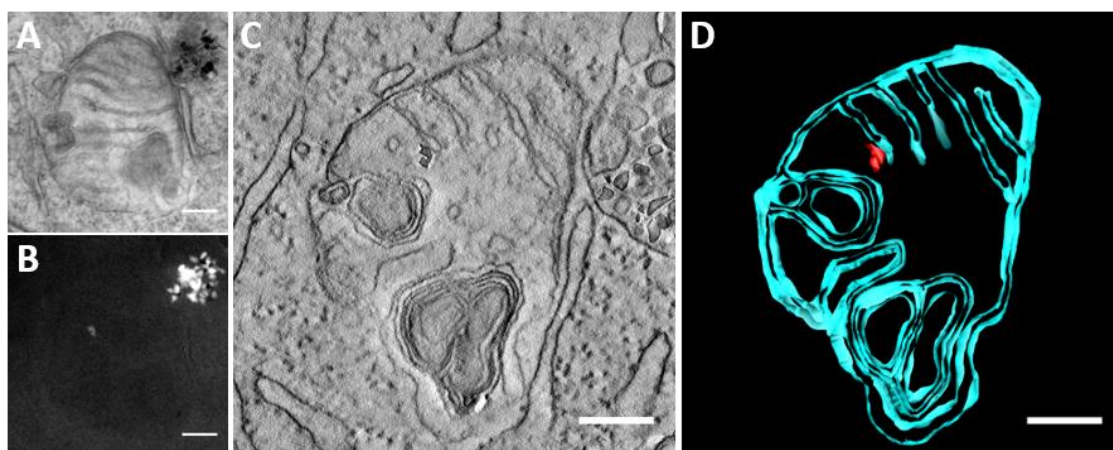
Figure 21 (A) Transmission electron microscopy (TEM) image of a mitochondrion and a cluster of nanodiamonds located at the top right. (B) Energy-filtered TEM of the same region like in (A) revealing a better signal-to-noise signal of nanodiamonds. (C) TEM tomogram and (D) 3D model of the mitochondrion illustrating two single nanodiamonds (red) inside the mitochondrion. Scale bar = (A–D) 200 nm. (A–D) are adapted with permission from Han, S.; Raabe, M.; Hodgson, L.; Mantell, J.; Verkade, P.; Lasser, T.; Landfester, K.; Weil, T.; Lieberwirth, I. High-Contrast Imaging of Nanodiamonds in Cells by Energy Filtered and Correlative Light-Electron Microscopy: Toward a Quantitative Nanoparticle-Cell Analysis. *Nano Lett.* **2019**, *19* (3), 2178–2185.

In summary, we demonstrated a powerful way to visualize and identify FND clusters in cells using CLEM. In addition, we identified single FND using EFTEM. A bioinspired

protein coating was used to enhance uptake and prevent aggregation. Mainly, FND clusters were found in cells. Hereby, the EM and LM signals merged perfectly. The EM resolution was of such a high quality that even individual FNDs in a cluster could be distinguished and counted. EFTEM was used to identify single FND beyond clusters. For the first time, a single FND uptake by a mammalian cancer cell line could be visualized. In addition, EFTEM allows to identify single FNDs in intracellular organelles such as mitochondria.

We believe that our approach can help to gain a better understanding of the cellular behavior of FNDs in nanoscale. This would give information about bioactivities and potential toxic effects of such nanomaterials based on quantitative data which is very relevant for the whole field of nanotherapeutics, bioimaging and sensing probes.

All results are presented and discussed comprehensively in the manuscript (chapter 6.1).[114]

3.2 An *In Vivo* Study of Coated Fluorescent Nanodiamonds Showing Successful Crossing of the Blood–Brain Barrier

After a cellular study of uptake and trafficking of coated FNDs at the nanoscale, we further explored our system *in vivo*. Therefore, we preformed experiments with coated FNDs in mice and studied a potential crossing of the BBB. Transport through the BBB is of high interest because the therapy or diagnosis of many neurological diseases is often limited by the hindered transport of compounds through the BBB. The main role of the BBB is, next to separate the circulating blood from the brain and extracellular fluid in the central nervous system, to maintain a constant homeostatic environment and to prevent xenobiotics from entering the brain.[229] To achieve this, the BBB is composed of many different cell types including endothelial cells, pericytes, astrocytes, and neurons.[230] However, this complicated and tight natural barrier makes it difficult to deliver drugs over the blood into the brain.

In the last decades, many nanomaterials have been tested for a successful crossing of the BBB such as antibodies, liposomes, polymers, and micelles.[231] However, these systems were always limited in imaging. Microscopic imaging by fluorescent dyes, expression of fluorescent proteins or luciferase was difficult due to bleaching of fluorophores, a high autofluorescence of the tissue or a low transfection efficiency.[232–235] One of the best studied nanomaterial in crossing the BBB are poly(lactic-co-glycolic acid) NPs.[236] However, these NPs possess no optical properties which would be beneficial for diagnosis. Furthermore, it was demonstrated that these NPs only cross the BBB in diseased animals with impaired BBB but not in healthy animals.[237,238] NPs with better optical properties such as QD have been considered as an alternative but their application is limited due to their high toxicity.[239,240] Similar problems were found for carbon dots which require new functionalization strategies to avoid clearance and heart accumulation which might be toxic.[241,242] To overcome these hurdles, we used FNDs which show no photobleaching, a good biocompatibility, and a potential for imaging *in vivo* in future.

The coating material was prepared in the same way as reported in the publication above.[114] In summary, native HSA was cationized followed by PEGylation (Figure 22A). 20 PEG units were introduced which was proofed by matrix-assisted laser desorption/ionization time of flight mass spectrometry (Maldi-Tof MS). For multi-color imaging, either the dyes BODIPY or rhodamine were attached. The successful coating of the NDs was characterized by zeta-potential, TEM, and DLS. After coating, the negative surface charge of the uncoated ND (−28.5 mV ± 1.0 mV) changed to a positive surface charge (26.3 mV ± 0.7 mV) due to the positive charged coating material. DLS revealed a significant size increase after coating of the NDs. Two ND samples differing in size were used with averaged diameters of 28.47 nm ± 0.22 nm and 36.68 nm ± 0.18 nm, respectively. After coating, the averaged diameter changed to 41.55 nm ± 0.20 nm and 55.87 nm ± 0.92 nm, respectively. From the TEM images a histogram was created for

both ND samples revealing sizes of 18.70 nm ± 3.40 nm and 25.50 nm ± 5.50 nm. The diameter after coating cannot be determined by TEM because the coating is not visible in the TEM. However, we saw a clear difference in the aggregation behavior of the NDs. Uncoated NDs were strongly aggregating in contrast to coated NDs which were uniformly distributed over the TEM grid.
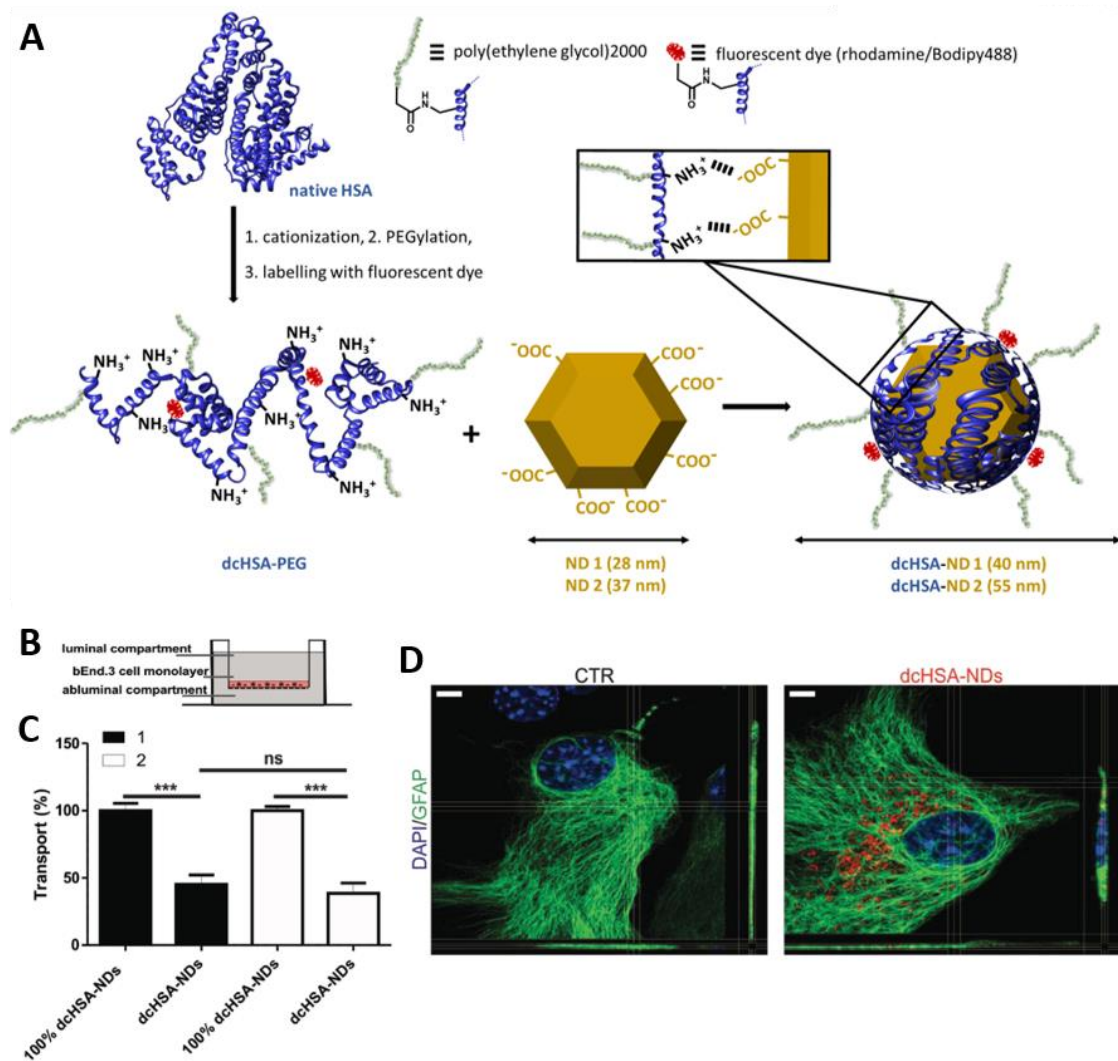

Figure 22 (A) Overview of the coating material and the coating procedure. Human serum albumin (HSA) was cationized, PEGylated, and labelled with a dye before two different sizes (28 nm and 37 nm) of nanodiamonds (NDs) were coated by non-covalent adsorption. (B) Scheme of the *in vitro* blood–brain barrier (BBB) model. (C) Transport of coated NDs through the BBB in the *in vitro* model. (D) Confocal laser scanning microscopy images of astrocytes (left) and astrocytes after uptake of coated NDs (right; red). Scale bar = 5 µm. (A–D) are adapted with permission from Moscariello, P.; Raabe, M.; Liu, W.; Bernhardt, S.; Qi, H.; Kaiser, U.; Wu, Y.; Weil, T.; Luhmann, H. J.; Hedrich, J. Unraveling In Vivo Brain Transport of Protein-Coated Fluorescent Nanodiamonds. *Small* **2019**, 1902992.

The transport of the coated NDs was investigated by an *in vitro* model. Endothelia cells (bEnd.3) were seeded on the luminal side of a transwell insert. Hereby, the luminal side represents the bloodstream while the abluminal compartment represents the brain. To proof that the cells are forming a tight barrier, the transendothelial electrical

resistance (TEER) was monitored. TEER values higher than 40 Ω × cm² indicate a tight barrier which excludes paracellular transport.

To investigate how the size of the NDs influences the crossing of the BBB, both coated ND samples were applied to the BBB *in vitro* model (Figure 22B). After 24 h, the fraction of coated NDs which reached the abluminal area was quantified by fluorescence intensity measurements. A transport of 100% represents the passive diffusion of coated NDs through the transwell insert on which no cells were seeded. The slightly smaller coated NDs (DLS=41 nm) showed a transport of 45.17±7.0% and the larger NDs (DLS=56 nm) showed a transport of 38.6±7.6% (Figure 22C). Thus, there was no significant difference in the crossing of the BBB between the smaller and bigger NDs.

To get a better understanding of the crossing mechanism of the BBB, we investigated the cellular uptake of the coated NDs into bEnd.3. Endothelia cells are forming a tight cell barrier around the blood vessels and are the first cell types which nanomaterials need to pass for crossing the BBB. Firstly, we checked the uptake by CLSM. To enable CLSM we changed to FNDs and we attached the dye BODIPY to the coating protein. CLSM revealed colocalization of the fluorescent signals of the FNDs and the BODIPY proofing the stability of the coating *in vitro*. Secondly, we investigated the uptake process of the coated FNDs. There are two well studied uptake mechanisms, the clathrin-mediated uptake and the caveolae-mediated uptake. To investigate which uptake mechanism is used, bEnd.3 cells were incubated with the coated FNDs in combination with either fluorescein-labeled transferrin (incorporated *via* clathrin-mediated uptake) or the B subunit of cholera toxin-alexa-488 (incorporated *via* caveolae-mediated uptake). Afterwards, colocalization was determined by CLSM. We showed that 27.2±3.07% of the coated FNDs were colocalized with fluorescein-labeled transferrin and 70.55±3.90% of the coated FNDs were colocalized with the B subunit of cholera toxin-alexa-488. These data indicate a preference of the caveolae-mediated uptake which is in accordance with literature.[243,244] During uptake and cell trafficking, different cellular compartments are formed starting from early endosomes, over late endosomes, and finally develop into lysosomes. To study in which compartment the coated FNDs are localized, we performed costaining with early endosome antigen markers or lysosomal-associated membrane protein 1 markers. CLSM revealed that only 2.40±0.50% of fluorescence signals of the coated FNDs are colocalized with signals of the early endosome markers but 15.14±4.15% are colocalized with the lysosome markers after 24 h. It is not surprising that almost no coated FNDs are localized in the early endosome because the retention time is usually only a few minutes. In addition, we performed costaining with an autophagosome marker (microtubule-associated protein 1A/1B-light chain 3). Only 0.98±0.52% of the fluorescence signals of coated FNDs were colocalized with signals of the autosomal marker. An increase of autophagy is highly related to cellular stress. Therefore, our results indicate that the coated FNDs should not induce cellular stress.

After showing the successful uptake of coated FNDs into endothelia cells, we examined other cell types which are located in the BBB. CLSM revealed strong uptake of coated FNDs in the perinuclear region of astrocytes (Figure 22D). In contrast, in neurons coated FNDs were mainly located in axons and dendrites. Taken together, these data proofed the successful uptake of coated FNDs into endothelia cells, astrocytes, and neurons which might be one of the reasons why coated FNDs are crossing the BBB *in vitro* model.

To further understand the process of crossing the BBB, we studied the transport of coated FNDs from one to another cell. Interestingly, we found vesicles with coated FNDs located in a cell structure connecting two adjacent cells. Tunneling nanotubes have been described before as actin bridges between different cells which are responsible for transporting various cellular compartments over long distances.[245] To visualize the transport of coated FNDs we tracked their fluorescent signal by CLSM. During 45 min of tracking, we saw a clear unidirectional movement of the vesicles with FNDs from one to another cell. Even an increasing of the speed was found when the vesicles came closer to the target cell. We speculate that this difference in speed is caused by a "bottle-neck" effect. In the cytosol, the vesicles show a more random diffusion and once the vesicles entered the tunneling nanotubes a unidirectional movement starts. In addition, we proofed that there is also transport of coated FNDs in vesicles along the tunneling nanotubes in neurons. Our data agree with previously reported transport of FNDs in HEK293T and SH-SY5Y cells.[151] To summarize, we proofed transport of coated FND in vesicles *via* tunneling nanotubes between different cells. This cell-to-cell transport is highly interesting regarding crossing of the BBB.

Next, we investigated the biocompatibility of our coated FNDs. Therefore, a monolayer of bEnd.3 cells was seeded in a transwell and the TEER was constantly measured. The TEER values of untreated cells and cells incubated with coated FNDs showed no significant difference indicating that the cell integrity was not harmed by the coated FNDs and they still formed a dense monolayer. Cell viability of astrocytes and neurons was proofed by alamar blue assay. There was no significant difference in the cell viability for untreated astrocytes or neurons compared to astrocytes or neurons treated with coated FNDs (0.5 µg/ml, 10 µg/ml or 30 µg/ml). These data revealed a high biocompatibility of different cells, which are all located in the BBB, after treatment with coated FNDs.

Finally, we investigated whether coated FNDs are able to cross the BBB and end up in the brain *in vivo*. 24 h after intravenously injection of the coated FNDs (500 µg/ml of blood), mice were sacrificed, the organs removed, cut into slices, and analyzed by CLSM. The liver was used to proof successful injection because biodistributional studies have clearly shown that positively charged NPs are accumulating in the liver. We imaged the samples using the reflection mode, the emission of the FNDs, and the emission of the dye which was attached to the coating protein. The reflection mode is independent of

the fluorescent properties (number of NV centers) of the FNDs which can differ between individual FNDs. As expected, we saw a high signal in the reflection mode in liver slices. In addition, we identified several signals of the reflection mode and the emission of the coating protein which were colocalized indicating that the coating of the FNDs is still in intact. In brain slices, we could clearly visualize signals in the reflection mode. After costaining of the astrocytes and neurons, we could visualize FNDs on the single cell level, mostly located close to blood vessels.

In addition, we performed biodistribution studies. The highest uptake of coated FNDs was observed in liver and spleen after 24 h. However, the brain uptake indicates an adequate circulation time of the coated FNDs. The accumulation of the coated FNDs is in agreement with data reported in literature describing the accumulation of NDs with a diameter of 50 nm in liver, spleen, kidney, and lung.

In summary, we presented a nanodiamond-based carrier and imaging system which showed successful crossing of the BBB. We reported the entire procedure from material characterization, to 2D cell culture experiments, a BBB *in vitro* model, and finally uptake of the coated FNDs into the brain *in vivo*.

All results are presented and discussed comprehensively in the manuscript (chapter 6.2).[116]

3.3 A Bioinspired Albumin Nanotheranostic for Magnetic Resonance Imaging and Drug Delivery in Triple-Negative Breast Cancer Xenografts

After the demonstration that coated FNDs can cross the BBB *in vivo*, we were interested to further explore the potential of coated FNDs for bioimaging. As it has been already discussed in the introduction, FNDs are promising candidates as contrast agents for MRI in future. However, so far the hyperpolarization protocols are still under development and the polarization of the FNDs is not sufficient enough for *in vivo* imaging. As an alternative to study FNDs *in vivo* by MRI before hyperpolarization is applicable, we designed a protein coating which is attached to the contrast agent Gd^{3+}. In this preliminary study, we investigated the potential of only the coating material for MRI and therapy in a TNBC xenograft.

Despite extensive research in the fields of cancer diagnosis and treatment, cancer remains the disease with the highest mortal rate next to heart diseases. Breast cancer (BC) is the most diagnosed cancer type among women and ends fatal in 400,000 cases yearly.[246] BC accurse in different subtypes and four major intrinsic subtypes have been identified: the luminal subtypes A and B, expressing hormone receptor-related-genes, triple-negative/basal-like BC, and HER2-positive BC.[247–249] The diagnosis and treatment of TNBC is especially difficult because of the lack of estrogen, progesterone, and HER2 receptors which are normally used in targeted cancer treatment.[247] So far, there are no approved targeted therapies for TNBC but several systemic treatments are available such as taxanes (e.g. paclitaxel), anthracyclines (e.g. DOX), and platinum-agents (e.g. cisplatin) which find usage in adjuvant and neoadjuvant therapy.[247] However, their application is restricted due to their high cellular toxicity accompanied by many side effects among them nausea and vomiting, myelosuppression, alopecia, mucositis, and cardiotoxicity.[250,251]

To overcome these limitations, NP–drug carriers were explored reducing the systemic toxicity by delivering the drug directly into the tumor tissues.[252–256] Protein-based nanocarriers have shown great opportunity as a translational drug delivery platform with several clinical trials in different phases.[257] Especially HSA, the most abundant blood plasma protein, has been used frequently as drug-delivery system such as albumin NPs[258], albumin–drug conjugates[259,260], albumin-binding drug derivates[261], albumin-coated NPs[259,262], and prodrugs[263–265]. Even one member of the albumin-based nanocarrier family is approved by the FDA; Abraxane®, a 100–200 nm sized albumin aggregate NP which encapsulates paclitaxel, was approved for the treatment of metastatic BC[266] and other cancer types such as non-small-cell lung cancer[267], and pancreatic cancer[268]. In contrast to the free drug or individual HSA systems, HSA-based denatured nanocarriers benefit from the EPR effect because of their increased size.[269] Recently, also cell- or tissue-targeted delivery was achieved and marketed by functionalization of monoclonal antibodies or recombinant proteins (Kadcyla®, Ontak®).[270]

Because TNBC shows a high growth rate often together with high grading, a combination of therapy and diagnosis would be highly desirable to study the drug delivery and tumor growth. In routine clinical diagnosis, MRI is the preferential method because MRI is noninvasive with a high spatial resolution for soft tissue. While CT requires radioactive contrast agents, MRI neither needs radiation nor causes other health risks.[271]
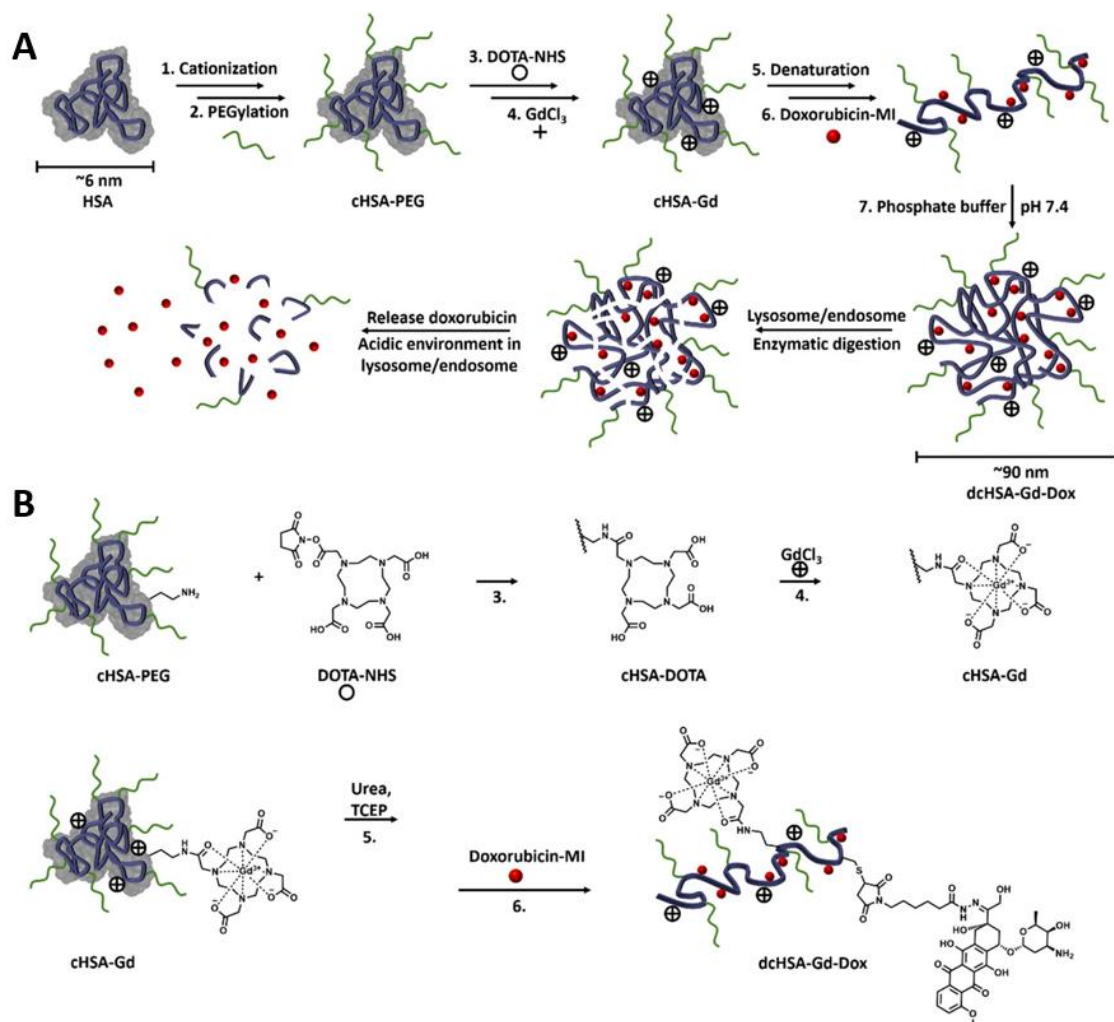

Figure 23 (A) Overview of the preparation of functionalized human serum albumin with Gd^{3+} and doxorubicin. (B) Details of the attachment of Gd^{3+} and doxorubicin. (A–B) are adapted with permission from Hafner, S.; Raabe, M.; Wu, Y.; Wang, T.; Zuo, Z.; Rasche, V.; Syrovets, T.; Weil, T.; Simmet, T. High-Contrast Magnetic Resonance Imaging and Efficient Delivery of an Albumin Nanotheranostic in Triple-Negative Breast Cancer Xenografts. *Adv. Ther.* **2019**, 1900084.

Albumin-based NPs which allow MR/fluorescence imaging have been fabricated before but there are still challenges for the treatment of cancer.[272–275] Mostly, the active compound, such as drug or contrast agent, is attached to the NP by non-covalent adsorption. This interaction is very vulnerable to unwanted leakage of the drug or contrast agent during *in vivo* circulation causing serious problems like systemic toxicity. Next to this, the concentration of the NP which is needed for the treatment of the cancer differs often from that used for imaging. Concentrations suitable for treatment would

provide a too low signal-to-noise ratio in imaging and vice versa, the optimal concentration for imaging would cause a high toxicity due to the too high drug concentration. Therefore, a nanocarrier system which balances drug load with contrast agent load would be highly beneficial.

To the best of our knowledge there is no albumin carrier available for the treatment of TNBC which enables diagnosis and therapy at the same time so far. Herein, we designed an albumin-based nanocarrier which addresses therapy and diagnosis; Both, the chemotherapeutic drug DOX as well as the contrast agent Gd(III)-1,4,7,10-tetraaza-cyclododecane-1,4,7,10-tetraacetic acid (DOTA) were attached covalently to the NP to avoid leakage during *in vivo* circulation (see Figure 23A). DOX contains a pH-cleavable hydrazone linker allowing release of the drug in the acidic endosomal or lysosomal compartments of cancer cells (see Figure 23B). Furthermore, we evaluated the nanocarrier in a TNBC xenograft bearing chick embryo model.

Native HSA contains a high number of functional groups which can be easily modified by simple chemistry. There are high numbers of primary amino groups ($-NH_2$ = 60 per HSA), carboxylic groups ($-COOH$ = 98 per HSA), and thiol groups ($-SH$ = 35 per HSA, but 34 thiol groups are forming disulfide bonds). In the first step, we transferred all negative charges of HSA into positive ones by adding ethylene diamine in high excess. During this process almost all carboxylic groups were converted into primary amino groups as confirmed by Maldi-Tof MS. This product as well as all following products were purified by ultracentrifugation (molecular weight cut-off 30 kDa). The increased number of amino groups allowed a higher number of functionalization and an enhanced cellular uptake of the nanocarrier due to the interaction of the positive charges of the nanocarrier with the negative charges of the cell membrane. Next, the cationized HSA (cHSA) was PEGylated by adding NHS-activated PEG (2,000 Da). The PEG units increase colloidal stability and prevent immune responses *in vivo*. In average 20 PEG units per protein were introduced as shown in Maldi-Tof MS. To attach the contrast agent Gd(III) later on, we synthesized DOTA-NHS according to literature. DOTA-NHS reacted with the PEGylated cHSA and in average 49 DOTA units were introduced as confirmed by Maldi-Tof MS (see Figure 23B). Gd(III) salt was added in high excess and the solution was heated up to 60 °C to load the DOTA with Gd(III). 44 of the 49 DOTA units were successfully loaded with Gd(III) according to Maldi-Tof MS.

To keep the number of drug molecules as precise as possible, which is crucial for dosing, we decided to attach the drug in a site-selective way. HSA possesses 35 cysteines among which 34 form disulfide bonds in the native state. Previously, we have shown that after denaturation and reduction of the disulfide bonds about 27–28 of the cysteines are accessible for Michael reactions.[276] The remaining 7–8 cysteines are sterically hindered because they are located closely to another cysteine. To attach the drug DOX, we synthesized the (6-maleimidocaproyl)hydrazine of DOX, a pH-cleavable hydrazine linker, which connects DOX to a maleimide group according to literature (see

Figure 23B). The modified HSA was denatured in 5 M urea buffer and the disulfide bonds were reduced by adding TCEP. To prevent oxidation, the buffer was degassed and the reaction was carried out under argon. About 27 DOX units were introduced according to Maldi-Tof MS.

After exchanging the denaturation buffer to Dulbecco's phosphate-buffered saline (50 mM, pH 7.4) the nanocarrier formed spherical structures as visualized by TEM. The determined diameter of the nanocarrier was 99.2 nm ± 17.7 nm (n=66) in average calculated from TEM and 87.8 nm ± 2.3 nm (n=3, PDI = 0.31 ± 0.05) calculated from DLS. According to literature, nanocarriers with a diameter of 100 nm benefit from the EPR effect but do not show a too fast clearance by the reticuloendothelial system.[277]

To enable MRI with a high signal-to-noise ratio, we investigated the relaxivity of the attached Gd(III). The relaxivity is a measure of the image-enhancing capability of a contrast agent and is proportional to the longitudinal (1/T1) or transverse (1/T2) relaxation rate. Gadolinium is a positive contrast agent and therefore enhances the T1 relaxation rate of water. The relaxivity is affected by three factors as described by the Solomon-Bloembergen-Morgan equation; (I) number of inner-sphere water molecules (q), (II) the water residence time (τ_m), and (III) the tumbling rate (1/τ_r).[278] While it is more sophisticated to change the first two factors, it is known that attaching the Gd(III) to macromolecules slows down τ_m which, in turn, enhances the image.[279] The relaxivity was determined by measurement of the relaxation rate at different Gd(III) concentrations. As expected, in contrast to the relaxivity of the clinically used contrast agent MultiHance® (4.6 mM^{-1} s^{-1}), our nanocarrier revealed significantly enhanced relaxivity (13.75 mM^{-1} s^{-1}). The increased relaxivity is comparable to other gadolinium-based macromolecular complexes.[280,281]

Next, we explored the cellular uptake and cytotoxic effect of our nanocarrier in MDA-MB-231 breast cancer cells. After incubating cells with our nanocarrier for 1 h, we could show successfully cell uptake of the nanocarrier by fluorescence microscopy following the emission of DOX. Cell viability was studied after incubation of cells with the nanocarrier and free DOX for 24 h, 48 h, and 72 h. At 72 h, the IC$_{50}$ value of our nanocarrier (77.5 nM) was slightly increased compared to free Dox (17.9 nM) but still in the nanomolar range.

The chorioallantoic membrane (CAM) of fertilized chick eggs is an attractive preclinical *in vivo* model because it enables fast screening of substances and represents an intermediate form between isolated, cultured cells, and animal experiments (see Figure 24A). In addition, data obtained from the CAM model correlate strongly with data received from mice experiments.[282,283] MDA-MB-231 xenografts were grown on the CAM of fertilized chick eggs to investigate the accumulation of the nanocarrier in tumor xenografts (see Figure 24A). In MRI, the nanocarrier showed a higher signal-to-noise ratio in tumor tissue compared to the clinical standard MultiHance® between 1 h to 15 h after injection (see Figure 24B). After 35 h, no contrast enhancement was visible

anymore. We did not see any contrast enhancement in other organs which proofs that the nanocarrier only accumulated in the tumor tissue. Furthermore, we determined the concentration of Gd(III) in the tumor tissue, liver, and blood plasma by inductively coupled plasma-optical emission spectrometry 6 h after intravenous injection. A high Gd(III) concentration was only determined in the tumor tissue but neither in the liver nor the blood plasma supporting the data from MRI.

Before we studied the therapeutic effect of our nanocarrier, we proofed that the embryo survival is not affected by the nanocarrier. We injected either a low dose (0.03 µmol/kg) or a high (0.09 µmol/kg) dose of the nanocarrier into chick embryos. In addition, chick embryos were treated with equimolar concentrations of free DOX or a physiological sodium chloride solution as control. Chick embryos treated with the nanocarrier showed a high survival rate even at high dose (low dose: 95% and high dose: 77%). In contrast, free DOX revealed significant lower chick embryo survival rate (low dose: 66% and high dose: 59%).
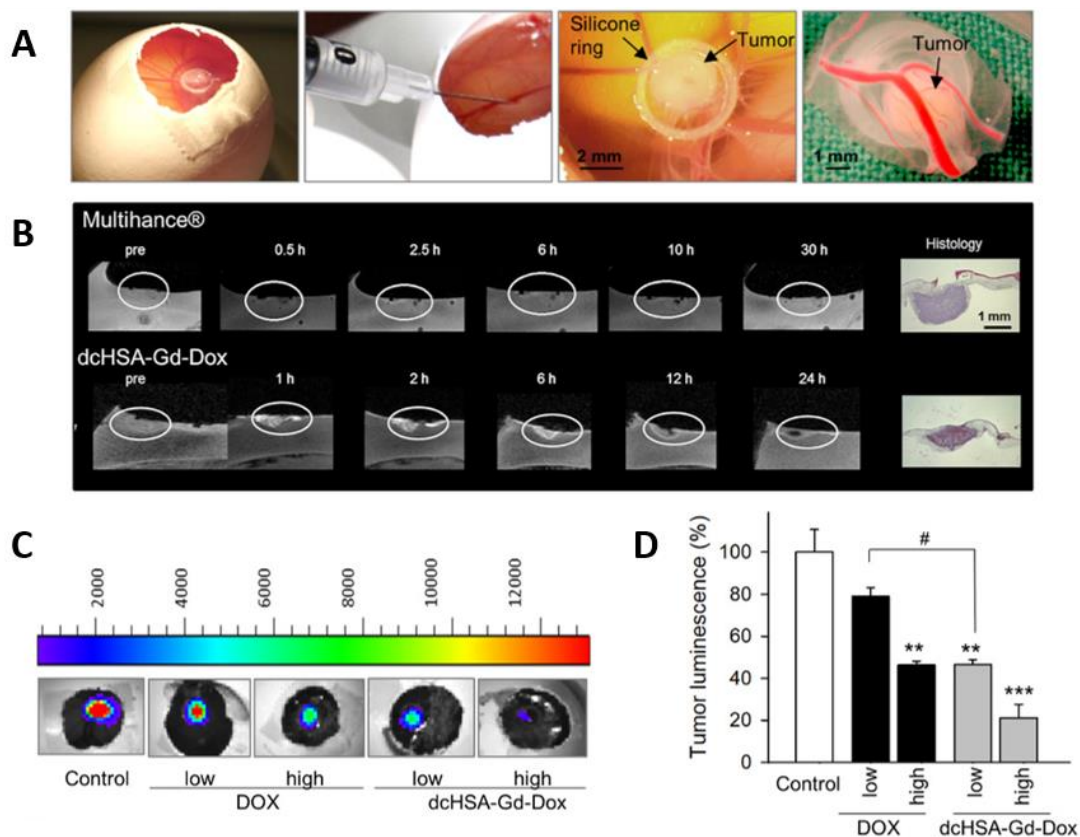
Figure 24 (A) MDA-MB-231 xenograft on the chorioallantoic membrane (first and third pictures from left), intravenous application of the nanocarrier (second from left) and xenograft after collection (forth from left). (B) Magnetic resonance images of representative breast cancer xenografts before and after intravenous injection of MultiHance (first row) or the nanocarrier (second row) and the same tumors after histochemical preparation. (C+D) Representative pictures of luminescent tumors *in vivo* (C) and mean luminescence of MDA-MB-231 cancer xenografts 72 h after treatment (D) with doxorubicin or the nanocarrier. (A–D) are adapted with permission from Hafner, S.; Raabe, M.; Wu, Y.; Wang, T.; Zuo, Z.; Rasche, V.; Syrovets, T.; Weil, T.; Simmet, T. High-Contrast Magnetic Resonance Imaging and Efficient

Often therapeutic and diagnostic applications of nanocarriers are hindered because different concentration of the nanocarrier are required. Hereby, mostly the concentration which is required for imaging shows high toxicity. However, our nanocarrier showed a high chick embryo survival rate at a comparable concentration which showed high contrast in MRI (0.09 µmol/kg of the nanocarrier for the chick embryo survival study, 0.08 µmol/kg of the nanocarrier for MRI).

Next to the diagnostic potential, we investigated the therapeutic potential of our nanocarrier. The transparency of the CAM enables easy observation of the tumor growth *in vivo*. We used a xenograft which consist of luciferase-expressing MDA-MB-231 cells (see Figure 24C). The tumor growth can be easily visualized by addition of D-luciferin. The bioluminescence was recorded using an *in vivo* imaging system (IVIS). The averaged bioluminescence intensity was significantly reduced of xenografts treated with our nanocarrier compared to DOX or the control (see Figure 24C+D). We confirmed the results by immunohistochemical analysis. Ki-67, a cell proliferation marker, indicates the mitotic phase of the cell cycle and is absent in resting G_0 cells. In addition, K-67 expression was defined as an indicator for lower disease-free and overall survival in a study including 3,500 breast cancer patients. In our work, the nanocarrier treated xenograft showed significantly reduction of the K-67 positive cells compared to treatment with DOX or the control. Furthermore, TUNEL staining, a marker for apoptotic cells, revealed that the nanocarrier and DOX induced an apoptotic effect in breast cancer xenografts.

In summary, we designed a nanocarrier based on cationized and PEGylated albumin containing 44 Gd(III) units providing high-contrast MRI. In addition, 27–28 DOX units were attached which are released in the acidic compartments of cancer cells due to a pH-cleavable hydrazone linker yielding in high toxicity (IC_{50} 77.5 nM). *In vivo*, our nanocarrier showed enrichment only in the breast cancer xenografts and reduced the proliferation Ki-67-positive fraction in breast cancer xenografts.

Furthermore, we were able to allow cancer treatment and diagnostic at the same concentration of the nanocarrier with a high signal-to-noise in imaging and a high survival rate of chick embryo.

All results are presented and discussed comprehensively in the manuscript (chapter 6.3).[284]

3.4 Functional L-DOPA Coating of Fluorescent Nanodiamonds Enabling Photothermal Applications in Cells

In the previous publications, we showed the unique properties of FNDs regarding imaging *in vitro* and *in vivo*. For these purposes, we used a bioinspired protein-based coating which prevented aggregation and enhanced cellular uptake. However, this coating is driven exclusively by non-covalent adsorption which strongly depends on the surface of the FND. Therefore, batch-to-batch variations of FNDs are affecting the coating quality and the reproducibility of the coating using different sources of FNDs without continual optimization.
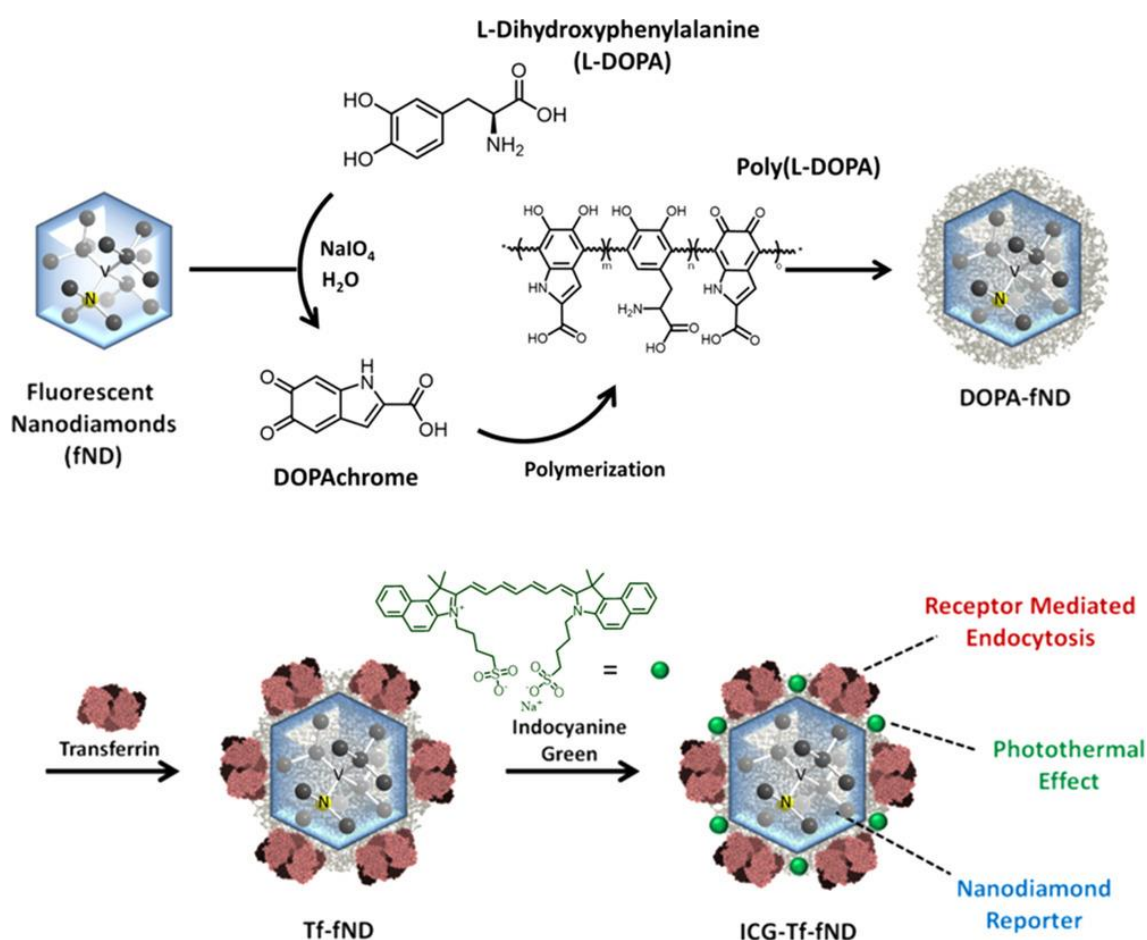
Figure 25 Schematic illustration of the polymerization of L-3,4-dihydroxyphenylalanine on the surface of nanodiamonds and further post-modification with transferrin and indocyanine green. Adapted with permission from Harvey, S.; Raabe, M.; Ermakova, A.; Wu, Y.; Zapata, T.; Chen, C.; Lu, H.; Jelezko, F.; Ng, D. Y. W.; Weil, T. Transferrin-Coated Nanodiamond–Drug Conjugates for Milliwatt Photothermal Applications. *Adv. Ther.* **2019**, 1900067.

To overcome these limitations, we were interested in designing a covalently bound coating. Nature offers an exemplary strategy to coat various surfaces. Dopamine, a bioinspired building block derived from mussel foot proteins, showed outstanding coating behaviors of different materials by self-polymerization as firstly reported by the group of Messersmith.[285] In the following years, dopamine found many applications in coating of surfaces or particles, and fabrication of membranes using different

polymerization methods such as dip-coating or electro-polymerization.[286] Next to dopamine, these properties were also observed for L-DOPA and norepinephrine. Post-functionalization after the coating is easy due to the presence of many functional groups including amines, alcohols, and conjugated Michael acceptors.[285–287] Recently, polydopamine has been demonstrated as a potential coating for NDs.[72,288] In contrast to dopamine, L-DOPA contains an additional carboxylic acid group resulting in a higher hydrophilicity of poly(L-DOPA).[289,290] In this work, we demonstrated that L-DOPA does not only act as a diverse coating for FNDs from different commercial sources (FND Biotech, Microdiamant) but also implements photothermal applications in addition to the optical properties of the FNDs.

We used NV$^-$ containing FNDs with an average size of 35 nm in diameter to ensure a small enough particle size after coating for further cellular studies. The polymerization of dopamine or L-DOPA was initiated by sodium periodate in MilliQ water to avoid destabilization of the FND by buffer salts (see Figure 25). In our experiment, FNDs were dispersed in MilliQ water under sonication followed by the addition of L-DOPA or dopamine reaching a final concentration of 1–10 mM of the catecholamine. The mixture was heated up to 55 °C and sonicated for 5 min. Next, we added a freshly prepared sodium periodate solution (0.5 equiv. compared to catecholamine). Afterwards, the solution was heated up to 55 °C again and shaken for additional 15 min. The coated FNDs were purified by ultracentrifugation.

FNDs coated with L-DOPA showed a good colloidal stability in contrast to dopamine coated FNDs which exhibited a high degree of aggregation, lower polymerization efficiency, and poorer aqueous stability. We assume that this is due to the additional carboxylic group of L-DOPA and, resulting from that, a higher hydrophilicity. The applicability of our coating methodology was confirmed by TEM testing three different batches and two different commercial sources of FNDs (FND Biotech, Microdiamant). All FNDs were clearly coated and were well distributed over the TEM grid. We further investigated the coating by DLS, X-ray photoelectron (XPS), Raman, and Fourier-transform infrared spectroscopy (FT-IR) spectroscopy which all proofed the successful coating among our FND sources.

In addition, we were able to control the thickness of the poly(L-DOPA) coating by varying the concentration of the monomer. The thickness of the coating varied linearly from 3–15 nm using concentrations of L-DOPA between 1–10 mM. We characterized the thickness of the coating by TEM and DLS (see Figure 26A). Furthermore, we investigated the molecular composition and bond formation of the L-DOPA coated FNDs with a shell thickness of 15 nm. XPS revealed the characteristic signals from the C–N–C, C=N–C demonstrating the cyclization of L-DOPA.

The polymerization of L-DOPA follows a radical mechanism. Because the NV$^-$ centers could be affected by this process it is essentially to control the magnetic properties of the FNDs. We investigated FNDs with two different thicknesses of the coating (3 nm and

15 nm). Spectra were recorded on a home-build confocal microscope with excitation light at 515 nm and 532 nm. The coated FNDs revealed a unique background signal triggered by the poly(L-DOPA) shell. The intensity of the background signal was strongly related on the thickness of the coating but the zero photon lines of the NV^- and NV^0 centers were clearly visible. In addition, a decrease in the initial intensity proportional to the thickness of the coating was observed caused by the broadband absorbance of the polycatecholamine. Interestingly, the fluorescence intensity increased by 60% compared to the initial excitation and reached a saturation level after a few minutes. Even after a few hours in darkness, the high level of fluorescence was stable which allows more sophisticated imaging with FNDs without double counting of the same particle. For sensing applications, the charge state of the NV center is crucial because only the NV^- center can be used. ODMR is the standard technique to measure the charge of NV centers. The ODMR spectra proved the presence of NV^- centers in poly(L-DOPA) coated FNDs. The decreased ODMR contrast is caused by the background light of the poly(L-DOPA) layer.
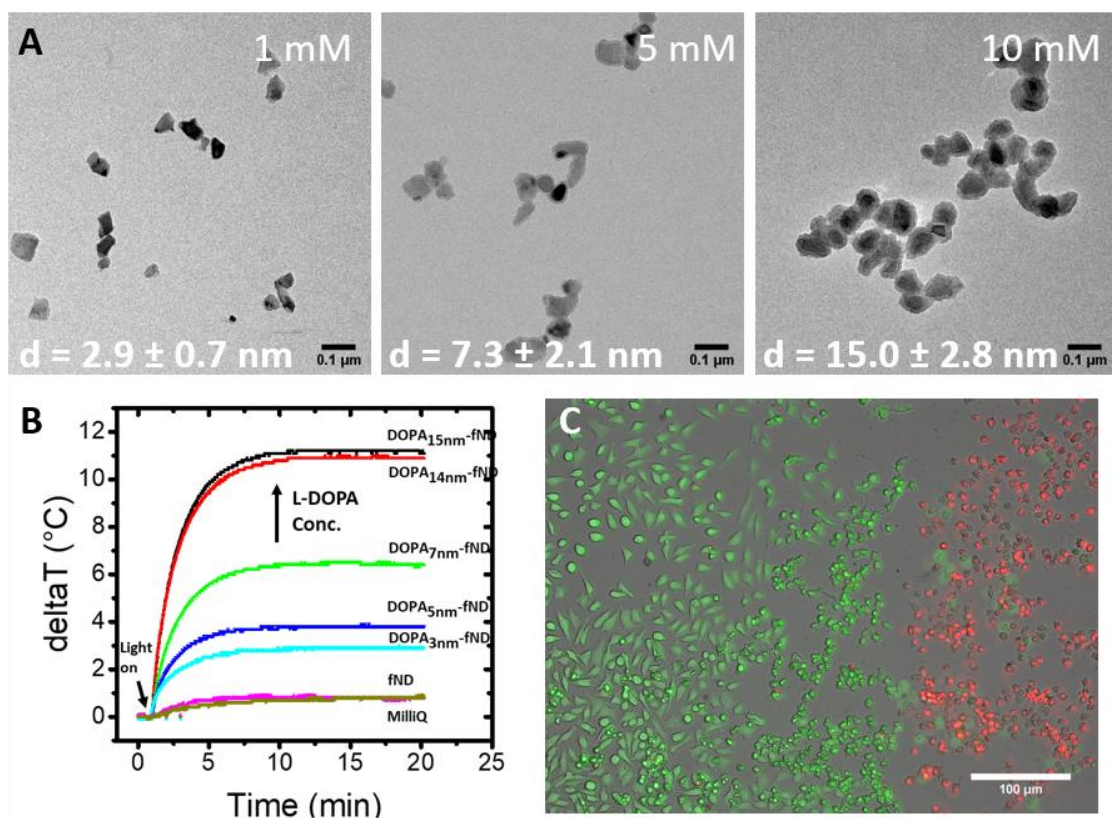
Figure 26 (A) Transmission electron microscopy images of poly(L-DOPA) coated nanodiamonds indicating the control of the thickness of the shell using different cencentrations of L-DOPA monomer. Scale bar = 0.1 μm. (B) Temperature increase of different nanodiamond samples after irradiation (810 nm lamp; 1 W/cm^2). (C) Live and dead staining (10 ×) of HeLa cells incubated overnight with imaged 4 h after 15 min irradiation with 810 nm lamp, 4 W/cm^2. Sharp border observed between live (green) and dead (red) cells. Scale bar = 100 μm. (A–C) are adapted with permission from Harvey, S.; Raabe, M.; Ermakova, A.; Wu, Y.; Zapata, T.; Chen, C.; Lu, H.; Jelezko, F.; Ng, D. Y. W.; Weil, T. Transferrin-Coated Nanodiamond–Drug Conjugates for Milliwatt Photothermal Applications. *Adv. Ther.* **2019**, 1900067.

Polycatecholamines are excellent energy absorbers from UV up to NIR light due to oligomeric and polymeric structures. The absorbed light is transferred into heat with high efficiency enabling applications as photothermal agents. Especially photothermal agents which are working in the NIR range are of high interest due to the low absorption by the body. We showed that poly(L-DOPA) coated FNDs exhibited enhanced photothermal effect compared to uncoated FNDs after irradiation at 810 nm resulting in a 10-fold increase in temperature (see Figure 26B). We have chosen coated FNDs with a poly(L-DOPA) thickness of 7 nm for further experiments to balance between the photothermal effect and the fluorescence intensity. We used the L-DOPA coating to homogenize FNDs and to enable easy post-functionalization. To proof post-functionalization, we used proteins to stabilize the poly(L-DOPA) coated FNDs further and to add biologically active functionalities. An important criterion of proteins is their conserved 3D structure which is important for the activity and must not be changed during the adsorption to surfaces.

Human transferrin (79.5 kDa) is a heme containing protein which binds and transports iron through transferrin receptors located in the membrane of many mammalian cell lines. Therefore, transferrin is often used to enhance the cellular uptake of NPs. We directly loaded the transferrin onto our poly(L-DOPA) coated FNDs benefiting from the amine-reactive Michael acceptors of the quinone moieties which are formed during polymerization (see Figure 25). The unbound protein was removed by ultrafiltration. After loading transferrin, the hydrodynamic diameter increased from 125 nm to 155 nm indicating successful coating of the protein. In addition, we proved the coating by FT-IR.

We evaluated the influence of transferrin to induce receptor-mediated uptake using an A549 lung adenocarcinoma cell line. Imaging by CLSM revealed efficient receptor-mediated uptake of the transferrin modified poly(L-DOPA) coated FNDs (Tf-FND) in contrast to uncoated FNDs or the precursor poly(L-DOPA) coated FND. In the next step, we attached ICG, a FDA approved small dye with excellent photothermal properties, onto Tf-FND (see Figure 25). ICG was loaded onto the Tf-FND by incubation overnight in dark followed by removal of free dye through ultrafiltration. We determined the amount of bound ICG by its specific absorbance at 400 nm and found that the loading was 180% by mass compared to the FND. In this way, a high local concentration of ICG was provided which could enhance the photothermal effect of poly(L-DOPA) coated FNDs. We explored the photothermal effect by using an 810 nm irradiation. ICG loaded Tf-FND (ICG-Tf-FND, ΔT=13.9 °C) showed a 120% and 12% improvement in temperature compared to poly(L-DOPA) coated FND (ΔT=6.4 °C) and ICG (ΔT=12.4 °C) after 20 min of irradiation. ICG-Tf-FND revealed a difference in the temperature profile compared to free ICG although the absolute ICG concentration were the same. This effect was observed before in hollow inorganic NPs and NP clusters.[291,292] After 24 h incubation of ICG-Tf-FND in cell media, we observed a negligible release of ICG (<5%) which demonstrated the strong interaction.

Finally, we investigated the photothermal effect in mammalian cancer cells (HeLa and A549). We compared the cellular uptake of ICG-Tf-FND and free ICG by confocal microscopy imaging the fluorescence signal of ICG (ex. 561 nm, em. 750–800 nm). ICG-Tf-FND showed a receptor-mediated uptake and was localized in endosomes without any leakage of ICG, whereas free ICG was diffusing throughout the whole cell and even ended up in the nucleus. To proof the photothermal effect we used a 810 nm lamp (200 mW) which was focused onto the cells by a fluorescence microscope. Depending on the magnification of the objective (10×, 20×, 40×) we were able to change the intensity of the light beam. Simultaneously, we recorded bright field images every 20 s to investigate morphological changes of the cells. Several light intensities (0.09 W/cm², 0.4 W/cm², 4.0 W/cm²) were used to study the optimum parameters for photothermal induced cytotoxicity within 15 min. Efficient and fast cell rounding was visually observed at light intensities of 0.4 W/cm² and 4.0 W/cm². However, even at very low light intensities (0.09 W/cm²) cell rounding was detected after 10 min. This is remarkable considering that the previously reported ICG-polydopamine-ND systems required light intensities of 2 W/cm². Next to alterations in the cell morphology, we performed dead/live staining using fluorescein diacetate/propidium iodide which further demonstrated the spatial control of the light induced cell death (see Figure 26C). The controls, Tf-FND and FND+ICG mixture, showed no morphological changes upon irradiation at any light intensities.

In summary, we presented a hierarchical design of a FND-based theranostic which benefits from the optical properties of the FND and the photothermal effect of poly(L-DOPA). The poly(L-DOPA) served as a sticky coating which enabled protein adsorption without effecting their activity. In addition, we loaded ICG onto the poly(L-DOPA) to increase the photothermal effect *in vitro*. The poly(L-DOPA) coating did not effect the magnetic properties of the NV⁻ centers which is crucial for sensing applications in future. In comparison to other ND-based systems, our system showed effective photothermal effect at least at a ten times lower intensity (~90 mW/cm²) *in vitro*.

All results are presented and discussed comprehensively in the manuscript (chapter 6.4).[75]

4. Conclusion and Outlook

Within this thesis, two bio-inspired coating systems were presented. The first coating strategy is based on the protein corona formation in Nature where proteins are non-covalently adsorbed to NPs. Starting from the blood plasma protein HSA, we designed a coating material which is easy to functionalize. To promote the electrostatic interactions between the proteins and the negatively-charged FND surfaces, all negatively-charged amino-acid side chains of HSA were transferred into positively. Furthermore, the proteins were PEGylated and denatured to increase their stability and flexibility. Moreover, this coating strategy offers chemical versatility in that different functionalities could be introduced easily *via* reactions with the high number of chemical groups, e.g. amines and carboxylic acids, which are present on the surface of HSA. For example, we attached small molecular dyes for multi-color imaging, introduced chelator molecules to bind Gd^{3+} ions, a contrast agent for MRI, or connected the drug doxorubicin *via* a pH-responsive linker. In the three publications presented in this thesis dealing with the protein coating (chapter 3.1–3.3)[114,116,284], we explored the applicability of FNDs coated through different modifications of HSA in biological models to investigate their cellular fate, as well as developed various bioimaging methods. In cells, we investigated the behavior of coated FNDs by CLEM and EFTEM. Coated FNDs showed a strong uptake and accumulated mostly in intracellular vesicles. The dense structure of the FND core allowed to perform TEM tomography of FND clusters and to visualize these clusters in 3D in such a high resolution that individual FNDs in a cluster could be distinguished. For the first time, we managed to image single FNDs which were not part of a cluster by EFTEM. Using this method, the visualization of a single FND uptake as well as the identification of single FNDs in a mitochondrion was made possible. This publication revealed the ideal properties of coated FNDs for CLEM and EFTEM. Therefore, coated FNDs functionalized with targeting groups such as peptides, antibodies or nanobodies could function as ideal intracellular markers in future which would allow imaging by fluorescence, super-resolution, and electron microscopy. However, there are still some obstacles to overcome before coated FNDs can be applied as markers in future. The protein coating stabilized the FNDs and promoted their uptake but most of the coated FNDs were trapped in intracellular vesicles where target groups could not bind to ligands. Therefore, it is absolutely necessary to ensure release of coated FNDs from endosomes first. One possibility to enhance release of the endosome is to use photo-induced endosomal escape.[293] Our group[228] has already shown that ruthenium complexes can be introduced to HSA. Upon laser irradiation, the ruthenium complex produced singlet oxygen which was toxic for cells in high dose especially when the HSA modified with a ruthenium-complex-modified was targeted to the mitochondria. However, in lower dose the singlet oxygen should not be toxic for the cell but could serve to destroy endosomes and to promote endosomal release of coated FNDs. Another benefit of singlet oxygen is its paramagnetic property which would allow to sense the spin of singlet oxygen by FNDs using magnetic relaxometry.

We also investigated the applicability of the protein coating for *in vivo* studies. Firstly, we showed that protein coated FNDs were taken up by endothelial cells and neuronal cells in a 2D cell culture and that FNDs crossed the BBB in an *in vitro* model. Afterwards, coated FNDs were injected into mice to investigate their behavior and a possible transport through the BBB *in vivo*. Mice were sacrificed and slices of organs were analyzed by fluorescence microscopy. Multi-color fluorescence microscopy imaging was enabled by labelling the protein coating material with a small dye. Colocalization of the fluorescence signals of FNDs and labelled coating protein revealed the stability of the coating material *in vivo*. Furthermore, FND were visualized by the reflection mode of a CLSM. Coated FNDs were clearly identified in brain tissue slices proofing the transport through the BBB *in vivo*. These data revealed the stability of the coating *in vivo* and the promising role of FNDs as imaging agent in mice. However, there are two major requirements which must be fulfilled to implement FNDs as imaging tools *in vivo*. Firstly, the imaging quality must be improved to allow live imaging in mice even at a deeper penetration depth. Secondly, targeting groups must be attached to the coating of FNDs to guide them to specific areas of the mice such as abnormal tissue.
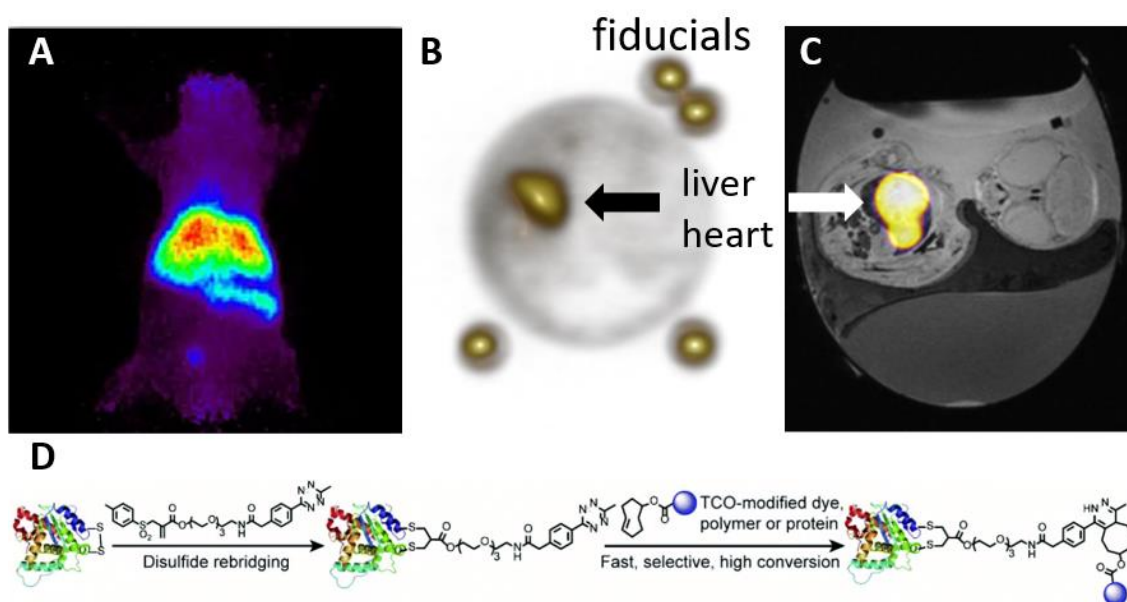
Figure 27 (A–C) Nanodiamonds (NDs) were coated with a protein containing the chelator desferal. After addition of radioactive ions, coated NDs were injected into mice or chick embryos. (A) Biodistribution analysis of ^{68}Ga-labelled NDs in a mouse by positron-emission tomography (PET) revealed a clear localization in liver and spleen. (B) Biodistribution analysis using PET imaging of ^{89}Zr-labelled NDs in the chick chorioallantoic membrane xenograft model showed a clear locally restricted enrichment. (C) The superposition of the PET data with the high-resolution anatomical information of the magnetic resonance imaging made it possible to identify the enriched regions as the liver and heart of the embryo. (D) Schematic illustration of site-selective re-bridging of a protein with a tetrazine-modified linker. Ultra-fast click reaction is performed after addition of *trans*-cyclooctene (TCO)-modified dyes, proteins or polyethylene glycol chains. (D) is reprinted with permission of Xu, L.; Raabe, M.; Zegota, M. M.; Nogueira, J. C. F.; Chudasama, V.; Kuan, S. L.; Weil, T. Site-Selective Protein Modification via Disulfide Rebridging for Fast Tetrazine/*Trans* -Cyclooctene Bioconjugation. *Org. Biomol. Chem.* **2020**, *18* (6), 1140–1147. CC BY 3.0, https://creativecommons.org/licenses/by/3.0.

As discussed in the introduction, hyperpolarization of FNDs could pave the way for MRI in future. However, so far polarization protocols are still very sophisticated and the time during which FNDs are polarized and therefore visible for MRI is too short for *in vivo* measurements. To investigate the biodistribution of FNDs in mice by MRI beforehand, we designed a protein coating which was functionalized with a contrast agent for MRI. The chelator agent DOTA was attached to the coating proteins and subsequently Gd^{3+} ions were loaded into the chelator. Furthermore, the coating proteins were site-specifically modified by attaching doxorubicin to the thiol groups of cysteines. A pH-responsive linker allowed release of the drug under acidic conditions such as in the tumor environment. Without FNDs these proteins formed spherical nanocarriers. The successful therapeutic effect and the high contrast in MRI was revealed in TNBC bearing chick embryos. After showing the proof-of-principle, these modified proteins will be used to coat FNDs by non-covalent adsorption in future. This will allow to study the biodistribution of coated FNDs by MRI before the polarization protocols are more applicable for bioimaging. To further investigate and explore bioimaging in future, we have started to develop a coating material which can be radiolabeled to enable PET imaging. Benefiting again from the fact that the coating proteins are easy to functionalize, we attached the chelator deferoxamine (desferal). After coating of FNDs with the functionalized proteins by adsorption, ^{89}Zr or ^{68}Ga ions were bound by deferoxamine. The radiolabeled FNDs were injected into mice or chick embryos to investigate their biodistribution by PET and MRI (Figure 27A–C).

However, these coated materials do not enable any specific targeting so far. The overarching goal is to use hyperpolarized FNDs for MRI in future. Because the process of hyperpolarization could be detrimental for sensitive targeting groups such as antibodies, the concept to perform the hyperpolarization before attaching the targeting groups was conceived. In order to achieve this, the major consideration is the short time of polarization of FNDs which is in the range of tens of minutes. Therefore, an ultrafast chemistry is required for attaching targeting groups to FNDs. One of the most promising reactions is the inverse electron demand Diels-Alder reaction of 1,2,4,5-tetrazine and *trans*-cyclooctene because of the fast reaction kinetics and excellent orthogonality. We have shown that we can site-selectively modify targeting groups (antibody fragment and somatostatin) with a tetrazine group *via* disulfide rebridging (Figure 27D). The modified antibody fragment and somatostatin retain bioactivity after chemical modification. Furthermore, we showed that the reaction of the site-selective modified targeting groups and a *trans*-cyclooctene bearing PEG or dye was possible. The publication is reprinted in chapter 6.5. In future, this allows us to quickly functionalize *trans*-cyclooctene bearing FNDs with targeting groups which were site-selectively modified with a tetrazine group. The proof that FNDs can be functionalized by this click chemistry was shown recently by the group of Shenderova[294].

To sum up the experiences of the protein coating, following **advantages** were figured out:

+ coating proteins can be easily chemically functionalized and offer a chemical versatility of reactive groups

+ coating proteins can be characterized in detail before adsorption onto NDs

+ coated NDs were applicable in different living systems using various imaging techniques

+ coated NDs showed strong cellular uptake which is beneficial for imaging

+ coated NDs crossed the BBB *in vivo*

The following **disadvantages** of the protein coating were revealed:

− coated NDs were mainly trapped in the cellular endosome

− coated NDs showed strong cellular uptake which might hinder targeting delivery

− stability of protein coating *in vivo* still needs to be studied further

− thick coating which is not suitable for sensing applications

As part of this thesis, we also reported the design of poly(L-DOPA) coated FNDs and their application in photothermal therapy.[75] The self-polymerization of L-DOPA on the surface of FNDs was inspired by mussel foot proteins in Nature. In contrast to the protein coating, L-DOPA polymerization allowed to tune the thickness of the shell around FNDs from a few up to tens of nm. Furthermore, poly(L-DOPA) showed a photothermal effect upon irradiation with an infrared laser. After loading of ICG and transferrin to increase the photothermal effect and to induce targeting, a high cytotoxic effect was revealed for HeLa cells even at a low power of the laser. These poly(L-DOPA) coated FNDs are also interesting candidates for photo-induced endosomal release because without ICG they showed only a weak photothermal effect which did not kill cells but could be strong enough to lead to endosomal release. In combination with CLEM, the release of the coated FND from endosomes or the damage of cell organelles induced by the photothermal effect of the coated FNDs could be studied. Furthermore, NV⁻ or better SiV containing FNDs would allow to measure the increase in temperature in nanoscale by ODMR or fluorescence spectroscopy. That NV⁻ containing FNDs which were coated by poly(L-DOPA) preserve their sensing properties was proven in our publication by ODMR spectroscopy.[75] This could pave the way for not only correlative microscopy but also to combine temperature mapping of a cell in nanoscale and subsequently merging this map with images from fluorescence and electron microscopy to gain a detailed information about the position of the FNDs as well as the effect of the temperature increase.

To sum up the experiences of the poly(L-DOPA) coating, following **advantages** were figured out:

+ thin coating which allows to tune the thickness in nanometer scale

+ possesses a photothermal effect

+ does not harm the magnetic properties of FNDs

+ easy to post-functionalize

The following **disadvantages** of the poly(L-DOPA) coating were revealed:

− needs further modification to prevent aggregation
− the photothermal effect is not strong enough to kill cells
− quenching of the fluorescence of the NV centers in FNDs

I would like to use the last paragraph to make some final remarks about the quality of NDs and how this influences the coating of NDs and their applications in biomedicine, imaging, and sensing. Even though we presented two coating strategies which could be applied broadly across different fields, batch-to-batch variations of NDs remain a problem. Variations in different batches of commercially available NDs can include shape and size, surfaces properties, as well as the number of NV centers per ND. Especially the surface properties are very important for further coating techniques and coating protocols need to be adjusted to every new batch of NDs if the surface properties differ too much. This is a huge drawback considering that biomedical treatments demand standardized protocols. Furthermore, it is aggravated by the fact that primary post-functionalization techniques of NDs are limited. Commercially available NDs are usually air and acid oxidized but still show significant differences from batch to batch. Another problem is the strongly decreasing number of NV centers for smaller commercial NDs (<30 nm). So far this hinders fluorescence imaging *in vivo* due to the weak brightness of these NDs. SiV containing NDs could enable imaging *in vivo* because of their infrared-shifted emission but up to now these NDs are of bad quality and show strong quenching upon laser irradiation. Finally, sensing applications are aggravated because FNDs possess different shapes, sizes, and numbers of NV^- centers. In addition, most of the coating shells are too thick and thus the distance between the NV^- centers and the analyte is too long. Therefore, deeper studies of the ND synthesis and primary post-functionalization are essential to improve coating strategies and guarantee that coating strategies are applicable for different ND batches.

5. References

(1)   Panwar, N.; Soehartono, A. M.; Chan, K. K.; Zeng, S.; Xu, G.; Qu, J.; Coquet, P.; Yong, K.-T.; Chen, X. Nanocarbons for Biology and Medicine: Sensing, Imaging, and Drug Delivery. *Chem. Rev.* **2019**, *119* (16), 9559–9656. https://doi.org/10.1021/acs.chemrev.9b00099.

(2)   Bezzon, V. D. N.; Montanheiro, T. L. A.; de Menezes, B. R. C.; Ribas, R. G.; Righetti, V. A. N.; Rodrigues, K. F.; Thim, G. P. Carbon Nanostructure-Based Sensors: A Brief Review on Recent Advances. *Adv. Mater. Sci. Eng.* **2019**, *2019*, 1–21. https://doi.org/10.1155/2019/4293073.

(3)   Patel, K. D.; Singh, R. K.; Kim, H.-W. Carbon-Based Nanomaterials as an Emerging Platform for Theranostics. *Mater. Horizons* **2019**, *6* (3), 434–469. https://doi.org/10.1039/C8MH00966J.

(4)   Kroto, H. W.; Heath, J. R.; O'Brien, S. C.; Curl, R. F.; Smalley, R. E. C60: Buckminsterfullerene. *Nature* **1985**, *318* (6042), 162–163. https://doi.org/10.1038/318162a0.

(5)   Bodenmann, A. K.; MacDonald, A. H. Graphene: Exploring Carbon Flatland. *Phys. Today* **2007**, *60* (8), 35–41. https://doi.org/10.1063/1.2774096.

(6)   Hu, C.; Li, M.; Qiu, J.; Sun, Y.-P. Design and Fabrication of Carbon Dots for Energy Conversion and Storage. *Chem. Soc. Rev.* **2019**, *48* (8), 2315–2337. https://doi.org/10.1039/C8CS00750K.

(7)   Ali, H.; Ghosh, S.; Jana, N. R. Fluorescent Carbon Dots as Intracellular Imaging Probes. *WIREs Nanomedicine and Nanobiotechnology* **2020**. https://doi.org/10.1002/wnan.1617.

(8)   Shenderova, O. A.; McGuire, G. E. Science and Engineering of Nanodiamond Particle Surfaces for Biological Applications (Review). *Biointerphases* **2015**, *10* (3), 030802. https://doi.org/10.1116/1.4927679.

(9)   Badziag, P.; Verwoerd, W. S.; Ellis, W. P.; Greiner, N. R. Nanometre-Sized Diamonds Are More Stable than Graphite. *Nature* **1990**, *343* (6255), 244–245. https://doi.org/10.1038/343244a0.

(10)   Nunn, N.; Torelli, M.; McGuire, G.; Shenderova, O. Nanodiamond: A High Impact Nanomaterial. *Curr. Opin. Solid State Mater. Sci.* **2017**, *21* (1), 1–9. https://doi.org/10.1016/j.cossms.2016.06.008.

(11)   Zaitsev, A. M. *Optical Properties of Diamond*; Springer Berlin Heidelberg: Berlin, Heidelberg, 2001. https://doi.org/10.1007/978-3-662-04548-0.

(12)   Wu, Y.; Jelezko, F.; Plenio, M. B.; Weil, T. Diamond Quantum Devices in Biology. *Angew. Chemie - Int. Ed.* **2016**, 6586–6598. https://doi.org/10.1002/anie.201506556.

(13)   Schirhagl, R.; Chang, K.; Loretz, M.; Degen, C. L. Nitrogen-Vacancy Centers in Diamond: Nanoscale Sensors for Physics and Biology. *Annu. Rev. Phys. Chem.* **2014**, *65* (1), 83–105. https://doi.org/10.1146/annurev-physchem-040513-

103659.

(14)   Alkahtani, M. H.; Alghannam, F.; Jiang, L.; Almethen, A.; Rampersaud, A. A.; Brick, R.; Gomes, C. L.; Scully, M. O.; Hemmer, P. R. Fluorescent Nanodiamonds: Past, Present, and Future. *Nanophotonics* **2018**, *7* (8), 1423–1453. https://doi.org/10.1515/nanoph-2018-0025.

(15)   Sekiguchi, T.; Sotoma, S.; Harada, Y. Fluorescent Nanodiamonds as a Robust Temperature Sensor inside a Single Cell. *Biophys. Physicobiology* **2018**, *15*, 229–234. https://doi.org/10.2142/biophysico.15.0_229.

(16)   Krueger, A.; Lang, D. Functionality Is Key: Recent Progress in the Surface Modification of Nanodiamond. *Adv. Funct. Mater.* **2012**, *22* (5), 890–906. https://doi.org/10.1002/adfm.201102670.

(17)   Liu, W.; Naydenov, B.; Chakrabortty, S.; Wuensch, B.; Hübner, K.; Ritz, S.; Cölfen, H.; Barth, H.; Koynov, K.; Qi, H.; et al. Fluorescent Nanodiamond–Gold Hybrid Particles for Multimodal Optical and Electron Microscopy Cellular Imaging. *Nano Lett.* **2016**, *16* (10), 6236–6244. https://doi.org/10.1021/acs.nanolett.6b02456.

(18)   Chu, Z.; Zhang, S.; Zhang, B.; Zhang, C.; Fang, C.-Y.; Rehor, I.; Cigler, P.; Chang, H.-C.; Lin, G.; Liu, R.; et al. Unambiguous Observation of Shape Effects on Cellular Fate of Nanoparticles. *Sci. Rep.* **2014**, *4*, 4495.

(19)   Reina, G.; Zhao, L.; Bianco, A.; Komatsu, N. Chemical Functionalization of Nanodiamonds: Opportunities and Challenges Ahead. *Angew. Chemie Int. Ed.* **2019**, *58* (50), 17918–17929. https://doi.org/10.1002/anie.201905997.

(20)   Turcheniuk, K.; Mochalin, V. N. Biomedical Applications of Nanodiamond (Review). *Nanotechnology* **2017**, *28* (25), 252001. https://doi.org/10.1088/1361-6528/aa6ae4.

(21)   Danilenko, V. V. On the History of the Discovery of Nanodiamond Synthesis. *Phys. Solid State* **2004**, *46* (4), 595–599. https://doi.org/10.1134/1.1711431.

(22)   Schrand, A. M.; Hens, S. A. C.; Shenderova, O. A. Nanodiamond Particles: Properties and Perspectives for Bioapplications. *Crit. Rev. Solid State Mater. Sci.* **2009**, *34* (1–2), 18–74. https://doi.org/10.1080/10408430902831987.

(23)   Schwander, M.; Partes, K. A Review of Diamond Synthesis by CVD Processes. *Diam. Relat. Mater.* **2011**, *20* (9), 1287–1301. https://doi.org/10.1016/j.diamond.2011.08.005.

(24)   Bini, R.; Schettino, V. *Materials under Extreme Conditions*, 1st ed.; Yap, D., Ed.; Imperial College Press: London, 2014.

(25)   Pezzagna, S.; Naydenov, B.; Jelezko, F.; Wrachtrup, J.; Meijer, J. Creation Efficiency of Nitrogen-Vacancy Centres in Diamond. *New J. Phys.* **2010**, *12* (6), 065017. https://doi.org/10.1088/1367-2630/12/6/065017.

(26)   Rabeau, J. R.; Reichart, P.; Tamanyan, G.; Jamieson, D. N.; Prawer, S.; Jelezko, F.; Gaebel, T.; Popa, I.; Domhan, M.; Wrachtrup, J. Implantation of Labelled Single Nitrogen Vacancy Centers in Diamond Using N15. *Appl. Phys. Lett.* **2006**, *88* (2), 023113. https://doi.org/10.1063/1.2158700.

(27)   Meijer, J.; Burchard, B.; Domhan, M.; Wittmann, C.; Gaebel, T.; Popa, I.; Jelezko, F.; Wrachtrup, J. Generation of Single Color Centers by Focused Nitrogen Implantation. *Appl. Phys. Lett.* **2005**, *87* (26), 261909. https://doi.org/10.1063/1.2103389.

(28)   Ohno, K.; Joseph Heremans, F.; Bassett, L. C.; Myers, B. A.; Toyli, D. M.; Bleszynski Jayich, A. C.; Palmstrøm, C. J.; Awschalom, D. D. Engineering Shallow Spins in Diamond with Nitrogen Delta-Doping. *Appl. Phys. Lett.* **2012**, *101* (8), 082413. https://doi.org/10.1063/1.4748280.

(29)   Alkahtani, M.; Lang, J.; Naydenov, B.; Jelezko, F.; Hemmer, P. Growth of High-Purity Low-Strain Fluorescent Nanodiamonds. *ACS Photonics* **2019**, *6* (5), 1266–1271. https://doi.org/10.1021/acsphotonics.9b00224.

(30)   Ekimov, E. A.; Kudryavtsev, O. S.; Mordvinova, N. E.; Lebedev, O. I.; Vlasov, I. I. High-Pressure Synthesis of Nanodiamonds from Adamantane: Myth or Reality? *ChemNanoMat* **2018**, *4* (3), 269–273. https://doi.org/10.1002/cnma.201700349.

(31)   Boudou, J.-P.; Curmi, P. A.; Jelezko, F.; Wrachtrup, J.; Aubert, P.; Sennour, M.; Balasubramanian, G.; Reuter, R.; Thorel, A.; Gaffet, E. High Yield Fabrication of Fluorescent Nanodiamonds. *Nanotechnology* **2009**, *20* (23), 235602. https://doi.org/10.1088/0957-4484/20/23/235602.

(32)   Choi, S.; Leong, V.; Davydov, V. A.; Agafonov, V. N.; Cheong, M. W. O.; Kalashnikov, D. A.; Krivitsky, L. A. Varying Temperature and Silicon Content in Nanodiamond Growth: Effects on Silicon-Vacancy Centres. *Sci. Rep.* **2018**, *8* (1), 3792. https://doi.org/10.1038/s41598-018-21953-2.

(33)   Iwasaki, T.; Ishibashi, F.; Miyamoto, Y.; Doi, Y.; Kobayashi, S.; Miyazaki, T.; Tahara, K.; Jahnke, K. D.; Rogers, L. J.; Naydenov, B.; et al. Germanium-Vacancy Single Color Centers in Diamond. *Sci. Rep.* **2015**, *5* (1), 12882. https://doi.org/10.1038/srep12882.

(34)   Wentorf, R. H. The Behavior of Some Carbonaceous Materials at Very High Pressures and High Temperatures. *J. Phys. Chem.* **1965**, *69* (9), 3063–3069. https://doi.org/10.1021/j100893a041.

(35)   Ekimov, E. A.; Kondrina, K. M.; Mordvinova, N. E.; Lebedev, O. I.; Pasternak, D. G.; Vlasov, I. I. High-Pressure, High-Temperature Synthesis of Nanodiamond from Adamantane. *Inorg. Mater.* **2019**, *55* (5), 437–442. https://doi.org/10.1134/S0020168519050042.

(36)   Spohn, M.; Alkahtani, M. H. A.; Leiter, R.; Qi, H.; Kaiser, U.; Hemmer, P.; Ziener, U. Poly(1-Vinyladamantane) as a Template for Nanodiamond Synthesis. *ACS Appl. Nano Mater.* **2018**, *1* (11), 6073–6080. https://doi.org/10.1021/acsanm.8b01238.

(37)   Schmidlin, L.; Pichot, V.; Josset, S.; Pawlak, R.; Glatzel, T.; Kawai, S.; Meyer, E.; Spitzer, D. Two-Dimensional Nanodiamond Monolayers Deposited by Combined Ultracentrifugation and Electrophoresis Techniques. *Appl. Phys. Lett.* **2012**, *101* (25), 253111. https://doi.org/10.1063/1.4772983.

(38)   Smith, B. R.; Gruber, D.; Plakhotnik, T. The Effects of Surface Oxidation on

Luminescence of Nano Diamonds. *Diam. Relat. Mater.* **2010**, *19* (4), 314–318. https://doi.org/10.1016/j.diamond.2009.12.009.

(39) Laube, C.; Oeckinghaus, T.; Lehnert, J.; Griebel, J.; Knolle, W.; Denisenko, A.; Kahnt, A.; Meijer, J.; Wrachtrup, J.; Abel, B. Controlling the Fluorescence Properties of Nitrogen Vacancy Centers in Nanodiamonds. *Nanoscale* **2019**, *11* (4), 1770–1783. https://doi.org/10.1039/C8NR07828A.

(40) Hu, W.; Li, Z.; Yang, J. Surface and Size Effects on the Charge State of NV Center in Nanodiamonds. *Comput. Theor. Chem.* **2013**, *1021*, 49–53. https://doi.org/10.1016/j.comptc.2013.06.015.

(41) Shenderova, O.; Nunn, N. Production and Purification of Nanodiamonds. In *Nanodiamonds*; Elsevier, 2017; pp 25–56. https://doi.org/10.1016/B978-0-32-343029-6.00002-7.

(42) Yeap, W. S.; Chen, S.; Loh, K. P. Detonation Nanodiamond: An Organic Platform for the Suzuki Coupling of Organic Molecules. *Langmuir* **2009**, *25* (1), 185–191. https://doi.org/10.1021/la8029787.

(43) Bertrand, J.-R.; Pioche-Durieu, C.; Ayala, J.; Petit, T.; Girard, H. A.; Malvy, C. P.; Le Cam, E.; Treussart, F.; Arnault, J.-C. Plasma Hydrogenated Cationic Detonation Nanodiamonds Efficiently Deliver to Human Cells in Culture Functional SiRNA Targeting the Ewing Sarcoma Junction Oncogene. *Biomaterials* **2015**, *45*, 93–98. https://doi.org/10.1016/j.biomaterials.2014.12.007.

(44) Barras, A.; Lyskawa, J.; Szunerits, S.; Woisel, P.; Boukherroub, R. Direct Functionalization of Nanodiamond Particles Using Dopamine Derivatives. *Langmuir* **2011**, *27* (20), 12451–12457. https://doi.org/10.1021/la202571d.

(45) Turcheniuk, V.; Turcheniuk, K.; Bouckaert, J.; Barras, A.; Dumych, T.; Bilyy, R.; Zaitsev, V.; Siriwardena, A.; Wang, Q.; Boukherroub, R.; et al. Affinity of Glycan-Modified Nanodiamonds towards Lectins and Uropathogenic Escherichia Coli. *ChemNanoMat* **2016**, *2* (4), 307–314. https://doi.org/10.1002/cnma.201500229.

(46) Zhang, D.; Zhao, Q.; Zang, J.; Lu, Y.-J.; Dong, L.; Shan, C.-X. Luminescent Hybrid Materials Based on Nanodiamonds. *Carbon N. Y.* **2018**, *127*, 170–176. https://doi.org/10.1016/j.carbon.2017.11.009.

(47) Wuest, K. N. R.; Trouillet, V.; Goldmann, A. S.; Stenzel, M. H.; Barner-Kowollik, C. Polymer Functional Nanodiamonds by Light-Induced Ligation. *Macromolecules* **2016**, *49* (5), 1712–1721. https://doi.org/10.1021/acs.macromol.5b02607.

(48) Akiel, R. D.; Zhang, X.; Abeywardana, C.; Stepanov, V.; Qin, P. Z.; Takahashi, S. Investigating Functional DNA Grafted on Nanodiamond Surface Using Site-Directed Spin Labeling and Electron Paramagnetic Resonance Spectroscopy. *J. Phys. Chem. B* **2016**, *120* (17), 4003–4008. https://doi.org/10.1021/acs.jpcb.6b00790.

(49) Barras, A.; Martin, F. A.; Bande, O.; Baumann, J.-S.; Ghigo, J.-M.; Boukherroub, R.; Beloin, C.; Siriwardena, A.; Szunerits, S. Glycan-Functionalized Diamond Nanoparticles as Potent E. Coli Anti-Adhesives. *Nanoscale* **2013**, *5* (6), 2307. https://doi.org/10.1039/c3nr33826f.

(50)   Khanal, M.; Larsonneur, F.; Raks, V.; Barras, A.; Baumann, J.-S.; Martin, F. A.; Boukherroub, R.; Ghigo, J.-M.; Ortiz Mellet, C.; Zaitsev, V.; et al. Inhibition of Type 1 Fimbriae-Mediated Escherichia Coli Adhesion and Biofilm Formation by Trimeric Cluster Thiomannosides Conjugated to Diamond Nanoparticles. *Nanoscale* **2015**, *7* (6), 2325–2335. https://doi.org/10.1039/C4NR05906A.

(51)   Lai, H.; Lu, M.; Lu, H.; Stenzel, M. H.; Xiao, P. PH-Triggered Release of Gemcitabine from Polymer Coated Nanodiamonds Fabricated by RAFT Polymerization and Copper Free Click Chemistry. *Polym. Chem.* **2016**, *7* (40), 6220–6230. https://doi.org/10.1039/C6PY01188H.

(52)   Wang, D.; Tong, Y.; Li, Y.; Tian, Z.; Cao, R.; Yang, B. PEGylated Nanodiamond for Chemotherapeutic Drug Delivery. *Diam. Relat. Mater.* **2013**, *36*, 26–34. https://doi.org/10.1016/j.diamond.2013.04.002.

(53)   Kivi, M. A.; Alinia, H.; Jafarzadeh, Y.; Yegani, R. High-density Polyethylene Membranes Embedded with Carboxylated and Polyethylene Glycol-grafted Nanodiamond to Be Used in Membrane Bioreactors. *J. Appl. Polym. Sci.* **2019**, *136* (35), 47914. https://doi.org/10.1002/app.47914.

(54)   Dong, Y.; Cao, R.; Li, Y.; Wang, Z.; Li, L.; Tian, L. Folate-Conjugated Nanodiamond for Tumor-Targeted Drug Delivery. *RSC Adv.* **2015**, *5* (101), 82711–82716. https://doi.org/10.1039/C5RA12383F.

(55)   Huang, H.; Liu, M.; Tuo, X.; Chen, J.; Mao, L.; Wen, Y.; Tian, J.; Zhou, N.; Zhang, X.; Wei, Y. One-Step Fabrication of PEGylated Fluorescent Nanodiamonds through the Thiol-Ene Click Reaction and Their Potential for Biological Imaging. *Appl. Surf. Sci.* **2018**, *439*, 1143–1151. https://doi.org/10.1016/j.apsusc.2017.12.233.

(56)   Lu, M.; Wang, Y. K.; Zhao, J.; Lu, H.; Stenzel, M. H.; Xiao, P. PEG Grafted-Nanodiamonds for the Delivery of Gemcitabine. *Macromol. Rapid Commun.* **2016**, *37* (24), 2023–2029. https://doi.org/10.1002/marc.201600344.

(57)   Zhang, X.; Fu, C.; Feng, L.; Ji, Y.; Tao, L.; Huang, Q.; Li, S.; Wei, Y. PEGylation and PolyPEGylation of Nanodiamond. *Polymer (Guildf).* **2012**, *53* (15), 3178–3184. https://doi.org/10.1016/j.polymer.2012.05.029.

(58)   Zhang, T.; Cui, H.; Fang, C.-Y.; Cheng, K.; Yang, X.; Chang, H.-C.; Forrest, M. L. Targeted Nanodiamonds as Phenotype-Specific Photoacoustic Contrast Agents for Breast Cancer. *Nanomedicine* **2015**, *10* (4), 573–587. https://doi.org/10.2217/nnm.14.141.

(59)   Li, T.-F.; Xu, Y.-H.; Li, K.; Wang, C.; Liu, X.; Yue, Y.; Chen, Z.; Yuan, S.-J.; Wen, Y.; Zhang, Q.; et al. Doxorubicin-Polyglycerol-Nanodiamond Composites Stimulate Glioblastoma Cell Immunogenicity through Activation of Autophagy. *Acta Biomater.* **2019**, *86*, 381–394. https://doi.org/10.1016/j.actbio.2019.01.020.

(60)   Sotoma, S.; Iimura, J.; Igarashi, R.; Hirosawa, K.; Ohnishi, H.; Mizukami, S.; Kikuchi, K.; Fujiwara, T.; Shirakawa, M.; Tochio, H. Selective Labeling of Proteins on Living Cell Membranes Using Fluorescent Nanodiamond Probes. *Nanomaterials* **2016**, *6* (4), 56. https://doi.org/10.3390/nano6040056.

(61)   Yoshino, F.; Amano, T.; Zou, Y.; Xu, J.; Kimura, F.; Furusho, Y.; Chano, T.; Murakami, T.; Zhao, L.; Komatsu, N. Preferential Tumor Accumulation of Polyglycerol Functionalized Nanodiamond Conjugated with Cyanine Dye Leading to Near-Infrared Fluorescence In Vivo Tumor Imaging. *Small* **2019**, 1901930. https://doi.org/10.1002/smll.201901930.

(62)   Li, T.-F.; Li, K.; Zhang, Q.; Wang, C.; Yue, Y.; Chen, Z.; Yuan, S.-J.; Liu, X.; Wen, Y.; Han, M.; et al. Dendritic Cell-Mediated Delivery of Doxorubicin-Polyglycerol-Nanodiamond Composites Elicits Enhanced Anti-Cancer Immune Response in Glioblastoma. *Biomaterials* **2018**, *181*, 35–52. https://doi.org/10.1016/j.biomaterials.2018.07.035.

(63)   Zhao, L.; Xu, Y. H.; Qin, H.; Abe, S.; Akasaka, T.; Chano, T.; Watari, F.; Kimura, T.; Komatsu, N.; Chen, X. Platinum on Nanodiamond: A Promising Prodrug Conjugated with Stealth Polyglycerol, Targeting Peptide and Acid-Responsive Antitumor Drug. *Adv. Funct. Mater.* **2014**, *24* (34), 5348–5357. https://doi.org/10.1002/adfm.201304298.

(64)   Hsieh, F.-J.; Sotoma, S.; Lin, H.-H.; Cheng, C.-Y.; Yu, T.-Y.; Hsieh, C.-L.; Lin, C.-H.; Chang, H.-C. Bioorthogonal Fluorescent Nanodiamonds for Continuous Long-Term Imaging and Tracking of Membrane Proteins. *ACS Appl. Mater. Interfaces* **2019**, *11* (22), 19774–19781. https://doi.org/10.1021/acsami.9b03640.

(65)   Terada, D.; Sotoma, S.; Harada, Y.; Igarashi, R.; Shirakawa, M. One-Pot Synthesis of Highly Dispersible Fluorescent Nanodiamonds for Bioconjugation. *Bioconjug. Chem.* **2018**, *29* (8), 2786–2792. https://doi.org/10.1021/acs.bioconjchem.8b00412.

(66)   Zhao, L.; Xu, Y.-H.; Akasaka, T.; Abe, S.; Komatsu, N.; Watari, F.; Chen, X. Polyglycerol-Coated Nanodiamond as a Macrophage-Evading Platform for Selective Drug Delivery in Cancer Cells. *Biomaterials* **2014**, *35* (20), 5393–5406. https://doi.org/10.1016/j.biomaterials.2014.03.041.

(67)   Zhao, L.; Takimoto, T.; Ito, M.; Kitagawa, N.; Kimura, T.; Komatsu, N. Chromatographic Separation of Highly Soluble Diamond Nanoparticles Prepared by Polyglycerol Grafting. *Angew. Chemie Int. Ed.* **2011**, *50* (6), 1388–1392. https://doi.org/10.1002/anie.201006310.

(68)   Genjo, T.; Sotoma, S.; Tanabe, R.; Igarashi, R.; Shirakawa, M. A Nanodiamond-Peptide Bioconjugate for Fluorescence and ODMR Microscopy of a Single Actin Filament. *Anal. Sci.* **2016**, *32* (11), 1165–1170. https://doi.org/10.2116/analsci.32.1165.

(69)   Lim, D. G.; Rajasekaran, N.; Lee, D.; Kim, N. A.; Jung, H. S.; Hong, S.; Shin, Y. K.; Kang, E.; Jeong, S. H. Polyamidoamine-Decorated Nanodiamonds as a Hybrid Gene Delivery Vector and SiRNA Structural Characterization at the Charged Interfaces. *ACS Appl. Mater. Interfaces* **2017**, *9* (37), 31543–31556. https://doi.org/10.1021/acsami.7b09624.

(70)   Zeng, Y.; Liu, W.; Wang, Z.; Singamaneni, S.; Wang, R. Multifunctional Surface Modification of Nanodiamonds Based on Dopamine Polymerization. *Langmuir* **2018**, *34* (13), 4036–4042. https://doi.org/10.1021/acs.langmuir.8b00509.

(71)   Qin, S.; Cui, M.; Qiu, S.; Zhao, H.; Wang, L.; Zhang, A. Dopamine@Nanodiamond as Novel Reinforcing Nanofillers for Polyimide with Enhanced Thermal, Mechanical and Wear Resistance Performance. *RSC Adv.* **2018**, *8* (7), 3694–3704. https://doi.org/10.1039/C7RA10688B.

(72)   Maziukiewicz, D.; Grześkowiak, B.; Coy, E.; Jurga, S.; Mrówczyński, R. NDs@PDA@ICG Conjugates for Photothermal Therapy of Glioblastoma Multiforme. *Biomimetics* **2019**, *4* (1), 3. https://doi.org/10.3390/biomimetics4010003.

(73)   Jung, H.-S.; Cho, K.-J.; Seol, Y.; Takagi, Y.; Dittmore, A.; Roche, P. A.; Neuman, K. C. Polydopamine Encapsulation of Fluorescent Nanodiamonds for Biomedical Applications. *Adv. Funct. Mater.* **2018**, *28* (33), 1801252. https://doi.org/10.1002/adfm.201801252.

(74)   Chen, X.; Zhou, J.; Zhang, Y.; Zhu, S.; Tian, X.; Meng, F.; Cui, L.; Xue, P.; Huang, R.; Sun, J. Polydopamine-Modified Polyaniline/Nanodiamond Ternary Hybrids with Brain Fold-like Surface for Enhanced Dual Band Electromagnetic Absorption. *ACS Appl. Polym. Mater.* **2019**, *1* (3), 405–413. https://doi.org/10.1021/acsapm.8b00127.

(75)   Harvey, S.; Raabe, M.; Ermakova, A.; Wu, Y.; Zapata, T.; Chen, C.; Lu, H.; Jelezko, F.; Ng, D. Y. W.; Weil, T. Transferrin-Coated Nanodiamond–Drug Conjugates for Milliwatt Photothermal Applications. *Adv. Ther.* **2019**, 1900067. https://doi.org/10.1002/adtp.201900067.

(76)   Lai, H.; Stenzel, M. H.; Xiao, P. Surface Engineering and Applications of Nanodiamonds in Cancer Treatment and Imaging. *Int. Mater. Rev.* **2019**, 1–37. https://doi.org/10.1080/09506608.2019.1622202.

(77)   Bumb, A.; Sarkar, S. K.; Billington, N.; Brechbiel, M. W.; Neuman, K. C. Silica Encapsulation of Fluorescent Nanodiamonds for Colloidal Stability and Facile Surface Functionalization. *J. Am. Chem. Soc.* **2013**, *135* (21), 7815–7818. https://doi.org/10.1021/ja4016815.

(78)   von Haartman, E.; Jiang, H.; Khomich, A. A.; Zhang, J.; Burikov, S. A.; Dolenko, T. A.; Ruokolainen, J.; Gu, H.; Shenderova, O. A.; Vlasov, I. I.; et al. Core–Shell Designs of Photoluminescent Nanodiamonds with Porous Silica Coatings for Bioimaging and Drug Delivery I: Fabrication. *J. Mater. Chem. B* **2013**, *1* (18), 2358. https://doi.org/10.1039/c3tb20308e.

(79)   Rehor, I.; Slegerova, J.; Kucka, J.; Proks, V.; Petrakova, V.; Adam, M.-P.; Treussart, F.; Turner, S.; Bals, S.; Sacha, P.; et al. Fluorescent Nanodiamonds Embedded in Biocompatible Translucent Shells. *Small* **2014**, *10* (6), 1106–1115. https://doi.org/10.1002/smll.201302336.

(80)   Rehor, I.; Mackova, H.; Filippov, S. K.; Kucka, J.; Proks, V.; Slegerova, J.; Turner, S.; Van Tendeloo, G.; Ledvina, M.; Hruby, M.; et al. Fluorescent Nanodiamonds with Bioorthogonally Reactive Protein-Resistant Polymeric Coatings. *Chempluschem* **2014**, *79* (1), 21–24. https://doi.org/10.1002/cplu.201300339.

(81)   Li, Y.; Zhou, X. Transferrin-Coupled Fluorescence Nanodiamonds as Targeting

Intracellular Transporters: An Investigation of the Uptake Mechanism. *Diam. Relat. Mater.* **2010**, *19* (10), 1163–1167. https://doi.org/10.1016/j.diamond.2010.05.003.

(82) Wang, Z.; Tian, Z.; Dong, Y.; Li, L.; Tian, L.; Li, Y.; Yang, B. Nanodiamond-Conjugated Transferrin as Chemotherapeutic Drug Delivery. *Diam. Relat. Mater.* **2015**, *58*, 84–93. https://doi.org/10.1016/j.diamond.2015.06.008.

(83) Cordina, N. M.; Sayyadi, N.; Parker, L. M.; Everest-Dass, A.; Brown, L. J.; Packer, N. H. Reduced Background Autofluorescence for Cell Imaging Using Nanodiamonds and Lanthanide Chelates. *Sci. Rep.* **2018**, *8* (1), 4521. https://doi.org/10.1038/s41598-018-22702-1.

(84) Chan, M. S.; Landig, R.; Choi, J.; Zhou, H.; Liao, X.; Lukin, M. D.; Park, H.; Lo, P. K. Stepwise Ligand-Induced Self-Assembly for Facile Fabrication of Nanodiamond–Gold Nanoparticle Dimers via Noncovalent Biotin–Streptavidin Interactions. *Nano Lett.* **2019**, *19* (3), 2020–2026. https://doi.org/10.1021/acs.nanolett.9b00113.

(85) Li, D.; Chen, X.; Wang, H.; Liu, J.; Zheng, M.; Fu, Y.; Yu, Y.; Zhi, J. Cetuximab-Conjugated Nanodiamonds Drug Delivery System for Enhanced Targeting Therapy and 3D Raman Imaging. *J. Biophotonics* **2017**, *10* (12), 1636–1646. https://doi.org/10.1002/jbio.201700011.

(86) Golyshev, S. A.; Berkovich, A. K.; Yakovlev, R. Y.; Bystrov, D. M.; Ivanov, N. M.; Balandina, G. N.; Rudenskaya, G. N. Nanodiamond-Chymotrypsin and Nanodiamond-Papain Conjugates, Their Synthesis and Activity and Visualization of Their Interaction with Cells Using Optical and Electron Microscopy. *Biointerphases* **2017**, *12* (3), 031004. https://doi.org/10.1116/1.4996108.

(87) Wang, X.; Gu, M.; Toh, T. B.; Abdullah, N. L. B.; Chow, E. K.-H. Stimuli-Responsive Nanodiamond-Based Biosensor for Enhanced Metastatic Tumor Site Detection. *SLAS Technol. Transl. Life Sci. Innov.* **2018**, *23* (1), 44–56. https://doi.org/10.1177/2472630317735497.

(88) Tsai, P.-C.; Chen, O. Y.; Tzeng, Y.-K.; Hui, Y. Y.; Guo, J. Y.; Wu, C.-C.; Chang, M.-S.; Chang, H.-C. Gold/Diamond Nanohybrids for Quantum Sensing Applications. *EPJ Quantum Technol.* **2015**, *2* (1), 19. https://doi.org/10.1140/epjqt/s40507-015-0031-3.

(89) Lai, H.; Chen, F.; Lu, M.; Stenzel, M. H.; Xiao, P. Polypeptide-Grafted Nanodiamonds for Controlled Release of Melittin to Treat Breast Cancer. *ACS Macro Lett.* **2017**, *6* (8), 796–801. https://doi.org/10.1021/acsmacrolett.7b00389.

(90) Balakin, S.; Missirlis, A.; Klemmed, B.; Lee, J.; Opitz, J.; Yeo, J.-S.; Cuniberti, G. Quantitative Analysis of BMP-2 Derived Peptide Covalently Grafted onto Oxidized Detonation Nanodiamonds. *Carbon N. Y.* **2019**, *152*, 740–745. https://doi.org/10.1016/j.carbon.2019.05.064.

(91) Knapinska, A. M.; Tokmina-Roszyk, D.; Amar, S.; Tokmina-Roszyk, M.; Mochalin, V. N.; Gogotsi, Y.; Cosme, P.; Terentis, A. C.; Fields, G. B. Solid-Phase Synthesis,

Characterization, and Cellular Activities of Collagen-Model Nanodiamond-Peptide Conjugates. *Biopolymers* **2015**, *104* (3), 186–195. https://doi.org/10.1002/bip.22636.

(92) Salaam, A. D.; Hwang, P.; McIntosh, R.; Green, H. N.; Jun, H.-W.; Dean, D. Nanodiamond-DGEA Peptide Conjugates for Enhanced Delivery of Doxorubicin to Prostate Cancer. *Beilstein J. Nanotechnol.* **2014**, *5*, 937–945. https://doi.org/10.3762/bjnano.5.107.

(93) Chan, M. S.; Liu, L. S.; Leung, H. M.; Lo, P. K. Cancer-Cell-Specific Mitochondria-Targeted Drug Delivery by Dual-Ligand-Functionalized Nanodiamonds Circumvent Drug Resistance. *ACS Appl. Mater. Interfaces* **2017**, *9* (13), 11780–11789. https://doi.org/10.1021/acsami.6b15954.

(94) Gaillard, C.; Girard, H. A.; Falck, C.; Paget, V.; Simic, V.; Ugolin, N.; Bergonzo, P.; Chevillard, S.; Arnault, J. C. Peptide Nucleic Acid–Nanodiamonds: Covalent and Stable Conjugates for DNA Targeting. *RSC Adv.* **2014**, *4* (7), 3566–3572. https://doi.org/10.1039/C3RA45158E.

(95) Kim, H.; Man, H. Bin; Saha, B.; Kopacz, A. M.; Lee, O.-S.; Schatz, G. C.; Ho, D.; Liu, W. K. Multiscale Simulation as a Framework for the Enhanced Design of Nanodiamond-Polyethylenimine-Based Gene Delivery. *J. Phys. Chem. Lett.* **2012**, *3* (24), 3791–3797. https://doi.org/10.1021/jz301756e.

(96) Zhang, X.-Q.; Chen, M.; Lam, R.; Xu, X.; Osawa, E.; Ho, D. Polymer-Functionalized Nanodiamond Platforms as Vehicles for Gene Delivery. *ACS Nano* **2009**, *3* (9), 2609–2616. https://doi.org/10.1021/nn900865g.

(97) Pichot, V.; Guerchoux, M.; Muller, O.; Guillevic, M.; Fioux, P.; Merlat, L.; Spitzer, D. Nanodiamond Coating by Polyethylenimine for Optical Limitation. *Diam. Relat. Mater.* **2019**, *95*, 55–59. https://doi.org/10.1016/j.diamond.2019.04.001.

(98) Petrakova, V.; Benson, V.; Buncek, M.; Fiserova, A.; Ledvina, M.; Stursa, J.; Cigler, P.; Nesladek, M. Imaging of Transfection and Intracellular Release of Intact, Non-Labeled DNA Using Fluorescent Nanodiamonds. *Nanoscale* **2016**, *8* (23), 12002–12012. https://doi.org/10.1039/C6NR00610H.

(99) Křivohlavá, R.; Neuhöferová, E.; Jakobsen, K. Q.; Benson, V. Knockdown of MicroRNA-135b in Mammary Carcinoma by Targeted Nanodiamonds: Potentials and Pitfalls of In Vivo Applications. *Nanomaterials* **2019**, *9* (6), 866. https://doi.org/10.3390/nano9060866.

(100) Wuest, K. N. R.; Lu, H.; Thomas, D. S.; Goldmann, A. S.; Stenzel, M. H.; Barner-Kowollik, C. Fluorescent Glyco Single-Chain Nanoparticle-Decorated Nanodiamonds. *ACS Macro Lett.* **2017**, *6* (10), 1168–1174. https://doi.org/10.1021/acsmacrolett.7b00659.

(101) Lee, J. W.; Lee, S.; Jang, S.; Han, K. Y.; Kim, Y.; Hyun, J.; Kim, S. K.; Lee, Y. Preparation of Non-Aggregated Fluorescent Nanodiamonds (FNDs) by Non-Covalent Coating with a Block Copolymer and Proteins for Enhancement of Intracellular Uptake. *Mol. Biosyst.* **2013**, *9* (5), 1004. https://doi.org/10.1039/c2mb25431j.

(102) Aramesh, M.; Shimoni, O.; Ostrikov, K.; Prawer, S.; Cervenka, J. Surface Charge Effects in Protein Adsorption on Nanodiamonds. *Nanoscale* **2015**, *7* (13), 5726–5736. https://doi.org/10.1039/C5NR00250H.

(103) Lin, C. L.; Lin, C. H.; Chang, H. C.; Su, M. C. Protein Attachment on Nanodiamonds. *J. Phys. Chem. A* **2015**, *119* (28), 7704–7711. https://doi.org/10.1021/acs.jpca.5b01031.

(104) Chen, M.; Zuo, X.; Xu, Q.; Wang, R.; Fan, S.; Wu, H. Investigating the Interaction of Nanodiamonds with Human Serum Albumin and Induced Cytotoxicity. *J. Spectrosc.* **2019**, *2019*, 1–9. https://doi.org/10.1155/2019/4503137.

(105) Chang, B.-M.; Lin, H.-H.; Su, L.-J.; Lin, W.-D.; Lin, R.-J.; Tzeng, Y.-K.; Lee, R. T.; Lee, Y. C.; Yu, A. L.; Chang, H.-C. Highly Fluorescent Nanodiamonds Protein-Functionalized for Cell Labeling and Targeting. *Adv. Funct. Mater.* **2013**, *23* (46), 5737–5745. https://doi.org/10.1002/adfm.201301075.

(106) Tzeng, Y.-K.; Faklaris, O.; Chang, B.-M.; Kuo, Y.; Hsu, J.-H.; Chang, H.-C. Superresolution Imaging of Albumin-Conjugated Fluorescent Nanodiamonds in Cells by Stimulated Emission Depletion. *Angew. Chemie Int. Ed.* **2011**, *50* (10), 2262–2265. https://doi.org/10.1002/anie.201007215.

(107) Moore, L.; Gatica, M.; Kim, H.; Osawa, E.; Ho, D. Multi-Protein Delivery by Nanodiamonds Promotes Bone Formation. *J. Dent. Res.* **2013**, *92* (11), 976–981. https://doi.org/10.1177/0022034513504952.

(108) Pham, M. D.; Epperla, C. P.; Hsieh, C.-L.; Chang, W.; Chang, H.-C. Glycosaminoglycans-Specific Cell Targeting and Imaging Using Fluorescent Nanodiamonds Coated with Viral Envelope Proteins. *Anal. Chem.* **2017**, *89* (12), 6527–6534. https://doi.org/10.1021/acs.analchem.7b00627.

(109) Ermakova, A.; Pramanik, G.; Cai, J.-M.; Algara-Siller, G.; Kaiser, U.; Weil, T.; Tzeng, Y.-K.; Chang, H. C.; McGuinness, L. P.; Plenio, M. B.; et al. Detection of a Few Metallo-Protein Molecules Using Color Centers in Nanodiamonds. *Nano Lett.* **2013**, *13* (7), 3305–3309. https://doi.org/10.1021/nl4015233.

(110) Su, L.-J.; Lin, H.-H.; Wu, M.-S.; Pan, L.; Yadav, K.; Hsu, H.-H.; Ling, T.-Y.; Chen, Y.-T.; Chang, H.-C. Intracellular Delivery of Luciferase with Fluorescent Nanodiamonds for Dual-Modality Imaging of Human Stem Cells. *Bioconjug. Chem.* **2019**, *30* (8), 2228–2237. https://doi.org/10.1021/acs.bioconjchem.9b00458.

(111) Liao, W.-S.; Ho, Y.; Lin, Y.-W.; Naveen Raj, E.; Liu, K.-K.; Chen, C.; Zhou, X.-Z.; Lu, K.-P.; Chao, J.-I. Targeting EGFR of Triple-Negative Breast Cancer Enhances the Therapeutic Efficacy of Paclitaxel- and Cetuximab-Conjugated Nanodiamond Nanocomposite. *Acta Biomater.* **2019**, *86*, 395–405. https://doi.org/10.1016/j.actbio.2019.01.025.

(112) Smith, A. H.; Robinson, E. M.; Zhang, X.-Q.; Chow, E. K.; Lin, Y.; Osawa, E.; Xi, J.; Ho, D. Triggered Release of Therapeutic Antibodies from Nanodiamond Complexes. *Nanoscale* **2011**, *3* (7), 2844. https://doi.org/10.1039/c1nr10278h.

(113) Zhang, T.; Neumann, A.; Lindlau, J.; Wu, Y.; Pramanik, G.; Naydenov, B.; Jelezko,

F.; Schüder, F.; Huber, S.; Huber, M.; et al. DNA-Based Self-Assembly of Fluorescent Nanodiamonds. *J. Am. Chem. Soc.* **2015**, *137* (31), 9776–9779. https://doi.org/10.1021/jacs.5b04857.

(114) Han, S.; Raabe, M.; Hodgson, L.; Mantell, J.; Verkade, P.; Lasser, T.; Landfester, K.; Weil, T.; Lieberwirth, I. High-Contrast Imaging of Nanodiamonds in Cells by Energy Filtered and Correlative Light-Electron Microscopy: Toward a Quantitative Nanoparticle-Cell Analysis. *Nano Lett.* **2019**, *19* (3), 2178–2185. https://doi.org/10.1021/acs.nanolett.9b00752.

(115) Wu, Y.; Ermakova, A.; Liu, W.; Pramanik, G.; Vu, T. M.; Kurz, A.; McGuinness, L.; Naydenov, B.; Hafner, S.; Reuter, R.; et al. Programmable Biopolymers for Advancing Biomedical Applications of Fluorescent Nanodiamonds. *Adv. Funct. Mater.* **2015**, *25* (42), 6576–6585. https://doi.org/10.1002/adfm.201502704.

(116) Moscariello, P.; Raabe, M.; Liu, W.; Bernhardt, S.; Qi, H.; Kaiser, U.; Wu, Y.; Weil, T.; Luhmann, H. J.; Hedrich, J. Unraveling In Vivo Brain Transport of Protein-Coated Fluorescent Nanodiamonds. *Small* **2019**, 1902992. https://doi.org/10.1002/smll.201902992.

(117) Shimkunas, R. A.; Robinson, E.; Lam, R.; Lu, S.; Xu, X.; Zhang, X.-Q.; Huang, H.; Osawa, E.; Ho, D. Nanodiamond–Insulin Complexes as PH-Dependent Protein Delivery Vehicles. *Biomaterials* **2009**, *30* (29), 5720–5728. https://doi.org/10.1016/j.biomaterials.2009.07.004.

(118) Leung, H. M.; Chan, M. S.; Liu, L. S.; Wong, S. W.; Lo, T. W.; Lau, C.-H.; Tin, C.; Lo, P. K. Dual-Function, Cationic, Peptide-Coated Nanodiamond Systems: Facilitating Nuclear-Targeting Delivery for Enhanced Gene Therapy Applications. *ACS Sustain. Chem. Eng.* **2018**, *6* (8), 9671–9681. https://doi.org/10.1021/acssuschemeng.8b00446.

(119) Morales-Zavala, F.; Casanova-Morales, N.; Gonzalez, R. B.; Chandía-Cristi, A.; Estrada, L. D.; Alvizú, I.; Waselowski, V.; Guzman, F.; Guerrero, S.; Oyarzún-Olave, M.; et al. Functionalization of Stable Fluorescent Nanodiamonds towards Reliable Detection of Biomarkers for Alzheimer's Disease. *J. Nanobiotechnology* **2018**, *16* (1), 1–14. https://doi.org/10.1186/s12951-018-0385-7.

(120) Badea, I.; Kaur; Michel; Chitanda; Maley; Yang; Borondics; Verrall. Lysine-Functionalized Nanodiamonds: Synthesis, Physiochemical Characterization, and Nucleic Acid Binding Studies. *Int. J. Nanomedicine* **2012**, 3851. https://doi.org/10.2147/IJN.S32877.

(121) Badea, I.; Alwani, S.; Kaur, R.; Michel, D.; Chitanda, J. M.; Verrall, R.; Karunakaran, C. Lysine-Functionalized Nanodiamonds as Gene Carriers: Development of Stable Colloidal Dispersion for in Vitro Cellular Uptake Studies and SiRNA Delivery Application. *Int. J. Nanomedicine* **2016**, 687. https://doi.org/10.2147/IJN.S92218.

(122) Lukowski, S.; Neuhoferova, E.; Kinderman, M.; Krivohlava, R.; Mineva, A.; Petrakova, V.; Benson, V. Fluorescent Nanodiamonds Are Efficient, Easy-to-Use Cyto-Compatible Vehicles for Monitored Delivery of Non-Coding Regulatory RNAs. *J. Biomed. Nanotechnol.* **2018**, *14* (5), 946–958.

https://doi.org/10.1166/jbn.2018.2540.

(123) Zhao, L.; Nakae, Y.; Qin, H.; Ito, T.; Kimura, T.; Kojima, H.; Chan, L.; Komatsu, N. Polyglycerol-Functionalized Nanodiamond as a Platform for Gene Delivery: Derivatization, Characterization, and Hybridization with DNA. *Beilstein J. Org. Chem.* **2014**, *10*, 707–713. https://doi.org/10.3762/bjoc.10.64.

(124) Xia, Y.; Deng, X.; Cao, M.; Liu, S.; Zhang, X.; Xiao, X.; Shen, S.; Hu, Q.; Sheng, W. Nanodiamond-Based Layer-by-Layer Nanohybrids Mediate Targeted Delivery of MiR-34a for Triple Negative Breast Cancer Therapy. *RSC Adv.* **2018**, *8* (25), 13789–13797. https://doi.org/10.1039/C8RA00907D.

(125) Hsieh, F.-J.; Chen, Y.-W.; Huang, Y.-K.; Lee, H.-M.; Lin, C.-H.; Chang, H.-C. Correlative Light-Electron Microscopy of Lipid-Encapsulated Fluorescent Nanodiamonds for Nanometric Localization of Cell Surface Antigens. *Anal. Chem.* **2018**, *90* (3), 1566–1571. https://doi.org/10.1021/acs.analchem.7b04549.

(126) Hsieh, F.-J.; Chen, Y.-W.; Hui, Y.; Lin, C.-H.; Chang, H.-C. Quantification and Imaging of Antigens on Cell Surface with Lipid-Encapsulated Fluorescent Nanodiamonds. *Micromachines* **2019**, *10* (5), 304. https://doi.org/10.3390/mi10050304.

(127) Vavra, J.; Rehor, I.; Rendler, T.; Jani, M.; Bednar, J.; Baksh, M. M.; Zappe, A.; Wrachtrup, J.; Cigler, P. Supported Lipid Bilayers on Fluorescent Nanodiamonds: A Structurally Defined and Versatile Coating for Bioapplications. *Adv. Funct. Mater.* **2018**, *28* (45), 1803406. https://doi.org/10.1002/adfm.201803406.

(128) van der Laan, K.; Hasani, M.; Zheng, T.; Schirhagl, R. Nanodiamonds for In Vivo Applications. *Small* **2018**, *14* (19), 1703838. https://doi.org/10.1002/smll.201703838.

(129) Lin, Y.-C.; Wu, K.-T.; Lin, Z.-R.; Perevedentseva, E.; Karmenyan, A.; Lin, M.-D.; Cheng, C.-L. Nanodiamond for Biolabelling and Toxicity Evaluation in the Zebrafish Embryo in Vivo. *J. Biophotonics* **2016**, *9* (8), 827–836. https://doi.org/10.1002/jbio.201500304.

(130) Zhang, X.; Yin, J.; Kang, C.; Li, J.; Zhu, Y.; Li, W.; Huang, Q.; Zhu, Z. Biodistribution and Toxicity of Nanodiamonds in Mice after Intratracheal Instillation. *Toxicol. Lett.* **2010**, *198* (2), 237–243. https://doi.org/10.1016/j.toxlet.2010.07.001.

(131) Yuan, Y.; Chen, Y.; Liu, J.-H.; Wang, H.; Liu, Y. Biodistribution and Fate of Nanodiamonds in Vivo. *Diam. Relat. Mater.* **2009**, *18* (1), 95–100. https://doi.org/10.1016/j.diamond.2008.10.031.

(132) Zhang, X.; Hu, W.; Li, J.; Tao, L.; Wei, Y. A Comparative Study of Cellular Uptake and Cytotoxicity of Multi-Walled Carbon Nanotubes, Graphene Oxide, and Nanodiamond. *Toxicol. Res. (Camb).* **2012**, *1* (1), 62. https://doi.org/10.1039/c2tx20006f.

(133) Zhu, Y.; Li, J.; Li, W.; Zhang, Y.; Yang, X.; Chen, N.; Sun, Y.; Zhao, Y.; Fan, C.; Huang, Q. The Biocompatibility of Nanodiamonds and Their Application in Drug Delivery Systems. *Theranostics* **2012**, *2* (3), 302–312.

https://doi.org/10.7150/thno.3627.

(134) Derfus, A. M.; Chan, W. C. W.; Bhatia, S. N. Probing the Cytotoxicity of Semiconductor Quantum Dots. *Nano Lett.* **2004**, *4* (1), 11–18. https://doi.org/10.1021/nl0347334.

(135) Huang, H.; Pierstorff, E.; Osawa, E.; Ho, D. Active Nanodiamond Hydrogels for Chemotherapeutic Delivery. *Nano Lett.* **2007**, *7* (11), 3305–3314. https://doi.org/10.1021/nl071521o.

(136) Chow, E. K.; Zhang, X.-Q.; Chen, M.; Lam, R.; Robinson, E.; Huang, H.; Schaffer, D.; Osawa, E.; Goga, A.; Ho, D. Nanodiamond Therapeutic Delivery Agents Mediate Enhanced Chemoresistant Tumor Treatment. *Sci. Transl. Med.* **2011**, *3* (73), 73ra21-73ra21. https://doi.org/10.1126/scitranslmed.3001713.

(137) Gao, G.; Guo, Q.; Zhi, J. Nanodiamond-Based Theranostic Platform for Drug Delivery and Bioimaging. *Small* **2019**, 1902238. https://doi.org/10.1002/smll.201902238.

(138) Liu, K.-K.; Zheng, W.-W.; Wang, C.-C.; Chiu, Y.-C.; Cheng, C.-L.; Lo, Y.-S.; Chen, C.; Chao, J.-I. Covalent Linkage of Nanodiamond-Paclitaxel for Drug Delivery and Cancer Therapy. *Nanotechnology* **2010**, *21* (31), 315106. https://doi.org/10.1088/0957-4484/21/31/315106.

(139) Jaque, D.; Martínez Maestro, L.; del Rosal, B.; Haro-Gonzalez, P.; Benayas, A.; Plaza, J. L.; Martín Rodríguez, E.; García Solé, J. Nanoparticles for Photothermal Therapies. *Nanoscale* **2014**, *6* (16), 9494–9530. https://doi.org/10.1039/C4NR00708E.

(140) Ryu, T.-K.; Baek, S. W.; Kang, R. H.; Choi, S.-W. Selective Photothermal Tumor Therapy Using Nanodiamond-Based Nanoclusters with Folic Acid. *Adv. Funct. Mater.* **2016**, *26* (35), 6428–6436. https://doi.org/10.1002/adfm.201601207.

(141) Ryu, T.-K.; Lee, G.-J.; Rhee, C.-K.; Choi, S.-W. Cellular Uptake Behavior of Doxorubicin-Conjugated Nanodiamond Clusters for Efficient Cancer Therapy. *Macromol. Biosci.* **2015**, *15* (10), 1469–1475. https://doi.org/10.1002/mabi.201500176.

(142) Ryu, T.-K.; Baek, S.-W.; Kang, R.-H.; Jeong, K.-Y.; Jun, D.-R.; Choi, S.-W. Photodynamic and Photothermal Tumor Therapy Using Phase-Change Material Nanoparticles Containing Chlorin E6 and Nanodiamonds. *J. Control. Release* **2018**, *270*, 237–245. https://doi.org/10.1016/j.jconrel.2017.12.008.

(143) Ahn, G. Y.; Yun, T. H.; Park, J.; Lee, M. J.; Choi, I.; Ryu, T.-K.; Na, K.; Choi, S.-W. Polyaniline-Grafted Nanodiamonds for Efficient Photothermal Tumor Therapy. *Colloids Surfaces B Biointerfaces* **2019**, *180*, 273–280. https://doi.org/10.1016/j.colsurfb.2019.04.063.

(144) Jimenez, C. M.; Knezevic, N. Z.; Rubio, Y. G.; Szunerits, S.; Boukherroub, R.; Teodorescu, F.; Croissant, J. G.; Hocine, O.; Seric, M.; Raehm, L.; et al. Nanodiamond-PMO for Two-Photon PDT and Drug Delivery. *J. Mater. Chem. B* **2016**, *4* (35), 5803–5808. https://doi.org/10.1039/c6tb01915c.

(145) Matshitse, R.; Ngoy, B. P.; Managa, M.; Mack, J.; Nyokong, T. Photophysical Properties and Photodynamic Therapy Activities of Detonated Nanodiamonds-BODIPY-Phthalocyanines Nanoassemblies. *Photodiagnosis Photodyn. Ther.* **2019**, *26*, 101–110. https://doi.org/10.1016/j.pdpdt.2019.03.007.

(146) Reineck, P.; Francis, A.; Orth, A.; Lau, D. W. M.; Nixon-Luke, R. D. V.; Rastogi, I. Das; Razali, W. A. W.; Cordina, N. M.; Parker, L. M.; Sreenivasan, V. K. A.; et al. Brightness and Photostability of Emerging Red and Near-IR Fluorescent Nanomaterials for Bioimaging. *Adv. Opt. Mater.* **2016**, *4* (10), 1549–1557. https://doi.org/10.1002/adom.201600212.

(147) Fu, C.-C.; Lee, H.-Y.; Chen, K.; Lim, T.-S.; Wu, H.-Y.; Lin, P.-K.; Wei, P.-K.; Tsao, P.-H.; Chang, H.-C.; Fann, W. Characterization and Application of Single Fluorescent Nanodiamonds as Cellular Biomarkers. *Proc. Natl. Acad. Sci.* **2007**, *104* (3), 727–732. https://doi.org/10.1073/pnas.0605409104.

(148) Chang, Y.-R.; Lee, H.-Y.; Chen, K.; Chang, C.-C.; Tsai, D.-S.; Fu, C.-C.; Lim, T.-S.; Tzeng, Y.-K.; Fang, C.-Y.; Han, C.-C.; et al. Mass Production and Dynamic Imaging of Fluorescent Nanodiamonds. *Nat. Nanotechnol.* **2008**, *3* (5), 284–288. https://doi.org/10.1038/nnano.2008.99.

(149) Zhang, B.; Li, Y.; Fang, C.-Y.; Chang, C.-C.; Chen, C.-S.; Chen, Y.-Y.; Chang, H.-C. Receptor-Mediated Cellular Uptake of Folate-Conjugated Fluorescent Nanodiamonds: A Combined Ensemble and Single-Particle Study. *Small* **2009**, *5* (23), 2716–2721. https://doi.org/10.1002/smll.200900725.

(150) Liu, W.; Yu, F.; Yang, J.; Xiang, B.; Xiao, P.; Wang, L. 3D Single-Molecule Imaging of Transmembrane Signaling by Targeting Nanodiamonds. *Adv. Funct. Mater.* **2016**, *26* (3), 365–375. https://doi.org/10.1002/adfm.201502883.

(151) Epperla, C. P.; Mohan, N.; Chang, C.-W.; Chen, C.-C.; Chang, H.-C. Nanodiamond-Mediated Intercellular Transport of Proteins through Membrane Tunneling Nanotubes. *Small* **2015**, *11* (45), 6097–6105. https://doi.org/10.1002/smll.201502089.

(152) Haziza, S.; Mohan, N.; Loe-Mie, Y.; Lepagnol-Bestel, A.-M.; Massou, S.; Adam, M.-P.; Le, X. L.; Viard, J.; Plancon, C.; Daudin, R.; et al. Fluorescent Nanodiamond Tracking Reveals Intraneuronal Transport Abnormalities Induced by Brain-Disease-Related Genetic Risk Factors. *Nat. Nanotechnol.* **2017**, *12* (4), 322–328. https://doi.org/10.1038/nnano.2016.260.

(153) Lin, H.-H.; Lee, H.-W.; Lin, R.-J.; Huang, C.-W.; Liao, Y.-C.; Chen, Y.-T.; Fang, J.-M.; Lee, T.-C.; Yu, A. L.; Chang, H.-C. Tracking and Finding Slow-Proliferating/Quiescent Cancer Stem Cells with Fluorescent Nanodiamonds. *Small* **2015**, *11* (34), 4394–4402. https://doi.org/10.1002/smll.201500878.

(154) Wu, T.-J.; Tzeng, Y.-K.; Chang, W.-W.; Cheng, C.-A.; Kuo, Y.; Chien, C.-H.; Chang, H.-C.; Yu, J. Tracking the Engraftment and Regenerative Capabilities of Transplanted Lung Stem Cells Using Fluorescent Nanodiamonds. *Nat. Nanotechnol.* **2013**, *8* (9), 682–689. https://doi.org/10.1038/nnano.2013.147.

(155) Lien, Z.-Y.; Hsu, T.-C.; Liu, K.-K.; Liao, W.-S.; Hwang, K.-C.; Chao, J.-I. Cancer Cell

Labeling and Tracking Using Fluorescent and Magnetic Nanodiamond. *Biomaterials* **2012**, *33* (26), 6172–6185. https://doi.org/10.1016/j.biomaterials.2012.05.009.

(156) McGuinness, L. P.; Yan, Y.; Stacey, A.; Simpson, D. A.; Hall, L. T.; Maclaurin, D.; Prawer, S.; Mulvaney, P.; Wrachtrup, J.; Caruso, F.; et al. Quantum Measurement and Orientation Tracking of Fluorescent Nanodiamonds inside Living Cells. *Nat. Nanotechnol.* **2011**, *6* (6), 358–363. https://doi.org/10.1038/nnano.2011.64.

(157) Zhang, H.; Aharonovich, I.; Glenn, D. R.; Schalek, R.; Magyar, A. P.; Lichtman, J. W.; Hu, E. L.; Walsworth, R. L. Silicon-Vacancy Color Centers in Nanodiamonds: Cathodoluminescence Imaging Markers in the Near Infrared. *Small* **2014**, *10* (10), 1908–1913. https://doi.org/10.1002/smll.201303582.

(158) Bray, K.; Cheung, L.; Hossain, K. R.; Aharonovich, I.; Valenzuela, S. M.; Shimoni, O. Versatile Multicolor Nanodiamond Probes for Intracellular Imaging and Targeted Labeling. *J. Mater. Chem. B* **2018**, *6* (19), 3078–3084. https://doi.org/10.1039/C8TB00508G.

(159) Merson, T. D.; Castelletto, S.; Aharonovich, I.; Turbic, A.; Kilpatrick, T. J.; Turnley, A. M. Nanodiamonds with Silicon Vacancy Defects for Nontoxic Photostable Fluorescent Labeling of Neural Precursor Cells. *Opt. Lett.* **2013**, *38* (20), 4170. https://doi.org/10.1364/OL.38.004170.

(160) Kuo, Y.; Hsu, T.-Y.; Wu, Y.-C.; Chang, H.-C. Fluorescent Nanodiamond as a Probe for the Intercellular Transport of Proteins in Vivo. *Biomaterials* **2013**, *34* (33), 8352–8360. https://doi.org/10.1016/j.biomaterials.2013.07.043.

(161) Mohan, N.; Chen, C.-S.; Hsieh, H.-H.; Wu, Y.-C.; Chang, H.-C. In Vivo Imaging and Toxicity Assessments of Fluorescent Nanodiamonds in Caenorhabditis Elegans. *Nano Lett.* **2010**, *10* (9), 3692–3699. https://doi.org/10.1021/nl1021909.

(162) Igarashi, R.; Yoshinari, Y.; Yokota, H.; Sugi, T.; Sugihara, F.; Ikeda, K.; Sumiya, H.; Tsuji, S.; Mori, I.; Tochio, H.; et al. Real-Time Background-Free Selective Imaging of Fluorescent Nanodiamonds in Vivo. *Nano Lett.* **2012**, *12* (11), 5726–5732. https://doi.org/10.1021/nl302979d.

(163) Simpson, D. A.; Thompson, A. J.; Kowarsky, M.; Zeeshan, N. F.; Barson, M. S. J.; Hall, L. T.; Yan, Y.; Kaufmann, S.; Johnson, B. C.; Ohshima, T.; et al. In Vivo Imaging and Tracking of Individual Nanodiamonds in Drosophila Melanogaster Embryos. *Biomed. Opt. Express* **2014**, *5* (4), 1250. https://doi.org/10.1364/BOE.5.001250.

(164) Hui, Y. Y.; Su, L.-J.; Chen, O. Y.; Chen, Y.-T.; Liu, T.-M.; Chang, H.-C. Wide-Field Imaging and Flow Cytometric Analysis of Cancer Cells in Blood by Fluorescent Nanodiamond Labeling and Time Gating. *Sci. Rep.* **2015**, *4* (1), 5574. https://doi.org/10.1038/srep05574.

(165) Su, L.-J.; Wu, M.-S.; Hui, Y. Y.; Chang, B.-M.; Pan, L.; Hsu, P.-C.; Chen, Y.-T.; Ho, H.-N.; Huang, Y.-H.; Ling, T.-Y.; et al. Fluorescent Nanodiamonds Enable Quantitative Tracking of Human Mesenchymal Stem Cells in Miniature Pigs. *Sci.*

Rep. **2017**, *7* (1), 45607. https://doi.org/10.1038/srep45607.

(166) Chang, C.-C.; Zhang, B.; Li, C.-Y.; Hsieh, C.-C.; Duclos, G.; Treussart, F.; Chang, H.-C. Exploring Cytoplasmic Dynamics in Zebrafish Yolk Cells by Single Particle Tracking of Fluorescent Nanodiamonds. *Proc. SPIE* **2012**, *8272*, 827205. https://doi.org/10.1117/12.907181.

(167) Yoshinari, Y.; Mori, S.; Igarashi, R.; Sugi, T.; Yokota, H.; Ikeda, K.; Sumiya, H.; Mori, I.; Tochio, H.; Harada, Y.; et al. Optically Detected Magnetic Resonance of Nanodiamonds In Vivo; Implementation of Selective Imaging and Fast Sampling. *J. Nanosci. Nanotechnol.* **2015**, *15* (2), 1014–1021. https://doi.org/10.1166/jnn.2015.9739.

(168) Robinson, M. E.; Ng, J. D.; Zhang, H.; Buchman, J. T.; Shenderova, O. A.; Haynes, C. L.; Ma, Z.; Goldsmith, R. H.; Hamers, R. J. Optically Detected Magnetic Resonance for Selective Imaging of Diamond Nanoparticles. *Anal. Chem.* **2018**, *90* (1), 769–776. https://doi.org/10.1021/acs.analchem.7b03157.

(169) Hegyi, A.; Yablonovitch, E. Molecular Imaging by Optically Detected Electron Spin Resonance of Nitrogen-Vacancies in Nanodiamonds. *Nano Lett.* **2013**, *13* (3), 1173–1178. https://doi.org/10.1021/nl304570b.

(170) Prabhakar, N.; Peurla, M.; Koho, S.; Deguchi, T.; Näreoja, T.; Chang, H.-C.; Rosenholm, J. M.; Hänninen, P. E. STED-TEM Correlative Microscopy Leveraging Nanodiamonds as Intracellular Dual-Contrast Markers. *Small* **2018**, *14* (5), 1701807. https://doi.org/10.1002/smll.201701807.

(171) Hsieh, F.-J.; Chen, Y.-W.; Huang, Y.-K.; Lee, H.-M.; Lin, C.-H.; Chang, H.-C. Correlative Light-Electron Microscopy of Lipid-Encapsulated Fluorescent Nanodiamonds for Nanometric Localization of Cell Surface Antigens. *Anal. Chem.* **2018**, *90* (3), 1566–1571. https://doi.org/10.1021/acs.analchem.7b04549.

(172) Zurbuchen, M. A.; Lake, M. P.; Kohan, S. A.; Leung, B.; Bouchard, L.-S. Nanodiamond Landmarks for Subcellular Multimodal Optical and Electron Imaging. *Sci. Rep.* **2013**, *3* (1), 2668. https://doi.org/10.1038/srep02668.

(173) Hemelaar, S. R.; de Boer, P.; Chipaux, M.; Zuidema, W.; Hamoh, T.; Martinez, F. P.; Nagl, A.; Hoogenboom, J. P.; Giepmans, B. N. G.; Schirhagl, R. Nanodiamonds as Multi-Purpose Labels for Microscopy. *Sci. Rep.* **2017**, *7* (1), 720. https://doi.org/10.1038/s41598-017-00797-2.

(174) Torelli, M. D.; Nunn, N. A.; Shenderova, O. A. A Perspective on Fluorescent Nanodiamond Bioimaging. *Small* **2019**, 1902151. https://doi.org/10.1002/smll.201902151.

(175) Rittweger, E.; Wildanger, D.; Hell, S. W. Far-Field Fluorescence Nanoscopy of Diamond Color Centers by Ground State Depletion. *EPL (Europhysics Lett.* **2009**, *86* (1), 14001. https://doi.org/10.1209/0295-5075/86/14001.

(176) Wildanger, D.; Patton, B. R.; Schill, H.; Marseglia, L.; Hadden, J. P.; Knauer, S.; Schönle, A.; Rarity, J. G.; O'Brien, J. L.; Hell, S. W.; et al. Solid Immersion Facilitates Fluorescence Microscopy with Nanometer Resolution and Sub-

Ångström Emitter Localization. *Adv. Mater.* **2012**, *24* (44), OP309–OP313. https://doi.org/10.1002/adma.201203033.

(177)   Han, K. Y.; Willig, K. I.; Rittweger, E.; Jelezko, F.; Eggeling, C.; Hell, S. W. Three-Dimensional Stimulated Emission Depletion Microscopy of Nitrogen-Vacancy Centers in Diamond Using Continuous-Wave Light. *Nano Lett.* **2009**, *9* (9), 3323–3329. https://doi.org/10.1021/nl901597v.

(178)   Arroyo-Camejo, S.; Adam, M.-P.; Besbes, M.; Hugonin, J.-P.; Jacques, V.; Greffet, J.-J.; Roch, J.-F.; Hell, S. W.; Treussart, F. Stimulated Emission Depletion Microscopy Resolves Individual Nitrogen Vacancy Centers in Diamond Nanocrystals. *ACS Nano* **2013**, *7* (12), 10912–10919. https://doi.org/10.1021/nn404421b.

(179)   Valluru, K. S.; Willmann, J. K. Clinical Photoacoustic Imaging of Cancer. *Ultrasonography* **2016**, *35* (4), 267–280. https://doi.org/10.14366/usg.16035.

(180)   Prabhakar, N.; Rosenholm, J. M. Nanodiamonds for Advanced Optical Bioimaging and Beyond. *Curr. Opin. Colloid Interface Sci.* **2019**, *39*, 220–231. https://doi.org/10.1016/j.cocis.2019.02.014.

(181)   Fang, C.-Y.; Chang, C.-C.; Mou, C.-Y.; Chang, H.-C. Preparation and Characterization of Ion-Irradiated Nanodiamonds as Photoacoustic Contrast Agents. *J. Nanosci. Nanotechnol.* **2015**, *15* (2), 1037–1044. https://doi.org/10.1166/jnn.2015.9741.

(182)   Zhang, B.; Fang, C.-Y.; Chang, C.-C.; Peterson, R.; Maswadi, S.; Glickman, R. D.; Chang, H.-C.; Ye, J. Y. Photoacoustic Emission from Fluorescent Nanodiamonds Enhanced with Gold Nanoparticles. *Biomed. Opt. Express* **2012**, *3* (7), 1662. https://doi.org/10.1364/BOE.3.001662.

(183)   Zhang, T.; Cui, H.; Fang, C.-Y.; Jo, J.; Yang, X.; Chang, H.-C.; Forrest, M. L. In Vivo Photoacoustic Imaging of Breast Cancer Tumor with HER2-Targeted Nanodiamonds. *Proc. SPIE* **2013**, *8815*, 881504. https://doi.org/10.1117/12.2027253.

(184)   Lee, D.; Park, E.-J.; Lee, S.-E.; Jeong, S. H.; Lee, J. Y.; Kang, E. Energy-Absorbing and Local Plasmonic Nanodiamond/Gold Nanocomposites for Sustained and Enhanced Photoacoustic Imaging. *ACS Sustain. Chem. Eng.* **2017**, *5* (9), 8284–8293. https://doi.org/10.1021/acssuschemeng.7b01944.

(185)   Zhang, T.; Cui, H.; Fang, C.-Y.; Su, L.-J.; Ren, S.; Chang, H.-C.; Yang, X.; Forrest, M. L. Photoacoustic Contrast Imaging of Biological Tissues with Nanodiamonds Fabricated for High Near-Infrared Absorbance. *J. Biomed. Opt.* **2013**, *18* (2), 026018. https://doi.org/10.1117/1.JBO.18.2.026018.

(186)   Chen, X.; Wang, H.; Li, D.; Yu, Y.; Zhi, J. The Effect of Carboxylated Nanodiamond (CNDs) on the Migration of HepG2 Cells. *Phys. status solidi* **2016**, *213* (8), 2131–2137. https://doi.org/10.1002/pssa.201600094.

(187)   Li, D.; Chen, X.; Wang, H.; Yu, Y.; Liu, J.; Wang, Y.; Zhang, J.; Zheng, M.; Zhi, J. Nanodiamonds as Raman Probes for Specifically Targeted Bioimaging: Visualization and Mechanism Study of the Biorecognition between

Nanodiamonds–EGF and EGFR. *RSC Adv.* **2017**, *7* (21), 12835–12841. https://doi.org/10.1039/C6RA28139G.

(188) Chen, X.; Li, D.; Wang, H.; Jiao, Y.; Wang, H.; Yu, Y.; Zhi, J. Fabrication of an EGF Modified Nanodiamonds-Based Anti-Cancer Drug Targeted Delivery System and Drug Carrier Uptake Visualization by 3D Raman Microscopy. *RSC Adv.* **2016**, *6* (50), 44543–44551. https://doi.org/10.1039/C6RA04753J.

(189) Pope, I.; Payne, L.; Zoriniants, G.; Thomas, E.; Williams, O.; Watson, P.; Langbein, W.; Borri, P. Coherent Anti-Stokes Raman Scattering Microscopy of Single Nanodiamonds. *Nat. Nanotechnol.* **2014**, *9* (11), 940–946. https://doi.org/10.1038/nnano.2014.210.

(190) Manus, L. M.; Mastarone, D. J.; Waters, E. A.; Zhang, X.-Q.; Schultz-Sikma, E. A.; MacRenaris, K. W.; Ho, D.; Meade, T. J. Gd(III)-Nanodiamond Conjugates for MRI Contrast Enhancement. *Nano Lett.* **2010**, *10* (2), 484–489. https://doi.org/10.1021/nl903264h.

(191) Rammohan, N.; MacRenaris, K. W.; Moore, L. K.; Parigi, G.; Mastarone, D. J.; Manus, L. M.; Lilley, L. M.; Preslar, A. T.; Waters, E. A.; Filicko, A.; et al. Nanodiamond–Gadolinium(III) Aggregates for Tracking Cancer Growth In Vivo at High Field. *Nano Lett.* **2016**, *16* (12), 7551–7564. https://doi.org/10.1021/acs.nanolett.6b03378.

(192) Panich, A. M.; Salti, M.; Goren, S. D.; Yudina, E. B.; Aleksenskii, A. E.; Vul', A. Y.; Shames, A. I. Gd(III)-Grafted Detonation Nanodiamonds for MRI Contrast Enhancement. *J. Phys. Chem. C* **2019**, *123* (4), 2627–2631. https://doi.org/10.1021/acs.jpcc.8b11655.

(193) Nakamura, T.; Ohana, T.; Yabuno, H.; Kasai, R.; Suzuki, T.; Hasebe, T. Simple Fabrication of Gd(III)-DTPA-Nanodiamond Particles by Chemical Modification for Use as Magnetic Resonance Imaging (MRI) Contrast Agent. *Appl. Phys. Express* **2013**, *6* (1), 015001. https://doi.org/10.7567/APEX.6.015001.

(194) Qin, S.-R.; Zhao, Q.; Cheng, Z.-G.; Zhang, D.-X.; Zhang, K.-K.; Su, L.-X.; Fan, H.-J.; Wang, Y.-H.; Shan, C.-X. Rare Earth-Functionalized Nanodiamonds for Dual-Modal Imaging and Drug Delivery. *Diam. Relat. Mater.* **2019**, *91*, 173–182. https://doi.org/10.1016/j.diamond.2018.11.015.

(195) Lin, B.-R.; Chen, C.-H.; Chang, C.-H.; Kunuku, S.; Chen, T.-Y.; Hsiao, T.-Y.; Yu, H.-K.; Chang, Y.-J.; Liao, L.-C.; Chen, F.-H.; et al. Iron Embedded Magnetic Nanodiamonds for in Vivo MRI Contrast Enhancement. *J. Phys. D. Appl. Phys.* **2019**, *52* (50), 505402. https://doi.org/10.1088/1361-6463/ab41e8.

(196) Lin, B.-R.; Chen, C.-H.; Kunuku, S.; Chen, T.-Y.; Hsiao, T.-Y.; Niu, H.; Lee, C.-P. Fe Doped Magnetic Nanodiamonds Made by Ion Implantation as Contrast Agent for MRI. *Sci. Rep.* **2018**, *8* (1), 7058. https://doi.org/10.1038/s41598-018-25380-1.

(197) Waddington, D. E. J.; Sarracanie, M.; Zhang, H.; Salameh, N.; Glenn, D. R.; Rej, E.; Gaebel, T.; Boele, T.; Walsworth, R. L.; Reilly, D. J.; et al. Nanodiamond-Enhanced MRI via in Situ Hyperpolarization. *Nat. Commun.* **2017**, *8* (1), 15118. https://doi.org/10.1038/ncomms15118.

(198) Ajoy, A.; Liu, K.; Nazaryan, R.; Lv, X.; Zangara, P. R.; Safvati, B.; Wang, G.; Arnold, D.; Li, G.; Lin, A.; et al. Orientation-Independent Room Temperature Optical 13 C Hyperpolarization in Powdered Diamond. *Sci. Adv.* **2018**, *4* (5), eaar5492. https://doi.org/10.1126/sciadv.aar5492.

(199) Waddington, D. E. J.; Boele, T.; Rej, E.; McCamey, D. R.; King, N. J. C.; Gaebel, T.; Reilly, D. J. Phase-Encoded Hyperpolarized Nanodiamond for Magnetic Resonance Imaging. *Sci. Rep.* **2019**, *9* (1), 5950. https://doi.org/10.1038/s41598-019-42373-w.

(200) Xiong, W.; Wang, W.; Wang, Y.; Zhao, Y.; Chen, H.; Xu, H.; Yang, X. Dual Temperature/PH-Sensitive Drug Delivery of Poly(N-Isopropylacrylamide-Co-Acrylic Acid) Nanogels Conjugated with Doxorubicin for Potential Application in Tumor Hyperthermia Therapy. *Colloids Surfaces B Biointerfaces* **2011**, *84* (2), 447–453. https://doi.org/10.1016/j.colsurfb.2011.01.040.

(201) Radtke, M.; Bernardi, E.; Slablab, A.; Nelz, R.; Neu, E. Nanoscale Sensing Based on Nitrogen Vacancy Centers in Single Crystal Diamond and Nanodiamonds: Achievements and Challenges. *Nano Futur.* **2019**, *3* (4), 042004. https://doi.org/10.1088/2399-1984/ab5f9b.

(202) Tetienne, J.-P.; Hingant, T.; Rondin, L.; Cavaillès, A.; Mayer, L.; Dantelle, G.; Gacoin, T.; Wrachtrup, J.; Roch, J.-F.; Jacques, V. Spin Relaxometry of Single Nitrogen-Vacancy Defects in Diamond Nanocrystals for Magnetic Noise Sensing. *Phys. Rev. B* **2013**, *87* (23), 235436. https://doi.org/10.1103/PhysRevB.87.235436.

(203) Kaufmann, S.; Simpson, D. A.; Hall, L. T.; Perunicic, V.; Senn, P.; Steinert, S.; McGuinness, L. P.; Johnson, B. C.; Ohshima, T.; Caruso, F.; et al. Detection of Atomic Spin Labels in a Lipid Bilayer Using a Single-Spin Nanodiamond Probe. *Proc. Natl. Acad. Sci.* **2013**, *110* (27), 10894–10898. https://doi.org/10.1073/pnas.1300640110.

(204) Sushkov, A. O.; Chisholm, N.; Lovchinsky, I.; Kubo, M.; Lo, P. K.; Bennett, S. D.; Hunger, D.; Akimov, A.; Walsworth, R. L.; Park, H.; et al. All-Optical Sensing of a Single-Molecule Electron Spin. *Nano Lett.* **2014**, *14* (11), 6443–6448. https://doi.org/10.1021/nl502988n.

(205) Gorrini, F.; Giri, R.; Avalos, C. E.; Tambalo, S.; Mannucci, S.; Basso, L.; Bazzanella, N.; Dorigoni, C.; Cazzanelli, M.; Marzola, P.; et al. Fast and Sensitive Detection of Paramagnetic Species Using Coupled Charge and Spin Dynamics in Strongly Fluorescent Nanodiamonds. *ACS Appl. Mater. Interfaces* **2019**, *11* (27), 24412–24422. https://doi.org/10.1021/acsami.9b05779.

(206) Maze, J. R.; Stanwix, P. L.; Hodges, J. S.; Hong, S.; Taylor, J. M.; Cappellaro, P.; Jiang, L.; Dutt, M. V. G.; Togan, E.; Zibrov, A. S.; et al. Nanoscale Magnetic Sensing with an Individual Electronic Spin in Diamond. *Nature* **2008**, *455* (7213), 644–647. https://doi.org/10.1038/nature07279.

(207) Taylor, J. M.; Cappellaro, P.; Childress, L.; Jiang, L.; Budker, D.; Hemmer, P. R.; Yacoby, A.; Walsworth, R.; Lukin, M. D. High-Sensitivity Diamond Magnetometer with Nanoscale Resolution. *Nat. Phys.* **2008**, *4* (10), 810–816.

https://doi.org/10.1038/nphys1075.

(208) Balasubramanian, G.; Chan, I. Y.; Kolesov, R.; Al-Hmoud, M.; Tisler, J.; Shin, C.; Kim, C.; Wojcik, A.; Hemmer, P. R.; Krueger, A.; et al. Nanoscale Imaging Magnetometry with Diamond Spins under Ambient Conditions. *Nature* **2008**, *455* (7213), 648–651. https://doi.org/10.1038/nature07278.

(209) Dolde, F.; Fedder, H.; Doherty, M. W.; Nöbauer, T.; Rempp, F.; Balasubramanian, G.; Wolf, T.; Reinhard, F.; Hollenberg, L. C. L.; Jelezko, F.; et al. Electric-Field Sensing Using Single Diamond Spins. *Nat. Phys.* **2011**, *7* (6), 459–463. https://doi.org/10.1038/nphys1969.

(210) Hall, L. T.; Hill, C. D.; Cole, J. H.; Stadler, B.; Caruso, F.; Mulvaney, P.; Wrachtrup, J.; Hollenberg, L. C. L. Monitoring Ion-Channel Function in Real Time through Quantum Decoherence. *Proc. Natl. Acad. Sci.* **2010**, *107* (44), 18777–18782. https://doi.org/10.1073/pnas.1002562107.

(211) Kucsko, G.; Maurer, P. C.; Yao, N. Y.; Kubo, M.; Noh, H. J.; Lo, P. K.; Park, H.; Lukin, M. D. Nanometre-Scale Thermometry in a Living Cell. *Nature* **2013**, *500* (7460), 54–58. https://doi.org/10.1038/nature12373.

(212) Simpson, D. A.; Morrisroe, E.; McCoey, J. M.; Lombard, A. H.; Mendis, D. C.; Treussart, F.; Hall, L. T.; Petrou, S.; Hollenberg, L. C. L. Non-Neurotoxic Nanodiamond Probes for Intraneuronal Temperature Mapping. *ACS Nano* **2017**, *11* (12), 12077–12086. https://doi.org/10.1021/acsnano.7b04850.

(213) Zhang, T.; Liu, G.-Q.; Leong, W.-H.; Liu, C.-F.; Kwok, M.-H.; Ngai, T.; Liu, R.-B.; Li, Q. Hybrid Nanodiamond Quantum Sensors Enabled by Volume Phase Transitions of Hydrogels. *Nat. Commun.* **2018**, *9* (1), 3188. https://doi.org/10.1038/s41467-018-05673-9.

(214) Fujisaku, T.; Tanabe, R.; Onoda, S.; Kubota, R.; Segawa, T. F.; So, F. T.-K.; Ohshima, T.; Hamachi, I.; Shirakawa, M.; Igarashi, R. PH Nanosensor Using Electronic Spins in Diamond. *ACS Nano* **2019**, *13* (10), 11726–11732. https://doi.org/10.1021/acsnano.9b05342.

(215) Russell, L. W.; Ralph, S. G.; Wittick, K.; Tetienne, J.-P.; Simpson, D. A.; Reece, P. J. Manipulating the Quantum Coherence of Optically Trapped Nanodiamonds. *ACS Photonics* **2018**, *5* (11), 4491–4496. https://doi.org/10.1021/acsphotonics.8b00946.

(216) Horowitz, V. R.; Aleman, B. J.; Christle, D. J.; Cleland, A. N.; Awschalom, D. D. Electron Spin Resonance of Nitrogen-Vacancy Centers in Optically Trapped Nanodiamonds. *Proc. Natl. Acad. Sci.* **2012**, *109* (34), 13493–13497. https://doi.org/10.1073/pnas.1211311109.

(217) Berthelot, J.; Aćimović, S. S.; Juan, M. L.; Kreuzer, M. P.; Renger, J.; Quidant, R. Three-Dimensional Manipulation with Scanning near-Field Optical Nanotweezers. *Nat. Nanotechnol.* **2014**, *9* (4), 295–299. https://doi.org/10.1038/nnano.2014.24.

(218) Kayci, M.; Chang, H.-C.; Radenovic, A. Electron Spin Resonance of Nitrogen-Vacancy Defects Embedded in Single Nanodiamonds in an ABEL Trap. *Nano Lett.*

2014, *14* (9), 5335–5341. https://doi.org/10.1021/nl5023964.

(219) Schermelleh, L.; Heintzmann, R.; Leonhardt, H. A Guide to Super-Resolution Fluorescence Microscopy. *J. Cell Biol.* **2010**, *190* (2), 165–175. https://doi.org/10.1083/jcb.201002018.

(220) Sahl, S. J.; Hell, S. W.; Jakobs, S. Fluorescence Nanoscopy in Cell Biology. *Nat. Rev. Mol. Cell Biol.* **2017**, *18* (11), 685–701. https://doi.org/10.1038/nrm.2017.71.

(221) Giepmans, B. N. G.; Deerinck, T. J.; Smarr, B. L.; Jones, Y. Z.; Ellisman, M. H. Correlated Light and Electron Microscopic Imaging of Multiple Endogenous Proteins Using Quantum Dots. *Nat. Methods* **2005**, *2* (10), 743–749. https://doi.org/10.1038/nmeth791.

(222) Butterworth, K. T.; Coulter, J. A.; Jain, S.; Forker, J.; McMahon, S. J.; Schettino, G.; Prise, K. M.; Currell, F. J.; Hirst, D. G. Evaluation of Cytotoxicity and Radiation Enhancement Using 1.9 Nm Gold Particles: Potential Application for Cancer Therapy. *Nanotechnology* **2010**, *21* (29), 295101. https://doi.org/10.1088/0957-4484/21/29/295101.

(223) Bianco, S.; Grigolini, P.; Paradisi, P. Fluorescence Intermittency in Blinking Quantum Dots: Renewal or Slow Modulation? *J. Chem. Phys.* **2005**, *123* (17), 174704. https://doi.org/10.1063/1.2102903.

(224) He, H.; Xie, C.; Ren, J. Nonbleaching Fluorescence of Gold Nanoparticles and Its Applications in Cancer Cell Imaging. *Anal. Chem.* **2008**, *80* (15), 5951–5957. https://doi.org/10.1021/ac8005796.

(225) Chipaux, M.; van der Laan, K. J.; Hemelaar, S. R.; Hasani, M.; Zheng, T.; Schirhagl, R. Nanodiamonds and Their Applications in Cells. *Small* **2018**, *14* (24), 1704263. https://doi.org/10.1002/smll.201704263.

(226) Chu, Z.; Zhang, S.; Zhang, B.; Zhang, C.; Fang, C.-Y.; Rehor, I.; Cigler, P.; Chang, H.-C.; Lin, G.; Liu, R.; et al. Unambiguous Observation of Shape Effects on Cellular Fate of Nanoparticles. *Sci. Rep.* **2015**, *4* (1), 4495. https://doi.org/10.1038/srep04495.

(227) Nisman, R.; Dellaire, G.; Ren, Y.; Li, R.; Bazett-Jones, D. P. Application of Quantum Dots as Probes for Correlative Fluorescence, Conventional, and Energy-Filtered Transmission Electron Microscopy. *J. Histochem. Cytochem.* **2004**, *52* (1), 13–18. https://doi.org/10.1177/002215540405200102.

(228) Chakrabortty, S.; Agrawalla, B. K.; Stumper, A.; Vegi, N. M.; Fischer, S.; Reichardt, C.; Kögler, M.; Dietzek, B.; Feuring-Buske, M.; Buske, C.; et al. Mitochondria Targeted Protein-Ruthenium Photosensitizer for Efficient Photodynamic Applications. *J. Am. Chem. Soc.* **2017**, *139* (6), 2512–2519. https://doi.org/10.1021/jacs.6b13399.

(229) Pardridge, W. M. The Blood-Brain Barrier: Bottleneck in Brain Drug Development. *NeuroRX* **2005**, *2* (1), 3–14. https://doi.org/10.1602/neurorx.2.1.3.

(230) Hawkins, B. T.; Davis, T. P. The Blood-Brain Barrier/Neurovascular Unit in Health and Disease. *Pharmacol. Rev.* **2005**, *57* (2), 173–185. https://doi.org/10.1124/pr.57.2.4.

(231) Kievit, F. M.; Zhang, M. Cancer Nanotheranostics: Improving Imaging and Therapy by Targeted Delivery Across Biological Barriers. *Adv. Mater.* **2011**, *23* (36), H217–H247. https://doi.org/10.1002/adma.201102313.

(232) Wang, H.; Cao, F.; De, A.; Cao, Y.; Contag, C.; Gambhir, S. S.; Wu, J. C.; Chen, X. Trafficking Mesenchymal Stem Cell Engraftment and Differentiation in Tumor-Bearing Mice by Bioluminescence Imaging. *Stem Cells* **2009**, *27* (7), 1548–1558. https://doi.org/10.1002/stem.81.

(233) Kajstura, J.; Rota, M.; Hall, S. R.; Hosoda, T.; D'Amario, D.; Sanada, F.; Zheng, H.; Ogórek, B.; Rondon-Clavo, C.; Ferreira-Martins, J.; et al. Evidence for Human Lung Stem Cells. *N. Engl. J. Med.* **2011**, *364* (19), 1795–1806. https://doi.org/10.1056/NEJMoa1101324.

(234) Chalfie, M.; Tu, Y.; Euskirchen, G.; Ward, W.; Prasher, D. Green Fluorescent Protein as a Marker for Gene Expression. *Science (80-.).* **1994**, *263* (5148), 802–805. https://doi.org/10.1126/science.8303295.

(235) Weir, C.; Morel-Kopp, M.-C.; Gill, A.; Tinworth, K.; Ladd, L.; Hunyor, S. N.; Ward, C. Mesenchymal Stem Cells: Isolation, Characterisation and In Vivo Fluorescent Dye Tracking. *Hear. Lung Circ.* **2008**, *17* (5), 395–403. https://doi.org/10.1016/j.hlc.2008.01.006.

(236) Zhou, Y.; Peng, Z.; Seven, E. S.; Leblanc, R. M. Crossing the Blood-Brain Barrier with Nanoparticles. *J. Control. Release* **2018**, *270*, 290–303. https://doi.org/10.1016/j.jconrel.2017.12.015.

(237) Dong, X. Current Strategies for Brain Drug Delivery. *Theranostics* **2018**, *8* (6), 1481–1493. https://doi.org/10.7150/thno.21254.

(238) Medina, D. X.; Householder, K. T.; Ceton, R.; Kovalik, T.; Heffernan, J. M.; Shankar, R. V.; Bowser, R. P.; Wechsler-Reya, R. J.; Sirianni, R. W. Optical Barcoding of PLGA for Multispectral Analysis of Nanoparticle Fate in Vivo. *J. Control. Release* **2017**, *253*, 172–182. https://doi.org/10.1016/j.jconrel.2017.02.033.

(239) Ferreira, L.; Karp, J. M.; Nobre, L.; Langer, R. New Opportunities: The Use of Nanotechnologies to Manipulate and Track Stem Cells. *Cell Stem Cell* **2008**, *3* (2), 136–146. https://doi.org/10.1016/j.stem.2008.07.020.

(240) Solanki, A.; Kim, J. D.; Lee, K.-B. Nanotechnology for Regenerative Medicine: Nanomaterials for Stem Cell Imaging. *Nanomedicine* **2008**, *3* (4), 567–578. https://doi.org/10.2217/17435889.3.4.567.

(241) Ruan, S.; Qian, J.; Shen, S.; Zhu, J.; Jiang, X.; He, Q.; Gao, H. A Simple One-Step Method to Prepare Fluorescent Carbon Dots and Their Potential Application in Non-Invasive Glioma Imaging. *Nanoscale* **2014**, *6* (17), 10040. https://doi.org/10.1039/C4NR02657H.

(242) Baldrighi, M.; Trusel, M.; Tonini, R.; Giordani, S. Carbon Nanomaterials Interfacing with Neurons: An In Vivo Perspective. *Front. Neurosci.* **2016**, *10*. https://doi.org/10.3389/fnins.2016.00250.

(243) Thöle, M.; Nobmann, S.; Huwyler, J.; Bartmann, A.; Fricker, G. Uptake of Cationized Albumin Coupled Liposomes by Cultured Porcine Brain Microvessel Endothelial Cells and Intact Brain Capillaries. *J. Drug Target.* **2002**, *10* (4), 337–344. https://doi.org/10.1080/10611860290031840.

(244) Lu, W.; Sun, Q.; Wan, J.; She, Z.; Jiang, X.-G. Cationic Albumin-Conjugated Pegylated Nanoparticles Allow Gene Delivery into Brain Tumors via Intravenous Administration. *Cancer Res.* **2006**, *66* (24), 11878–11887. https://doi.org/10.1158/0008-5472.CAN-06-2354.

(245) Mittal, R.; Karhu, E.; Wang, J.-S.; Delgado, S.; Zukerman, R.; Mittal, J.; Jhaveri, V. M. Cell Communication by Tunneling Nanotubes: Implications in Disease and Therapeutic Applications. *J. Cell. Physiol.* **2019**, *234* (2), 1130–1146. https://doi.org/10.1002/jcp.27072.

(246) Ferlay, J.; Soerjomataram, I.; Dikshit, R.; Eser, S.; Mathers, C.; Rebelo, M.; Parkin, D. M.; Forman, D.; Bray, F. Cancer Incidence and Mortality Worldwide: Sources, Methods and Major Patterns in GLOBOCAN 2012. *Int. J. Cancer* **2015**, *136* (5), E359–E386. https://doi.org/10.1002/ijc.29210.

(247) Jerusalem, G.; Collignon, J.; Schroeder, H.; Lousberg, L. Triple-Negative Breast Cancer: Treatment Challenges and Solutions. *Breast Cancer Targets Ther.* **2016**, 93. https://doi.org/10.2147/BCTT.S69488.

(248) Perou, C. M.; Sørlie, T.; Eisen, M. B.; van de Rijn, M.; Jeffrey, S. S.; Rees, C. A.; Pollack, J. R.; Ross, D. T.; Johnsen, H.; Akslen, L. A.; et al. Molecular Portraits of Human Breast Tumours. *Nature* **2000**, *406* (6797), 747–752. https://doi.org/10.1038/35021093.

(249) Sorlie, T.; Perou, C. M.; Tibshirani, R.; Aas, T.; Geisler, S.; Johnsen, H.; Hastie, T.; Eisen, M. B.; van de Rijn, M.; Jeffrey, S. S.; et al. Gene Expression Patterns of Breast Carcinomas Distinguish Tumor Subclasses with Clinical Implications. *Proc. Natl. Acad. Sci.* **2001**, *98* (19), 10869–10874. https://doi.org/10.1073/pnas.191367098.

(250) Teles, R. H. G.; Moralles, H. F.; Cominetti, M. R. Global Trends in Nanomedicine Research on Triple Negative Breast Cancer: A Bibliometric Analysis. *Int. J. Nanomedicine* **2018**, *Volume 13*, 2321–2336. https://doi.org/10.2147/IJN.S164355.

(251) Lao, J.; Madani, J.; Puértolas, T.; Álvarez, M.; Hernández, A.; Pazo-Cid, R.; Artal, Á.; Antón Torres, A. Liposomal Doxorubicin in the Treatment of Breast Cancer Patients: A Review. *J. Drug Deliv.* **2013**, *2013*, 1–12. https://doi.org/10.1155/2013/456409.

(252) Liu, L.; Wang, Y.; Miao, L.; Liu, Q.; Musetti, S.; Li, J.; Huang, L. Combination Immunotherapy of MUC1 MRNA Nano-Vaccine and CTLA-4 Blockade Effectively Inhibits Growth of Triple Negative Breast Cancer. *Mol. Ther.* **2018**, *26* (1), 45–55.

https://doi.org/10.1016/j.ymthe.2017.10.020.

(253) Yang, D.; Yao, X.; Dong, J.; Wang, N.; Du, Y.; Sun, S.; Gao, L.; Zhong, Y.; Qian, C.; Hong, H. Design and Investigation of Core/Shell GQDs/HMSN Nanoparticles as an Enhanced Drug Delivery Platform in Triple-Negative Breast Cancer. *Bioconjug. Chem.* **2018**, *29* (8), 2776–2785. https://doi.org/10.1021/acs.bioconjchem.8b00399.

(254) Goyal, R.; Kapadia, C. H.; Melamed, J. R.; Riley, R. S.; Day, E. S. Layer-by-Layer Assembled Gold Nanoshells for the Intracellular Delivery of MiR-34a. *Cell. Mol. Bioeng.* **2018**, *11* (5), 383–396. https://doi.org/10.1007/s12195-018-0535-x.

(255) Bellat, V.; Ting, R.; Southard, T. L.; Vahdat, L.; Molina, H.; Fernandez, J.; Aras, O.; Stokol, T.; Law, B. Functional Peptide Nanofibers with Unique Tumor Targeting and Enzyme-Induced Local Retention Properties. *Adv. Funct. Mater.* **2018**, *28* (44), 1803969. https://doi.org/10.1002/adfm.201803969.

(256) Zhang, N.; Liang, X.; Gao, C.; Chen, M.; Zhou, Y.; Krueger, C. J.; Bao, G.; Gong, Z.; Dai, Z. Loading Lovastatin into Camptothecin–Floxuridine Conjugate Nanocapsules for Enhancing Anti-Metastatic Efficacy of Cocktail Chemotherapy on Triple-Negative Breast Cancer. *ACS Appl. Mater. Interfaces* **2018**, *10* (35), 29385–29397. https://doi.org/10.1021/acsami.8b11723.

(257) Elsadek, B.; Kratz, F. Impact of Albumin on Drug Delivery — New Applications on the Horizon. *J. Control. Release* **2012**, *157* (1), 4–28. https://doi.org/10.1016/j.jconrel.2011.09.069.

(258) Ruttala, H. B.; Ramasamy, T.; Shin, B. S.; Choi, H.-G.; Yong, C. S.; Kim, J. O. Layer-by-Layer Assembly of Hierarchical Nanoarchitectures to Enhance the Systemic Performance of Nanoparticle Albumin-Bound Paclitaxel. *Int. J. Pharm.* **2017**, *519* (1–2), 11–21. https://doi.org/10.1016/j.ijpharm.2017.01.011.

(259) Wu, Y.; Ihme, S.; Feuring-Buske, M.; Kuan, S. L.; Eisele, K.; Lamla, M.; Wang, Y.; Buske, C.; Weil, T. A Core-Shell Albumin Copolymer Nanotransporter for High Capacity Loading and Two-Step Release of Doxorubicin with Enhanced Anti-Leukemia Activity. *Adv. Healthc. Mater.* **2013**, *2* (6), 884–894. https://doi.org/10.1002/adhm.201200296.

(260) Chakrabortty, S.; Sison, M.; Wu, Y.; Ladenburger, A.; Pramanik, G.; Biskupek, J.; Extermann, J.; Kaiser, U.; Lasser, T.; Weil, T. NIR-Emitting and Photo-Thermal Active Nanogold as Mitochondria-Specific Probes. *Biomater. Sci.* **2017**, *5* (5), 966–971. https://doi.org/10.1039/C6BM00951D.

(261) Gao, J.; Jiang, S.; Zhang, X.; Fu, Y.; Liu, Z. Preparation, Characterization and in Vitro Activity of a Docetaxel–Albumin Conjugate. *Bioorg. Chem.* **2019**, *83*, 154–160. https://doi.org/10.1016/j.bioorg.2018.10.032.

(262) Wu, Y.; Eisele, K.; Doroshenko, M.; Algara-Siller, G.; Kaiser, U.; Koynov, K.; Weil, T. A Quantum Dot Photoswitch for DNA Detection, Gene Transfection, and Live-Cell Imaging. *Small* **2012**, *8* (22), 3465–3475. https://doi.org/10.1002/smll.201200409.

(263) Pes, L.; Koester, S. D.; Magnusson, J. P.; Chercheja, S.; Medda, F.; Abu Ajaj, K.;

Rognan, D.; Daum, S.; Nollmann, F. I.; Garcia Fernandez, J.; et al. Novel Auristatin E-Based Albumin-Binding Prodrugs with Superior Anticancer Efficacy in Vivo Compared to the Parent Compound. *J. Control. Release* **2019**, *296*, 81–92. https://doi.org/10.1016/j.jconrel.2019.01.010.

(264) Elsadek, B.; Graeser, R.; Warnecke, A.; Unger, C.; Saleem, T.; El-Melegy, N.; Madkor, H.; Kratz, F. Optimization of an Albumin-Binding Prodrug of Doxorubicin That Is Cleaved by Prostate-Specific Antigen. *ACS Med. Chem. Lett.* **2010**, *1* (5), 234–238. https://doi.org/10.1021/ml100060m.

(265) Kratz, F.; Müller, I. A.; Ryppa, C.; Warnecke, A. Prodrug Strategies in Anticancer Chemotherapy. *ChemMedChem* **2008**, *3* (1), 20–53. https://doi.org/10.1002/cmdc.200700159.

(266) Tomao, S. Albumin-Bound Formulation of Paclitaxel (Abraxane&Reg; ABI-007) in the Treatment of Breast Cancer. *Int. J. Nanomedicine* **2009**, 99. https://doi.org/10.2147/IJN.S3061.

(267) Socinski, M. A.; Langer, C. J.; Okamoto, I.; Hon, J. K.; Hirsh, V.; Dakhil, S. R.; Page, R. D.; Orsini, J.; Zhang, H.; Renschler, M. F. Safety and Efficacy of Weekly Nab(R)-Paclitaxel in Combination with Carboplatin as First-Line Therapy in Elderly Patients with Advanced Non-Small-Cell Lung Cancer. *Ann. Oncol.* **2013**, *24* (2), 314–321. https://doi.org/10.1093/annonc/mds461.

(268) Ma, W. W.; Hidalgo, M. The Winning Formulation: The Development of Paclitaxel in Pancreatic Cancer. *Clin. Cancer Res.* **2013**, *19* (20), 5572–5579. https://doi.org/10.1158/1078-0432.CCR-13-1356.

(269) Chen, Q.; Liang, C.; Wang, C.; Liu, Z. An Imagable and Photothermal "Abraxane-Like" Nanodrug for Combination Cancer Therapy to Treat Subcutaneous and Metastatic Breast Tumors. *Adv. Mater.* **2015**, *27* (5), 903–910. https://doi.org/10.1002/adma.201404308.

(270) Weissig, V.; Pettinger, T.; Murdock, N. Nanopharmaceuticals (Part 1): Products on the Market. *Int. J. Nanomedicine* **2014**, 4357. https://doi.org/10.2147/IJN.S46900.

(271) Chalela, J. A.; Kidwell, C. S.; Nentwich, L. M.; Luby, M.; Butman, J. A.; Demchuk, A. M.; Hill, M. D.; Patronas, N.; Latour, L.; Warach, S. Magnetic Resonance Imaging and Computed Tomography in Emergency Assessment of Patients with Suspected Acute Stroke: A Prospective Comparison. *Lancet* **2007**, *369* (9558), 293–298. https://doi.org/10.1016/S0140-6736(07)60151-2.

(272) Chen, Q.; Wang, X.; Wang, C.; Feng, L.; Li, Y.; Liu, Z. Drug-Induced Self-Assembly of Modified Albumins as Nano-Theranostics for Tumor-Targeted Combination Therapy. *ACS Nano* **2015**, *9* (5), 5223–5233. https://doi.org/10.1021/acsnano.5b00640.

(273) Hu, D.; Sheng, Z.; Gao, G.; Siu, F.; Liu, C.; Wan, Q.; Gong, P.; Zheng, H.; Ma, Y.; Cai, L. Activatable Albumin-Photosensitizer Nanoassemblies for Triple-Modal Imaging and Thermal-Modulated Photodynamic Therapy of Cancer. *Biomaterials* **2016**, *93*, 10–19. https://doi.org/10.1016/j.biomaterials.2016.03.037.

(274) Zuo, Z.; Syrovets, T.; Wu, Y.; Hafner, S.; Vernikouskaya, I.; Liu, W.; Ma, G.; Weil, T.; Simmet, T.; Rasche, V. The CAM Cancer Xenograft as a Model for Initial Evaluation of MR Labelled Compounds. *Sci. Rep.* **2017**, *7* (1), 46690. https://doi.org/10.1038/srep46690.

(275) Zuo, Z.; Syrovets, T.; Genze, F.; Abaei, A.; Ma, G.; Simmet, T.; Rasche, V. High-Resolution MRI Analysis of Breast Cancer Xenograft on the Chick Chorioallantoic Membrane. *NMR Biomed.* **2015**, *28* (4), 440–447. https://doi.org/10.1002/nbm.3270.

(276) Wu, Y.; Ihme, S.; Feuring-Buske, M.; Kuan, S. L.; Eisele, K.; Lamla, M.; Wang, Y.; Buske, C.; Weil, T. A Core-Shell Albumin Copolymer Nanotransporter for High Capacity Loading and Two-Step Release of Doxorubicin with Enhanced Anti-Leukemia Activity. *Adv. Healthc. Mater.* **2013**, *2* (6), 884–894. https://doi.org/10.1002/adhm.201200296.

(277) Wei, Y.; Quan, L.; Zhou, C.; Zhan, Q. Factors Relating to the Biodistribution & Clearance of Nanoparticles & Their Effects on in Vivo Application. *Nanomedicine* **2018**, *13* (12), 1495–1512. https://doi.org/10.2217/nnm-2018-0040.

(278) Raymond, K. N.; Pierre, V. C. Next Generation, High Relaxivity Gadolinium MRI Agents †. *Bioconjug. Chem.* **2005**, *16* (1), 3–8. https://doi.org/10.1021/bc049817y.

(279) Klemm, P. J.; Floyd, W. C.; Smiles, D. E.; Fréchet, J. M. J.; Raymond, K. N. Improving T1 and T2 Magnetic Resonance Imaging Contrast Agents through the Conjugation of an Esteramide Dendrimer to High-Water-Coordination Gd(III) Hydroxypyridinone Complexes. *Contrast Media Mol. Imaging* **2012**, *7* (1), 95–99. https://doi.org/10.1002/cmmi.483.

(280) Tang, J.; Sheng, Y.; Hu, H.; Shen, Y. Macromolecular MRI Contrast Agents: Structures, Properties and Applications. *Prog. Polym. Sci.* **2013**, *38* (3–4), 462–502. https://doi.org/10.1016/j.progpolymsci.2012.07.001.

(281) Li, Y.; Beija, M.; Laurent, S.; Elst, L. vander; Muller, R. N.; Duong, H. T. T.; Lowe, A. B.; Davis, T. P.; Boyer, C. Macromolecular Ligands for Gadolinium MRI Contrast Agents. *Macromolecules* **2012**, *45* (10), 4196–4204. https://doi.org/10.1021/ma300521c.

(282) Syrovets, T.; Gschwend, J. E.; Büchele, B.; Laumonnier, Y.; Zugmaier, W.; Genze, F.; Simmet, T. Inhibition of IκB Kinase Activity by Acetyl-Boswellic Acids Promotes Apoptosis in Androgen-Independent PC-3 Prostate Cancer Cells in Vitro and in Vivo. *J. Biol. Chem.* **2005**, *280* (7), 6170–6180. https://doi.org/10.1074/jbc.M409477200.

(283) Estrada, A. C.; Syrovets, T.; Pitterle, K.; Lunov, O.; Büchele, B.; Schimana-Pfeifer, J.; Schmidt, T.; Morad, S. A. F.; Simmet, T. Tirucallic Acids Are Novel Pleckstrin Homology Domain-Dependent Akt Inhibitors Inducing Apoptosis in Prostate Cancer Cells. *Mol. Pharmacol.* **2010**, *77* (3), 378–387. https://doi.org/10.1124/mol.109.060475.

(284) Hafner, S.; Raabe, M.; Wu, Y.; Wang, T.; Zuo, Z.; Rasche, V.; Syrovets, T.; Weil, T.;

Simmet, T. High-Contrast Magnetic Resonance Imaging and Efficient Delivery of an Albumin Nanotheranostic in Triple-Negative Breast Cancer Xenografts. *Adv. Ther.* **2019**, 1900084. https://doi.org/10.1002/adtp.201900084.

(285) Lee, H.; Dellatore, S. M.; Miller, W. M.; Messersmith, P. B. Mussel-Inspired Surface Chemistry for Multifunctional Coatings. *Science (80-.).* **2007**, *318* (5849), 426–430. https://doi.org/10.1126/science.1147241.

(286) Ryu, J. H.; Messersmith, P. B.; Lee, H. Polydopamine Surface Chemistry: A Decade of Discovery. *ACS Appl. Mater. Interfaces* **2018**, *10* (9), 7523–7540. https://doi.org/10.1021/acsami.7b19865.

(287) Yang, J.; Cohen Stuart, M. A.; Kamperman, M. Jack of All Trades: Versatile Catechol Crosslinking Mechanisms. *Chem. Soc. Rev.* **2014**, *43* (24), 8271–8298. https://doi.org/10.1039/C4CS00185K.

(288) Zeng, Y.; Liu, W.; Wang, Z.; Singamaneni, S.; Wang, R. Multifunctional Surface Modification of Nanodiamonds Based on Dopamine Polymerization. *Langmuir* **2018**, *34* (13), 4036–4042. https://doi.org/10.1021/acs.langmuir.8b00509.

(289) Kuang, J.; Guo, J. L.; Messersmith, P. B. High Ionic Strength Formation of DOPA-Melanin Coating for Loading and Release of Cationic Antimicrobial Compounds. *Adv. Mater. Interfaces* **2014**, *1* (6), 1400145. https://doi.org/10.1002/admi.201400145.

(290) Yu, L.; Liu, X.; Yuan, W.; Brown, L. J.; Wang, D. Confined Flocculation of Ionic Pollutants by Poly(L-Dopa)-Based Polyelectrolyte Complexes in Hydrogel Beads for Three-Dimensional, Quantitative, Efficient Water Decontamination. *Langmuir* **2015**, *31* (23), 6351–6366. https://doi.org/10.1021/acs.langmuir.5b01084.

(291) Lapotko, D. Plasmonic Nanoparticle-Generated Photothermal Bubbles and Their Biomedical Applications. *Nanomedicine* **2009**, *4* (7), 813–845. https://doi.org/10.2217/nnm.09.59.

(292) Vaz, B.; Salgueiriño, V.; Pérez-Lorenzo, M.; Correa-Duarte, M. A. Enhancing the Exploitation of Functional Nanomaterials through Spatial Confinement: The Case of Inorganic Submicrometer Capsules. *Langmuir* **2015**, *31* (32), 8745–8755. https://doi.org/10.1021/acs.langmuir.5b00098.

(293) Tan, X.; Bruchez, M. P.; Armitage, B. A. Efficient Cytoplasmic Delivery of Antisense Probes Assisted by Cyclized-Peptide-Mediated Photoinduced Endosomal Escape. *ChemBioChem* **2019**, *20* (5), 727–733. https://doi.org/10.1002/cbic.201800709.

(294) Torelli, M. D.; Rickard, A. G.; Backer, M. V.; Filonov, D. S.; Nunn, N. A.; Kinev, A. V.; Backer, J. M.; Palmer, G. M.; Shenderova, O. A. Targeting Fluorescent Nanodiamonds to Vascular Endothelial Growth Factor Receptors in Tumor. *Bioconjug. Chem.* **2019**, *30* (3), 604–613. https://doi.org/10.1021/acs.bioconjchem.8b00803.

6. Publications

6.1 High-Contrast Imaging of Nanodiamonds in Cells by Energy Filtered and Correlative Light-Electron Microscopy: Toward a Quantitative Nanoparticle-Cell Analysis

Shen Han,• Marco Raabe,• Lorna Hodgson, Judith Mantell, Paul Verkade, Theo Lasser, Katharina Landfester, Tanja Weil,* and Ingo Lieberwirth*

•shared first authorship, *corresponding authors

Abstract:

Fluorescent nanodiamonds (fNDs) represent an emerging class of nanomaterials offering great opportunities for ultrahigh resolution imaging, sensing and drug delivery applications. Their biocompatibility, exceptional chemical and consistent photostability renders them particularly attractive for correlative light-electron microscopy studies providing unique insights into nanoparticle-cell interactions. Herein, we demonstrate a stringent procedure to image and quantify fNDs with a high contrast down to the single particle level in cells. Individual fNDs were directly visualized by energy-filtered transmission electron microscopy, that is, inside newly forming, early endosomal vesicles during their cellular uptake processes as well as inside cellular organelles such as a mitochondrion. Furthermore, we demonstrate the unequivocal identification, localization, and quantification of individual fNDs in larger fND clusters inside intracellular vesicles. Our studies are of great relevance to obtain quantitative information on nanoparticle trafficking and their various interactions with cells, membranes, and organelles, which will be crucial to design-improved sensors, imaging probes, and nanotherapeutics based on quantitative data.

High-Contrast Imaging of Nanodiamonds in Cells by Energy Filtered and Correlative Light-Electron Microscopy: Toward a Quantitative Nanoparticle-Cell Analysis

Shen Han,[†] Marco Raabe,[†,‡] Lorna Hodgson,[§] Judith Mantell,[§] Paul Verkade,[§] Theo Lasser,[†,∥] Katharina Landfester,[†] Tanja Weil,*[,†,‡] and Ingo Lieberwirth*[,†]

[†]Max-Planck Institute for Polymer Research, Ackermannweg 10, 55128 Mainz, Germany
[‡]Institute of Inorganic Chemistry I, Ulm University, Albert-Einstein-Allee 11, 89081 Ulm, Germany
[§]School of Biochemistry, University of Bristol, Medical Sciences Building, University Walk, BS8 1TD Bristol, United Kingdom
[∥]Laboratoire d'Optique Biomédical, École Polytechnique Fédérale de Lausanne, CH-1015 Lausanne, Switzerland

S *Supporting Information*

light microscopy   electron microscopy   segmentation

ABSTRACT: Fluorescent nanodiamonds (fNDs) represent an emerging class of nanomaterials offering great opportunities for ultrahigh resolution imaging, sensing and drug delivery applications. Their biocompatibility, exceptional chemical and consistent photostability renders them particularly attractive for correlative light-electron microscopy studies providing unique insights into nanoparticle-cell interactions. Herein, we demonstrate a stringent procedure to image and quantify fNDs with a high contrast down to the single particle level in cells. Individual fNDs were directly visualized by energy-filtered transmission electron microscopy, that is, inside newly forming, early endosomal vesicles during their cellular uptake processes as well as inside cellular organelles such as a mitochondrion. Furthermore, we demonstrate the unequivocal identification, localization, and quantification of individual fNDs in larger fND clusters inside intracellular vesicles. Our studies are of great relevance to obtain quantitative information on nanoparticle trafficking and their various interactions with cells, membranes, and organelles, which will be crucial to design-improved sensors, imaging probes, and nanotherapeutics based on quantitative data.

KEYWORDS: *Correlative light-electron microscopy, energy-filtered transmission electron microscopy, nanoparticle quantification, nanodiamond, particle-cell interactions*

During the past decades, nanoparticles have transformed biomedicine as traceable drug carriers and sensitive probes for therapy and diagnostics.[1] They have provided important insights into diseases and serve as a valuable platform for imaging and therapy of, for example, cancer cells and tissue in (pre)clinical studies.[2] To further advance nanomedicine approaches and to avoid risks of nanoparticle-induced toxicity, a deeper understanding of nanoparticle-cell interactions[3,4] during their cellular uptake processes,[5,6] intracellular release, and trafficking[7] is crucial. Light microscopy (LM) and transmission electron microscopy (TEM) have been applied to visualize nanoparticle−cell interactions. However, classical LM is limited by the wavelength of light and does not provide resolution beyond the diffraction limit (∼200 nm).[8]

Super-resolution techniques such as stimulated emission depletion (STED), stochastic optical reconstruction microscopy (STORM), photoactivated localization microscopy (PALM), or super-resolution optical fluctuation imaging (SOFI) enabled resolutions down to the nanometer scale[9,10] but these optical imaging techniques require very photostable fluorescent markers. Super-resolution microscopy techniques like STED provide spatial resolution of 40 nm in HeLa cells, which is still about 100 times lower compared to the resolution

2178

LM
EM
CLEM
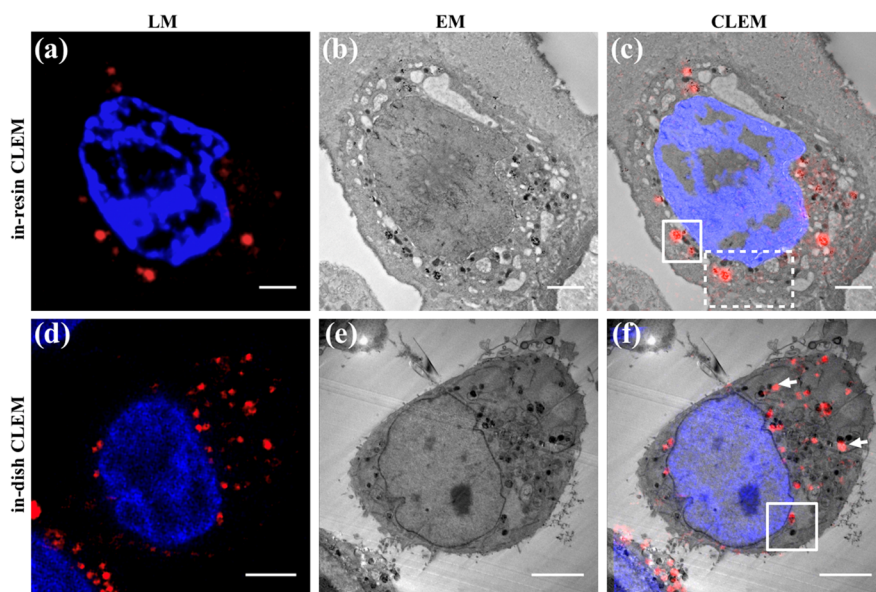
Figure 1. Correlative light-electron microscopy (CLEM) of fNDs in HeLa cells showing the results of the in-resin (top) and in-dish (bottom) preparation. (a) Confocal laser scanning microscopy (CLSM) of fNDs (red) and nucleus (blue, Hoechst) on ultrathin section (120 nm nominal thickness). (b) Transmission electron microscopy (TEM) of the same section as in (a). (c) Overlay of (a,b). (d) A selected image (of LM stack) with fNDs (red) and nucleus (blue, Hoechst) of a paraformaldehyde (PFA) fixed HeLa cell. (e) Corresponding epoxy resin section of the same cell as shown in (d) and the resulting CLEM overlay (f). Scale bar: (a–c) 2 μm, (d–f) 5 μm. The white boxes denoted in (c) refer to the areas displayed in Figure 3, and the box denoted in (f) refers to the area shown in Figure 2.

of TEM (below 1 nm) and surrounding structures could not be imaged.[11,12] In contrast, electron microscopy provides morphological visualization at unmatched resolution without the need to apply specific marker molecules. Recently, correlative light-electron microscopy (CLEM) has emerged as the method of choice to gain unique insights into exo- and endogenous cellular structures and to precisely localize endogenous proteins[11,13,14] or nanoparticles with high resolution providing important information on, for example, transporter trafficking[15] and membrane uptake.[16,17] Quantum dots (QDs) and gold nanoparticles have been applied as imaging probes for CLEM but they are limited by their weak fluorescence,[18] blinking problems of QDs,[19] and their inherent cytotoxicity, raising various concerns for long-term in vitro and in vivo studies.[20,21]

Fluorescent nanodiamonds (fNDs) have emerged as promising and biocompatible[22] imaging probes in LM, and they have been used for traceable drug delivery as well as nanoscale-sensing applications.[22] These carbon-based nanoparticles with nitrogen vacancy (NV⁻) defect color centers[23−26] provide stable fluorescence without blinking, which represents an ideal prerequisite for single-particle tracking[23,27] and super-resolution studies[28] in cells. In addition, the unique magneto-optical properties of NV⁻ centers in diamond allow sensing of local magnetic fields,[29] temperature,[30−32] electric potentials,[33] and pH value[30] with high sensitivity in living cells.

We have established a straightforward imaging approach using high-precision CLEM and dark-field energy filtered transmission electron microscopy (EFTEM) to localize fNDs in cells down to the single particle level. Until now, single fND tracking remained challenging[34−36] and only information on their approximate location and tracking paths was resolved. In previous work, image quality of NDs in CLEM studies was limited due to the weak contrast of the all-carbon composition of the diamond lattice, which has a similar chemical composition as the resin matrix used in EM preventing

imaging of individual fNDs[37,38] due to their low contrast within cells.[38−40] Attempts to increase contrast and detectability in EM and/or LM focused on labeling of the fNDs by gold nanoparticles[37] or by coating with a silica shell.[38]

Herein, dark-field contrast enhancement provided high image quality with greatly enhanced contrast suitable for resolving unlabeled single fNDs during their cellular uptake process and within cellular organelles for the first time. In a first demonstration experiment, the number of fNDs inside an endosomal vesicle was quantified. We envision that the technique developed herein will provide quantitative understanding of the various interactions of nanoparticles with cells and ultimately pave the way to a rational design of nanoscale markers, sensors, and reliable and reproducible nanotherapeutics.

After synthesis, fNDs strongly aggregate in aqueous buffer due to their high number of negatively charged surface groups. Therefore, uncoated fNDs could not be used as single particle probes for cellular studies, and fND surface coating is essential to stabilize them in cellular environments. Herein, fNDs with 35 nm mean-diameter have been used whose surface was oxidized under harsh conditions in oxidizing acids (Figure S1d) and their dispersibility was enhanced in Milli-Q water at low concentrations (0.1 mg/mL) by ultrasonification. We have developed previously a copolymer derived from the blood plasma protein human serum albumin (dcHSA-PEG(2000)₁₈), termed dcHSA-PEG, containing multiple positively charged primary amino groups and grafted poly(ethylene oxide) side chains (for further details see SI, Figure S1c; the synthesis of this polymer was reported before[41,42]) that readily adsorbed to the surface of fNDs. Coated fNDs were purified by centrifugation (18 000×g) and separated from the unbound biopolymer. After coating with dcHSA-PEG, the surface charges changed from a negative to a positive value (Figure S1d) and their hydrodynamic radius R_h increased from 44.5 to 61.7 nm (dynamic light scattering, DLS, Figures S2 and 3).
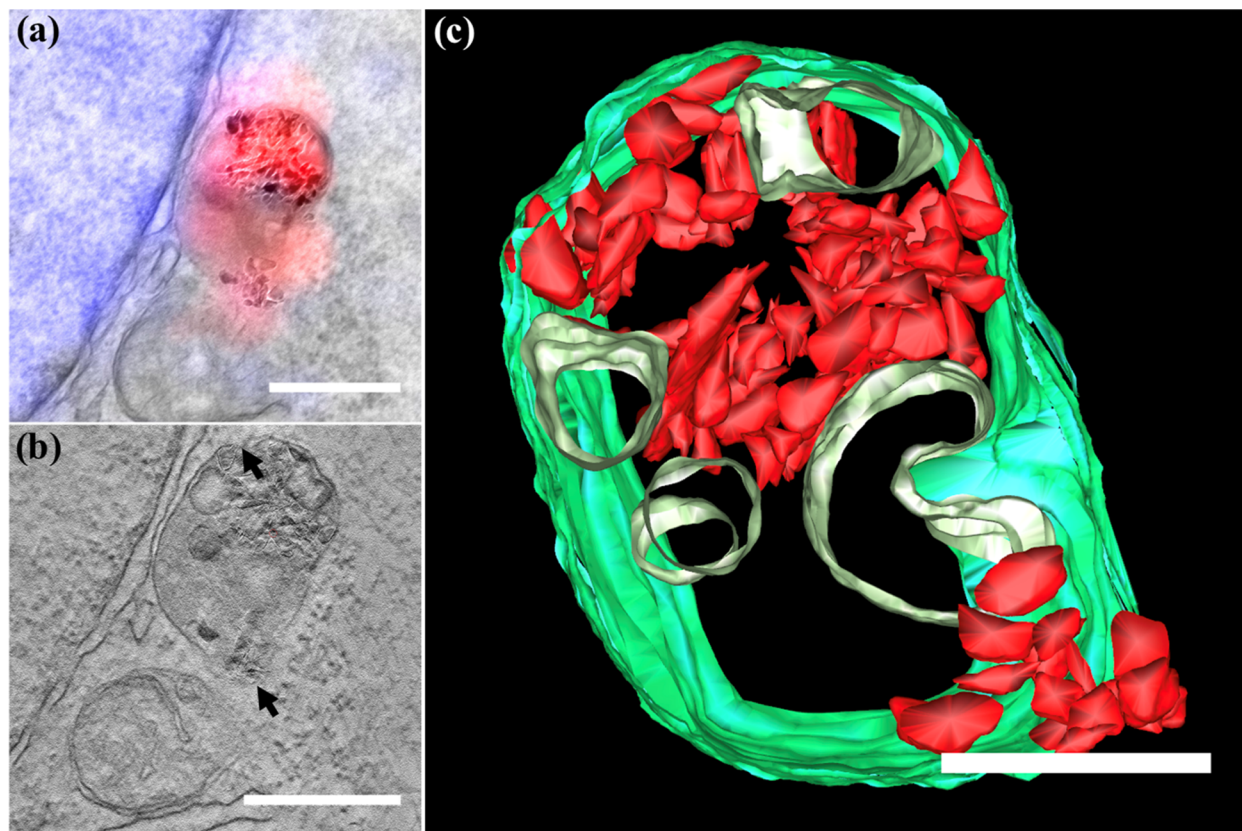
Figure 2. (a) CLEM micrograph constructed from the overlay of LM and TEM micrograph showing the area denoted by the box in Figure 1f. The localization of the fNDs by LM is shown in red, whereas the nucleus appears in blue. (b) Tomogram section of the same region; black arrows indicate the disappearance of the vesicle membrane. (c) The 3D model of fNDs clusters inside the endosomal vesicle; fNDs appear in red and the cellular membrane is shown in green; five vesicles are given in light green. Scale bar: (a,b) 500 nm, (c) 250 nm.

This relatively large increase of about 17 nm was also due to the loss of small fNDs during purification by ultracentrifugation. For the in vitro studies, narrowly dispersed fNDs of high colloidal stability in Dulbecco's phosphate-buffered saline (DPBS) were required. A monomodal distribution of coated fNDs was detected in the dynamic light scattering (DLS) recorded at different angles indicating no fND aggregate formation (Figures S2 and 3). Subsequently, the fNDs dissolved in DPBS were visualized by TEM revealing well-dispersed single nanoparticles distributed over the TEM grid (Figure S1b), whereas uncoated fNDs appeared mostly aggregated in DPBS on the TEM grid (Figure S1a). The negatively charged nitrogen vacancy (NV^-) centers in fNDs emit light at a wavelength of 680 nm after excitation with a 561 nm laser. Their emission intensity depends on the number, size, and shape of the fNDs. Herein, about 15 NV^- on average were present statistically distributed within the fNDs and their optical properties were not affected by the biopolymer coating (Figure S1e). These coated fNDs were then used to study their cellular uptake and trafficking by confocal laser scanning microscopy (CLSM) and TEM in HeLa cells.

First, the coated fNDs were vitrified and embedded prior to LM and EM acquisition providing images from the same cellular location ("in-resin CLEM"). Then, fNDs were examined by LM followed by EM acquisition ("in-dish CLEM"). The correlative imaging method provided localization of fNDs in fluorescence microscopy and high-resolution EM micrographs from the same cellular region of interest (ROI). Because of their stable emission intensity, fNDs could

be identified in CLSM as well as in EM despite their all-carbon composition. Figure 1a,b reveals LM and EM images from the in-resin CLEM imaging of the same section, where fND fluorescence was retained after the harsh resin and polymerization treatment. The cellular structures appeared well preserved even after staining with low amounts (0.1%) of uranyl acetate (UA). Noteworthy, our imaging procedure did not rely on osmium tetroxide (OsO_4) as contrast enhancer. Compared to previously reported epoxy resins for embedding,[38] the Lowicryl matrix applied herein allowed efficient nucleus staining with Hoechst dye (blue) on the section facilitating the selection of the cells of interest in LM. Figure 1c shows fNDs clusters of different sizes, whose emission was precisely colocalized with CLEM with high contrast.[38,39]

The structural information (in-resin CLEM) was obtained within one thin cell slice. In addition, we performed in-dish CLEM aiming for three-dimensional (3D) tomography. Since z-stack images of the sample were recorded with CLSM first (Figure 1d), spatial information on the sample as well as the fluorescence signals of the fNDs were obtained before the EM preparation. Cellular structures such as mitochondria remained well preserved, and they could be imaged with high resolution and contrast. Pronounced vesicle membranes around the fNDs clusters were detected (Figures S4 and S5). Background fluorescence was largely suppressed for an improved colocalization and the CLSM and EM images appeared only slightly shifted (white arrows, Figure 1f), which was mainly due to small changes in the position or shape changes of the living cells before fixation.

Table 1. Comparison of Different Methods to Image Single Intracellular fNDs Including a Qualitative Assessment on Their Performance

technique	specificity for fND clusters	specificity for single NDs	resolution	fluorescence (FL)
CLEM	high specificity depending on the fND emission	low specificity	high resolution (EM grade)	FL information from both fNDs and labeled organelles
EFTEM	high specificity depending on the fND unique energy absorption	high specificity depending on the unique energy adsorption of fNDs	high resolution (EM grade)	no FL information
HAADF STEM	medium specificity depending on the fND orientation	medium specificity depending on the fND orientation	high resolution (EM grade)	no FL information
TEM (overfocus)	medium specificity depending on the fND Fresnel contrast fringes	medium specificity depending on the fND Fresnel contrast fringes	high resolution (EM grade)	no FL information
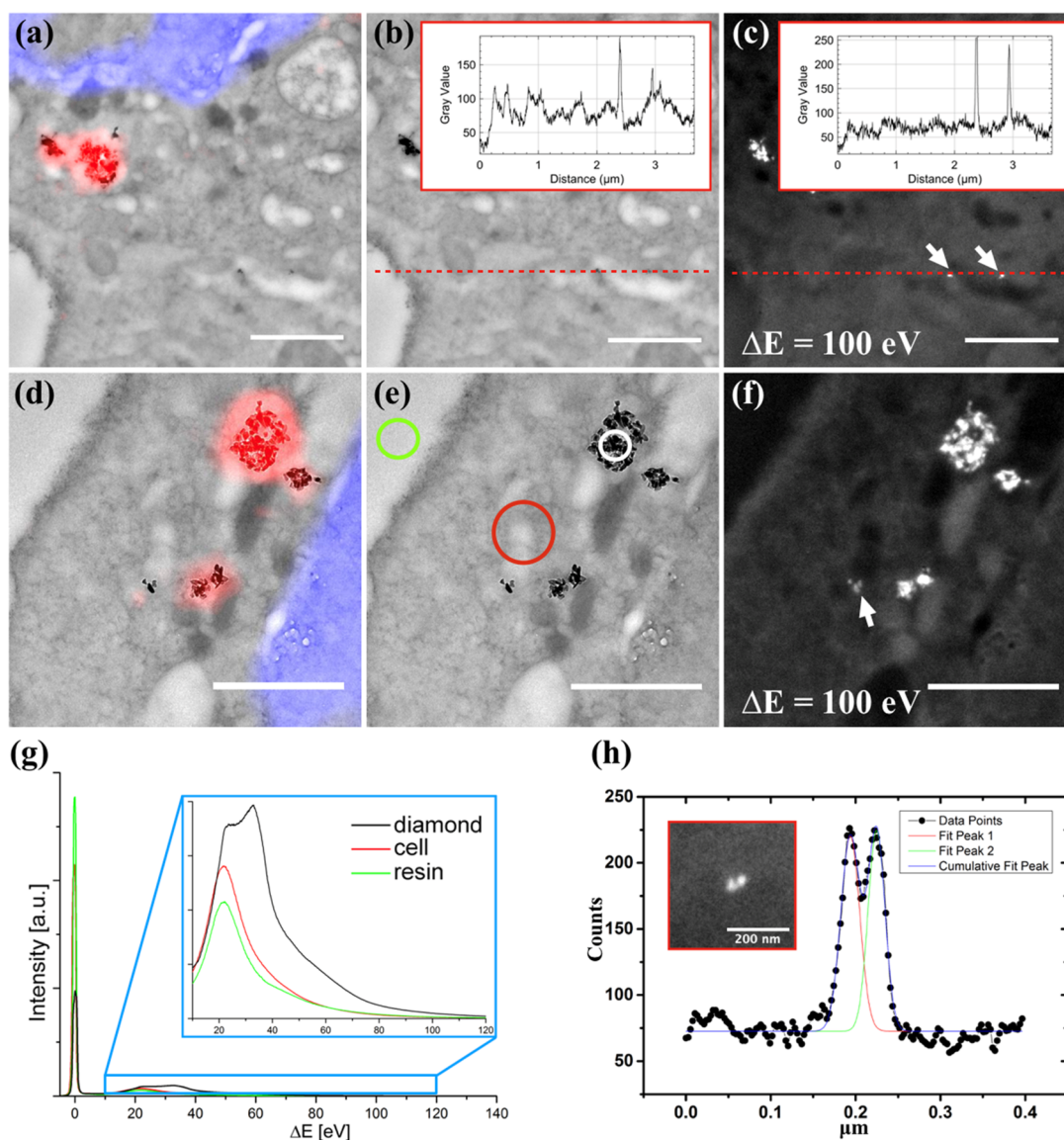
Figure 3. Single fND and fND clusters imaged by energy-filtered transmission electron microscopy (EFTEM). (a,d) CLEM overlay; (b,e) the corresponding TEM bright-field micrograph. (c,f) EFTEM micrograph acquired at an energy loss of 100 eV with 10 eV slit width. The white arrows indicate the detection of individual fNDs. The insets in (b,c) represent line profile values of respective selected line (red dots line). (g) EEL spectra of embedded fNDs (black), the embedded cell (red) and a resin-only area (green), corresponding to the positions indicated in (e) (the inset of (g) shows a zoom into the energy loss range from 10 to 120 eV). The spectra were acquired by focusing the electron beam on the respective area. (h) The line profile value of the inset (EFTEM micrograph of two closely located fNDs, Gaussian function fit of the data. (a,c) The magnification of the region marked by the dashed box in Figure 2c; (d−f)Magnification of the area marked by the solid box in Figure 2c. Scale bar: 1 μm.

The coated fNDs showed pronounced cellular uptake due to attractive electrostatic interactions with the negatively charged cellular membrane as reported previously.[41] They mainly localized in spherical clusters inside intracellular vesicles such as endosomes, lysosomes, or autophagosomes (Figure 1). EM provided the required nanoscale resolution required to precisely quantify fNDs inside these intracellular vesicles and to image their endosomal escape. Figure 2 is an enlargement of
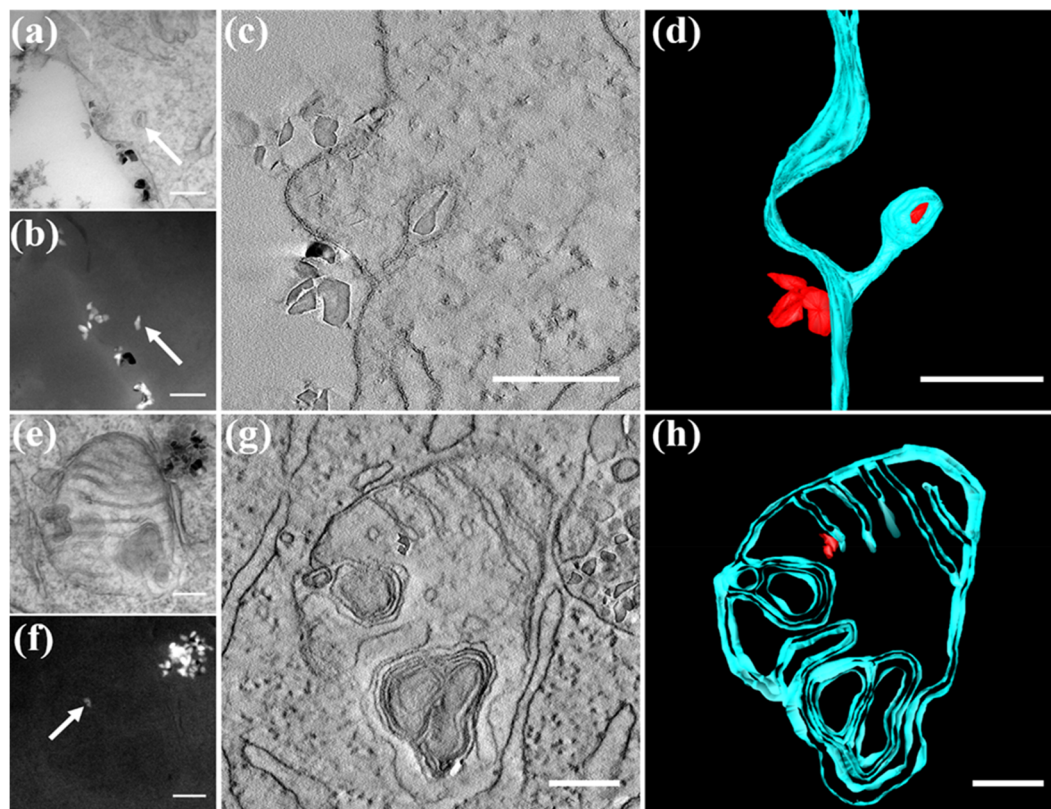
Figure 4. Interactions of single fNDs with cellular substructures. (a,b) Bright-field TEM and dark-field EFTEM of single fND uptake; (e,f) Bright-field TEM and dark-field EFTEM of fNDs inside a mitochondrion. (c,g) Virtual slices from the tomogram, whereas (d,h) give the segmentation of the tomograms of single fND uptake and localization inside a mitochondrion, respectively. Scale bar: 200 nm.

the area indicated in Figure 1f and clearly reveals a vesicle in close proximity to the cell nucleus (blue staining) and a mitochondrion located below. In total, three clusters of fNDs were found inside the vesicle: two at the top and a third smaller cluster at the bottom right close to the membrane of the vesicle. Tomography of this vesicle was performed to study the vesicle integrity. Figure 2b shows a cross section matching the LM overlay of Figure 2a. Despite the high resolution, some parts (black arrows) of the membrane appeared disrupted, especially at positions where the upper left and lower right fNDs clusters were localized. This effect appeared even more pronounced when analyzing the entire tomogram (see SI Movie 1). Obviously, fNDs induced disruption of the vesicular membrane, which likely allowed their escape from vesicles as suggested also by previous studies with labeled nanoparticles.[37,43] Segmentation of the vesicle together with fNDs is shown in Figure 2c and as a result of the high-resolution TEM tomography; even single fNDs in the cluster were identified. In Figure 2c, a total number of 101 fNDs (in red) and the outer membrane of the endosome were segmented (in green) now allowing a quantification of the fNDs per cluster. The fND clusters in the endosomal vesicles were divided into three subvolumes: (1) the cluster located close to the vesicle membrane at the upper left part contained 27 fNDs in total (reconstructed in red), (2) the cluster located in the mid of the endosome was formed by 61 fNDs, whereas (3) the clusters located at the bottom right consisted of 13 fNDs. In addition, five small vesicles were identified and segmented (in light green) within the endosome.

TEM micrographs did not provide sufficient contrast for the detection of single fNDs within the embedding resin as both

materials mainly consist of carbon-based structures. In addition, their detection by LM was limited by low fND concentrations within the thin sections (in-resin CLEM) as well as the varying fluorescence quantum yields among individual NDs, which resulted in fNDs occasionally not emitting and therefore remaining invisible. Although previous CLEM studies demonstrated an improvement for the visualization of intracellular NDs with STED,[38] the discrimination of individual ND in larger clusters still remains challenging if not impossible. In order to compare and optimize fND imaging at the nanoscale, we evaluated additional EM imaging methods summarized in Table 1 highlighting the specificity and resolution of the different techniques for detecting fNDs in clusters as well as single fNDs.

HAADF STEM. Dark-field imaging (DF) using a high-angular annular dark-field detector with scanning TEM (HAADF STEM, Figures S6 and 7) could in principle visualize single fNDs. However, diffraction-based identification techniques like HAADF STEM and conventional DF imaging rely on the correct orientation of the crystal with regard to the incident electron beam and therefore, only few individual nanodiamond crystals were detected, as demonstrated in Figure S7.

EFTEM. EFTEM allows the identification and localization of individual fNDs in the in-resin and in-dish preparations as this technique depends on the electron density but not on the orientations of the fNDs. EFTEM has been applied previously to image gold particles and QDs in HEp-2 cells for correlative microscopy studies[44] but it has not yet been used to identify intracellular fNDs. Figure 3 shows the corresponding CLEM micrographs, TEM bright-field micrographs and EFTEM micrographs of fNDs in HeLa cells. Three fNDs clusters

(Figure 3a,b) were detected in the TEM micrograph, which was confirmed by the fluorescence signal in the LM image. The EFTEM micrograph in Figure 3c reveals the presence of two single fNDs (arrows), which were barely visible in the bright field micrographs and could not be detected by fluorescence imaging. After inverting Figure 3b, we calculated the line value (red dotted line) crossing two single fNDs (Figure 3b,c). A Gaussian fit was used to calculate the signal-to-noise ratio (Figure S10 and 11) in the EFTEM image (Figure 3c), which was significantly improved (4.0 and 3.3) compared to the signal-to-noise ratio (2.3 and 1.5) of the TEM bright field image. In addition, we estimated the resolution using the line profile crossing two fNDs (Figure 3h). The distance between the two peaks was 30 nm as calculated by a Gaussian function (Figure S12) and the Gaussian fitting result highly matched the line value ($R^2 = 0.974$). The detection limit of fluorescence imaging becomes apparent in Figure 3d,e. The cluster in the left corner of Figure 3d consists of three fNDs, whose fluorescence signal could still be resolved (the slight mismatch was due to the time gap of the in-dish preparation), whereas EFTEM (Figure 3f) clearly shows the presence of three individual fNDs. The remarkable contrast of fNDs in EFTEM imaging was attributed to the higher density of NDs compared to the surrounding resin. The mean free path λ (the average distance an electron propagates through the specimen before being scattered) was lower in diamond compared to the surrounding material and hence, the inelastic scattering intensity was increased, which was experimentally confirmed by the electron energy loss (EEL) spectra in Figure 3g. Accordingly, fNDs appeared with bright contrast when imaged with an energy loss ΔE ranging from 50 eV up to 190 eV (Figure S8). This assumption was further corroborated by the observation, that fNDs could be detected easily in bright field imaging at large overfocus (Figure S9).

TEM (Overfocus). The bright Fresnel contrast fringes, which were formed around the individual fNDs in TEM bright-field imaging, indicated that the fNDs were phase objects attributed to their higher electron density, which also offers potential for detecting individual fNDs without the need for EFTEM or CLEM. The Fresnel fringes in the TEM micrograph appeared due to the discontinuous potential change at the edge of the fND. In overfocus conditions, this yielded a bright fringe around the object in the TEM micrograph.[45] However, also other phase objects presented in the specimen could be misinterpreted as fND by this method.

Our results clearly indicate that the EFTEM approach represents the method of choice for detecting single fNDs with high contrast and great spatial resolution within cells. EFTEM even allowed an autonomous TEM screening of the entire sample and subsequent qualitative data analysis was accomplished conveniently, which offers the great potential to accelerate the precise identification and quantification of intracellular fNDs.

Figure 4a reveals a TEM image of fNDs close to the extracellular matrix of the cellular membrane. The presence of the single fND was clearly confirmed by EFTEM (Figure 4b), which was not detectable by CLEM and standard TEM. It seemed that several fNDs formed clusters close to the extracellular matrix, and a single fND was located already inside the cell, presumably inside an early endosomal vesicle. Electron tomography was performed on this site and Figure 4c shows a virtual slice of the tomogram (see SI Movie 2).

Obviously, the formation of the early endosome was still in process, and the membrane of the endosome appeared still connected to the membrane of the cell. In order to gain deeper insights into this process, the tomogram of this site was segmented yielding a 3D model (Figure 4d) in which four fNDs were localized close to the cellular membrane (in green), and a single fND appeared inside the newly formed endosomal vesicle, highlighted in red. This 3D tomography captured for the first time the process of cellular uptake of a single fND as well as the presence of a membrane tunnel connecting the endosome with the cellular membrane.

Inside the cell, we screened for single fNDs that were taken up into organelles, which is of great interest for sensing,[22] drug delivery,[46] as well as understanding nanoparticle-related toxicity.[22] Single fNDs localized in cellular organelles are particularly challenging to detect. Figure 4e shows the TEM image of a cluster of fNDs in direct proximity to a mitochondrion. The fND cluster with dimensions of around 200 nm in diameter was detected in the upper right corner in close vicinity to the mitochondrion, which was probably too bulky to enter the cell organelle. EFTEM clearly showed the presence of individual fNDs inside this mitochondrion (Figure 4f). The virtual section from the tomogram (Figure 4g; see SI Movie 3) reveals two fNDs inside the mitochondrion and the segmentation (Figure 4h) of the tomogram clearly supported that the fNDs were located close to the inner membrane. Interestingly, there was no membrane formed around the fNDs suggesting that during their uptake process into the mitochondrion, the endosomal membrane surrounding the two fNDs most likely coalesced with the mitochondrial membrane. One could speculate that the two fNDs might originate from the larger fND cluster located close to the mitochondrion. However, additional studies are necessary to unravel the intracellular transport processes of nanoparticles into mitochondria.

In summary, we have demonstrated a stringent procedure to image and quantify coated fNDs as clusters as well as down to the single particle level inside cells. A bioinspired protein coating was used to stabilize the fNDs inside cells, which has similarities to the natural protein corona, formed when nanoparticles are subjected to blood serum providing high colloidal stability and biocompatibility. fNDs were detected at different stages during their cellular uptake and intracellular trafficking highlighting that many cellular barriers have to be crossed inside cells (Figure 5a). fND clusters appeared outside the cellular membrane as well as in endosomal vesicles as detected by CLEM with a high contrast by colocalization of LM and EM signals (Figure 5b). EM images of fND clusters were obtained with the highest resolution reported yet, which even allowed quantification of individual fNDs in the larger fND clusters inside intracellular vesicles. Moreover, individual fNDs were detected for the first time by EFTEM. In this way, the cellular uptake process of a single fND inside a newly forming, early endosomal vesicle was imaged (Figure 5d), and the presence of single fNDs inside a mitochondrion (Figure 5c) was demonstrated. The localization and quantification of fNDs inside mitochondria is of particular interest because drug delivery into these organelles represents an emerging strategy in cancer cell treatment.[46] Conventional LM studies could not unambiguously differentiate whether nanoparticles were taken up into mitochondria or if they only colocalized with their outer membranes. Applying dark-field EFTEM, we were able to resolve the presence of individual fNDs inside the
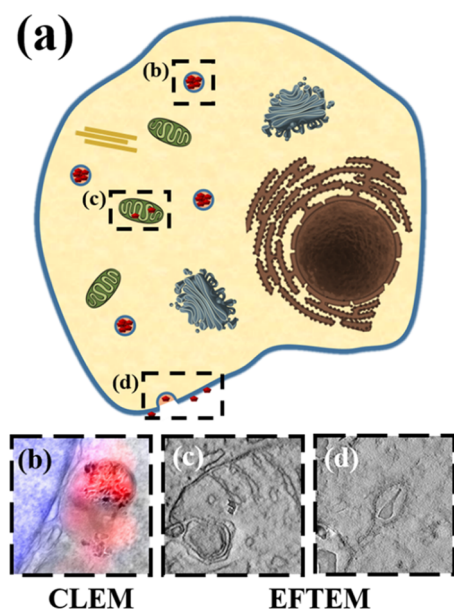
Figure 5. (a) Visualization of fNDs in different cellular environments. (b) Identification and quantification of fNDs in intracellular vesicles using CLEM. In addition, single fND detection was achieved by EFTEM (c) inside a mitochondrion as well as (d) in the cellular membrane during fND uptake.

mitochondrion, whereas a larger fND cluster remained outside this organelle in close vicinity to its outer membrane.

We believe that our approach offers the great potential to resolve fNDs within clusters as well as single fNDs and to allow the quantification of their exact number and image their locations within the various cellular compartments. In this way, one could gain fundamental insights into intracellular transport processes of fNDs and how these pathways are interconnected, which provides great opportunities to ultimately correlate bioactivities and potential toxic effects of nanomaterials based on quantitative data. We believe that such studies will be of great relevance to obtain reliable and reproducible information on nanotherapeutics that ultimately facilitate rational design of efficient and safe drug transporter and imaging probes.

■ ASSOCIATED CONTENT

Ⓢ Supporting Information

The Supporting Information is available free of charge on the ACS Publications website at DOI: 10.1021/acs.nano-lett.9b00752.

> Material and Synthesis as well as Figures S1−S12 (PDF)
> Movie contains the whole tomogram reconstruction of Figure 2 (AVI)
> Movie shows the whole tomogram reconstruction of Figure 4c (AVI)
> Movie shows the whole tomogram reconstruction of Figure 4g (AVI)

■ AUTHOR INFORMATION

Corresponding Authors
*E-mail: (T.W.) weil@mpip-mainz.mpg.de.
*E-mail: (I.L.) lieberw@mpip-mainz.mpg.de.
ORCID Ⓞ
Katharina Landfester: 0000-0001-9591-4638
Ingo Lieberwirth: 0000-0003-1323-524X

Author Contributions
S.H. and M.R. contributed equally.
Notes
The authors declare no competing financial interest.

■ ACKNOWLEDGMENTS

■ REFERENCES

(1) Pelaz, B.; Alexiou, C. H.; Alvarez -Puebla, R. A.; Alves, F.; Andrews, A. M.; Ashraf, S.; Balogh, L. P.; Ballerini, L.; Bestetti, A.; Brendel, C.; Bosi, S.; Carril, M.; Chan, W. C. W.; Chen, C. Y.; Chen, X. D.; Chen, X. Y.; Cheng, Z.; Cui, D. X.; Du, J. Z.; Dullin, C.; Escudero, A.; Feliu, N.; Gao, M. Y.; George, M.; Gogotsi, Y.; Grunweller, A.; Gu, Z. W.; Halas, N. J.; Hampp, N.; Hartmann, R. K.; Hersam, M. C.; Hunziker, P.; Jian, J.; Jiang, X. Y.; Jungebluth, P.; Kadhiresan, P.; Kataoka, K.; Khademhosseini, A.; Kopecek, J.; Kotov, N. A.; Krug, H. F.; Lee, D. S.; Lehr, C. M.; Leong, K. W.; Liang, X. J.; Lim, M. L.; Liz-Marzan, L. M.; Ma, X. M.; Macchiarini, P.; Meng, H.; Mohwald, H.; Mulvaney, P.; Nel, A. E.; Nie, S. M.; Nordlander, P.; Okano, T.; Oliveira, J.; Park, T. H.; Penner, R. M.; Prato, M.; Puntes, V.; Rotello, V. M.; Samarakoon, A.; Schaak, R. E.; Shen, Y. Q.; Sjoqvist, S.; Skirtach, A. G.; Soliman, M. G.; Stevens, M. M.; Sung, H. W.; Tang, B. Z.; Tietze, R.; Udugama, B. N.; VanEpps, J. S.; Weil, T.; Weiss, P. S.; Willner, I.; Wu, Y. Z.; Yang, L. L.; Yue, Z.; Zhang, Q.; Zhang, Q.; Zhang, X. E.; Zhao, Y. L.; Zhou, X.; Parak, W. J. ACS Nano 2017, 11, 2313−2381.
(2) Velasco-Aguirre, C.; Morales, F.; Gallardo-Toledo, E.; Guerrero, S.; Giralt, E.; Araya, E.; Kogan, M. J. Int. J. Nanomed. 2015, 10, 4919−36.
(3) Mailänder, V.; Landfester, K. Biomacromolecules 2009, 10, 2379−400.
(4) Baier, G.; Baumann, D.; Siebert, J. M.; Musyanovych, A.; Mailänder, V.; Landfester, K. Biomacromolecules 2012, 13, 2704−2715.
(5) Ritz, S.; Schottler, S.; Kotman, N.; Baier, G.; Musyanovych, A.; Kuharev, J.; Landfester, K.; Schild, H.; Jahn, O.; Tenzer, S.; Mailänder, V. Biomacromolecules 2015, 16, 1311−1321.
(6) Kokkinopoulou, M.; Simon, J.; Landfester, K.; Mailänder, V.; Lieberwirth, I. Nanoscale 2017, 9, 8858−8870.
(7) Salvati, A.; Pitek, A. S.; Monopoli, M. P.; Prapainop, K.; Bombelli, F. B.; Hristov, D. R.; Kelly, P. M.; Aberg, C.; Mahon, E.; Dawson, K. A. Nat. Nanotechnol. 2013, 8, 137−43.
(8) Schermelleh, L.; Heintzmann, R.; Leonhardt, H. J. J. Cell Biol. 2010, 190, 165−75.
(9) Vandenberg, W.; Leutenegger, M.; Lasser, T.; Hofkens, J.; Dedecker, P. Cell Tissue Res. 2015, 360, 151−78.
(10) Sahl, S. J.; Hell, S. W.; Jakobs, S. Nat. Rev. Mol. Cell Biol. 2017, 18, 685−701.
(11) Giepmans, B. N. G.; Deerinck, T. J.; Smarr, B. L.; Jones, Y. Z.; Ellisman, M. H. Nat. Methods 2005, 2, 743−749.
(12) Tzeng, Y. K.; Faklaris, O.; Chang, B. M.; Kuo, Y.; Hsu, J. H.; Chang, H. C. Angew. Chem., Int. Ed. 2011, 50, 2262−2265.
(13) Mari, M.; Geerts, W. J.; Reggiori, F. Traffic 2014, 15, 1164−78.
(14) Mateos, J. M.; Barmettler, G.; Doehner, J.; Ojeda Naharros, I.; Guhl, B.; Neuhauss, S. C. F.; Kaech, A.; Bachmann-Gagescu, R.; Ziegler, U. J. Visualized Exp. 2017, 129, 56113.
(15) Hodgson, L.; Tavare, J.; Verkade, P. Protoplasma 2014, 251, 403−16.
(16) van Weering, J. R. T.; Brown, E.; Sharp, T. H.; Mantell, J.; Cullen, P. J.; Verkade, P. Methods Cell Biol. 2010, 96, 619−648.

(17) Olmos, Y.; Hodgson, L.; Mantell, J.; Verkade, P.; Carlton, J. G. *Nature* **2015**, *522*, 236−9.

(18) He, H.; Xie, C.; Ren, J. *Anal. Chem.* **2008**, *80*, 5951−7.

(19) Bianco, S.; Grigolini, P.; Paradisi, P. *J. Chem. Phys.* **2005**, *123*, 174704.

(20) Derfus, A. M.; Chan, W. C. W.; Bhatia, S. N. *Nano Lett.* **2004**, *4*, 11−18.

(21) Butterworth, K. T.; Coulter, J. A.; Jain, S.; Forker, J.; McMahon, S. J.; Schettino, G.; Prise, K. M.; Currell, F. J.; Hirst, D. G. *Nanotechnology* **2010**, *21*, 295101.

(22) Chipaux, M.; van der Laan, K. J.; Hemelaar, S. R.; Hasani, M.; Zheng, T.; Schirhagl, R. *Small* **2018**, *14*, No. 1704263.

(23) Fu, C. C.; Lee, H. Y.; Chen, K.; Lim, T. S.; Wu, H. Y.; Lin, P. K.; Wei, P. K.; Tsao, P. H.; Chang, H. C.; Fann, W. P. *Proc. Natl. Acad. Sci. U. S. A.* **2007**, *104*, 727−732.

(24) Mohan, N.; Tzeng, Y. K.; Yang, L.; Chen, Y. Y.; Hui, Y. Y.; Fang, C. Y.; Chang, H. C. *Adv. Mater.* **2010**, *22*, 843−847.

(25) Prabhakar, N.; Nareoja, T.; von Haartman, E.; Sen Karaman, D.; Jiang, H.; Koho, S.; Dolenko, T. A.; Hanninen, P. E.; Vlasov, D. I.; Ralchenko, V. G.; Hosomi, S.; Vlasov, I. I.; Sahlgren, C.; Rosenholm, J. M. *Nanoscale* **2013**, *5*, 3713−3722.

(26) Wu, Y. Z.; Jelezko, F.; Plenio, M. B.; Weil, T. *Angew. Chem., Int. Ed.* **2016**, *55*, 6586−6598.

(27) Hsiao, W. W. W.; Hui, Y. Y.; Tsai, P. C.; Chang, H. C. *Acc. Chem. Res.* **2016**, *49*, 400−407.

(28) Arroyo-Camejo, S.; Adam, M. P.; Besbes, M.; Hugonin, J. P.; Jacques, V.; Greffet, J. J.; Roch, J. F.; Hell, S. W.; Treussart, F. *ACS Nano* **2013**, *7*, 10912−10919.

(29) Glenn, D. R.; Lee, K.; Park, H.; Weissleder, R.; Yacoby, A.; Lukin, M. D.; Lee, H.; Walsworth, R. L.; Connolly, C. B. *Nat. Methods* **2015**, *12*, 736−738.

(30) Tsai, P.-C.; Chen, O. Y.; Tzeng, Y.-K.; Hui, Y. Y.; Guo, J. Y.; Wu, C.-C.; Chang, M.-S.; Chang, H.-C. *EPJ. Quantum Technology* **2015**, *2*, 19.

(31) Simpson, D. A.; Morrisroe, E.; McCoey, J. M.; Lombard, A. H.; Mendis, D. C.; Treussart, F.; Hall, L. T.; Petrou, S.; Hollenberg, L. C. L. *ACS Nano* **2017**, *11*, 12077−12086.

(32) Sekiguchi, T.; Sotoma, S.; Harada, Y. *Biophysics and physicobiology* **2018**, *15*, 229−234.

(33) Dolde, F.; Fedder, H.; Doherty, M. W.; Nöbauer, T.; Rempp, F.; Balasubramanian, G.; Wolf, T.; Reinhard, F.; Hollenberg, L. C. L.; Jelezko, F.; Wrachtrup, J. *Nat. Phys.* **2011**, *7*, 459.

(34) Chang, Y. R.; Lee, H. Y.; Chen, K.; Chang, C. C.; Tsai, D. S.; Fu, C. C.; Lim, T. S.; Tzeng, Y. K.; Fang, C. Y.; Han, C. C.; Chang, H. C.; Fann, W. *Nat. Nanotechnol.* **2008**, *3*, 284−8.

(35) Liu, W. L.; Yu, F. L.; Yang, J. B.; Xiang, B.; Xiao, P.; Wang, L. *Adv. Funct. Mater.* **2016**, *26*, 365−375.

(36) Hui, Y. Y.; Hsiao, W. W. W.; Haziza, S.; Simonneau, M.; Treussart, F.; Chang, H. C. *Curr. Opin. Solid State Mater. Sci.* **2017**, *21*, 35−42.

(37) Liu, W. N.; Naydenov, B.; Chakrabortty, S.; Wuensch, B.; Hubner, K.; Ritz, S.; Colfen, H.; Barth, H.; Koynov, K.; Qi, H. Y.; Leiter, R.; Reuter, R.; Wrachtrup, J.; Boldt, F.; Scheuer, J.; Kaiser, U.; Sison, M.; Lasser, T.; Tinnefeld, P.; Jelezko, F.; Walther, P.; Wu, Y. Z.; Weil, T. *Nano Lett.* **2016**, *16*, 6236−6244.

(38) Prabhakar, N.; Peurla, M.; Koho, S.; Deguchi, T.; Nareoja, T.; Chang, H. C.; Rosenholm, J. M.; Hanninen, P. E. *Small* **2018**, *14*, 1701807.

(39) Hemelaar, S. R.; de Boer, P.; Chipaux, M.; Zuidema, W.; Hamoh, T.; Martinez, F. P.; Nagl, A.; Hoogenboom, J. P.; Giepmans, B. N. G.; Schirhagl, R. *Sci. Rep.* **2017**, *7*, 720.

(40) Hsieh, F. J.; Chen, Y. W.; Huang, Y. K.; Lee, H. M.; Lin, C. H.; Chang, H. C. *Anal. Chem.* **2018**, *90*, 1566−1571.

(41) Wu, Y. Z.; Ermakova, A.; Liu, W. N.; Pramanik, G.; Vu, T. M.; Kurz, A.; McGuinness, L.; Naydenov, B.; Hafner, S.; Reuter, R.; Wrachtrup, J.; Isoya, J.; Fortsch, C.; Barth, H.; Simmet, T.; Jelezko, F.; Weil, T. *Adv. Funct. Mater.* **2015**, *25*, 6576−6585.

(42) Zhang, T.; Neumann, A.; Lindlau, J.; Wu, Y. Z.; Prarnanik, G.; Naydenov, B.; Jelezko, F.; Schuder, F.; Huber, S.; Huber, M.; Stehr, F.; Hogele, A.; Weil, T.; Liedl, T. *J. Am. Chem. Soc.* **2015**, *137*, 9776−9779.

(43) Chu, Z. Q.; Zhang, S. L.; Zhang, B. K.; Zhang, C. Y.; Fang, C. Y.; Rehor, I.; Cigler, P.; Chang, H. C.; Lin, G.; Liu, R. B.; Li, Q. *Sci. Rep.* **2015**, *4*, 4495.

(44) Nisman, R.; Dellaire, G.; Ren, Y.; Li, R.; Bazett-Jones, D. P. *J. Histochem. Cytochem.* **2004**, *52*, 13−18.

(45) Dunin-Borkowski, R. E. *Ultramicroscopy* **2000**, *83*, 193−216.

(46) Chakrabortty, S.; Agrawalla, B. K.; Stumper, A.; Vegi, N. M.; Fischer, S.; Reichardt, C.; Kogler, M.; Dietzek, B.; Feuring-Buske, M.; Buske, C.; Rau, S.; Weil, T. *J. Am. Chem. Soc.* **2017**, *139*, 2512−2519.

SUPPLEMENTARY INFORMATION

High-Contrast Imaging of Nanodiamonds in Cells by Energy Filtered and Correlative Light-Electron Microscopy: Toward A Quantitative Nanoparticle-Cell Analysis

Shen Han,[‡, 1] Marco Raabe,[‡, 1, 2] Lorna Hodgson,[3] Judith Mantell,[3] Paul Verkade,[3] Theo Lasser,[1,4] Katharina Landfester,[1] Tanja Weil,[*, 1, 2] Ingo Lieberwirth,[*, 1]

Material. Fluorescent nanodiamonds (fND) were bought from FND Biotech (Taiwan).

Synthesis of dcHSA-PEG. The cationization, denaturation and the attachment of polyethylene glycol of human serum albumin (HSA) was synthesized as reported before.[1] In summary, HSA was converted to cationic HSA (cHSA) by adding ethylenediamine in high access resulting in ≈158 positive charges per protein. The positive surface charge enables high uptake into human cancer cells due to interactions with the negative charged cell membrane. Afterwards, in average 18 PEG chains (MW = 2000 g/mol) were attached to the cHSA. The PEG chains are necessary to enable colloidal stability, reduce interaction with plasma proteins and prevent immunoresponse. The obtained cHSA-PEG(2000)$_{18}$ was denatured using an urea buffer (phosphate buffer 50 mM, pH 7.4, 5 M urea, 200 mM ethylenediaminetetraacetic acid) and the disulfide bridges were reduced by tris(2-carboxyethyl)phosphine (TCEP). N-(2-aminoethyl)maleimide trifluoroacetic acid salt was added to cap the free thiol groups to prevent rebinding and to form the final dcHSA-PEG(2000)$_{18}$.

Characterization of coated fNDs. The successful coating of fNDs can be controlled by dynamic light scattering (DLS), zeta-potential and transmission electron microscopy (TEM) measurements. Usually, uncoated fNDs aggregate strongly in aqueous buffer solutions; however, in MilliQ water DLS of fNDs can be measured without aggregation. The DLS measurements showed an increase of R_h from 44.5 nm to 61.7 nm (Figure S2-3) after coating the fNDs with dcHSA-PEG(2000)$_{18}$. One of

the reasons of the relatively large increase in R_h (17.2 nm) is the loss of small fND during the purification by centrifugation. Furthermore, the coated fNDs showed only one population in the DLS measurement recorded at different angles indicating the presence of only single fNDs (Figure S2-3). The surface of these commercial available fNDs is oxidized and therefore, the fND possess a negative surface charge (Figure S1d). Due to the negative charge and the strong aggregation in aqueous buffer, uncoated fNDs were not taken up into human mammalian cancer cells. After the adsorption of dcHSA-PEG onto the fNDs, the surface charge changed from a negative to positive value (Figure S1d) caused by the positive charge of the dcHSA-PEG(2000)$_{18}$. The coated fNDs showed strong uptake into human mammalian cancer cells even at low concentrations.

fNDs can be easily visualized by TEM due to their high density. Uncoated fNDs showed mostly aggregation in DPBS on the TEM grid (Figure S1a). In contrast, coated fNDs in DPBS were nicely distributed over the TEM grid (Figure S1b). Monodispersed coated fNDs in DPBS are highly important for further in vitro studies.
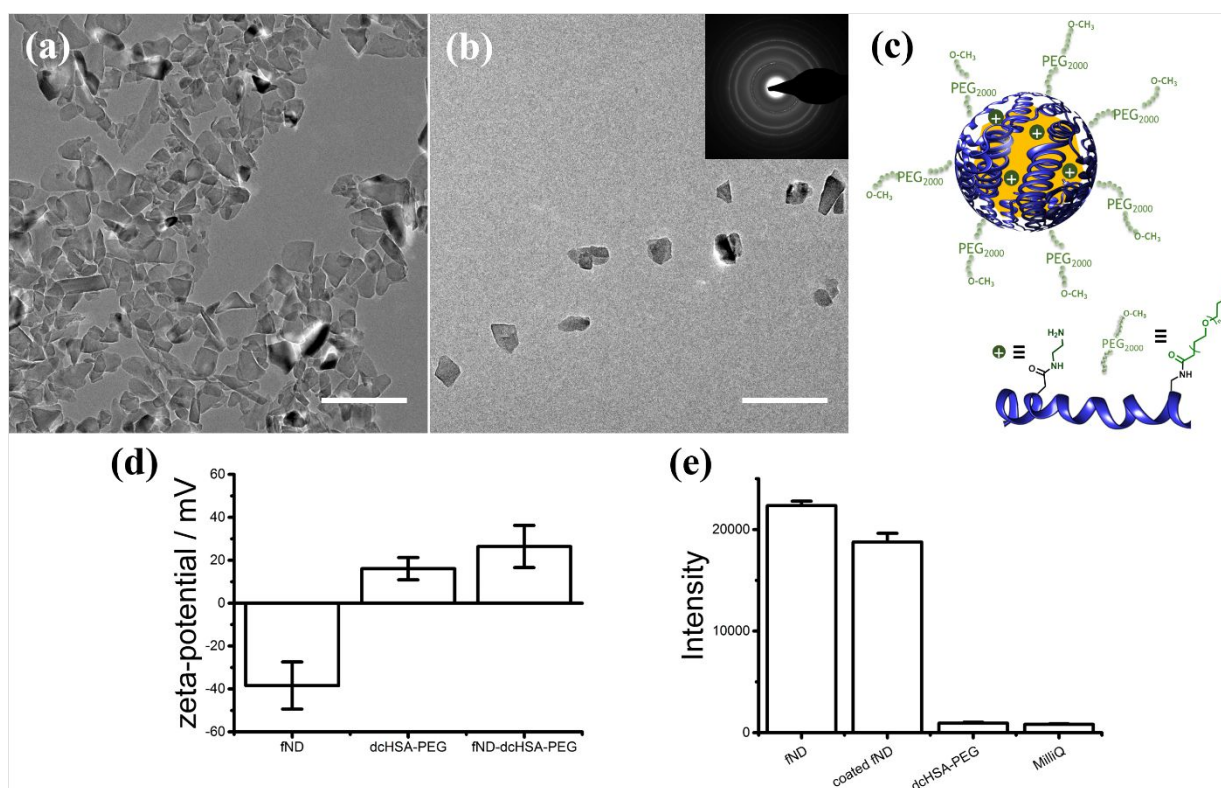
Figure S1: Characterization of fND. (a) Transmission electron microscopy (TEM) images of uncoated fND aggregates diluted in PBS. (b) Coated single fNDs diluted in PBS; fresnel

diffraction pattern of ND. (c) Scheme of protein coated fNDs. (d) Zeta-potential values. (e) Fluorescence intensity of uncoated fNDs, coated fNDs (both 0.5 mg/ml), dcHSA-PEG (2 mg/ml) and MilliQ water. Scale bar: 200 nm.

Coating of NDs. 500 μg of fluorescent NDs were dispersed in 5 ml of MilliQ water. Afterwards, the solution was dropped into a mixture of 2 mg dcHSA-PEG in 20 ml MilliQ water and shaken overnight at room temperature. The next day, free protein was removed by centrifugation (18 000 g, three times with MilliQ).

For further *in vitro* experiments, the fNDs were dispersed in Dulbecco's Phosphate Buffered Saline at a concentration of 1 mg/ml.

Fluorescence measurement. Fluorescence was measured using Tecan (SPARK 20M). Uncoated and dcHSA-PEG coated fNDs were dispersed in MilliQ water at a concentration of 0.5 mg/ml. dcHSA-PEG was dissolved in MilliQ water at a concentration of 2 mg/ml. 10 μl of each sample were transferred into a 96-well plate and the emission at a wavelength of 680 nm was measured at a fixed gain of 167. The excitation wavelength was 561 nm.

DLS. Dynamic light scattering measurements were performed on an ALV spectrometer consisting of a goniometer and an ALV-5004 multiple-tau full-digital correlator (320 channels). A He-Ne Laser (wavelength of 632.8 nm) was used as light source. For temperature controlled measurements, the light scattering instrument was equipped with a thermostat from Julabo. Measurements were performed at 20 °C at 9 angles ranging from 30° to 150°. The full measurements are depicted in Figure S2-3 left. The autocorrelation curve of the measurements at 90° is shown in Figure S2-3 right. The autocorrelation curve was transferred into a time based function to visualize the monodispersity of the samples using the software contin algorithm (Figure S2-3 right blue).

Uncoated and dcHSA-PEG coated fND were prepared at a concentration of 0.5 mg/ml in MilliQ water for DLS measurements.
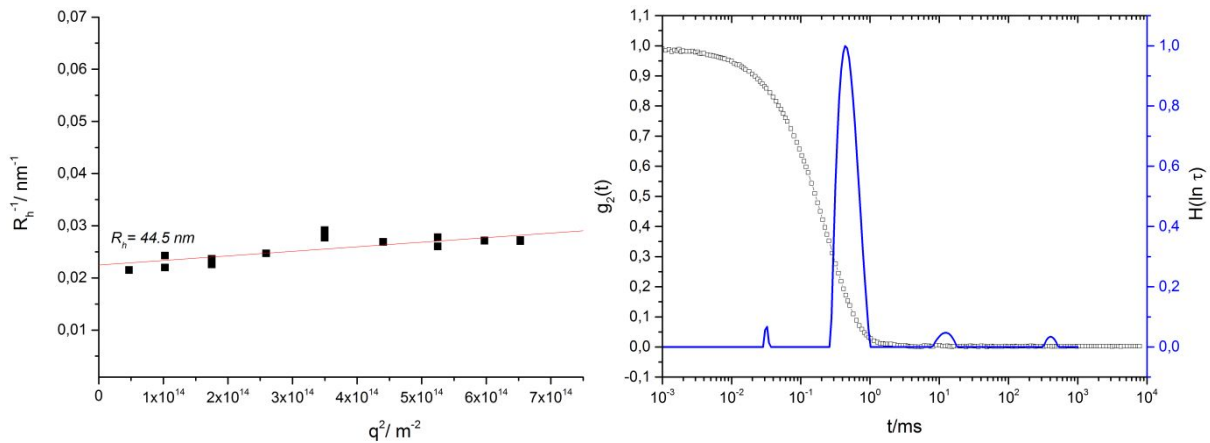
Figure S2: DLS of uncoated fNDs. Left DLS measurements from 30° to 150°. Right Autocorrelation curve (black dotted line) and time based function (blue) at 90°.
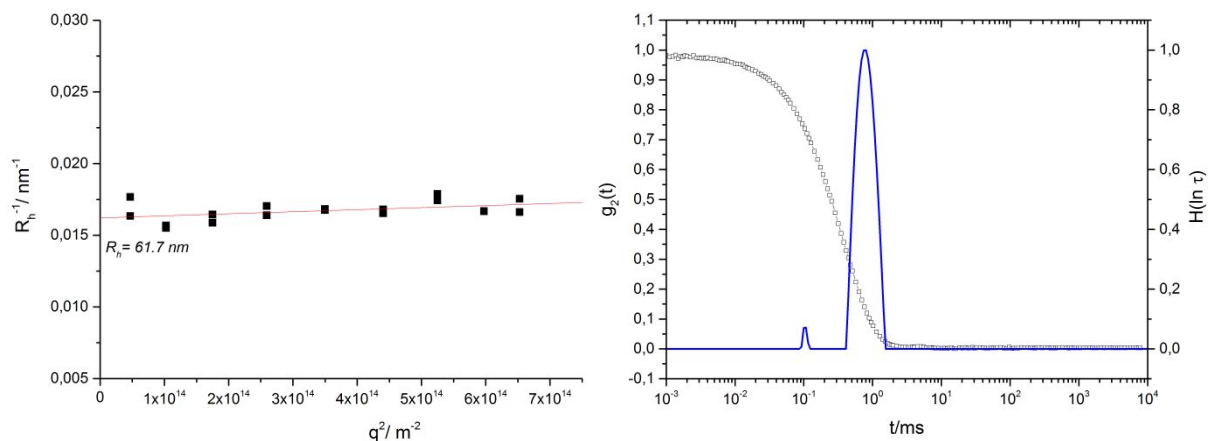
Figure S3: DLS of fNDs coated with dcHSA-PEG. Left DLS measurements from 30° to 150°. Right Autocorrelation curve (black dotted line) and time based function (blue) at 90°.

Zeta-Potential. Uncoated (0.5 mg/ml), dcHSA-PEG coated fND (0.5 mg/ml) and dcHSA-PEG (0.5 mg/ml) were prepared in a 1 mM KCl solution and the zeta-potential was measured using a Zetasizer (Nano series) from Malvern.

Cell culture. HeLa cells were cultured in Dulbecco's modified eagle medium (DMEM; Invitrogen, Germany) supplement with 10% fetal bovine serum (FBS; Sigma Aldrich, Germany), 1% glutamine, and 1% penicillin/streptomycin (Invitrogen, Germany) in a humidified incubator at 37 °C and 5%

CO_2.

Preparation of in-dish correlative light-electron microscopy (CLEM) specimens for confocal light scanning microscopy (CLSM) and transmission electron microscopy (TEM). In-dish CLEM was defined as the detection of fluorescence signals prior to EM preparation. HeLa cells were incubated with fNDs (75 µg/ml) at 37 °C (5% CO_2) for 4 h and then fixed in 4% formaldehyde (Carl Roth, Germany) for 10 min in MatTek gridded glass bottom dishes (Ashland, USA). Nucleus counterstaining with Hoechst 33342 dye in DMEM (1:1000) was performed after the paraformaldehyde (PFA) fixation for 5 min. Three times of washing in PBS were performed after nucleus staining. Prepared samples were investigated on Leica SP8 AOBS system attached to a Leica DM I6000 inverted microscope with a 63X 1.4 NA oil immersion objective. The Hoechst 33342 dye and fNDs were excited with 50 mW diode laser at 405 nm and 20 mW solid state yellow laser at 561 nm. Fluorescence signals were collected at 461 nm for Hoechst and 660-700 nm for fNDs. Stack images of ROIs with the step of ~0.2 µm were recorded. The position of the cell of interest was simultaneously recorded. After fluorescent imaging, samples were subjected to a postfixation in 4% glutaraldhyde in phosphate buffer (pH = 7). Staining with OsO_4 and uranyl acetate were performed sequentially, each step followed by three times washing in phosphate buffer. Samples were then subjected to dehydration through ethanol in ddH_2O with the gradient of 70%, 80%, 90%, 100% for 10 min each and subsequently embedded in EPON. Polymerized blocks were trimmed to the ROIs recorded by CLSM, and cut into 300 nm thick sections using a 45º diamond knife (Diatome, Switzerland) in EM UC6 ultramicrotome (Leica, Germany). Sections were then collected onto formvar coated slot copper grid (Plano, Germany) and air dried overnight for TEM imaging and tomography. Region of interests (ROIs) were retraced in TEM and tomography was performed with a single-axis tilt series from -65.5° to +67° using tilt increments of 1.5º above +/- 45° and 2.5º between -45° and +45°. Totally 65 images were collected using a CCD Camera. TEM imaging and

tomography were performed with a Tecnai G20 - FEI 200 kV Twin Lens with Lab6 filament and FEI

Eagle 4k x 4k CCD camera and with a Tecnai F20 – FEI 200 kV with FEG and Gatan US1000 CCD

camera.

Preparation of in-resin CLEM specimens for CLSM and TEM. In-resin CLEM requires samples

to be vitrified and embedded into resin prior LM and EM acquisition. HeLa cells were incubated with

fNDs (75 μg/ml) for 4 h at 37 °C (5% CO_2). After the cell uptake experiment, cells in the petri dish

were harvested and transferred into 2 ml Eppendorf tubes. After centrifugation at 1000 g for 5 min, 1

μl of thick cell suspension were collected and loaded into a 100 μm deep membrane carrier (Leica,

Germany) and vitrified in Leica EM PACT2 (Leica, Germany). Frozen membrane carriers were then

transferred into flow through containers with freeze substitution cocktail (0.1% uranyl acetate, 0.01%

tannic acid, 5% water in acetone). Freeze substitution was done in an AFS2 automated freeze

substitution device (Leica, Germany) equipped with an attachment for automated exchange of reagent

(Freeze substitution processor, FSP, Leica, Germany). Samples were kept at -90 °C for 5 h and

gradually warmed up to -45 °C at the rate of 5°C/h. After being held at -45 °C for 2 h, samples were

washed twice in acetone for 30 min each. Samples were then infiltrated in 25%, 50%, 75% of

Lowicryl HM20 resin in acetone for 2.5 h each and finally infiltrated in 100% resin overnight. Resin

was exchanged for twice with the duration of 3 h each after the overnight infiltration. Polymerization

of resin was carried out under UV light for 43 h, with the first 19 h being held at -45 °C, followed by

warming up to 0 °C within 12 h, and finally being kept at 0 °C for another 12 h.

After polymerization, resin blocks were removed from the containers. The carriers were detached

from the resin blocks by using liquid nitrogen and the warmed up specimen carrier detaching tool

(Leica, Germany). The blocks were then trimmed to desired sizes and sectioned to 120 nm thick

sections using a 45º diamond knife (Diatome, Switzerland) in EM UC6 ultramicrotome (Leica,

Germany). Sections were collected onto carbon coated formvar films on F1 copper finder grids (Agar Scientific). After being air dried, grids were stained with Hoechst 33342 dye in ddH$_2$O (1:1000) for 5 min, and washed three times in ddH$_2$O for 1 min each. Each stained grid was then mounted between a coverslip and a glass slide in 15 µl of 50% glycerol in ddH$_2$O. Mounted grids were then imaged by Leica DMI4000 B inverted epifluorescence microscope with 20X 0.75 NA dry lens for fluorescence detection. After imaging, the grids were carefully retrieved using a sharp razor blade and washed in H$_2$O. The grids were then post-stained with uranyl acetate and lead citrate before TEM imaging.
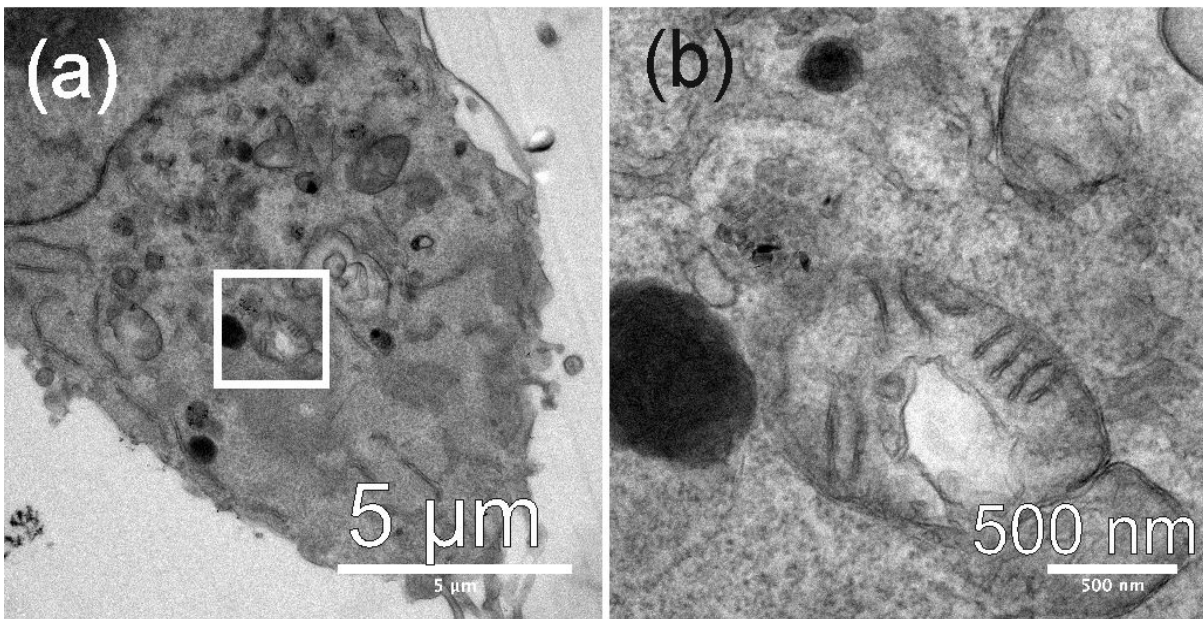
Figure S4: TEM bright field (BF) micrographs showing the preservation quality of the in-dish preparation method.
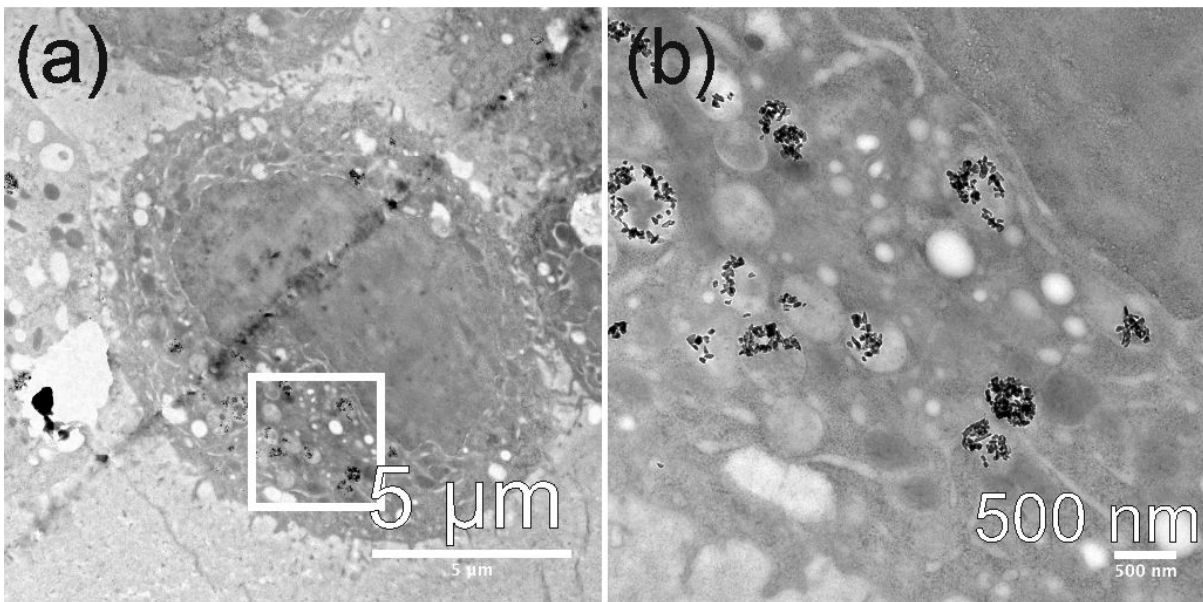
Figure S5: TEM BF micrographs showing the preservation quality of the in-resin preparation. Compared to the in-dish method, the contrast of the cellular structures is lower, presumably due to the missing OsO_4 staining and lower uranyl acetate concentration. However, post staining of the sections should be possible.

Images alignment and analysis. For tomogram alignment and reconstruction, IMOD software (version 4.9.7) was used. Acquired images from the tilt series were initially aligned and stacked in the software. The stacked file was then computationally reconstructed using a weighted back-projection algorithm. For CLEM image registration, images from light and electron microscopy were manually tracked and aligned using eC-CLEM plugin in Icy.[2]

The alignment of the in-resin acquired data was straightforward, because both, electron and light microscopical imaging originate from the very same specimen. However, for the in-dish preparation, there is a certain time span between the LM imaging and the final fixation for EM preparation and subsequent imaging. This time span already leads to systematic mismatch in the alignment. In addition, the preparation of the ultrathin sections might lead to problems with the CLEM alignment. The sections suffer a certain compression during sectioning, which can be easily compensated by a simple affine transformation (stretching of the EM micrographs parallel to the cutting direction). However, we did not observe noticeable compression of the sections and within the accuracy of the

LM images we did not need to compensate for this. On the other hand, the normal of the sections and the optical axis of the LM might not coincide. With other words, there is a certain angle between the cutting direction and the imaging direction of the LM. For this case, there is a certain tolerance of the preparation method due to the rather large confocal optical section thickness compared to ultramicrotomy sections. A confocal microscope can reach thicknesses down to 500 nm. The effect of a misaligned cutting angle would result in the disappearance of (correlative) objects, especially at the image periphery. Accordingly, we put much effort in aligning the block phase of the resin block as parallel as possible to the diamond knife and we did not encounter any problems with a misalignment of the cutting angle with regards to the imaging plane of the LM.

Transmission electron microscopy. TEM examination was performed on a Tecnai F20 transmission electron microscope operated at an acceleration voltage of 200 kV. The instrument was equipped with a scanning unit for scanning TEM (STEM) and a Tridiem 863 (Gatan) post column electron energy loss spectrometer capable of both, electron energy loss spectroscopy (EELS) and image filtering (EFTEM). Conventional image acquisition was done with a Gatan US 1000 CCD Camera at on-axis position. In post-filter position another Gatan US1000 CCD camera was used for EFTEM and EELS. For bright field imaging and for the acquisition of tomogram tilt series an objective aperture with diameter of 20 μm was used. The same aperture was used for dark field imaging; the beam tilt was adjusted to a value around 2 x 6.1 mrad, which is the angle of the diamond (111) diffraction for 200 kV electrons. Under these conditions, only electrons that have been diffracted (or inelastically scattered) exactly to the hole of the objective aperture contribute to the image formation. With this imaging mode it is possible, to identify and highlight crystalline areas in the specimen.

STEM was done using a fishione high-angle annual dark-field (HAADF) detector and if not otherwise stated, the camera length was adjusted to 520 mm. At this camera length the diamond (111) diffraction angle falls into the acceptance angle of the HAADF detector and hence the crystalline areas yield

bright contrast.

EFTEM was done using an energy selecting slit width of 10 eV, if not otherwise stated.

Imaging of NDs in the TEM. Imaging of NDs and especially individual NDs in TEM can be facilitated by using different imaging methods, depending on the configuration of the respective instrument. The main problem when imaging ND in a resin matrix, as commonly prepared for TEM ultrastructural examination of biological samples, is their low contrast with regard to the surrounding resin. However, there are some physical features of NDs that promote their discrimination from the resin matrix. The density of a diamond is with 3.5 g/cm^3 much higher than that of the surrounding resin and, as every diamond, NDs are crystalline.

Imaging crystalline areas is one of the strengths of the TEM. By simply selecting the position of the objective aperture, it is possible to select electrons, that have left the sample under a certain angle, e.g. due to diffraction. This method is called dark field mode and can be easily achieved in any TEM. The strongest diffraction spot of diamond is the (111) with a d-spacing of 2.058 Å. This corresponds to a diffraction angle of $2\Theta = 12.2$ mrad for 200 keV electrons. When the objective aperture of the TEM is adjusted in a way that electrons leaving the sample under this angle can pass (but the transmitted beam is blocked), the crystalline areas appear with bright contrast. But because the aperture allows only a small azimuth area of the diffraction ring to pass, only those crystals with the correct orientation become visible (arrow in Figure S6c).
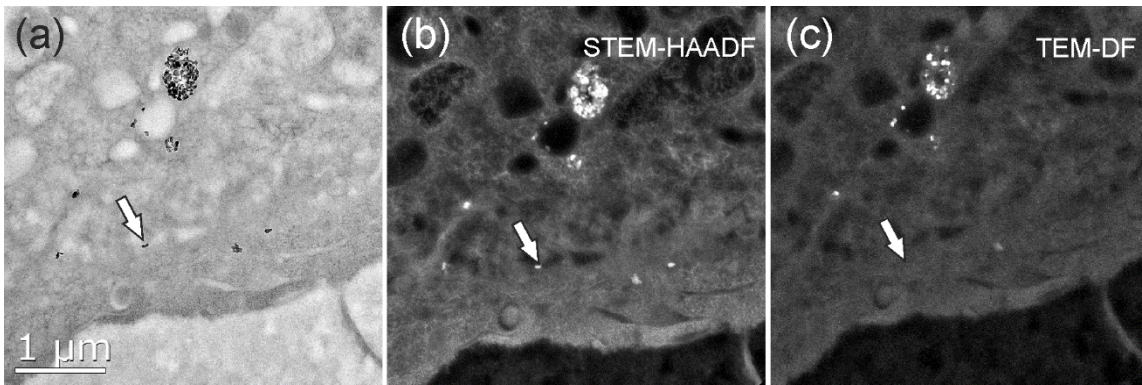
Figure S6: TEM and STEM micrographs showing the same area. In the bright field micrograph (a) the NDs are clearly visible by their dark contrast and in the STEM micrograph (b) the NDs appear bright because their diffraction contributes to the HAADF signal. All the NDs in the bright field micrograph are also visible in the STEM micrograph. When using the conventional TEM dark field (c) mode, some of the NDs are not visible, as exemplarily marked by the arrow.

In order to overcome this azimuthal restriction, annular detection methods like conical dark field or HAADF-STEM can be used. Due to the annular geometry of the HAADF detector all directions of the diffraction ring are detected and the crystal areas appear with bright contrast (Figure S6b). But even using the whole (111) diffraction ring does not guarantee that every ND crystal becomes visible, because this depends on the crystalline orientation; if the Bragg-condition is not fulfilled due to an odd orientation of the crystal there is no signal in the dark field micrograph. This is exemplarily demonstrated in Figure S7, where the ND marked by the arrow is clearly seen in the TEM BF (a) and in the EFTEM micrograph (c), but not in the HAADF-STEM (b).
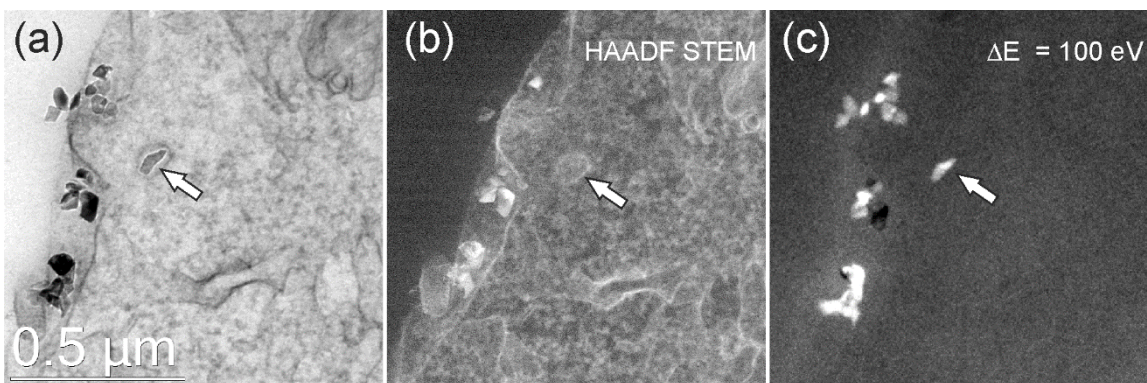
Figure S7: TEM-BF (a), STEM-HAADF (b) and EFTEM (c) micrographs of the same area. The ND marked with an arrow is visible in the BF and the EFTEM micrograph, but it does not appear in the HAADF-STEM mode.

Another alternative to image NDs in a resin matrix is to use EFTEM imaging. Here, the identification does not rely on the correct orientation of the crystal but rather on the difference in electron density between the ND and the surrounding matrix. NDs are a pure carbon material and the surrounding matrix of polymerized resin is a carbon rich material as well. Accordingly, element specific discrimination by EFTEM is eliminated. But the mean free electron path λ depends on the local electron density and then finally on the density of the respective material. In a simplified explanation the probability for inelastic scattering depends on the local electron density and with that on the material density. This is shown in the electron energy loss (EEL) spectra Figure 3g. The intensity in the areas of the nanodiamonds is greater in the entire spectral range measured from 50 to 200 eV than where resin or cellular material is present in the sample. Therefore, the nanodiamonds appear brighter in the EFTEM micrographs. Figure S8 shows an EFTEM series acquired at different energy losses using an energy selecting slit width of 10 eV. The NDs are clearly visible up to 190 eV energy loss. We did not checked higher loss values because this would unnecessarily increase the exposure time without yielding more information. Accordingly, EFTM imaging is the appropriate way to identify and image NDs in an embedded cell samples. Even single fNDs can be detected this way, which is not possible by fluorescence imaging at all.
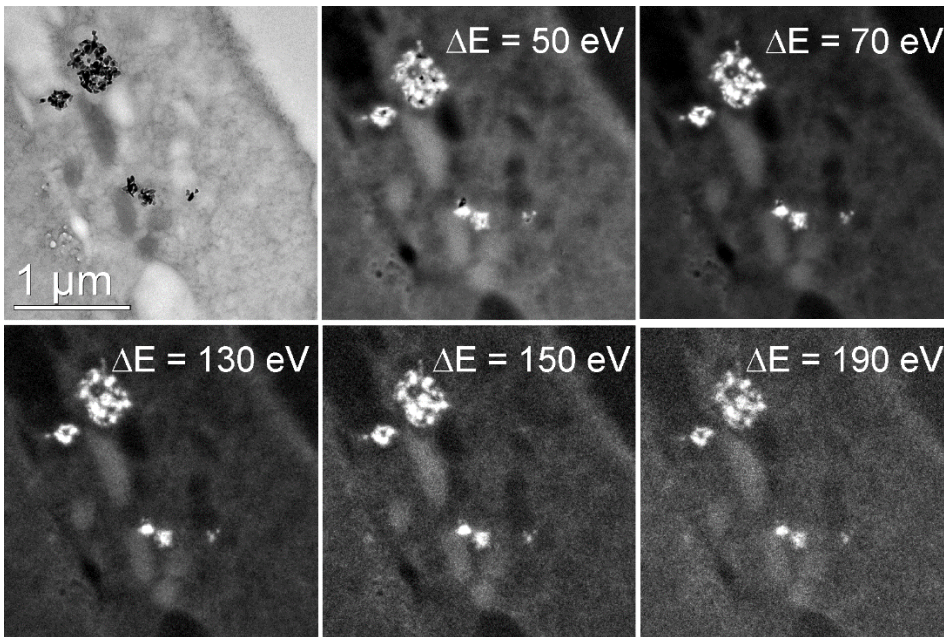
Figure S8: energy filtered TEM micrographs: The sample area is imaged with increasing energy loss from bright field (0 eV, upper left) to 190 eV (lower right). The slit width of the spectrometer was adjusted to 10 eV. In the bright field micrograph the ND are clearly visible by their dark contrast.

However, if you have neither an energy filter nor a scanning unit at the TEM, there is another, very easy way to locate the embedded NDs. Hereby one can simplify the tedious search for the NDs considerably. Like other objects, NDs are phase objects that change the phase of the electron waves as they exit the sample.

If the TEM is now heavily overfocused, this will cause the resulting Fresnel fringes of the NDs to show bright contrast on the resulting image, as shown in Figure 9b. Although these images are useless for further processing, they clearly show the position of the NDs. For comparison, Figure 9c shows the corresponding EFTEM image, on which individual NDs can be recognized as well (marked by the arrow).
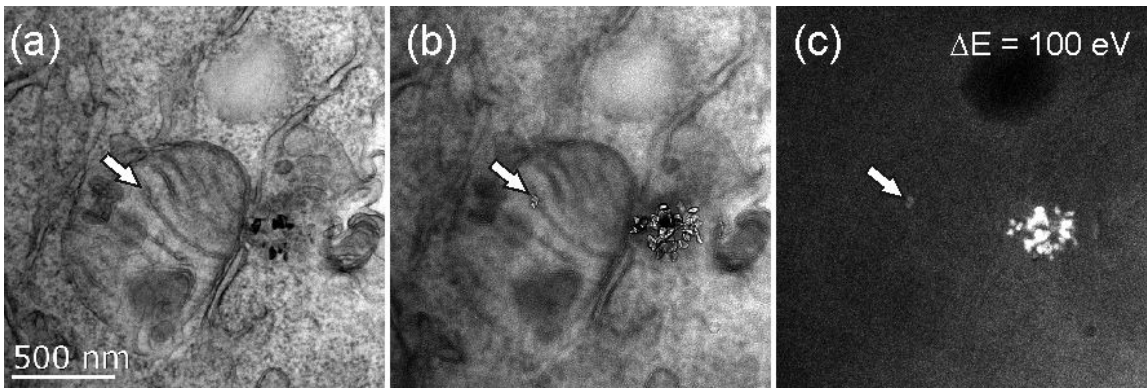
Figure S9: TEM and EFTEM micrographs of the same sample area demonstrating the ease and power of overfocus identification of phase objects like NDs in a resin matrix. (a) The TEM BF micrograph does not reveal the presence of a ND at the position marked with an arrow. Over focused TEM micrograph (b) clearly shows the ND which can be seen in the EFTEM micrograph (c) as well.

Calculation of signal to noise ratio

The signal-to-noise ratio of the gray value depicted in Figure 3b-c was calculated by Gaussian fitting. The two Gaussian fits for the TEM bright field image and the EFTEM image are shown in Figure S10-11.
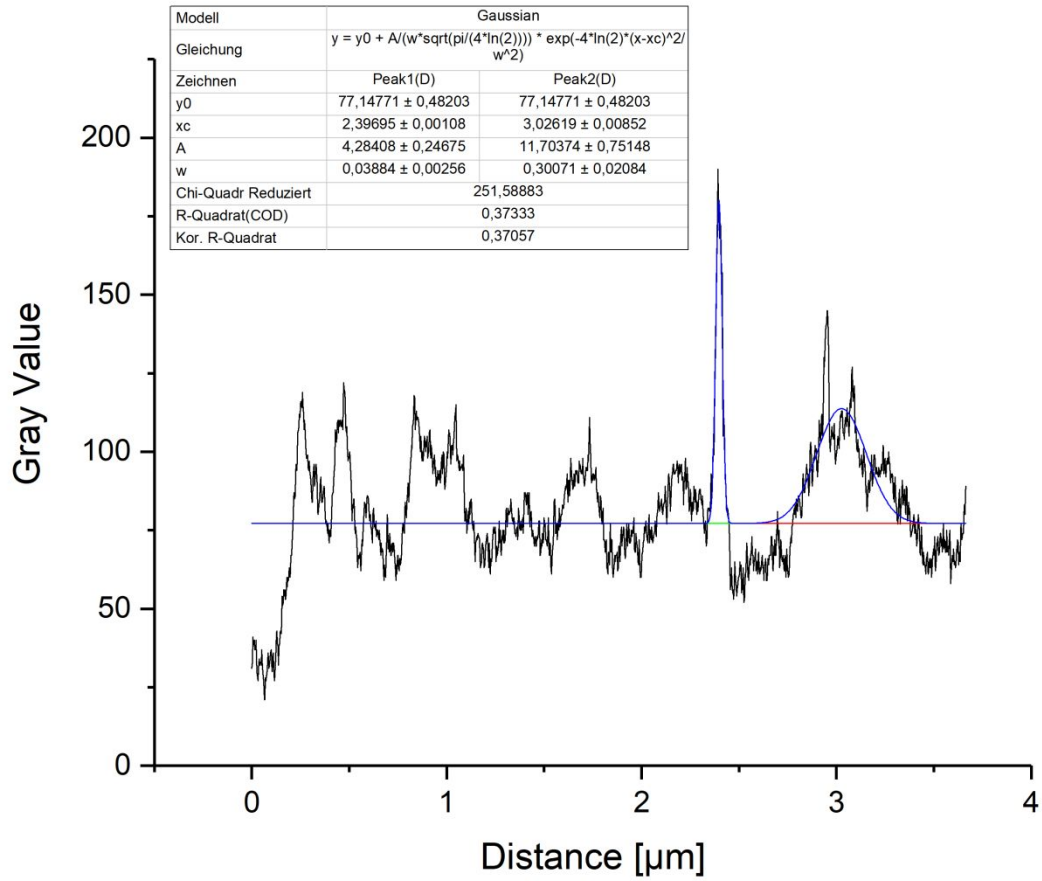
Figure S10 The Gaussian fit of the gray value graph from the TEM bright field image (Figure 3b).
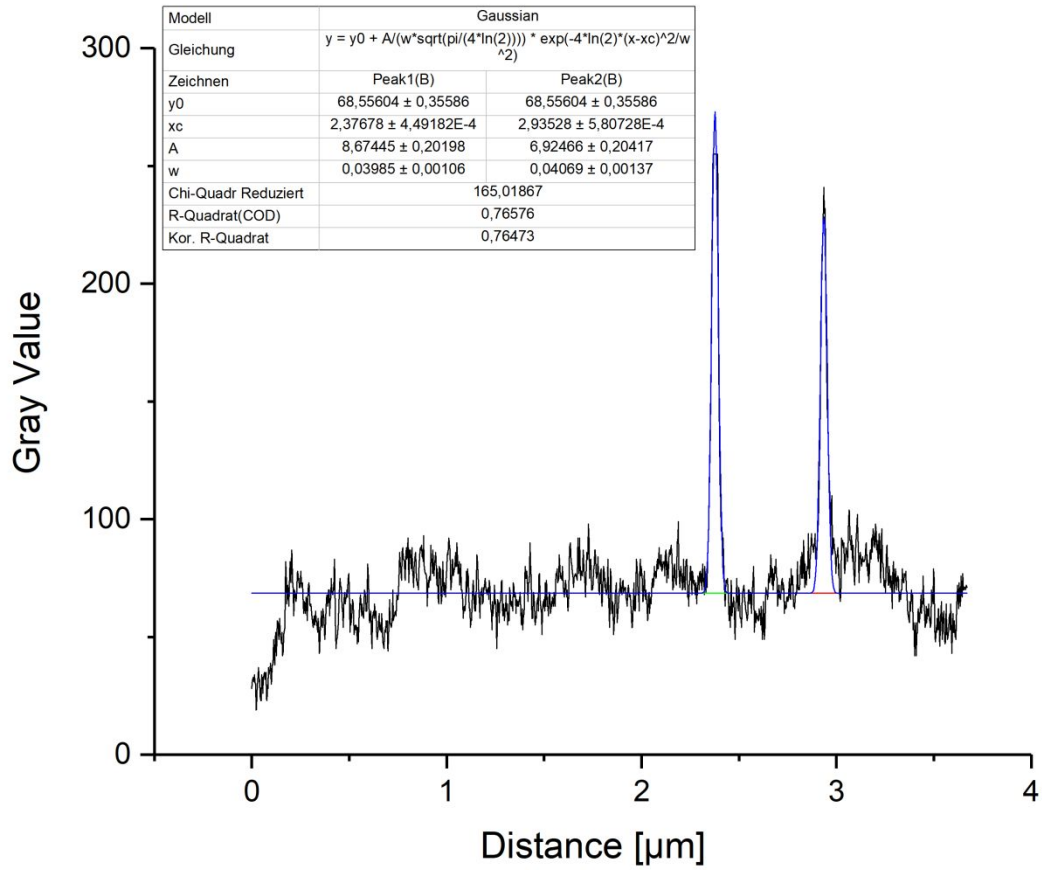
Figure S11 The Gaussian fit of the Gray Value graph from the EFTEM image (Figure 3c).

Calculation of resolution
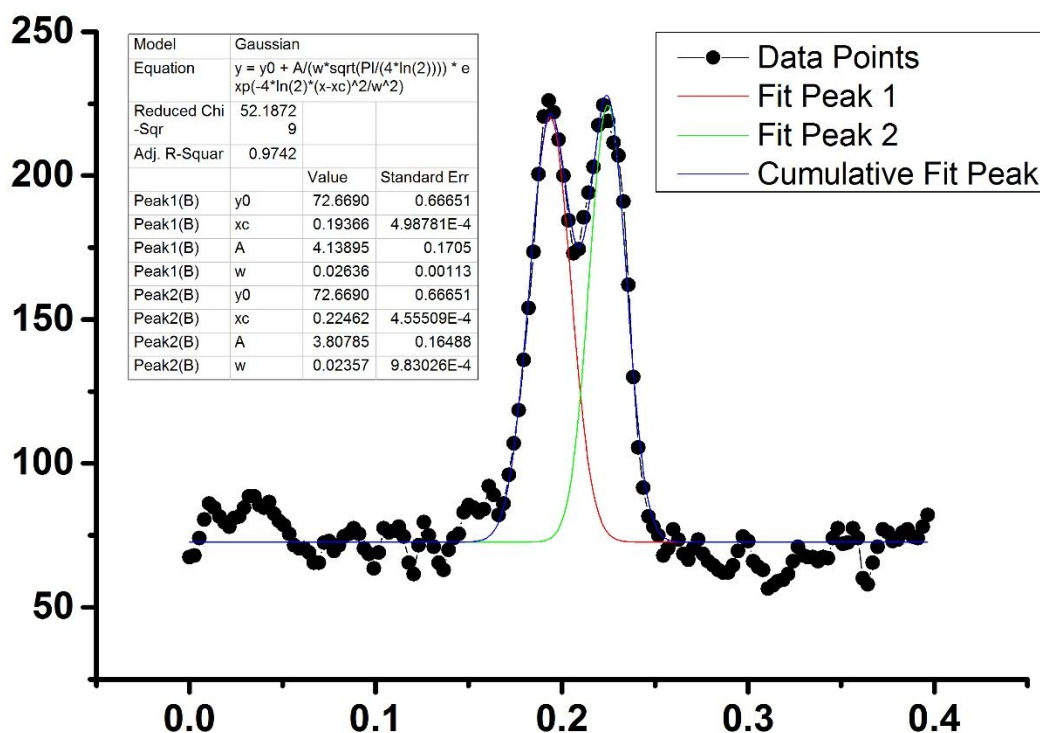
Figure S12 The two peaks were fitted by a Gaussian which was used to calculate the resolution.

References:

1.   Wu, Y. Z.; Ermakova, A.; Liu, W. N.; Pramanik, G.; Vu, T. M.; Kurz, A.; McGuinness, L.; Naydenov, B.; Hafner, S.; Reuter, R.; Wrachtrup, J.; Isoya, J.; Fortsch, C.; Barth, H.; Simmet, T.; Jelezko, F.; Weil, T. *Adv. Funct. Mater.* **2015,** 25, (42), 6576-6585.

2.   Paul-Gilloteaux, P.; Heiligenstein, X.; Belle, M.; Domart, M. C.; Larijani, B.; Collinson, L.; Raposo, G.; Salamero, J. *Nat. Methods* **2017,** 14, (2), 102-103.

6.2 Unraveling In Vivo Brain Transport of Protein-Coated Fluorescent Nanodiamonds

Pierpaolo Moscariello, Marco Raabe, Weina Liu, Sandra Bernhardt, Yuzhou Wu, Haoyuan Qi, Ute Kaiser, Tanja Weil,* Heiko J. Luhmann,* and Jana Hedrich*

*corresponding authors

Abstract:

Nanotheranostics, combining diagnostics and therapy, has the potential to revolutionize treatment of neurological disorders. But one of the major obstacles for treating central nervous system diseases is the blood–brain barrier (BBB) preventing systemic delivery of drugs and optical probes into the brain. To overcome these limitations, nanodiamonds (NDs) are investigated in this study as they are a powerful sensing and imaging platform for various biological applications and possess outstanding stable far-red fluorescence, do not photobleach, and are highly biocompatible. Herein, fluorescent NDs encapsulated by a customized human serum albumin–based biopolymer (polyethylene glycol) coating (dcHSA-PEG) are taken up by target brain cells. In vitro BBB models reveal transcytosis and an additional direct cell–cell transport via tunneling nanotubes. Systemic application of dcHSA-NDs confirms their ability to cross the BBB in a mouse model. Tracking of dcHSA-NDs is possible at the single cell level and reveals their uptake into neurons and astrocytes in vivo. This study shows for the first time systemic NDs brain delivery and suggests transport mechanisms across the BBB and direct cell–cell transport. Fluorescent NDs are envisioned as traceable transporters for in vivo brain imaging, sensing, and drug delivery.

Unraveling In Vivo Brain Transport of Protein-Coated Fluorescent Nanodiamonds

Pierpaolo Moscariello, Marco Raabe, Weina Liu, Sandra Bernhardt, Haoyuan Qi, Ute Kaiser, Yuzhou Wu, Tanja Weil,* Heiko J. Luhmann,* and Jana Hedrich*

Nanotheranostics, combining diagnostics and therapy, has the potential to revolutionize treatment of neurological disorders. But one of the major obstacles for treating central nervous system diseases is the blood–brain barrier (BBB) preventing systemic delivery of drugs and optical probes into the brain. To overcome these limitations, nanodiamonds (NDs) are investigated in this study as they are a powerful sensing and imaging platform for various biological applications and possess outstanding stable far-red fluorescence, do not photobleach, and are highly biocompatible. Herein, fluorescent NDs encapsulated by a customized human serum albumin–based biopolymer (polyethylene glycol) coating (dcHSA-PEG) are taken up by target brain cells. In vitro BBB models reveal transcytosis and an additional direct cell–cell transport via tunneling nanotubes. Systemic application of dcHSA-NDs confirms their ability to cross the BBB in a mouse model. Tracking of dcHSA-NDs is possible at the single cell level and reveals their uptake into neurons and astrocytes in vivo. This study shows for the first time systemic NDs brain delivery and suggests transport mechanisms across the BBB and direct cell–cell transport. Fluorescent NDs are envisioned as traceable transporters for in vivo brain imaging, sensing, and drug delivery.

1. Introduction

Reaching the brain with an effective therapy or imaging reagent is still considered one of the most challenging tasks in treating neurological diseases. The complexity of neurological causes and syndromes as well as the limited understanding of the exact disease pathophysiology have impeded the development of efficient therapies without long-term side effects.[1] In addition, the blood–brain barrier (BBB) still represents a major challenge for effective central nervous system (CNS) delivery of therapeutics and imaging probes. The BBB consists of brain capillary endothelial cells, pericytes, astrocytes, and neurons, all referred to as the neurovascular unit (NVU).[2] The role of the NVU is to maintain a constant homeostatic environment and to prevent xenobiotics (including many potential drugs) from entering the brain.[3] The BBB is not only a physical barrier but also a dynamic interface influenced by the individual physiological and pathophysiological conditions.[4] Thus, there is a need for a more personalized therapy for patients with CNS diseases. However, translating science into solutions for personalized therapies is still a major challenge in research and development. Personalized medicine is based on the knowledge of the individual genetics, disease status, and pharmacokinetics. Theranostics, a combination of diagnosis and therapy in one system, is becoming an attractive research field to address the transition from conventional to personalized therapeutic plans.[5,6] Many nanomaterials, such as different types of radionuclide-labeled particles like antibodies, liposomes, polymers, and micelles have already been used for theranostic applications, both in animal models and in patients.[7] Most optical tools such as fluorescent dye labels,[8] expression of fluorescent[9,10] or nonfluorescent proteins like luciferase[11] are limited by photobleaching, strong interference with autofluorescence from background tissue, and low transfection efficiencies. Poly(lactic-co-glycolic acid; PLGA) NPs are the most studied nanosystems for successful BBB crossing.[12] Nonetheless, they do not possess intrinsic optical properties useful for nanotheranostics. Additionally, in a recent study Medina et al. demonstrated that PLGA NPs were not transported to the brain in healthy animals but only in diseased animals with impaired BBB.[13,14] Inorganic nanomaterials such as quantum dots have been considered as alternatives for

Dr. P. Moscariello, S. Bernhardt, Prof. H. J. Luhmann, Dr. J. Hedrich
Institute of Physiology
University Medical Center of Johannes Gutenberg University Mainz
Duesbergweg 6, 55128 Mainz, Germany
E-mail: luhmann@uni-mainz.de; hedrich@mpip-mainz.mpg.de

Dr. P. Moscariello, M. Raabe, Dr. W. Liu, Prof. Y. Wu,
Prof. T. Weil, Dr. J. Hedrich
Max Planck Institute for Polymer Research
Ackermannweg 10, 55128 Mainz, Germany
E-mail: weil@mpip-mainz.mpg.de

M. Raabe, Dr. W. Liu, Prof. T. Weil
Institute of Inorganic Chemistry I
Ulm University
Albert-Einstein-Allee 11, 89081 Ulm, Germany

Dr. H. Qi, Prof. U. Kaiser
Central Facility of Electron Microscopy
Electron Microscopy Group of Materials Science
Ulm University
Albert-Einstein-Allee 11, 89081 Ulm, Germany

The ORCID identification number(s) for the author(s) of this article can be found under https://doi.org/10.1002/smll.201902992.

brain targeting, but their cytotoxicity, for example due to release of toxic metal cations, represents a major limitation for in vivo studies.[15–17] Carbon dots (CDs) also exhibit desirable optical properties and a few studies report their spontaneous BBB crossing ability.[18,19] Given their recent discovery, the potential of CDs as a platform in the diagnosis and therapy of CNS diseases still needs further investigation addressing new functionalization strategies to avoid rapid clearance and heart accumulation that might induce toxicity.[20]

Here, fluorescent nanodiamonds (NDs) were investigated as an emerging class of carbon nanomaterials providing essential features of nanotheranostics. NDs are characterized by peculiar optical and magnetic properties, biocompatibility, high thermal conductivity and electrical resistivity as well as chemical stability and nondegradability even in harsh environments.[21] The implementation of elemental defects (e.g., nitrogen vacancy; NV) in the carbon lattice leads to an outstanding photostable far-red fluorescence with an emission maximum at 700 nm, which is higher than most cellular autofluorescence.[22,23] It was shown that NV-NDs improve the sensitivity of magnetic resonance imaging (MRI) due to their dynamic nuclear spin polarization from the NV center.[24] However, the high potential of NDs as in vivo theranostics is still limited by their tendency to aggregate in biological surroundings. Typical commercial suspensions of NDs usually contain larger aggregates hindering their biological applicability.[22] Haziza et al. have previously shown in vitro tracking of fluorescent NDs in mouse hippocampal neurons for monitoring the biological effects of nocodazole and genetic factors.[25] Another recent study demonstrated the neuronal action potential magnetic sensing in marine worms using fluorescent NDs.[26] The great potential of NDs for therapeutic and bioimaging applications in neuronal diseases has been highlighted. However, in vivo studies are lacking that demonstrate NDs delivery after systemic administration across an intact BBB in vivo.[27,28] The study of Xi and colleagues, for example, showed delivery of the anticancer drug doxorubicin by NDs, which adsorbed doxorubicin at the surface, after direct location into brain tumor tissue via invasive convection-enhanced delivery.[29] Therefore, to our knowledge, it has not yet been demonstrated whether NDs are able to cross an intact BBB without invasive strategies, which would be of fundamental importance to evaluate their application in neuroscience.[20] Consequently, there is an urgent need for new studies, which assess the trafficking and transport of NDs across the most restrictive biological barrier, i.e., the blood–brain barrier.

In this study, NDs stabilized by a protein-derived biopolymer coating (cationic, PEGylated denatured human serum albumin; dcHSA-PEG) (**Figure 1**) were evaluated for their ability to cross an intact BBB in vitro and in vivo, which is a prerequisite for their application as nanotheranostic platform for neurological disease treatment. dcHSA-NDs reveal high colloidal stability over a broad pH range (pH 2–8). The high number of reactive functional groups of the dcHSA-PEG coating provides an easy to functionalize platform for the attachment of drugs or targeting sequences, thus circumventing the disadvantage of challenging surface chemistry of uncoated NDs.[24,30]

We believe that none of the reported nanoplatforms for brain targeting exhibit, simultaneously, all of the dcHSA-NDs features: 1) stable fluorescence, 2) potential for hyperpolarization of

nuclear spin for magnetic resonance imaging, 3) temperature sensing, 4) colloidal stability, 5) multitude of functionalization groups on dcHSA-PEG, 6) biocompatibility. Transport of dcHSA-NDs across the BBB after intravenous injection would allow brain delivery of multiple drugs, possibility of treatment tracking via magnetic resonance and sensing of brain temperature changes occurring in a number of common human diseases in one platform. Thus, dcHSA-NDs provide not only a potential biomedical strategy but also an efficient platform to study biological processes in vivo.

To evaluate dcHSA-NDs for brain targeting in vivo via BBB crossing, we demonstrated that dcHSA-NDs 1) were able to cross the BBB in an in vitro model and 2) were endocytosed by brain endothelial cells partly incorporated in endosomal compartments and lysosomes and released on the abluminal side. Here the particles 3) were taken up by neurons and astrocytes, and 4) were transported via cell-to-cell connections of tunneling nanotubes. 5) Cell viability or BBB integrity in vitro was not affected. 6) Most importantly, investigated fluorescent dcHSA-NDs crossed BBB in healthy mice reaching the brain parenchyma and could be tracked at the single cell level. Our results clearly demonstrate the great potential of fluorescent dcHSA-NDs as a delivery platform for BBB transport and provide promising evidence for future personalized nanotheranostic applications in neurological diseases and the study of disease mechanisms in the brain.

2. Results and Discussion

2.1. Characterization of dcHSA-NDs

To design a NDs system, which is able to cross an intact blood–brain barrier, their transport needs to be controlled addressing endocytosis and transcytosis. Therefore, we selected denatured and cationized albumin as NDs coating, which facilitates cell penetration and intracellular trafficking and final release on the brain side after transcytosis.[30,31] Cationization of HSA is accomplished by reacting about 100 carboxylic acid groups of the aspartic acid and glutamic acid side chains with ethylenediamine in excess yielding cHSA with about 159 primary amino groups as reported previously.[30,32] cHSA provides the positive charges necessary for NDs coating by electrostatic interactions with the negatively surface charges of NDs (Figure 1A) and facilitates to enhanced cellular uptake due to interactions with the negatively charged cellular membrane.[30,33] Furthermore, about 20 polyethylene glycol (PEG) polymer chains with an average molecular weight of 2000 g mol^{-1} were covalently attached addressing about 20 of the about 159 amino groups on the denatured HSA (Figure S1, Supporting Information) to form the final dcHSA-PEG depicted in Figure 1.[30] PEG(2000) chains, which provide an extended hydration shell, impart high colloidal stability in biological solutions, and reduce protein binding in plasma.[30] For coating, the NDs were first dispersed in boric acid buffer (20×10^{-3} M, pH 8.4) by sonication. Then, the dispersion was added to dcHSA-PEG-BDP or dcHSA-PEG-Rho (12 mg) and dissolved in a larger volume of boric acid buffer (pH 8.4) by a dropping funnel. The mixture was stirred at room temperature overnight. After coating overnight, dcHSA-NDs were separated from the unbound dcHSA-PEG by centrifugation.
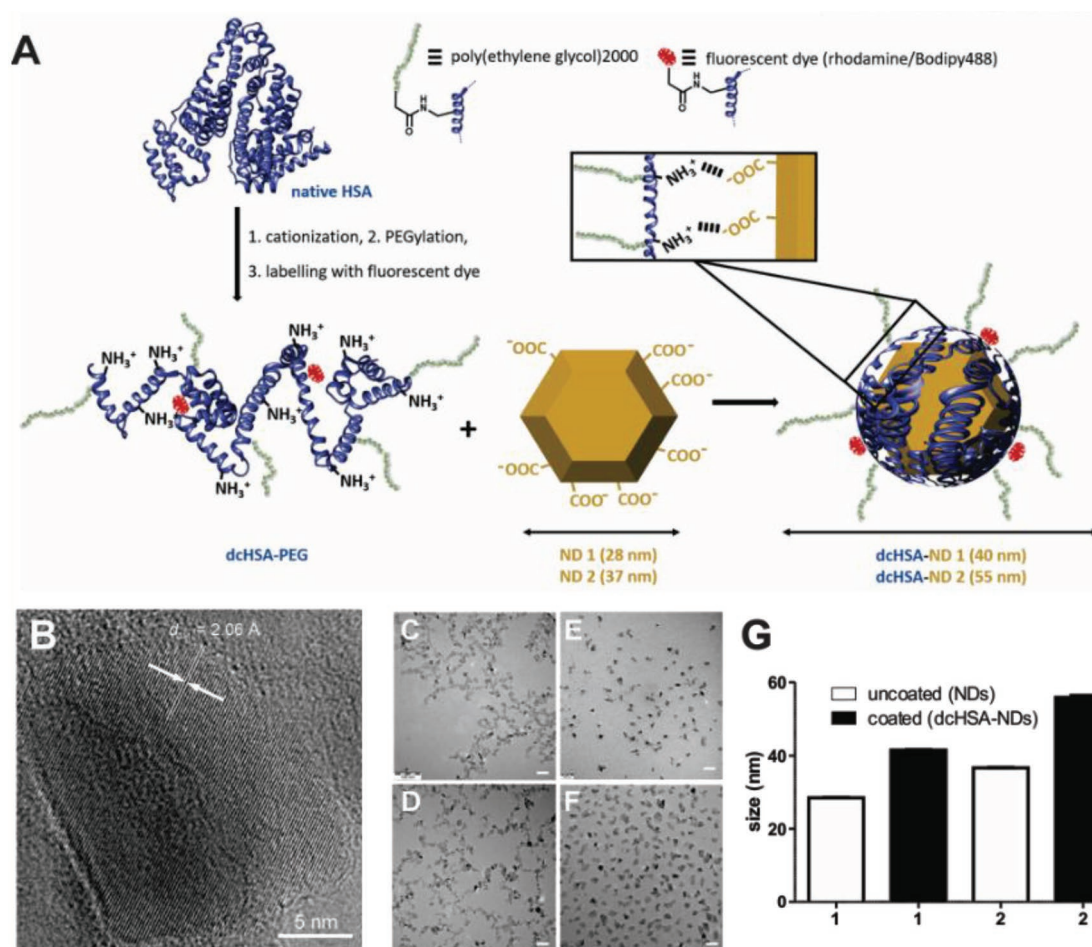
**ADVANCED
SCIENCE NEWS**

www.advancedsciencenews.com

NANO · MICRO

small

www.small-journal.com

Figure 1. NDs are encapsulated by a HSA-based biopolymer. A) Preparation of dcHSA-NDs starts from native HSA, which is cationized, conjugated to PEG2000 chains and denaturated to afford dcHSA-PEG. The positively charged dcHSA-PEG offers multiple electrostatic interactions with the negatively charged NDs surface, and NDs are coated with the biopolymer to yield dcHSA-NDs. B) HRTEM of nanodiamonds which reveals the typical carbon lattice structure. C–F) TEM images of NDs **1** (18.7 nm) C) and NDs **2** (25.5 nm) D), and TEM images of dcHSA-PEG-coated **1** E) and **2** NDs F); scale bar = 50 nm. G) Hydrodynamic diameter (nm) of **1** and **2** NDs without (white) or with (black) coating.

All synthesis steps and all characterizations are given in the Supporting Information.

The zeta-potential measurement clearly showed a change from the negatively-charged, uncoated NDs to positively-charged, protein-coated dcHSA-NDs (zeta potentials: NDs (−28.5 ± 1.0 mV), dcHSA-NDs (26.3 ± 0.7 mV), and dcHSA-PEG (11.9 ± 3.7 mV); Figure S3, Supporting Information). To address the size-dependent impact of dcHSA-NDs on in vitro BBB transport, dcHSA-NDs of two different sizes (about 40 nm for dcHSA-NDs **1** and 55 nm for dcHSA-NDs **2**) were separated from the same batch. The hydrodynamic diameter after coating was assessed by DLS (dynamic light scattering) in MilliQ water. The average diameters changed from 28.47 ± 0.22 nm before coating to 41.55 ± 0.20 nm for dcHSA-NDs **1** (40 nm) and 36.68 ± 0.18 nm to 55.87 ± 0.92 nm for dcHSA-NDs **2** (55 nm), respectively (Figure 1G). The morphology of the NDs before and after coating was characterized by transmission electron microscopy (TEM). From the TEM images, histograms were created displaying the sizes of NDs **1** (18.7 ± 3.4 nm) and NDs **2** (25.5 ± 5.5 nm) that support the results obtained from the DLS measurements

(Figure S2, Supporting Information). Furthermore, uncoated NDs formed clusters visible in TEM images (Figure 1C,D). In contrast, discrete nanoparticles of dcHSA-NDs were observed (Figure 1E,F) indicating the successful coating and stabilization of the NDs by the dcHSA-PEG shell. In addition, we recorded high-resolution TEM (HRTEM); it was accomplished to visualize the typical diamond lattice structure (Figure 1B).

The stability of the coated polymer shell on the surface of NDs (dcHSA-NDs **1** and **2**), was further assessed in agarose gel (Figure S4, Supporting Information). The overlap of the three signals for NDs, the protein coating, and its rhodamine label proved that the coating of dcHSA-NDs even remained stable in harsh condition during gel electrophoresis (1× TAE (Tris base-Acetic acid-EDTA) buffer and electric field).

2.2. dcHSA-NDs Are Transported Across BBB in an In Vitro Model

To investigate the ability of dcHSA-NDs to cross the BBB, an in vitro model composed of the endothelial cell line bEnd.3 cells

ADVANCED
SCIENCE NEWS
www.advancedsciencenews.com

NANO · MICRO
small
www.small-journal.com

A

luminal compartment
bEnd.3 cell monolayer
abluminal compartment

B

C
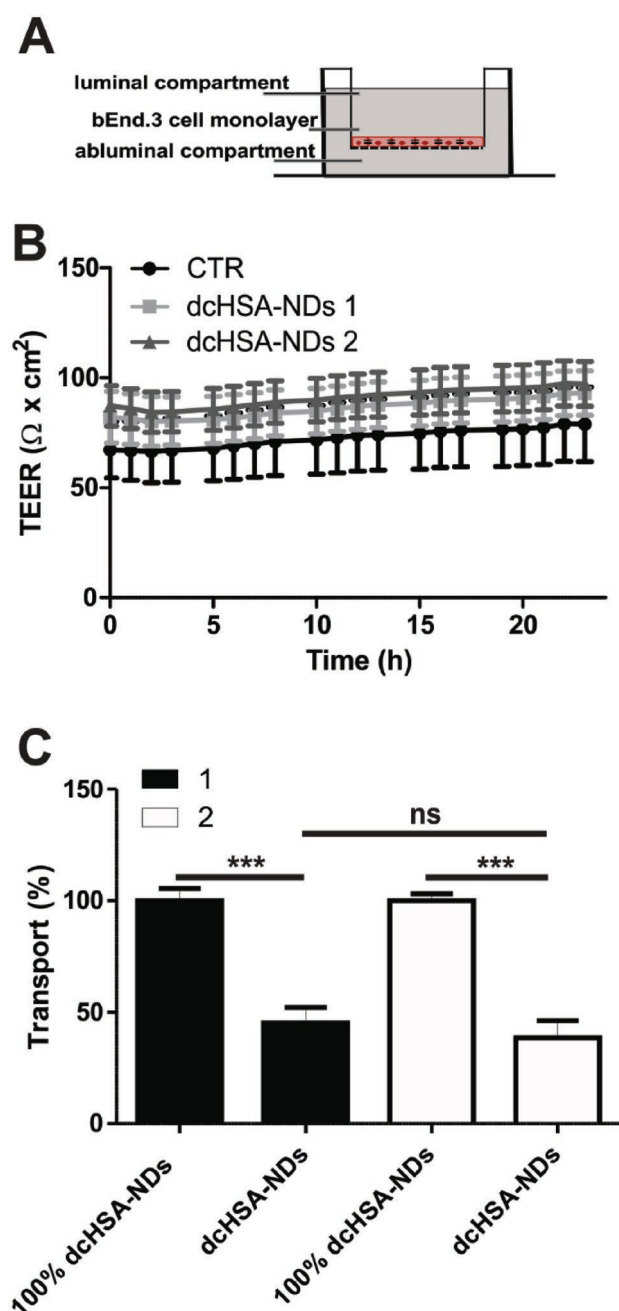
Figure 2. dcHSA-NDs are transported across BBB in vitro. A) Schematic presentation of in vitro model with bEnd.3 cells seeded in monoculture on transwell inserts. B) Absolute TEER values automatically measured during the whole experiment by CellZscope from t_0 of dcHSA-NDs application to t_{24} of transport assay. Data are expressed as $\Omega \times cm^2$. C) Mean transport across bEnd.3 cell monolayer for 1 or 2 dcHSA-NDs. dcHSA-NDs were applied at a concentration of 30 μg mL^{-1} for 24 h. Abluminal fluorescence is expressed as relative values compared to the 100% of dcHSA-NDs transport in inserts without cells (100% dcHSA-NDs); $n \geq 6$ wells from 3 cultures, one-way ANOVA, ***$p < 0.001$, ns = not significant.

seeded on the luminal side of a transwell insert was applied (**Figure 2**A). In this in vitro model, the luminal compartment represents the bloodstream and the abluminal compartment represents the brain. The in vitro BBB model has been

validated after bEnd.3 cell seeding by continuously monitoring the transendothelial electrical resistance (TEER) using the CellZscope system, which indicates whether these cells have formed a tight cell barrier. TEER values higher than 40 $\Omega \times cm^2$ were considered adequate to exclude relevant paracellular transport (Figure 2B).[34] Additionally, the apparent permeability coefficient (P_{app}) as a validation parameter of a hydrophilic tracer, FITC-dextran 4 kDa, was measured to ensure the formation of tight cell junctions restricting paracellular diffusion. The mean P_{app} was $2.98 \pm 1.23 \times 10^{-6}$ cm s^{-1}, which is in the range of optimal P_{app} for BBB model.[35]

The two different sizes of tested nanodiamonds, dcHSA-NDs **1** (40 nm) and dcHSA-NDs **2** (55 nm), were applied with a concentration of 30 μg mL^{-1} in the luminal compartment of the transwell BBB model to assess their ability to traffic from luminal across bEnd.3 cells to abluminal and to assess the impact of NDs size changes on BBB transport. After 24 h treatment, dcHSA-NDs fluorescence was quantified in collected abluminal medium to determine the transport rate. A transport of 100% indicated passive diffusion of dcHSA-NDs in transwell inserts without cells. dcHSA-NDs were capable to efficiently cross the BBB in vitro. Transport of $45.17 \pm 7\%$ (one-way analysis of variance (ANOVA); $p < 0.05$; $n = 6$ wells from 3 cultures) for dcHSA-NDs 1 (40 nm) and $38.6 \pm 7.6\%$ (one-way ANOVA; $p < 0.05$; $n = 6$ wells from 3 cultures) for dcHSA-NDs 2 (55 nm) was measured compared to the 100% control (100% dcHSA-NDs 1: $100 \pm 5.4\%$; 100% dcHSA-NDs 2: $100 \pm 3\%$; $n = 6$ wells from 3 cultures) (Figure 2C). The transport rate did not show a significant size dependent difference (dcHSA-NDs **1** vs dcHSA-NDs **2**: one-way ANOVA, $p > 0.05$).

2.3. dcHSA-NDs Undergo Internalization and Intracellular Trafficking in Brain Endothelial Cells

In order to understand the mechanisms underlying the dcHSA-NDs endothelial transport, their uptake and intracellular localization were studied in more details. Using fluorocytochemistry, dcHSA-NDs-containing vesicles were detected in bEnd.3 cells (**Figure 3**A) indicating that the transport of dcHSA-NDs is an active endocytosis and transcytosis process. Fluorescent NDs were tracked by reflection as well as NV signals and the dcHSA-PEG-shell was detected independently by following the signal of bodipy-488-labelling on dcHSA-PEG to evaluate, whether the NDs coating remains stable in the cellular environment. Colocalization of the signals was observed (Figure S5, Supporting Information) demonstrating that dcHSA-NDs reached intracellular compartments and that the biopolymer shell remained attached to the NDs during uptake and intracellular trafficking. Furthermore, comparing dcHSA-NDs with and without NV-centers, we found no difference in cell uptake, hence dcHSA-NDs with and without NV-centers were used.

Next, we studied some of the mechanisms involved in cellular uptake and intracellular trafficking. bEnd.3 cells were treated with dcHSA-NDs in combination with FITC-labeled transferrin (TF, via clathrin-mediated uptake) or the B subunit of cholera toxin-alexa-488 (CTX, via caveolae-mediated uptake) for 24 h to identify their endocytotic pathway. Cellular couptake was

**ADVANCED
SCIENCE NEWS**

www.advancedsciencenews.com

NANO · MICRO

small

www.small-journal.com

analyzed by quantification of colocalizing vesicles in confocal z-stacks. dcHSA-NDs vesicles colocalized $27.7 \pm 3.07\%$ with TF and $70.55 \pm 3.9\%$ with CTX positive vesicles showing a significantly higher preference of dcHSA-NDs for caveolae-mediated endocytosis (TF vs CTX: $n = 12$ regions of interest from 3 cultures, Mann–Whitney U test, $p < 0.0001$) (Figure 3B,C). Caveolae-mediated uptake has been shown to be fundamental, specifically for cationized-albumin, more than native albumin in brain endothelial cells[36,37] and our data clearly showed that dcHSA-NDs also followed predominantly this pathway.

After cellular uptake via both clathrin-mediated or caveolae-mediated endocytosis, early endosomes (EE) typically mature to late endosomes (LE) and lysosomes.[38] To assess whether dcHSA-NDs localize in EE or LE/lysosomes, costainings were performed with early endosome antigen (EEA) marker or lysosomal-associated membrane protein 1 (LAMP-1) marker, respectively. Confocal microscopy revealed that dcHSA-NDs appear within both EE and LE/lysosomes (Figure 3D). Quantitative analysis showed a minor colocalization of $2.4 \pm 0.5\%$ with EE and about $15.14 \pm 4.15\%$ with LE/lysosomes ($n = 12$ regions of interest from 3 cultures, Mann–Whitney U test, $p < 0.0001$) (Figure 3E). These results can be expected, considering that the retention time in EE usually is only a few minutes.[38] After 24 h most of the dcHSA-NDs-containing-EE already undergo maturation in LE and LE/lysosome fusion, which explains why LE/lysosomes represent the endosomal compartments with most pronounced colocalization. These data correspond to previous data of dcHSA-NDs in LE/lysosomes of cancer cells. Cells treated with doxorubicin-loaded-dcHSA-NDs released the drug doxorubicin into the cytosol by an endosome/lysosome escape mechanisms.[30] The transport data confirm these results, although part of dcHSA-NDs localize in LE/lysosomes, a consistent percentage of dcHSA-NDs is able to follow a transcytotic pathway thus avoiding intracellular entrapment. We further assessed whether dcHSA-NDs induced autophagy and were subsequently internalized in autophagosomes. Costaining with the autophagosome marker microtubule-associated protein 1A/1B-light chain 3 (LC3) was performed to study possible dcHSA-NDs autophagosome incorporation. Representative orthogonal z-stacks showed LC3-positive vesicles in both CTR and dcHSA-NDs treated cultures (Figure S6A, Supporting Information). Only $0.98 \pm 0.52\%$ ($n = 10$ regions of interest from 3 cultures) of dcHSA-NDs colocalized with LC3-positive-vesicles (Figure S6B, Supporting Information), which is a negligible value considering the high rate of basal autophagy in endothelial cells.[39] Thus, no induction of autophagy and no dcHSA-NDs in autophagosomes were observed. Since an increase in autophagy is also a marker for cellular stress, dcHSA-NDs-related cellular stress could be excluded by this test.

2.4. dcHSA-NDs Are Taken up by Neurons and Astrocytes

High intracellular trafficking into endothelial cells underlines the potential of dcHSA-NDs to cross the BBB after transcytosis

Figure 3. dcHSA-NDs are taken up by bEnd.3 cells and localize in endosomal compartments. Representative confocal orthogonal view and 3D reconstruction of dcHSA-NDs (red) uptake A) or colocalization with CTX or TF (green) B); scale bar = 5 µm. C) Percentage of colocalizing dcHSA-NDs-containing-vesicles with CTX or TF containing vesicles; $n = 12$ ROIs from 3 cultures, Mann–Whitney U test, ***$p < 0.001$. D) Representative orthogonal view of dcHSA-NDs with EEA as early endosomes marker or LAMP-1 as late endosomes marker; scale bar = 7 µm. E) Quantification of colocalization for dcHSA-NDs-containing vesicles with EE or LE; $n = 12$ ROIs from 3 cultures, Mann–Whitney U test, ***$p < 0.001$.

ADVANCED
SCIENCE NEWS
www.advancedsciencenews.com

NANO · MICRO
small
www.small-journal.com

to reach the abluminal compartment in vitro. In physiological conditions dcHSA-NDs may also interact with other cell types such as neurons and astrocytes after trafficking from blood to the brain parenchyma. Therefore, we studied whether dcHSA-NDs were also taken up by murine primary neuronal cells. Astrocytes were stained against glial fibrillary acidic protein (GFAP) while neurons were stained against the neuronal nuclear protein NeuN to visualize the cell body or β-III-tubulin for imaging of axons and dendrites. Orthogonal view from z-stacks of dcHSA-NDs-treated astrocytes showed high uptake predominantly in the perinuclear region (**Figure** 4A). However, in neurons, confocal microscopy showed higher localization of dcHSA-NDs in axons and dendrites than in the perinuclear region, which is clearly visible in the β-III-tubulin and in the NeuN staining (Figure 4B). In summary,

our data demonstrate that dcHSA-NDs are able to cross the BBB model system under in vitro conditions and provide high potential for passing the BBB to reach different target cells in the brain, which is an essential feature to track delivery and modulate pathophysiology of neurological disorders at different target sites.

2.5. dcHSA-NDs Tracking Reveals Direct Cell–Cell Transport

Most dcHSA-NDs-containing vesicles were localized in the perinuclear region in bEnd.3 cells and astrocytes. However, dcHSA-NDs-containing vesicles were also detected in distal subcellular areas, and this peripheral localization was mostly in neuronal cells, which prompted us to investigate distal
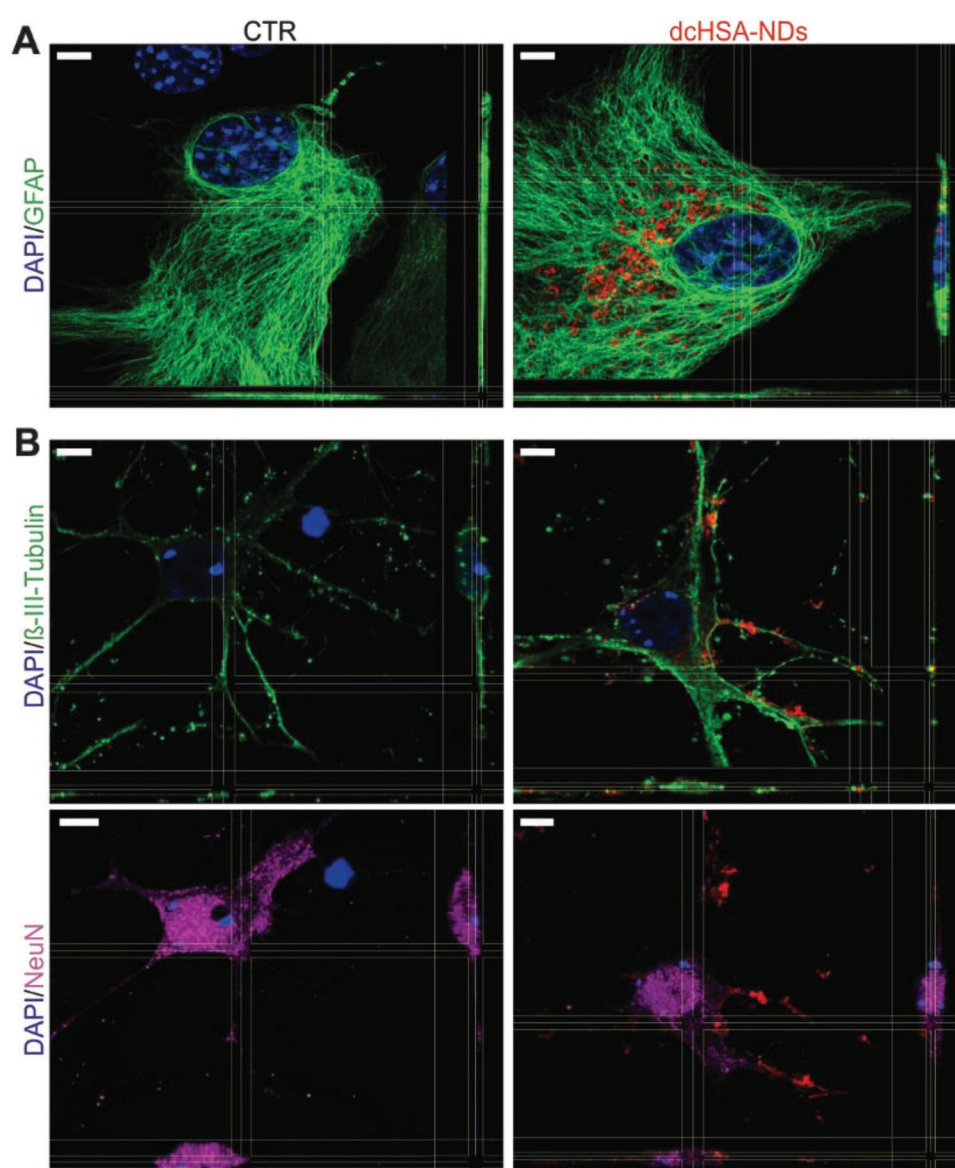
Figure 4. dcHSA-NDs are taken up by neurons and astrocytes in vitro. A) Representative confocal orthogonal views of dcHSA-NDs (red) uptake in astrocytes labeled by GFAP marker (green). B) Neuronal uptake of dcHSA-NDs. Neuronal cell body stained by NeuN (magenta) and dendrites and axons stained by β-III-tubulin (green); scale bar = 5 µm.
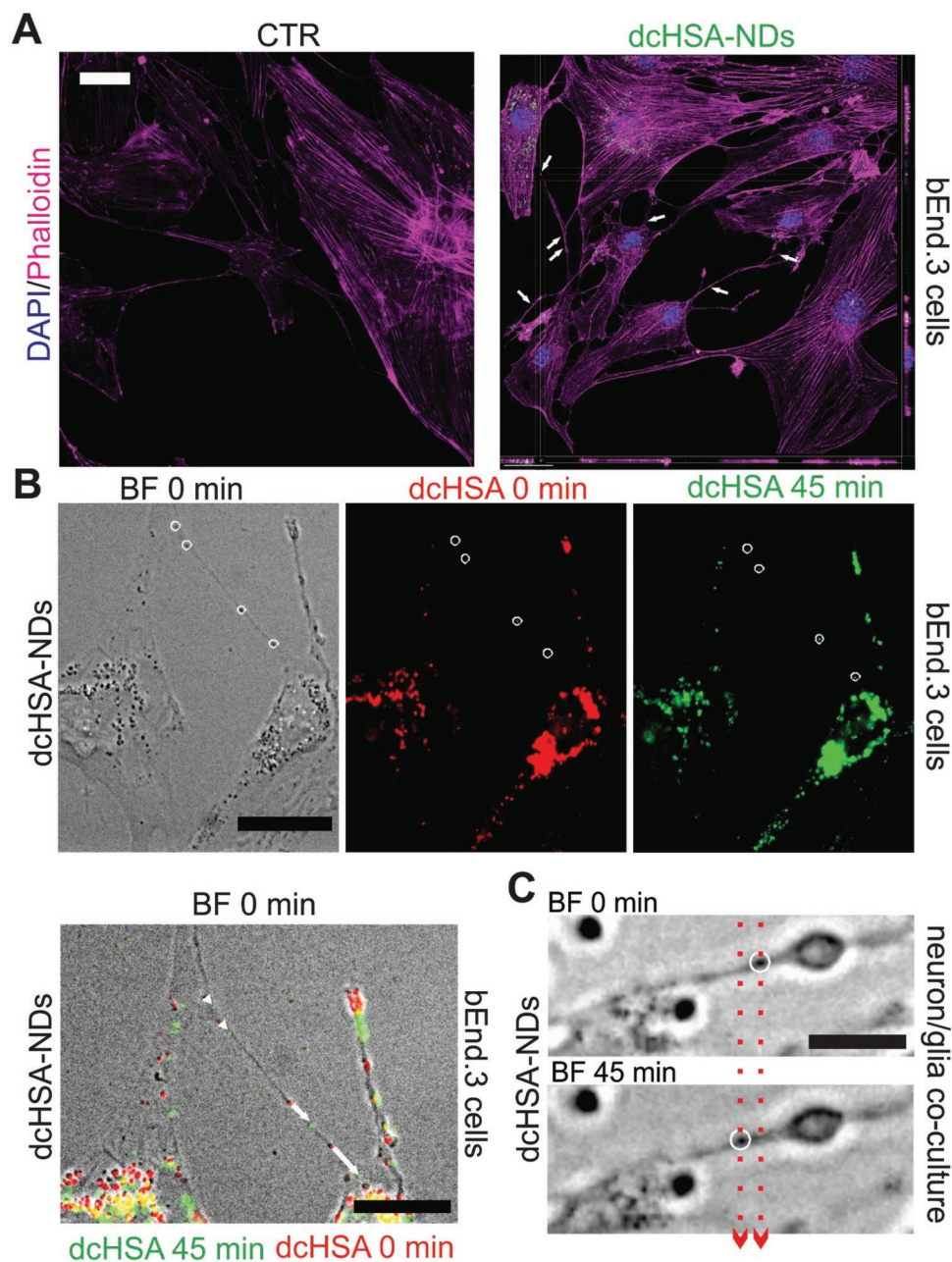
Figure 5. Tracking of fluorescent dcHSA-NDs direct cell–cell migration via TNTs. A) Representative confocal orthogonal view of dcHSA-NDs (green) localization in phalloidin-labeled-actin (magenta) bridges in bEnd.3 cells. White arrows indicate dcHSA-NDs localized in TNTs. B) Time-lapse tracking of dcHSA-NDs movements along TNTs in bEnd.3 cells merging BF picture with those of fluorescence at 0 min (red) and 45 min (green). White circles indicate the tracked dcHSA-NDs; white arrows indicate length and direction of dcHSA-NDs migration. C) Representative time lapse of dcHSA-NDs movement along TNTs in neurons. Dashed lines indicate the edges of dcHSA-NDs-containing vesicle movement. Scale bar = 20 µm.

localization of dcHSA-NDs. Intriguingly, after staining the cellular cytoskeleton with rhodamine–phalloidin, fluorescent dcHSA-NDs vesicles were detected in a cell structure connecting two adjacent cells (**Figure 5**A). Actin bridges have been identified as tunneling nanotubes (TNT) that have been observed in vitro for many cell types as well as in in vivo for developing embryos of different species.[40,41] TNTs are thin membranous bridges connecting cells over long distances and transferring various cellular components from cell to cell.[41]

In order to study cell–cell migration of dcHSA-NDs, live cell imaging was carried out to track dcHSA-NDs-vesicles moving along TNTs (Video S1, Supporting information). Detection of dcHSA-NDs fluorescence at 0 and 45 min merged with brightfield pictures at 0 min allowed visualization of different vesicle movements at varying positions along the same TNT (Figure 5B). Time-lapse tracking clearly showed a unidirectional migration of dcHSA-NDs-vesicles from an initiating cell to a target cell and accelerated movement when
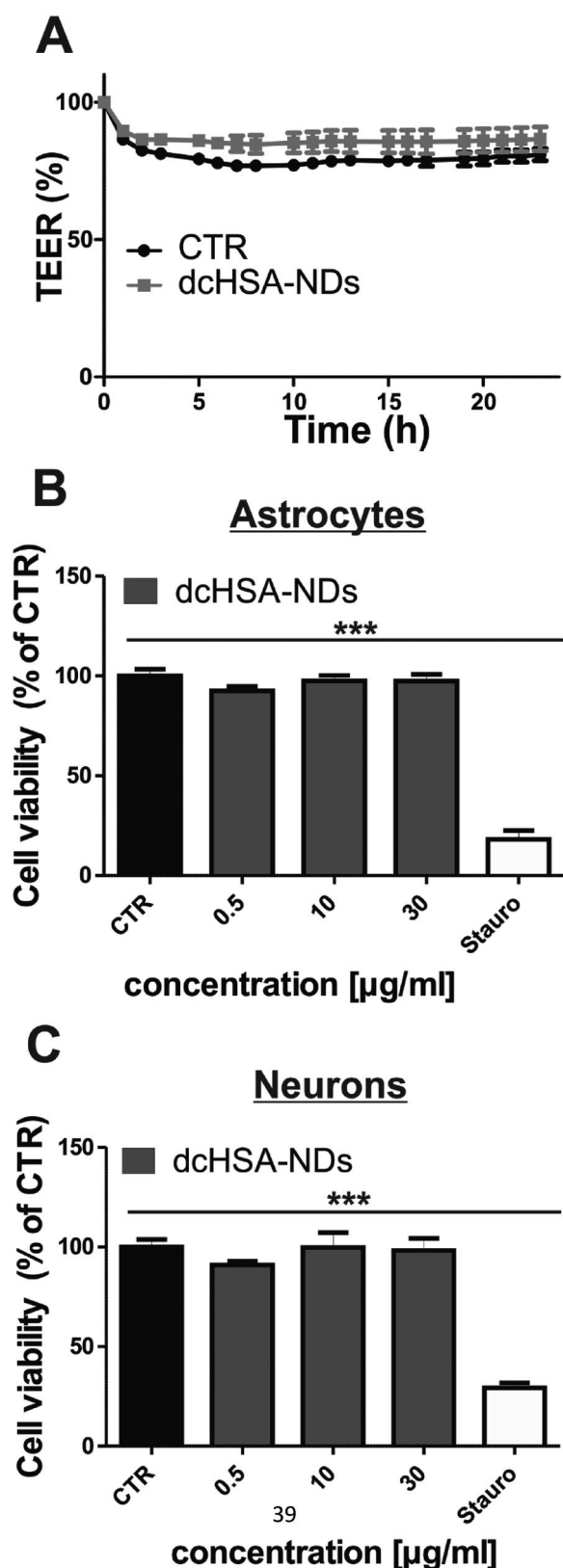
**ADVANCED
SCIENCE NEWS**

www.advancedsciencenews.com

**NANO · MICRO
small**

www.small-journal.com

dcHSA-NDs-vesicles approached the target cell (Figure 5B; white arrows). We speculate that the differences in movement could be due to restricted available space, a "bottle-neck," during the entry phase, in which the vesicle diffuses randomly in the cytosol. This could explain the observed slower migration of dcHSA-NDs vesicles close to the beginning of the TNTs (Figure 5B), which then changes to a directional motion in the TNT, induced by molecular motors in actin- and tubulin-mediated transport. [42]

TNT formation was also demonstrated in neurons and astrocytes.[41,43,44] In an immature neuronal/glial coculture, fluorescent dcHSA-NDs-vesicles could also be tracked by live cell imaging in membrane cell–cell connections as observed for bEnd.3 cells (Figure 5C; Video S2, Supporting Information). Costainings with GFAP, β-III-tubulin, and rhodamine–phalloidin showed TNTs connecting astrocytes and neurons (Figure S7, Supporting Information). Our data complements previous studies on TNT transport of fluorescent NDs in HEK293T and SH-SY5Y neuroblastoma cells in vitro for intercellular cargo delivery.[42] However, we demonstrate for the first time intercellular transport of fluorescent dcHSA-NDs in brain endothelial cell line and primary neuronal/glial cells. Our data show migration of dcHSA-NDs from cell to cell for NVU cells along TNTs without the need of being released to the extracellular environment. Intriguingly, these data strongly suggests direct cell–cell transfer of dcHSA-NDs across a biological barrier for brain delivery. The direct cell–cell migration across the BBB would be of high value due to a possible faster and more specific delivery pathway avoiding extracellular interactions of dcHSA-NDs.

To summarize, these in vitro results suggest intracellular trafficking leading to transcytosis and direct cell–cell transport of dcHSA-NDs from the luminal to abluminal compartment with no involvement and induction of autophagy.

2.6. dcHSA-NDs Have No Impact on BBB Integrity and Cell Viability

The biocompatibility of dcHSA-NDs is crucial for bioapplications. Thus, the impact of dcHSA-NDs on bEnd.3 cell monolayer integrity and astrocyte and neuron viability was investigated. TEER was constantly measured using a CellZscope during the dcHSA-NDs treatment in transwell inserts to monitor bEnd.3 monolayer integrity. Comparing TEER measurement of control (CTR) and dcHSA-NDs-treated inserts, showed a slight tendency of the CTR to decrease compared to dcHSA-NDs samples ($n = 6$ wells from 3 cultures, two-way ANOVA, $p > 0.05$) (**Figure 6**A). These results indicate preservation of BBB integrity after dcHSA-NDs treatment. The general decrease of TEER values at the beginning of the treatment is due to perturbations in the assay related to medium exchange. The treatment at time = 0 produced a fluctuation-dependent instability in the TEER measurement that became stable again within the following hours.

Figure 6. dcHSA-NDs do not affect BBB integrity and cell viability. A) BBB in vitro integrity investigated for 24 h of dcHSA-NDs treatment on bEnd.3 cell monolayer. TEER was measured by CellZscope and the values at $t = 0$ were set to 100% and each following measurement was expressed in relative percentage; $n = 6$ wells from 3 cultures. B,C) Cell viability after dcHSA-NDs treatment in astrocytes B) or in neurons C) for 24 h with concentrations from 0.5–30 μg mL^{-1} quantified by Alamar Blue assay. Dead cell control: cell toxin staurosporine (Stauro). $n > 7$ from 3 cultures; one-way ANOVA; ***$p < 0.001$.

ADVANCED
SCIENCE NEWS
www.advancedsciencenews.com

NANO · MICRO
small
www.small-journal.com

Cell vitality in astrocytes and neurons was assessed in an alamar blue assay applying different concentrations (0.5, 10, or 30 µg mL^{-1}) of dcHSA-NDs. Our results showed no significant change in cell vitality of both astrocytes ($n > 7$ wells from 3 cultures, one-way ANOVA, $p > 0.05$) (Figure 6B) and neurons ($n > 7$ wells from 3 cultures, one-way ANOVA, $p > 0.05$) (Figure 6C) for all investigated concentrations. Staurosporine, a cell toxin serving as control, resulted in a significant decrease in cell viability compared to CTR ($n > 7$ wells from 3 cultures, one-way ANOVA, $p < 0.0001$) (Figure 6B,C). These data indicate that dcHSA-NDs are well tolerated by cells of the NVU in vitro, which is a first indication of high biocompatibility and which is crucial for conducting in vivo experiments.

2.7. Fluorescent dcHSA-NDs Cross the BBB and Can be Tracked at the Single Cell Level in Astrocytes and Neurons In Vivo

To assess the potential of fluorescent dcHSA-NDs for clinical applications, we investigated whether fluorescent dcHSA-NDs injected intravenously in mice were able to reach the brain. 24 h after dcHSA-NDs application (500 µg mL^{-1} of blood), brain and liver were screened for dcHSA-NDs signals. Liver was used as positive control since biodistributional studies have clearly demonstrated that many cationic nanoparticles are highly taken up in the liver.[45] Thus, high uptake in liver slices allowed comparison of dcHSA-NDs signals (reflection, bodipy488-labeled-dcHSA-shell, NV) intensity in tissue (Figure S8, Supporting Information). Colocalization of signals originating from NDs and Bodipy-488 labeling on dcHSA-PEG-shell suggest that at least the dcHSA-NDs, which show colocalization, maintain their integrity in vivo. Detection by reflection represents the most reliable detection system since it images all NDs in the sample, independent of the presence or absence of NV centers (not all NDs have NV centers). Therefore, brain slices were carefully analyzed for dcHSA-NDs reflection signals. The orthogonal view of confocal z-stacks showed dcHSA-NDs in brain slices (**Figure 7**A). In order to identify dcHSA-NDs-positive cells, astrocytes and neuronal cell bodies were stained for GFAP and NeuN, respectively. dcHSA-NDs were clearly detectable at the single cell level close to blood vessels and some NPs-containing vesicles colocalized with GFAP-positive astrocytes surrounding vessels or NeuN-positive neurons as observable from 3D reconstructions (Figure 7B,C). Biodistribution studies were accomplished to identify organs showing dcHSA-NDs uptake. Liver and spleen showed the highest uptake after 24 h (Figure S9, Supporting Information). However, the observed brain uptake indicates an adequate circulation time of dcHSA-NDs in the bloodstream required for transport into the brain. Additionally, the organs with the highest uptake are also the ones involved in the clearance of drugs and exogenous molecules. Observed kidney uptake in particular in an area identified as the glomeruli, the region of ultrafiltration, suggests clearance of the particle (Figure S9, Supporting Information). It is important to underline that after dcHSA-NDs ultrafiltration from blood to primary urine, they might still be reabsorbed to the bloodstream. Comparing the biodistribution of dcHSA-NDs to published data for 50 nm uncoated NDs, both systems were found in liver, spleen,

kidney, and lung, while our dcHSA-NDs clearly revealed uptake in the brain, more uptake in spleen and less in lung. Both particle systems exhibit low uptake rates for the heart.[46] Also, for other brain-targeted particles such as liposomes, bispecific antibodies or gold nanoparticles targeting the transferrin receptor, high uptake in liver, kidney, and spleen was observed, while uptake into the brain of healthy WT mice was in most cases about 20 times less pronounced.[47–49]

Thus, these data clearly confirm the ability of dcHSA-NDs to cross the BBB and reach the brain parenchyma in vivo. Combined with the in vitro data, we assume a transcytotic process involving also direct cell–cell migration from brain endothelial cells to neurons via astrocytes incorporation occurring in vivo as also observed in vitro.

3. Conclusions

Previous studies on NDs were exclusively based on invasive in situ brain delivery approaches that were not able to solve the challenge of systemic NDs delivery into the brain after intravenous injection.[20,27] Herein, for the first time, we evaluated fluorescent NDs with a dcHSA-PEG protein coating in mice after systemic application and revealed efficient transport across an intact BBB in vivo. The NDs reached the abluminal side via intracellular trafficking and were taken up by astrocytes and neurons. We also provided new insights in dcHSA-NDs trafficking via direct cell–cell interactions mediated by TNTs. We demonstrate successful BBB crossing and tracking of fluorescent dcHSA-NDs at the single cell level within a complex neuronal system, thus achieving for the first time systemic delivery of fluorescent dcHSA-NDs into the brain.

Fluorescent NDs offer great potential as nanotheranostics due to their optical properties such as stable fluorescence, the option for nuclear spin polarization allowing hyperpolarization and MRI detection[50,51] and biocompatibility.[24] Therefore, we propose dcHSA-NDs as nanotheranostic for neurological diseases such as glioma, as they combine within one platform 1) the fluorescent properties of fluorescent NDs and detection by refraction due to the diamond lattice, 2) the natural albumin-mediated "recruitment" at the tumor site as well as 3) multiple available groups to attach anticancer drugs. It is conceivable that HSA conjugates enrich at tumor sites in vivo. Matsumura and Maeda have shown that the accumulation of intravenously injected Evans blue-albumin complex accumulates in tumor tissue.[52] Since then others have demonstrated accumulation of albumin in many other carcinomas as well[53] and these attractive features were also reported for cationized albumin.[54,55] dcHSA-NDs conjugated with multiple copies of the antitumor drug doxorubicin were applied previously to target cancer cells in a human breast cancer xenograft model and pronounced antitumor efficacy was demonstrated, as well as high particle stability, which is a critical concern for further clinical application.[30]

In summary, we show for the first time successful brain delivery and tracking of fluorescent dcHSA-NDs at the single cell level in vivo. Our data in combination with the observed antitumor efficiency of doxorubicin-coated dcHSA-NDs in the peripheral breast cancer model suggest that dcHSA-NDs could
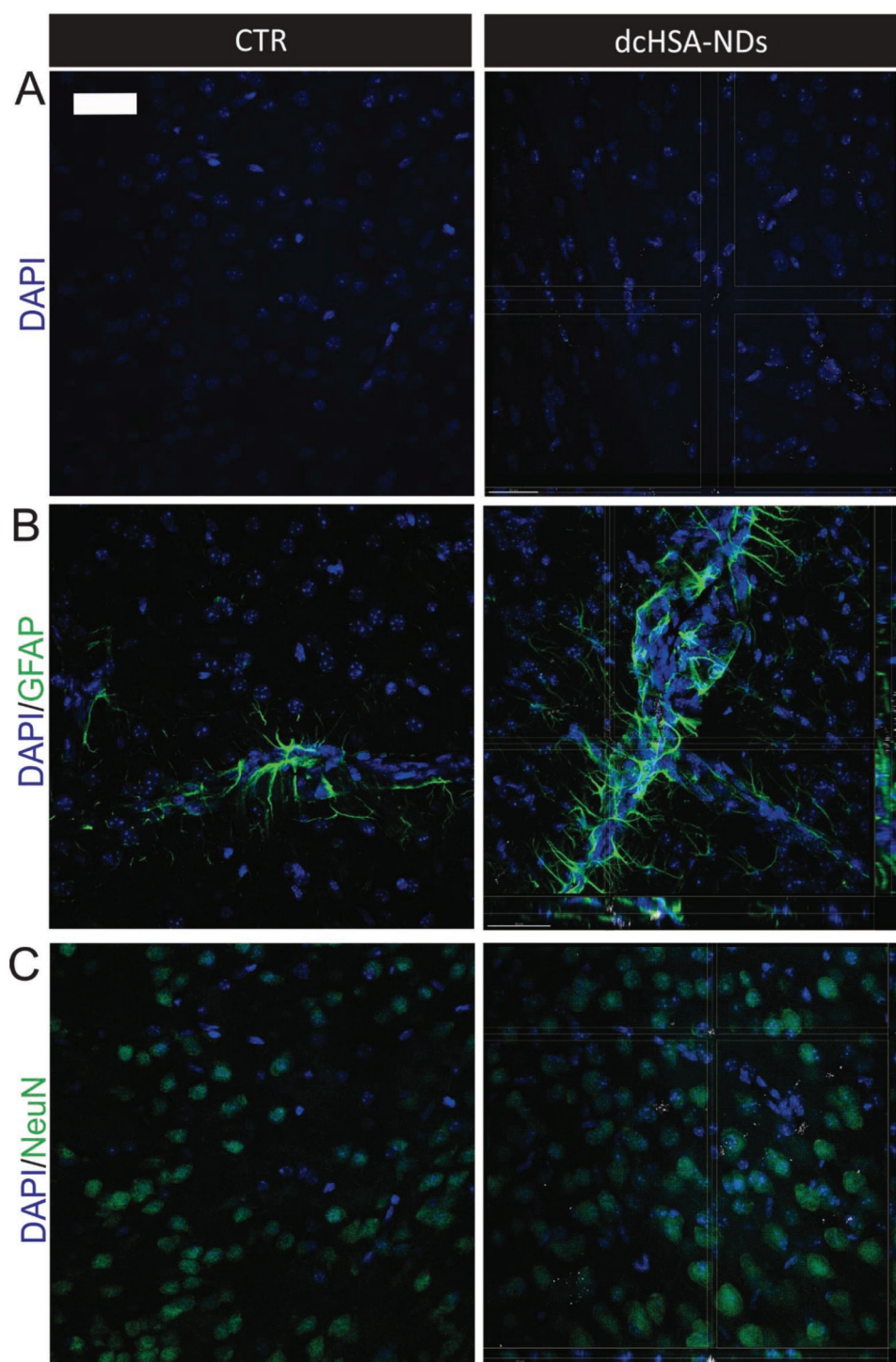
ADVANCED
SCIENCE NEWS
www.advancedsciencenews.com

NANO · MICRO
small
www.small-journal.com

Figure 7. In vivo fluorescent dcHSA-NDs cross the BBB and are tracked on single cell level in neurons and astrocytes. A) Representative confocal orthogonal views of dcHSA-NDs (white) signals in brain slices. B,C) Representative confocal orthogonal view of dcHSA-NDs (white) localization in GFAP-positive astrocytes (green) B) and NeuN-positive neurons (green) C); scale bar = 40 µm.

emerge as nanotheranostics for systemic applications in personalized treatment of neurological diseases such as glioma.

4. Experimental Section

Ethical Approval: All experimental procedures were approved by the ethical committee of the "Landesuntersuchungsamt Rheinland-Pfalz" and the authority "Landesuntersuchungsamt Rheinland-Pfalz" protocol number: "Aktenzeichen: 23 177-07/G 16-1-024." Principles of laboratory animal care (European, national and international laws) were followed.

Materials: If not stated otherwise, chemicals were obtained from Sigma-Aldrich, Seelze or Hamburg, Germany.

In Vitro Transport Assay: With mean TEER values of at least $40 \ \Omega \times cm^2$, dcHSA-NDs **1** (40 nm) and **2** (55 nm) were applied in the luminal compartment of the in vitro BBB model with a concentration

of 30 µg mL^{-1}. Crossing rate was quantified by rhodamine labeling of dcHSA-NDs. Fluorescence was measured with Infinite F1000 TECAN plate reader. Fluorescence intensity in abluminal compartment of transwell inserts without cells was set to 100% and the percentage of crossing was calculated as relative values.

Uptake and Couptake of dcHSA-NDs in bEnd.3 Cells: dcHSA-NDs or fluorescent dcHSA-NDS were applied in a final concentration of 30 µg mL^{-1} to bEnd.3 cells, primary murine astrocytes or neurons seeded on coverslips for 24 h. For couptake studies, dcHSA-NDs were applied in combination with 120 µg mL^{-1} transferrin-Alexa Fluor 488 (T13342, Invitrogen) or 15 µg mL^{-1} cholera toxin B subunit-FITC (C1655). Cells were finally fixed with paraformaldehyde (PFA) 4%.

Live Cell Imaging: bEnd.3 cells or neurons/glia cocultures (DIV 2) were treated with fluorescent dcHSA-NDs (30 µg mL^{-1}) for 24 h. Cells were washed with PBS and fresh medium was added to start live cell imaging. 45-minutes live cell imaging was carried out with IX81 microscope and a monochrome fluorescence CCD camera XM10 using the cell^F Software (Olympus). Movies were edited with Windows Live Movie Maker. 45 min recording time are presented in 2 s videos for bEnd.3 or 6 s videos for neurons.

Quantification of Colocalization: Images were taken by TCS SP5 confocal (Leica). For quantification of intracellular colocalization, z-stacks were deconvolved by Huygens Essential software. Using Image J software, the percentage of vesicles containing dcHSA-NDs colocalizing with a certain intracellular compartment was analyzed setting arbitrary a threshold of 40% of colocalization for each vesicle to avoid false positive values. In addition, deconvolved z-stacks were analyzed by JacoP plugin in ImageJ to calculate Van Steensel's cross-correlation functions (CCFs) as proof of colocalization data.[56]

Cell Viability Assay: Cytotoxity on astrocytes and neurons was investigated using the cell viability Alamar Blue assay. Cells were treated with dcHSA-NDs for 24 h after reaching confluence for astrocytes and at a cell density of 200 000 cells/well for neurons. Cells were washed with HBSS-/-, and resazurin (R7017) was applied in each well with a final concentration of 16.66 µg mL^{-1} in HBSS+++ (100 µL). After 1 h incubation, fluorescence was measured spectrophotometrically using Tecan Infinite F1000 plate reader (Tecan, Salzburg, Austria). Fluorescence values were corrected to fluorescence of media without cells (blank). Cell viability (%) was related to untreated control cells (100%).

In Vivo Fluorescent dcHSA-NDs Uptake: Fluorescent dcHSA-NDs with bodipy488-labeled-dcHSA-PEG in PBS were intravenously injected (500 µg mL^{-1}) in C57BL/6 P21-29 mice for 24 h. After treatment mice were perfused with PBS/heparin-natrium (Ratiopharm, 5000 E.I.) and subsequently with PFA 4%. Liver and brain were collected and incubated overnight in PFA 4%. The day after, organs were washed with PBS followed by equilibration in 30% of sucrose. 30 µm slices were obtained using a freezing microtome (Leica CM 1325).

Data Analysis: Data were analyzed with GraphPad Prism 5 software (Graph Pad, La Jolla, CA, USA) and presented as mean ± SEM. Statistical analyses were performed with Mann–Whitney U test, ANOVA one way. $p < 0.05$ was considered as statistically significant*, $p < 0.01$**, $p < 0.001$***.

Supporting Information

Supporting Information is available from the Wiley Online Library or from the author.

Conflict of Interest

The authors declare no conflict of interest.

Keywords

[1] World Health Organization, *Neurological Disorders: Public Health Challenges*, World Health Organization, Geneva **2006**.

[2] B. T. Hawkins, T. P. Davis, *Pharmacol. Rev.* **2005**, *57*, 173.

[3] W. M. Pardridge, *NeuroRx* **2005**, *2*, 3.

[4] N. J. Abbott, A. Friedman, *Epilepsia* **2012**, *53*, 1.

[5] S. Jeelani, R. C. Reddy, T. Maheswaran, G. S. Asokan, A. Dany, B. Anand, *J. Pharm. BioAllied Sci.* **2014**, *6*, S6.

[6] T. H. Kim, S. Lee, X. Chen, *Expert Rev. Mol. Diagn.* **2013**, *13*, 257.

[7] F. M. Kievit, M. Zhang, *Adv. Mater.* **2011**, *23*, H217.

[8] C. Weir, M. C. Morel-Kopp, A. Gill, K. Tinworth, L. Ladd, S. N. Hunyor, C. Ward, *Heart, Lung Circ.* **2008**, *17*, 395.

[9] M. Chalfie, Y. Tu, G. Euskirchen, W. W. Ward, D. C. Prasher, *Science* **1994**, *263*, 802.

[10] J. Kajstura, M. Rota, S. R. Hall, T. Hosoda, D. D'Amario, F. Sanada, H. Zheng, B. Ogorek, C. Rondon-Clavo, J. Ferreira-Martins, A. Matsuda, C. Arranto, P. Goichberg, G. Giordano, K. J. Haley, S. Bardelli, H. Rayatzadeh, X. Liu, F. Quaini, R. Liao, A. Leri, M. A. Perrella, J. Loscalzo, P. Anversa, *N. Engl. J. Med.* **2011**, *364*, 1795.

[11] H. Wang, F. Cao, A. De, Y. Cao, C. Contag, S. S. Gambhir, J. C. Wu, X. Chen, *Stem Cells* **2009**, *27*, 1548.

[12] Y. Zhou, Z. Peng, E. S. Seven, R. M. Leblanc, *J. Controlled Release* **2018**, *270*, 290.

[13] D. X. Medina, K. T. Householder, R. Ceton, T. Kovalik, J. M. Heffernan, R. V. Shankar, R. P. Bowser, R. J. Wechsler-Reya, R. W. Sirianni, *J. Controlled Release* **2017**, *253*, 172.

[14] X. Dong, *Theranostics* **2018**, *8*, 1481.

[15] L. Ferreira, J. M. Karp, L. Nobre, R. Langer, *Cell Stem Cell* **2008**, *3*, 136.

[16] A. Solanki, J. D. Kim, K. B. Lee, *Nanomedicine* **2008**, *3*, 567.

[17] A. B. Rosen, D. J. Kelly, A. J. Schuldt, J. Lu, I. A. Potapova, S. V. Doronin, K. J. Robichaud, R. B. Robinson, M. R. Rosen, P. R. Brink, G. R. Gaudette, I. S. Cohen, *Stem Cells* **2007**, *25*, 2128.

[18] J. Qian, S. Ruan, X. Cao, X. Cun, J. Chen, S. Shen, X. Jiang, Q. He, J. Zhu, H. Gao, *J. Colloid Interface Sci.* **2014**, *436*, 227.

[19] S. Ruan, J. Qian, S. Shen, J. Zhu, X. Jiang, Q. He, H. Gao, *Nanoscale* **2014**, *6*, 10040.

[20] M. Baldrighi, M. Trusel, R. Tonini, S. Giordani, *Front. Neurosci.* **2016**, *10*, 250.

**ADVANCED
SCIENCE NEWS**

www.advancedsciencenews.com

**NANO · MICRO
small**

www.small-journal.com

[21] Y. Zhu, J. Li, W. Li, Y. Zhang, X. Yang, N. Chen, Y. Sun, Y. Zhao, C. Fan, Q. Huang, *Theranostics* **2012**, *2*, 302.

[22] V. N. Mochalin, O. Shenderova, D. Ho, Y. Gogotsi, *Nat. Nanotechnol.* **2011**, *7*, 11.

[23] G. Balasubramanian, I. Y. Chan, R. Kolesov, M. Al-Hmoud, J. Tisler, C. Shin, C. Kim, A. Wojcik, P. R. Hemmer, A. Krueger, T. Hanke, A. Leitenstorfer, R. Bratschitsch, F. Jelezko, J. Wrachtrup, *Nature* **2008**, *455*, 648.

[24] Y. Wu, F. Jelezko, M. B. Plenio, T. Weil, *Angew. Chem., Int. Ed. Engl.* **2016**, *55*, 6586.

[25] S. Haziza, N. Mohan, Y. Loe-Mie, A. M. Lepagnol-Bestel, S. Massou, M. P. Adam, X. L. Le, J. Viard, C. Plancon, R. Daudin, P. Koebel, E. Dorard, C. Rose, F. J. Hsieh, C. C. Wu, B. Potier, Y. Herault, C. Sala, A. Corvin, B. Allinquant, H. C. Chang, F. Treussart, M. Simonneau, *Nat. Nanotechnol.* **2017**, *12*, 322.

[26] J. F. Barry, M. J. Turner, J. M. Schloss, D. R. Glenn, Y. Song, M. D. Lukin, H. Park, R. L. Walsworth, *Proc. Natl. Acad. Sci. USA* **2016**, *113*, 14133.

[27] J. Saraf, K. Kalia, P. Bhattacharya, R. K. Tekade, *Drug Discovery Today* **2018**, *24*, 584.

[28] O. Shimoni, B. Shi, P. A. Adlard, A. I. Bush, *J. Mol. Neurosci.* **2016**, *60*, 405.

[29] G. Xi, E. Robinson, B. Mania-Farnell, E. F. Vanin, K. W. Shim, T. Takao, E. V. Allender, C. S. Mayanil, M. B. Soares, D. Ho, T. Tomita, *Nanomedicine* **2014**, *10*, 381.

[30] Y. Wu, A. Ermakova, W. Liu, G. Pramanik, T. M. Vu, A. Kurz, L. McGuinness, B. Naydenov, S. Hafner, R. Reuter, J. Wrachtrup, J. Isoya, C. Förtsch, H. Barth, T. Simmet, F. Jelezko, T. Weil, *Adv. Funct. Mater.* **2015**, *25*, 6576.

[31] F. Helm, G. Fricker, *Pharmaceutics* **2015**, *7*, 27.

[32] Y. Z. Wu, S. Ihme, M. Feuring-Buske, S. L. Kuan, K. Eisele, M. Lamla, Y. R. Wang, C. Buske, T. Weil, *Adv. Healthcare Mater.* **2013**, *2*, 884.

[33] Y. Z. Wu, K. Eisele, M. Doroshenko, G. Algara-Siller, U. Kaiser, K. Koynov, T. Weil, *Small* **2012**, *8*, 3465.

[34] P. Moscariello, D. Y. W. Ng, M. Jansen, T. Weil, H. J. Luhmann, J. Hedrich, *Adv. Sci.* **2018**, *5*, 1700897.

[35] P. J. Gaillard, A. G. de Boer, *Eur. J. Pharm. Sci.* **2000**, *12*, 95.

[36] M. Thöle, S. Nobmann, J. Huwyler, A. Bartmann, G. Fricker, *J. Drug Targeting* **2002**, *10*, 337.

[37] W. Lu, Q. Sun, J. Wan, Z. She, X. G. Jiang, *Cancer Res.* **2006**, *66*, 11878.

[38] J. Huotari, A. Helenius, *EMBO J.* **2011**, *30*, 3481.

[39] T. Urbanek, W. Kuczmik, A. Basta-Kaim, B. Gabryel, *Brain Res.* **2014**, *1553*, 1.

[40] R. Mittal, E. Karhu, J. S. Wang, S. Delgado, R. Zukerman, J. Mittal, V. M. Jhaveri, *J. Cell. Physiol.* **2019**, *234*, 1130.

[41] H. H. Gerdes, A. Rustom, X. Wang, *Mech. Dev.* **2013**, *130*, 381.

[42] C. P. Epperla, N. Mohan, C. W. Chang, C. C. Chen, H. C. Chang, *Small* **2015**, *11*, 6097.

[43] X. Sun, Y. Wang, J. Zhang, J. Tu, X. J. Wang, X. D. Su, L. Wang, Y. Zhang, *Cell Death Dis.* **2012**, *3*, e438.

[44] M. Tardivel, S. Bégard, L. Bousset, S. Dujardin, A. Coens, R. Melki, L. Buée, M. Colin, *Acta Neuropathol. Commun.* **2016**, *4*, 117.

[45] E. Blanco, H. Shen, M. Ferrari, *Nat. Biotechnol.* **2015**, *33*, 941.

[46] Y. Yuan, Y. Chen, J.-H. Liu, H. Wang, Y. Liu, *Diamond Relat. Mater.* **2009**, *18*, 95.

[47] K. B. Johnsen, M. Bak, P. J. Kempen, F. Melander, A. Burkhart, M. S. Thomsen, M. S. Nielsen, T. Moos, T. L. Andresen, *Theranostics* **2018**, *8*, 3416.

[48] K. B. Johnsen, A. Burkhart, F. Melander, P. J. Kempen, J. B. Vejlebo, P. Siupka, M. S. Nielsen, T. L. Andresen, T. Moos, *Sci. Rep.* **2017**, *7*, 10396.

[49] D. Sehlin, X. T. Fang, S. R. Meier, M. Jansson, S. Syvanen, *Sci. Rep.* **2017**, *7*, 17254.

[50] E. Rej, T. Gaebel, T. Boele, D. E. Waddington, D. J. Reilly, *Nat. Commun.* **2015**, *6*, 8459.

[51] D. E. J. Waddington, M. Sarracanie, H. Zhang, N. Salameh, D. R. Glenn, E. Rej, T. Gaebel, T. Boele, R. L. Walsworth, D. J. Reilly, M. S. Rosen, *Nat. Commun.* **2017**, *8*, 15118.

[52] Y. Matsumura, H. Maeda, *Cancer Res.* **1986**, *46*, 6387.

[53] H. Sinn, H. H. Schrenk, E. A. Friedrich, U. Schilling, W. Maier-Borst, *Int. J. Radiat. Appl. Instrum., Part B* **1990**, *17*, 819.

[54] S. Abbasi, A. Paul, W. Shao, S. Prakash, *J. Drug Delivery* **2012**, *2012*, 8.

[55] H. J. Byeon, l. Q. Thao, S. Lee, S. Y. Min, E. S. Lee, B. S. Shin, H. G. Choi, Y. S. Youn, *J. Controlled Release* **2016**, *225*, 301.

[56] S. Bolte, F. P. Cordelières, *J. Microsc.* **2006**, *224*, 213.

NANO ■■ MICRO

small

Supporting Information

Unraveling In Vivo Brain Transport of Protein-Coated Fluorescent Nanodiamonds

Pierpaolo Moscariello, Marco Raabe, Weina Liu, Sandra Bernhardt, Haoyuan Qi, Ute Kaiser, Yuzhou Wu, Tanja Weil,* Heiko J. Luhmann,* and Jana Hedrich*

Supporting Information

Unraveling in Vivo Brain Transport of Protein-Coated Fluorescent Nanodiamonds

Pierpaolo Moscariello[1,2], Marco Raabe[2,3], Weina Liu[2,3], Sandra Bernhardt[1], Haoyuan Qi[4], Ute Kaiser[4], Yuzhou Wu[2], Tanja Weil[2,3]*, Heiko J. Luhmann[1]*, Jana Hedrich[1,2]*

Supporting Experimental Section

Alpha-methoxy-omega-carboxylic acid succinimidyl ester poly(ethylene glycol) was purchased from Rapp Polymer. BODIPY® FL NHS was purchased from Lumiprobe. Fluorescent nanodiamonds were ordered from FND Biotech (Taiwan) and non-fluorescent nanodiamonds were ordered from Microdiamond. All other chemicals were purchased from Sigma Aldrich.

Preparation of cHSA[1]

Human serum albumin (HSA) was converted to cationized HSA (cHSA) by adding an ethylenediamine hydrochloride solution (EDC, 2.5 M, pH 4.75) with 2000 equivalents of EDC for 75 min. The product was purified by Vivaspin 20 (30 kDa molecular weight cut-off filter) centrifugal concentrator. Native HSA possesses (UniProt P02768) 99 –COOH groups (Asp + Glu + C-terminus) as well as 60 –NH$_2$ groups (Lys + N-terminus). Assuming all – COOH groups are reacting with ethylenediamine the theoretical molecular weight of cHSA is 70.9 kDa which fits to our result in Figure S1. See further discussion in our previous publications.[1, 2]

Preparation of dcHSA-PEG[1]

dcHSA-PEG was synthesized as reported before.[1] cHSA was subsequently reacted with alpha-methoxy-omega-carboxylic acid succinimidyl ester poly(ethylene glycol) (MeO-PEG2000-NHS, 30 equivalents) in sodium phosphate buffer (50 mM, pH 8.0) to obtain cHSA-PEG. Finally, cHSA-PEG was denatured in urea-phosphate buffer (50 mM phosphate buffer, pH 7.4, 5 M urea and 2 mM ethylenediaminetetraacetic acid (EDTA)) and reacted with 20 equivalents tris(2-carboxyethyl)phosphine hydrochloride (TCEP) and 200 equivalents N-(2-aminoethyl)maleimide trifluoroacetate to reduce disulfide bonds and cap the thiol groups. dcHSA-PEG was isolated and Maldi- TOF analysis gave an average increase in the molecular weight of about 40 KDa indicating the attachment of about 20 PEG(2000) chains to the cHSA backbone (Figure S1).

Maldi-TOF was performed on a Bruker Daltonics Reflex III spectrometer. Saturated solution of sinapinic acid dissolved in a 1:1 water:acetonitrile with 0.1% trifluoroacetic acid was used as matrix solution.

Preparation of dcHSA-PEG-BDP and dcHSA-PEG-Rho

Afterwards, dcHSA-PEG was labelled by adding BODIPY® FL NHS-ester (BDP NHS-ester, Lumiprobe). In detail, dcHSA-PEG (35 mg, 0.34 µmol, 1 equivalent) was dissolved in 17 ml of phosphate buffer (50 mM, pH 8.0). After a few minutes, the BDP FL NHS-ester (1 mg, 2.7 µmol, 8 equivalents) dissolved in 1.5 ml dimethyl sulfoxide was added and the reaction mixture was stirred at room temperature for 2 h. The free dye was removed by ultrafiltration using Vivaspin 20 (30 kDa molecular weight cut-off filter) and washed 3× with MilliQ water. The product was freeze dried to obtain dcHSA-PEG-BDP. Rhodamine labelled dcHSA-PEG-Rho was prepared and purified with the same protocol by adding 5(6)-carboxy-X-rhodamine N-succinimidyl ester (Sigma-Aldrich, Germany).

Preparation of coated NDs

2

Fluorescent NDs (35 nm, 3 mg, FND Biotech, Taiwan), or NDs (25 nm, 3 mg, Microdiamant GmbH, Germany) were dispersed in 30 ml MilliQ water or boric acid buffer (20 mM, pH 8.4), respectively, by sonication. Afterwards, the fluorescent NDs or NDs mixture was added to dcHSA-PEG-BDP or dcHSA-PEG-Rho (12 mg) and dissolved in 120 ml of MilliQ water or boric acid buffer, 20 mM, pH 8.4) by dropping funnel. The mixture was stirred at room temperature overnight. The coated fluorescent NDs were concentrated using Vivaspin 20 (30 kDa molecular weight cut-off filter) and afterwards free protein was removed by centrifugation (2× MilliQ water, 1× Dulbecco's phosphate-buffered saline, DPBS, 18000 g). Finally, a 4 mg ml^{-1} solution of coated fluorescent NDs in DPBS was prepared for further in vivo studies. In the case of size different batches for initial in vitro transport, different sized NDs were obtained by ultracentrifugation, and were coated by dcHSA-PEG-Rho with the above described coating protocol.

Calculation of the amount of dcHSA-PEG attached to nanodiamonds

The fluorescence intensity of BODIPY attached to dcHSA-PEG was used to calculate the amount of dcHSA-PEG which is present on the nanodiamond. As described above, the NDs were coated with dcHSA-PEG. Afterwards, the free protein was removed by centrifugation and collected. The concentration of free protein was calculated by fluorescence intensity of the BODIPY. The fluorescence intensity of the free dcHSA-PEG as well as of four known dcHSA-PEG concentrations (62.5 µg/ml, 125.0 µg/ml, 250 µg/ml and 500 µg/ml) for further calibration was measured using Tecan reader (Spark20M, excitation: 480 nm, emission: 520 nm, gain: 82.). After linear fitting (Pearson R=0.99734, y=87394.46x+699.04) using OriginPro, the fluorescence intensity of the free protein was determined. The amount of free protein enabled to calculate the amount of protein, which was attached to the nanodiamond. In a sample with 200 µg of NDs, 123 µg of protein was determined. Therefore, a mass to mass ratio of protein to nanodiamond of 1:1.6 was found.

Measurement of zeta-potential

The zeta-potential was measured using a Zetasizer (Nano series) from Malvern. Uncoated NDs, dcHSA-NDs and dcHSA-PEG were all prepared as a 0.5 mg/ml solution in MilliQ water or DPBS buffer. Zeta-potentials are shown in Figure S3.

Transmission electron microscopy characterization

5 μl of NDs **1** (40 nm) or NDs **2** (55 nm) water suspension (0.01 mg ml^{-1}) was dropped on a 300 mesh size copper grid covered with a continuous carbon film and freshly glowed, discharged hydrophilic surface. The dcHSA-NDs **1** and dcHSA-NDs **2** TEM samples were prepared by the same method. TEM samples were dried overnight at room temperature. TEM images were obtained by A Jeol 1400 Transmissions electron microscope. Histogram was created by measuring the diameter of ND using ImageJ.

Dynamic light scattering size measurement

The DLS sizes of NDs **1** and NDs **2**, dcHSA-NDs **1** and dcHSA-NDs **2** (0.5 mg ml^{-1} in MilliQ water, 600 μl) were measured by a Malvern Zeta sizer ZEN3600 (Malvern Ltd, Malvern, UK) at 25°C with 173° angle.

High-resolution transmission electron microscopy

High-resolution transmission electron microscopy (HRTEM) imaging was conducted by using an aberration-corrected FEI Titan 80-300 TEM operated at an acceleration voltage of 80 kV. Negative Cs imaging technique was applied to increase the contrast of the nanodiamond (Cs ≈ - 20 μm, over focus). To minimize the contrast from the supporting film, nanodiamond

were supported by a graphene film. Firstly, chemical vapor deposited (CVD) graphene was transferred to a Quantifoil® grid. Then, 2 μL of dcHSA-ND solution (1μg/mL) was drop casted onto the graphene grid. The solution was subsequently dried in ambience for approximately 30 min.

Culturing bEnd.3 cells

The murine line, bEnd.3, from brain endothelioma (ATCC® CRL-2299™, American Type Culture Collection, Manassas, VA, USA) was cultured as recommended by the manufacturer.[3] Cells were cultivated at a humidified atmosphere with 37°C and 5% CO_2 in DMEM (Glutamax, gibco by life technology, Darmstadt, Germany) supplemented with 10% fetal calf serum (Biochrom, S0115) and 2% penicillin/streptomycin (Invitrogen GmbH, Karlsruhe, Germany). Cells were seeded with 80000 cells per insert (0.3 cm^2) or 100000 cells per coverslip.

Primary murine astrocytes

Primary astrocyte cultures were prepared from six newborn mice (postnatal day P 3). Forebrains were isolated and after meninges depletion the tissue was minced and incubated with 0.05% trypsin/EDTA for 20 min. Horse serum 10% (HS; S9135, Biochrom) diluted in HBSS -/- (gibco by life technology, Darmstadt, Germany) was used in order to stop the digestion process. Cells were dispersed using Pasteur pipettes and filtered by a 40 μm cell strainer. Isolated astrocytes were seeded on poly-ornithine (P4538) coated T75-flasks in MEM supplemented with 10% horse serum and 5 μg ml^{-1} gentamycin. Cells were splitted 1:3 after getting to confluence. Astrocytes were seeded with 100000 cells per coverslip or per well of a 24-well plate as requested from experimental design.

Primary murine neurons

Primary neuronal dissociated cell culture from mice were performed as introduced by Kaech and Banker[4] and optimized by the protocol of Beaudoin and colleagues[5]. Forebrains were isolated from newborn mice (P0-1). After meninges depletion tissue was washed three times with ice cold HBSS -/- and incubated for 20 min in 0.05% trypsin/EDTA (gibco by life technology, Darmstadt, Germany). DNase I (Roche, 11284932001) (2000U in 5 ml) was added for 5 min. Tissue was homogenized in Neuronal Plating Medium (MEM, 10% horse serum, 0.6% glucose) and trypan blue (T8154) was used for cell counting of viable cells. Primary neurons were seeded in plating medium with cell numbers of 200000 cells per coverslip (SDS treated and poly-ornithine coated) or well of 24-well plate. After 30 min medium was replaced with Neuronal Maintenance Medium [Neurobasal Medium (gibco by life technology, Darmstadt, Germany) with 2 mM glutamine (gibco by life technology, 25030024) and supplemented with B27 Supplement (gibco, 17504044)]. Every 7 days one-third of the medium was replaced with fresh Neuronal Maintenance Medium.

In vitro BBB model and validation by TEER and Papp measurements:

bEnd.3 cells (passage 10–30) were seeded with 80.000 cells per insert (0.3 cm^2) on the luminal side of BD Fluoroblok TM Inserts (pore size 3 µm, Corning Incorporated, Corning, USA). Cells were grown in DMEM (Glutamax, gibco by life technology, Darmstadt, Germany) supplemented with 10% fetal calf serum (Biochrom, S0115) and 2% penicillin/streptomycin (Invitrogen GmbH, Karlsruhe, Germany). In vitro TEER was measured automatically using CellZscope system (NanoAnalytics, Münster, Germany). When the mean TEER values were at least 40 $\Omega \times$ cm^2, FITC-dextran 4 KDa (46944) was applied at a concentration of 100 µg ml^{-1} to the luminal side of the transwell system for apparent permeability (Papp) determination. After 24 h medium from the abluminal compartment was collected and the fluorescence intensity for FD4 was measured by Infinite F1000 TECAN plate reader. FD4 concentration was defined respect to a calibration curve obtained by the

6

measurement of serial dilutions values and the Papp was calculated according to the following equation[6]:

Papp = dQ/dt × 1/A × C_0 [cm/s].

dQ/dt is the amount of transported FITC-dextran per minute (µg/sec.), A is the surface area of the filter (0.3 cm^2), C_0 is the initial FITC-dextran concentration (100 µg ml^{-1}).

Immunocytochemistry

Cells on coverslips were fixed with PFA 4%. Probes were blocked and permeabilized with 7% normal donkey serum (Dianova, Hamburg, Germany)/0.3% Triton (T-8787) in PBS for 2 h at RT. Primary antibody was incubated in 2% bovine serum albumin (Dianova, 001-000-161, Hamburg, Germany) with 0.05% azide and 0.1% Triton/PBS overnight at RT. Secondary antibody and DAPI (32670) were incubated in 2% bovine serum albumin with 0.05% azide for 2 hr at RT, followed by PBS washing. Finally, coverslips were embedded in Fluoromount (Biozol, Eching, Germany).

Immunohistochemistry

Slices were blocked and permeabilized with 7% normal donkey serum (Dianova, Hamburg, Germany)/0.8% Triton (T-8787) in PBS for 2 h at RT and incubated with donkey anti-mouse FAB fragment (Dianova, 715-007-003, Hamburg, Germany) in PBS 10×10^{-3}M for at RT for 2 h. Primary antibody was incubated in 2% bovine serum albumin (Dianova, 001-000-161, Hamburg, Germany) with 0.05% azide and 0.3% Triton/PBS overnight at RT. Secondary antibody and DAPI (32670) were incubated in 2% bovine serum albumin with 0.05% azide at RT for 2 h, followed by PBS washing. Slices were finally washed with Tris-HCl (50×10^{-3} M) at pH of 6.5 and embedded in CFM-3R (Citifluor Ltd., London, UK).

Antibodies and fluorescent markers

7

Anti-early endosome antigen-1 (rabbit, Abcam, ab50313, 1:50), anti-lysosomal-associated membrane protein 1 (rat, BD Biosciences, 553792, 1:50), anti-microtubule-associated protein 1A/1B-light chain 3 (mouse, Nanotools, 0260S/LC3-2G6, 1:200), anti-glial fibrillary acidic protein (mouse, Synaptic Systems, 173011, 1:500), anti-neuronal nuclear antigen (rabbit, Merck Millipore, ABN78, 1:500), anti- neuronal class III ß-Tubulin (mouse, BioLegend, MMS-435P, 1:1000), Alexa Fluor 647 donkey anti-rabbit IgG (Jackson, Dianova, 711-605-152, 1:200), dyLight 488 anti-rat IgG (Bethyl Lab, Biomol, 1:200), dylight 488 donkey anti-mouse IgG (Bethyl Lab, Biomol, A90-337D2, 1:200), dylight 488 donkey anti-rabbit IgG (Jackson, Dianova, 711-485-152, 1:200), Rhodamine-Phalloidin (Invitrogen, R415, 1:40).

Supporting Figures
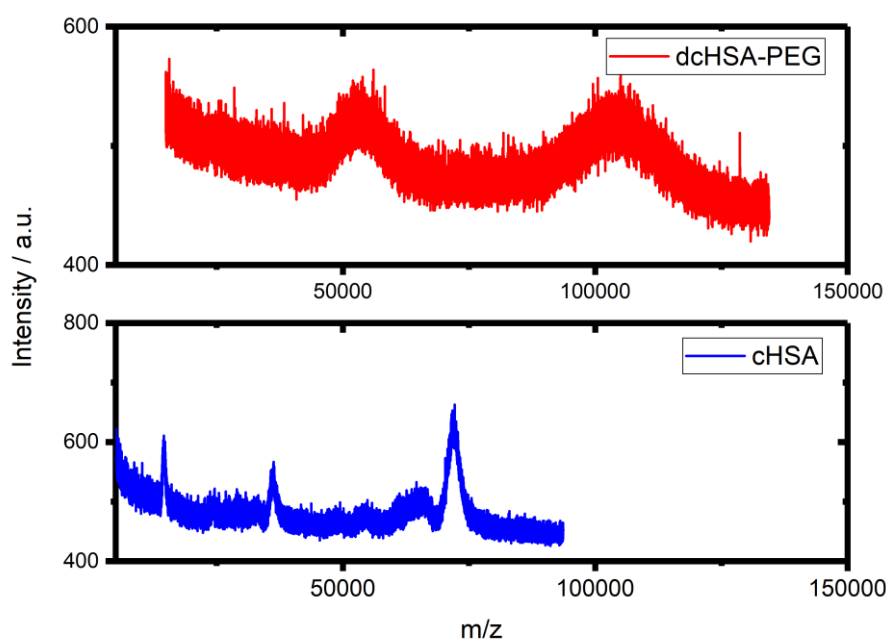
Figure S1. Maldi-TOF spectra of dcHSA-PEG (112 KDa) and cHSA (72 KDa).
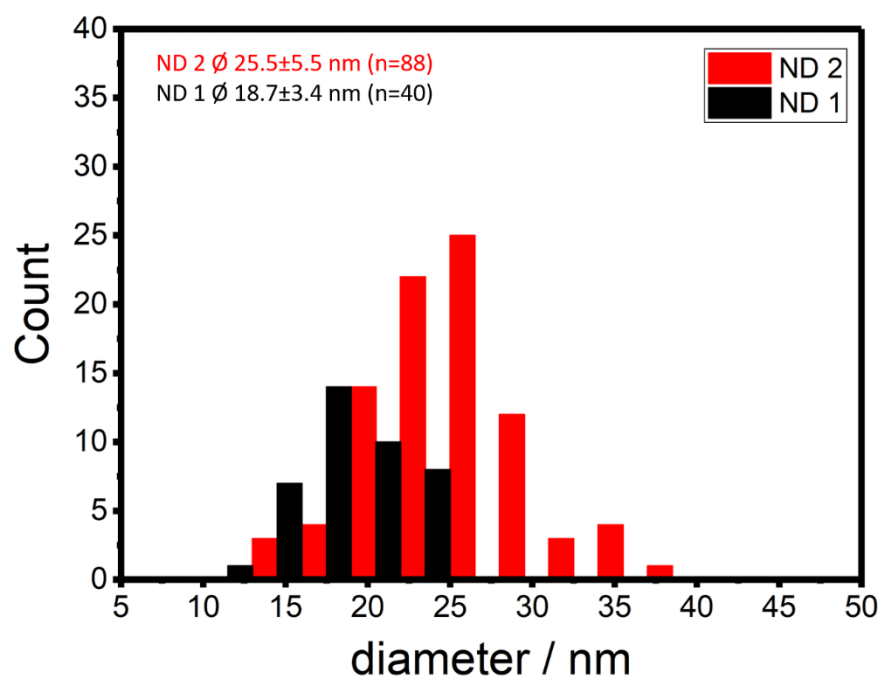
Figure S2. Histogram of size distribution for dcHSA-NDs 1 and dcHSA-NDs 2 calculated from TEM.
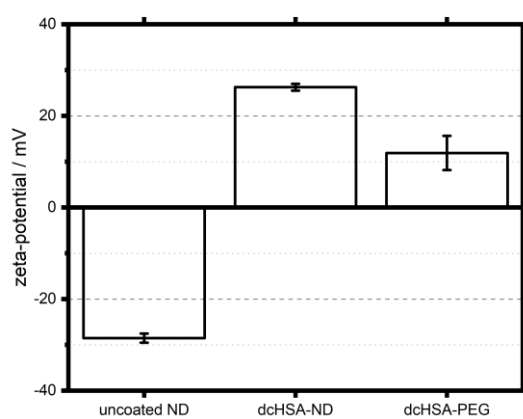
Figure S3. Zeta-potential measurement. Zeta-potential of uncoated NDs (-28.5±1.0 mV), dcHSA-ND*s* (26.3±0.7 mV) and dcHSA-PEG (11.9±3.7 mV).

9

UV channel   Coomassie channel   Photo of NDs
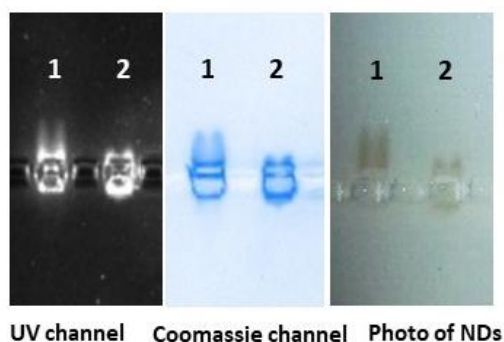
Figure S4. dcHSA-NDs 1 (40 nm) and 2 (55 nm) gel electrophoresis. Images of dcHSA-ND **1** (40 nm) and dcHSA-ND **2** (55 nm) shifted in a 0.8% agarose gel by electrophoresis (80 V for 40 min). Images were captured with ultra violet light for rhodamin (left) or for dcHSA-PEG with bright field after coomassie staining (middle) or for NDs before coomassie staining (right). Due to the size difference, smaller dcHSA-ND **1** showed further migration distance than dcHSA-ND **2**. Overlapping of ultra violet and bright field signals; indicate that the coating of dcHSA-ND was stable under electric field during gel electrophoresis.
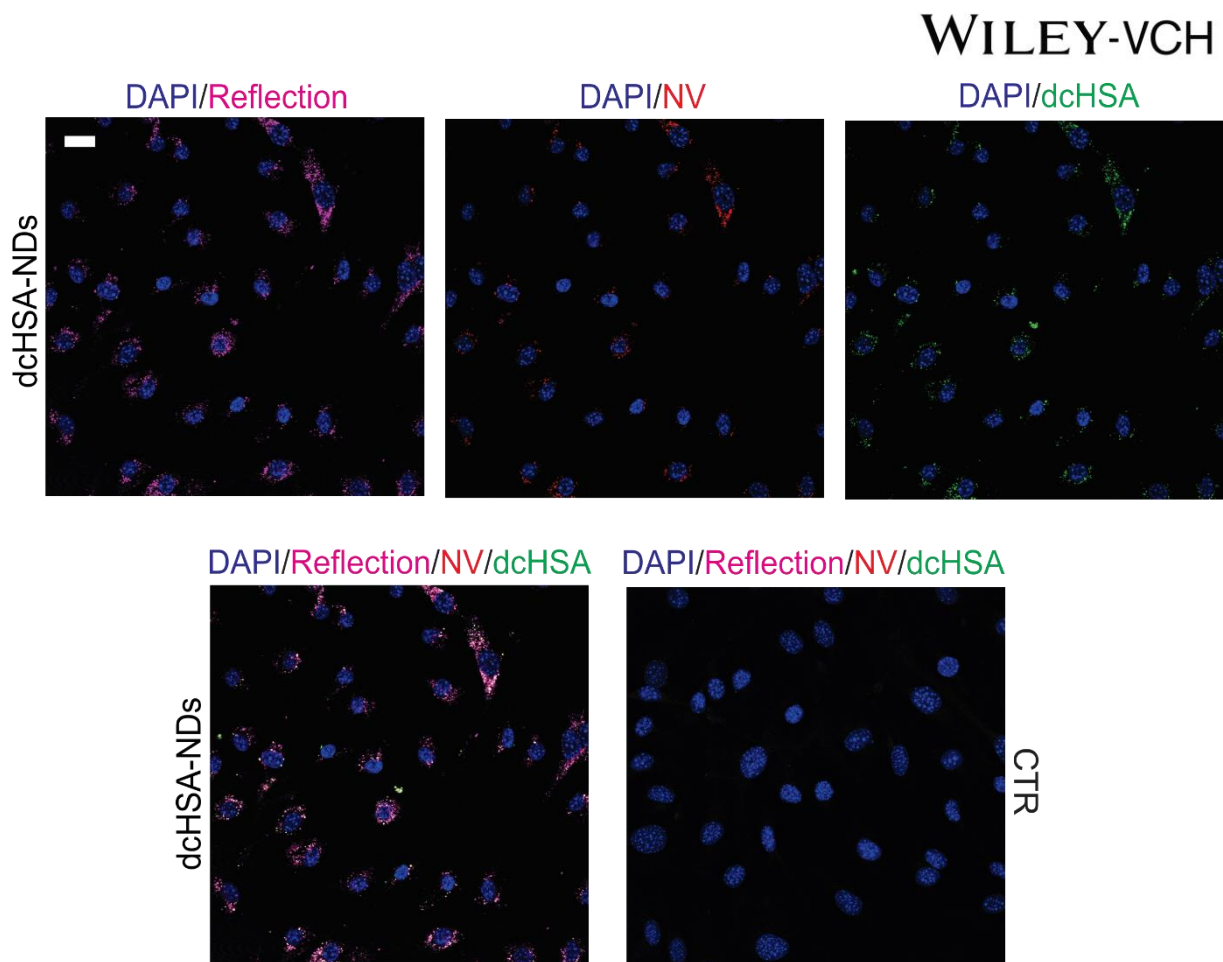
Figure S5. Intracellular colocalization of fluorescent NDs coated with bodipy488-labeled-dcHSA-PEG. Representative confocal picture of reflection- (magenta), NV- (red), dcHSA-PEG-shell- (green) signals for dcHSA-NDs in bEnd.3 cells; scale bar = 20 µm.
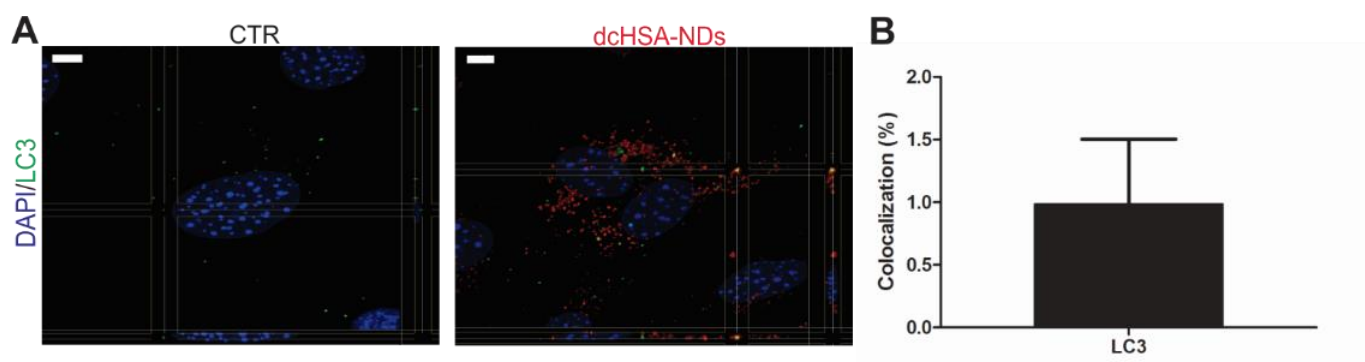
Figure S6. **dcHSA-NDs autophagosomes colocalization analysis.** **(A)** Representative confocal orthogonal view of dcHSA-NDs (red) co-staining with LC3 (green); scale bar = 5 µm. **(B)** Percentage of colocalizing dcHSA-NDs with LC3; n = 10 ROIs from 3 cultures.
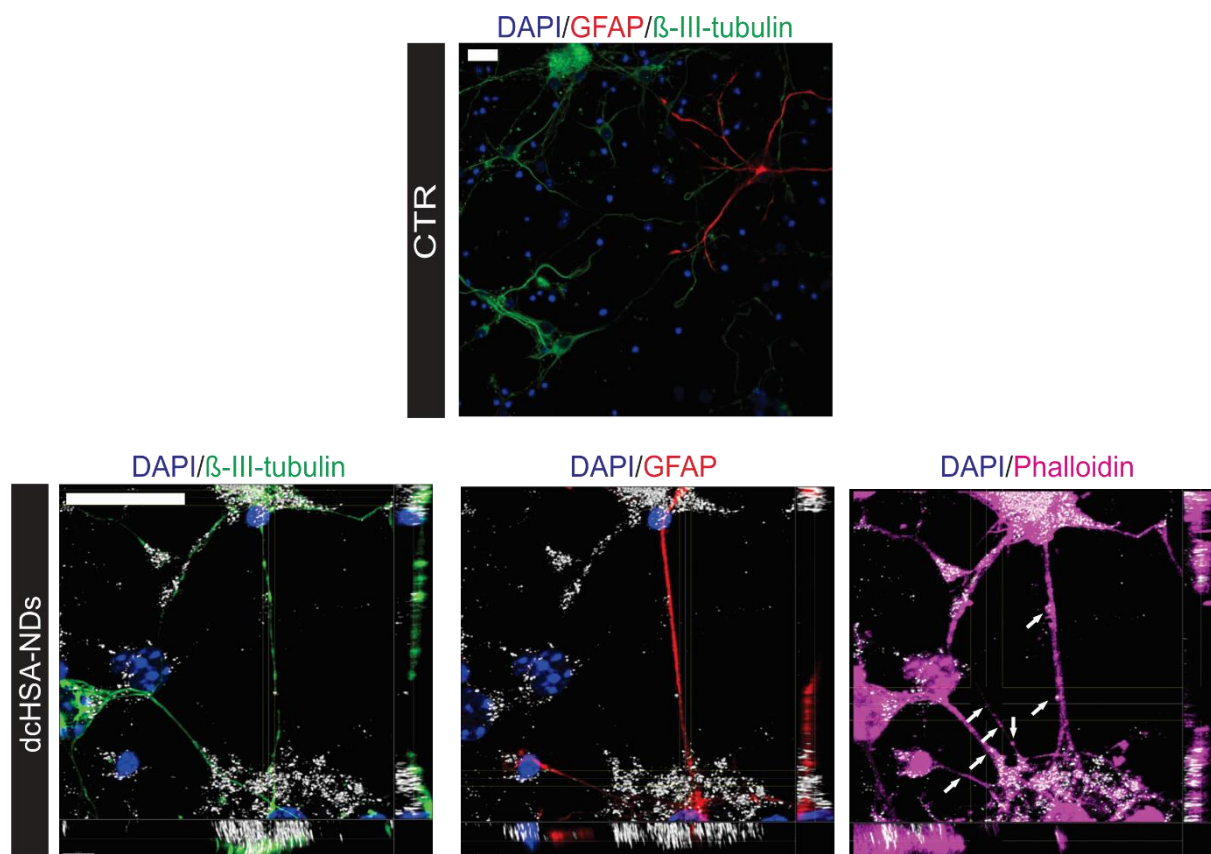
Figure S7. **dcHSA-NDs are localized in actin bridges in neurons/glia cocultures.** Representative confocal orthogonal view of dcHSA-NDs (white) colocalization with TNTs (white arrows) observable via phalloidin staining (magenta) and cellular specific markers: GFAP for astrocytes (red) and ß-III-tubulin for neurons (green). Scale bar = 20 μm
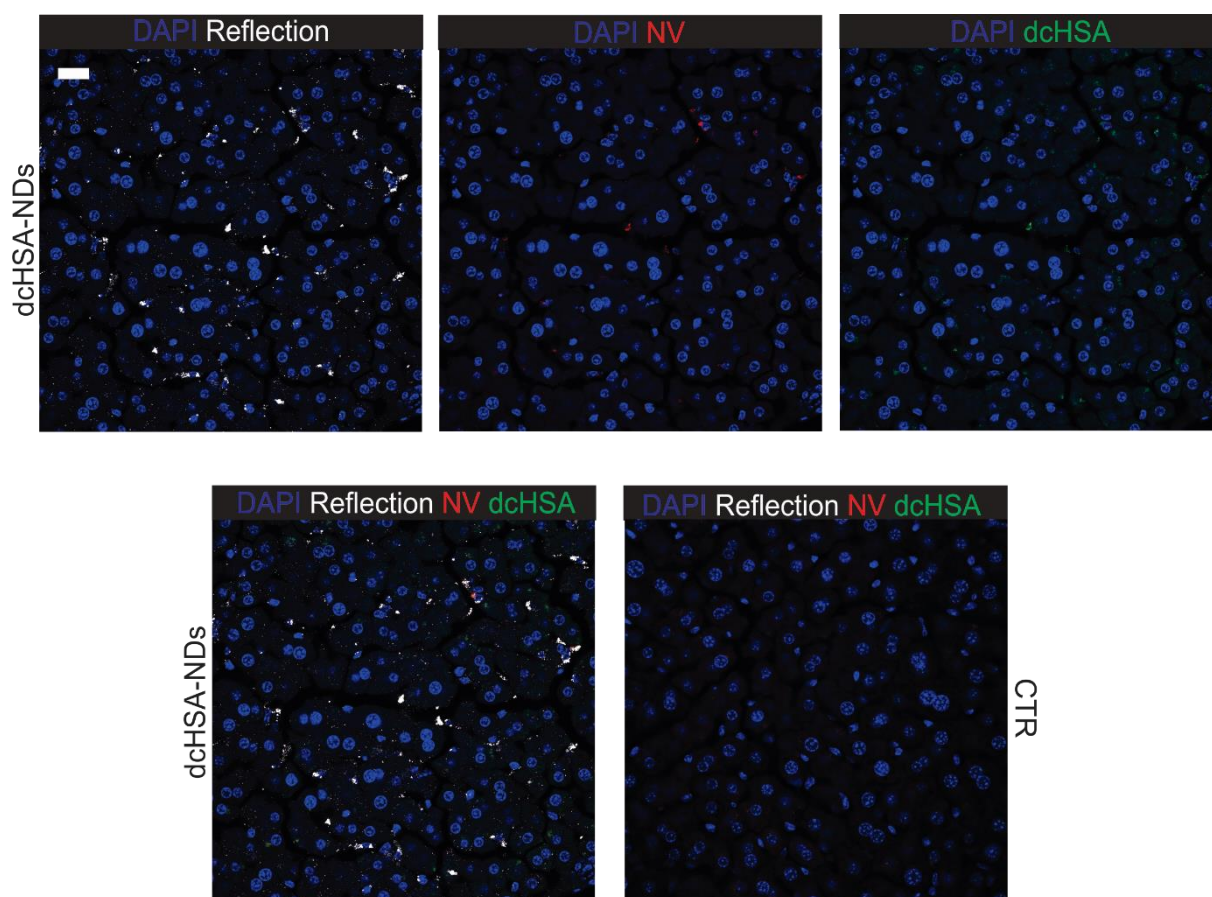
Figure S8. Fluorescent dcHSA-NDs liver uptake in vivo. Representative confocal picture of reflection (white), NV (red), dcHSA-PEG-shell (green) signals for dcHSA-NDs in liver; scale bar = 20 µm.
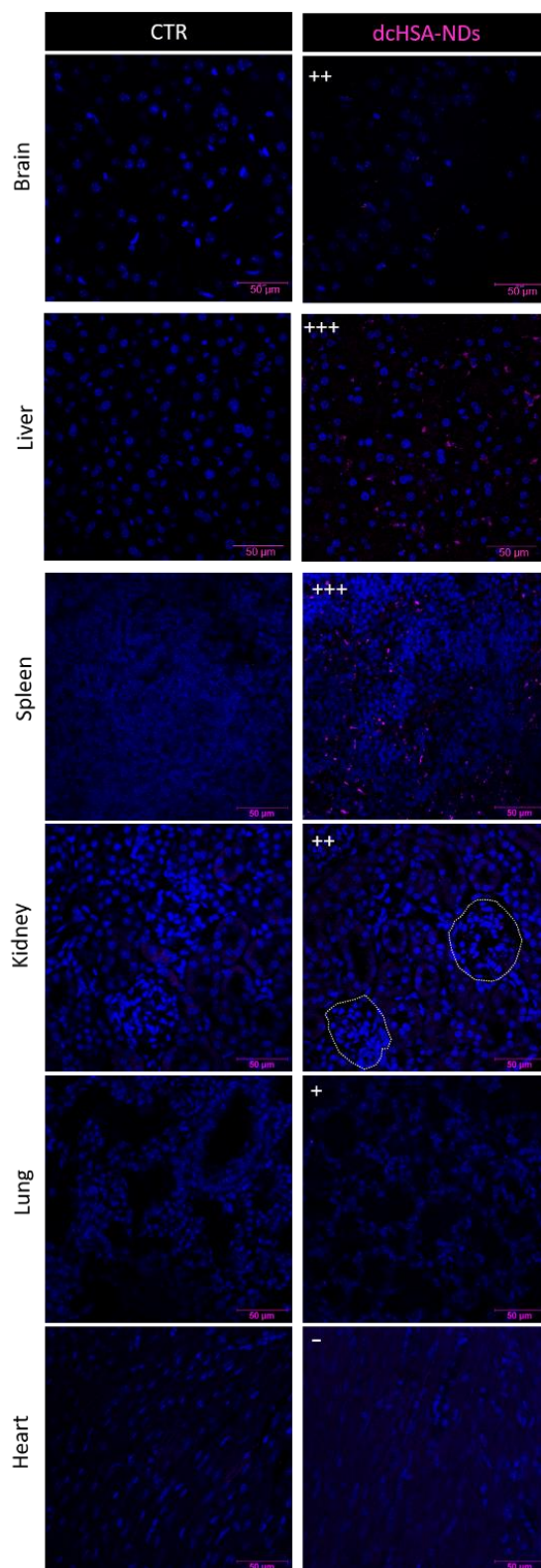
Figure S9. Fluorescent dcHSA-NDs biodistribution. Representative confocal picture of fluorescent dcHSA-NDs (magenta) in different organs; (+) or (-) represent the rate of observed uptake in each organ; dashed circles in kidney indicate renal glomeruli perimeter; scale bar = 50 μm.

References

[1]   Y. Z. Wu, S. Ihme, M. Feuring-Buske, S. L. Kuan, K. Eisele, M. Lamla, Y. R. Wang, C. Buske, T. Weil, *Adv Healthc Mater* **2013,** *2* (6), 884-894. DOI 10.1002/adhm.201200296.

[2]   Y. Wu, A. Ermakova, W. Liu, G. Pramanik, T. M. Vu, A. Kurz, L. McGuinness, B. Naydenov, S. Hafner, R. Reuter, J. Wrachtrup, J. Isoya, C. Förtsch, H. Barth, T. Simmet, F. Jelezko, T. Weil, *Advanced Functional Materials* **2015,** *25* (42), 6576-6585. DOI doi:10.1002/adfm.201502704.

[3]   R. Montesano, M. S. Pepper, U. Möhle-Steinlein, W. Risau, E. F. Wagner, L. Orci, *Cell* **1990,** *62* (3), 435-45.

[4]   S. Kaech, G. Banker, *Nat Protoc* **2006,** *1* (5), 2406-15. DOI 10.1038/nprot.2006.356.

[5]   G. M. Beaudoin, S. H. Lee, D. Singh, Y. Yuan, Y. G. Ng, L. F. Reichardt, J. Arikkath, *Nat Protoc* **2012,** *7* (9), 1741-54. DOI 10.1038/nprot.2012.099.

[6]   P. Artursson, *J Pharm Sci* **1990,** *79* (6), 476-82.

6.3 High-Contrast Magnetic Resonance Imaging and Efficient Delivery of an Albumin Nanotheranostic in Triple-Negative Breast Cancer Xenografts

Susanne Hafner,• Marco Raabe,• Yuzhou Wu, Tao Wang, Zhi Zuo, Volker Rasche, Tatiana Syrovets, Tanja Weil,* and Thomas Simmet*

•shared first authorship, *corresponding authors

Abstract:

Triple-negative breast cancer (TNBC) is a fast growing and strong metastasizing tumor, which presents almost no cellular receptors that can be addressed by targeted therapeutics. In addition, TNBC is often characterized by high tumor grading, fast growth rates, and early metastasis. Therefore, multifunctional drug carriers allowing efficient drug delivery and bioimaging to treat and track TNBC tissue in vivo would be highly desirable. A human serum albumin-based polyethylene glycol copolymer (dcHSA-Gd-Dox) is synthesized combining multiple copies of the chemotherapeutic drug doxorubicin and gadolinium (III) (Gd(III))-based magnetic resonance imaging (MRI) contrast agent. The biodegradable albumin-based nanocarriers reveal high-contrast tumor imaging and efficient drug delivery in a preclinical TNBC xenograft model, where the xenografts are grown on the chorioallantoic membrane of fertilized chick eggs. dcHSA-Gd-Dox is injected intravenously, and the distribution of the compound is monitored by MRI and inductively coupled optical plasma emission spectrometry. dcHSA-Gd-Dox is rapidly taken up into MDA-MB-231 cells and exhibits significant cytotoxic efficacy. dcHSA-Gd-Dox combines high tissue enrichment with low systemic toxicity and high-contrast MRI rendering it an attractive nanotheranostic for TNBC.

High-Contrast Magnetic Resonance Imaging and Efficient Delivery of an Albumin Nanotheranostic in Triple-Negative Breast Cancer Xenografts

Susanne Hafner, Marco Raabe, Yuzhou Wu, Tao Wang, Zhi Zuo, Volker Rasche, Tatiana Syrovets, Tanja Weil,* and Thomas Simmet*

Triple-negative breast cancer (TNBC) is a fast growing and strong metastasizing tumor, which presents almost no cellular receptors that can be addressed by targeted therapeutics. In addition, TNBC is often characterized by high tumor grading, fast growth rates, and early metastasis. Therefore, multifunctional drug carriers allowing efficient drug delivery and bioimaging to treat and track TNBC tissue in vivo would be highly desirable. A human serum albumin-based polyethylene glycol copolymer (dcHSA-Gd-Dox) is synthesized combining multiple copies of the chemotherapeutic drug doxorubicin and gadolinium (III) (Gd(III))-based magnetic resonance imaging (MRI) contrast agent. The biodegradable albumin-based nanocarriers reveal high-contrast tumor imaging and efficient drug delivery in a preclinical TNBC xenograft model, where the xenografts are grown on the chorioallantoic membrane of fertilized chick eggs. dcHSA-Gd-Dox is injected intravenously, and the distribution of the compound is monitored by MRI and inductively coupled optical plasma emission spectrometry. dcHSA-Gd-Dox is rapidly taken up into MDA-MB-231 cells and exhibits significant cytotoxic efficacy. dcHSA-Gd-Dox combines high tissue enrichment with low systemic toxicity and high-contrast MRI rendering it an attractive nanotheranostic for TNBC.

1. Introduction

Among women, breast cancer (BC) is the most frequently diagnosed cancer worldwide and every year, it accounts for more than 400 000 cases of death.[1] It is well known that BC is not a homogeneous disease, but it consists of different subtypes.[1,2] Four major intrinsic subtypes have been identified by genomic studies: the luminal subtypes A and B, which express hormone receptor-related genes, triple-negative/basal-like BC, and human epidermal growth factor receptor 2 (HER2)-positive BC.[2–4] Triple-negative breast cancer (TNBC) accounts for about 15% of BC cases and is associated with a poor prognosis as TNBC cells do not express estrogen, progesterone, and HER2 receptors that are usually addressed in targeted BC therapies.[2] The heterogeneity of the disease and lack of receptors has limited the successful development of receptor-specific therapeutics and currently, there are no approved targeted therapies available for TNBC.[1,2]

Today, only a few systemic drug treatment options exist for TNBC like taxanes (e.g., paclitaxel), anthracyclines (e.g.,

Dr. S. Hafner, Prof. T. Syrovets, Prof. T. Simmet
Institute of Pharmacology of Natural Products and Clinical Pharmacology
Ulm University
Helmholtzstr. 20, 89081 Ulm, Germany
E-mail: thomas.simmet@uni-ulm.de
M. Raabe, Prof. Y. Wu, Prof. T. Weil
Max-Planck Institute for Polymer Research
Ackermannweg 10, 55128 Mainz, Germany
E-mail: weil@mpip-mainz.mpg.de

M. Raabe, Prof. T. Weil
Department of Inorganic Chemistry I
Ulm University
Albert-Einstein-Allee 11, 89081 Ulm, Germany

Prof. Y. Wu
Hubei Key Laboratory of Bioinorganic Chemistry and Materia Medica
School of Chemistry and Chemical Engineering
Huazhong University of Science and Technology
Wuhan 430074, P. R. China

Prof. T. Wang
School of Materials Science and Engineering
Southwest Jiaotong University
Chengdu 610031, P. R. China

Dr. Z. Zuo, Prof. V. Rasche
Internal Medicine II, Core Facility Small Animal MRI, Medical Faculty
Ulm University
Albert-Einstein-Allee 23, 89081 Ulm, Germany

**ADVANCED
SCIENCE NEWS**
www.advancedsciencenews.com

**ADVANCED
THERAPEUTICS**
www.advtherap.com

doxorubicin [Dox]), and platinum agents (e.g., cisplatin) for adjuvant and neoadjuvant therapies.[2] However, their high cellular toxicity affects healthy human cells as well, resulting in severe and partially dose-limiting adverse effects.[5,6] For example, anthracyclines like the widely used drug Dox frequently induce nausea and vomiting, myelosuppression, alopecia, mucositis, and cardiotoxicity.[5,6]

Therefore, various nanocarrier-drug complexes have been reported aiming at the treatment of TNBC.[7–15] Among these, protein-based therapeutics are a promising class of nanocarriers, which earned great interest as translational drug delivery platform with increasing numbers of clinical trials in different phases.[16] In particular, the abundant blood plasma protein human serum albumin (HSA) has been applied as drug delivery system, and albumin nanoparticles,[17] albumin-drug conjugates,[18,19] albumin-binding drug derivatives,[20] albumin-coated nanoparticles,[19,21] and prodrugs[22–24] have been developed and advanced into clinical trials. Nanoparticle albumin-bound (Nab) formulations consist of denatured albumin aggregates that form nanoparticles with sizes of ≈100–200 nm with encapsulated lipophilic drug molecules. Abraxane, a Nab formulation of paclitaxel, has been approved by the FDA to treat metastatic BC,[25] and other cancers such as non-small-cell lung cancer,[26] and pancreatic cancer.[27] Nab formulations showed enhanced permeability and retention effect (EPR) in cancer tissue compared to the free drug.[28] Hence, in contrast to individual HSA proteins, HSA-based denatured nanocarriers benefit from the EPR effect due to their increased sizes of 100–200 nm.[29–33] Recently, cell- or tissue-targeted therapeutics have received much attention, and monoclonal antibodies or recombinant fusion proteins functionalized with drug molecules (Kadcyla, Ontak) have been approved and marketed.[34] It has been proposed that albumin nanocarriers accumulate in the tumor space by both passive and active drug targeting[23,24] through the EPR effect as well as binding to matricellular glycoproteins, for example, albondin on the endothelium and SPARC (osteonectin and BM-40) in the tumor interstitium.[24,35]

As TNBC appears to have high growth rates often with high grading, the combination of therapy and imaging in one system would be highly desirable to study drug tissue enrichment and follow therapeutic progress. To date, there is no albumin carrier available that targets TNBC and allows concurrent in vivo imaging.

In routine clinical diagnostics and screenings, magnetic resonance imaging (MRI) is the method of choice due to its noninvasiveness and high spatial resolution for soft tissue. Compared to computed tomography (CT), it is devoid of radiation or other health risks, and it offers diagnostic accuracy of various diseases, for example, acute and chronic cerebral hemorrhage, that is, stroke.[36] In breast cancer imaging, MRI plays an essential role with multiple indications and has shown superior sensitivity compared to other modalities like ultrasound and mammography.[37,38] Therefore, attempts were made to fabricate albumin nanoparticles for tumor-targeted imaging by MRI, for example, in combination with the photosensitizer chelator chlorin e6 that binds MRI-active Mn^{2+}.[31,33] Recently, albumin nanoparticles have been fabricated for MR/fluorescence imaging and photothermal therapy by attaching gadolinium (Gd) (III) and indocyanine green.[39] Gd-based bioimaging still

represents a method of choice as it features high relaxivity, stability, and safety[40] and albumin-based formulations containing (Gd(III)) were applied for MR tumor imaging in an avian in vivo model.[41,42] However, there are still serval challenges associated with the design of an in vivo theranostic for treating TNBC. There is the high risk that nanocarriers build up by noncovalent adsorption of the active compounds (ICG, chlorin e6, GD-1,4,7,10-tetraazacyclododecane-1,4,7,10-tetraacetic acid (Gd-DOTA), and cytotoxic drugs) to HSA show rapid loss of imaging signals and a high systemic toxicity due to leakage of active compounds during in vivo circulation. Therefore, TNBC tissue selective and effective albumin nanocarriers with combining high cytotoxicity and high-contrast imaging with minimized leakage of the drugs or imaging agents are still elusive.

Herein, we designed an albumin-based nanocarrier dcHSA-Gd-Dox, which provides multiple copies of covalently attached MRI contrast agent Gd(III)-DOTA and the chemotherapeutic agent Dox that has been linked via a pH-controlled hydrazone linker to facilitate drug release at the target tissue and minimize systemic drug leakage. dcHSA-Gd-Dox exhibits TNBC tissue selectivity and low systemic toxicity combined with high antitumor efficacy in a preclinical TNBC in vivo model. High-contrast bioimaging due to covalent loading of high numbers of MRI contrast agents and toxicity due to multiple Dox molecules and their controlled pH-triggered release in the lysosomal or endosomal compartments of the tumor cells paves the way to effective TNBC theranostics with great potential for personalized disease monitoring and translational applications.

2. Results and Discussion

2.1. Synthesis and Characterization of dcHSA-Gd-Dox

HSA provides many attractive features as a nanocarrier such as high numbers of amino groups ($-NH_2$ = 60 per HSA) and carboxylic acid groups ($-COOH$ = 98 per HSA) of the lysine, glutamic, and aspartic acid side chains that allow the introduction of various functionalities.[19] First, the carboxylic acid side chains were converted into primary amino groups by reacting HSA with ethylenediamine yielding cationized HSA (cHSA, **Figure 1**A, step 1; see details in Figure S7A, Supporting Information) as reported.[43] The additional positive surface charge at physiological pH enhances cellular uptake of HSA[19] and allows further chemical modifications of the amine groups. Almost all of the carboxylic acid side chains were converted into primary amino groups as quantified by matrix-assisted laser desorption/ionization-time of flight (MALDI-TOF; Figure S6, Supporting Information, cHSA) yielding monodisperse cHSA. In the next step, about 20 PEG chains with molecular weight of 2000 g mol⁻¹ were attached to the cHSA as indicated by the increase in molecular weight of 40 kDa yielding cHSA-PEG (Figure 1A, step 2; see for details Figures S7A and S6, Supporting Information, cHSA-PEG). In order to facilitate sensitive MRI of the nanocarrier, multiple copies of the complex agent DOTA were introduced by reacting DOTA-*N*-hydroxysuccinimide (DOTA-NHS) with the remaining primary amino groups at the surface of cHSA-PEG (Figure 1A,B, step 3). The molecular weight increased by 19 kDa indicating the introduction of about 49 DOTA

**ADVANCED
SCIENCE NEWS**

www.advancedsciencenews.com

**ADVANCED
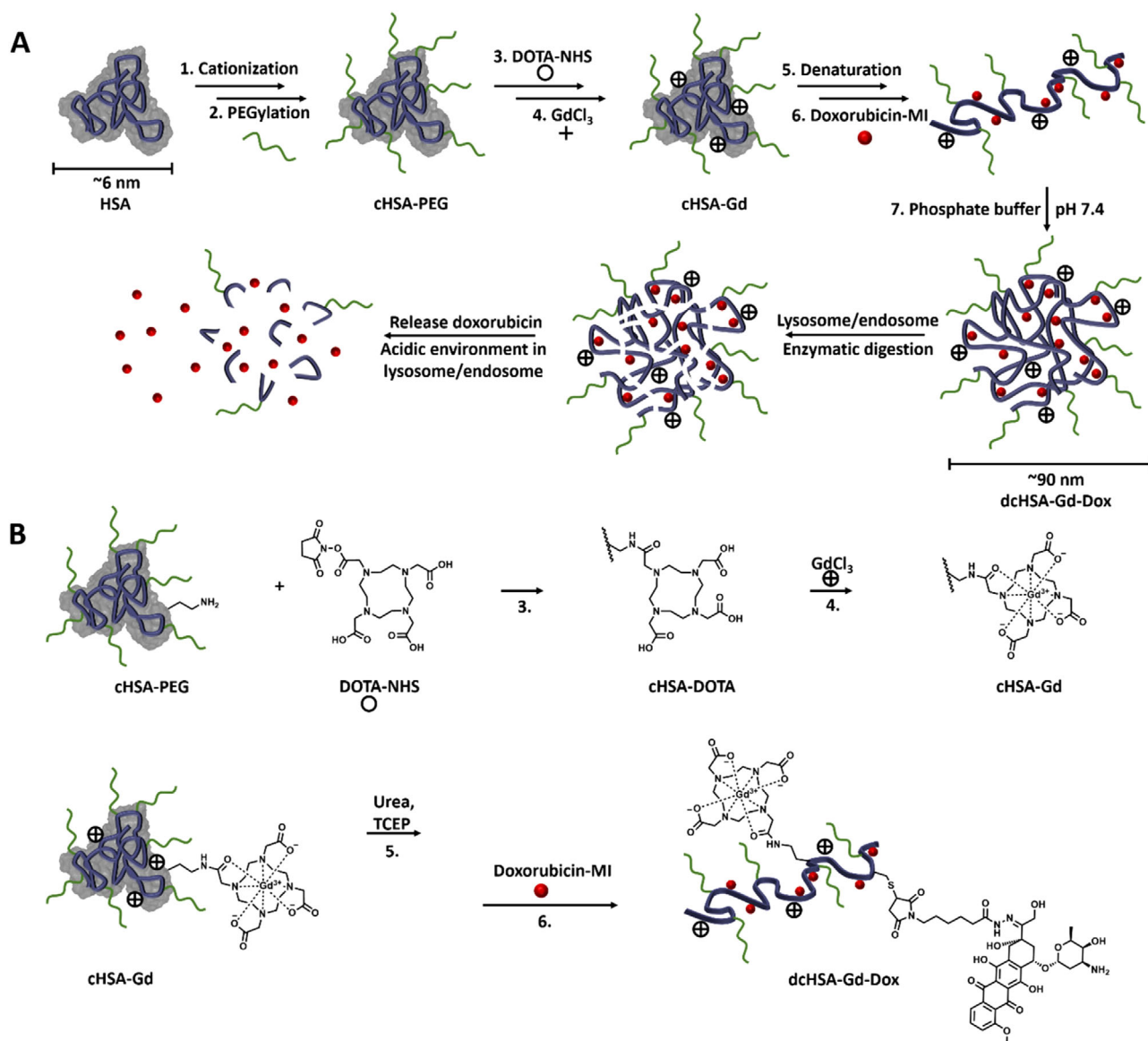THERAPEUTICS**

www.advtherap.com

Figure 1. Synthesis of dcHSA-Gd-Dox. A) General scheme of dcHSA-Gd-Dox synthesis. dcHSA-Gd-Dox was synthesized starting from native HSA in seven steps. Amino acids with a carboxylic group as side group and the C-terminus were cationized by addition of ethylenediamine (step 1 "cationization"). Afterward PEG-NHS was added to form cHSA-PEG (step 2 "PEGylation"). To enable MRI, DOTA-NHS reacted with the cHSA-PEG (step 3 "DOTA-NHS," see details in B top panel) and then, DOTA complexed Gd(III) (step 4 "GdCl₃," see details in B top panel). After denaturation and reduction of the disulfide bonds (step 5 "denaturation," see details in B bottom panel), Dox-maleimide (MI) was conjugated to the free thiols (step 6 "Dox-MI," see details in B bottom panel). After changing to a physiological buffer (step 7 "phosphate buffer"), dcHSA-Gd-Dox formed spherical nanocarriers. At tumor sites, dcHSA-Gd-PEG is digested by enzymes and the acid-responsive linker of the Dox-maleimide is cleaved due to the acidic environment resulting in release of Dox.[19] B) Detailed scheme of dcHSA-Gd-Dox synthesis, steps 3–6.

units on average (**Figure 2**E top; Figure S6, Supporting Information, cHSA-DOTA). Gadolinium cations were complexed by about 44 of the attached DOTA groups by addition of GdCl₃ to cHSA-DOTA in Milli-Q at 60 °C and overnight stirring forming cHSA-Gd (Figure 1A,B, step 4 and Figure 2E center; Figure S6, Supporting Information, cHSA-Gd). cHSA-Gd was separated from free gadolinium by ultracentrifugation (molecular weight cut off [MWCO] 30 kDa). Even though the PEG and DOTA groups were attached in a statistical fashion to cHSA, the synthesis procedures are robust, allow upscaling, and possess only negligible

batch-to-batch variations in the attached functionalities. Furthermore, quality control is feasible by applying mass spectrometry.

As the number of drug molecules is particularly crucial for dosing, we have attached Dox in a site-specific manner to the thiols of the cysteine residues at the polypeptide backbone after denaturation and reduction of cHSA-Gd (Figure 1A,B, steps 5 and 6). HSA provides 17 disulfide groups and 1 unpaired cysteine. We have reported previously that after denaturation, about 27–28 cysteines of the total number of 35 cysteines of HSA are accessible for Michael reactions.[19,44] About 7–8 cysteines of

**ADVANCED
SCIENCE NEWS**
www.advancedsciencenews.com

**ADVANCED
THERAPEUTICS**
www.advtherap.com
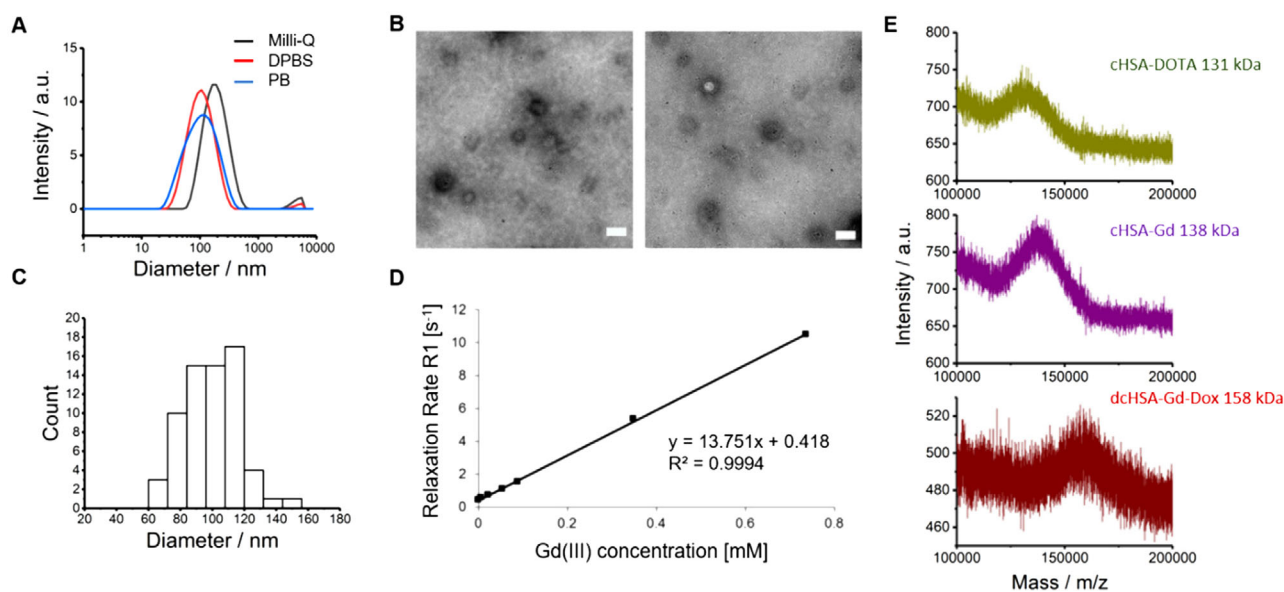
Figure 2. Characterization and magnetic properties of dcHSA-Gd-Dox. A) DLS chromatogram of dcHSA-Gd-Dox in water, DPBS, and PB (50 mm, pH 7.4). B) TEM images of dcHSA-Gd-Dox in DPBS revealed spherical structures. Scale bar 200 nm. C) The diameter of 66 spherical structures was determined and plotted in a histogram. D) Magnetic properties of dcHSA-Gd-Dox. The r_1 relaxation of dcHSA-Gd-Dox was 13.75 mm^{-1} s^{-1}. E) MALDI-TOF MS spectra of cHSA-DOTA (MW: 131 kDa), cHSA-Gd (MW: 138 kDa) and the final dcHSA-Gd-Dox (MW: 158 kDa).

the HSA sequence are colocalized (see Figure S7C, Supporting Information) and due to steric hindrance, no second Michael addition occurs after the first thiol has reacted.[19,44] Therefore the number of drug molecules per modified protein is consistent and very reproducible with little batch-to-batch variations.

The (6-maleimidocaproyl)hydrazone of Dox, a pH-cleavable hydrazone linker connecting Dox to maleimide, was synthesized according to the literature.[45] cHSA-Gd was denatured in a 5 m urea buffer and the disulfide bridges were reduced by TCEP. About 27 available thiol groups of the denatured cHSA-Gd were reacted with Dox-maleimide according to MALDI-TOF (Figure 2E bottom; Figure S6, Supporting Information, dcHSA-Gd-Dox) yielding dcHSA-Gd-Dox in quantitative yield. A pH-responsive release has many advantages over nanocarriers with noncovalently adsorbed drug molecules as unwanted leakage of the drugs during biodistribution in vivo is minimized. We have demonstrated previously that dcHSA-Dox conjugates connected via the hydrazone linker revealed a controlled two-step release of Dox.[19] The first step has to be triggered by proteases such as trypsin and cathepsin B, which digest the polypeptide backbone of the protein carrier. These proteases are usually located in the endosome or lysosome and overexpressed in various cancer types.[19] Only then, release of the Dox is triggered by the acidic pH value in the endosome or lysosome resulting in the cleavage of the hydrazone bond.[19]

2.2. Size Determination of dcHSA-Gd-Dox

The dimensions of the nanocarriers were determined by dynamic light scattering (DLS) and transmission electron microscopy (TEM). DLS was measured in a 0.5 mg mL^{-1} solution of dcHSA-Gd-Dox in Milli-Q, Dulbecco's Phosphate Buffered

Saline (DPBS), and phosphate buffer (PB, 50 mm, pH 7.4). In Milli-Q water, dcHSA-Gd-Dox showed a diameter of about 151.2 ± 3.5 nm ($n = 3$) with a polydispersity index (PDI) of 0.41 ± 0.08. Under more physiological conditions (DPBS), dcHSA-Gd-Dox formed nanostructures with diameters of about 87.8 ± 2.3 nm ($n = 3$) and a PDI of 0.31 ± 0.05. In the presence of a higher concentrated PB (50 mm, pH 7.4), nanoobjects of about 86.8 ± 1.6 nm ($n = 3$) with a PDI of 0.31 ± 0.04 (Figure 2A) were detected. Noteworthy, no smaller or larger particle populations were detected. TEM images showed spherical nanostructures of dcHSA-Gd-PEG with a diameter of about 99.2 ± 17.7 nm ($n = 66$, Figure 2B,C). The contrast in TEM results only from the high load of Dox and gadolinium as no protein stains were applied. Previously, nanoparticles with mean diameters of around 100 nm revealed a significant EPR effect.

2.3. Relaxivity Measurements of dcHSA-Gd-Dox

dcHSA-Gd-Dox showed favorable predispositions for MRI. As shown in Figure 2D, a linear correlation between the relaxation rate $r_1 = 1/T1$ and dcHSA-Gd-Dox concentration was observed, yielding a T1 relaxivity of $r_1 = 13.75$ mm^{-1} s^{-1}. Compared to the r_1 relaxivity of clinically used Gd(III) contrast agent Gd-BOPTA (MultiHance, 4.6 mm^{-1} s^{-1}), dcHSA-Gd-Dox (13.75 mm^{-1} s^{-1}) exhibited significantly improved enhancement indicating higher sensitivity compared to other gadolinium-based macromolecular contrast agents. The paramagnetic properties were at high levels comparable to published gadolinium-based macromolecular complexes.[46–48] Overall, the high number of Gd(III) per polymer provided a high relaxation time and therefore a high contrast.
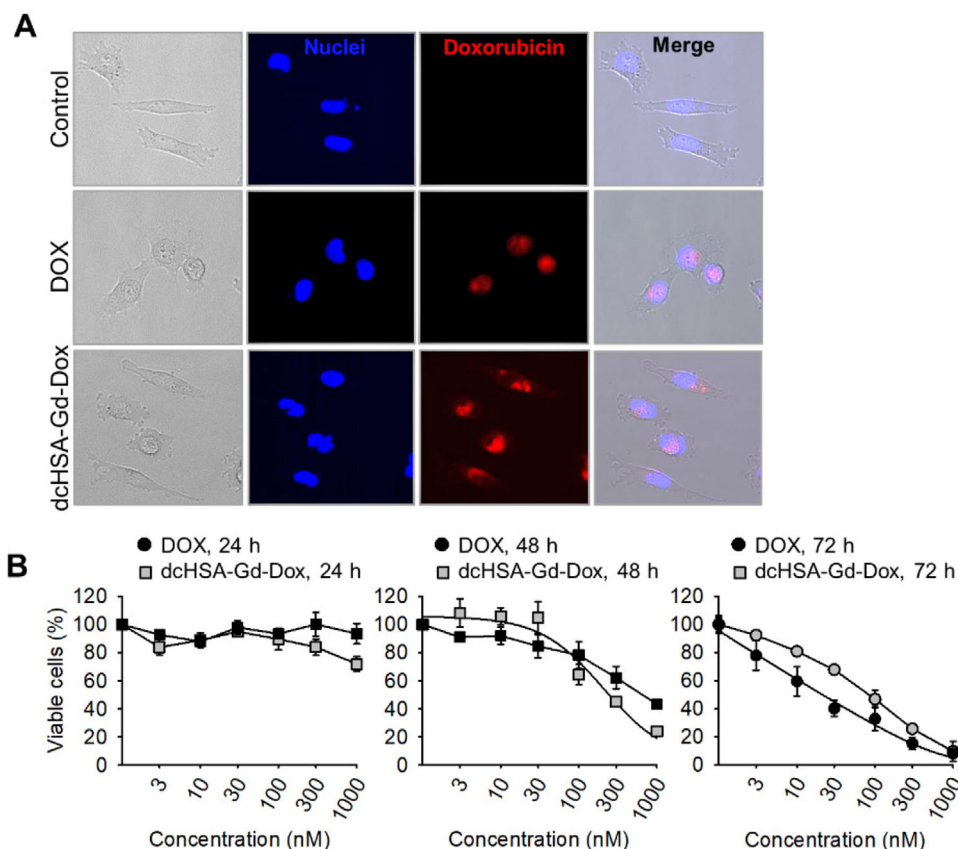
Figure 3. Tumor cell uptake and cytotoxicity of dcHSA-Gd-Dox. MDA-MB-231 breast cancer cells were incubated with dcHSA-Gd-Dox or equimolar Dox, washed, and the fluorescence of Dox was exploited to visualize dcHSA-Gd-Dox in tumor cells by fluorescence microscopy. A) Representative fluorescent images of MDA-MB-231 cells incubated with 0.36 µM dcHSA-Gd-Dox or equimolar Dox for 1 h and stained with Hoechst 33342 (from left to right: DIC, DAPI, Cy3, and merged fluorescent image). Original magnification 200×. B) Cell viability of MDA-MB-231 cells in vitro, incubated with dcHSA-Gd-Dox or Dox for 24, 48, and 72 h. XTT assay, mean ± SEM of $n = 3$ (each experiment performed in triplicates).

2.4. Uptake and Cytotoxicity of dcHSA-Gd-Dox in Breast Cancer Cells In Vitro

The fluorescence of Dox was exploited to visualize dcHSA-Gd-Dox by fluorescence microscopy. Breast cancer cells were incubated with dcHSA-Gd-Dox or Dox for 1 h and unbound nanocarriers were removed by washing. Subsequent fluorescence microscopy showed uptake of dcHSA-Gd-Dox into MDA-MB-231 breast cancer cells (**Figure 3**A). MDA-MB-231 cells were incubated for 24–72 h and cell viability was analyzed by monitoring mitochondrial dehydrogenase activity (Figure 3B). After 72 h, the IC_{50} of dcHSA-Gd-Dox (77.5 nM) appeared slightly higher than the IC_{50} of conventional Dox (17.9 nM), but was still in the nanomolar range (Figure 3B).

2.5. dcHSA-Gd-Dox Accumulates in Tumor Xenografts

The application of dcHSA-Gd-Dox was studied in vivo in tumor xenografts grown on the chorioallantoic membrane (CAM) of fertilized chick eggs as a preclinical in vivo model (**Figure 4**A). Because of its simplicity and direct accessibility, the CAM is an attractive preclinical in vivo model with proven applicability in tumor-related research to explore, for example, tumor biology, growth, and angiogenesis.[49,50] It enables rapid screening of substances with reliable assessment of substance activity, distribution, and toxicity in an in vivo environment[51] and it has been widely implemented for the evaluation of drug delivery and kinetics of, for example, drug conjugates,[52] prodrugs,[53] or nanoparticles.[54] We have previously confirmed that data obtained from the CAM model correlate with in vivo experiments in mice.[55–57] Therefore, the CAM model represents an intermediate form between isolated cultured cells and animal experiments in rodents and contributes to animal welfare by saving mammalian laboratory animals and matches the 3Rs recommendations.

Previously, MRI and the measurement of tumor growth in the CAM model has been combined based on our MRI protocols.[41,58,59] Compared to the standard gadolinium-based MRI contrast agent MultiHance, dcHSA-Gd-Dox showed a much higher signal-to-noise ratio (SNR) in tumor tissue 1–15 h after intravenous injection indicating dcHSA-Gd-Dox accumulation in tumor specimens (Figure 4B,C and **Table 1**). Only after 35 h, no contrast enhancement was detectable anymore (Figure 4B,C). Moreover, we did not observe significant contrast enhancement

**ADVANCED
SCIENCE NEWS**

www.advancedsciencenews.com

**ADVANCED
THERAPEUTICS**

www.advtherap.com
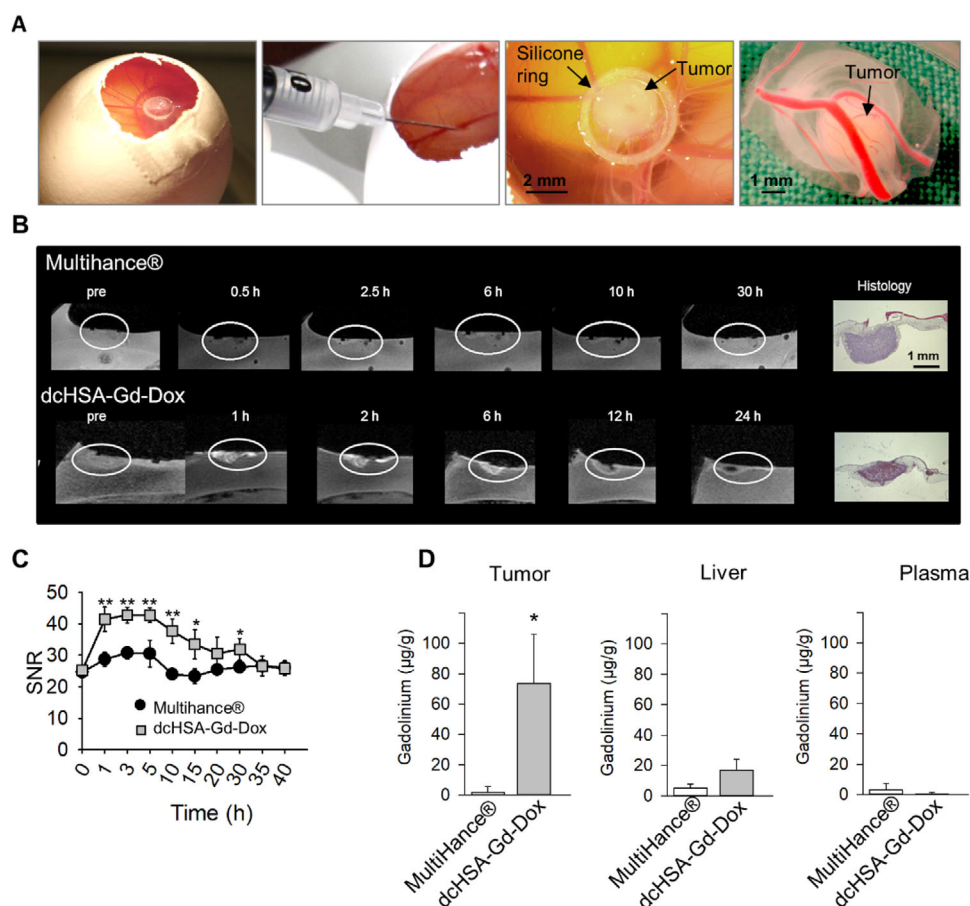
Figure 4. dcHSA-Gd-Dox accumulation in breast cancer xenografts in vivo. 1×10^6 MDA-MB-231 stably expressing firefly luciferase were grafted onto the chorioallantoic membrane (CAM) of the chick embryo. Six days later, 50 µL of Dox covalently linked to gadolinium (dcHSA-Gd-Dox) or a commercial gadolinium-containing MRI contrast agent (MultiHance) were intravenously injected at equimolar concentrations of gadolinium (3.6 µmol kg^{-1}, egg weight 50 g). MRI scans were conducted before and after the injection up to 40 h. A) MDA-MB-231 xenograft on the CAM (first and third pictures from left), intravenous application of dcHSA-Gd-Dox (second from left) and xenograft after collection (rightmost picture). B) MRI images of representative breast cancer xenografts before and after intravenous injection of MultiHance (first row) or dcHSA-Gd-Dox (second row) and the same tumors after histochemical preparation (HE, magnification 50×). C) Mean signal to noise ratio (SNR) in tumor tissue after injection of dcHSA-Gd-Dox or MultiHance, measured over time. Mean ± SD of five tumor-bearing eggs/group; Mann–Whitney rank sum test, **$p < 0.001$, *$p < 0.05$. D) Gadolinium in tumor, liver, and blood plasma 6 h after i.v. injection of dcHSA-Gd-Dox or MultiHance as measured by inductively coupled plasma optical emission spectrometry (ICP-OES). Data are mean ± SEM of 3–4 embryos per group; Mann–Whitney rank sum test, *$p < 0.05$.

Table 1. Substance doses used for in vivo diagnostic and therapeutic applications.

	dcHSA-Gd-Dox [µmol kg^{-1}]	Gd(III) [µmol kg^{-1}]	Dox [µmol kg^{-1}]
MRI	0.08	3.60	2.21
Therapy, low dose	0.03	1.22	0.75
Therapy, high dose	0.09	4.1	2.50

in any other organ or embryonic compartment but only in the tumor xenografts (Figure S8, Supporting Information).

To further analyze dcHSA-Gd-Dox biodistribution, we collected breast cancer xenografts, chick embryo blood, and livers 6 h after injection of dcHSA-Gd-Dox or MultiHance and an-

alyzed the gadolinium contents in tissues using inductively coupled plasma optical emission spectrometry (ICP-OES). This technique is highly sensitive and accurately quantifies single elements in tissue samples.[60] ICP-OES analysis confirmed the preferable accumulation of dcHSA-Gd-Dox in tumor tissue (Figure 4D). Furthermore, dcHSA-Gd-Dox was detectable in chick embryo livers, but liver distribution did not differ significantly from the standard gadolinium-based contrast agent MultiHance (Figure 4D). At that time point, dcHSA-Gd-Dox was not detectable in embryonic blood samples (Figure 4D). Thus, both MRI and ICP-OES analyses revealed dcHSA-Gd-Dox enrichment in breast cancer xenografts. Therefore, dcHSA-Gd-Dox seems to overcome intrinsic limitations associated with low relaxivity and unspecific tissue uptake of small molecule Gd(III) complexes, and proves applicability as an MR contrast agent for breast cancer xenograft imaging in ovo.

2.6. Biocompatibility of dcHSA-Gd-Dox

Embryo survival is highly predictive for compound toxicity because living organisms in the embryonic stage are highly vulnerable to external toxic influences. Three days after intravenous administration, dcHSA-Gd-Dox was well tolerated by chick embryos as embryo survival rates did not significantly differ from embryos injected with physiological sodium chloride solution; 95% and 77% of embryos injected with dcHSA-Gd-Dox 0.75 and 2.5 μmol kg^{-1}, respectively, survived indicating high biocompatibility of dcHSA-Gd-Dox. In contrast, injections of equimolar doses of commercial Dox resulted in significantly reduced survival rates, that is, 66% and 59% after low and high dosages, respectively (**Figure 5**A and Table 1). Thus, dcHSA-Gd-Dox exhibits much lower systemic toxicity than conventional Dox.

Often, divergent concentrations of nanocarriers are being used for diagnostic and therapeutic applications because the therapeutic concentration of the nanocarrier is below the imaging threshold, and, on the other hand, the concentration used for imaging is accompanied by high toxicity. However, we could clearly demonstrate that dcHSA-Gd-Dox provides low toxicity in embryos at therapeutic concentrations allowing MRI at a comparable concentration (Table 1).

2.7. dcHSA-Gd-Dox Inhibits the Growth of Tumor Xenografts

In addition to its diagnostic applications, we investigated the therapeutic efficacy of dcHSA-Gd-Dox in tumor tissue. The transparency of the CAM facilitates continuous observation of the tumor site and in vivo monitoring after treatment.[51] In our studies, we used luminescence-based tumor monitoring that has previously been validated.[61,62] Recently, we have shown antitumor efficacy of multidomain protein complexes by luminescence monitoring of tumor viability in vivo.[63]

Breast cancer growth was assessed in ovo by measuring tumor-cell-derived bioluminescence upon topical application of D-luciferin (Figure 5B). Mean bioluminescence of xenografts treated with dcHSA-Gd-Dox was significantly reduced compared to control or Dox-treated samples (Figure 5C and Table 1). These results were confirmed by subsequent immunohistochemical analysis of the cell proliferation marker Ki-67 (Figure 5D,F). This nuclear protein is indicative of mitotic phases of the cell cycle and peaking in the M phase, whereas it is not detectable in resting G_0 cells.[64] A cohort study including more than 3500 breast cancer patients identified Ki-67 expression of tumor tissue as a prognostic parameter correlated with lower disease-free and overall survival.[65] In our study, dcHSA-Gd-Dox significantly reduced the proliferative Ki-67-positive fraction in breast cancer xenografts compared to the vehicle control group, whereas conventional Dox had a minor effect on this parameter. Furthermore, TUNEL staining revealed that dcHSA-Gd-Dox and conventional Dox induced apoptosis in cancer xenografts (Figure 5E,F). Thus, in the preclinical CAM in vivo model, the theranostic dcHSA-Gd-Dox inhibits the growth of breast cancer xenografts and exerts higher biocompatibility and better antitumor efficacy than conventional Dox.

In vivo measurements of tumor bioluminescence and immunohistochemical analysis of cell proliferation (Ki-67) and apoptosis (TUNEL) demonstrated dose-dependent inhibition of tumor growth by dcHSA-Gd-Dox. The therapeutic efficacy of dcHSA-Gd-Dox was significantly stronger compared to free Dox at the same molar concentrations.

3. Conclusion

dcHSA-Gd-Dox nanocarriers were designed based on denatured, cationized, and PEGylated HSA biopolymers and about 44 Gd(III)-DOTA groups providing MRI with high relaxation time and imaging contrast. 27 Dox molecules were attached via a pH-cleavable hydrazone linker that releases Dox in acidic environments thus yielding nanocarriers with high toxicity (IC$_{50}$ of about 77.5 nM) in MDA-MB-231 TNBC cells. dcHSA-Gd-Dox significantly reduced the proliferative Ki-67-positive fraction in breast cancer xenografts, whereas conventional Dox only had a minor effect. Both MRI and ICP-OES analyses revealed dcHSA-Gd-Dox enrichment in tumor tissue, where it rapidly accumulated and persisted for at least 15 h. Thus, the accumulation of dcHSA-Gd-Dox in tumor tissue facilitated higher local concentrations, which could account for the observed significant antitumor potency, which was even outperforming equimolar dosages of conventional Dox.

The preferential enrichment of dcHSA-Gd-Dox within tumor xenografts facilitates its simultaneous usage for diagnostic and therapeutic purposes and implies a lower risk of systemic side effects. Nanocarriers exhibiting tumor selectivity and low systemic toxicity combined with high antitumor efficacy are not available for the treatment of TNBC. We envision that in TNBC patients, MR imaging after dcHSA-Gd-Dox application could be useful i) to evaluate if the chemotherapeutics reach the tumor site and ii) to assess tumor response to therapy over time. Therefore, we believe that dcHSA-Gd-Dox represents a promising theranostic awaiting further exploration and translational applications.

4. Experimental Section

Statistical Analysis: SigmaPlot software 12.0 (Systat Software GmbH, Erkrath, Germany) was used for statistical analysis. IC$_{50}$ values were calculated by nonlinear regression analysis. Two-group comparisons were analyzed using Mann–Whitney rank sum test, whereas multi-group comparisons were performed by Kruskal–Wallis one-way analysis of variance (ANOVA) with Newman–Keuls post hoc test, alpha = 0.05. For the analysis of qualitative data (embryo survival rate), Chi-square test (Fisher's exact test) was performed. *p*-values were indicated as *$p < 0.05$, **$p < 0.01$, and ***$p < 0.001$. Experimental results were usually presented as means ± SEM (standard error of the mean) or SD (standard deviation) of *n* independent experiments or samples ($n \geq 3$). *n* is defined in the main text for each experiment. Data of cytotoxicity, embryo survival, and tumor luminescence were normalized to the values under control conditions upon vehicle treatment as 100%. Further details on data presentation and sample size of each data set can be found in the respective figure legend.

Reagents and Equipment: Dox hydrochloride from Cayman Chemical (Ann Arbor, MI) was used for in vitro studies. For in vivo experiments, Dox hydrochloride from Teva or NeoCorp (both 2 mg mL^{-1}) was purchased. D-Luciferin potassium salt (Biomol, Hamburg, Germany) was dissolved in phosphate-buffered saline and stored in aliquots at −20 °C. Gadolinium (III) chloride hexahydrate was purchased from Alfa Aesar, REacton
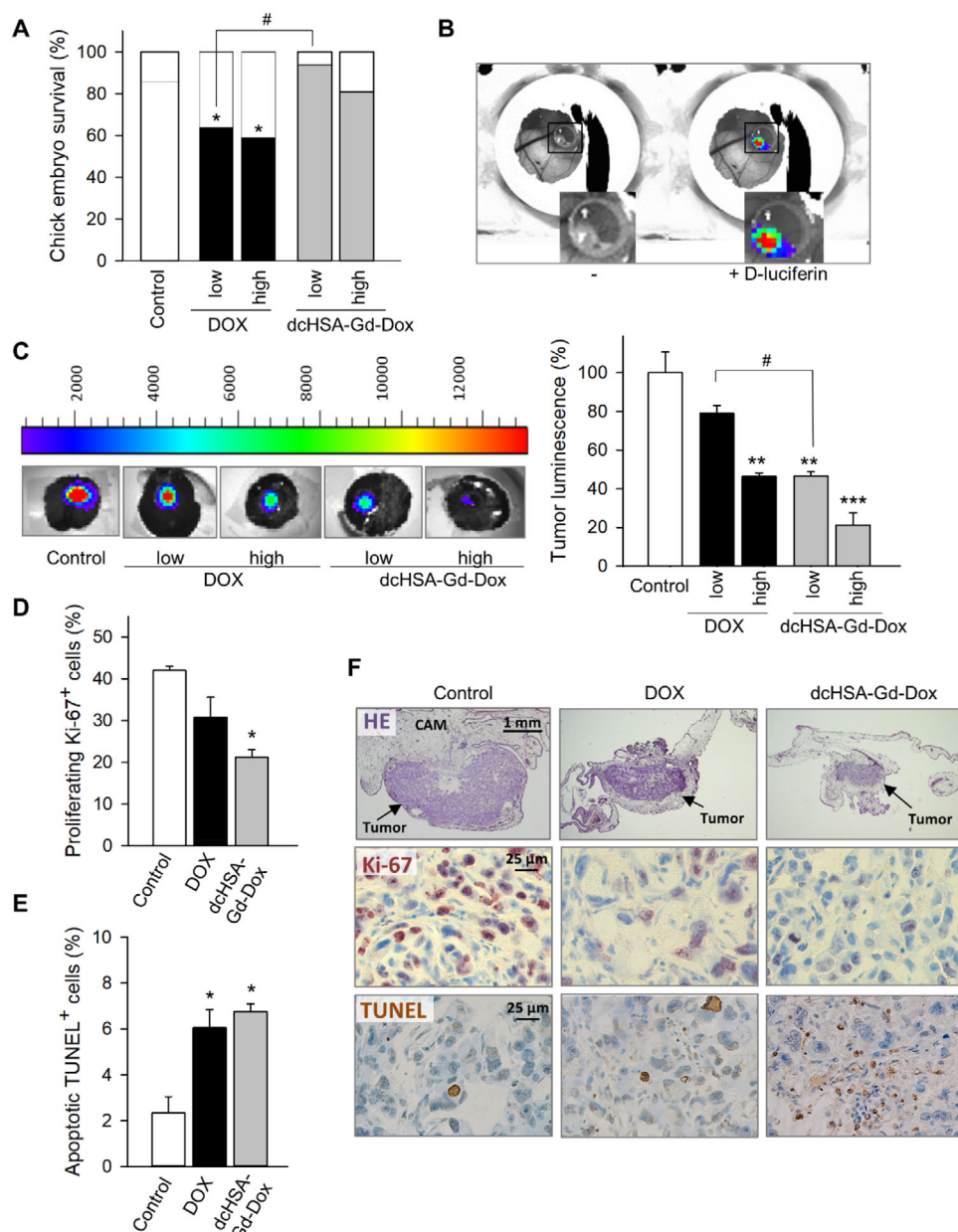
Figure 5. dcHSA-Gd-Dox inhibits the growth of breast cancer cells xenografts in vivo. 0.5×10^6 MDA-MB-231 stably expressing firefly luciferase were grafted onto the chorioallantoic membrane (CAM) of the chick embryo. Three days later, treatment commenced by i.v. injection of 50 µL of either Dox (Dox, low dose, 0.75 µmol kg^{-1}, and high dose, 2.5 µmol kg^{-1}) or Dox covalently linked to dcHSA-Gd-Dox (containing the same amount of Dox molecules as the positive control). Tumor luminescence was analyzed 72 h after i.v. injection, 10 min after addition of ᴅ-luciferin (0.75 mg mL^{-1}, 10 µL) with integration time 1 s. A) Survival rates of chick embryos 72 h after treatment (16–39 eggs per group). Chi-square test, Fisher's exact test. B) In vivo luminescent imaging of breast cancer xenografts before and after the addition of ᴅ-luciferin as indicated. C) Representative pictures of luminescent tumors in vivo (left panel) and mean luminescence of MDA-MB-231 cancer xenografts 72 h after treatment (right panel). Mean ± SEM of two experiments, $n = 6$ tumors/group. Newman–Keuls test. Immunohistochemical analysis of breast cancer xenografts. Three days after treatment, tumor xenografts were collected, paraffin embedded, and stained to analyze the number of proliferating and apoptotic MDA-MB-231 breast cancer cells. D) Percentage of Ki-67$^+$ proliferating breast cancer cells. E) Percentage of apoptotic TUNEL$^+$ cells in tumor xenografts. In every tumor, 205–619 cells were analyzed. Data are mean ± SEM of 3–4 tumors per group, Newman–Keuls test. F) Representative pictures of tumor sections after immunohistochemical staining. Upper row: HE, hematoxylin and eosin, original magnification 25×, center row: Ki-67 antigen, red-brown nuclei are indicative of proliferating cells, original magnification 200×; lower row: TUNEL staining (brown) to detect cells with fragmented DNA as apoptosis marker, original magnification 400×. ***$p < 0.001$, **$p < 0.01$, *$p < 0.05$, #$p < 0.05$.

ADVANCED
SCIENCE NEWS
www.advancedsciencenews.com

ADVANCED
THERAPEUTICS
www.advtherap.com

(99.9% purity). HSA was bought from Sigma-Aldrich. PEG-2000-NHS was purchased from Rapp Polymere and Vivaspin20 from Sartorius.

Absorbance, fluorescence, and luminescence were measured in vitro using an Infinite M1000 PRO plate reader (Tecan Group, Maennedorf, Switzerland), whereas an IVIS in vivo imaging system (PerkinElmer, Waltham, MA) was used for bioluminescence analysis of breast cancer xenografts in vivo. ICP-OES was performed by using an Ultima 2 (Horiba, Kyoto, Japan). For MRI and ICP-OES measurements, conventional MRI gadolinium contrast agent Gd-BOPTA (MultiHance, Bracco Imaging, Konstanz, Germany) served as a control. MALDI-TOF was performed on a Bruker Daltonics Reflex III spectrometer. Saturated solution of sinapinic acid dissolved in a 1:1 water:acetonitrile with 0.1% trifluoroacetic acid was used as the matrix solution.

Cell Lines: MDA-MB-231 breast adenocarcinoma cells (ACC 732) were obtained from the Leibnitz Institute, German Collection of Microorganisms and Cell Cultures (DSMZ, Braunschweig, Germany).

MDA-MB-231/luc cells stably transfected with firefly luciferase (AKR-231-GVO-CB) were purchased from Cell Biolabs (BioCat, Heidelberg, Germany).

MDA-MB-231 cells were cultured in DMEM medium (high glucose) supplemented with 2 mM glutamine, 0.1 mM MEM nonessential amino acids (NEAA), 10% heat-inactivated fetal calf serum, and 1% penicillin/streptomycin with regular passaging 2–3 times per week.

Synthesis and Characterization of dcHSA-Gd-Dox: The synthesis of 2,2′,2″-(10-(2-((2,5-dioxopyrrolidin-1-yl)oxy)-2-oxoethyl)-1,4,7,10-tetra-aza-cyclo-dodecane-1,4,7-triyl)-triacetic acid (DOTA-NHS) was done according to the literature with slight changes.[66] The synthesis is reported in the Supporting Information and all intermediates and products of the DOTA-NHS synthesis were characterized by ^{1}H-, ^{13}C-NMR and/or liquid chromatography-mass spectrometry (LC-MS, Figures S1–5, Supporting Information). (6-Maleimidocaproyl)hydrazine of doxorubicin (Dox-MI) was synthesized as reported before.[45]

cHSA and PEGylated cHSA (cHSA-PEG) were synthesized as reported.[43,67] Briefly, HSA was cationized yielding polycationic HSA (cHSA) by reacting ethylenediamine hydrochloride (2.5 M, pH 4.75) with 2000 equiv. of 1-ethyl-3-(3-dimethylaminopropyl)carbodiimide for 75 min. The crude product was purified using Vivaspin 20 ultracentrifugation tubes (30 kDa MWCO) and subsequently reacted with methoxy-PEG2000-NHS (28 equiv.) in degassed phosphate buffer (PB, 50 mM, pH 8.0) to obtain cHSA-PEG containing around 20 PEG units. Again, the product was purified by Vivaspin 20 ultracentrifugation tubes (30 kDa MWCO). Both compounds were characterized by MALDI-TOF mass spectroscopy (cHSA, 72 kDa; cHSA-PEG, 112 kDa; Figure S6, Supporting Information).

Synthesis of cHSA-DOTA: cHSA-PEG (97 mg, 0.84 µmol) was dissolved in 60 mL PB (50 mM, pH 8.0). After 20 min, DOTA-NHS (501 g mol^{-1}, 340 mg) dissolved in 4 mL dimethyl sulfoxide was added and the mixture was stirred at room temperature overnight. The crude product was purified by Vivaspin 20 ultracentrifugation tubes (30 kDa MWCO, 1 ×× PB, 3 × Milli-Q) and lyophilized to yield cHSA-DOTA (131 kDa, Figure 2E; Figure S6, Supporting Information) with 49 DOTA groups attached on average.

Synthesis of cHSA-Gd: cHSA-DOTA (110 mg, 0.84 µmol) was dissolved in Milli-Q water and after 20 min, gadolinium (III) chloride hexahydrate (2 g, 5.3 mmol) was added, and the mixture was stirred for two nights at 60 °C. Afterward, the mixture was purified by Vivaspin 20 ultracentrifugation tubes (30 kDa MWCO, 1× PB, 3 × Milli-Q) to yield cHSA-Gd (138 kDa, Figure 2E; Figure S6, Supporting Information) with 44 Gd-DOTA groups attached on average.

Synthesis of dcHSA-Gd-Dox: cHSA-Gd (110 mg, 0.8 µmol) was dissolved in 80 mL degassed PB (50 mM, pH 7.4, 5 M urea, 2 mM ethylenediaminetetraacetic acid [EDTA]) under argon atmosphere. After 20 min, tris(2-carboxyethyl)phosphine (TCEP, 21 µmol) was added and the mixture was stirred for another 20 min. Finally, Dox-maleimide (107 mg, 143 µmol) was added and the mixture was stirred at room temperature under argon atmosphere overnight. Unreacted Dox-maleimide was removed by Vivaspin 20 ultracentrifugation tubes (30 kDa MWCO, 5 × PB [50 mM, pH 7.4, 5 M urea, 2 mM EDTA], 10 × Milli-Q) and the product was lyophilized

yielding dcHSA-Gd-Dox (158 kDa, Figure 2E; Figure S6, Supporting Information).

Dynamic Light Scattering: 200 µL of a 0.5 mg mL^{-1} dcHSA-Gd-PEG solution in Milli-Q, DPBS and PB (50 mM, pH 7.4), were transferred into a borosilicate glass cuvette. The sample was measured at 20 °C with a 90° angle using a Malvern Zetasizer Nano-S90 (Nano series) and the distribution of the hydrodynamic diameter was presented as intensity.

Transmission Electron Microscopy: One drop of a 0.1 mg mL^{-1} solution of dcHSA-Gd-Dox in DPBS was placed onto an oxygen-treated copper grid. A Jeol 1400 TEM was used to obtain bright field images. The diameter of 66 spherical structures in TEM images were determined by ImageJ and plotted as a histogram.

Cell Viability Analysis and Fluorescent Microscopy In Vitro: For in vitro studies of dcHSA-Gd-Dox cytotoxicity, MDA-MB-231 were seeded in 96-well plates the day before the experiment (5000 cells per well). After 24 h, medium was replaced by medium containing dcHSA-Gd-Dox or Dox at equimolar concentrations. After the indicated incubation time, XTT tetrazolium salt was added to the wells. In viable cells, mitochondrial dehydrogenases reduce XTT to formazan and the colorimetric measurement of formazan dye yields the relative amount of viable cells compared to control cells treated with vehicle only. The XTT cell proliferation assay kit was purchased from Roche Diagnostics (Filderstadt, Germany).

In addition, cells seeded in ibidi slides were incubated with dcHSA-Gd-Dox for 1 h at 37 °C, stained with Hoechst 33342 (Molecular Probes, 1 µg mL^{-1}) and analyzed by fluorescent microscopy using a Ti-E inverse fluorescence microscope (Nikon, Düsseldorf, Germany) with 20× objective and a filter set with broad 75-nm emission passband (573–648 nm).

Analysis of Anticancer Activity in an Avian Breast Cancer Xenograft Model In Vivo: All experiments were conducted in compliance with the European directive for "Protection of Animals Used for Experimental and Scientific Purposes" and the respective German juridical implementation. For in vivo experiments, fertilized eggs from *Gallus domesticus* were bought from a hatchery (LSL Rhein-Main Geflügelvermehrungsbetriebe GmbH & Co.KG, Dieburg, Germany), cleaned, and incubated at 37 °C. Four days after fertilization, a circular part of the egg shell was carefully removed to uncover the subjacent CAM. The area was covered with tape to avoid evaporation. Three days later, a silicone ring (interior diameter 5 mm) was placed onto the CAM and MDA-MB-231 cells stably expressing firefly luciferase were resuspended in matrigel/medium (1:1) and xenotransplanted inside the ring onto the CAM (0.5 × 10^6 cells in 20 µL per egg). Matrigel was purchased from BD Biosciences (Heidelberg, Germany). In our studies, avian embryos were sacrificed no later than 8days before hatching.

Three days after cancer cell xenotransplantation, 50 µL of either Dox (low dose, 0.75 µmol kg^{-1}, or high dose, 2.5 µmol kg^{-1}) or Dox covalently linked to dcHSA-Gd-Dox (low dose, 0.03 µmol kg^{-1} or high dose, 0.09 µmol kg^{-1} containing the same amount of Dox molecules as the positive control, see Table 1) were intravenously injected. Compounds were dissolved in 0.9% NaCl solution for infusion.

To measure tumor growth, tumor luminescence was analyzed 72 h after intravenous injection of dcHSA-Gd-Dox and 10 min after addition of D-luciferin (0.75 mg mL^{-1}, 10 µL) with an integration time of 1 s, using an IVIS in vivo imaging system. Afterward, tumor xenografts were extracted from the CAM, fixed, and embedded in paraffin, and cut into 5 µm sections for immunohistological analysis.

Antibody against the human proliferation antigen Ki-67 was used to analyze the proportion of proliferating cells within cancer xenografts (Dako Cytomation, Glostrup, Denmark). To detect apoptotic tumor cells, the TUNEL method to visualize DNA strand breaks by the terminal deoxynucleotidyl transferase (Tdt)-mediated dUTP biotin nick-end labeling was applied.

MR Imaging and Contrast Analysis: The longitudinal relaxivity r_1 was derived from quantification of the resulting T1 relaxation constants as a function of Gd(III) concentration. A dilution series of dcHSA-Gd-Dox and Gd-BOPTA (MultiHance) resulting in Gd(III) concentrations from 15to 760 µM (dcHSA-Gd-Dox) and 1 µM to 1 mM (MultiHance) diluted in 0.9% NaCl aqueous solution was measured at room temperature at 11.7 Tesla field strength. T1 values were derived by fitting a monoexponential

decay curve to multi-repetition time data (TR = 300, 800, 1500, 5000, 7500, 10 000 ms).

MR imaging and intravenous injection of compounds was performed as previously described.[41] In short, MRI in vivo was performed on a small-animal MRI device (11.7 Tesla Bruker Biospec 117/16, Bruker Biospin, Ettlingen, Germany). A 72 mm quadrature volume T/R resonator was used for signal reception. A T_1-weighted 3D FLASH (3D-T_1 FLASH) sequence was used for assessment of the contrast agent distribution (acquisition parameters: TR/TE = 6/2 ms, matrix = 400 × 439 × 96, spatial resolution = 100 × 100 × 560 µm^3 and NSA = 2). Additionally, anatomic images were acquired applying a multi-slice RARE sequence (acquisition parameters: TR/TE = 4320/45 ms, matrix size = 650 × 650, in-plane resolution = 77 × 91 µm^2, slice thickness = 0.5 mm, no inter-slice gap, RARE factor = 8, and NSA = 4). During scanning, the eggs were reproducibly positioned in a polystyrene holder after cooling at 4 °C for 110 min to avoid motion artifacts. For acquisition and visualization, ParaVision 6.01 software (Bruker Biospin, Ettlingen, Germany) was used. MRI scans were conducted before and after the injection of 50 µL of dcHSA-Gd-Dox or a commercial gadolinium-containing MRI contrast agent (MultiHance) at equimolar concentrations of gadolinium (3.6 µmol kg^{-1}, respective egg weight 50 g). Consecutive MRI scans were performed starting 30 min after injection and continued for up to 40 h. To analyze SNR, regions of interest (ROIs) were manually selected at the same position at different time points. The value was corrected for the SNR of the background using the formula: SNR = (S_{ROI} − S_{BG})/δ_{BG} with S_{ROI} and S_{BG} being the mean value over the ROI and background and δ_{BG} the standard deviation of the background.

Inductively Coupled Plasma Optical Emission Spectrometry Measurement of Gadolinium: To follow dcHSA-Gd-Dox distribution, embryos were sacrificed 6 h after intravenous injection, breast cancer xenografts and chick embryo organs (blood, liver) were collected, weighed, and the content of gadolinium was analyzed by ICP-OES. To facilitate elemental analytics of gadolinium, tissue was digested in *aqua regia* (nitrohydrochloric acid) by a microwave-assisted procedure (Microwave 3000, Anton Paar, Graz, Austria).

Supporting Information

Supporting Information is available from the Wiley Online Library or from the author.

Acknowledgements

Conflict of Interest

The authors declare no conflict of interest.

Keywords

[1] J. Ferlay, I. Soerjomataram, R. Dikshit, S. Eser, C. Mathers, M. Rebelo, D. M. Parkin, D. Forman, F. Bray, *Int. J. Cancer* **2015**, *136*, E359.

[2] J. Collignon, L. Lousberg, H. Schroeder, G. Jerusalem, *Breast Cancer (Dove Med Press)* **2016**, *8*, 93.

[3] C. M. Perou, T. Sorlie, M. B. Eisen, M. van de Rijn, S. S. Jeffrey, C. A. Rees, J. R. Pollack, D. T. Ross, H. Johnsen, L. A. Akslen, O. Fluge, A. Pergamenschikov, C. Williams, S. X. Zhu, P. E. Lonning, A. L. Borresen-Dale, P. O. Brown, D. Botstein, *Nature* **2000**, *406*, 747.

[4] T. Sorlie, C. M. Perou, R. Tibshirani, T. Aas, S. Geisler, H. Johnsen, T. Hastie, M. B. Eisen, M. van de Rijn, S. S. Jeffrey, T. Thorsen, H. Quist, J. C. Matese, P. O. Brown, D. Botstein, P. E. Lonning, A. L. Borresen-Dale, *Proc. Natl. Acad. Sci. U. S. A.* **2001**, *98*, 10869.

[5] R. H. G. Teles, H. F. Moralles, M. R. Cominetti, *Int. J. Nanomed.* **2018**, *13*, 2321.

[6] J. Lao, J. Madani, T. Puertolas, M. Alvarez, A. Hernandez, R. Pazo-Cid, A. Artal, A. Anton Torres, *J. Drug Delivery* **2013**, *2013*, 456409.

[7] L. Liu, Y. Wang, L. Miao, Q. Liu, S. Musetti, J. Li, L. Huang, *Mol. Ther.* **2018**, *26*, 45.

[8] B. Darvishi, L. Farahmand, A. K. Majidzadeh, *Mol. Ther. – Nucleic Acids* **2017**, *7*, 164.

[9] D. Yang, X. Yao, J. Dong, N. Wang, Y. Du, S. Sun, L. Gao, Y. Zhong, C. Qian, H. Hong, *Bioconjugate Chem.* **2018**, *29*, 2776.

[10] M. W. Kim, H. Y. Jeong, S. J. Kang, I. H. Jeong, M. J. Choi, Y. M. You, C. S. Im, I. H. Song, T. S. Lee, J. S. Lee, A. Lee, Y. S. Park, *Theranostics* **2019**, *9*, 837.

[11] R. Goyal, C. H. Kapadia, J. R. Melamed, R. S. Riley, E. S. Day, *Cell Mol. Bioeng.* **2018**, *11*, 383.

[12] K. Greish, A. Mathur, R. Al Zahrani, S. Elkaissi, M. Al Jishi, O. Nazzal, S. Taha, V. Pittala, S. Taurin, *J. Controlled Release* **2018**, *291*, 184.

[13] C. Mei, N. Wang, X. Zhu, K. H. Wong, T. Chen, *Adv. Funct. Mater.* **2018**, *28*, 1805225.

[14] V. Bellat, R. Ting, T. L. Southard, L. Vandat, H. Molina, J. Fernandez, O. Aras, T. Stokol, B. Law, *Adv. Funct. Mater.* **2018**, *28*, 1803969.

[15] N. Zhang, X. Liang, C. Gao, M. Chen, Y. Zhou, C. J. Krueger, G. Bao, Z. Gong, Z. Dai, *ACS Appl. Mater. Interfaces* **2018**, *10*, 29385.

[16] B. Elsadek, F. Kratz, *J. Controlled Release* **2012**, *157*, 4.

[17] H. B. Ruttala, T. Ramasamy, B. S. Shin, H. G. Choi, C. S. Yong, J. O. Kim, *Int. J. Pharm.* **2017**, *519*, 11.

[18] S. Chakrabortty, M. Sison, Y. Wu, A. Ladenburger, G. Pramanik, J. Biskupek, J. Extermann, U. Kaiser, T. Lasser, T. Weil, *Biomater. Sci.* **2017**, *5*, 966.

[19] Y. Wu, S. Ihme, M. Feuring-Buske, S. L. Kuan, K. Eisele, M. Lamla, Y. Wang, C. Buske, T. Weil, *Adv. Healthcare Mater.* **2013**, *2*, 884.

[20] J. Gao, S. Jiang, X. Zhang, Y. Fu, Z. Liu, *Bioorg. Chem.* **2019**, *83*, 154.

[21] Y. Wu, K. Eisele, M. Doroshenko, G. Algara-Siller, U. Kaiser, K. Koynov, T. Weil, *Small* **2012**, *8*, 3465.

[22] L. Pes, S. D. Koester, J. P. Magnusson, S. Chercheja, F. Medda, K. Abu Ajaj, D. Rognan, S. Daum, F. I. Nollmann, J. Garcia Fernandez, P. Perez Galan, H. K. Walter, A. Warnecke, F. Kratz, *J. Controlled Release* **2019**, *296*, 81.

[23] F. Kratz, I. A. Müller, C. Ryppa, A. Warnecke, *ChemMedChem* **2008**, *3*, 20.

[24] B. Elsadek, R. Graeser, A. Warnecke, C. Unger, T. Saleem, N. El-Melegy, H. Madkor, F. Kratz, *ACS Med. Chem. Lett.* **2010**, *1*, 234.

[25] D. J. Bharali, M. Khalil, M. Gurbuz, T. M. Simone, S. A. Mousa, *Nanomedicine* **2009**, *4*, 1.

[26] M. A. Socinski, C. J. Langer, I. Okamoto, J. K. Hon, V. Hirsh, S. R. Dakhil, R. D. Page, J. Orsini, H. Zhang, M. F. Renschler, *Ann. Oncol.* **2013**, *24*, 314.

[27] W. W. Ma, M. Hidalgo, *Clin. Cancer Res.* **2013**, *19*, 5572.

[28] R. Kinoshita, Y. Ishima, V. T. G. Chuang, H. Nakamura, J. Fang, H. Watanabe, T. Shimizu, K. Okuhira, T. Ishida, H. Maeda, M. Otagiri, T. Maruyama, *Biomaterials* **2017**, *140*, 162.

[29] Q. Chen, C. Liang, C. Wang, Z. Liu, *Adv. Mater.* **2015**, *27*, 903.

**ADVANCED
SCIENCE NEWS**

www.advancedsciencenews.com

**ADVANCED
THERAPEUTICS**

www.advtherap.com

[30] H. Jeong, M. Huh, S. J. Lee, H. Koo, I. C. Kwon, S. Y. Jeong, K. Kim, *Theranostics* **2011**, *1*, 230.

[31] Q. Chen, X. Wang, C. Wang, L. Feng, Y. Li, Z. Liu, *ACS Nano* **2015**, *9*, 5223.

[32] Z. Sheng, D. Hu, M. Zheng, P. Zhao, H. Liu, D. Gao, P. Gong, G. Gao, P. Zhang, Y. Ma, L. Cai, *ACS Nano* **2014**, *8*, 12310.

[33] D. Hu, Z. Sheng, G. Gao, F. Siu, C. Liu, Q. Wan, P. Gong, H. Zheng, Y. Ma, L. Cai, *Biomaterials* **2016**, *93*, 10.

[34] V. Weissig, T. K. Pettinger, N. Murdock, *Int. J. Nanomed.* **2014**, *9*, 4357.

[35] N. Desai, V. Trieu, B. Damascelli, P. Soon-Shiong, *Transl. Oncol.* **2009**, *2*, 59.

[36] J. A. Chalela, C. S. Kidwell, L. M. Nentwich, M. Luby, J. A. Butman, A. M. Demchuk, M. D. Hill, N. Patronas, L. Latour, S. Warach, *Lancet* **2007**, *369*, 293.

[37] P. Mehnati, M. J. Tirtash, *Asian Pac. J. Cancer Prev.* **2015**, *16*, 6177.

[38] K. Pinker, T. H. Helbich, E. A. Morris, *Br. J. Radiol.* **2017**, *90*, 20160715.

[39] L. Wang, H. Lin, X. Chi, C. Sun, J. Huang, X. Tang, H. Chen, X. Luo, Z. Yin, J. Gao, *Small* **2018**, *14*, 1801612.

[40] D. Hao, T. Ai, F. Goerner, X. Hu, V. M. Runge, M. Tweedle, *J. Magn. Reson. Imaging* **2012**, *36*, 1060.

[41] Z. Zuo, T. Syrovets, Y. Wu, S. Hafner, I. Vernikouskaya, W. Liu, G. Ma, T. Weil, T. Simmet, V. Rasche, *Sci. Rep.* **2017**, *7*, 46690.

[42] Z. Zuo, T. Syrovets, F. Genze, A. Abaei, G. Ma, T. Simmet, V. Rasche, *NMR Biomed.* **2015** *28*, 440.

[43] K. Eisele, R. A. Gropeanu, C. M. Zehendner, A. Rouhanipour, A. Ramanathan, G. Mihov, K. Koynov, C. R. Kuhlmann, S. G. Vasudevan, H. J. Luhmann, T. Weil, *Biomaterials* **2010**, *31*, 8789.

[44] Y. Wu, G. Pramanik, K. Eisele, T. Weil, *Biomacromolecules* **2012**, *13*, 1890.

[45] D. Willner, P. A. Trail, S. J. Hofstead, H. D. King, S. J. Lasch, G. R. Braslawsky, R. S. Greenfield, T. Kaneko, R. A. Firestone, *Bioconjugate Chem.* **1993**, *4*, 521.

[46] J. Tang, Y. Sheng, H. Hu, Y. Shen, *Prog. Polym. Sci.* **2013**, *38*, 462.

[47] Y. Li, M. Beija, S. Laurent, L. vander Elst, R. N. Muller, H. T. T. Duong, A. B. Lowe, T. P. Davis, C. Boyer, *Macromolecules* **2012**, *45*, 4196.

[48] Y. D. Xiao, R. Paudel, J. Liu, C. Ma, Z. S. Zhang, S. K. Zhou, *Int. J. Mol. Med.* **2016** *38*, 1319.

[49] P. Nowak-Sliwinska, T. Segura, M. L. Iruela-Arispe, *Angiogenesis* **2014**, *17*, 779.

[50] C. P. Dagg, D. A. Karnofsky, J. Roddy, *Cancer Res.* **1956**, *16*, 589.

[51] A. Vargas, M. Zeisser-Labouebe, N. Lange, R. Gurny, F. Delie, *Adv. Drug Delivery Rev.* **2007**, *59*, 1162.

[52] W. W. Chin, W. K. Lau, R. Bhuvaneswari, P. W. Heng, M. Olivo, *Cancer Lett.* **2007**, *245*, 127.

[53] N. Fotinos, M. A. Campo, F. Popowycz, R. Gurny, N. Lange, *Photochem. Photobiol.* **2006** *82*, 994.

[54] A. Vargas, B. Pegaz, E. Debefve, Y. Konan-Kouakou, N. Lange, J. P. Ballini, H. van den Bergh, R. Gurny, F. Delie, *Int. J. Pharm.* **2004**, *286*, 131.

[55] T. Syrovets, J. E. Gschwend, B. Büchele, Y. Laumonnier, W. Zugmaier, F. Genze, T. Simmet, *J. Biol. Chem.* **2005**, *280*, 6170.

[56] M. Vogler, H. Walczak, D. Stadel, T. L. Haas, F. Genze, M. Jovanovic, J. E. Gschwend, T. Simmet, K. M. Debatin, S. Fulda, *Cancer Res.* **2008**, *68*, 7956.

[57] A. C. Estrada, T. Syrovets, K. Pitterle, O. Lunov, B. Büchele, J. Schimana-Pfeifer, T. Schmidt, S. A. Morad, T. Simmet, *Mol. Pharmacol.* **2010**, *77*, 378.

[58] Y. Wu, A. Ermakova, W. Liu, G. Pramanik, T. M. Vu, A. Kurz, L. McGuinness, B. Naydenov, S. Hafner, R. Reuter, J. Wrachtrup, J. Isoya, C. Fortsch, H. Barth, T. Simmet, F. Jelezko, T. Weil, *Adv. Funct. Mater.* **2015**, *25*, 6576.

[59] M. Trautmann, J. Menzel, C. Bertling, M. Cyra, I. Isfort, K. Steinestel, S. Elges, I. Gunewald, B. Altvater, C. Rossig, S. Fröhling, S. Hafner, T. Simmet, P. Aman, E. Wardelmann, S. Huss, W. Hartmann *Clin. Cancer Res.* **2017**, *23*, 6227.

[60] E. M. Frame, E. E. Uzgiris, *Analyst* **1998**, *123*, 675.

[61] A. L. Puaux, L. C. Ong, Y. Jin, I. Teh, M. Hong, P. K. Chow, X. Golay, J. P. Abastado, *Int. J. Mol. Imaging* **2011**, *2011*, 321538.

[62] M. Rovithi, A. Avan, N. Funel, L. G. Leon, V. E. Gomez, T. Wurdinger, A. W. Griffioen, H. M. Verheul, E. Giovannetti, *Sci. Rep.* **2017**, *7*, 44686.

[63] S. L. Kuan, S. Fischer, S. Hafner, T. Wang, T. Syrovets, W. Liu, Y. Tokura, D. Y. W. Ng, A. Riegger, C. Fortsch, D. Jager, T. F. E. Barth, T. Simmet, H. Barth, T. Weil, *Adv. Sci.* **2018**, *5*, 1701036.

[64] P. H. Tan, B. H. Bay, G. Yip, S. Selvarajan, P. Tan, J. Wu, C. H. Lee, K. B. Li, *Mod. Pathol.* **2005** *18*, 374.

[65] E. C. Inwald, M. Klinkhammer-Schalke, F. Hofstädter, F. Zeman, M. Koller, M. Gerstenhauer, O. Ortmann, *Breast Cancer Res. Treat.* **2013**, *139*, 539.

[66] K. Kono, S. Nakashima, D. Kokuryo, I. Aoki, H. Shimomoto, S. Aoshima, K. Maruyama, E. Yuba, C. Kojima, A. Harada, Y. Ishizaka, *Biomaterials* **2011**, *32*, 1387.

[67] D. Palesch, F. Boldt, J. A. Müller, K. Eisele, C. M. Sturzel, Y. Wu, J. Münch, T. Weil, *ChemBioChem* **2016**, *17*, 1504.

Supporting Information

High-Contrast Magnetic Resonance Imaging and Efficient Delivery of an Albumin Nanotheranostic in Triple-Negative Breast Cancer Xenografts

Susanne Hafner, Marco Raabe, Yuzhou Wu, Tao Wang, Zhi Zuo, Volker Rasche, Tatiana Syrovets, Tanja Weil*, and Thomas Simmet*

Material

All chemical compounds and solvents were purchased from commercial sources.

NMR spectra were measured on a Bruker 400 MHz NMR spectrometer and the chemical shifts were referenced to residual solvent shifts in the respective deuterated solvents. LC-MS analysis was performed on a Shimadzu LC-MS 2020 equipped with an electrospray ionization source and a SPD-20A UV/Vis detector (Shimadzu, Duisburg, Germany). Samples (40 µl) were injected onto a Luna C-18 reverse phase column (50 × 4.6 mm, 5 µm, Phenomenex, CA, Torrance). The column temperature was set at 40 °C. The mobile phase consisted of 0.1% formic acid in water (A) and 0.1% formic acid in acetonitrile (B). The gradient was linearly increased from 5% to 95% A over 20 min, held at 95% for an additional 8 min, and then immediately stepped back down to 5% for re-equilibration. The mobile phase flow rate was 0.4 mL min^{-1}.

Synthesis of DOTA-NHS
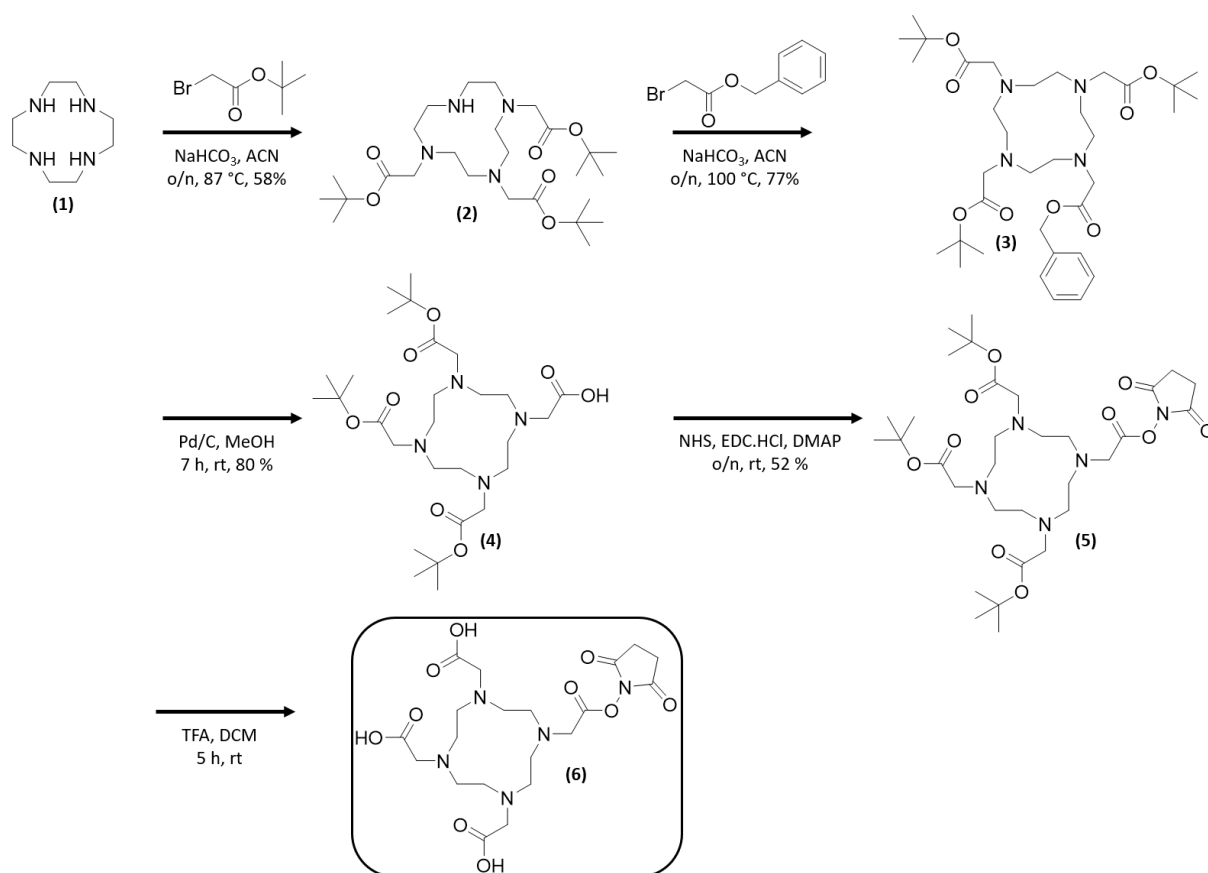
Figure S1. Overview of the synthesis route of 2,2',2''-(10-(2-((2,5-dioxopyrrolidin-1-yl)oxy)-2-oxoethyl)-1,4,7,10-tetraazacyclododecane-1,4,7-triyl)triacetic acid.
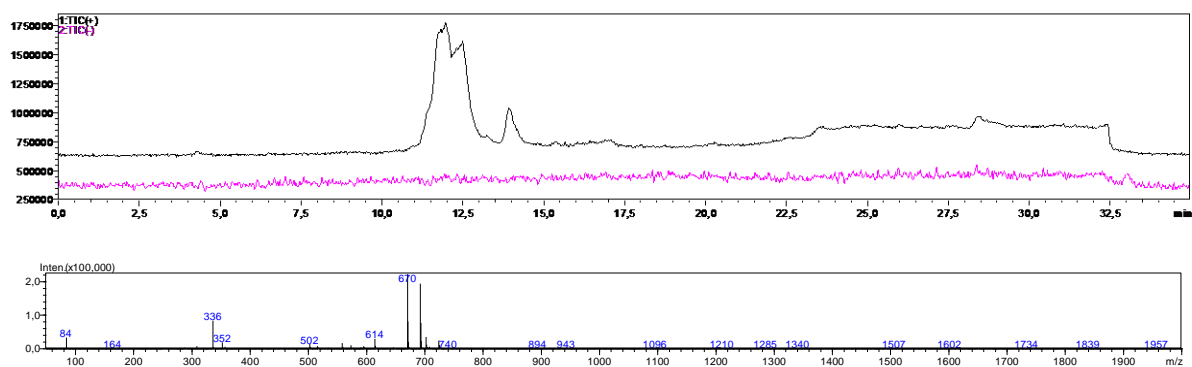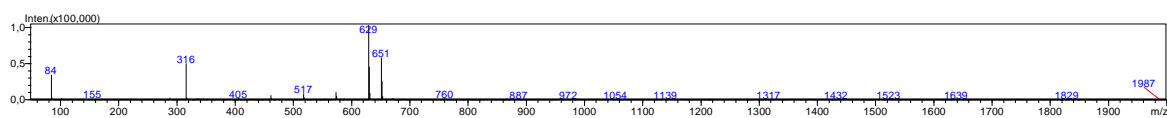
Tri-*tert*-butyl 2,2',2''-(1,4,7,10-tetraazacyclododecane-1,4,7-triyl)triacetate (2)
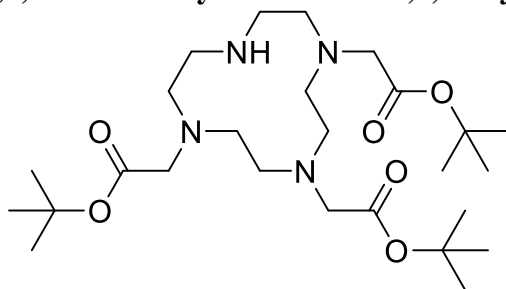
Cyclen (**1**, 750 mg, 4.35 mmol) and NaHCO$_3$ (1200 mg, 13.9 mmol) were dissolved in 540 mL anhydrous acetonitrile (ACN). *Tert*-butyl 2-bromoacetate (2710 mg, 13.9 mmol) in 180 mL

anhydrous ACN was added dropwise over 30 min at room temperature (rt). The reaction mixture was refluxed at 87 °C overnight (o/n). The reaction was carried out under argon. The solvent was filtered to remove undissolved $NaHCO_3$ and afterwards removed under high vacuum. The crude product was purified by silica gel column chromatography ($CHCl_3$ 97%, methanol (MeOH) 3%). The solvent was removed to give a colorless oil (1290 mg, 2.5 mmol, 58%).

^{1}H-NMR (400 MHz, methanol-d4 (MeOD)) σ [ppm] 3.43 (s, 4 H), 3.37 (s, 2 H), 3.16 – 3.13 (m, 4 H), 3.01 – 2.98 (m, 2 H), 2.82 – 2.79 (m, 2 H), 2.72 – 2.70 (m, 2 H), 1.48 (s, 27 H).

^{13}C-NMR (100 MHz, MeOD) σ [ppm] 172.52, 172.34, 82.71, 82.49, 79.51, 57.62, 55.21, 54.69, 51.73, 50.43, 47.05, 28.43.

LC-MS: m/z 515 [M$^+$] (calc. 514.17 g mol^{-1})
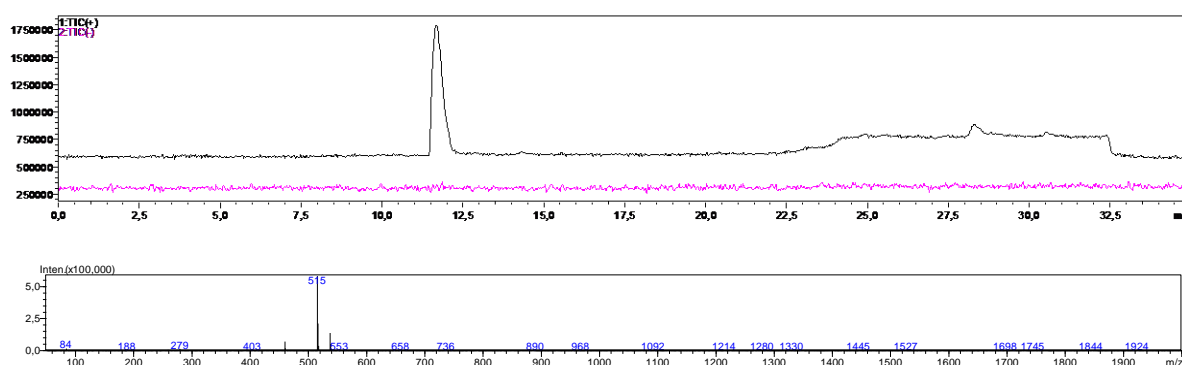
T_r = 11.7 min, m/z 515 [M$^+$]

Figure S2. LC-MS spectrum of tri-*tert*-butyl 2,2',2''-(1,4,7,10-tetraazacyclododecane-1,4,7-triyl)triacetate. The mass chromatogram is given due to too weak signal in the UV chromatogram.

Tri-*tert*-butyl 2,2',2''-(10-(2-(benzyloxy)-2-oxoethyl)-1,4,7,10-tetraazacyclododecane-1,4,7-triyl)triacetate (3)
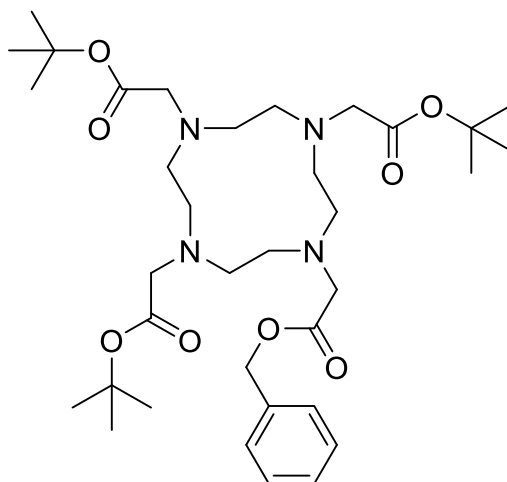
Tri-*tert*-butyl 2,2',2''-(1,4,7,10-tetraazacyclododecane-1,4,7-triyl)triacetate (**2**, 1264 mg, 2.5 mmol) and NaHCO$_3$ (840 mg, 10 mg) were dissolved in 25 mL anhydrous ACN. Benzyl bromoacetate (859 mg, 3.75 mmol) was added and the mixture was refluxed at 100 °C o/n. The reaction was carried out under argon. The reaction mixture was cooled and filtered, before purification by silica gel column chromatography (CHCl$_3$ 92%, MeOH 8%). The solvent was removed to give a yellow oil (1279.3 mg, 1.93 mmol, 77%).

^{1}H-NMR (400 MHz, MeOD) σ [ppm] 7.41 - 7.33 (m, 5 H), 5.21 (s, 2 H), 3.65 – 2.14 (m, 24 H) 1.53 (s, 27 H).

^{13}C-NMR (100 MHz, MeOD) σ [ppm] 175.22, 174.63, 174.53, 137.03, 129.64, 129.52, 129.48, 82.97, 82.93, 79.53, 67.88, 56.67, 56.59, 55.97, 28.38.

LC-MS: m/z 663 [M$^+$] (calc. 662.87 g mol^{-1})
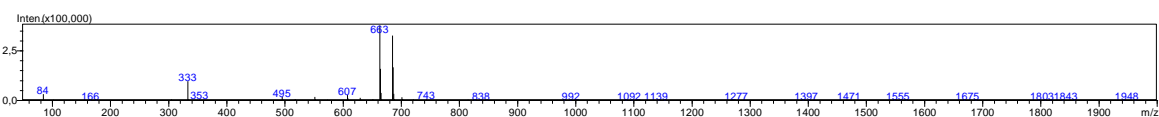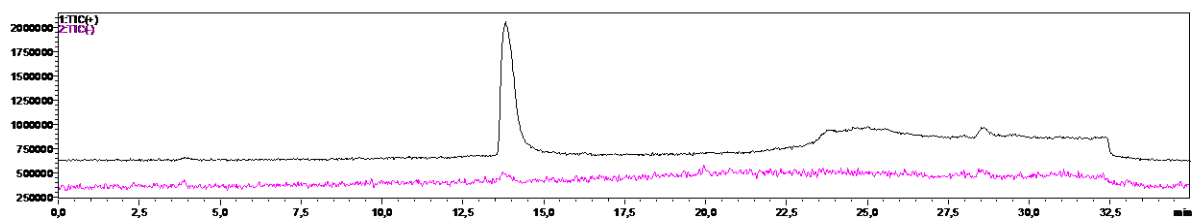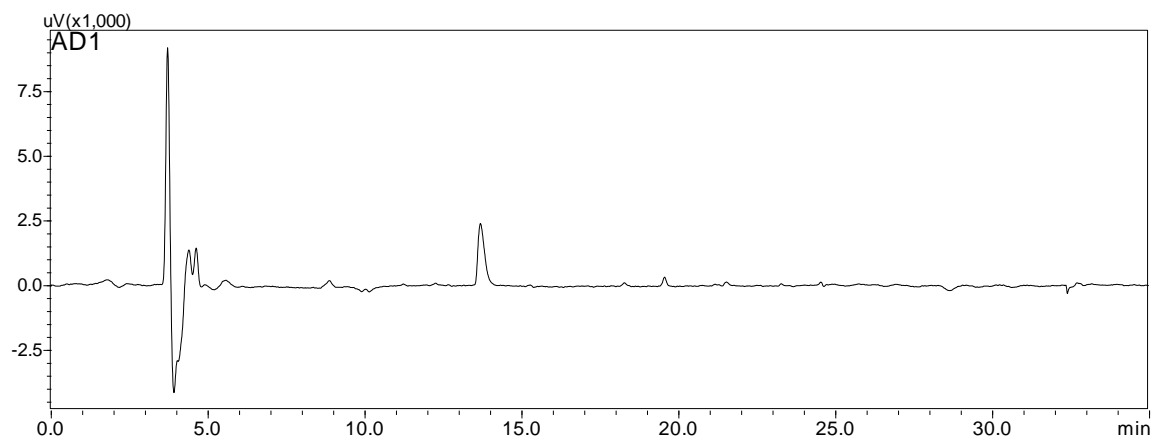
T$_r$ = 13.8 min, m/z 663 [M$^+$]

Figure S3. LC-MS spectrum of tri-*tert*-butyl 2,2',2''-(10-(2-(benzyloxy)-2-oxoethyl)-1,4,7,10-tetraazacyclododecane-1,4,7-triyl)triacetate. Top UV chromatogram (254 nm) and bottom mass chromatogram.

2-(4,7,10-tris(2-(*tert*-butoxy)-2-oxoethyl)-1,4,7,10-tetraazacyclododecan-1-yl)acetic   acid (4)
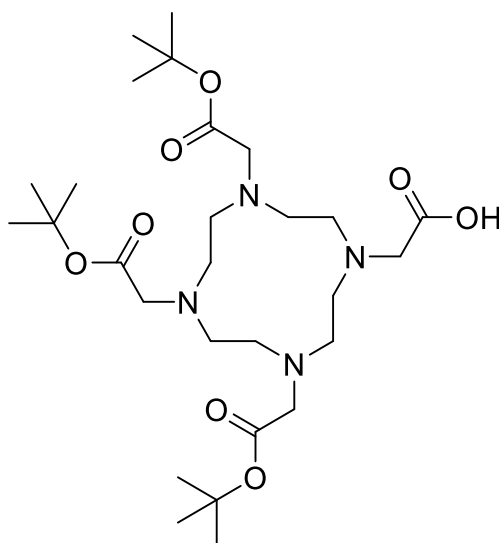
3 mL MeOH was added very gently to 10 mg palladium on carbon. Tri-*tert*-butyl 2,2',2"-(10-(2-(benzyloxy)-2-oxoethyl)-1,4,7,10-tetraazacyclododecane-1,4,7-triyl)triacetate (**3**, 196 mg, 0.29 mmol) in 7 mL MeOH was added and the solvent degassed using freeze-pump-thaw cycles (3x). Hydrogen was added. The mixture was shaken for 7 h using an ultrasonic bath. Afterwards, the mixture was filtered and the solvent removed under vacuum to give a colorless oil (133 mg, 0.23 mmol, 80%).

LC-MS: m/z 573 [M$^+$] (calc. 572.74 g mol^{-1})
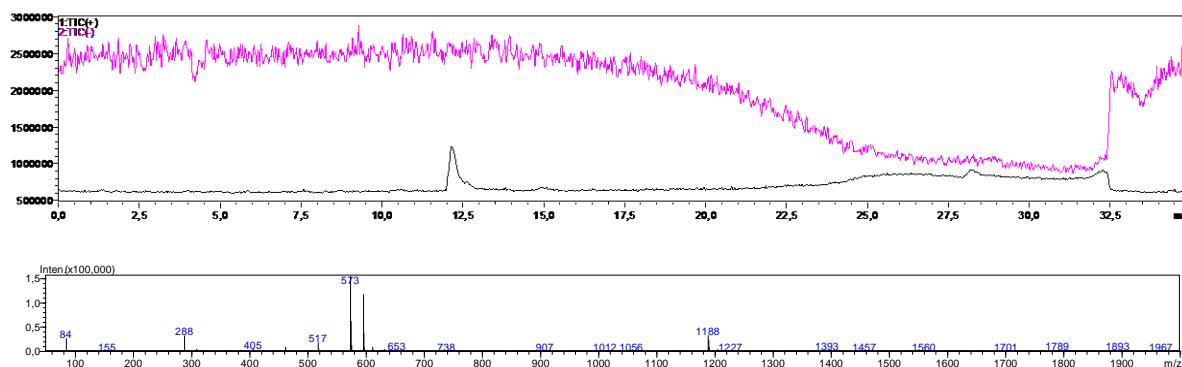
$T_r = 12.2$ min, m/z 573 [M+], 595 [M+Na$^+$]

Figure S4. LC-MS spectrum of 2-(4,7,10-tris(2-(*tert*-butoxy)-2-oxoethyl)-1,4,7,10-tetra-azacyclododecan-1-yl)acetic acid. The mass chromatogram is given due to too weak signal in the UV chromatogram.

Tri-*tert*-butyl 2,2',2''-(10-(2-((2,5-dioxopyrrolidin-1-yl)oxy)-2-oxoethyl)-1,4,7,10-tetraaza-cyclododecane-1,4,7-triyl)triacetate (5)
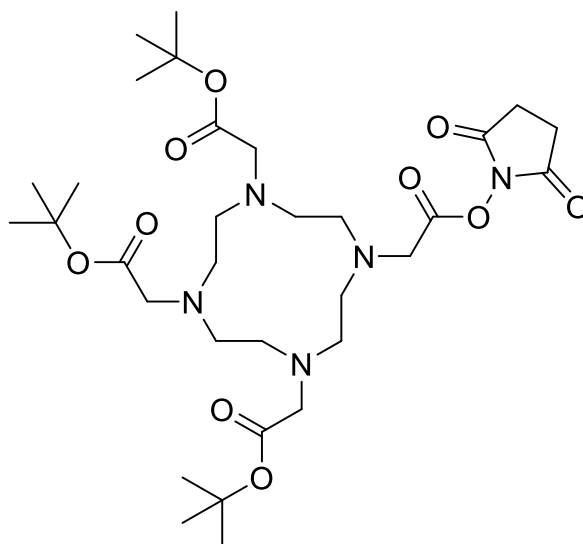
2-(4,7,10-tris(2-(*tert*-butoxy)-2-oxoethyl)-1,4,7,10-tetraazacyclododecan-1-yl)acetic acid (**4**, 213.1 mg, 0.73 mmol), *N*-hydroxysuccinimide (47.19 mg, 0.41 mmol), 1-ethyl-3-(3-dimethyl-aminopropyl)carbodiimid hydrochloride (84.35 mg, 0.44 mmol) and 4-dimethylamino-pyridine (5.37 mg, 0.044 mmol) were dissolved in 15 mL anhyd. dichloromethane (DCM) and

7

stirred overnight at room temperature. The solvent was removed and the crude product purified by silica gel column chromatography (CHCl$_3$ 90%, MeOH 10%). After removing the solvent, a colorless oil (130 mg, 0.19 mmol, 52%) remained.

LC-MS: m/z 670 [M+] (calc. 669.82 g mol^{-1}), but also methyl ester

Afterwards, tri-*tert*-butyl 2,2',2''-(10-(2-((2,5-dioxopyrrolidin-1-yl)oxy)-2-oxoethyl)-1,4,7,10-tetraazacyclododecane-1,4,7-triyl)triacetate (**5**, 130 mg, 0.19 mmol) in 6 mL dimethyl sulfoxide (DMSO) was deprotected by adding 12 mL trifluoroacetic acid (TFA) and the mixture was stirred for 4 h. The deprotected product (**6**) was dissolved in DMSO after removing TFA under high vacuum.

T_r = 11.88 min, m/z 670 [M+]
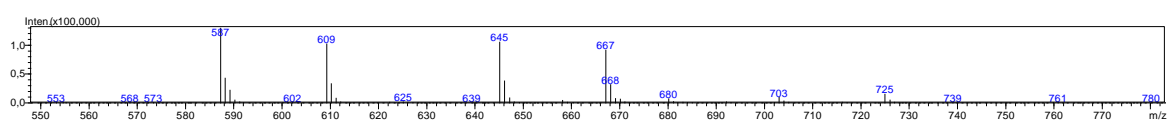
T_r = 12.44 min, m/z 587 [M+] (methyl ester); m/z 645 [M+]

T_r = 13.91 min, m/z 629 [M+]

Figure S5. LC-MS spectrum of tri-*tert*-butyl 2,2',2''-(10-(2-((2,5-dioxopyrrolidin-1-yl)oxy)-2-oxoethyl)-1,4,7,10-tetraazacyclododecane-1,4,7-triyl)triacetate. The mass chromatogram is given due to too weak signal in the UV chromatogram.

9
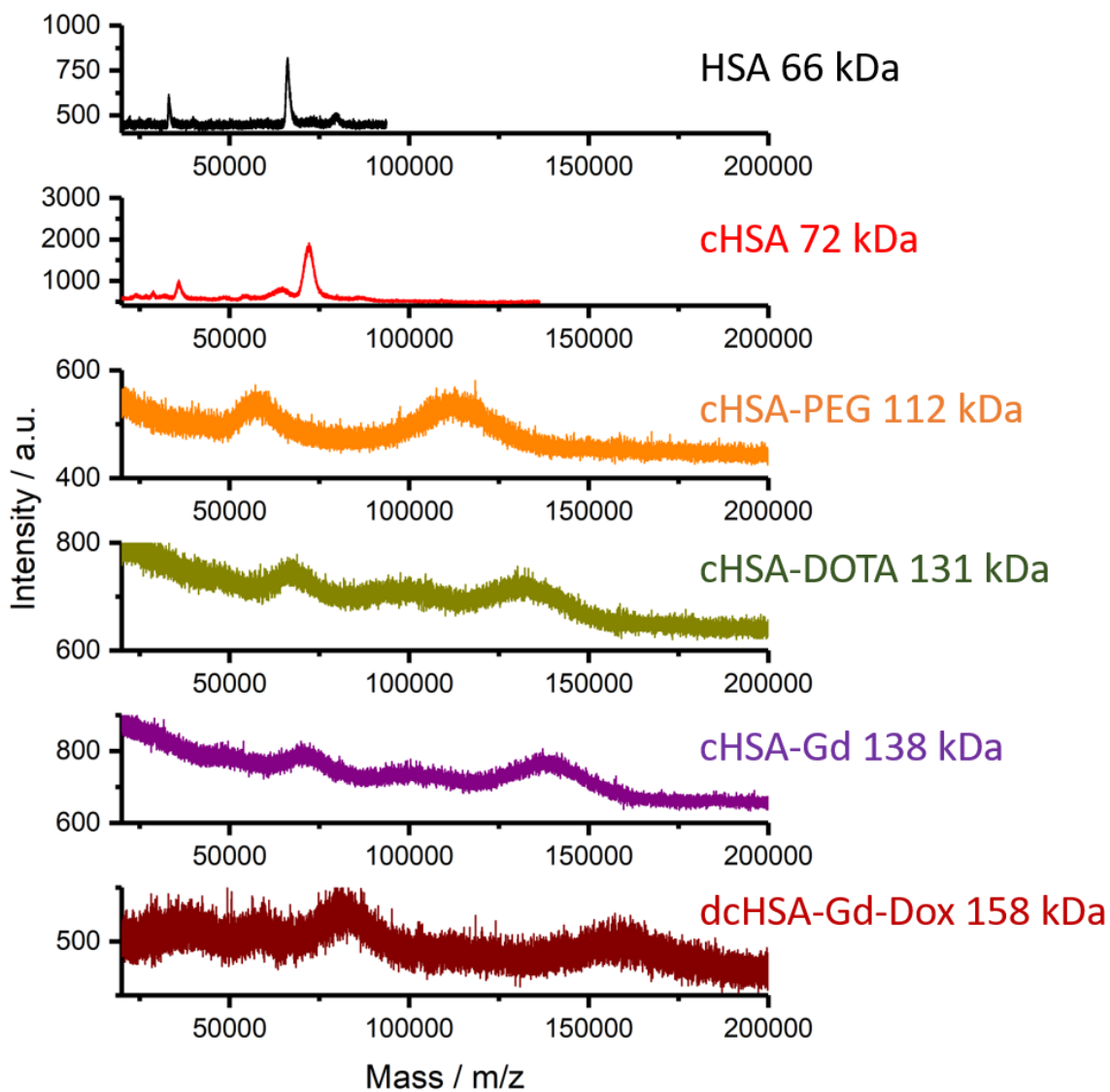
Figure S6. Maldi-TOF spectra of all intermediates and the final product.
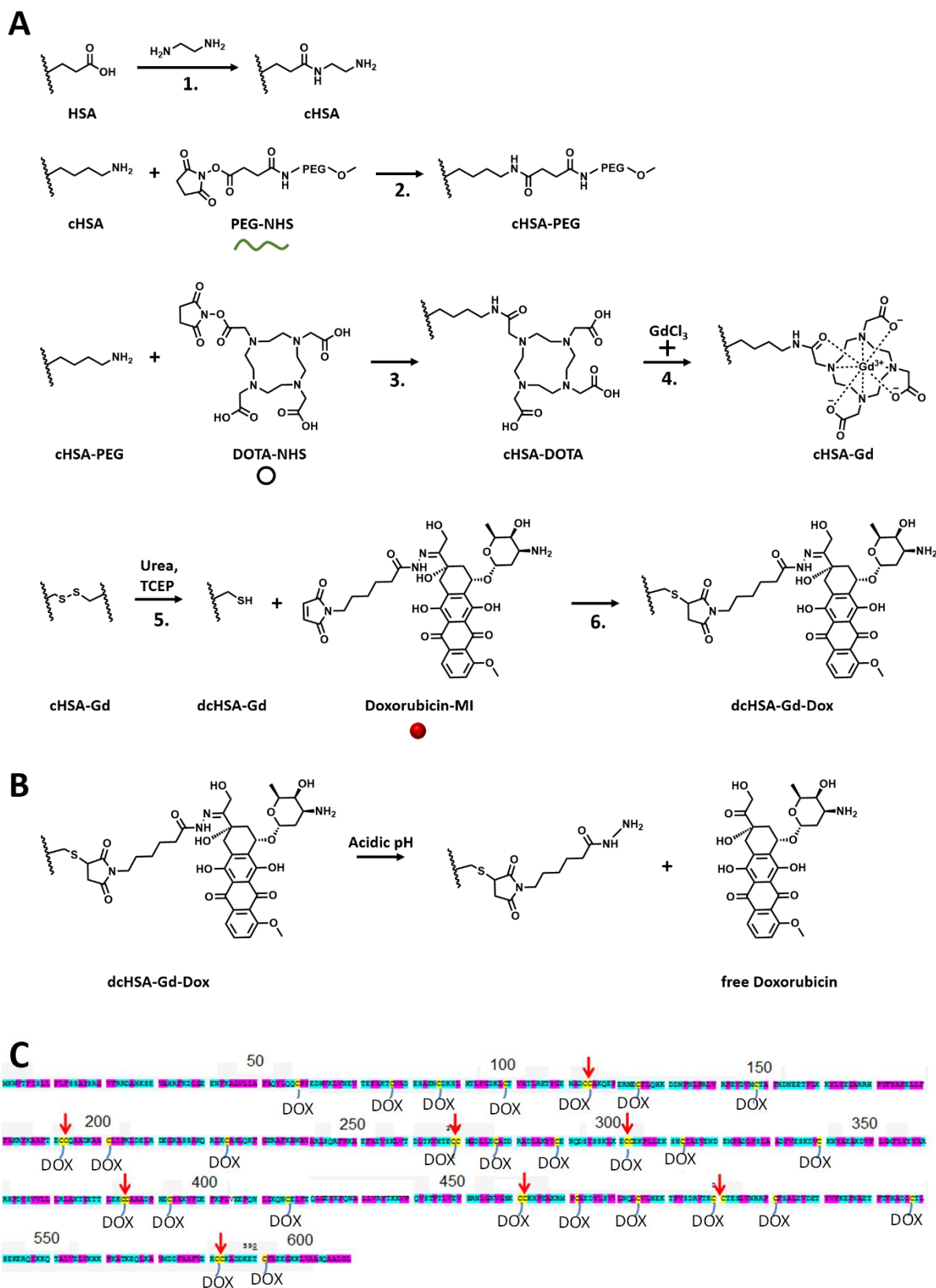
Figure S7. (A) Details of the modification of human serum albumin (HSA, see Figure 1). (B) Release of doxorubicin under acidic pH values. Dox: doxorubicin; HSA: human serum

albumin; Gd: gadolinium; MI: maleimide; PEG: polyethylene glycol. (C) Amino acid sequence of HSA. Blue color denotes hydrophilic amino acid residues, purple color stands for lipophilic amino acids and yellow color indicates cysteine residues and red arrows indicate the presence of two neighboring cysteine residues. Due to steric hindrance, DOX is most likely only attached to one of these cysteine residue.
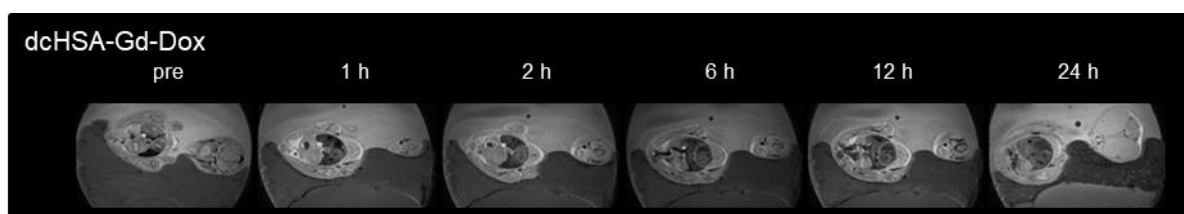
Figure S8. MRI of the chick egg after intravenous injection of dcHSA-Gd-Dox. MRI scans were conducted before and after the injection of dcHSA-Gd-Dox (3.6 µmol kg^{-1}, egg weight 50 g) to monitor for contrast enhancement in particular embryonic compartments.

6.4 Transferrin-Coated Nanodiamond–Drug Conjugates for Milliwatt Photothermal Applications

Sean Harvey,• Marco Raabe,• Anna Ermakova, Yingke Wu, Todd Zapata, Chaojian Chen, Hao Lu, Fedor Jelezko, David Y.W. Ng, and Tanja Weil*

•shared first authorship, *corresponding author

Abstract:

Fluorescent nanodiamonds (fNDs) are unique carbon-based nanomaterials due to their outstanding optical and magnetic properties. However, realization of the full potential of fNDs is often limited by their processability because fNDs aggregate strongly in both organic and aqueous solutions. Therefore, robust and potentially universal coating strategies are urgently needed to address these limitations. Derived from mussel foot proteins, the polymerization of L-3,4-dihydroxyphenylalanine (L-DOPA) provides important surface functional groups including amines, carboxylic acid, alcohols, and conjugated Michael acceptors. Herein, L-DOPA is polymerized on fNDs with a high control over the shell thickness. Photoluminescence and optically detected magnetic resonance studies reveal that the unique photophysical properties of fNDs are preserved after thin poly(L-DOPA) film coating. Subsequently, conjugation of transferrin, a heme protein that provides efficient receptor-specific cellular transport, improves the colloidal stability and cellular uptake of the poly(L-DOPA)-coated fNDs. The loading of FDA-approved indocyanine green as a photothermal agent yields an integrated biohybrid material exhibiting an amplified photothermal effect in cells at very low energy intake ($\approx$90 mW cm^{-2}).

Transferrin-Coated Nanodiamond–Drug Conjugates for Milliwatt Photothermal Applications

Sean Harvey, Marco Raabe, Anna Ermakova, Yingke Wu, Todd Zapata, Chaojian Chen, Hao Lu, Fedor Jelezko, David Y. W. Ng, and Tanja Weil*

Fluorescent nanodiamonds (fNDs) are unique carbon-based nanomaterials due to their outstanding optical and magnetic properties. However, realization of the full potential of fNDs is often limited by their processability because fNDs aggregate strongly in both organic and aqueous solutions. Therefore, robust and potentially universal coating strategies are urgently needed to address these limitations. Derived from mussel foot proteins, the polymerization of L-3,4-dihydroxyphenylalanine (L-DOPA) provides important surface functional groups including amines, carboxylic acid, alcohols, and conjugated Michael acceptors. Herein, L-DOPA is polymerized on fNDs with a high control over the shell thickness. Photoluminescence and optically detected magnetic resonance studies reveal that the unique photophysical properties of fNDs are preserved after thin poly(L-DOPA) film coating. Subsequently, conjugation of transferrin, a heme protein that provides efficient receptor-specific cellular transport, improves the colloidal stability and cellular uptake of the poly(L-DOPA)-coated fNDs. The loading of FDA-approved indocyanine green as a photothermal agent yields an integrated biohybrid material exhibiting an amplified photothermal effect in cells at very low energy intake ($\approx$90 mW cm^{-2}).

S. Harvey, M. Raabe, Dr. A. Ermakova, Y. Wu, Dr. T. Zapata, C. Chen, Dr. H. Lu, Dr. D. Y. W. Ng, Prof. T. Weil
Max Planck Institute for Polymer Research
Ackermannweg 10, 55128 Mainz, Germany
E-mail: weil@mpip-mainz.mpg.de
S. Harvey, M. Raabe, C. Chen, Prof. T. Weil
Institute of Inorganic Chemistry I
Ulm University
Albert-Einstein-Allee 11 89081 Ulm, Germany
Prof. F. Jelezko
Institute for Quantum Optics
Ulm University
Albert-Einstein-Allee 11 89081 Ulm, Germany

1. Introduction

Among carbon-based materials, fluorescent nanodiamonds (fNDs) are unique as they do not only possess excellent photoluminescence properties, but they are also very precise local sensors of magnetic and electric fields, temperature, or mechanical forces.[1,2] These characteristics are predominantly derived from the defect centers in nanodiamonds (NDs) where impurity atoms such as nitrogen,[3] silicon,[4,5] and germanium[6] are localized alongside lattice vacancies. Consequently, the type of such crystallographic defects defines its unique optical spectrum as well as spin properties. Hence, the optical behavior of fNDs is independent of its size, in contrast to other classes of nano-emitters such as quantum/carbon dots and gold nanoparticles.[7] The best studied color center is the nitrogen-vacancy (NV) center.[2,3,8–11] The remarkable properties of this atom-like defect in the diamond lattice allow application for high-resolution magnetic (bio)sensing,[12] energy transfer,[13] bioimaging,[12] and even quantum computing technologies.[14] Due to this, in the present work, nanodiamonds with NV centers were selected as base material for designing a potent theranostic system.

In order to achieve these aims, the processability of NDs is a recurring challenge. The colloidal stability of NDs in solution, both organic and aqueous, is extremely poor and is further aggravated with the reduction in the size of the diamond particle.[9,15] Hence, the capability to chemically introduce novel functions tends to be severely hampered by the aggregation of the NDs. To alleviate this primary issue, nanodiamond coating technologies have been developed using adsorption mechanisms deriving from weak attractive forces (electrostatic, van der Waals, hydrogen bonding) and/or strong covalent interactions.[8,16,17] However, these coating technologies have persistent difficulties due to batch to batch production variability impacting the surface composition of NDs. In addition, it is crucial to understand that the coating material has to fulfill many important criteria, including 1) chemical multifunctionality, 2) reproducibility of the coating strategy on NDs from different sources and sizes, 3) colloidal stability of the fND conjugate in biological media and inside cells, and 4) minimally affecting the photoluminescence and magnetic sensing capabilities.

**ADVANCED
SCIENCE NEWS**

www.advancedsciencenews.com

**ADVANCED
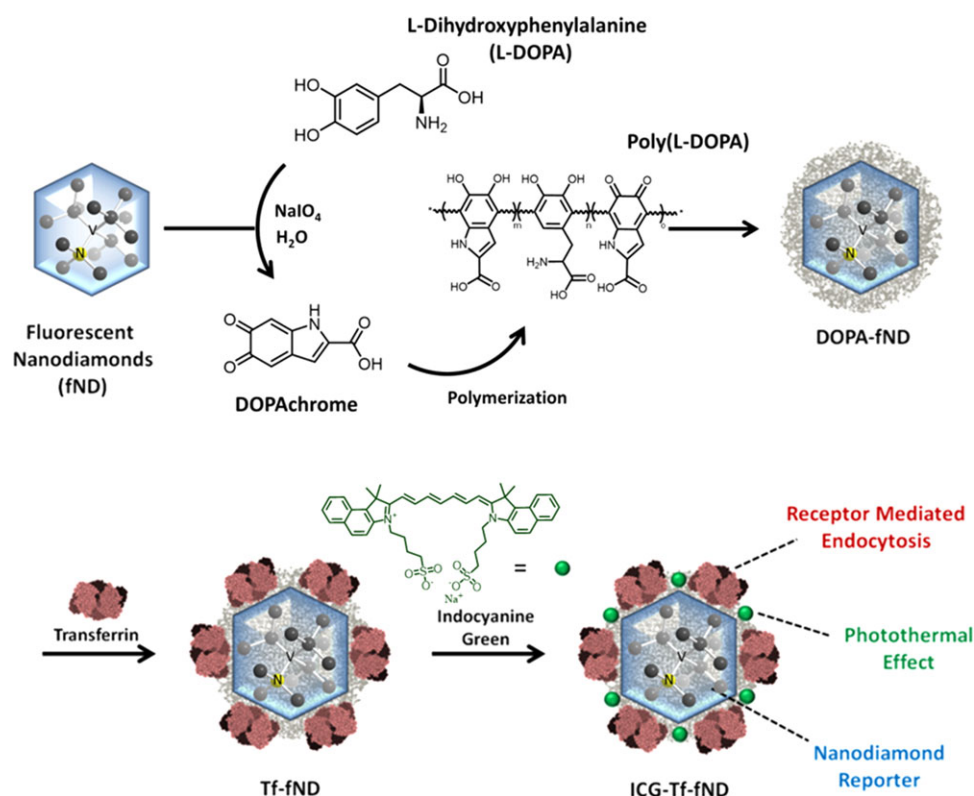THERAPEUTICS**

www.advtherap.com

Figure 1. Schematic illustration of fND nanosystem preparation.

While it is synthetically challenging for a coating methodology that performs consistently well regardless of surface properties, nature has aptly demonstrated otherwise. Derived from mussel foot proteins, the polymerization of catechol pendant groups is the key for the attachment of mussel bivalves onto virtually any surface. Messersmith et al. first showed that polymers of catecholamines, in particular dopamine, can replicate the adhesiveness of the mussel foot.[18] The significance of polydopamine was quickly realized resting on its capability to adapt to various surface functions. This behavior was also observed for other catecholamines, such as L-3,4-dihydroxyphenylalanine (L-DOPA)[19–22] and norepinephrine.[23–25] Chemically, polycatecholamine films possess important functional groups including amines, alcohols, and conjugated Michael acceptors leading to a massive variety of post-functionalized surfaces.[18,26,27] In this context, polydopamine has been demonstrated recently as a proof of concept to functionalize NDs.[28,29] Polydopamine–ND systems represent an attractive platform. However, post-functionalization with, for example, polyethylene glycol has been crucial due to the high adhesiveness of polydopamine that potentially contributes to the aggregation of the coated nanodiamonds, especially under physiological buffer conditions.[30] In comparison, L-DOPA contains an additional carboxylic group giving poly(L-DOPA) coatings a higher hydrophilicity compared to polydopamine.[18,19]

Herein, we show that poly(L-DOPA) does not only act as a polar and versatile bridging entity to conjugate multiple functional entities onto fNDs but also enhances its photothermal capability to develop a complex fND therapeutic platform (**Figure 1**). Furthermore, we establish the strategy of polymerization of L-DOPA

on fNDs from different sources (FND Biotech, Microdiamant) by monitoring the kinetics of polymerization, the control over thickness and colloidal stability under physiological conditions. The effect of the poly(L-DOPA) coating on the photoluminescence and optically detected magnetic resonance were studied, and these unique photophysical properties were preserved for fNDs with thin surface coating. Subsequently, the coated fNDs were further decorated by transferrin, a heme cell membrane protein involved in receptor-specific cellular uptake that stabilizes the biohybrid in cellular media and the FDA-approved indocyanine green (ICG) as a photothermal agent. By localizing a high concentration of ICG in cellular vesicle nanoenvironments, we envision that the integrated material will provide high photothermal toxicity even at very low energy intake.

2. Results and Discussion

2.1. Preparation and Characterization of L-DOPA-Coated Nanodiamonds

Nanodiamonds with 35 nm average diameter were purchased from FND Biotech (Taiwan) and used without further surface treatment. Sodium periodate initiated polymerization of dopamine, and L-DOPA in pure MilliQ water was used to avoid buffer salts, which are known to destabilize colloidal NDs.[15] In addition, this method provides faster deposition times than polymerization in alkaline buffers[31–33] further reducing ND aggregation. In contrast to the well-established dopamine surface
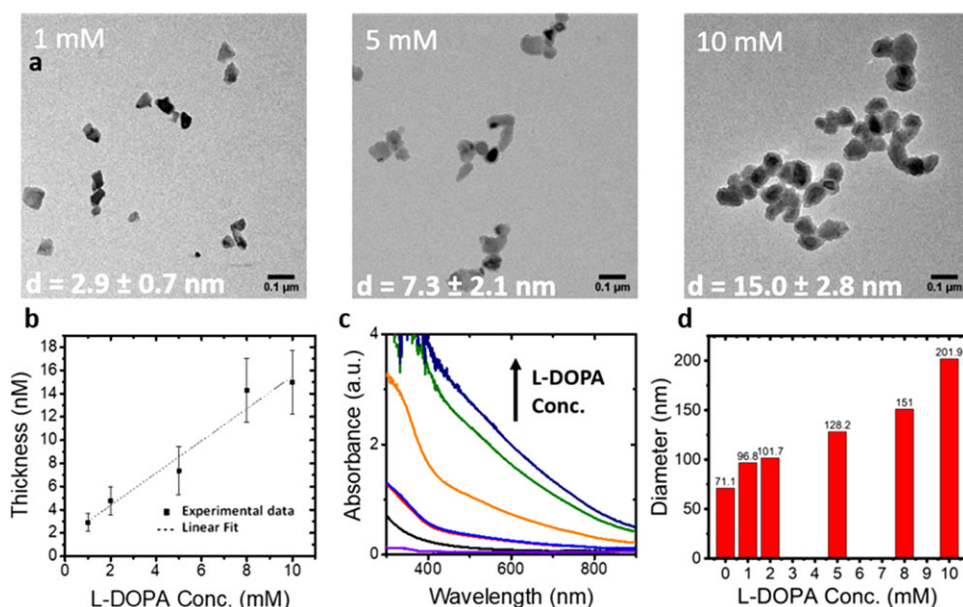
**ADVANCED
SCIENCE NEWS**
www.advancedsciencenews.com

**ADVANCED
THERAPEUTICS**
www.advtherap.com

Figure 2. a) Transmission electron microscope images of DOPA-fND prepared with different concentrations of L-DOPA. Data presented as mean ± SEM, $n = 44$. b) Poly(L-DOPA) shell thickness increases linearly with L-DOPA concentration ($n = 44$). c) UV–vis absorption spectra of aqueous solutions of DOPA-fND (100 µg mL^{-1}) showing broadband absorbance into the NIR. d) Dynamic light scattering data. Hydrodynamic diameter of DOPA-fND increases with increasing L-DOPA concentrations.

polymerization, L-DOPA provides an additional carboxylic group and poly(L-DOPA) coatings exhibit higher hydrophilicity than polydopamine.[20,21] We anticipate that poly(L-DOPA) would show a greater potential in enhancing the aqueous stability of fNDs. In our experimental setup, 100 µg fNDs were dispersed in MilliQ water under sonication. To this solution was added a volume of freshly prepared L-DOPA or dopamine (2.5 mg mL^{-1}) solution in MilliQ to bring the final catecholamine concentration to 1–10 mM. This mixture was heated to 55 °C and sonicated for 5 min to ensure thorough mixing. Finally, an appropriate volume of freshly prepared sodium periodate solution (10.84 mg mL^{-1}) was added to give 0.5 molar equivalents (sodium periodate to catecholamine) and bring the final volume to 1 mL. The solution was sonicated for further 5 min at 55 °C. The reaction was continued on a shaker at 500 rpm for additional 15 min. The coated fNDs were purified by five centrifugation and washing cycles through an ultrafiltration tube (100 kDa). UV–vis spectroscopy showed that unreacted monomer and excess oxidation products were removed after three cycles (Figure S1e, Supporting Information). While fNDs coated in the L-DOPA were colloidally stable, fNDs coated with polydopamine exhibited a high degree of aggregation, lower polymerization efficiency, and poorer aqueous stability (Figures S1 and S12, Supporting Information). The applicability of the L-DOPA coating methodology was evaluated under transmission electron microscopy with three different batches and two different sources of fNDs (FND Biotech, Microdiamant) yielding the DOPA-fNDs (**Figure 2**a and Figure S2, Supporting Information). The poly(L-DOPA) coating can be clearly seen on each fND, which are well dispersed across the TEM grid with small aggregates attributed to drying effects (Figure 2a,b and Figure S2, Supporting Information). The poly(L-DOPA) coating was further confirmed by dynamic light scattering (DLS; Figure S12, Supporting Information), X-ray photoelectron spectroscopy

(XPS), and Raman and Fourier transform Infrared (FT-IR) spectroscopies demonstrating a positive outlook toward its applicability across different ND sources (Figure 2d and Figures S3–S5, Supporting Information). In addition, the polymerization method allows controlling the thickness of poly(L-DOPA) by simply varying the concentration of the monomer. Between 1–10 mM of L-DOPA, the thickness varies linearly from 3–15 nm, suggesting that the synthesis is robust and predictable. The aforementioned thicknesses were simultaneously characterized by the absorbance of poly(L-DOPA), DLS, and TEM (Figure 2). DOPA$_{15nm}$-fND with 15 nm shell thickness was obtained using 10 mM L-DOPA, and XPS was used to elucidate molecular information and ascertain the bonds formed during polymerization. Against pure fND, L-DOPA, and poly(L-DOPA) as controls, the characteristic signals from the C—N—C, C=N—C bonds clearly demonstrate the cyclization of L-DOPA as an intermediate into its polymeric form (Figure S3, Supporting Information). Moreover, the relative photoelectron count of the C–O, C=O, C—C$_{sp3}$, and C—C$_{sp2}$ signals indicate contributions from both the fND surface as well as from poly(L-DOPA). As the polymerization of L-DOPA proceeds via a radical mechanism,[26,34] it is essential to characterize the influence of the coating toward the magnetic properties of the fND.

2.2. Physical Properties of L-DOPA Coated Nanodiamonds

In this respect, the effect of poly(L-DOPA) with two different thicknesses (3 and 15 nm) to the NV's properties in fNDs was investigated. Spectra measurements were performed on a custom-built confocal microscope with the excitation laser light at 515 and 532 nm. The spectra of coated fNDs reveal that the poly(L-DOPA) layer adds a unique background signal (**Figure 3**a). The
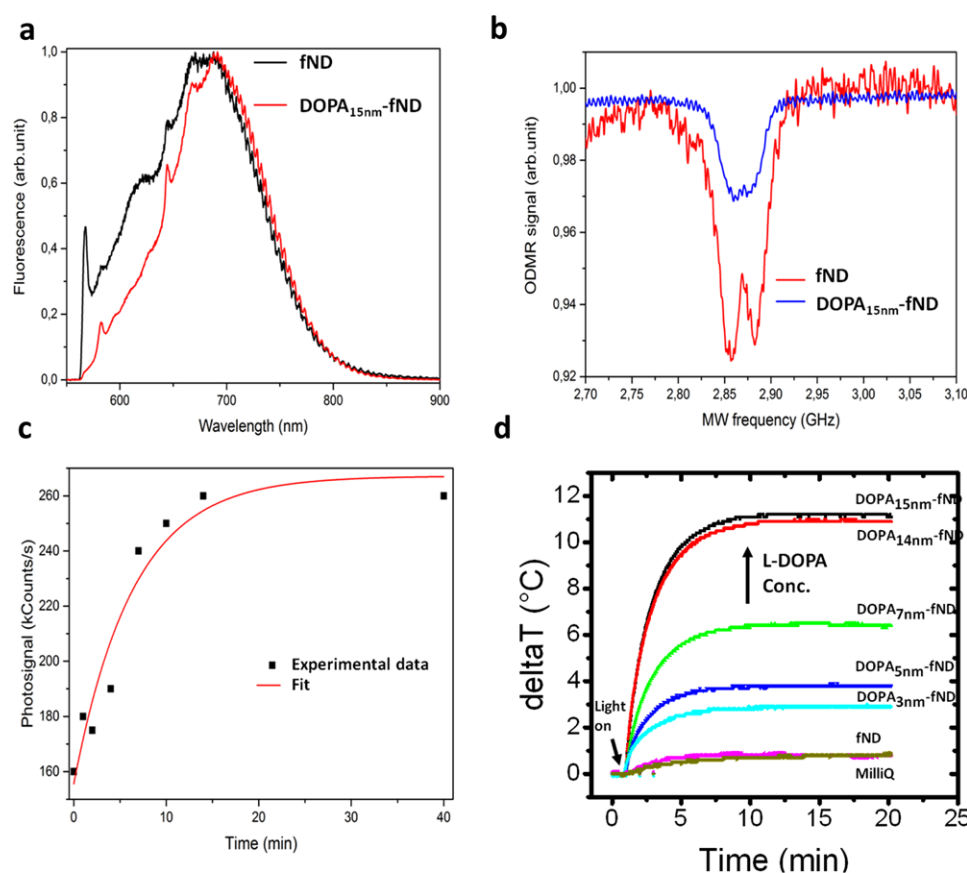
ADVANCED
SCIENCE NEWS
www.advancedsciencenews.com

ADVANCED
THERAPEUTICS
www.advtherap.com

Figure 3. a) Normalized emission spectra (ex. 532 nm) for fND and DOPA$_{15nm}$-fND. NV^0 and NV$^-$ zero phonon lines are visible in both spectra. Fluorescence of poly(L-DOPA) coating evident between 570 and 700 nm. b) Nanodiamonds with PDA layer (15 nm) demonstrate stable ODMR lines; however, the presence of PDA layer decrease the contrast of ODMR. It can be related to background fluorescence from PDA. c) The fluorescence of DOPA-fND increases with time of laser illumination. Fluorescence increase is stable in time. d) Temperature increase of aqueous solutions of various concentrations of DOPA-fND (100 µg mL^{-1} fND) after near-infrared (NIR) irradiation (810 nm lamp; 1 W cm^{-2}).

intensity of the background signal depends on the thickness of the layer but the zero phonon lines of NV$^-$ and NV^0 centers are well visible in each sample. A decrease in the initial fluorescence intensity proportional to the coating thickness was observed for DOPA-fND (Figure S6, Supporting Information) attributed to the broadband absorbance of polycatecholamines. Unexpectedly, independent of the wavelength of the laser light, the detected fluorescence increased over 60% from the initial excitation and reached saturation level within a few minutes (Figure 3c) as measured for 20 DOPA$_{15nm}$-fND. The high level of fluorescence is stable in time after cessation of laser excitation and remains so even after 4 h in darkness (Figures S7 and S8, Supporting Information), which enables more advanced imaging with tracking of nanodiamonds without double counting of the same particle.

To study the charge properties of NV centers in fNDs, optically detected magnetic resonance (ODMR) was observed. Resolved ODMR lines (Figure 3b) prove the presence of NV$^-$ centers in NDs after poly(L-DOPA) coating, indicating its suitability for sensing applications. The decrease of ODMR contrast is attributed to background light from the poly(L-DOPA) layer. However, deeper investigations of the spin properties of NV center in poly(L-DOPA)-coated NDs are currently ongoing.

Due to the presence of oligomeric and polymeric components of various order within the structure, polycatecholamines are good energy absorbers from UV to NIR.[26,35–37] Furthermore, absorbed light is converted to heat with high efficiency allowing their application as photothermal agents.[38] Photothermal agents that are active in the NIR range are of greater interest due to the reduced absorbance by the body in this region.[39,40] We demonstrated that all poly(L-DOPA)-coated fNDs exhibited an enhanced photothermal effect over pure fNDs when irradiated at 810 nm, and achieving greater than 10-fold increase (ΔT = 11.1 °C vs 0.8 °C) in temperature change for DOPA$_{15nm}$-fND (Figure 3d). Although, a higher photothermal effect was observed for DOPA$_{15nm}$-fND, we chose to continue our experiments with DOPA$_{7nm}$-fND (ΔT = 6.4 °C) providing an appropriate balance between fluorescence intensity and photothermal effects.

2.3. Post-Modification of DOPA-fND for Uptake Studies In Vitro

To investigate the poly(L-DOPA) coating as a homogenized platform for the post-functionalization of fNDs, we examined the conjugation of proteins as stabilizing and biologically active functional entities.[41–43] As a conserved 3D structure of the adsorbed
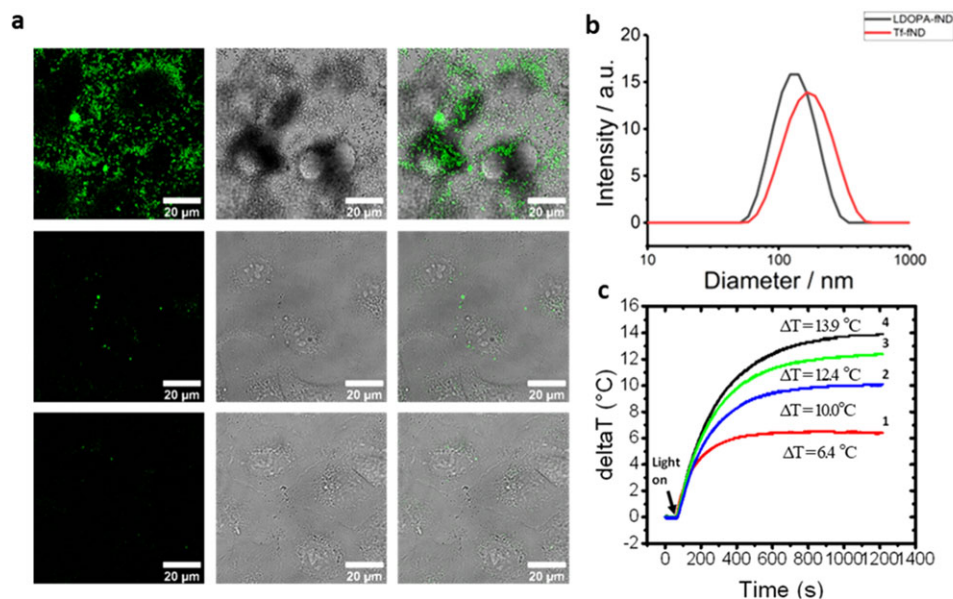
**ADVANCED
SCIENCE NEWS**

www.advancedsciencenews.com

**ADVANCED
THERAPEUTICS**

www.advtherap.com

Figure 4. a) Confocal microscopy images of uptake of DOPA$_{7nm}$-fND (top row) and Tf-fND (middle) in A549 cells (250 µg mL^{-1}). Significant aggregation and sedimentation of DOPA$_{7nm}$-fND visible. Tf-fND uptaken without sedimentation. Bottom row is blank sample. b) Dynamic light scattering data for DOPA$_{7nm}$-fND and Tf-fND. c) Temperature increase of aqueous solutions of DOPA$_{7nm}$-fND (100 µg mL^{-1}) (1), free ICG (100 and 200 µg mL^{-1}) (2 and 3), and ICG-Tf-fND (100 µg mL^{-1}; 190 µg mL^{-1} ICG equiv) (4) after near-infrared (NIR) irradiation (810 nm lamp; 1 W cm^{-2}).

protein is essential for its activity, the impact of its conjugation onto the poly(L-DOPA) coating can be directly assessed in a biological assay system.

Human transferrin (Tf, 79.5 kDa), a heme-containing protein that binds and transports iron through transferrin receptors expressed at the membrane of many cells and has been used to enhance the uptake of nanoparticles,[44,45] was loaded directly onto DOPA-fND by mixing overnight in a mildly alkaline phosphate buffer. Adsorption of transferrin to the surface was likely accomplished through a combination of non-covalent interactions and covalent bonding via the amine-reactive Michael acceptors or carbonyls (Schiff base) of the quinone moieties formed during the polymerization of L-DOPA (Figure S13, Supporting Information), which has been also discussed before for L-DOPA polymers.[46] Unbound protein was removed from the reaction mixture by ultrafiltration (molecular weight cut off = 100 kDa) to afford Tf-fND. Upon loading, the hydrodynamic radius increased from 63 nm for DOPA-fND, to ≈78 nm for Tf-fND, indicating the successful formation of a protein corona around the fND (**Figure 4**b). Successful loading was also confirmed by FT-IR (Figure S9, Supporting Information). The capability of transferrin to initiate receptor-mediated endocytosis of Tf-fND was evaluated using A549 lung adenocarcinoma cell line. In contrast to fND alone or the precursor DOPA-fND, efficient receptor-mediated uptake of Tf-fND was observed through confocal laser scanning microscopy (Figure 4a). Next, we adsorbed ICG, a small molecule dye with innate photothermal properties, onto Tf-fND. The loading of ICG onto Tf-fND was accomplished by overnight incubation of Tf-fND and ICG in the dark with subsequent removal of excess ICG through extensive ultrafiltration to afford ICG-Tf-fND. The amount of ICG loaded was determined through its characteristic absorbance at 400 nm and found to be >180% by

mass compared to the fND (1.89 mg mg^{-1} fND). In this way, a high local concentration of ICG was obtained, which could enhance the photothermal effect of poly(L-DOPA)-coated fNDs. Subsequently, we quantify the photothermal effect of ICG-Tf-fND by observing the differential temperature increase in water upon irradiation at 810 nm. In comparison to DOPA$_{7nm}$-fND (ΔT = 6.4 °C) and ICG (ΔT = 12.4 °C), ICG-Tf-fND (ΔT = 13.9 °C) showed a 120% and 12% improvement, respectively, in terms of temperature increase attained after 20 min of irradiation (Figure 4c). Comparing absolute ICG concentrations, the magnitude difference in temperature profile produced by ICG-Tf-fND suggests that there is an enhancement for the loaded ICG over that of molecularly free ICG. This amplified photothermal effect by confinement was also characteristically observed in hollow inorganic nanoparticles and plasmonic nanoparticle clusters.[47,48] The strong interaction of ICG with Tf-fND was demonstrated by the negligible release of ICG (<5%) from ICG-Tf-fND when incubated in cell media for 24 h (Figure S10, Supporting Information).

2.4. Photothermal Applications In Vitro

We subsequently evaluated ICG-Tf-fND in HeLa and A549 cells. The internalization pathway of ICG-Tf-fND was elucidated by confocal microscopy. The fluorescence signal from ICG (ex. 561 nm, em. 750–800 nm) was imaged. It is interesting to note that the transport of ICG-Tf-fND is represented in a receptor-mediated manner by formation of endosomal vesicles where the fluorescence signals are highly localized (Figure S11, Supporting Information) and no freely diffusing ICG are obtained.
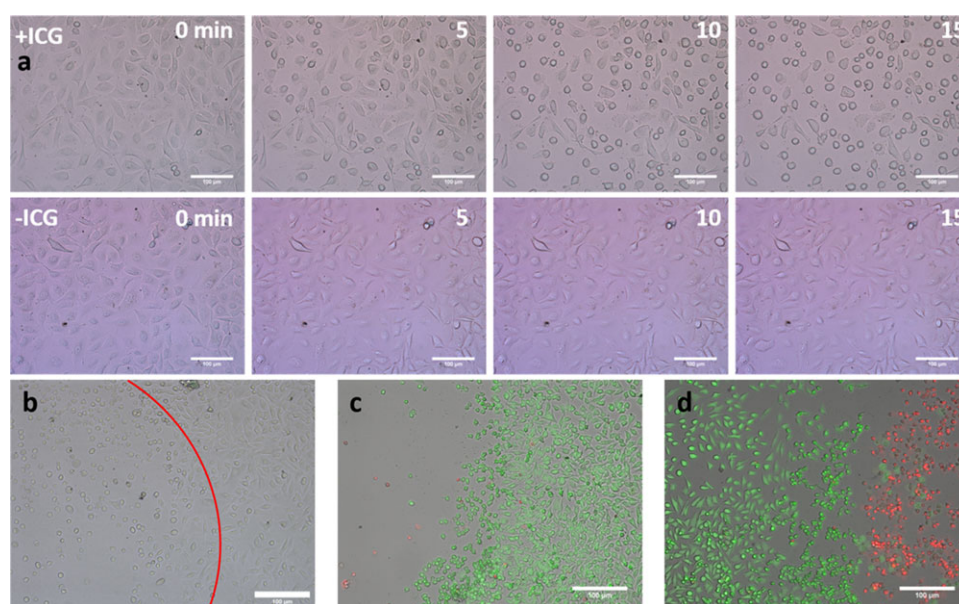
**ADVANCED
SCIENCE NEWS**

www.advancedsciencenews.com

**ADVANCED
THERAPEUTICS**

www.advtherap.com

Figure 5. a) Optical images (20 ×) of HeLa cells incubated overnight with ICG-Tf-fND and Tf-fND at 0, 5, 10, and 15 min after irradiation with 810 nm lamp, 430 mW cm^{-2}. Cell rounding is evident within 5 min in ICG-Tf-fND sample. No morphological changes observed with Tf-fND after 15 min. Scale bar = 100 µm. b) Brightfield image (10 ×) of A549 cells incubated overnight with ICG-Tf-fND imaged 4 h after 15 min irradiation with 810 nm lamp, 90 mW cm^{-2}. Border (marked with red line) between irradiated area and non-irradiated area clearly visible. Scale bar = 100 µm. c) Live and dead staining (10 ×) of HeLa cells incubated overnight with ICG-Tf-fND imaged 4 h after 15 min irradiation with 810 nm lamp, 430 mW cm^{-2}. Dead cells were washed away during preparation leaving an empty region bordered by healthy cells. Scale bar = 100 µm. d) Live and dead staining (10 ×) of HeLa cells incubated overnight with ICG-Tf-fND imaged 4 h after 15 min irradiation with 810 nm lamp, 4 W cm^{-2}. Sharp border clearly observed between live (green) and dead (red) cells. Scale bar = 100 µm.

Molecularly, free ICG rampantly diffuses throughout the cell (Figure S11, Supporting Information), clearly different to ICG-Tf-fND, which also indicates the strong interaction between ICG and Tf-fND.

Upon internalization, the photothermal effect was initiated using an 810 nm lamp (200 mW) concentrated through the objective onto the sample area. Light densities were varied by the magnification of the objective (10 ×, 20 ×, 40 ×) and supplied current. Simultaneously, time-lapsed optical images were recorded in 20 s intervals to visualize the morphological changes due to the localized heating effect by ICG-Tf-fND. First, various light densities (0.09, 0.4, and 4.0 W cm^{-2}) for the irradiation process were conducted to identify the optimum power for photothermal-induced cytotoxicity within 15 min. Efficient and immediate cell rounding (under 5 min) was visually observed at light densities of 0.4 and 4.0 W cm^{-2} (**Figure 5**a and Movies S1 and S2, Supporting Information). Even very low light densities down to 0.09 W cm^{-2} induced cell rounding visually detected within 10 min with cell death thereafter (Figure 5b and Movie S3, Supporting Information), a remarkably low power density compared to the previously reported ICG–polydopamine–ND conjugate which required over an order of magnitude higher power (2 W cm^{-2}).[29] Live/dead staining of the cells using fluorescein diacetate/propidium iodide combination further demonstrates the characteristic spatial control of the light-induced cell death (Figure 5c,d). In comparison, no cell death and only minor morphological changes upon irradiation were observed for Tf-fND or fND + ICG mixture at any power density (Figure 5a and Movies S4 and S5, Supporting Information).

3. Conclusion

In summary, we have described a hierarchical construction of a nanodiamond-based theranostic system through a poly(L-DOPA) coating that serves as a sticky layer for chemical functionalization. By selecting the protein transferrin and the small molecule dye ICG as two biologically active molecular components, we demonstrate that the poly(L-DOPA) is an excellent avenue for post-modification with both small molecules and proteins. Notably, the poly(L-DOPA) coating stabilizes the optical properties of NV centers in the nanocrystals, and at the same time, it has no negative effects on the charge state of NV$^-$ defects, which is crucial for future imaging and sensing applications.

Critical for effective dosing of deep-seated tumors due to the exponential attenuation of light, the activation threshold for the photothermal effect was at least ten times lower compared to other nanodiamond-based systems.[49–52] The endocytic transport behavior and the immediate cellular response toward localized heating, observed in confocal and time-lapsed microscopy, clearly demonstrate the efficiency of the system.

Compared to other fluorescent nanoparticles, fNDs have shown promise for in vitro and in vivo application due to their high photostability. Tracking of particles in real time over long periods can reveal information about biodistribution whereas the defect centers (e.g., NV$^-$, Si) enable sensing of temperature as a nanoscale thermometer to monitor photothermal effects in situ. To date, nanodiamonds have already been applied successfully in vivo for many animal models (mouse,[16] chicken embryo,[53] and miniature pig[54]).[55]

**ADVANCED
SCIENCE NEWS**

www.advancedsciencenews.com

**ADVANCED
THERAPEUTICS**

www.advtherap.com

We envision that the combination of optical and magnetic detection and ultra-low power density required for phototoxicity could open new avenues to the noninvasive treatment of malignant tumors deep within the body, which could reach tissue in the brain, prostate, colorectal, and pancreas. Collectively, the presented methodology rapidly facilitates the general preparation of customized multifunctional fNDs, in which a broad selection of functional components such as proteins and drugs could be used in combination.

Supporting Information

Supporting Information is available from the Wiley Online Library or from the author.

Acknowledgements

Conflict of Interest

The authors declare no conflict of interest.

Keywords

[1] V. N. Mochalin, O. Shenderova, D. Ho, Y. Gogotsi, *Nat. Nanotechnol.* **2012**, *7*, 11.

[2] Y. Wu, F. Jelezko, M. B. Plenio, T. Weil, *Angew. Chem., Int. Ed.* **2016**, *55*, 6586.

[3] R. Schirhagl, K. Chang, M. Loretz, C. L. Degen, *Annu. Rev. Phys. Chem.* **2014**, *65*, 83.

[4] R. L. Walsworth, H. Zhang, I. Aharonovich, J. W. Lichtman, D. R. Glenn, R. Schalek, E. L. Hu, A. P. Magyar, *Small* **2014**, *10*, 1908.

[5] S. Choi, V. Leong, V. A. Davydov, V. N. Agafonov, M. W. O. Cheong, D. A. Kalashnikov, L. A. Krivitsky, *Sci. Rep.* **2018**, *8*, 3792.

[6] T. Inubushi, N. Mizuochi, F. Ishibashi, M. Hatano, Y. Doi, Y. Miyamoto, L. J. Rogers, S. Kobayashi, S. Yamasaki, F. Jelezko, S. Nagamachi, B. Naydenov, K. Tahara, K. D. Jahnke, T. Iwasaki, T. Miyazaki, *Sci. Rep.* **2015**, *5*, 12882.

[7] M. H. Alkahtani, F. Alghannam, L. Jiang, A. Almethen, A. A. Rampersaud, R. Brick, C. L. Gomes, M. O. Scully, P. R. Hemmer, *Nanophotonics* **2018**, *7*, 1423.

[8] M. Chipaux, K. J. van der Laan, S. R. Hemelaar, M. Hasani, T. Zheng, R. Schirhagl, *Small* **2018**, *14*, 1704263.

[9] K. van der Laan, M. Hasani, T. Zheng, R. Schirhagl, *Small* **2018**, *14*, 1703838.

[10] S. Claveau, J. R. Bertrand, F. Treussart, *Micromachines* **2018**, *9*, 1.

[11] D. Ho, C.-H. K. Wang, E. K.-H. Chow, *Sci. Adv.* **2015**, *1*, e1500439.

[12] W. W. W. Hsiao, Y. Y. Hui, P. C. Tsai, H. C. Chang, *Acc. Chem. Res.* **2016**, *49*, 400.

[13] A. Nagl, S. R. Hemelaar, R. Schirhagl, *Anal. Bioanal. Chem.* **2015**, *407*, 7521.

[14] S. Mouradian, B. Lienhard, M. Walsh, H. Bakhru, B. J. Shields, T. Schröder, D. Englund, D. Kim, N. H. Wan, *Nano Lett.* **2018**, *18*, 2787.

[15] S. R. Hemelaar, A. Nagl, F. Bigot, M. M. Rodríguez-García, M. P. de Vries, M. Chipaux, R. Schirhagl, *Microchim. Acta* **2017**, *184*, 1001.

[16] M. D. Torelli, A. G. Rickard, M. V. Backer, D. S. Filonov, N. A. Nunn, A. V. Kinev, J. M. Backer, G. M. Palmer, O. A. Shenderova, *Bioconjugate Chem.* **2019**, *30*, 604.

[17] D. Wang, Y. Tong, Y. Li, Z. Tian, R. Cao, B. Yang, *Diamond Relat. Mater.* **2013**, *36*, 26.

[18] H. Lee, S. M. Dellatore, W. M. Miller, P. B. Messersmith, *Science* **2007**, *318*, 426.

[19] S. Azari, L. Zou, *J. Membr. Sci.* **2012**, *401–402*, 68.

[20] J. Kuang, J. L. Guo, P. B. Messersmith, *Adv. Mater. Interfaces* **2014**, *1*, 1400145.

[21] L. Yu, X. Liu, W. Yuan, L. J. Brown, D. Wang, *Langmuir* **2015**, *31*, 6351.

[22] H. Guo, Y. Sun, X. Niu, N. Wei, C. Pan, G. Wang, H. Zhang, H. Chen, T. Yi, X. Chen, *J. Chromatogr. A* **2018**, *1578*, 91.

[23] S. M. Kang, J. Rho, I. S. Choi, P. B. Messersmith, H. Lee, *J. Am. Chem. Soc.* **2009**, *131*, 13224.

[24] Y. Liu, G. Zhou, Z. Liu, M. Guo, X. Jiang, M. Berat Taskin, Z. Zhang, J. Liu, J. Tang, R. Bai, F. Besenbacher, M. Chen, C. Chen, *Sci. Rep.* **2017**, *7*, 8197.

[25] S. Hong, J. Kim, Y. Suk Na, J. Park, S. Kim, K. Singha, G.-I. Im, D.-K. Han, W. Jong Kim, H. Lee, *Angew. Chem., Int. Ed.* **2013**, *52*, 9187.

[26] J. Yang, M. A. Cohen Stuart, M. Kamperman, *Chem. Soc. Rev.* **2014**, *43*, 8271.

[27] J. H. Ryu, P. B. Messersmith, H. Lee, *ACS Appl. Mater. Interfaces* **2018**, *10*, 7523.

[28] Y. Zeng, W. Liu, Z. Wang, S. Singamaneni, R. Wang, *Langmuir* **2018**, *34*, 4036.

[29] D. Maziukiewicz, B. Grześkowiak, E. Coy, S. Jurga, R. Mrówczyński, *Biomimetics* **2019**, *4*, 3.

[30] H.-S. Jung, K.-J. Cho, Y. Seol, Y. Takagi, A. Dittmore, P. A. Roche, K. C. Neuman, *Adv. Funct. Mater.* **2018**, *28*, 1801252.

[31] F. Ponzio, J. Barthès, J. Bour, M. Michel, P. Bertani, J. Hemmerlé, M. D'Ischia, V. Ball, *Chem. Mater.* **2016**, *28*, 4697.

[32] M. Salomäki, L. Marttila, H. Kivelä, T. Ouvinen, J. Lukkari, *J. Phys. Chem. B* **2018**, *122*, 6314.

[33] D. Kyoung Yeon, S. Ko, S. Jeong, S.-P. Hong, S. Min Kang, W. Kyung Cho, *Langmuir* **2019**, *35*, 1227.

[34] G. Brucheltc, V. A. Roginsky, P. Schuler, H. B. Stegmann, H. Köhle, *Z. Naturforsch. C* **2018**, *50*, 715.

[35] J. Liebscher, R. Mrówczyński, H. A. Scheidt, C. Filip, N. D. Haìdade, R. Turcu, A. Bende, S. Beck, *Langmuir* **2013**, *29*, 10539.

[36] E. Kaxiras, A. Tsolakidis, G. Zonios, S. Meng, *Phys. Rev. Lett.* **2006**, *97*, 218102.

[37] M. L. Tran, B. J. Powell, P. Meredith, *Biophys. J.* **2006**, *90*, 743.

[38] Y. Liu, K. Ai, J. Liu, M. Deng, Y. He, L. Lu, *Adv. Mater.* **2013**, *25*, 1353.

[39] E. Pastrana, *Nat. Methods* **2013**, *10*, 36.

**ADVANCED
SCIENCE NEWS**

www.advancedsciencenews.com

**ADVANCED
THERAPEUTICS**

www.advtherap.com

[40] L. Zou, H. Wang, B. He, L. Zeng, T. Tan, H. Cao, X. He, Z. Zhang, S. Guo, Y. Li, *Theranostics* **2016**, *6*, 762.

[41] C. D. Spicer, C. Jumeaux, B. Gupta, M. M. Stevens, *Chem. Soc. Rev.* **2018**, *47*, 3574.

[42] A. Beck, L. Goetsch, C. Dumontet, N. Corvaïa, *Nat. Rev. Drug Discovery* **2017**, *16*, 315.

[43] C. L. Ventola, *Pharm. Ther.* **2017**, *42*, 742.

[44] J. Young Yhee, S. J. Lee, S. Lee, S. Song, H. S. Min, S.-W. Kang, S. Son, S. Y. Jeong, I. C. Kwon, S. H. Kim, K. Kim, S. Korea, *Bioconjugate Chem.* **2013**, *24*, 1850.

[45] D. Hauser, M. Estermann, A. Milosevic, L. Steinmetz, D. Vanhecke, D. Septiadi, B. Drasler, A. Petri-Fink, V. Ball, B. Rothen-Rutishauser, *Nanomaterials* **2018**, *8*, 1065.

[46] L. Zhu, J. Yu, Y. Xu, Z. Xi, B. Zhu, *Colloids Surf., B* **2009**, *69*, 152.

[47] D. Lapotko, *Nanomedicine* **2009**, *4*, 813.

[48] B. Vaz, V. Salgueiriño, M. Pérez-Lorenzo, M. A. Correa-Duarte, *Langmuir* **2015**, *31*, 8745.

[49] D. Maziukiewicz, B. Grześkowiak, E. Coy, S. Jurga, R. Mrówczyński, *Biomimetics* **2019**, *4*, 3.

[50] L.-C. Cheng, H. M. Chen, T.-C. Lai, Y.-C. Chan, R.-S. Liu, J. C. Sung, M. Hsiao, C.-H. Chen, L.-J. Her, D. P. Tsai, *Nanoscale* **2013**, *5*, 3931.

[51] T. K. Ryu, S. W. Baek, R. H. Kang, S. W. Choi, *Adv. Funct. Mater.* **2016**, *26*, 6428.

[52] T.-K. Ryu, S.-W. Baek, R.-H. Kang, K.-Y. Jeong, D.-R. Jun, S.-W. Choi, *J. Controlled Release* **2018**, *270*, 237.

[53] Y. Wu, A. Ermakova, W. Liu, G. Pramanik, T. M. Vu, A. Kurz, L. McGuinness, B. Naydenov, S. Hafner, R. Reuter, J. Wrachtrup, J. Isoya, C. Förtsch, H. Barth, T. Simmet, F. Jelezko, T. Weil, *Adv. Funct. Mater.* **2015**, *25*, 6576.

[54] L.-J. Su, M.-S. Wu, Y. Y. Hui, B.-M. Chang, L. Pan, P.-C. Hsu, Y.-T. Chen, H.-N. Ho, Y.-H. Huang, T.-Y. Ling, H.-H. Hsu, H.-C. Chang, *Sci. Rep.* **2017**, *7*, 45607.

[55] K. van der Laan, M. Hasani, T. Zheng, R. Schirhagl, *Small* **2018**, *14*, 1703838.

WILEY-VCH

Supporting Information

Transferrin-Coated Nanodiamond-Drug Conjugates for Milliwatt Photothermal Applications

Sean Harvey, Marco Raabe, Anna Ermakova, Yingke Wu, Todd Zapata, Chaojian Chen, Hao Lu, Fedor Jelezko, David Y.W. Ng, Tanja Weil*

Materials and Methods

Fluorescent nanodiamonds were bought from FND Biotech or provided from Microdiamond. Dulbecco's Modified Eagle's Medium (DMEM, 1x), Dulbecco's Phosphate-Buffered Saline (DPBS, 1x), Fetal Bovine Serum (FBS), MEM Non-Essential Amino Acids Solution (MEM NEAA, 100x) and Penicillin Streptomycin (Pen Strep) were purchased from gibco. Dopamine, L-DOPA and human transferrin were purchased from Sigma-Aldrich.

Statistical Analysis

Where given the data are presented as mean ± SD. Sample sizes are given in figure caption.

Preparation of DOPA-fND

Fluorescent nanodiamonds (fNDs) were dispersed in MilliQ water using an ultrasonic bath for 30 min. For a typical 500 μl batch of DOPA-fND 5mM, 50 μg of fNDs and 197.2 μl of L-DOPA (2.5 mg mL^{-1}) were mixed in MilliQ water and sonicated in a water batch at 55 °C for 5 min. To the fND L-DOPA solution was added 24.7 μl of sodium periodate solution in water (10.84 mg mL^{-1}). The final concentrations of fND, L-Dopa and sodium periodate were 100 μg mL^{-1}, 5 mM, and 2.5 mM, respectively. The mixture was sonicated in a water batch at 55 °C for 5 min and shaken at room temperature at 500 rpm for 15 min. The coated fNDs (DOPA-fND) were purified by ultrafiltration (100 kDa cutoff, 4000 xg, 5 min); washing 5 times.

Preparation of Tf-fND

DOPA-fND was re-dispersed using an ultrasonic bath for 90 min. For a typical 500 μl batch of DOPA-fND 5 mM transferrin, DOPA-fND (50 μg fND) was added to a 500 μl of transferrin (1 mg mL^{-1}) in phosphate buffer (10 mM, pH 8.5) under sonication for 5 min. The mixture was shaken overnight at room temperature at 500 rpm. The DOPA-fND transferrin (Tf-fND) was purified by ultrafiltration (100 kDa cutoff, 4000 xg, 5 min); washing 5 times.

Preparation of ICG-Tf-fND

Tf-fND was re-dispersed using an ultrasonic bath for 90 min. For a typical 500 μl batch of ICG-Tf-fND, Tf-fND (50 μg fND) was added to 500 μl of indocyanine green (ICG, 1 mg mL^{-1}) in MilliQ water under sonication for 5 min in the dark. The mixture was shaken overnight at room temperature at 500 rpm in the dark. The Tf-fND loaded with ICG (ICG-Tf-fND) was purified by ultrafiltration (100 kDa cutoff, 4000 xg, 5 min); washing 5 times.

Transmission Electron Microscopy

One drop of a 0.1 mg mL^{-1} solution of DOPA-fND (different concentration of L-dopa) in MilliQ was placed onto an oxygen treated copper grid. A Jeol 1400 transmissions electron microscope was used to obtain bright field images. See Figure S2.

UV-Vis Absorbance

10 µl of fND, **DOPA-fND, Tf-fND, or ICG-Tf-fND s**olutions in MilliQ water (100 µg mL^{-1}) were prepared in separate wells of 384 well low volume well plate. Absorbance scans from 200 to 1000 nm were obtained using a Tecan Spark20M.

Dynamic Light Scattering

200 µl of 0.2 mg mL^{-1} solutions of fND, DOPA-fND and ICG-Tf-fND in MilliQ were transferred into a borosilicate glass cuvette. The size was measured at 20 °C with a 90° angle using a Malvern Zetasizer Nano-S90 (Nano series). The hydrodynamic diameter distribution was presented as intensity.

Fluorescence

10 µl of fND, **DOPA-fND, Tf-fND, or ICG-Tf-fND s**olutions in MilliQ water (100 µg mL^{-1}) were prepared in separate wells of 384 well low volume well plate. Fluorescence Intensity scans were obtained using a Tecan Spark20M. An excitation wavelength of 520 nm was used for emission scans. An emission wavelength of 700 nm was monitored for excitation scans

Optically Detected Magnetic Resonance

To investigate the effect from polydopamine coating to spin properties of Nitrogen-Vacancy (NV) centers in fNDs Optically Detected Magnetic Resonance (ODMR) measurements were performed. It was done at the home build confocal microscope. FNDs were dropped on a glass substrate. Next to fNDs a wire was placed, which was used to apply microwave (MW) field to manipulate spin state of NV- centers. FNDs were constantly illuminated by laser light (532 nm), MW was tuned from 2.7 to 3.1 GHz. Fluorescence was detected by avalanche photodiode for better sensitivity

Confocal Microscopy

To study the cellular uptake mechanism, A549 cells were plated onto a Greiner Bio-One™ CELLview™ Cell Culture Slides 10-well plate at a density of 75 000 cells mL^{-1} in 100 µl cell medium (Dulbecco's Modified Eagle's Medium + 10% FBS, 1% MEM NEAA, 1% PenStrep). The cells were incubated overnight for attachment at 37 °C in 5% CO$_2$. The next day, the cell medium was removed and replaced by DOPA-fND (250 µg mL^{-1}) and Tf-fND (250 µg mL^{-1}) or free ICG (0.4 mg mL^{-1}) and ICG-Tf-fND (250 µg mL^{-1}) each in 100 µl cell medium. The cells were incubated at 37 °C in 5% CO$_2$ for overnight or 2 h. For imaging, the cells were washed once with Dulbecco's Phosphate-Buffered Saline (DPBS) and 100 µl of fresh cell media was added. Imaging was then performed using a Leica TCS SP5 scanning confocal microscope system coupled to a 63× water immersion objective. The emission of DOPA-fND, Tf-fND, free ICG and ICG-Tf-fND was recorded using a 561 nm laser for excitation and 660–700 nm filter for emission.

X-ray Photoelectron Spectroscopy

3 µl of fND or **DOPA-fND** solutions in MilliQ water (1 mg mL^{-1}) were deposited on a gold substrate and dried at 40 °C. XPS was conducted using a Kratos Axis UltraDLD spectrometer

(Kratos, Manchester, England) using an Al Kα excitation source with a photon energy of 1487 eV. The data was acquired in the hybrid mode using a 0° take-off angle, defined as the angle between the surface normal and the axis of the analyzer lens. Detailed region XP spectra were collected with setting analyzer pass energy at 80 eV, and a linear background was subtracted for all peak quantifications. The peak areas were normalized by the manufacturer supplied sensitivity factors and surface concentrations were calculated using CasaXPS software. N 1s, C 1s and O 1s high-resolution spectra were collected with analyzer pass energy of 20 eV. Neutralizer was always used during spectra collection.

RAMAN Spectroscopy

3 µl of fND or **DOPA-fND** solutions in MilliQ water (1 mg mL^{-1}) were deposited on a gold substrate and dried at 40 °C. RAMAN spectroscopy was conducted a Bruker Senterra instrument. A 785 nm laser (20 mW) focused through a 20× objective was used with an acquisition time of 25 seconds.

Fourier Transform Infrared Spectroscopy

Three microliters of fND or **DOPA-fND** solutions in MilliQ water (1 mg mL^{-1}) were deposited on a gold substrate and dried at 40 °C. FT-IR spectra were obtained by a Nicolet 730 FT‐IR spectrometer in ATR mode using 32 scans.

In vitro **Photothermal**

200 µl of fND, **DOPA-fND, Tf-fND, and ICG-Tf-fND** solutions in MilliQ water (100 µg mL^{-1}) were prepared in separate wells of a 96 well plate. The wells were covered with parafilm and a thin thermocouple lead was inserted into liquid. Each sample was irradiated with a 810 nm lamp (Thorlabs M810L3-C1) focused through the 10x objective of a Leica DMi8 microscope. The temperature was recorded over a 20 min period. The power density was calculated to be 1 W cm^{-2}.

A549 or HeLa cells were plated onto µ-Dish ibidi (35 mm, low) at a density of 75 000 cells mL^{-1} in 500 µl cell medium (Dulbecco's Modified Eagle's Medium + 10% FBS, 1% MEM NEAA, 1% PenStrep). The cells were incubated overnight for attachment at 37 °C in 5% CO$_2$. The next day, the medium was removed and replaced by Tf-fND (100 µg mL^{-1}) and ICG-Tf-fND (100 µg mL^{-1}) each in 500 µl cell medium. The cells were incubated at 37 °C in 5% CO$_2$ overnight. For photothermal experiments, the cells were washed once with Dulbecco's Phosphate-Buffered Saline (DPBS) and 500 µl of fresh cell media was added.

The culture dishes were placed in an incubator to maintain the temperature at 37 °C. Each sample was irradiated with a 810 nm lamp (Thorlabs M810L3-C1) focused through the 20× objective of a Leica DMi8 microscope for a period of 15 min. Every twenty seconds images were taken on a full color CCD camera (Leica MC170) attached to the microscope. The images were combined into a time-lapse video with a framerate of 8 images per second. An adjustable power source (Thorlabs LEDD1B) was used to change the light power delivered to the samples.

Dead/Life Staining

After photothermal experiments, cells were incubated 1 h at 37 °C in 5% CO$_2$. Dead/life staining solution was prepared accordingly to the ibidi protocol. In summary, 8 µl fluorescein diacetate (5 mg mL^{-1}) and 100 µl propidium iodide (1 mg mL^{-1}) were added to 5 mL DPBS.

Cell medium was removed and 500 µl of the staining solution was added. After 5 min, the cells were washed three times with DPBS.

Imaging was performed using a Leica DMi8 microscope equipped with a Leica MC170 ND camera, DFC9000GT and a sola light engine lumencor®.
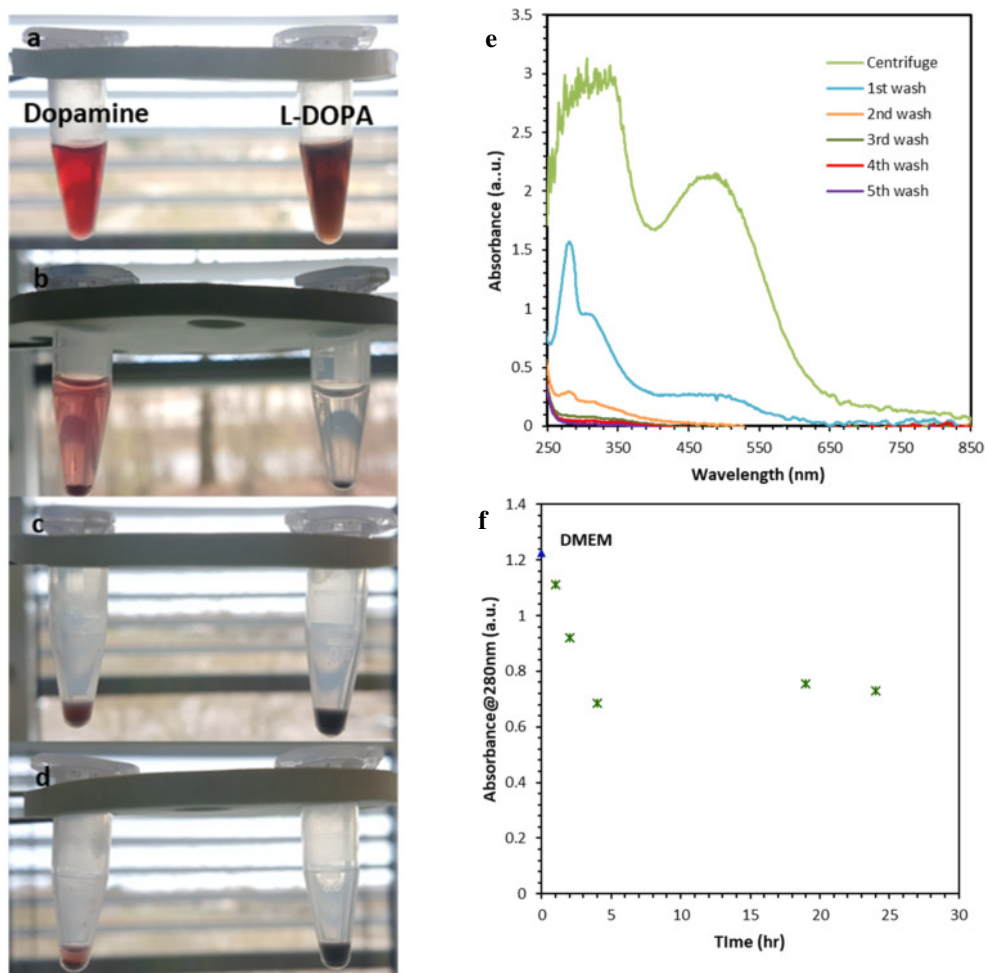
Figure S1. Images of nanodiamonds coated in dopamine (left) or L-DOPA (right) solutions at various stages. (a) 20 min after NaIO₄ addition. L-DOPA shows brown coloration indicative of polycatecholamines. (b) After two centrifugation and washing cycles. Red color remains in supernatant of dopamine sample suggesting incomplete polymerization. (c) Resuspension of nanodiamond pellet. (d) 15 min after resuspension. Sedimentation is visible in dopamine sample. (e) UV-Vis spectroscopy of centrifugation and washing cycles. unreacted monomer and excess oxidation products removed after 3 centrifugation and washing cycles. (f) Release of L-DOPA from **DOPA-fND** in DMEM media monitored at absorption peak of L-DOPA (280 nm). No release of free L-DOPA observed after 24 hours. Decrease in absorbance attributed to absorption of tryptophan and other UV absorbing compounds into poly(L-DOPA) matrix.
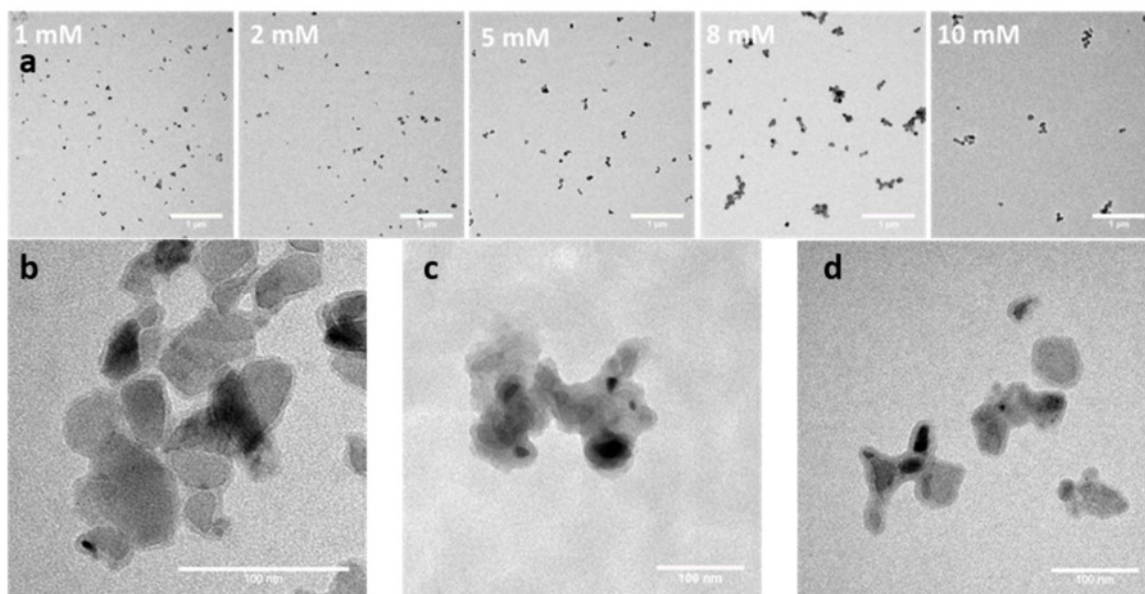
Figure S2. (a) Transmission electron microscope images of **DOPA-fND** prepared with different concentrations of L-DOPA showing lack of agglomeration. (b) Poly(L-DOPA) coating is universal for various batches and sources of nanodiamonds. Microdiamont Leipzig II L-DOPA 1 mM. (c) Microdiamont Leipzig II L-DOPA 10 mM. (d) Microdiamont MD 05 L-DOPA 1 mM.
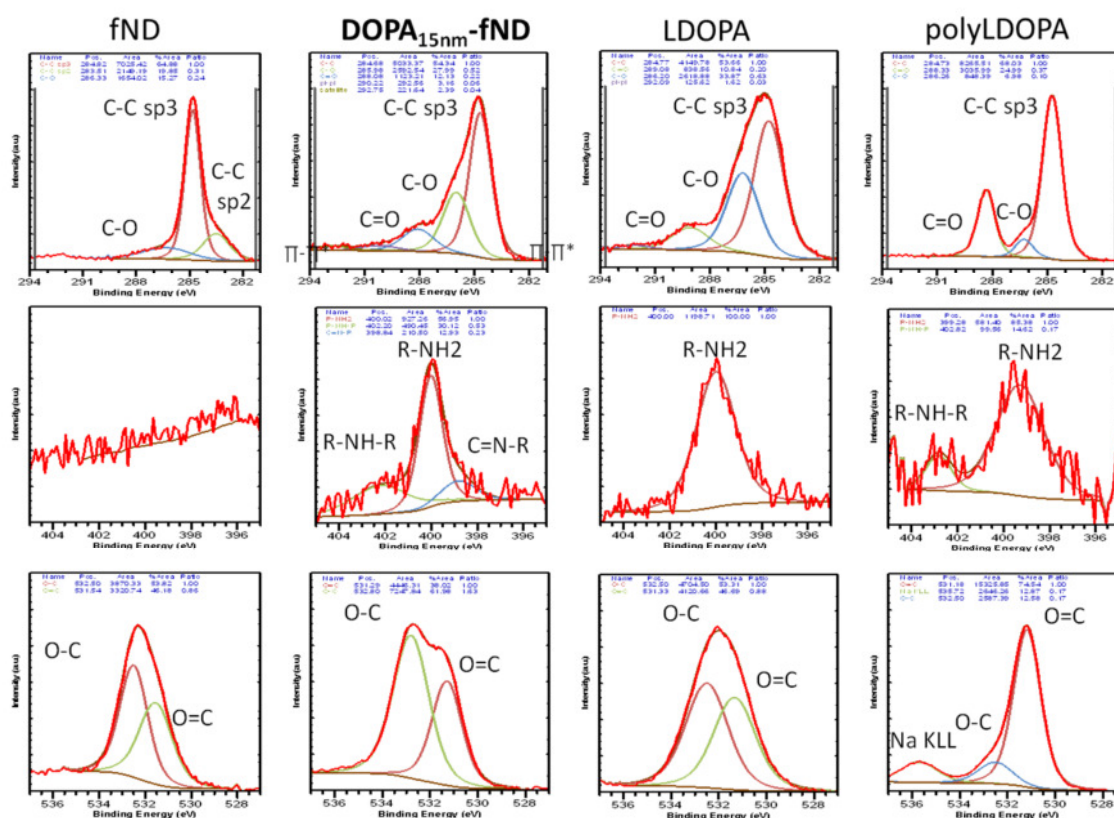
Figure S3. X-ray photoelectron spectrographs for raw nanodiamonds (fND), **DOPA₁₅ₙₘ-fND**, L-DOPA, and poly(L-DOPA) nanoparticles. Appearance of carbonyl/carboxyl groups and indole nitrogen indicative of poly(L-DOPA) coating on nanodiamonds. Higher ratio of carbonyl/carboxyl to hydroxyl groups in poly(L-DOPA) attributed to longer incubation of reaction mixture. Top row: C1s; Middle row: N1s; Bottom row: O1s.
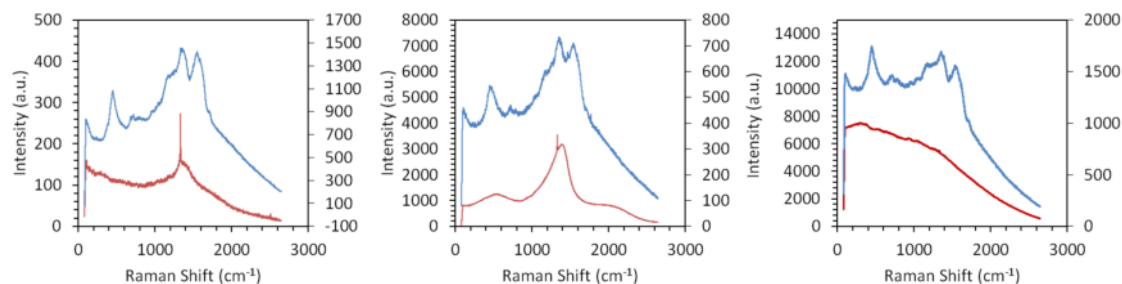
Figure S4. Raman spectra for different batches of nanodiamonds with poly(L-DOPA) coating. Spectra of raw nanodiamonds in red and coated nanodiamonds (1 mM L-DOPA concentration) in blue. Although spectra of raw nanodiamonds are significantly different, indicating different levels of impurities and surface compositions, the spectra of the coated nanodiamonds are strikingly similar. Verifying the universality of the coating. Left: fND BIOTECH; Center: Microdiamont Leipzig II; Right: Microdiamont MD 05. Peak Assignments (a) Diamond (~1336 cm^{-1}) (b) catechol deformation (1385 cm^{-1}) (c) catechol deformation (1557 cm^{-1}).
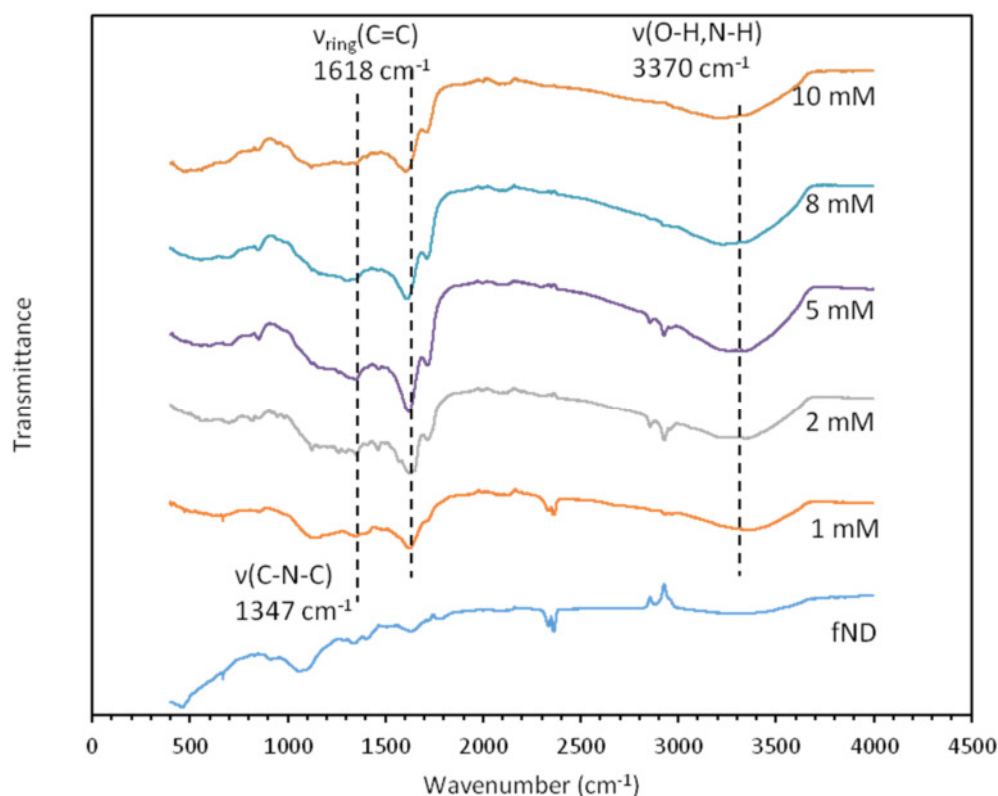
Figure S5. Fourier Transmission Infrared (FTIR) spectra of **DOPA-fND** (fND BIOTECH) prepared with different concentrations of L-DOPA. Peak assignments for poly(L-DOPA) given.
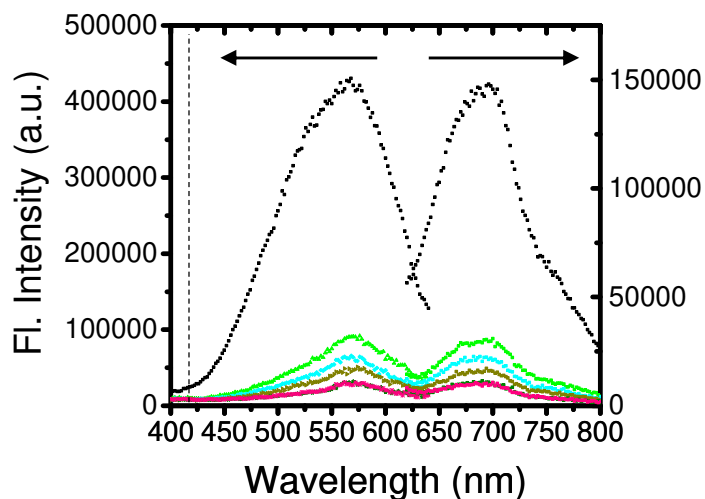
Figure S6. Fluorescence excitation and emission spectra of fND (black) and **DOPA-fND** (colored). Fluorescence decreases with increasing thickness of poly(L-DOPA) shell.
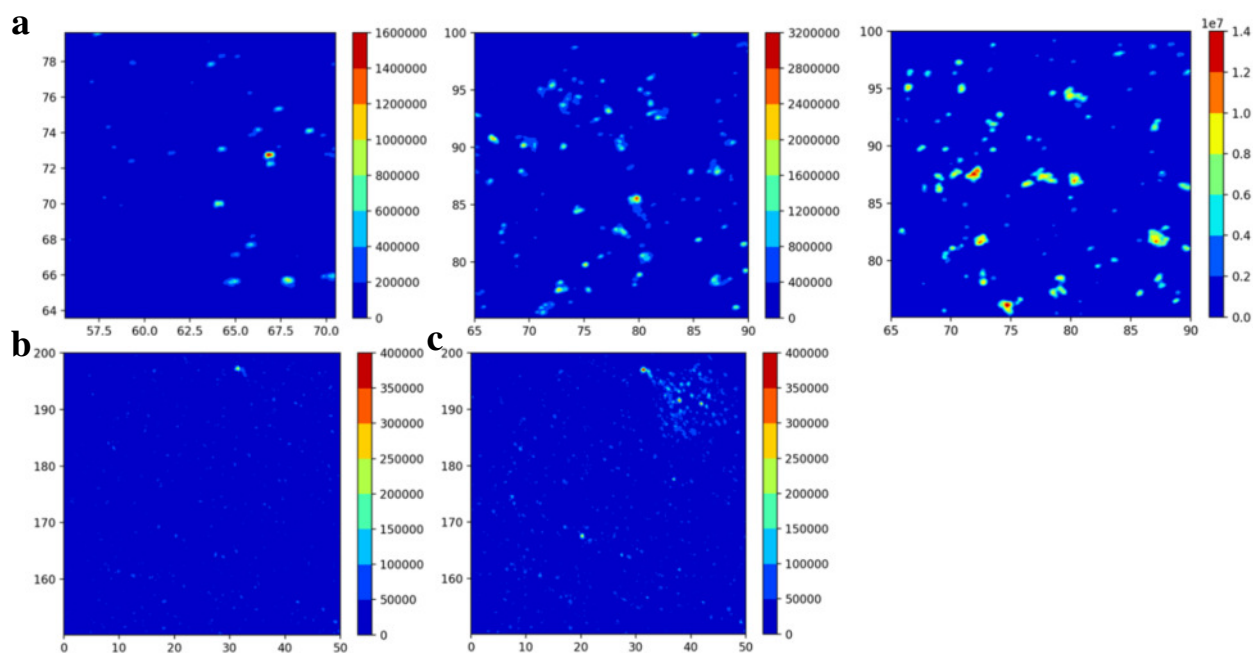
Figure S7. (a) Confocal imaging of coated fNDs. Left: **DOPA₃ₙₘ-fND**. Center: **DOPA₁₅ₙₘ-fND**. Right: raw nanodiamonds. Same area of NDs sample before (b) and after (c) local laser illumination. Increasing of fluorescence is stable in time (checked after 4 h).
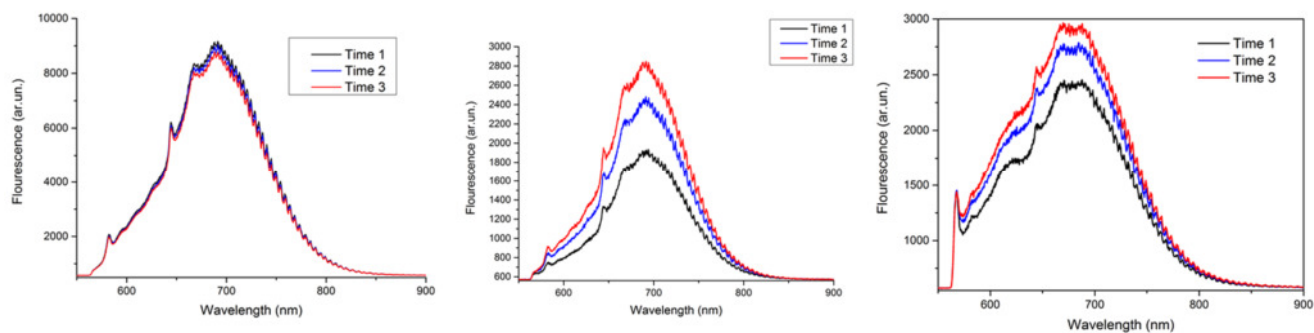
Figure S8. Increase in fluorescence after laser irradiation (laser 514 nm with 100 mkW) for **DOPA-fND** (a) Left: raw nanodiamonds; Center: **DOPA$_{3nm}$-fND**; Right: **DOPA$_{15nm}$-fND**. No increase in fluorescence observed for raw nanodiamonds. Time of signal accumulation was 10 sec and a time interval of about 2 min was selected in each measurement.
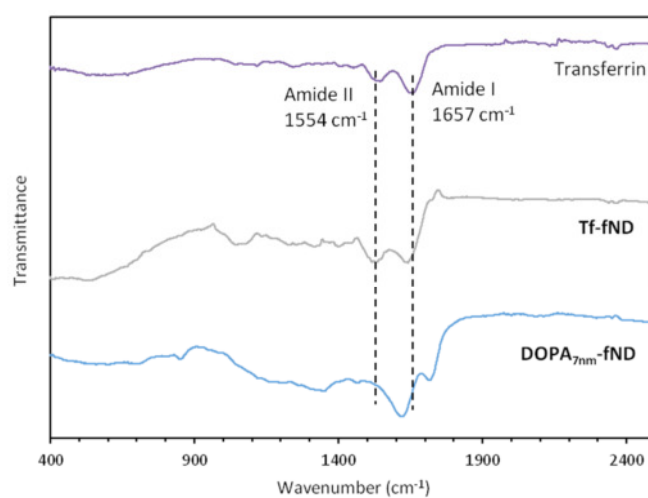
Figure S9. FTIR spectra of human Transferrin, **Tf-fND,** and **DOPA$_{7nm}$-fND**. The amide bands observed in **Tf-fND** spectra indicate successful conjugation of transferrin to surface.
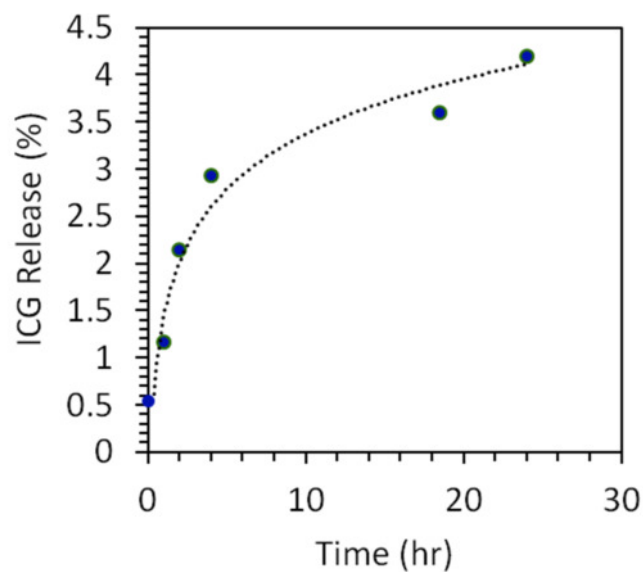
Figure S10. Indocyanine green (ICG) release profile *in vitro*. Negligible loss (< 5%) of ICG after 24 hours.
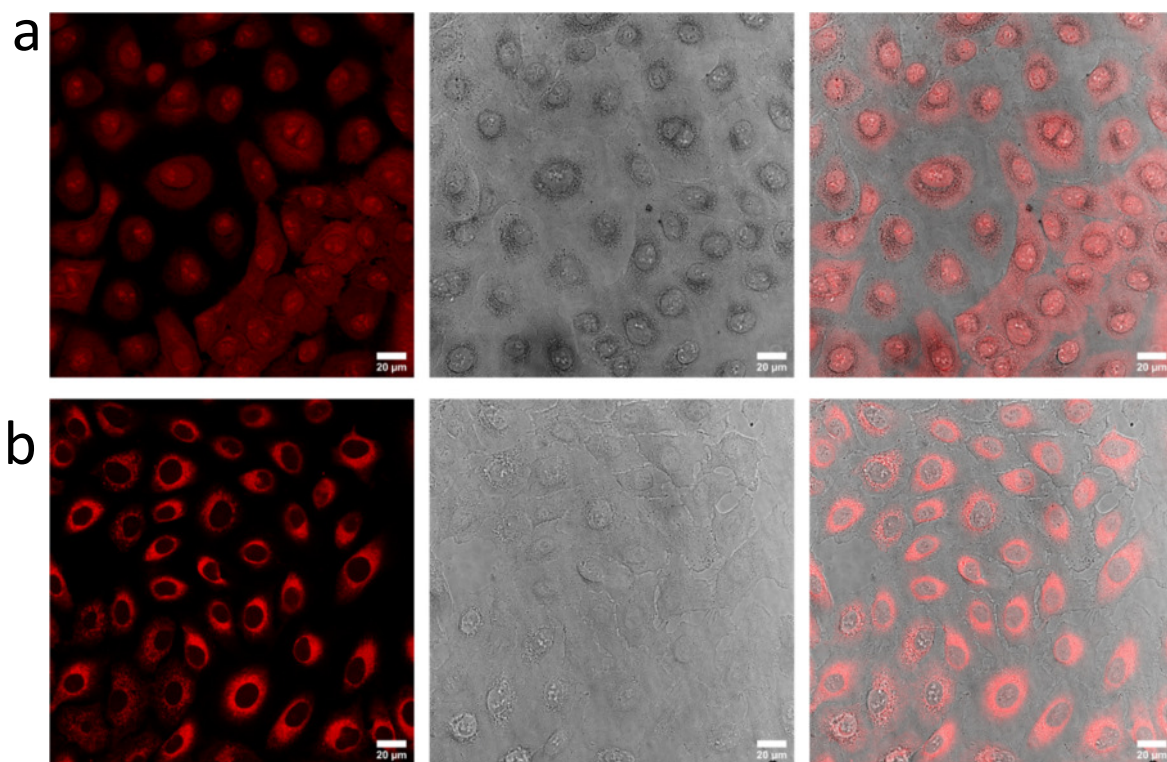
Figure S11. (a) Free indocyanine green (ICG, 0.4 mg mL^{-1}) was incubated with A549 cells for 2 h at 37 °C in 5% CO_2. (b) ICG-Tf-ND (250 µg mL^{-1}) was incubated with A549 cells for 2 h at 37 °C in 5% CO_2.
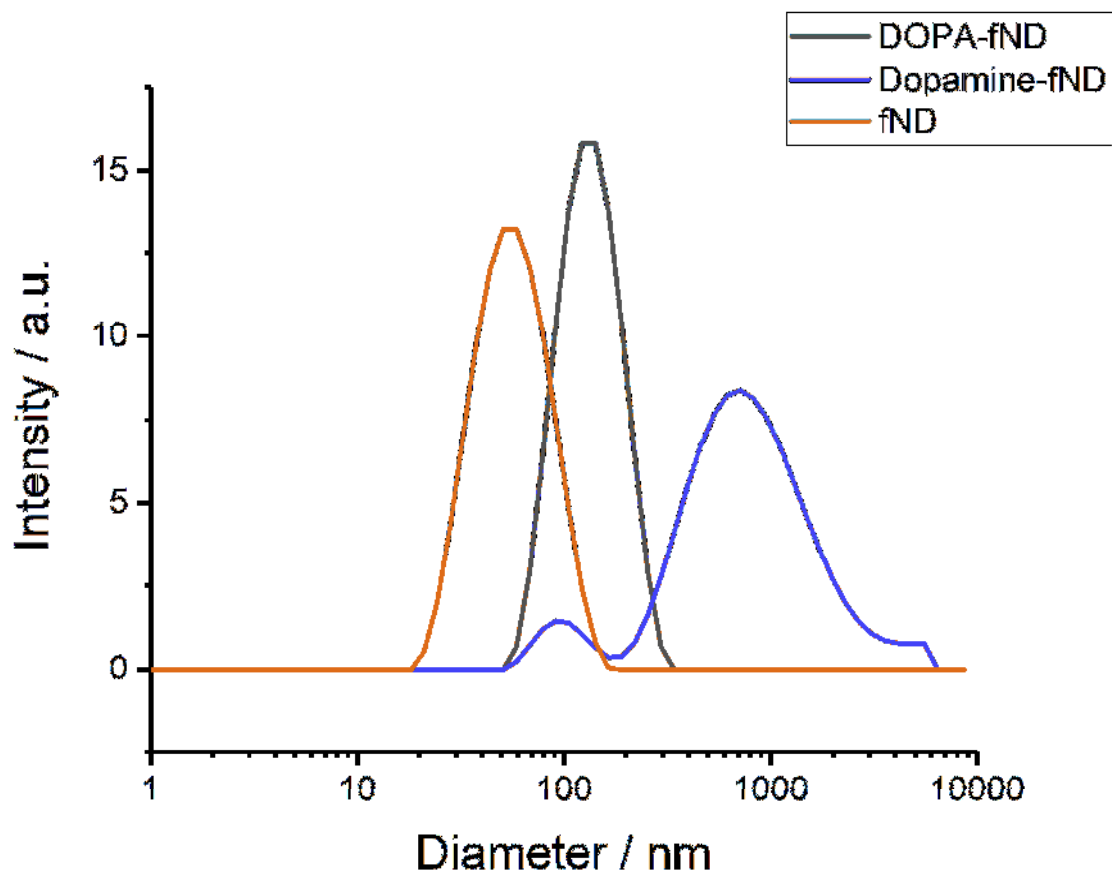
Figure S12. DLS spectra of fND coated with either L-DOPA or dopamine.
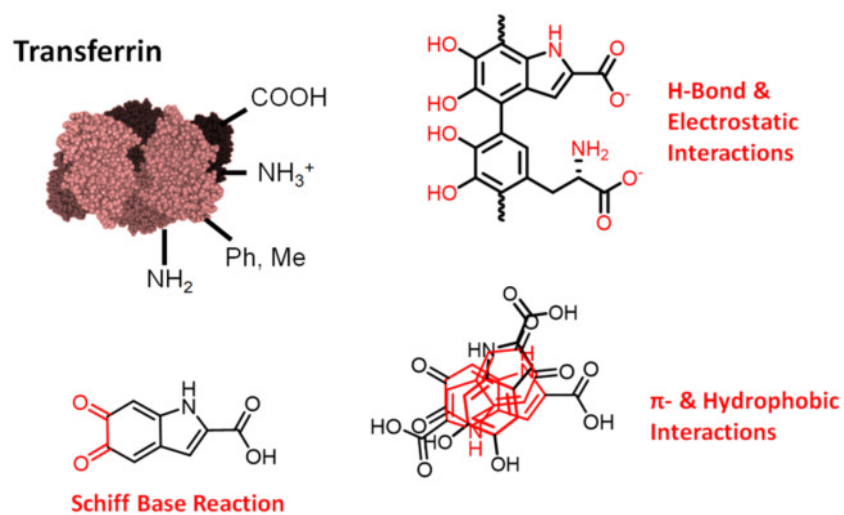
Figure S13. Summary of covalent and non-covalent interactions that enables the adsorption/conjugation of Transferrin to poly(L-DOPA).

6.5 Site-selective Protein Modification via Disulfide Rebridging for Fast Tetrazine/*trans*-Cyclooctene Bioconjugation

Lujuan Xu, Marco Raabe, Maksymilian Marek Zegota, João C. F. Nogueira, Vijay Chudasama, Seah Ling Kuan,* and Tanja Weil*

*corresponding authors

Abstract:

The inverse electron demand Diels-Alder reaction between tetrazine and trans-cyclooctene (TCO) holds great promise in protein modification and manipulation. Herein, we report the design and synthesis of a tetrazine-based disulfide rebridging reagent, which allows the site-selective installation of a tetrazine group to disulfide-containing peptides and proteins such as the hormone somatostatin (SST) and the antigen binding fragment (Fab) of human immunoglobulin G (IgG). The fast and efficient conjugation of the tetrazine modified proteins with three different TCO-containing substrates to form a set of bioconjugates in a site-selective manner was successfully demonstrated for the first time. Homogeneous, well-defined bioconjugates were obtained underlining the great potential of our method for fast bioconjugation of emerging protein therapeutics. The formed bioconjugates were stable against glutathione and in serum and they maintained their secondary structure. With this work, we broaden the scope of tetrazine chemistry for the site-selective protein modification to prepare well-defined SST and Fab conjugates with preserved structure and good stability in biologically relevant conditions.

PAPER

Check for updates

Site-selective protein modification *via* disulfide rebridging for fast tetrazine/*trans*-cyclooctene bioconjugation†

Lujuan Xu,[a,b] Marco Raabe, [ID] [a,b] Maksymilian M. Zegota,[a,b] João C. F. Nogueira,[c] Vijay Chudasama, [ID] [c] Seah Ling Kuan [ID] *[a,b] and Tanja Weil [ID] *[a,b]

An inverse electron demand Diels–Alder reaction between tetrazine and *trans*-cyclooctene (TCO) holds great promise for protein modification and manipulation. Herein, we report the design and synthesis of a tetrazine-based disulfide rebridging reagent, which allows the site-selective installation of a tetrazine group into disulfide-containing peptides and proteins such as the hormone somatostatin (SST) and the antigen binding fragment (Fab) of human immunoglobulin G (IgG). The fast and efficient conjugation of the tetrazine modified proteins with three different TCO-containing substrates to form a set of bioconjugates in a site-selective manner was successfully demonstrated for the first time. Homogeneous, well-defined bioconjugates were obtained underlining the great potential of our method for fast bioconjugation in emerging protein therapeutics. The formed bioconjugates were stable against glutathione and in serum, and they maintained their secondary structure. With this work, we broaden the scope of tetrazine chemistry for site-selective protein modification to prepare well-defined SST and Fab conjugates with preserved structures and good stability under biologically relevant conditions.

Introduction

Peptides and proteins are emerging as powerful treatment options, as exemplified by the application of antibodies and antibody fragments (Fab) in immunotherapy and antibody–drug conjugates in targeted cancer therapy.[1] Nevertheless, protein stability, immunogenicity and the time required to engineer recombinant antibodies could limit their development for *in vivo* studies.[2] In this regard, nature has evolved an optimal synthetic factory in the form of posttranslational processes, in which diverse functionalities can be attached to proteins in a site-directed fashion.[3] Inspired by this, chemists strive to develop methodologies to impart diverse functionalities to native proteins with similar levels of precision.

Site-selective modification of therapeutically relevant peptides and proteins to introduce reactive bioorthogonal handles has emerged for post-modification in an "on-demand" fashion to expand the features and functions of proteins to address the challenges in fundamental biological and medical applications.[4] In this manner, protein therapeutics can be synthetically customized to program their properties for envisaged applications.

Over the past decades, several bioorthogonal reactions, including the [3 + 2] azide–alkyne cycloaddition, photoclick 1,3-dipolar cycloaddition and the inverse electron demand Diels–Alder (IEDDA) reactions, have been developed and applied for protein modifications.[5] Among these, the IEDDA reaction of 1,2,4,5-tetrazine with *trans*-cyclooctene (TCO) stands out, providing fast reaction kinetics (rate constant of up to 10^6 M^{-1} s^{-1}), excellent orthogonality, catalyst-free conditions and good biocompatibility, and is a widely employed bioorthogonal approach in chemical biology.[6] Previously, the IEDDA reaction has been applied for the preparation of antibody conjugates, mainly *via* statistical modifications using *N*-hydroxysuccinimide (NHS) ester chemistry for cell imaging,[7] nanoparticle functionalization,[8] and antibody targeted therapy.[6a,9] In the literature, two common approaches to site-selectively modify proteins utilizing the IEDDA reaction are, the introduction of a diene or dienophile by genetic code expansion methods *via* the incorporation of noncanonical amino acids[10] and tag-based posttranslational attachment strategies using enzymes (*e.g.* lipoic acid protein ligase A).[11] Nevertheless, the genetic code expansion method suffers from low yields and tedious synthesis. This in turn limits its scal-

aMax Planck Institute for Polymer Research, Ackermannweg 10, 55128 Mainz, Germany. E-mail: weil@mpip-mainz.mpg.de, kuan@mpip-mainz.mpg.de

bInstitute of Inorganic Chemistry I, University of Ulm, Albert-Einstein-Allee 11, 89081 Ulm, Germany

cDepartment of Chemistry, University College London, London, UK

†Electronic supplementary information (ESI) available. See DOI: 10.1039/c9ob02687h

1140 | *Org. Biomol. Chem.*, 2020, **18**, 1140–1147

This journal is © The Royal Society of Chemistry 2020

ability and accessibility for further applications, while tag-based posttranslational attachment strategies first require the genetic fusion of a specific peptide sequence (*e.g.* lipoate acceptor peptide) to the protein of interest.[11] A single tetrazine or TCO group has also been introduced site-selectively into peptides or proteins at an unpaired cysteine site *via* the thiol-maleimide reaction.[6a,12]

However, very few native proteins contain free cysteine residues.[13] Furthermore, thiol–maleimide chemistry easily undergoes the retro-Michael reaction resulting in a maleimide exchange with other reactive thiols present, for example glutathione, under physiological conditions causing off-target effects.[4a] Therefore, other methods, which can introduce a tetrazine or TCO group in a site-selective fashion into proteins for subsequent IEDDA reactions are highly desirable to expand the scope of their applications. Since many therapeutically relevant peptides and proteins contain at least one disulfide bond close to the protein surface, the disulfide rebridging strategy provides a versatile technique to modify the solvent accessible disulfide bonds on these proteins and peptides to install suitable bioorthogonal tags.[13,14] Smith and coworkers presented an elegant approach to introduce the tetrazine group at the disulfide site of proteins/peptides *via* dichlorotetrazine.[15] However, a significantly reduced activity of the protein was reported after the modification. In this context, disulfide modification based on bis-alkylating reagents to form bisthioether conjugates gained wide applications for site-selective protein modifications without compromising their bioactivity. Furthermore, it has been reported that bisthioether conjugates formed by disulfide rebridging are more stable than thiol-maleimide conjugates[16] suggesting that it could be a viable strategy for the installation of IEEDA reaction handles. Herein, we present a simple and straightforward method for the site-selective incorporation of a tetrazine group into native peptides and proteins through disulfide rebridging with the allyl sulfone scaffold reported previously.[17] In comparison with known bis-sulfone disulfide rebridging reagents, allyl sulfone reagents provide improved reactivity and higher water solubility, which greatly facilitates protein bioconjugations.[17] The disulfide rebridging reactions of allyl sulfones proceed *in situ* without side reactions *e.g.* with reducing agents such as tris(2-carboxyethyl)-phosphine hydrochloride (TCEP). In comparison, disubstituted maleimide disulfide rebridging reagents, such as 3,4-dibromomaleimide, show side reactions with TCEP, presumably due to the nucleophilic addition of

phosphine to the electron-poor alkene moiety.[18] The versatility of the method was demonstrated by modifying two model substrates: SST and IgG Fab under mild conditions which yielded a set of well-defined protein conjugates (Fig. 1). The formed protein conjugates showed good stability and maintained their secondary structures after bioconjugation. The reported methodology provides a rapid, robust and straightforward strategy for site-selective protein labeling and expands the scope of using IEDDA chemistry in the functionalization of therapeutically relevant peptides and proteins in a precise manner.

Results and discussion

Synthesis and characterization of the tetrazine-based disulfide rebridging reagent

For the site-selective installation of bioorthogonal handles on the proteins, a longer incubation time (usually overnight) is often required.[13] Therefore, the diene "6-methyl-1,2,4,5-tetrazine" instead of the dienophile "TCO" was introduced into the protein. This strategy fully utilizes the fast kinetics of the IEDDA reaction but minimizes the inherent isomerization issues of TCO to nonreactive *cis*-cyclooctene, which occurs at a longer incubation time or in the presence of thiols.[4c,19] In this context, a tetrazine-based allylsulfone disulfide rebridging reagent (IC-Tetrazine, Scheme 1) was designed and readily
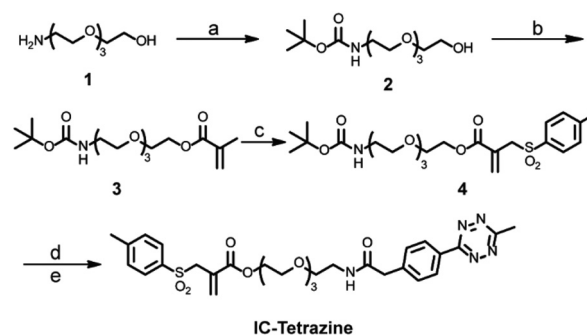
Scheme 1 Synthesis of the tetrazine-containing disulfide rebridging reagent (IC-Tetrazine). (a) Di-*tert*-butyl dicarbonate, CH$_2$Cl$_2$, overnight. (b) Methacryloyl chloride, Et$_3$N, CH$_2$Cl$_2$, 90%. (c) 1. I$_2$, sodium *p*-toluenesulfinate, CH$_2$Cl$_2$, 3 days. 2. Et$_3$N, CH$_2$Cl$_2$, overnight. 3. Et$_3$N, ethyl acetate, 95 °C, overnight, final yield: 60%. (d) Trifluoroacetic acid (TFA), CH$_2$Cl$_2$, 98%. (e) Methyltetrazine NHS ester, Et$_3$N, CH$_2$Cl$_2$, overnight, 40%.
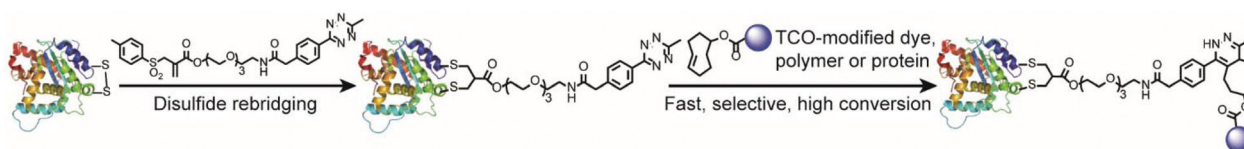

Fig. 1 Schematic overview of site-selective incorporation of a reactive tetrazine tag into a solvent-accessible disulfide site of a cell-targeting peptide or antibody fragment. The tetrazine-modified peptide/protein is used for post-functionalization to construct a small set of protein bioconjugates with a (1) dye, (2) polymer and (3) protein in a fast and highly selective manner with high conversions (one isomer is shown as a representation).

This journal is © The Royal Society of Chemistry 2020

Org. Biomol. Chem., 2020, **18**, 1140–1147 | **1141**

Paper

obtained through a four-step synthesis. As shown in Scheme 1, tetraethylene glycol monoamine (**1**) was protected to afford 2-(2-boc-aminoethoxy)ethanol (**2**) that underwent condensation with methacryloyl chloride yielding the corresponding methacrylate derivative (**3**). After a tandem iodosulfonylation–dehydroiodination reaction, the tosyl group was introduced to form allyl-sulfone (**4**). The *tert*-butoxycarbonyl group was subsequently removed in an acidic medium to afford the primary amino group, which then reacted with methyl-tetrazine NHS ester to afford the IC-Tetrazine reagent.

Site-selective protein modification

Subsequently, two model substrates (somatostatin and human IgG Fab) were selected for site-selective modification with IC-Tetrazine. Somatostatin (SST) regulates the endocrine system and mediates signal transduction *via* five G protein-coupled receptors (SSTR) that are overexpressed in high levels in various kinds of cancer cells and tumor blood vessels.[20] SST conjugates have been widely investigated for targeted drug delivery into SSTR-expressing cancer cells.[20,21] IC-Tetrazine was reacted with SST after its single accessible disulfide bond was reduced to generate free thiol groups by the addition of two equivalents of TCEP at room temperature (Fig. 2a). The product (SST-Tetrazine) was purified by high-performance liquid chromatography (HPLC) yielding SST-Tetrazine in 30% yield, which is comparable to that reported in the literature (20% to 40%).[13] Characterization by matrix assisted laser desorption/ionization time of flight mass spectrometry (MALDI-TOF-MS) revealed two signals corresponding to the desired SST-Tetrazine (m/z = 2110.95 $[M + H]^+$, Fig. 2b, the molecular weight of native SST is 1637 g mol^{-1}) and the laser fragmentation species of SST-Tetrazine (m/z = 2041.93, the

chemical structure of the fragmentation species is shown in Fig. S3†), respectively. Notably, SST-Tetrazine is stable for more than one year when stored as a solid at −20 °C (Fig. S4†).

Next, we applied the modification method to an antibody fragment (Fab) from human immunoglobulin G (IgG). Fab fragments have been successfully used for constructing antibody–drug and antibody–nanoparticle conjugates providing several advantages compared to the complete antibody.[22] The conjugate retains the antigen-binding region which is crucial for active targeting, but circumvents the non-specific binding of the Fc region of antibodies.[22a] Since the interchain disulfides are much more exposed to the solvent and less stable relative to the intrachain disulfides that are buried between the two layers of anti-parallel β-sheet structures,[23] IgG Fab was incubated with 50 equivalents of TCEP (optimization of the amounts of TCEP is shown in Fig. S5†) to reduce the solvent accessible interchain disulfide bonds and subsequently reacted with IC-Tetrazine overnight (Fig. 2a). The tetrazine modified Fab fragment (Fab-Tetrazine) was purified by ultrafiltration to remove residual TCEP and IC-Tetrazine. The MALDI-TOF-MS analysis of Fab-Tetrazine revealed a molecular weight of 48.5 kDa (Fig. 2c), showing an increase of ~500 Da compared to that of the native Fab (48.0 kDa, Fig. S5B†) demonstrating its successful site-selective modification. Sodium dodecyl sulfate polyacrylamide gel electrophoresis (SDS-PAGE) of Fab-Tetrazine revealed a single band at ~48 kDa showing that only a slight reduction occurred after site-selective modification even in the presence of 100 equivalents of TCEP after one hour (Fig. 2d, band 2). In contrast, under the same conditions, the native IgG Fab was almost completely reduced exhibiting a single band appearing at ~24 kDa on SDS-PAGE (Fig. 2d, band 1). Based on the concentration calcu-
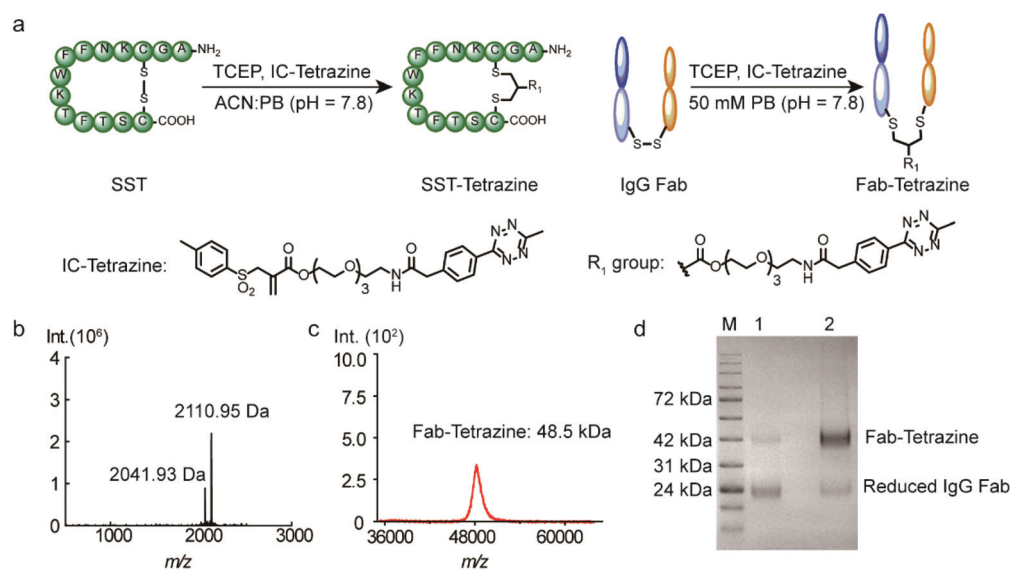

Fig. 2 (a) Site-selective modification of SST and IgG Fab with IC-Tetrazine. (b) MALDI–TOF-MS spectrum of SST-Tetrazine (found: 2110.95 $[M + H]^+$, calculated: 2110.95 $[M + H]^+$). The m/z peak at 2041.93 corresponds to the fragmentation of SST-Tetrazine. (c) MALDI–TOF-MS spectrum of Fab-Tetrazine (Fab-Tetrazine: found: 48.5k $[M + H]^+$, calculated: 48.5k $[M + H]^+$). (d) SDS-PAGE analysis of native Fab and Fab-Tetrazine (M: Applichem Protein Marker VI, 1: Fab (native) + 100 eq. TCEP incubation for one hour, and 2: Fab-Tetrazine + 100 eq. TCEP incubation for one hour).

1142 | *Org. Biomol. Chem.*, 2020, **18**, 1140–1147

This journal is © The Royal Society of Chemistry 2020

Organic & Biomolecular Chemistry

lated from gel densitometry (Fig. 2d), about 80% of the Fab fragment was successfully modified. A thiol quantification experiment using the thiol reagent 4,4′-dithiodipyridine was performed and the result showed that about 73% of IgG Fab were successfully modified, which is consistent with the result obtained from gel densitometry (details are shown in the ESI, Fig. S5c†). Taken together, the results clearly indicated that the disulfide bonds in IgG Fab were successfully rebridged using IC-Tetrazine.

Bioconjugation with a chromophore, PEG and enzyme

The versatility of the tetrazine-modified SST and IgG Fab for the construction of well-defined bioconjugates was demonstrated through post-modification with a fluorophore (cyanine-5, Cy5) and a PEG chain. In addition, SST-Tetrazine was also conjugated to a protein enzyme (cytochrome C, CytC) to form a peptide–protein conjugate with high conversion. A TCO-terminated PEG chain of a precise chain length with 12 repeating units (TCO-PEG12) was selected to facilitate the characterization by MALDI-TOF-MS. TCO-PEG12 was incubated with SST-Tetrazine in phosphate buffer (PB, 50 mM, pH = 7.4) and the pink color of the tetrazine group disappeared immediately after mixing, indicating that the reaction took place instantaneously. The bioconjugation reaction was carried out for 30 minutes to ensure completion. Thereafter, the reaction mixture was injected into the HPLC column and a predominant peak of SST-PEG12 was obtained (Fig. S7, ESI†). SST-PEG12 was isolated in nearly quantitative yield (95%) and characterized by MALDI-TOF-MS (Fig. 3b). SST-Tetrazine was also conjugated to TCO-Cy5 under similar conditions yielding

the desired conjugate SST-Cy5 in 90% yield. MALDI-TOF-MS showed the m/z signal at 3041.17 (Fig. 3c).

Due to the much larger molecular weight of Fab-Tetrazine compared to SST-Tetrazine, a longer PEG chain with a molecular weight of 5000 Da containing 113 repeating units on average (TCO-PEG113) was incubated with Fab-Tetrazine in phosphate buffer (pH = 7.4) for 30 minutes to afford Fab-PEG113. The characteristic band of Fab-Tetrazine at ~48 kDa almost entirely disappeared after PEGylation and a new band emerged, which was broader due to the polydispersity of the PEG chain (Fig. 3d). A control experiment of mixing native Fab and TCO-PEG113 did not show any unspecific absorption on SDS-PAGE (Fig. 3d). MALDI-TOF-MS spectra revealed a signal at 53.5 kDa indicating the successful conjugation (Fig. S11D†). Under similar conditions, the widely applied chromophore Cy5 was also attached to Fab-Tetrazine to afford Fab-Cy5 (molecular weight: 49.5 kDa, Fig. 3e) in 73% yield (the calculation is shown in the ESI†). Successful conjugation was confirmed by an increase in the molecular weight of ~1.5 kDa in the MALDI-TOF-MS spectra in comparison with those of native Fab (molecular weight: 48 kDa, Fig. 3e).

CytC is a 12 kDa hemeprotein typically located in the mitochondria of viable cells.[24] Iso-yeast CytC has a single thiol group on its surface for modification via thiol-maleimide chemistry.[25] TCO-PEG3-maleimide was reacted with CytC to introduce the TCO group via thiol-maleimide chemistry affording CytC-PEG3-TCO (Scheme S4†). MALDI-TOF-MS data revealed the successful modification of CytC (Fig. S6, ESI†). In addition, a tetrazine-based dye (tetrazine-5-fluorescein, Tetrazine-FAM, excitation wavelength: 492 nm and emission
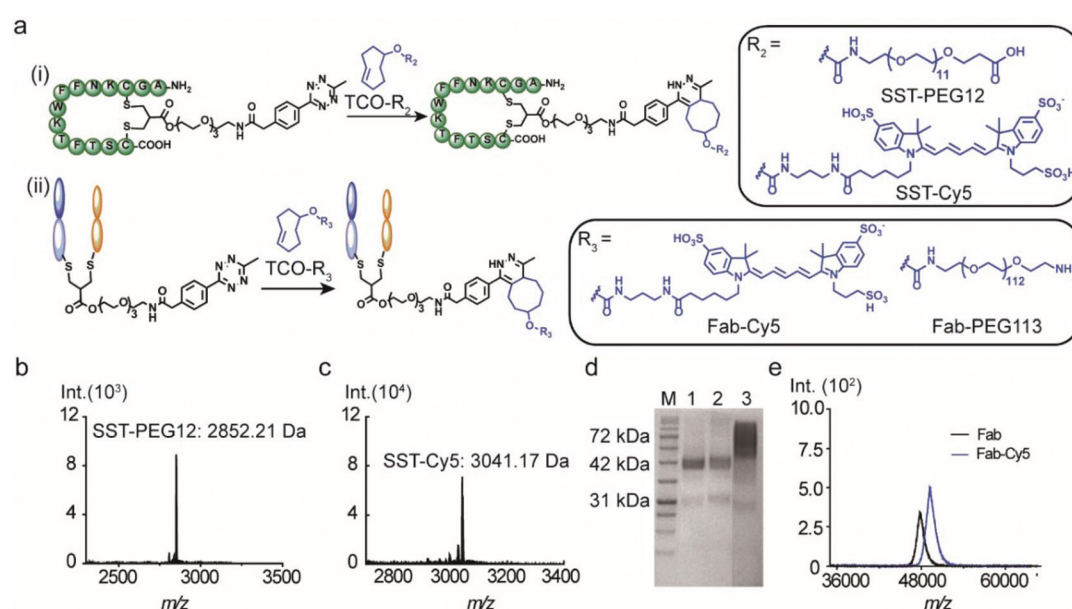

Fig. 3 (a) Bioconjugation between (i) SST-Tetrazine with TCO-PEG12 and TCO-Cy5. (ii) Fab-Tetrazine with TCO-Cy5 and TCO-PEG113 via a fast click reaction. (b) MALDI-TOF-MS spectrum of SST-PEG12 (found: 2852.21 [M + H]⁺, calculated: 2852.28 [M + H]⁺). (c) MALDI-TOF-MS spectrum of SST-Cy5 (found: 3041.17 [M + H]⁺, calculated: 3041.28 [M + H]⁺). Sinapic acid was used as the matrix for all MALDI-TOF-MS measurements. (d) SDS-PAGE analysis of Fab-PEG113 (M: Applichem Protein Marker VI, 1: Fab-Tetrazine, and 2: Fab + TCO-PEG113, 3: Fab-PEG113). (e) MALDI-TOF-MS spectra of Fab-Cy5 (found: 49.5k [M + H]⁺, calculated: 49.5k [M + H]⁺) and native Fab (found: 48.0k [M + H]⁺, calculated: 48.0k [M + H]⁺).

This journal is © The Royal Society of Chemistry 2020

Org. Biomol. Chem., 2020, 18, 1140–1147 | 1143

wavelength: 517 nm) was used to react with CytC-PEG3-TCO to assess the modification yield of CytC. Based on the absorbance of CytC at 280 nm and the FAM dye at 490 nm, about 90% of CytC was successfully modified with the TCO group (experimental details are shown in the ESI†). Thereafter, the targeting peptide SST-Tetrazine was conjugated to CytC-PEG3-TCO by mixing and shaking for 30 minutes.

After ultrafiltration to remove the residual SST-Tetrazine, SST-PEG3-CytC was obtained and characterized by MALDI-TOF-MS and SDS-PAGE. In the MALDI-TOF-MS spectra, the signal at 15 315 Da corresponds to the desired SST-PEG3-CytC conjugate (Fig. 4b), whereas the signal for CytC-PEG3-TCO (13 233 Da) completely disappeared. On SDS-PAGE, a slight band shift was observed indicating the successful conjugation between SST-Tetrazine and CytC-PEG3-TCO (Fig. 4c). The conjugation of Fab-Tetrazine with CytC-PEG3-TCO was

also performed. However, MALDI-Tof-MS data showed almost no conjugation product, presumably due to the steric hindrance of the two bulky macromolecules.

Stability studies of SST-Tetrazine, Fab-Tetrazine and Fab-Cy5

The stability of the bioconjugates after disulfide modification is an important consideration for their intended applications in cellular environments. Therefore, the stability of the modified protein with the newly synthesized disulfide rebridging reagent in glutathione (GSH) was investigated using liquid chromatography mass spectrometry (LC-MS). SST-Tetrazine (10 μM) was incubated with two-fold excess of GSH at biologically relevant concentrations (20 μM)[26] at 37 °C and SST-Tetrazine and the degradation product (GSH-Tetrazine, 1085 $[M + H]^+$; the chemical structure is shown in Scheme S9†) were identified by simultaneous detection by UV-Vis spectroscopy at an absorption wavelength of 254 nm and selective ion monitoring (SIM). The amount of SST-Tetrazine in each sample was determined as a ratio of the integration of the chromatogram at 254 nm of SST-Tetrazine to the standard (Fmoc-L-phenylalanine) (Fig. 5a and b). LC-MS data showed that SST-Tetrazine remained intact after 24 hours of incubation and no degradation products were detected in the SIM profile (Fig. S12C†). Next, the stability of the Fab conjugates was investigated based on the literature protocol.[22b] Fab-Tetrazine and Fab-Cy5 were incubated with 1% fetal bovine serum (FBS) at 37 °C and monitored using SDS-PAGE. SDS-PAGE data revealed no change in Fab-Tetrazine after 24 hours, indicating no obvious degradation (Fig. 5c). The stability of Fab-Cy5 was also investigated based on the quantification of the fluorescence of the conjugate (shown in the ESI,† page 15). The data indicated a good stability of Fab-Cy5 after incubation with FBS for 24 hours (Fig. 5d). Taken together, these experiments showed that the resultant peptide and protein bioconjugates formed by the disulfide rebridging strategy and the subsequent IEDDA reaction remained stable under physiological conditions, e.g. in the presence of GSH or in media containing serum proteins.
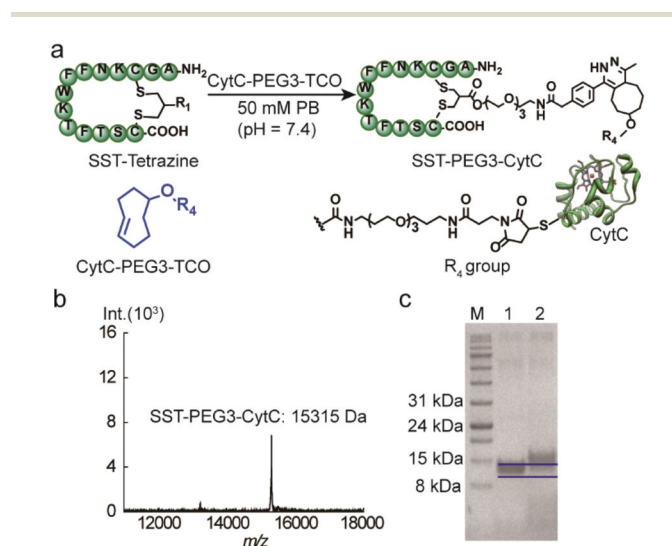

Fig. 4 (a) Bioconjugation between SST-Tetrazine and CytC-PEG3-TCO. (b) MALDI-TOF-MS spectrum of SST-PEG3-CytC (found: 15 315 [M + H]$^+$, calculated: 15 314 [M + H]$^+$) matrix: sinapic acid. (c) SDS-PAGE analysis of SST-PEG3-CytC (M: Applichem Protein Marker VI, 1: CytC-PEG3-TCO, and 2: SST-PEG3-CytC).
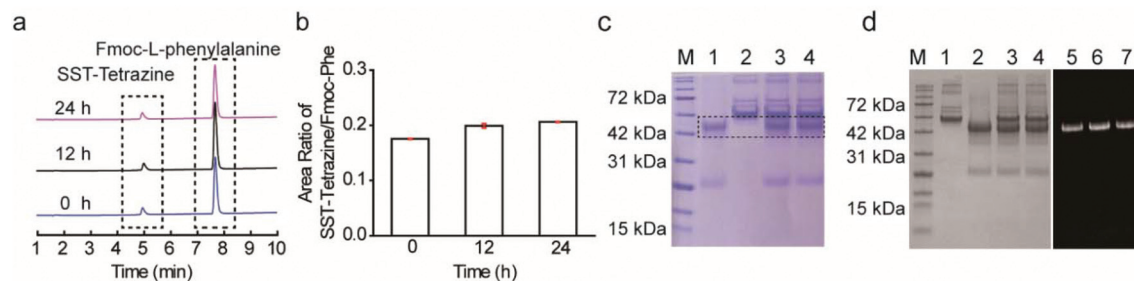

Fig. 5 (a) Stability study of SST-Tetrazine via LC-MS. (b) Area ratio of SST-Tetrazine at 254 nm compared to Fmoc-L-phenylalanine (standard) at three time points (n = 3, values are given as mean ± SD). (c) Stability study of Fab-Tetrazine by SDS-PAGE (M: Applichem Protein Marker VI, 1: Fab-Tetrazine, 2: 1% FBS, 3: Fab-Tetrazine + 1% FBS incubated for 12 hours, and 4: Fab-Tetrazine + 1% FBS incubated for 24 hours), (d) Stability study of Fab-Cy5 by SDS-PAGE with (left) and without (right) Coomassie blue (M: Applichem Protein Marker VI, 1: 1% FBS, 2: Fab-Cy5, 3: Fab-Cy5 + 1% FBS incubated for 12 h, 4: Fab-Cy5 + 1% FBS incubated for 24 h, 5: fluorescence of Fab-Cy5, 6: fluorescence of Fab-Cy5 after incubation with 1% FBS for 12 h, and 7: fluorescence of Fab-Cy5 after incubation with 1% FBS for 24 h).
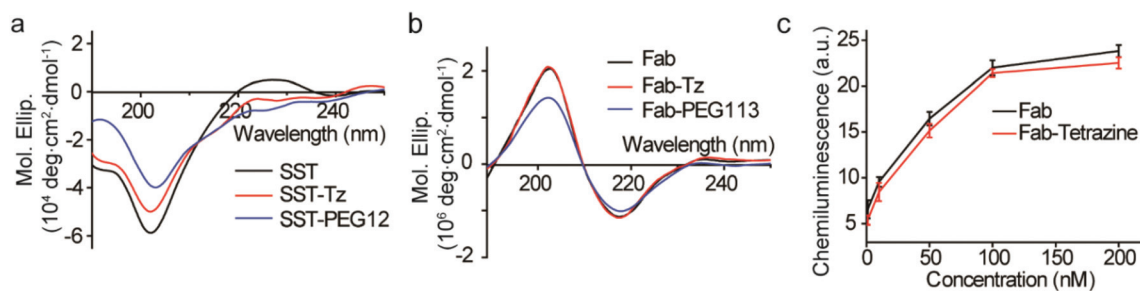
1144 | Org. Biomol. Chem., 2020, 18, 1140–1147

This journal is © The Royal Society of Chemistry 2020

Fig. 6 (a) CD spectra of SST, SST-Tetrazine and SST-PEG12 (SST, SST-Tetrazine and SST-PEG12 were diluted to 0.1 mg mL^{-1} in PBS, the data are the average of three runs). (b) CD spectra of Fab, Fab-Tetrazine and Fab-PEG113 (Fab, Fab-Tetrazine and Fab-PEG113 were measured at 0.1 mg mL^{-1} in PBS, the data are the average of three runs). (c) ELISA data of Fab and Fab-Tetrazine (five different concentration points: 1 nM, 10 nM, 50 nM, 100 nM, and 200 nM). Data are plotted as mean $\pm$ SD (n = 3).

Structural and functional studies

Circular dichroism (CD) is a versatile technique to determine the secondary and tertiary structures of proteins. According to Fig. 6a, SST, SST-Tetrazine and SST-PEG12 showed typical random coil structures with a negative band at 201 nm. The peak at 225 nm of SST is attributed to the presence of a higher degree of polyproline (PPII) conformation.[27]

Both native IgG Fab, Fab-Tetrazine and Fab-PEG113 conjugates, possess well-defined antiparallel β-pleated sheets confirmed by the peaks at 218 nm and 202 nm consistent with the literature report,[23] which confirmed that the secondary structure of Fab was preserved after modification (Fig. 6b). Next, we assessed whether the modification of IgG Fab affects its function to bind to protein L, a bacterial protein known to interact with Fab fragments of immunoglobulins.[28] The binding and recognition of native Fab and Fab-Tetrazine were thus investigated by enzyme-linked immunosorbent assay (ELISA). Different concentrations (1 nM, 10 nM, 50 nM, 100 nM, and 200 nM) of IgG Fab and Fab-Tetrazine were added to the protein L coated well plate and incubated for one hour. After removing the unbound protein, anti-human IgG (Fab specific)-peroxidase antibody was added to the well plate and incubated for one hour. Enhanced chemiluminescence solution was added to the well plate after washing three times with PBS. As shown in Fig. 6c, the binding affinities between IgG Fab and Fab-Tetrazine are comparable, suggesting that the binding of Fab-Tetrazine to protein L was preserved.

Conclusions

Herein, we report a straightforward and broadly applicable bioconjugation method for introducing a single tetrazine group into a targeting peptide and antibody fragment at a predefined, distinct site in aqueous media through disulfide modification. The tetrazine functionalized peptide or Fab was further conjugated with a series of TCO-modified functionalities, such as dyes, polymers, or proteins/enzymes yielding a small library of stable bioconjugates within a short reaction time. Such bulky functionalities could only be introduced by a two-step procedure as the disulfide rebridging reaction is greatly limited by the steric demand of the reagent. Bulky substituents attached to the rebridging reagent such as polymers, proteins or drug molecules have only limited access to the reduced disulfide residues resulting in complex product mixtures with large amounts of unreacted starting materials and very low product yield.[29] Therefore, the two-step approach presented herein based on the site-selective installation of the tetrazine tag first followed by the IEDDA reaction provides convenient access to compound libraries, in which a broad range of small and bulky TCO-modified functionalities could be attached to the corresponding tetrazine-modified proteins in a convenient, fast, and efficient way.

Notably, the modified proteins exhibited good stability under biologically relevant conditions and their secondary structure was preserved after modification. We envision that this method would enable the preparation of the desired bioconjugates "on site", e.g. in hospitals for the desired applications. In this way, the final conjugate would be applied to the patient immediately after preparation, preventing long term storage, quality control and loss of bioactivity of the final conjugate. The approach presented herein is a valuable addition to the chemical toolbox for site-selective protein labelling and manipulation, offering a fast, robust and straightforward method to be easily adapted in any laboratory.

Conflicts of interest

There are no conflicts to declare.

Acknowledgements

This journal is © The Royal Society of Chemistry 2020

Org. Biomol. Chem., 2020, **18**, 1140–1147 | **1145**

Notes and references

1 L. M. Weiner, R. Surana and S. Wang, *Nat. Rev. Immunol.*, 2010, **10**, 317.

2 V. Chudasama, A. Maruani and S. Caddick, *Nat. Chem.*, 2016, **8**, 114.

3 J. M. Chalker, G. J. Bernardes, Y. A. Lin and B. G. Davis, *Chem. – Asian J.*, 2009, **4**, 630–640.

4 (*a*) N. Krall, F. P. da Cruz, O. Boutureira and G. J. Bernardes, *Nat. Chem.*, 2016, **8**, 103–113; (*b*) O. Boutureira and G. J. L. Bernardes, *Chem. Rev.*, 2015, **115**, 2174–2195; (*c*) C. D. Spicer and B. G. Davis, *Nat. Commun.*, 2014, **5**, 4740; (*d*) G. Zhang, S. Zheng, H. Liu and P. R. Chen, *Chem. Soc. Rev.*, 2015, **44**, 3405–3417; (*e*) T. B. Nielsen, R. P. Thomsen, M. R. Mortensen, J. Kjems, P. F. Nielsen, T. E. Nielsen, A. L. B. Kodal, E. Cló and K. V. Gothelf, *Angew. Chem., Int. Ed.*, 2019, **58**, 9068–9072; (*f*) J. B. Trads, T. Tørring and K. V. Gothelf, *Acc. Chem. Res.*, 2017, **50**, 1367–1374; (*g*) C. D. Spicer, E. T. Pashuck and M. M. Stevens, *Chem. Rev.*, 2018, **118**, 7702–7743; (*h*) C. D. Spicer, T. Triemer and B. G. Davis, *J. Am. Chem. Soc.*, 2012, **134**, 800–803; (*i*) C. D. Spicer, C. Jumeaux, B. Gupta and M. M. Stevens, *Chem. Soc. Rev.*, 2018, **47**, 3574–3620.

5 (*a*) A.-C. Knall and C. Slugovc, *Chem. Soc. Rev.*, 2013, **42**, 5131–5142; (*b*) E. M. Sletten and C. R. Bertozzi, *Angew. Chem., Int. Ed.*, 2009, **48**, 6974–6998.

6 (*a*) B. L. Oliveira, Z. Guo and G. J. L. Bernardes, *Chem. Soc. Rev.*, 2017, **46**, 4895–4950; (*b*) A. C. Knall and C. Slugovc, *Chem. Soc. Rev.*, 2013, **42**, 5131–5142.

7 (*a*) N. K. Devaraj, R. Weissleder and S. A. Hilderbrand, *Bioconjugate Chem.*, 2008, **19**, 2297–2299; (*b*) N. K. Devaraj and R. Weissleder, *Acc. Chem. Res.*, 2011, **44**, 816–827; (*c*) N. K. Devaraj, R. Upadhyay, J. B. Haun, S. A. Hilderbrand and R. Weissleder, *Angew. Chem., Int. Ed.*, 2009, **48**, 7013–7016.

8 (*a*) J. B. Haun, N. K. Devaraj, S. A. Hilderbrand, H. Lee and R. Weissleder, *Nat. Nanotechnol.*, 2010, **5**, 660; (*b*) M. K. Rahim, R. Kota, S. Lee and J. B. Haun, *Nanotechnol. Rev.*, 2013, **2**, 215–227.

9 B. Oller-Salvia, G. Kym and J. W. Chin, *Angew. Chem., Int. Ed.*, 2018, **57**, 2831–2834.

10 (*a*) J. L. Seitchik, J. C. Peeler, M. T. Taylor, M. L. Blackman, T. W. Rhoads, R. B. Cooley, C. Refakis, J. M. Fox and R. A. Mehl, *J. Am. Chem. Soc.*, 2012, **134**, 2898–2901; (*b*) K. Lang, L. Davis, S. Wallace, M. Mahesh, D. J. Cox, M. L. Blackman, J. M. Fox and J. W. Chin, *J. Am. Chem. Soc.*, 2012, **134**, 10317–10320; (*c*) K. Lang, L. Davis, J. Torres-Kolbus, C. Chou, A. Deiters and J. W. Chin, *Nat. Chem.*, 2012, **4**, 298; (*d*) R. J. Blizzard, D. R. Backus, W. Brown, C. G. Bazewicz, Y. Li and R. A. Mehl, *J. Am. Chem. Soc.*, 2015, **137**, 10044–10047; (*e*) T. Machida, K. Lang, L. Xue, J. W. Chin and N. Winssinger, *Bioconjugate Chem.*, 2015, **26**, 802–806; (*f*) Y. Kurra, K. A. Odoi, Y.-J. Lee, Y. Yang, T. Lu, S. E. Wheeler, J. Torres-Kolbus, A. Deiters and W. R. Liu, *Bioconjugate Chem.*, 2014, **25**, 1730–1738.

11 (*a*) M. Baalmann, M. J. Ziegler, P. Werther, J. Wilhelm and R. Wombacher, *Bioconjugate Chem.*, 2019, **30**, 1405–1414; (*b*) D. S. Liu, A. Tangpeerachaikul, R. Selvaraj, M. T. Taylor, J. M. Fox and A. Y. Ting, *J. Am. Chem. Soc.*, 2012, **134**, 792–795.

12 (*a*) M. L. Blackman, M. Royzen and J. M. Fox, *J. Am. Chem. Soc.*, 2008, **130**, 13518–13519; (*b*) C. Canovas, M. Moreau, C. Bernhard, A. Oudot, M. Guillemin, F. Denat and V. Goncalves, *Angew. Chem., Int. Ed.*, 2018, **57**, 10646–10650.

13 S. L. Kuan, T. Wang and T. Weil, *Chem. – Eur. J.*, 2016, **22**, 17112–17129.

14 (*a*) S. Brocchini, S. Balan, A. Godwin, J.-W. Choi, M. Zloh and S. Shaunak, *Nat. Protoc.*, 2006, **1**, 2241–2252; (*b*) S. Shaunak, A. Godwin, J.-W. Choi, S. Balan, E. Pedone, D. Vijayarangam, S. Heidelberger, I. Teo, M. Zloh and S. Brocchini, *Nat. Chem. Biol.*, 2006, **2**, 312–313.

15 S. P. Brown and A. B. Smith, *J. Am. Chem. Soc.*, 2015, **137**, 4034–4037.

16 G. Badescu, P. Bryant, M. Bird, K. Henseleit, J. Swierkosz, V. Parekh, R. Tommasi, E. Pawlisz, K. Jurlewicz, M. Farys, N. Camper, X. Sheng, M. Fisher, R. Grygorash, A. Kyle, A. Abhilash, M. Frigerio, J. Edwards and A. Godwin, *Bioconjugate Chem.*, 2014, **25**, 1124–1136.

17 T. Wang, A. Riegger, M. Lamla, S. Wiese, P. Oeckl, M. Otto, Y. Wu, S. Fischer, H. Barth, S. L. Kuan and T. Weil, *Chem. Sci.*, 2016, **7**, 3234–3239.

18 (*a*) F. F. Schumacher, M. Nobles, C. P. Ryan, M. E. B. Smith, A. Tinker, S. Caddick and J. R. Baker, *Bioconjugate Chem.*, 2011, **22**, 132–136; (*b*) M. Henkel, N. Röckendorf and A. Frey, *Bioconjugate Chem.*, 2016, **27**, 2260–2265.

19 R. Rossin, S. M. van den Bosch, W. ten Hoeve, M. Carvelli, R. M. Versteegen, J. Lub and M. S. Robillard, *Bioconjugate Chem.*, 2013, **24**, 1210–1217.

20 S. L. Kuan, S. Fischer, S. Hafner, T. Wang, T. Syrovets, W. Liu, Y. Tokura, D. Y. W. Ng, A. Riegger, C. Förtsch, D. Jäger, T. F. E. Barth, T. Simmet, H. Barth and T. Weil, *Adv. Sci.*, 2018, 1701036.

21 T. Wang, N. Zabarska, Y. Wu, M. Lamla, S. Fischer, K. Monczak, D. Y. Ng, S. Rau and T. Weil, *Chem. Commun.*, 2015, **51**, 12552–12555.

22 (*a*) D. A. Richards, A. Maruani and V. Chudasama, *Chem. Sci.*, 2017, **8**, 63–77; (*b*) A. Maruani, M. E. Smith, E. Miranda, K. A. Chester, V. Chudasama and S. Caddick, *Nat. Commun.*, 2015, **6**, 6645.

1146 | *Org. Biomol. Chem.*, 2020, **18**, 1140–1147

This journal is © The Royal Society of Chemistry 2020

23 S. Sun, P. Akkapeddi, M. C. Marques, N. Martinez-Saez, V. M. Torres, C. Cordeiro, O. Boutureira and G. J. L. Bernardes, *Org. Biomol. Chem.*, 2019, **17**, 2005–2012.

24 F. R. Salemme, *Annu. Rev. Biochem.*, 1977, **46**, 299–330.

25 K. Qu, J. L. Vaughn, A. Sienkiewicz, C. P. Scholes and J. S. Fetrow, *Biochemistry*, 1997, **36**, 2884–2897.

26 T. Wang, D. Y. W. Ng, Y. Wu, J. Thomas, T. TamTran and T. Weil, *Chem. Commun.*, 2014, **50**, 1116–1118.

27 (*a*) Y. Tachibana, G. L. Fletcher, N. Fujitani, S. Tsuda, K. Monde and S.-I. Nishimura, *Angew. Chem., Int. Ed.*, 2004, **43**, 856–862; (*b*) S. Sun, I. Compañón, N. Martínez-Sáez, J. D. Seixas, O. Boutureira, F. Corzana and G. J. L. Bernardes, *ChemBioChem*, 2018, **19**, 48–52.

28 A. C. A. Roque, M.Â Taipa and C. R. Lowe, *J. Chromatogr. A*, 2005, **1064**, 157–167.

29 T. Wang, Y. Wu, S. L. Kuan, O. Dumele, M. Lamla, D. Y. W. Ng, M. Arzt, J. Thomas, J. O. Mueller, C. Barner-Kowollik and T. Weil, *Chem. Eur. J.*, 2015, **21**, 228–238.

This journal is © The Royal Society of Chemistry 2020

Org. Biomol. Chem., 2020, **18**, 1140–1147 | **1147**

Supporting Information for

Site-selective protein modification via disulfide rebridging for fast tetrazine/*trans*-cyclooctene bioconjugation

Lujuan Xu[a,b], Marco Raabe[a, b], Maksymilian Marek Zegota,[a, b] João C. F. Nogueira[c,], Vijay Chudasama[c], Seah Ling Kuan*[a,b], Tanja Weil*[a,b]

a. Max Planck Institute for Polymer Research, Ackermannweg 10, 55128 Mainz, Germany

b. Institute of Inorganic Chemistry I, University of Ulm, Albert-Einstein-Allee 11, 89081 Ulm, Germany

c. Department of Chemistry, University College London, London, UK

1. General experimental details

2. Synthetic Protocol of IC-Tetrazine

3. Synthesis of tetrazine modified somatostatin (SST-Tetrazine)

4. Synthesis of tetrazine modified Fab fragment (Fab-Tetrazine)

5. Synthesis and characterization of CytC-PEG3-TCO

6. SST-Tetrazine conjugation with TCO-PEG12, TCO-Cy5 and CytC-PEG3-TCO

7. Fab-Tetrazine conjugation with TCO-Cy5, TCO-PEG113

8. Stability study of SST-Tetrazine, Fab-Tetrazine and Fab-Cy5

9. CD experiment of SST-Tetrazine and Fab-Tetrazine

10. Enzyme-linked immunosorbent assay (ELISA) experiment

11. Reference

1. General experimental details

Unless otherwise stated, all the operations were performed without taking precautions to exclude moisture and air. All the organic solvents (CH_2Cl_2, $CHCl_3$, Ethyl Acetate (EA), acetonitrile (ACN)) were bought from commercial sources (Merck, Sigma Aldrich and so on) and are used directly without further purification. IgG Fab Fragment from Human (polyclonal) was obtained from Dianova GmbH and used as bought. Methyltetrazine *N*-hydroxysuccinimide (NHS) ester, *trans*-cyclooctene (TCO)-PEG3-maleimide were bought from Click Chemistry Tools. Sulfo-Cy5-TCO was bought from Santa Cruz Biotechnology. Tetrazine-5-FAM were purchased from Jena Bioscience. TCO-PEG113 was obtained from NANOCS. TCO-PEG12 was bought from Broadpharm. Iso-yeast Cytochrome C was purchased from Sigma-Aldrich. Glutathione was bought from Sigma-Aldrich. Protein L coated well plate, BCA assay and enhanced chemiluminescence (ECL) solution were purchased from Thermo Fisher Scientific. 4,4′-dithiodipyridine was bought from ACROS organics. Zeba spin desalting column (7K MWCO) was obtained from Thermo Fisher Scientific. H_2O used for the reactions was obtained from the Millipore purification system. Vivaspin sample concentrators were purchased from GE Healthcare. Reaction progress was monitored by thin layer chromatography (TLC) using Merck 60 F_{254} pre-coated silica gel plates and visualized under ultraviolet lamp (254 nm) or using appropriate staining solution ($KMnO_4$, ninhydrin, iodine). Flash column chromatography was carried out using Merck silica gel 60 mesh. High performance liquid chromatography (HPLC) was carried out using Shimadzu Analytical HPLC system. NMR spectra were recorded on Bruker Avance 300 NMR spectrometer and the chemical shifts (δ) were reported as parts per million (ppm) referenced with respect to the residual solvent peaks. MALDI-TOF-MS spectra were acquired on a Bruker Time-of-flight MS rapifleX. Fluorescence (or absorbance) spectra or intensities were measured on microplate reader (Tecan Spark 20M). The chemiluminescence was measured by GloMax Discover Microplate Reader.

2. Synthetic Protocol of IC-Tetrazine
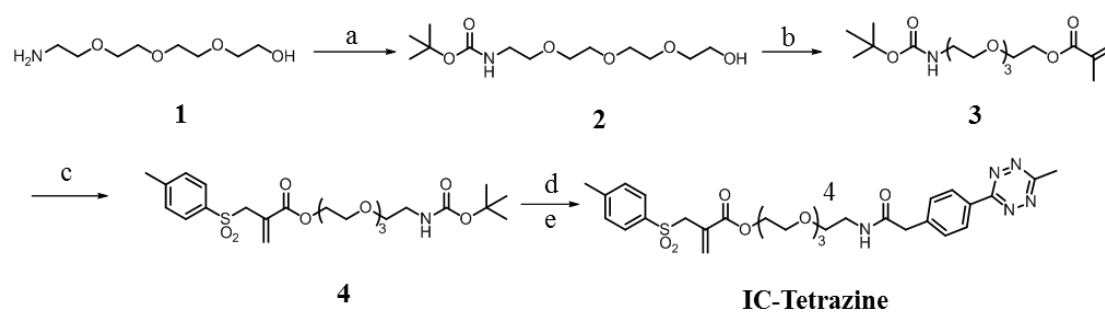
Scheme 1 Synthesis of tetrazine-containing disulfide rebridging reagent (IC-Tetrazine). (a) Di-*tert*-butyl dicarbonate, CH_2Cl_2, overnight. (b) methacrylchloride, Et_3N, CH_2Cl_2, 90%. (c)

1. I$_2$, sodium *p*-toluenesulfinate, CH$_2$Cl$_2$, 3 days. 2. Et$_3$N, CH$_2$Cl$_2$, overnight. 3. Et$_3$N, ethyl acetate, 95 °C, overnight, yield after all three steps: 60%. (d) Trifluoroacetic acid (TFA), CH$_2$Cl$_2$, 98%. (e) methyltetrazine NHS ester, Et$_3$N, CH$_2$Cl$_2$, overnight, 40%.

Synthesis of 2,2-dimethyl-4-oxo-3,8,11,14-tetraoxa-5-azahexadecan-16-yl methacrylate (compound 3)

Step a: 2-(2-(2-(2-aminoethoxy)ethoxy)ethoxy)ethanol (**1**, 0.50 g, 2.59 mmol) was dissolved in 6 mL CH$_2$Cl$_2$. Di-*tert*-butyl dicarbonate (0.68 g, 3.10 mmol) was also dissolved in 6 mL CH$_2$Cl$_2$ and then was added to the former solution dropwise with a syringe pump. The reaction mixture was stirred at room temperature overnight and the solvent was removed under vacuum. The compound **2** was got as a colorless oil and used directly for the next step without further purification.

Step b: To a 10 mL CH$_2$Cl$_2$ solution of crude product from step a (200 mg, 0.68 mmol) was added Et$_3$N (82.9 mg, 114 μL, 0.82 mmol) followed by methacryloyl chloride (85.7 mg, 0.82 mmol) at 0 °C. The mixture was stirred at room temperature overnight. The solvent was evaporated under high vacuum and the crude product was dissolved in 30 mL CH$_2$Cl$_2$. Subsequently, the crude product was washed with 1 M HCl and brine solution. The organic layer was dried over anhydrous Na$_2$SO$_4$ and the solvent was removed under vacuum. The crude product was purified by column chromatography (EA : hexane = 1:1) to afford the compound **3** as colorless oil in 90% yield.

^{1}H NMR (300 MHz, chloroform-d) δ 6.10 (s, 1H), 5.57–5.53 (s, 1H), 4.32 – 4.23 (m, 2H), 3.77 – 3.54 (m, 12H), 2.47 (t, J = 6.6 Hz, 2H), 1.92 (s, 3H), 1.42 (s, 9H).

^{13}C NMR (75 MHz, chloroform-d) δ 167.09, 155.92, 135.98, 125.83, 70.58, 70.24, 69.16, 63.86, 28.42, 18.31.

LC-MS: *m/z* = 362 [M+H]$^+$, 384 [M+Na]$^+$ (calculated exact mass: 362.21 [M+H]$^+$, 384.21 [M+Na]$^+$, formula: C$_{17}$H$_{31}$NO$_7$)

Synthesis of 2,2-dimethyl-4-oxo-3,8,11,14-tetraoxa-5-azahexadecan-16-yl 2-(tosylmethyl)-acrylate (compound 4)

Compound **3** (211 mg, 0.58 mmol) was dissolved in 5 mL CH$_2$Cl$_2$ followed by adding the sodium *p*-toluenesulfinate (156 mg, 0.87 mmol) and I$_2$ (222 mg, 0.87 mmol) sequentially. The reaction mixture was stirred at room temperature for 3 days. Next, Et$_3$N (176 mg, 242 μL, 1.74 mmol) was added to the mixture and stirred overnight. Then the organic layer was washed with 1 M HCl solution, saturated NaHCO$_3$ solution, Na$_2$S$_2$O$_3$ solution and brine solution. The organic layer was dried over MgSO$_4$ and the solvent was removed by high vacuum. The residue was dissolved in 10 mL ethyl acetate and Et$_3$N (176 mg, 242 μL, 1.74 mmol) was added dropwise at 0 ℃. The mixture was refluxed overnight. After that, the solvent was evaporated

and the crude product was purified by column chromatography (EA : hexane = 3:1) to afford compound **4** as slight yellow oil in 60% yield.

^{1}H NMR (300 MHz, chloroform-d) δ 7.72 (d, J = 8.3 Hz, 2H), 7.31 (d, J = 8.0 Hz, 2H), 6.50 (s, 1H), 5.86 (s, 1H), 4.17 – 4.11 (m, 4H), 3.68 – 3.58 (m, 10H), 3.52 (t, J = 5.2 Hz, 2H), 3.28 (t, J = 4.8 Hz, 2H), 2.42 (s, 3H), 1.42 (s, 9H).

^{13}C NMR (75 MHz, chloroform-d) δ 164.82, 155.98, 144.87, 135.37, 133.44, 129.61, 128.67, 79.25, 70.49, 70.23, 68.81, 64.50, 57.57, 40.52, 28.42, 21.54.

LC-MS: m/z = 516 [M+H]$^+$, 538 [M+Na]$^+$ (calculated exact mass: 516.22 [M+H]$^+$, 538.22 [M+Na]$^+$, formula:$C_{24}H_{37}NO_9S$)

Synthesis of 1-(4-(6-methyl-1,2,4,5-tetrazin-3-yl)phenyl)-2-oxo-6,9,12-trioxa-3-azatetradecan-14-yl 2-(tosylmethyl)acrylate (IC-Tetrazine)

Step d: In a 10 mL flask, compound **4** (15.1 mg, 0.03 mmol) was dissolved in 3 mL CH_2Cl_2. Trifluoroacetic acid (TFA, 171.2 mg, 1.54 mmol) was also added. The resulting mixture was stirred at room temperature overnight. The solvent and TFA was removed in vacuum to obtain 11.9 mg boc-deprotected product in 98%.

Step e: Boc-deprotected product (11.9 mg, 0.03 mmol) was dissolved in 2 mL CH_2Cl_2 followed by adding *N,N*-diisopropylethylamine (DIEA, 7.5 mg, 0.06 mmol) to ensure a basic condition. Methyltetrazine-NHS ester (11.4 mg, 0.03 mmol) was dissolved in 1 mL CH_2Cl_2 and added to the aforementioned mixture above. The reaction mixture was stirred at room temperature overnight and the solvent was evaporated under high vacuum. The residue was dissolved in 20 mL CH_2Cl_2 and was washed with brine solution. The organic layer was dried over anhydrous MgSO$_4$ and the solvent was removed under high vacuum. The residue was purified by column chromatography (CH_2Cl_2 : MeOH = 20:1) to afford compound **IC-Tetrazine** as red oil in 40% yield. The purify of IC-Tetrazine is 98% based on the quantification of the peak at 214 nm in LC-MS.

^{1}H NMR (300 MHz, chloroform-d) δ 8.54 (d, J = 7.5 Hz, 2H), 7.72 (d, J = 7.6 Hz, 2H), 7.51 (d, J = 7.8 Hz, 2H), 7.33 (d, J = 7.5 Hz, 2H), 6.50 (s, 1H), 5.83 (s, 1H), 4.25 – 4.08 (m, 4H), 3.75 – 3.37 (m, 16H), 3.09 (s, 3H), 2.44 (s, 3H).

^{13}C NMR (75 MHz, CDCl$_3$) δ 170.10, 167.24, 164.70, 163.85, 145.37, 144.96, 140.00, 135.50, 135.21, 133.46, 130.23, 129.73, 128.93, 128.73, 128.28, 70.62, 70.49, 70.25, 69.77, 68.81, 64.48, 57.60, 55.28, 43.48, 39.53, 35.78, 21.72, 21.12.

LC-MS: m/z = 628 [M+H]$^+$, 650 [M+Na]$^+$(calculated exact mass: 628.24 [M+H]$^+$, 650.24 [M+Na]$^+$, formula:$C_{30}H_{37}N_5O_8S$)
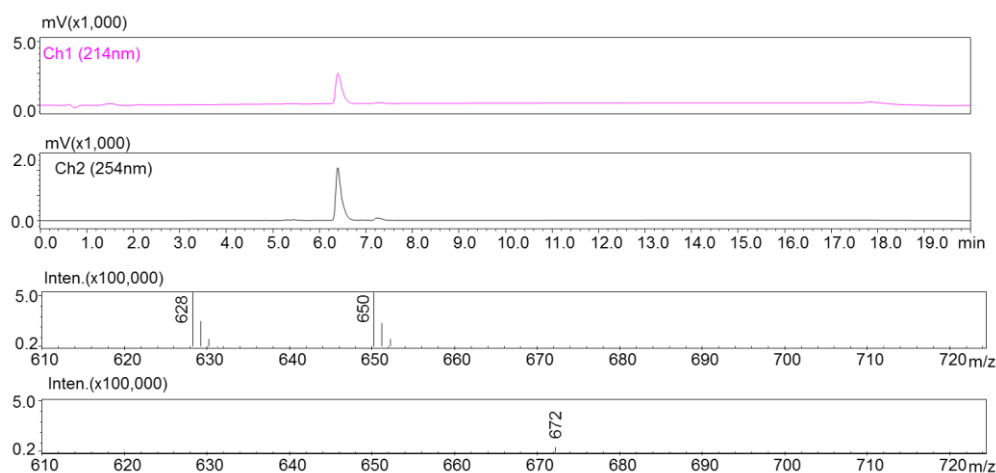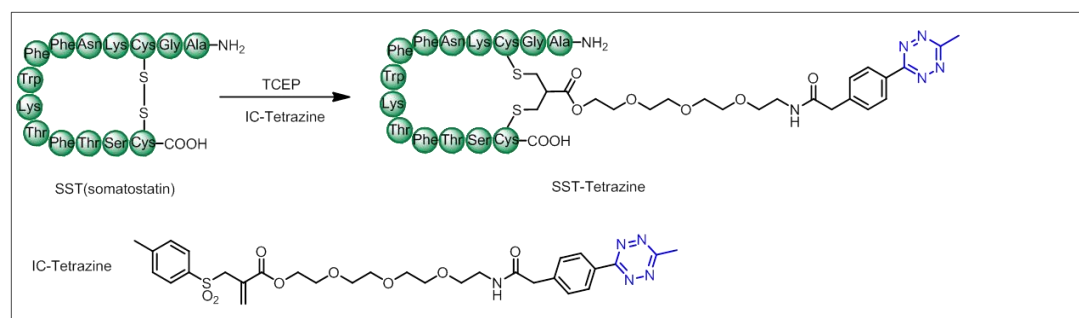
Figure S1 LC-MS data of IC-Tetrazine

3. Synthesis of tetrazine modified somatostatin (SST-Tetrazine)

Scheme S2 Synthesis of SST-Tetrazine

Somatostatin (SST, 2 mg, 1.22 μmol) was dissolved in 1 mL ACN/phosphate buffer (PB, 50 mM, pH = 7.8) mixture (v/v = 2:3). Tris(2-carboxyethyl)phosphine (TCEP, 0.7 mg, 2.44 μmol) was dissolved in 100 μL ACN/PB mixture and added to the somatostatin solution. The mixture was incubated at room temperature for 30 min. Afterwards, IC-Tetrazine (1.9 mg, 3.05 μmol) was dissolved in 1 mL ACN/PB mixture as well which was added to the SST and TCEP solution. The reaction mixture was degassed for several minutes to exclude air in the solvent and gently shaken at room temperature overnight. The crude product was purified by Prep HPLC using Atlantis Prep OBD T3 Column (19×100 mm, 5 μm) with the mobile phase starting from 100% solvent A (0.1% TFA in MilliQ water) and 0% solvent B (0.1% TFA in ACN), reaching 45% B at 35 min and finally reaching 100% B at 42 min with a flow rate of 10 mL/min. The absorbance was monitored at 280 nm, 254 nm and 515 nm. The retention time for SST-Tetrazine was 34 min. About 0.8 mg SST-Tetrazine was obtained after lyophilisation (30% yield).

LC-MS: m/z = 1056 [M+2H]$^{2+}$, 705 [M+3H]$^{3+}$, 1054 [M-2H]$^{2-}$

MALDI-TOF-MS (matrix: sinapinic acid): $m/z = 2110.95$ [M+H]$^+$ (calculated exact mass: 2110.95 [M+H]$^+$, formula: $C_{99}H_{135}N_{23}O_{25}S_2$)
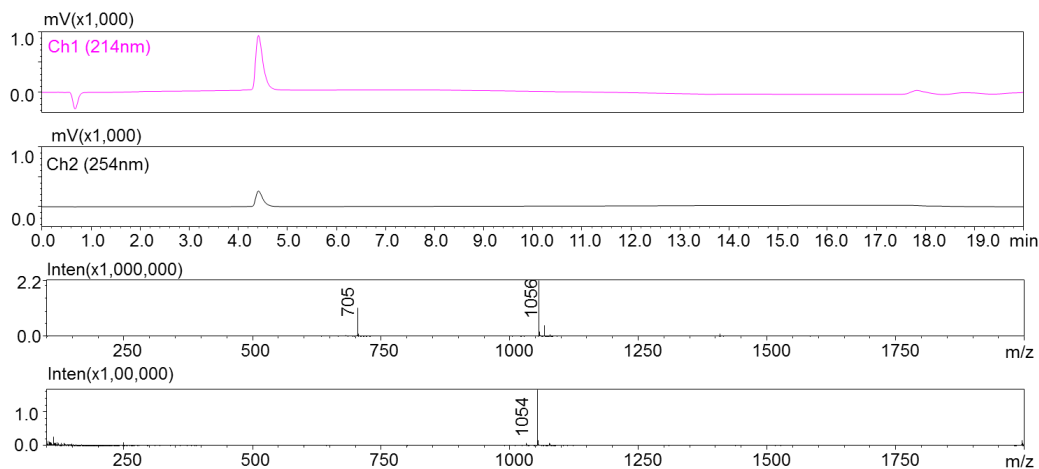
Figure S2 LC-MS data of purified SST-Tetrazine
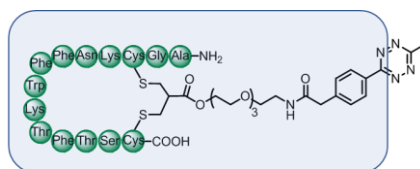
Fragmentation of SST-Tetrazine
Mr = 2041.93 Da

Figure S3 The chemical structure of the fragmentation part (in the frame) of SST-Tetrazine in MALDI-TOF-MS spectrum

Furthermore, SST-Tetrazine is also showing no obvious degradation after one year storage in the freezer based on the LC-MS data.
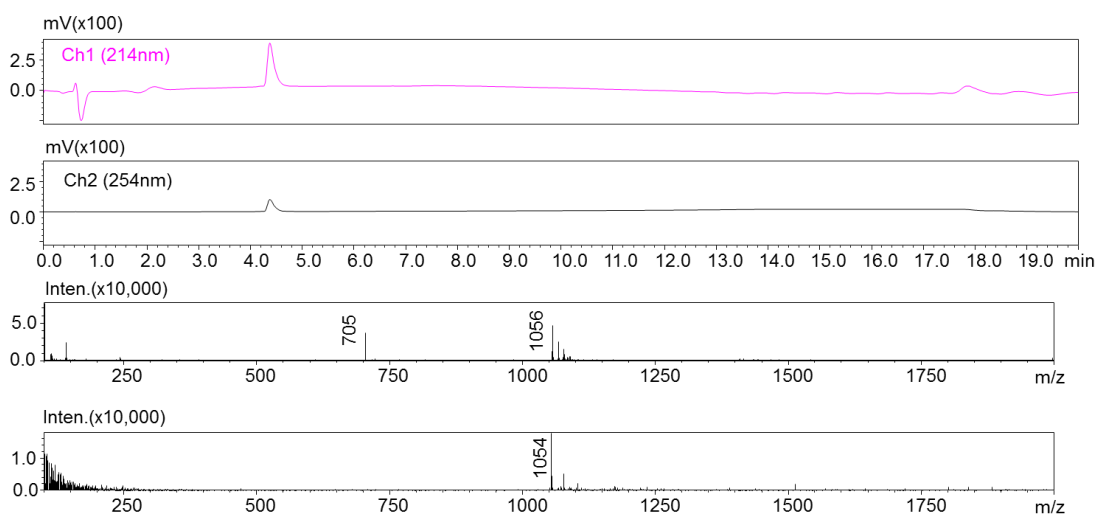
Figure S4 LC-MS data of SST-Tetrazine after one year storage in the freezer (−20 ℃)

4. Synthesis of tetrazine modified Fab fragment (Fab-Tetrazine)
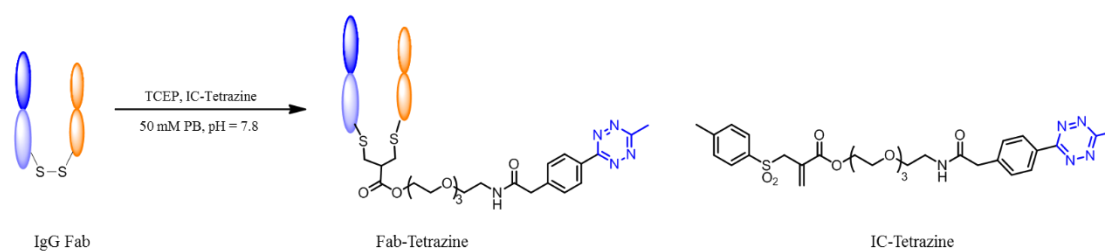
Scheme S3 Synthesis of Fab-Tetrazine

First, native IgG Fab was incubated with different amounts of TCEP to determine how much TCEP is necessary to totally reduce the interchain disulfide bond of IgG Fab. IgG Fab (3.2 µg, 0.067 nmol, 4.8 mg/mL, 1 eq) was mixed with 1 eq, 5 eq, 10 eq, 25 eq, 50 eq, 100 eq TCEP for incubation for 1 hour. Then, the mixture was loaded to the SDS-PAGE. SDS-PAGE data (Figure S5A) showed that 50 eq TCEP is necessary to fully reduce the interchain disulfide bond of IgG Fab.

Second, the buffer of the Fab solution (100 µg, 4.8 mg/mL, 2.08 nmol) was changed to PB (50 mM, pH = 7.8) by using 10 kDa MWCO ultrafiltration tube and diluted to 1 mg/mL with PB (50 mM, pH = 7.8). TCEP (30 µg, 0.10 µmol) was dissolved in 10 µL PB (50 mM, pH = 7.8) and added to the Fab solution. Next the mixture was incubated at room temperature for 1 hour. IC-Tetrazine (65.5 µg, 0.10 µmol, 20 mg/mL in dimethyl sulfoxide (DMSO)) was first dissolved in 5.5 µL DMSO and then added to the Fab solution. The mixture was incubated at room temperature overnight. Excess reagents were removed by repeated ultrafiltration in water using Vivaspin sample concentrator (10 kDa MWCO). The sample was analyzed by sodium dodecyl sulfate–polyacrylamide gel electrophoresis (SDS-PAGE). Based on the concentration calculated from gel densitometry, about 80% of the Fab fragment was successfully modified (SDS-PAGE is shown in Figure S5B).

SDS gel electrophoresis: 10% separating gel was prepared in the following order: 2.5 mL 40% acrylamide solution, 5 mL water, 2.5 mL 4× Bis-Tris gel buffer, 100 µL of 10% sodium dodecyl sulfate buffer, 50 µL ammonium persulfate (v/w) solution, 5 µL tetramethylethylenediamine. The mixed gel solution was added to the Bio-Rad Mini-Gel apparatus and stand for 15 min for polymerization. The isopropanol was added above the separating gel to exclude air. Next, 6% stacking gel was prepared in the following order: 0.75 mL 40% acrylamide solution, 3 mL water, 1.25 mL 4× Bis-Tris gel buffer, 30 µL 10% sodium dodecyl sulfate buffer, 25 µL ammonium persulfate (v/w) solution, 2.5 µL tetramethylethylenediamine. The stacking gel was also added above the separating gel after totally removing the isopropanol. A 10-well comb was inserted and the stacking gel was polymerized for another 10 min. For the sample loading to the SDS-PAGE, 16 µL protein solution was mixed with 6 µL loading dye and 1 µL TCEP solution. The mixture was incubated for one hour and then loaded to the gel.

On the other hand, a thiol-quantification experiment was performed to quantify how much thiol groups are still left in Fab-Tetrazine sample. 4,4′-Dithiodipyridine is a disulfide-containing reagent which reacts with protein thiols to form stoichiometric amounts of the chromogenic compound 4-thiopyridone (4-TP), absorbing at 324 nm. In this experiment, cysteine was selected as a standard compound. The procedure is described below:

1. 30 μL of 4,4′-dithiodipyridine (2 mM in 100 mM citrate buffer, pH = 4.5) incubated with 30 μL cysteine solution (concentration: 0.01 mM, 0.05 mM, 0.1 mM, 0.25 mM, 0.5 mM, dissolved in 100 mM citrate buffer, pH = 4.5) for 15 minutes at room temperature. 50 μL of cysteine and 4,4′-dithiodipyridine mixture were taken in 384-well plate. Absorbance was monitored at 324 nm and the standard curve is shown in Figure S5C.

2. 50 μL of Fab-Tetrazine sample was mixed with 100 eq TCEP (100 mM PB, pH = 7.8) and incubated for 1 hour to tally reduce the unmodified disulfide bonds.

3. Zeba spin desalting columns (7K MWCO) was buffer exchanged to the 100 mM citrate buffer first following the protocol provided by the supplier. Next, the Fab-Tetrazine solution was loaded to the column and the desalting steps was repeated six to eight times to tally remove the residue TCEP. After desalting, the protein concentration was determined to be 3.21 mg/mL based on the BCA assay following the protocol provided by the supplier.

4. Next, 30 μL of 4,4′-dithiodipyridine (2 mM in 100 mM citrate buffer, pH = 4.5) was incubated with 30 μL the Fab-Tetrazine solution at room temperature for 15 minutes. 50 μL of the protein and 4,4′-dithiodipyridine mixture were taken in 384-well plate. Absorbance was monitored at 324 nm and 0.51 was obtained for the Fab-Tetrazine sample.

Based on the standard curve, 0.51 indicated the concentration of thiol groups in 60 μL protein and 4,4′-dithiodipyridine mixture is 0.018 mM. The concentration of unmodified disulfide bond is 0.009 mM. The concentration of Fab-Tetrazine is 1.6 mg/mL (0.033 mM) in 60 μL protein and 4,4′-dithiodipyridine mixture. From this readout, about 73% of IgG Fab was successfully modified.
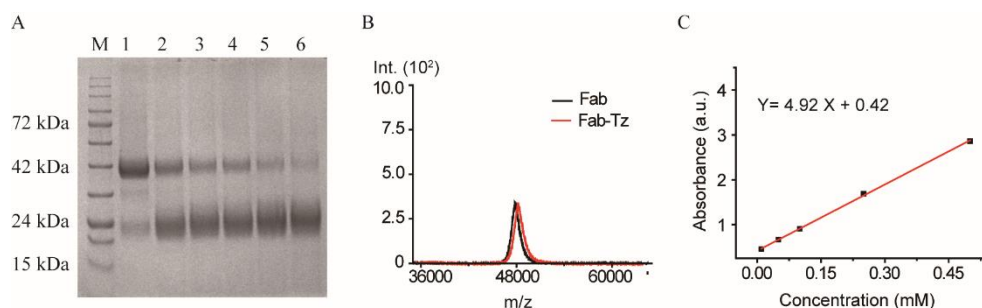

Figure S5 (A) SDS-PAGE analysis of Fab fragment which was incubated with different amounts of TCEP (M: Protein Marker, 1: Fab + 1 eq TCEP, 2: Fab + 5 eq TCEP, 3: Fab + 10 eq TCEP, 4: Fab + 20 eq TCEP, 5: Fab + 40 eq TCEP, 6: Fab + 50 eq TCEP) (B) MALDI-

TOF-MS of native IgG Fab (found: 48.0k [M+H]+, calculated: 48.0k [M+H]+) and Fab-Tetrazine (found: 48.5k [M+H]+, calculated: 48.5k [M+H]+) (C) standard curve based on checking the absorbance of cysteine and 4,4′-dithiodipyridine solution at 324 nm

5. Modification and characterization of Cytochrome C (CytC) with *trans*-cyclooctene (TCO) group
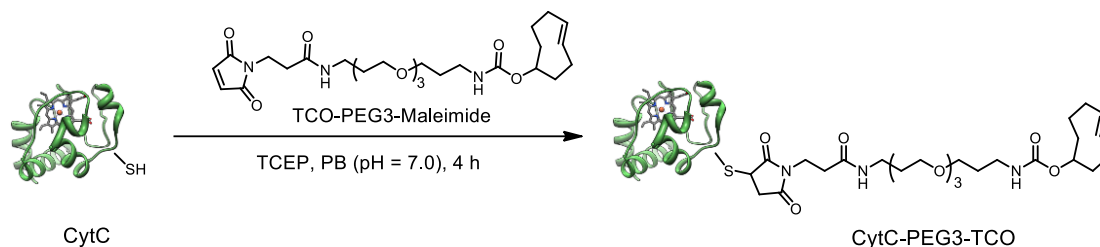
Scheme S4 Modification of Cytochrome C with TCO-PEG3-Maleimide

CytC (212 µg, 0.02 µmol) was dissolved in 212 µL PB (50 mM, pH = 7.0) and mixed with TCEP (9.7 µg, 0.03 µmol). The mixture was shaken at room temperature for 1 hour. TCO-PEG3-Maleimide (267 µg, 0.51 µmol) was added to the mixture above and shaken at room temperature for 4 hours. Afterwards, the crude product was purified by repeated ultrafiltration in water using Vivaspin sample concentrator (5 kDa MWCO). The MALDI-TOF-MS of the modified product (CytC-PEG3-TCO) is shown in Figure S6B. Compared to the native CytC (Figure S6A), the molecular weight of CytC-PEG3-TCO increased by 525 Da which corresponds to the molecular weight of TCO-PEG3-Maleimide (523.62 Da).
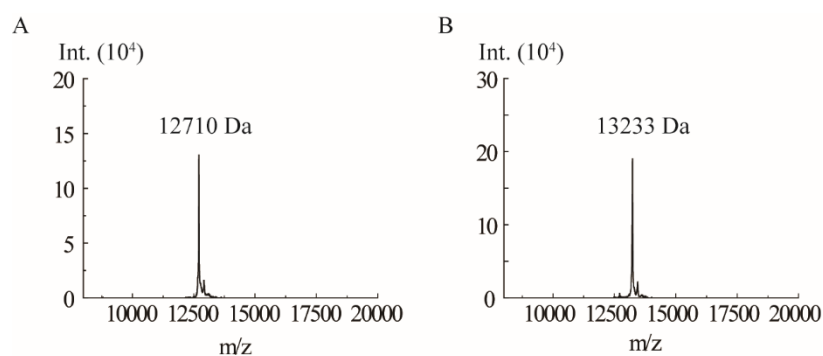
Figure S6 MALDI-TOF-MS of (A) native CytC (found: 12710 [M+H]+, calculated: 12588 [M+H]+) and (B) CytC-PEG3-TCO (found: 13233 [M+H]+, calculated: 13235 [M+H]+)
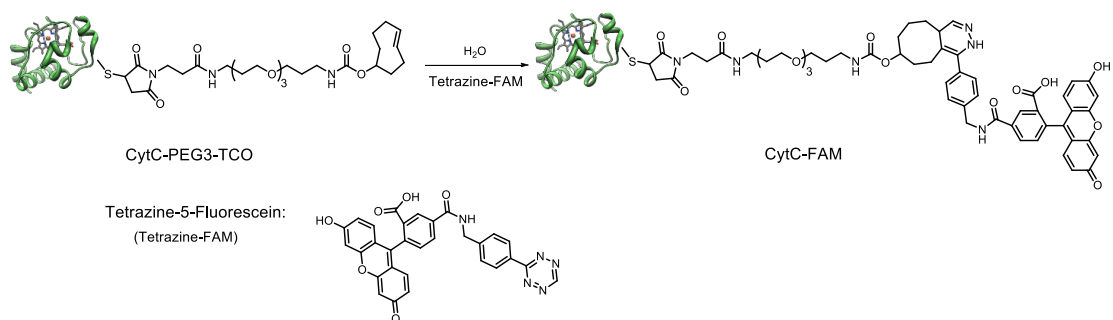
Scheme S5 Reaction between CytC-PEG3-TCO and Tetrazine-FAM

In order to check the modification yield of CytC with the TCO group, CytC-PEG3-TCO was used to react with a dye (Tetrazine-FAM) in H_2O. After reaction, the modification yield was estimated based on the absorbance of CytC at 280 nm and the FAM dye at 490 nm.

CytC-PEG3-TCO (70 μg, 5.29 nmol) was mixed with 2.27 μL Tetrazine-FAM (25.7 μg, 0.05 μmol, 10 mg/mL stock solution in DMSO) in H_2O. The mixture was shaken at room temperature for 1 hour. After that, the crude product was purified by repeated ultrafiltration in water using Vivaspin sample concentrator (5 kDa MWCO) to get the purified CytC-PEG3-FAM. The degree of labelling (DOL) was calculated based on the following equation:

$$DOL = \frac{A_{max} \times \varepsilon_{280}\,(protein)}{(A_{280} - A_{max} \times CF) \times \varepsilon_{max}}$$

We check the absorbance of CytC-PEG3-TCO at 280 nm and 490 nm, the values are listed below:

A_{280} (the absorbance of the sample at 280 nm) = 0.42,

A_{490} (the absorbance of the sample at 490 nm) = 0.89

ε_{280} (the extinction coefficient of CytC at 280 nm) = 13075 $M^{-1}cm^{-1}$

ε_{max} (the extinction coefficient of FAM dye at 490 nm) = 83000 $M^{-1}cm^{-1}$

CF (correction factor) = 0.3

Based on the calculation, the DOL is 90%.

Absorbance at 280 nm (A_{280}) is used to determine the protein concentration in a sample. However, fluorescent dyes also absorb at 280 nm. Therefore, a correction factor must be used to adjust for A_{280} contributed by the dye. The correction factor (CF) equals the A_{280} of the dye divided by the A_{max} of the dye as shown in the equation above.

6. SST-Tetrazine conjugation with TCO-PEG12, TCO-Cy5 and CytC-PEG3-TCO
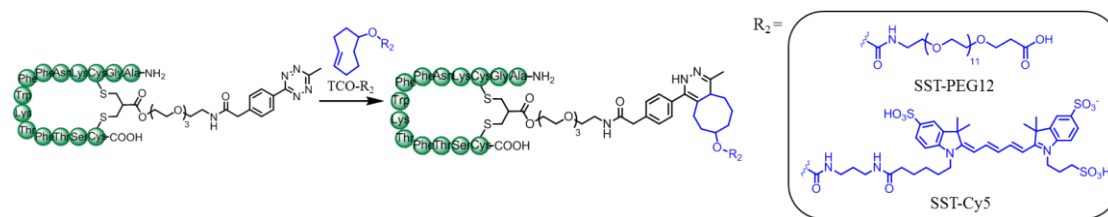
Scheme S6 Bioconjugation between SST-Tetrazine, TCO-PEG12 and TCO-Cy5

SST-Tetrazine (2 mg, 0.95 μmol) was dissolved in 1.332 mL PB (50 mM, pH = 7.4). TCO-PEG12 (730 μg, 1.00 μmol) was dissolved in 667 μL PB (50 mM, pH = 7.4) and added to the SST-Tetrazine solution. The reaction mixture was shaken for 30 min. After mixing the two components, the pink color originating from the tetrazine group disappeared immediately. The crude product was purified by semi-preparative HPLC using Agilent Eclipse XDB-C18 column (9.4 × 250 mm, 5 μm) with the mobile phase starting from 100% solvent A (0.1% TFA in MilliQ water) and 0% solvent B (0.1% TFA in ACN), reaching 43% B at 35 min and finally reaching 100% B at 38 min with a flow rate of 4 mL/min. The absorbance was monitored at 280 nm and 254 nm. The retention time for SST-PEG12 was 32 min. 2.56 mg SST-PEG12 was obtained (yield: 95%).

LC-MS: m/z = 718 [M+Na+3H]$^{4+}$, 959 [M+Na+2H]$^{3+}$, 966 [M+2Na+H]$^{3+}$, 1438 [M+Na+H]$^{2+}$, 1424 [M-H]$^-$

MALDI-TOF-MS (matrix: sinapinic acid): m/z = 2852.2102 [M+H]$^+$ (calculated exact mass: 2852.3873 [M+H]$^+$, formula: $C_{135}H_{202}N_{22}O_{41}S_2$).
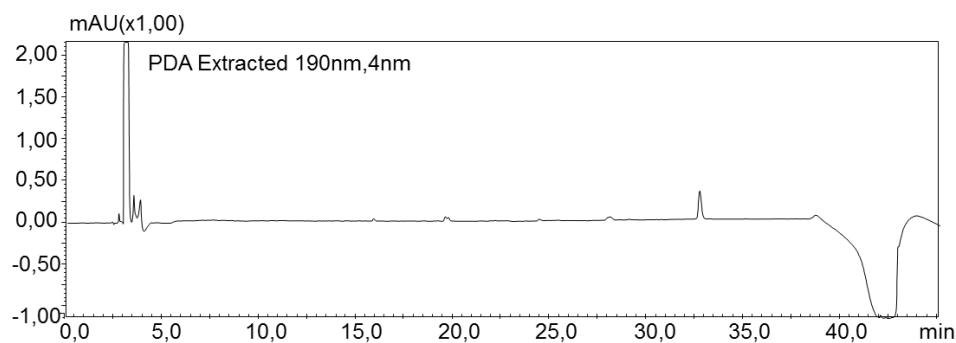
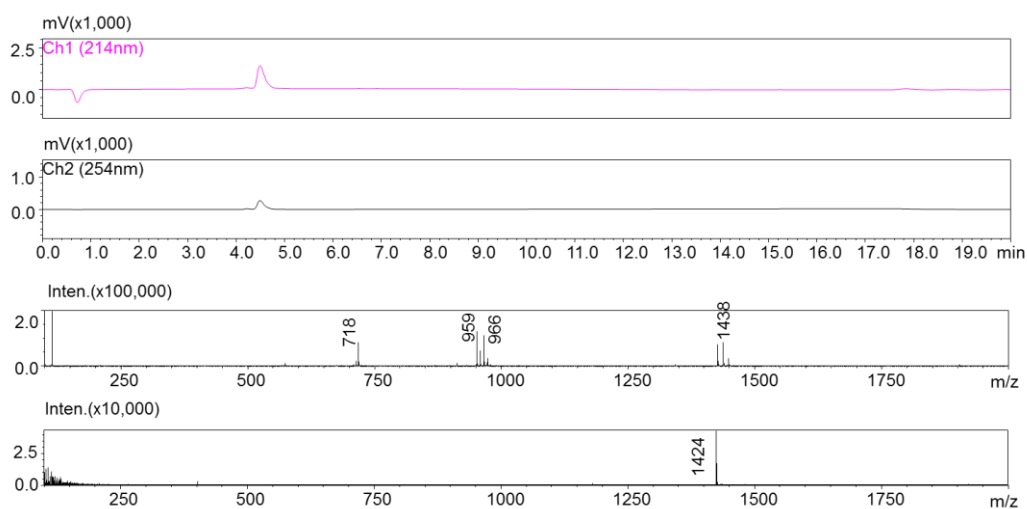Figure S7 HPLC chromatogram (280 nm detection wavelength) of SST-PEG12

Figure S8 LC-MS data of SST-PEG12

SST-Tetrazine (180 mg, 0.85 μmol) was dissolved in 1.26 mL PB (50 mM, pH = 7.4). TCO-Cy5 (1.03 μg, 0.9 μmol) was dissolved in 252 μL DMSO and added to the SST-Tetrazine solution. The reaction mixture was stirred for 30 min. The crude product was purified by Semipreparative HPLC using Agilent Eclipse XDB-C18 column (9.4×250 mm, 5 μm) with the mobile phase starting from 100% solvent A (0.1% TFA in MilliQ water) and 0% solvent B (0.1% TFA in ACN), reaching 43% B at 35 min and finally reaching 100% B at 38 min with a flow rate of 4 mL/min. The absorbance was monitored at 280 nm and 254 nm. The retention time for SST-Cy5 was 28.5 min. 2.3 mg SST-Cy5 was obtained (yield: 90%).

LC-MS: m/z = 1014 [M+3H]$^{3+}$, 1520 [M-2H]$^{2+}$, 1012 [M-3H]$^{3-}$

MALDI-TOF-MS (matrix: sinapinic acid): m/z = 3041.1742 [M+H]$^{+}$ (calculated exact mass: 3041.2939 [M+H]$^{+}$, formula: $C_{145}H_{197}N_{25}O_{37}S_5$)

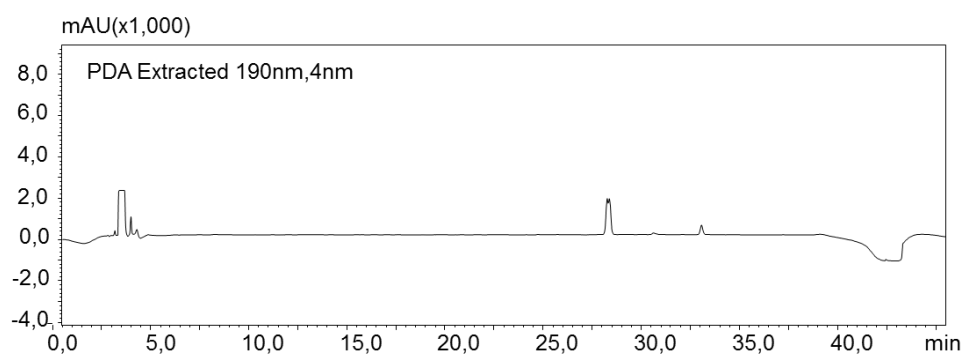
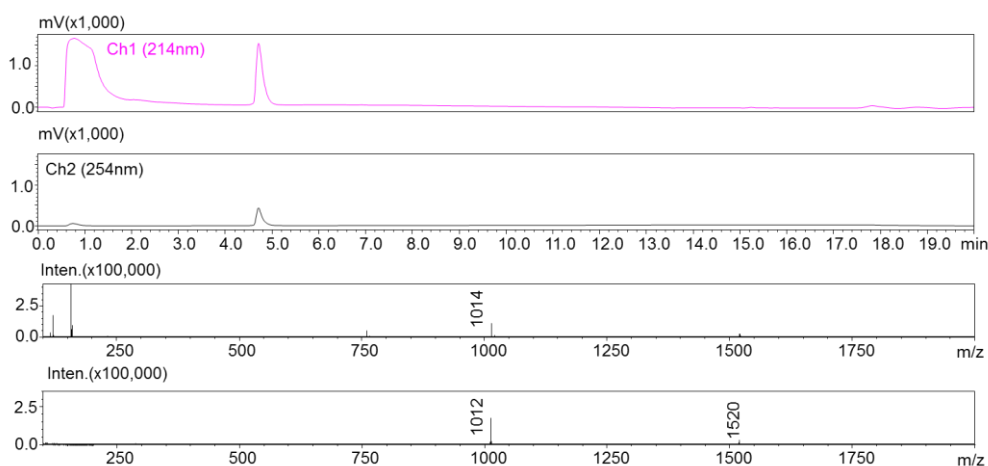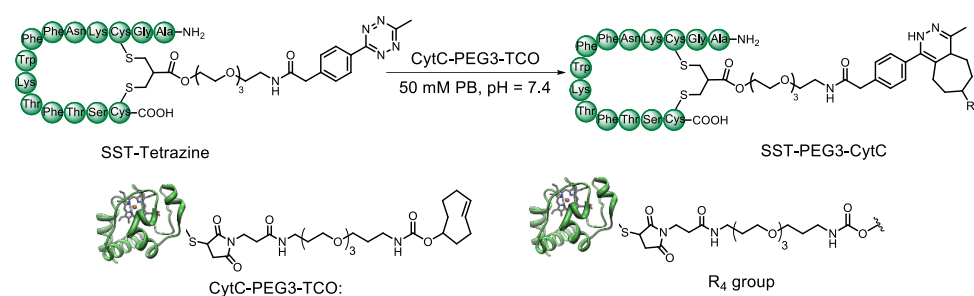Figure S9 HPLC chromatogram (280 nm detection wavelength) of SST-Cy5

Figure S10 LC-MS data of SST-Cy5

Scheme S7 Bioconjugation between SST-Tetrazine and CytC-PEG3-TCO

SST-Tetrazine (32 μg, 0.015 μmol) was mixed with CytC-PEG3-TCO (132 μg, 0.010 μmol) in PB (50 mM, pH = 7.4). The mixture was shaken for 30 min. Afterwards, the reaction mixture was purified by repeating ultrafiltration in water using Vivaspin sample concentrator (5 kDa MWCO) to get the purified SST-PEG3-CytC. The desired SST-PEG3-CytC was characterized by MALDI-TOF-MS and SDS-PAGE.

7. Fab-Tetrazine conjugation with TCO-Cy5 and TCO-PEG113
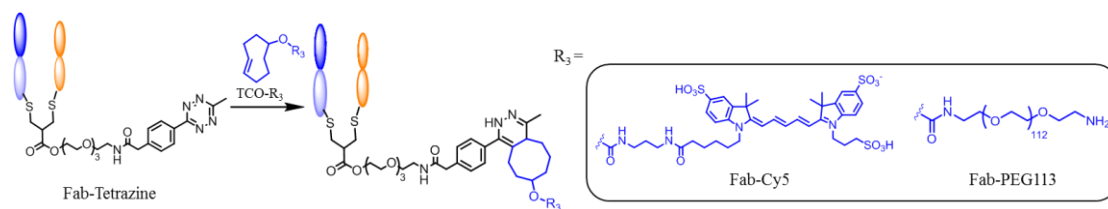
Scheme S8 Bioconjugation between Fab-Tetrazine, TCO-Cy5 and TCO-PEG113

Fab-Tetrazine (48 μg, 1.00 nmol) was dissolved in 85 μL PB (50 mM, pH = 7.4). TCO-Cy5 (5.7 μg, 5.00 nmol, 20 mg/mL in DMSO stock solution) was added to the Fab-Tetrazine solution. The reaction mixture was incubated at room temperature for 30 min. Afterwards, the crude product was purified by repeated ultrafiltration in water using Vivaspin sample

13

concentrator (10 kDa MWCO). Based on Figure S11A, Fab-Cy5 showed obvious fluorescence compared to the Fab-Tetrazine indicating the successful conjugation.

The degree of labelling of Fab-Cy5 was calculated using two different methods.
One method to determine the degree of labeling of Fab-Cy5 is based on the following equation:

$$DOL = \frac{A_{max} \times \varepsilon_{280}\,(protein)}{(A_{280} - A_{max} \times CF) \times \varepsilon_{max}}$$

After extensive desalting steps using Zeba spin desalting columns (repeated six to eight times to totally remove the free dye), we check the absorbance of Fab-Cy5 at 280 nm and 650 nm, the values are listed below:

A_{280} (the absorbance of the sample at 280 nm) = 0.23

A_{max} (the absorbance of the sample at 650 nm) = 0.56

ε_{280} (the extinction coefficient of native Fab at 280 nm) = 70000 $M^{-1}cm^{-1}$

ε_{max} (the extinction coefficient of Cy5 dye at 650 nm) = 250000 $M^{-1}cm^{-1}$

CF (correction factor) = 0.03

Based on the calculation, the DOL is 73%.

The other method to determine the degree of labelling is based on the gel densitometry. The absorbance of Fab-Cy5 at 650 nm is 0.56. The Cy5 concentration was 13.3 μg/mL (13.8 μM) calculated using the calibration curve (Figure 11C). Fab-Cy5 solution was diluted 10 times and then loaded to the SDS-PAGE. Based on the gel densitometry (FigureS11B), the concentration of Fab-Cy5 (1:10 dilution) is 0.094 mg/mL (1.96 μM). So the concentration of the original Fab-Cy5 (no dilution) is 0.94 mg/mL (19.6 μM). Therefore, the labelling efficiency was 70% (= 13.8/19.6×100%).
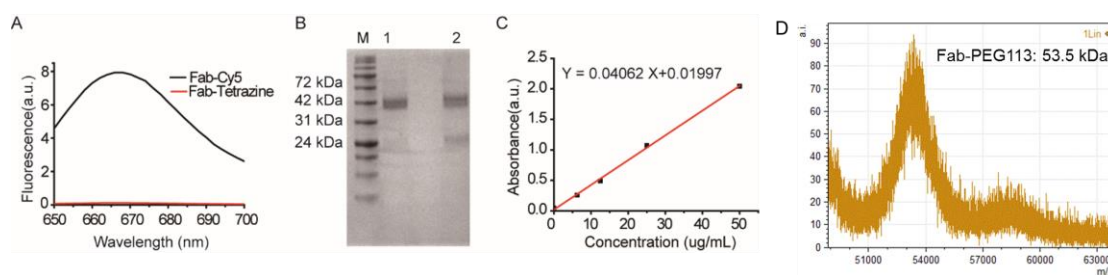

Figure S11 (A) Fluorescence spectra of Fab-Cy5 and Fab-Tetrazine (B) SDS-PAGE of IgG Fab and Fab-Cy5 (M: Protein marker, 1: Fab-Cy5 (based on the gel densitometry, the concentration of Fab-Cy5 is 0.094 mg/mL), 2: IgG Fab (0.1 mg/mL) (C) calibration curve of TCO-Cy5 based on the absorbance of 650 nm (D) MALDI-Tof-MS of Fab-PEG113 showing a signal at 53.5 kDa (found: 53.5k [M+H]$^+$, calculated: 53.5k [M+H]$^+$)

TCO-PEG113 (molecular weight: 5000 Da containing 113 repeating units on average) (25 μg, 5.00 nmol) was dissolved in PB (50 mM, pH = 7.4) and added to the Fab-Tetrazine (48 μg, 1.00

nmol) solution. The reaction mixture was stirred at room temperature for 30 min. After the reaction, the crude product was purified by repeated ultrafiltration in water using Vivaspin sample concentrator (10 kDa MWCO). The sample was analyzed by SDS-PAGE. Based on the gel, the band of Fab-Tetrazine totally disappeared and shifted to higher molecular weight (Fig. 3d in the main text). Because TCO-PEG113 is not monodisperse, the band of Fab-PEG113 also became broaden after conjugation. MALDI-Tof-MS of Fab-PEG113 also showed a signal at 53.55 kDa indicating the successful modification (Fig. S11D).

8. Stability test of SST-Tetrazine and Fab-Tetrazine

0.01 mM SST-Tetrazine solution was incubated with 20 μM Glutathione at 37 °C for 0 hours, 12 hours and 24 hours. For each sample, 10 μL of 10 mg/mL Fmoc-L-phenylalanine was added as internal standard. After incubation, the samples were injected into LC-MS. Identification of SST-Tetrazine product was performed simultaneously by UV-VIS detection at 254 nm and 214 nm and selective ion monitoring (SIM). The amount of SST-Tetrazine in each sample was determined as a ratio of the integration of the chromatogram at 254 nm of SST-Tetrazine to the internal standard.
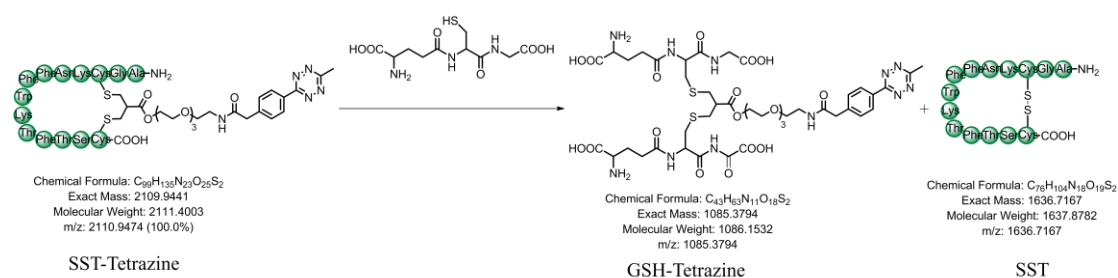
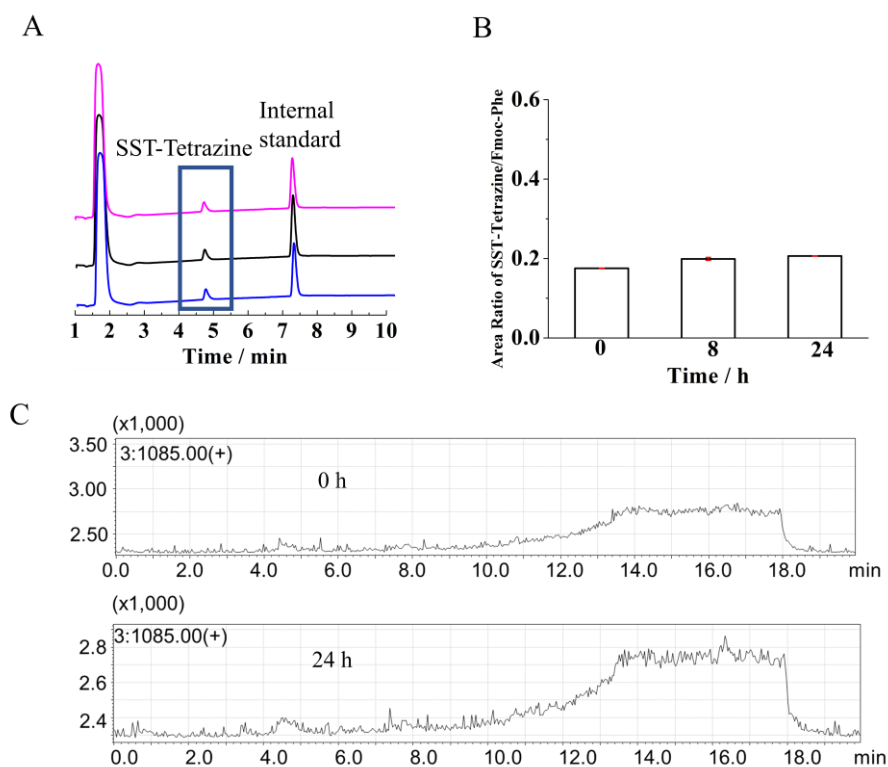Scheme S9 Reaction of GSH-mediated cleavage of SST-Tetrazine

Figure S12 (A) LC-MS chromatogram of SST-Tetrazine incubating with GSH at 214 nm (the peak at 2 min is from DMSO). (B) The area ratio of SST-Tetrazine at 214 nm compared to internal standard. (C) selective ion monitoring profile of m/z 1085 (GSH-Tetrazine) at 0 h and 24 h showing no degradation products were detected.

As suggested in the reference[1], the stability of Fab-Tetrazine and Fab-Cy5 were investigated through incubation with fetal bovine serum (FBS) at 37 °C. 0.01 mM Fab-Tetrazine and Fab-Cy5 were incubated with 1% FBS for 0 hour, 12 hours and 24 hours at 37 °C. After incubation, the mixture was analyzed by SDS-PAGE as described in the protocol in the section above. From the SDS-PAGE data, the protein band of Fab-Tetrazine did not have obvious change showing the good stability of Fab-Tetrazine. The stability of Fab-Cy5 was also investigated based on quantifying the fluorescence of the conjugate. The intensity of the fluorescence band of lane 5–7 is 23226.886, 24341.886 and 23008.664 using Image J. The data indicated good stability of Fab-Cy5 after incubation with FBS for 24 hours (Fig. 5d)

9. CD experiment of SST-Tetrazine and Fab-Tetrazine

Native SST, SST-Tetrazine and SST-PEG12 were dissolved in PBS to prepare 0.1 mg/mL solution. CD measurements were performed on JASCO J-1500 spectrometer in a 1 mm High Precision Cell by Hellma Analytics from 260 to 190 nm with a bandwidth of 1 nm. The data pitch was set to 0.2 nm, while the scanning speed was 10 nm/min. Each sample was measured

three times and the signal from the buffer blank was subtracted from the sample scan. The data was processed in the software Spectra Analysis and CD Multivariate SSE by JASCO.

Native IgG Fab, Fab-Tetrazine and Fab-PEG113 conjugate were dissolved in PBS at a final concentration of 0.1 mg/mL. CD experiment was performed as SST and SST-Tetrazine using the same machine with the same procedure. Each sample was measured three times and the signal from the buffer blank was subtracted from the sample scan. The data was processed in the softwares Spectra Analysis and CD Multivariate SSE by JASCO.

10. Enzyme-Linked immunosorbent assay (ELISA) experiment[2]

Protein L coated 96-well plate was washed with 100 µL wash buffer (PBS with added 0.05% Tween-20 detergent). Then dilution buffer (2% BSA in washing buffer) was used to dilute the native IgG Fab and Fab-Tetrazine to the following concentration: 1 nM, 10 nM, 50 nM, 100 nM, 200 nM and 100 µL of dilution solution were added to the corresponding well incubating for 2 hours. After 2 hours, the dilution solution was removed and each well was washed three times with wash buffer. Next, 100 µL of anti-human IgG, Fab-specific-HRP solution (prepared by taking 4 µL of a 1:5000 diluted solution and further diluting with 20 mL of PBS) was added to each well and incubate for 1 hour. Next, the solution was removed and washed with wash buffer 3 times (200 µL). For each well, 100 µL enhanced chemiluminescence solution (ECL solution, from Thermo Fisher Scientific) was added to each well and chemiluminescence was measured after 5 minutes.
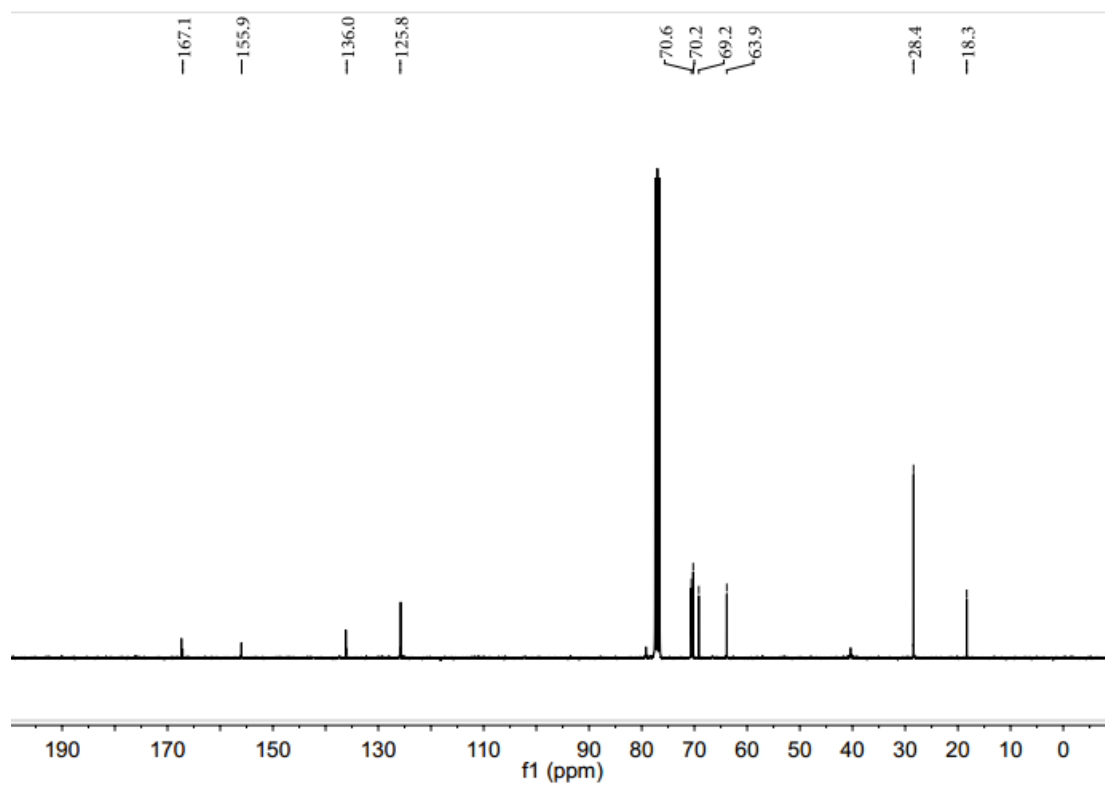
11. Reference

1. A. Maruani, M. E. Smith, E. Miranda, K. A. Chester, V. Chudasama and S. Caddick, *Nat. Commun.*, 2015, **6**, 6645.
2. M. K. Greene, D. A. Richards, J. C. F. Nogueira, K. Campbell, P. Smyth, M. Fernández, C. J. Scott and V. Chudasama, *Chem. Sci.*, 2018, **9**, 79-87.
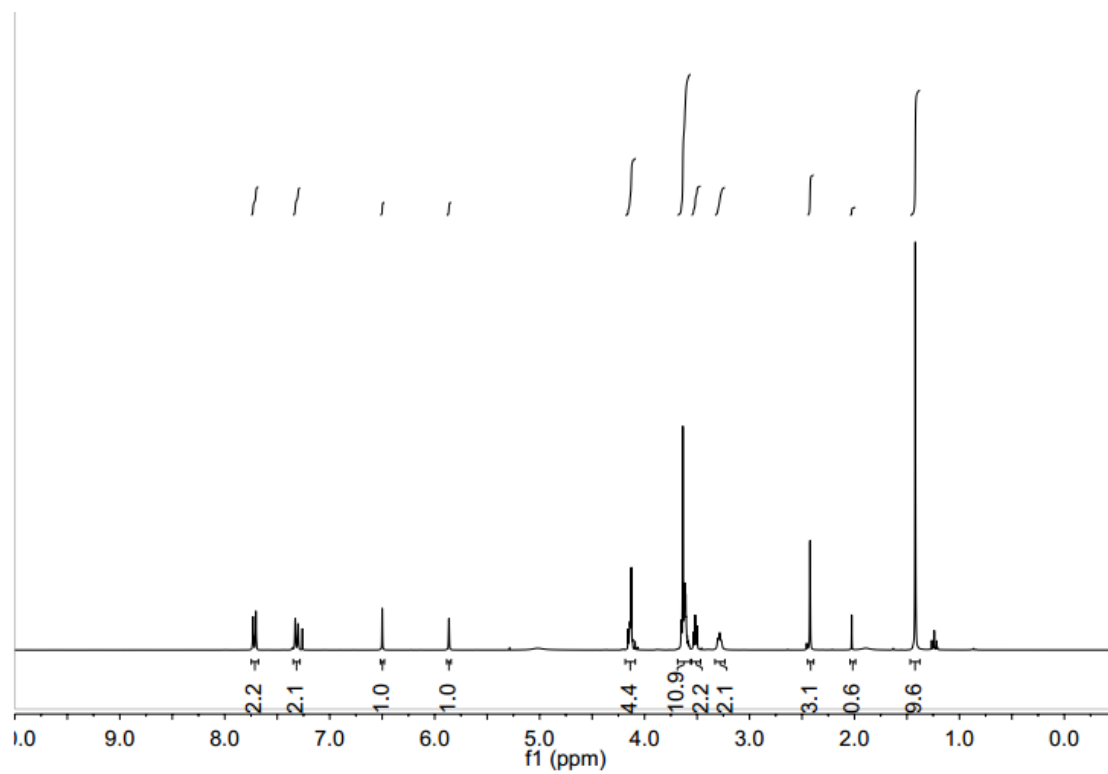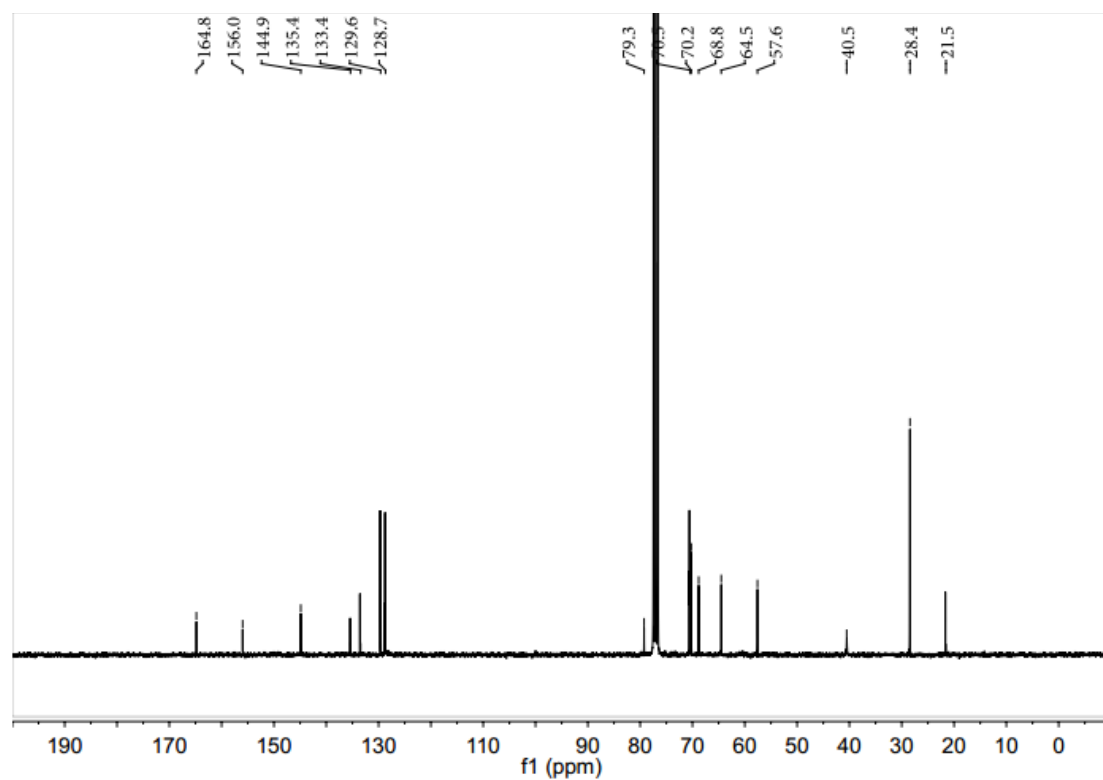
¹H NMR of compound **3**
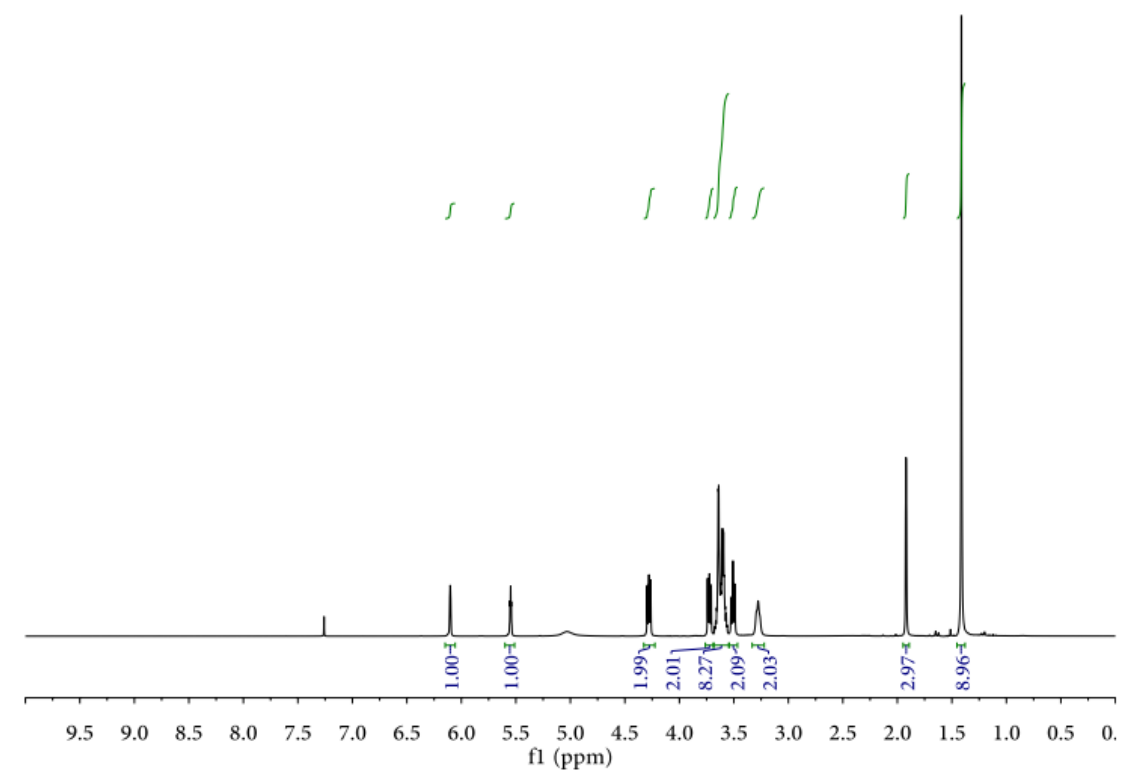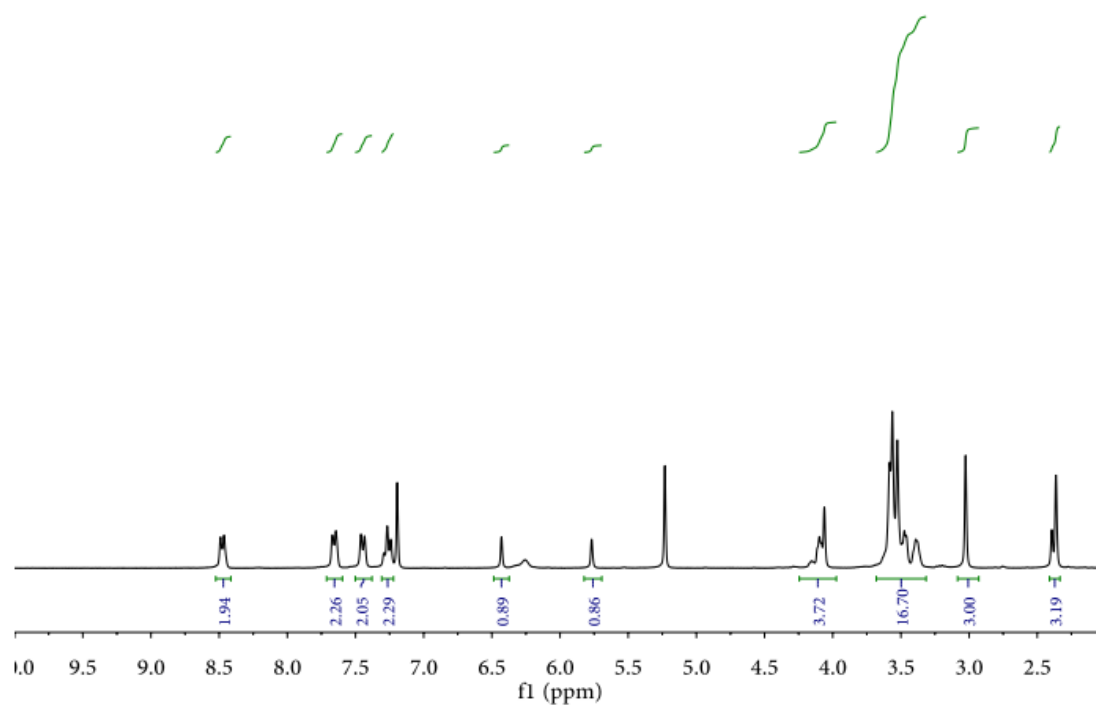

¹³C NMR of compound **3**

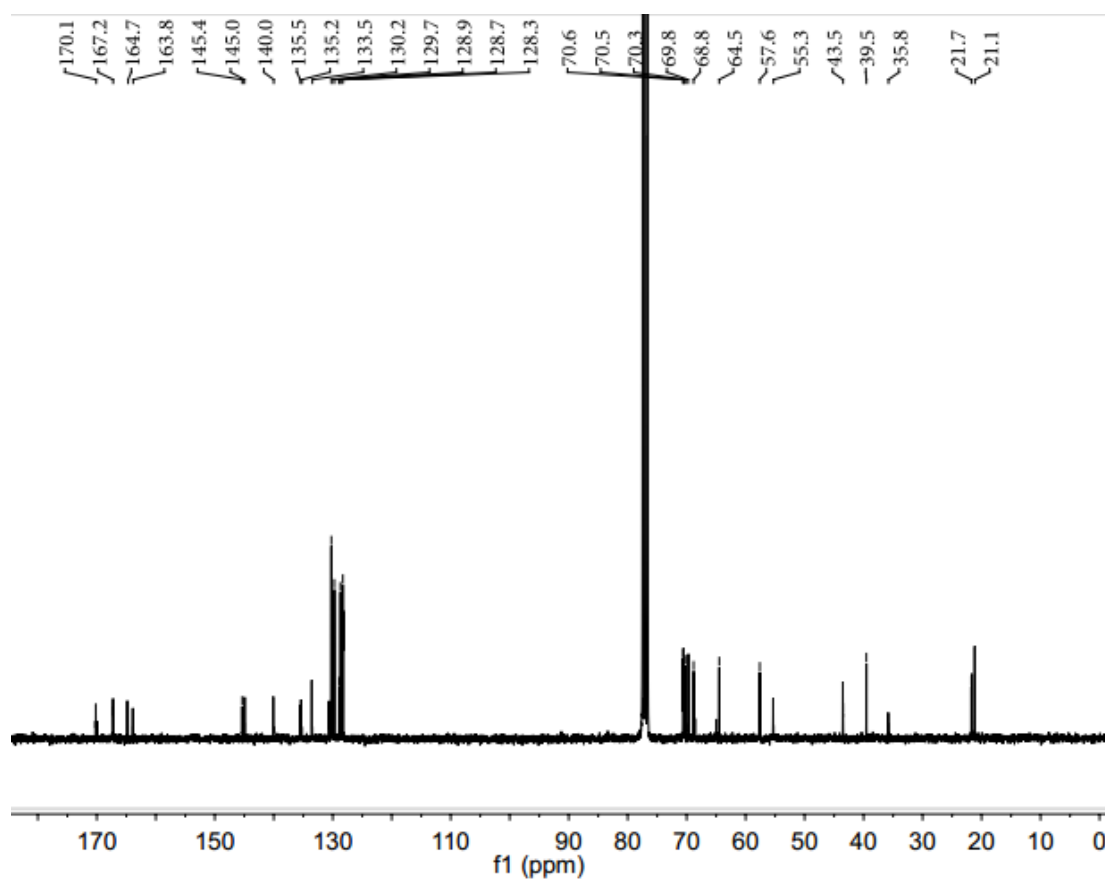
18

¹H NMR of compound **4**

¹³C NMR of compound **4**

¹H NMR of IC-Tetrazine

¹³C NMR of IC-Tetrazine

7. List of Publications

Publications

1. L. Xu, <u>M. Raabe</u>, M. M. Zegota, J. Nogueira, V. Chudasama, S. L. Kuan, and T. Weil, *Organic & Biomolecular Chemistry*. **2020**, 18, 1140–1147.

2. C. Chen, K. Wunderlich, D. Mukherji, K. Koynov, A. Heck, <u>M. Raabe</u>, M. Barz, G. Fytas, K. Kremer, D. Y. W. Ng, T. Weil, *Journal of the American Chemical Society*. **2020**, 142, 3, 1332–1340.

3. S. Hafner,• <u>M. Raabe</u>,• Y. Wu, T. Wang, Z. Zuo, V. Rasche, T. Syrovets, T. Weil, and T. Simmet, *Advanced Therapeutics.* **2019**, 1900084.

4. P. Moscariello, <u>M. Raabe</u>, W. Liu, S. Bernhardt, Y. Wu, T. Weil, H. J. Luhmann, and J. Hedrich, *Small.* **2019**, 1902992.

5. S. Harvey,• <u>M. Raabe</u>,• A. Ermakova, Y. Wu, T. Zapata, C. Chen, H. Lu, F. Jelezko, D. Y. W. Ng, and T. Weil, *Advanced Therapeutics.* **2019**, 1900067.

6. S. Han,• <u>M. Raabe</u>,• L. Hodgson, J. Mantell, P. Verkade, T. Lasser, K. Landfester, T. Weil, and I. Lieberwirth, *Nano Letters*. **2019**, 19, 2178–2185.

7. S. Harvey, D. Y. W. Ng, J. Szelwicka, L. Hueske, L. Veith, <u>M. Raabe</u>, I. Lieberwirth, G. Fytas, K. Wunderlich, and T. Weil, *Biointerphases*. **2018**, 13(6).

8. C. Seidler, M. M. Zegota, <u>M. Raabe</u>, S. L. Kuan, D. Y. W. Ng, and T. Weil, *Chemistry - An Asian Journal*. **2018**, 13, 3474–3479.

• shared first authorship

8. List of Conferences

"Polymer coating of fluorescent nanodiamonds", 25th Hasselt Diamond Workshop, Hasselt, Belgium, March 2020, oral presentation.

"Biopolymeric coating of fluorescent nanodiamonds as intracellular image probes for correlative microscopic strategies", Joint workshop Max Planck Institute for Polymer Research and Institute for Complex Molecular Systems, Mainz, Germany, November 2019, poster presentation.

"Fluorescent nanodiamonds as high-contrast imaging probes for correlative microscopic strategies", 14th International Conference on Materials Chemistry (MC14), Birmingham, United Kingdom, July 2019, poster presentation.

"Coated fluorescent nanodiamonds as high-contrast imaging probes in cells: From clusters to single nanodiamond analysis", Joint Twente/Mainz Mini-Symposium on Next Generation (Supra)Molecular Synthetic Materials, Mainz, Germany, May 2019, oral presentation.

"Quantification and single fluorescent nanodiamond detection in vitro using CLEM and EFTEM", Labeling & Nanoscopy, Heidelberg, Germany, November 2018, poster presentation.

"Advanced Materials Through Supramolecular and Macromolecular Functional Systems", Minisymposium, Mainz, Germany, April 2017.

"Precision Macromolecular Hybrids for Targeted Delivery and Imaging", CRC 1066 Symposium on CHEMICAL DESIGN – biomedical APPLICATIONS, Mainz, Germany, September 2016, poster presentation.

9. List of Abbreviation

ABEL	anti-Brownian electrokinetic trapping
AFM	atomic force microscopy
ATRP	atom transfer radical polymerization
BBB	blood–brain barrier
BC	breast cancer
bEnd.3	endothelia cells
BSA	bovine serum albumin
CAM	chorioallantoic membrane
CLEM	correlative light–electron microscopy
CLSM	confocal laser scanning microscopy
CT	computed tomography
CVD	chemical vapor deposition
DBCO	dibenzocyclooctyne
DCC	N,N'-dicyclohexylcarbodiimide
DLS	dynamic light scattering
DNA	deoxyribonucleic acid
DOTA	1,4,7,10-tetraazacyclododecane-1,4,7,10-tetraacetic acid
DOX	doxorubicin
EDC	1-ethyl-3-(3-dimethylaminopropyl)carbodiimide
EFTEM	energy filtered transmission electron microscopy
EGFR	epidermal growth factor receptor
EM	electron microscopy
EPR	enhanced permeability and retention
ESR	electron spin resonance
FND	fluorescent nanodiamond
FT-IR	Fourier-transform infrared spectroscopy
HER2	human epidermal growth factor receptor 2
HPHT	high pressure–high temperature
HSA	human serum albumin
ICG	indocyanine green
ICG-Tf-FND	transferrin-coated and ICG-loaded FNDs
L-DOPA	L-3,4-dihydroxyphenylalanine
LM	light microscopy
Maldi-Tof MS	matrix-assisted laser desorption/ionization time of flight mass spectrometry
MLS	mitochondrial localizing sequence
MRI	magnetic resonance imaging

ND	nanodiamond
NDX	NDs loaded with DOX
NHS	*N*-hydroxysuccinimide
NIR	near-infrared
NLS	nuclear localization signal
NP	nanoparticle
NV	nitrogen-vacancy
NV$^-$	negatively charged nitrogen-vacancy
ODMR	optically detected magnetic resonance
PA	photoacoustic
PAMAM	poly(amidoamine)
PEG	polyethylene glycol
PEI	polyethylenimine
PET	positron-emission tomography
PG	polyglycerol
PNA	peptide nucleic acid
QD	quantum dot
RAFT	reversible addition-fragmentation chain transfer
R_h	hydrodynamic radius
RNA	ribonucleic acid
siRNA	small interfering RNA
SiV	silicon-vacancy
SPT	single particle tracking
STED	stimulated emission depletion
STORM	stochastic optical reconstruction microscopy
TAT	trans-activator of transcription
TCEP	tris(2-carboxyethyl)phosphine
TEER	transendothelial electrical resistance
TEM	transmission electron microscopy
Tf-FND	transferrin-coated FNDs
TNBC	triple-negative breast cancer
UV	ultraviolet
XPS	X-ray photoelectron

10. Declaration of Honesty in Academic Work

Die vorliegende Arbeit entstand im Zeitraum von April 2016 bis März 2020 am Max-Planck-Institut für Polymerforschung im Arbeitskreis von Prof. Dr. Tanja Weil. Hiermit erkläre ich, dass ich die vorliegende Arbeit selbstständig angefertigt und keine anderen als die angegebenen Quellen und Hilfsmitteln benutzt sowie die wörtlich oder inhaltlich übernommenen Stellen als solche kenntlich gemacht und die Satzung der Universität Ulm zur Sicherung guter wissenschaftlicher Praxis in der aktuell gültigen Fassung vom 16.10.2009 beachtet habe.

_____   _____
             Ort, Datum   Marco Raabe